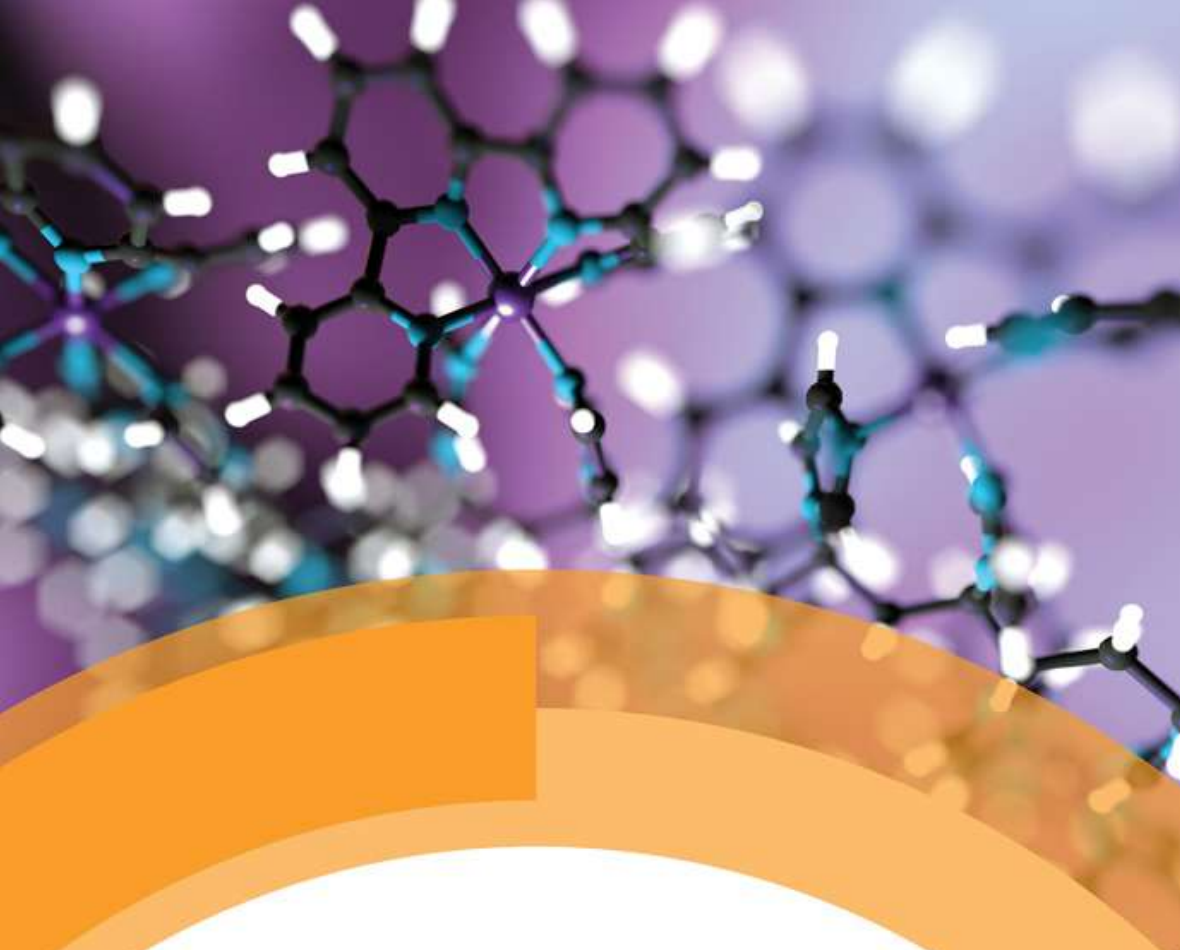

Polymer Chemistry Series

# Redox Polymers for Energy and Nanomedicine

Edited by Nerea Casado and David Mecerreyes

ROYAL SOCIETY OF CHEMISTRY

Redox Polymers for Energy and Nanomedicine

**Polymer Chemistry Series**



*Titles in the series:*

23: Fluorinated Polymers: Volume 1: Synthesis, Properties, Processing and Simulation
24: Fluorinated Polymers: Volume 2: Applications
25: Miktoarm Star Polymers: From Basics of Branched Architecture to Synthesis, Self-assembly and Applications
26: Mechanochemistry in Materials
27: Macromolecules Incorporating Transition Metals: Tackling Global Challenges
28: Molecularly Imprinted Polymers for Analytical Chemistry Applications
29: Photopolymerisation Initiating Systems
30: Click Polymerization
31: Organic Catalysis for Polymerisation
32: Synthetic Polymer Chemistry: Innovations and Outlook
33: Amphiphilic Polymer Co-networks: Synthesis, Properties, Modelling and Applications
34: Redox Polymers for Energy and Nanomedicine

*How to obtain future titles on publication:*
A standing order plan is available for this series. A standing order will bring delivery of each new volume immediately on publication.

*For further information please contact:*
Book Sales Department, Royal Society of Chemistry, Thomas Graham House, Science Park, Milton Road, Cambridge, CB4 0WF, UK
Telephone: +44 (0)1223 420066, Fax: +44 (0)1223 420247
Email: booksales@rsc.org
Visit our website at www.rsc.org/books

# *Redox Polymers for Energy and Nanomedicine*

Edited by

**Nerea Casado**
*University of the Basque Country, Spain*
*Email: nerea.casado@ehu.eus*

and

**David Mecerreyes**
*University of the Basque Country, Spain*
*Email: david.mecerreyes@ehu.es*

Polymer Chemistry Series No. 34

Print ISBN: 978-1-78801-871-5
PDF ISBN: 978-1-78801-974-3
EPUB ISBN: 978-1-78801-975-0
Print ISSN: 2044-0790
Electronic ISSN: 2044-0804

A catalogue record for this book is available from the British Library



The Royal Society of Chemistry is a charity, registered in England and Wales, Number 207890, and a company incorporated in England by Royal Charter (Registered No. RC000524), registered office: Burlington House, Piccadilly, London W1J 0BA, UK, Telephone: +44 (0) 20 7437 8656.

For further information see our web site at www.rsc.org

Printed in the United Kingdom by CPI Group (UK) Ltd, Croydon, CR0 4YY, UK

# *Contents*



Polymer Chemistry Series No. 34
Redox Polymers for Energy and Nanomedicine
Edited by Nerea Casado and David Mecerreyes

Published by the Royal Society of Chemistry, www.rsc.org

CHAPTER 1

# *Introduction to Redox Polymers: Classification, Characterization Methods and Main Applications*

NEREA CASADO*[a] AND DAVID MECERREYES*[a,b]

[a] University of the Basque Country UPV/EHU, Joxe Mari Korta Center, Avda. Tolosa 72, 20018 Donostia-San Sebastian, Spain; [b] Ikerbasque, Basque Foundation for Science, 48011 Bilbao, Spain
*Emails: Nerea.casado@ehu.eus; david.mecerreyes@ehu.eus

## 1.1 Introduction

Redox polymers are those polymers that can undergo reversible oxidation (loss of electrons) and reduction (gain of electrons) processes, as defined by the International Union of Pure and Applied Chemistry (IUPAC). They contain electroactive sites or groups that sustain these redox processes, which can be located in the main polymer backbone, as in the case of electrically conducting polymers such as polypyrrole,[1] or in the polymer's side-chain, as in the case of a polymer bearing a ferrocene group.[2]

The redox reaction implies the variation of the oxidation state of the polymer, which provokes changes in the properties of the polymeric material. Therefore, depending on the oxidation state (oxidized or reduced), the polymer may exhibit different chemical, optical, electronic or mechanical properties. The reversibility and easy external control of redox processes

Polymer Chemistry Series No. 34
Redox Polymers for Energy and Nanomedicine
Edited by Nerea Casado and David Mecerreyes

Published by the Royal Society of Chemistry, www.rsc.org

have made redox polymers interesting for different applications and for the development of new electrochemical devices such as organic batteries, electrochromic devices, optoelectronic devices, biosensors or biofuel cells.[3,4]

Moreover, the applications of redox polymers in medicine have increased in the last 20 years, for example, on the development of new types of actuators and drug-delivery systems.[5,6] As already mentioned, redox polymers are also interesting for electrochromic and electroluminescence devices and organic solar cells, due to their optoelectronic properties.[7,8] However, the developments of optoelectronic polymers are not reviewed in this book, as they are commonly known as conducting, conjugated, electroluminescent or electrochromic polymers, rather than as redox polymers.

Thus, this book highlights current trends in the chemistry, characterization and application of redox polymers. In this chapter, we will introduce the topic by showing an overview of the different types of redox polymers, state-of-the-art characterization techniques and their applications. In this last part, the role of redox polymers in energy devices, such as batteries, supercapacitors, solar cells, biofuel cells, as well as in medical applications such as tissue engineering, drug delivery, actuators and bioelectronic devices, will be highlighted.

## 1.2 Classification of Redox Polymers

Redox polymers became popular in the early 1980s as a new class of electroactive polymer. The first examples were based on conducting polymer backbones such as polyacetylene[1] and polymers containing ferrocene groups. Nowadays, the redox polymer portfolio is formed by a wide variety of chemical structures, including various conjugated polymer backbones and/or electroactive moieties which can be organic or inorganic/organometallic species. Historically, redox polymers have been classified mainly using the following criteria:

- Location of the redox center: in the polymer backbone or as a pendant group,
- Nature of polymer backbone: conjugated/semiconducting or nonconjugated,
- Nature of redox center: organic or inorganic.

These classifications always include exceptions and hybrid forms due to the large variety of redox polymers that have been synthesized over the years.

In this chapter, we will show first examples of organic redox polymers (formed by C, H, N, O and S), where we distinguish between semiconducting polymers and nonconjugated redox polymers. Next, we describe redox polymers having organometallic or alternative atoms in their redox moiety. Then, we will explain state-of-the-art characterization techniques of redox polymers and their most important applications in energy and medicine (Figure 1.1).

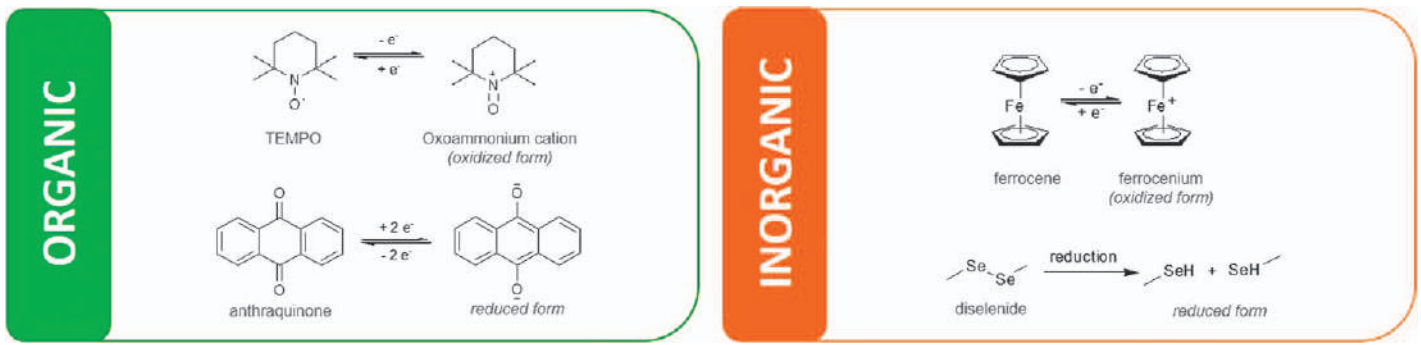


**Figure 1.1** Oxidation and reduction processes of representative organic and inorganic moieties included in redox polymers.

## 1.2.1 Organic Redox Polymers

### *1.2.1.1 Conjugated/Semiconducting Polymers*

Conjugated polymers (CPs) are composed of fully conjugated sequences of double bonds along the polymeric backbone. The extended conjugation and the additional doping provoke that conjugated polymers may exhibit bulk electric conductivity. Since the discovery of conductive polyacetylene by Shirakawa and co-workers in 1977,[9] conducting polymers have been widely investigated due to their interesting and tunable properties. In general, conducting polymers possess high electrical conductivity, easy processability, flexibility, low weight, low cost and the possibility of large-scale production.[10–12] Therefore, CPs have been employed in a wide range of applications including actuators, organic light-emitting diodes, batteries, supercapacitors, biosensors and drug-delivery systems.[10–15]

The most studied conducting polymers due to their high conductivity and easy synthesis are polypyrrole (Ppy), polyaniline (PANI), polythiophene (PT) and poly(3,4-ethylenedioxythiophene) (PEDOT). Among them, PEDOT is nowadays the most popular one due to its thermal and chemical stability, electro(chromic) properties and transparency, which are some of the reasons behind the success of its commercialization. Conducting polymers require partial oxidation or reduction processes to give rise to charged species, and thus, they can be considered as redox polymers. The generated charges are compensated by the appropriate counter ions, named dopants, to maintain the electroneutrality of the polymer.[16] The partial oxidation and reduction are known as p-doping and n-doping, respectively.[17] As a result of the doping process, charged defects such as *polarons* and *bipolarons* are created in the polymer chains, which are responsible for the electron conduction.

### *1.2.1.2 Nonconjugated Polymers*

Organic redox-active groups, such as nitroxides, quinones, phenothiazines or viologens, have been incorporated in polymer structures either as pendant groups or in the main polymeric backbone. The synthesis of new redox polymers and copolymers has been actively pursued in recent years for their application in batteries, biofuel cells, sensors and drug-delivery systems, among others.

Nitroxide radicals are one family of redox-active organic groups. Nishide and co-workers pioneered the synthesis of polymers containing nitroxide radicals such as 2,2,6,6,-tetramethyl-1-piperidinyloxy (TEMPO) (see Figure 1.2, polymer 1).[18,19] This type of radical is very stable and possesses fast electron transfer kinetics, thus they have been of great interest for organic batteries and supercapacitors.[20–22] Block copolymers, containing nitroxide radicals in one of the blocks, have been developed to tune the properties and obtain responsive polymers,[23] organic cathodes[24] and polymers with resistive memory properties.[25] The TEMPO group has also been incorporated as a pendant group in conjugated polymers, such as polythiophene[26] and PEDOT

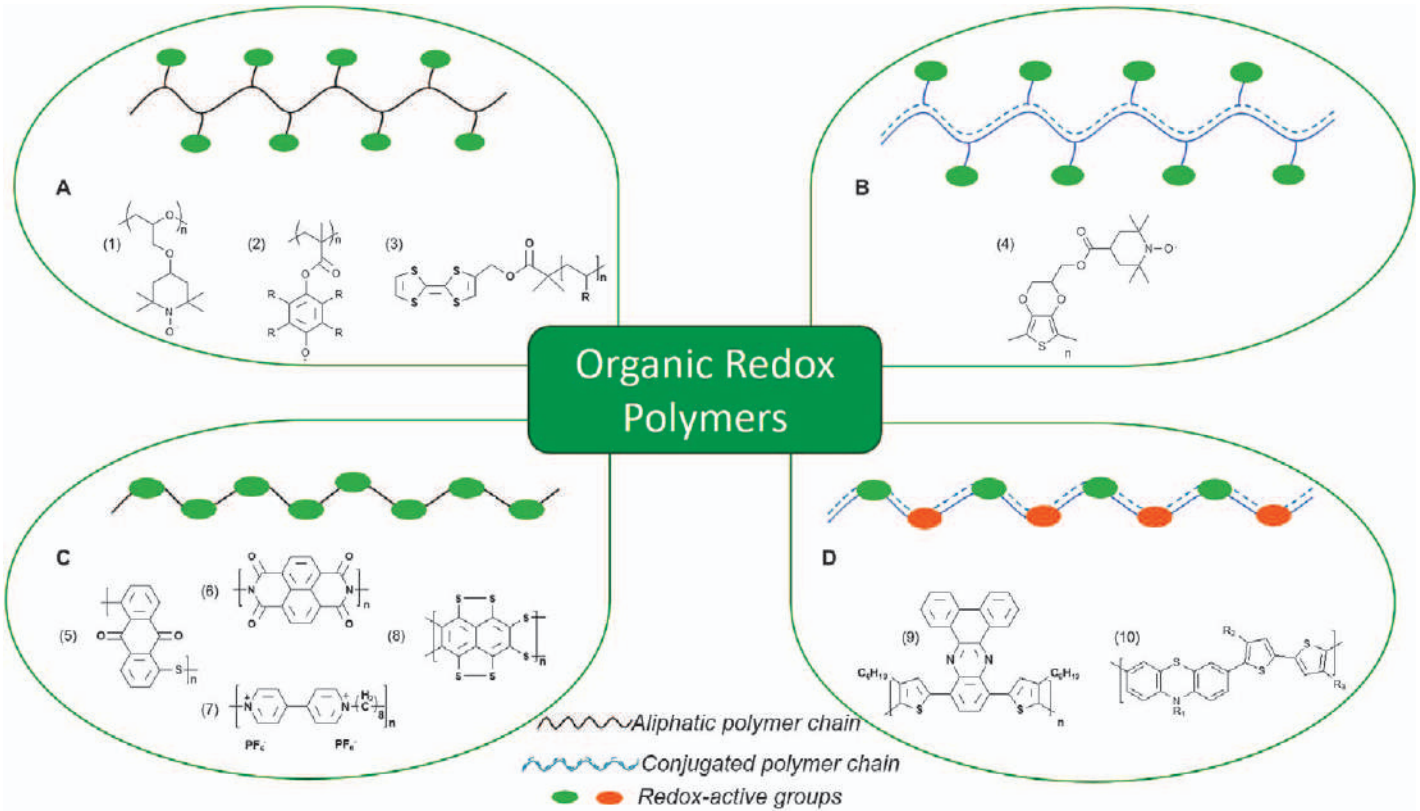


**Figure 1.2** Chemical structures of redox polymers containing electroactive organic moieties: as a pendant group (A, B) or in the polymer backbone (C, D), which can have at the same time conjugated (B, D) or aliphatic (nonconjugated) (A, C) backbones.

(polymer 4).[27] These polymers showed a synergetic effect between the redox properties of the conjugated backbone and the stable nitroxide radical, which are of great interest for battery applications.

Other types of stable radicals such as phenoxyl and verdazyl have been also incorporated in redox polymers with tuneable properties.[28] Phenoxyl radical polymers have found applications in energy storage.[29] For example, Schubert and co-workers synthesized phenoxyl-containing polymers with norbornene and methacrylate backbones[30] (polymer 2), which were applied as anode-active material in organic batteries due to the low redox potential. In a similar way, Price *et al.* reported the synthesis of 6-oxoverdazyl polymers with poly(phenyl methacrylate) backbone.[31]

Carbonyl-containing polymers are another relevant redox polymer family.[32] Carbonyls represent a common organic structural group, which can be found in a variety of redox moieties, such as anthraquinone, quinone, imide or anhydrides. Some examples in this area include polymers with anthraquinone derivatives[33] (polymer 5) or polyimides with naphthalene (polymer 6) or pyromellitic compounds.[34] Redox-active polyimides have been widely investigated as electrode materials for lithium,[34,35] sodium,[36] lithium-sulfur[37] and all-organic batteries,[38] as well as for applications in aerospace and electronics.[39] Quinone-containing polymers are very attractive for energy storage applications due to their high charge-storage capacity. Moreover, quinones are the principal redox center in natural organic materials, which makes them interesting in terms of sustainability.[40] Some examples include hybrid materials between conducting polymers, such as polypyrrole or PEDOT, and biopolymers like ligninsulfonates as electrode materials for batteries and supercapacitors.[41–43] Another interesting example is catechol-containing polymers,[44] which were applied as organic cathodes for lithium batteries,[45] while their ability to host various cations ($H^+$, $Li^+$, $K^+$, $Zn^{2+}$, $Mg^{2+}$, $Ca^{2+}$ and $Al^{3+}$) in aqueous batteries has been recently demonstrated.[46] This kind of bioinspired catechol polymer has also been synthesized as nanoparticles, which could be used in a variety of battery technologies.[47]

Other organic functional groups such as viologen, triphenylamine and phenothiazine are known to possess redox properties. Viologen and triphenylamine moieties have been incorporated into different polymer backbones to obtain linear, cross-linked or porous polymers.[48,49] Polymers with viologen moieties (polymer 7) combine redox and electrochromic properties, which make them interesting for several fields, including electrochromism, energy storage, gas storage and separation, and biochemistry.[50] Polymers with carbazole and phenazine units (polymer 9) and its derivatives (phenothiazine, thianthrene) have been used for energy storage,[51] photovoltaic[52] and optoelectronic devices.[53] The application of phenothiazine-containing redox polymers (polymer 10) in energy storage devices has increased in the last decade due to their fast redox process and high redox potential (3.5 V *vs.* $Li/Li^+$). Thus, they have been employed not only as electrode materials in Li/organic,[54,55] redox-flow[56] and all-organic[57,58] batteries but also as redox mediators in $Li/O_2$ batteries.[59]

The last family of organic redox polymers consists of organosulfur compounds. Polymers with disulfide bonds and polysulfide moieties (polymer 8) have been investigated as electrode materials in batteries.[60–62] Specially, copolymers with high sulfur content synthesized by inverse vulcanization are interesting cathode materials to replace elemental sulfur in lithium/sulfur (Li/S) batteries with good cycling stability.[63] Disulfide bonds are also very interesting for drug-delivery applications, as they degrade under physiological reducing conditions.[6] Tetrathiafulvalene (TTF) is an important redox moiety with disulfide linkages, which can undergo two reversible redox processes to radical cation ($TTF^{+}$) and dication ($TTF^{2+}$). TTF-containing polymers (polymer 3) have been widely studied due to their interesting charge-transfer properties for organic electronics.[64]

### 1.2.2 Inorganic Redox Polymers

Inorganic redox moieties have also been incorporated into polymer materials either in the backbone or as pendant groups. Ferrocene is the gold-standard organometallic moiety due to its redox stability and reversibility. The ferrocene group has been integrated into several polymer backbones, from the simplest poly(vinylferrocene)[60] (Figure 1.3, polymer 11) to block copolymers with ferrocene in one of the blocks. In this manner, functional polymers with ferrocene units have been developed with interesting mechanical robustness, photo-physical, optoelectronic properties and stimuli-responsive properties.[61,65] Poly(vinylferrocene), for example, has been copolymerized with poly(methyl methacrylate) to form nanocapsules,[63] or with poly(ethylene oxide) to obtain water-soluble star polymers[62] for biomedical applications. Poly(ferrocenylsilane) polymers (polymer 15) are the most important polymers where the ferrocene group is located in the polymer backbone.[66] As an example, poly(ferrocenylsilane)-based gels and hydrogels were synthesized as redox-responsive materials.[64]

In contrast to ferrocene polymers, cobaltocene-containing polymers have been much less developed, probably due to the difficulty of preparing substituted derivatives. Cobaltocenium-containing polymers (polymer 12) have been used in electrochemistry, catalysis and biosensing.[67,68]

Conjugated polymers comprising inorganic elements in their structure such as selenium, tellurium or phosphorous have been investigated to modify their redox and optoelectronic properties. In the last decade, polyselenophene conjugated polymers and copolymers (polymer 13) has been the most studied ones owing to their optical properties and their potential use in low-cost electronic devices.[69,70] As an example, Hollinger *et al.* synthesized selenophene–thiophene block copolymers, which phase-separate and exhibit interesting absorbance features for optoelectronic uses.[70] Moreover, the development of solution-processable poly(3-alkyltellurophene) polymers (polymer 14) proved their potential application for optoelectronic applications.[71] On the other hand, phosphole-containing polymers allow post-functionalization in the phosphorous center, as they

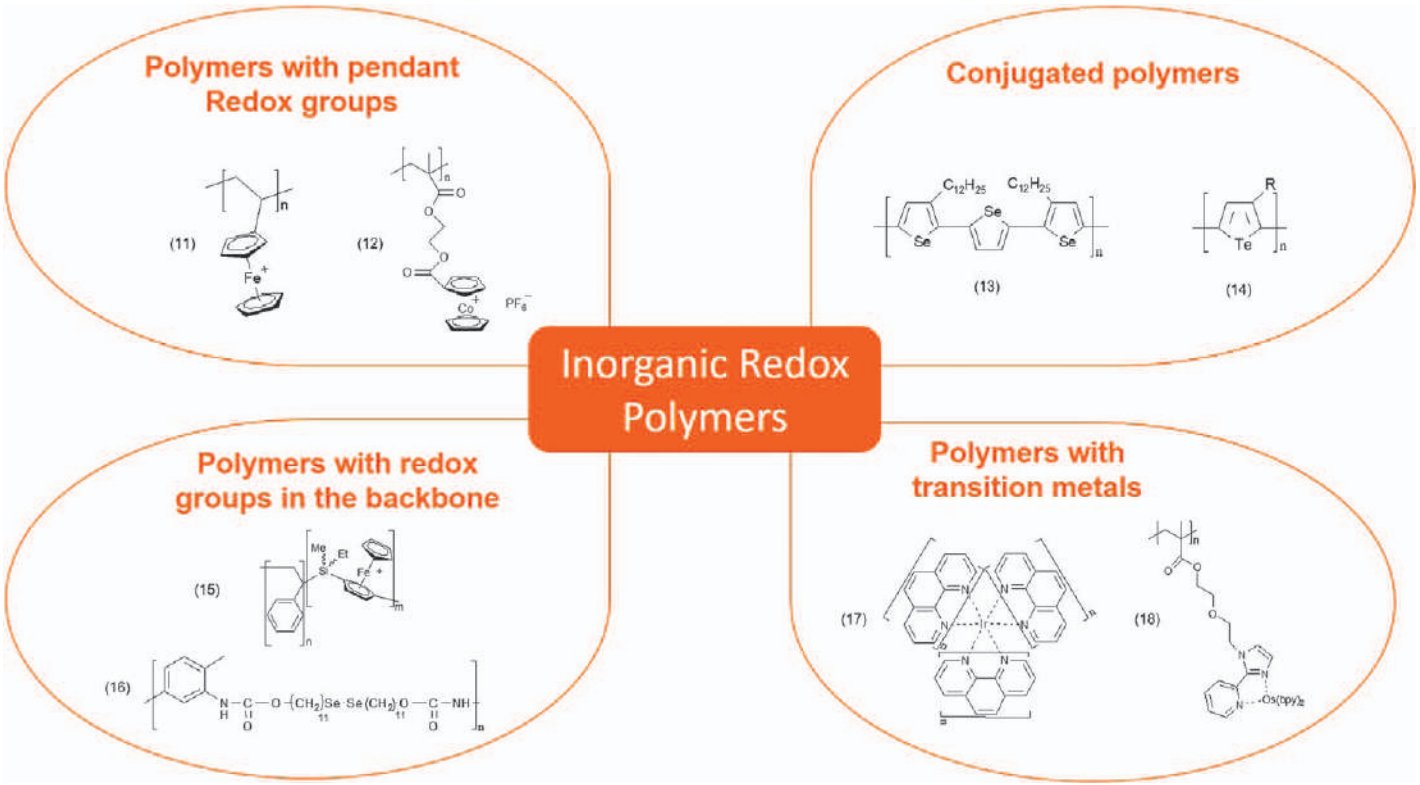


**Figure 1.3** Chemical structures of redox polymers containing electroactive inorganic moieties.

are able to tune the electronic properties. Phosphole-containing polymers have been applied in optoelectronic and sensing devices.[72,73]

Selenium is a nonmetal located in the chalcogen group of the periodic table between sulfur and tellurium elements. It possesses many similarities to the elements of its group, however, the bond energy of diselenide bond is smaller than the disulfide (Se–Se 172 kJ mol$^{-1}$ *vs.* S–S 226 kJ mol$^{-1}$). Therefore, selenium-containing polymers are promising materials as redox-responsive drug carriers.[74] As an example, a polyurethane triblock copolymer with diselenide bonds was reported by Xu and Zhang's group (polymer 16). This block copolymer forms multiresponsive micellar aggregates, which are responsive to both oxidant and reductant conditions and suitable for controlled drug-delivery systems.[75]

Polymers with transition metals, such as zinc, copper, platinum and iridium, have been widely developed due to their intrinsic properties including redox, catalytic, magnetic, light absorption and emission properties (polymer 17).[75–77] Depending on the interaction of the metal with the polymeric chain and the nature of the chain, whether conjugated or not, the electronic and electrochemical properties may vary.[78,79] In this family, zinc-containing polymers have been the most studied ones due to the coordination ability of Zn(II) to develop a wide variety of structures.[74] Moreover, platinum-, osmium- and palladium-containing polymers have been also investigated in biomedical applications such as biosensors and drug delivery (polymer 18).[80–82]

## 1.3 Characterization of Redox Polymers

Apart from the conventional polymer characterization techniques for molecular weight distribution, glass transition, crystallization, physicochemical, thermal and mechanical properties, redox-active polymers are commonly analyzed by electrochemical techniques. Cyclic voltammetry (CV) is the most widespread characterization method, together with electrochemical impedance spectroscopy (EIS). Moreover, CV can be combined simultaneously with additional techniques such as UV–Vis–NIR, infrared spectroscopy, photoemission, electrochemical quartz microbalance (EQCM) and atomic force microscopy to study the changes taking place in the polymer during the redox processes. As electrochemical characterizations are very sensitive, besides the intrinsic factors defined by the polymer nature, external factors related to the sample preparation and electrochemical technique have to be taken into account during the characterization of redox polymers. The most important external factors affecting the electrochemical characterization are: sample preparation, dimensions of the sample (thickness, weight and area), kinetics of the redox process, nature of the electrolyte, type of set-up, temperature and formulation of the electrode when binders and conductive additive are included.

### 1.3.1 Cyclic Voltammetry (CV)

Cyclic voltammetry is a powerful and popular electrochemical method to study the oxidation and reduction processes of redox polymers. It provides information about the redox behavior of the material at different potentials and is a fast and reliable characterization technique.[83] In this experiment, a potential is applied to the working electrode (E), which is swept at a certain rate (scan rate) and the resulting current ($i$) is measured. The obtained trace ($i$ *vs.* E) is called a voltammogram or cyclic voltammogram, which is dependent on the type of process occurring at the electrode.

Redox polymers can present different voltammogram shapes depending on the redox behavior (see Figure 1.4). Conducting polymers present typically two types of currents: the faradaic current caused by the redox reaction and the capacitive current resulting from the electrical double layer generated on the surface of the electrode.[3] These two current responses can be observed in the voltammogram trace of Figure 1.4a. Redox polymers with localized redox moieties, either in the backbone or as a pendant group, show

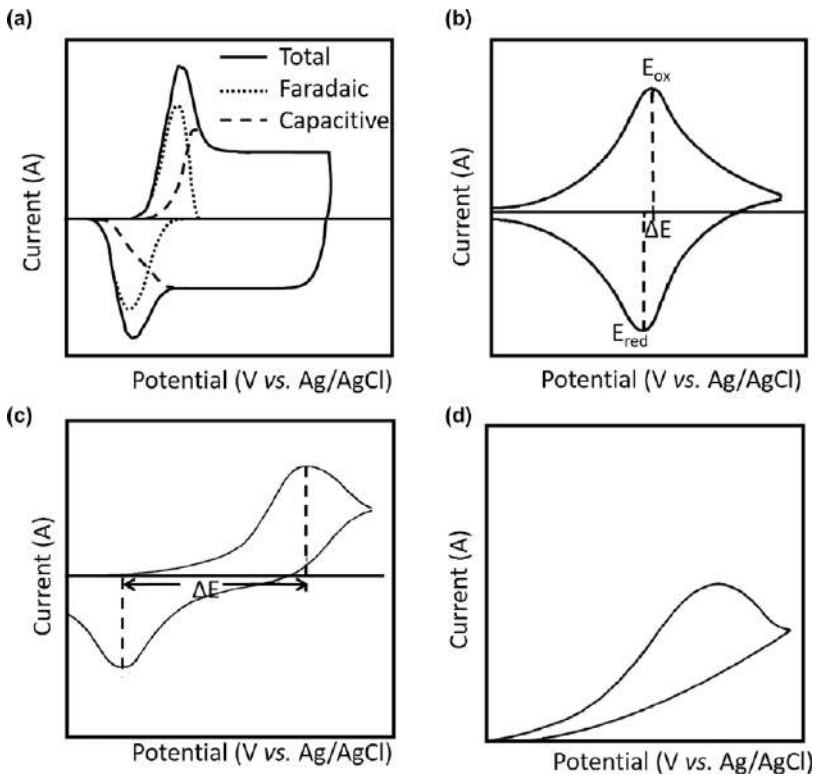


**Figure 1.4** Cyclic voltammograms of (a) conducting polymer, (b) diffusion-controlled reversible redox process, (c) quasi-reversible process and (d) irreversible process.

only the faradaic current. The maximum current peak corresponds to the oxidation potential ($E_{ox}$), while the minimum current peak to the reduction potential ($E_{red}$) is shown in Figure 1.4b. The redox potential is usually determined by the average potential ($E_{1/2}$) between the oxidation and reduction potentials, and is specific to the experimental conditions [$E_{1/2} = \Delta E = (E_{ox} + E_{red})/2$], as the two peaks are separated due to the diffusion of the analyte to and from the electrode surface. The separation of oxidation and reduction peaks reveals the reversibility of the redox reaction. Reversible redox reactions present small $\Delta E$ values ($\Delta E < 57$ mV),[84] while in quasi-reversible processes $\Delta E$ increases showing two separated and less sharp peaks in the cyclic voltammogram (Figure 1.4c). Moreover, if the process is completely irreversible, only one peak, oxidation or reduction, will be present in the cyclic voltammogram. Figure 1.4d shows a typical trace for a polymer with irreversible oxidation process.

The current response of redox polymers can be limited by two different processes. The first limiting process is related to the electron transfer kinetics between the electrode and the redox species, while the second one is due to the diffusion of the redox species to and from the electrode. Thus, diffusion is negligible for thin-layer electrodes, as the electroactive polymer deposited on the electrode surface is reacted very rapidly. On the contrary, electron transfer kinetics are not important for diluted solutions as the redox process will be affected only by the motion of the redox species. Most of redox polymers present an intermediate behavior between these two cases, which is called "finite diffusion."[3]

The determination of the limiting process is usually carried out by cyclic voltammetry experiments at different scan rates. The scan rate determines how fast the applied potential is changed. Faster scan rates result in the decrease of the diffusion layer size, generating higher current responses. When the redox polymer is deposited on the electrode, a linear variation of the peak current with the scan rate shows that the process is not limited by diffusion. The current response is described by the following equation:

$$i_p = \frac{n^2 F^2}{4RT} \nu A \Gamma$$

where $i_p$ is the peak current, $n$ is the number of electrons, $F$ is the Faraday constant, $\nu$ is the scan rate, $A$ is the electrode surface area, $\Gamma$ is the amount of redox-active material deposited in the electrode surface, $R$ is the gas constant and $T$ is the temperature in Kelvin.

When the redox polymer is dissolved in the electrolyte and involves freely diffusing redox species, the Randles–Sevcik equation describes how the peak current increases linearly with the square root of the scan rate.

$$i_p = 0.446 nFAC \left(\frac{nF\nu D}{RT}\right)^{1/2}$$

where $C$ is the bulk concentration of the redox-active species and $D$ is the diffusion coefficient of the redox-active species.[83]

Moreover, the cyclic voltammetry can be used to obtain additional information. For example, if the relationship between the oxidation and reduction current peaks is equal to one, the process is reversible, meaning that all the oxidized species are reduced back. The charge related to the oxidation and reduction processes can be quantified by measuring the area under the curve and dividing it by the scan rate. Additionally, by dividing this charge by the mass of the redox-active species, the specific capacity of the polymer is obtained, while the capacitance is the relationship between the current and the scan rate.[85]

Cyclic voltammetry characterization can be done using a rotating disc electrode (RDE) hydrodynamic working electrode to analyze the mechanism and kinetics of the redox processes. When the RDE reaches a steady state, a constant laminar flow of the electrolyte solution is created at the electrode surface. In this way, the mass transport of the redox species is not a limiting factor and the kinetics of the redox reaction can be calculated. This technique has been employed for the determination of electrocatalytic behavior of redox polymers.[86]

In conclusion, cyclic voltammetry is a versatile and powerful electrochemical technique to analyze the redox potential of the electroactive polymers. This redox potential value is specific and crucial for each application of the redox polymers. Figure 1.5 shows the redox potential of most common electroactive moieties included in redox polymers, however, it is important to note that these values are dependent on the experimental conditions, such as the type of electrolyte, cell configuration or sample preparation. In energy storage applications like batteries, the redox potential of the polymer is important as it will determine its application, whether it is used as an anode or cathode material, together with the voltage of the device, which is given by the potential difference between the two electrodes. In supercapacitors, polymers with fast and wide redox processes are required to obtain high specific capacitances. On the other hand, for applications such as biosensors and biofuel cells, as the polymers are used as redox mediators, their redox potential should be similar to the enzyme or the reaction where they will be involved.

### 1.3.2 Electrochemical Impedance Spectroscopy (EIS)

Together with cyclic voltammetry, electrochemical impedance spectroscopy (EIS) is a powerful and complex technique to analyze the electrical characteristics of the polymer films. The electrochemical impedance is the response of a system (cell) to an applied potential. In this technique, the current is measured when a small-amplitude alternating current (AC) potential is applied to a cell in equilibrium. In order to have a pseudo-linear response, the excitation signal should be small ($\sim$10 mV). In this way, when the sinusoidal potential is applied, the current response at the same

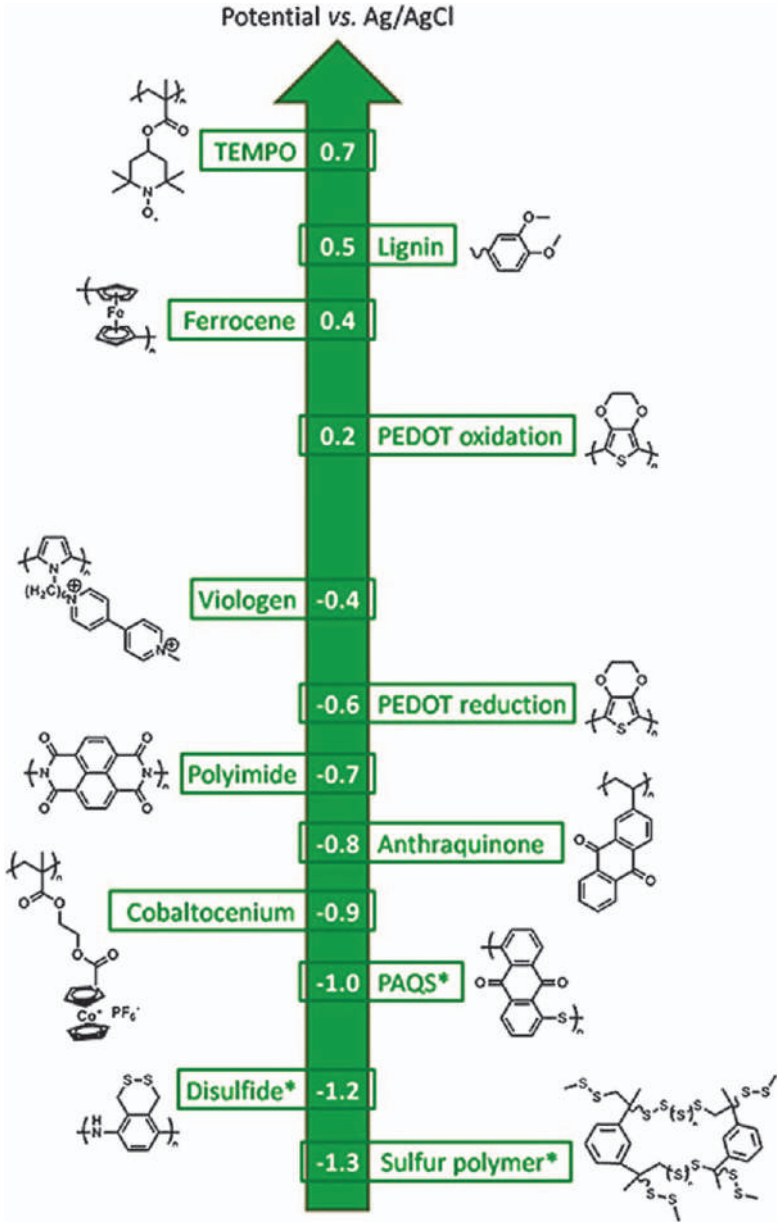


**Figure 1.5** Redox potentials of common electroactive groups included in redox polymers. *Potential values are taken from $Li/Li^+$ reference electrode and changed to Ag/AgCl ($Li/Li^+$ is $-3.26$ V *vs.* Ag/AgCl).
Reproduced from ref. 3 with permission from Elsevier, Copyright 2016.

frequency is a phase-shifted sinusoid. The frequency dependence of this impedance can reveal complex chemical processes. EIS also provides information about the rate of charge transfer and transport processes.[3]

The response of the system is usually represented in Nyquist plots, where the imaginary impedance is plotted against the real impedance. The variation of the impedance with the frequency is characteristic of an electrical circuit. Therefore, an equivalent electrical circuit model, which describes the system, is generally used to interpret the obtained EIS data. Parameters such as the charge transfer resistance, Warburg diffusion coefficient or the capacitance can be obtained from the interpretation of the equivalent circuit. It is worth mentioning that each electrochemical system should be modeled with the best appropriate equivalent circuit. For example, a simple electrode reaction can be described by the Randle equivalent circuit, containing the solution resistance ($R_s$), charge transfer resistance ($R_{ct}$), Warburg impedance ($Z_w$) and double-layer capacitance ($C_{dl}$).[87] The main advantage of EIS is that both the diffusion coefficient and the redox capacitance can be obtained from the same experiment, while multiple experiments are required to analyze these two values with cyclic voltammetry.

Another electrochemical technique used in the characterization of redox polymers is the chronocoulometry. This involves the measurement of charge as a function of time when a potential step waveform is applied. Chronocoulometry is used to determine the electrode surface area, diffusion coefficients, adsorption of electroactive species, and the kinetics of electron transfer and mechanisms of chemical reactions.[3]

### 1.3.3 Coupling of Electrochemical Methods with Additional Characterization Techniques

The coupling of electrochemical techniques with other characterization methods, such as UV–Vis spectroscopy, is a very interesting approach to get a better under understanding of the redox processes. These *in situ* analyses may also give information about the mechanism of the redox process. Next, the most widespread techniques that have been coupled with cyclic voltammetry will be explained.

- Optical absorption characterization. UV–Vis–NIR spectroscopy provides information about absorption bands and the optical band gap of redox polymers. The coupling of this technique with electrochemistry is named spectroelectrochemistry.[88,89] It is also used to determine the stability of radical species,[90] polaron and bipolaron formation,[91] as well as color change during the redox reaction.[92] Therefore, spectroelectrochemistry is mostly used for the analysis of electrochromic materials and the development of photovoltaic and electrochromic devices. As an example, the UV–Vis–NIR spectrum of a PEDOT:PSS sample in Figure 1.6a at different potentials denotes the absorbance

changes, showing a polaron band at −0.2 V *vs.* Ag/AgCl and increasing π–π* transition band at higher potentials.

- Other spectroscopy techniques such as Raman and FTIR have also been coupled to electrochemistry to analyze the structural change in the polymer during the redox reaction. The appearance of new peaks, or the shifting or intensity changes in the peaks during the oxidation and reduction processes can provide information on the alteration in the bonding nature of the polymers (Figure 1.6b).[89,93,94]
- Surface characterization techniques can be also coupled with electrochemistry. Thus, surface morphology of redox polymers can be analyzed by scanning electron microscopy (SEM),[95] scanning tunneling microscopy (STM) or atomic force microscopy (AFM).[96] As an example, Figure 1.6c shows AFM images for PEDOT at reduced and oxidized states.
- Electrochemical quartz crystal microbalance (EQCM) is a powerful *in situ* technique to complement electrochemical experiments. It is able to detect mass changes in the deposited film during electrochemical experiments. Thus, it is used to analyze processes involving mass changes such as adsorption, electrodeposition, polymerization or doping.[97] For example, the *in situ* CV-EQCM spectrum of a poly(amine-imide) polymer is shown in Figure 1.6d. During its oxidation, the ions of the electrolyte are absorbed into the polymer film to compensate the ions formed and thus, increasing the total mass, while in the reduction the contrary process is observed, desorption of ions together with the decrease of the total mass.
- Electron spin resonance (ESR) spectroscopy is another interesting method to analyze the presence of polaron charge carriers, as they have spin, opposite to bipolaron charge carriers. This technique provides the concentration of polaronic species and charged species. Therefore, it is used to study the polymerization processes that occur *via* radical intermediates, the redox processes in radical polymers and doping levels in conducting polymers. For example, polyaniline and PEDOT conducting polymers have been intensely characterized by ESR spectroscopy.[90]

## 1.4 Applications of Redox Polymers

The growing interest in redox polymers is due to their versatility and wide range of applications. The most important fields where redox polymers have been employed are batteries and biosensors. However, the search for more sustainable and environmentally friendly materials in the last decade has increased the application of redox polymers in other energy devices such as supercapacitors, solar cells, biofuel cells or thermoelectric devices. Moreover, redox polymers are finding new opportunities in the development of medical systems such as actuators, drug-delivery systems, tissue engineering

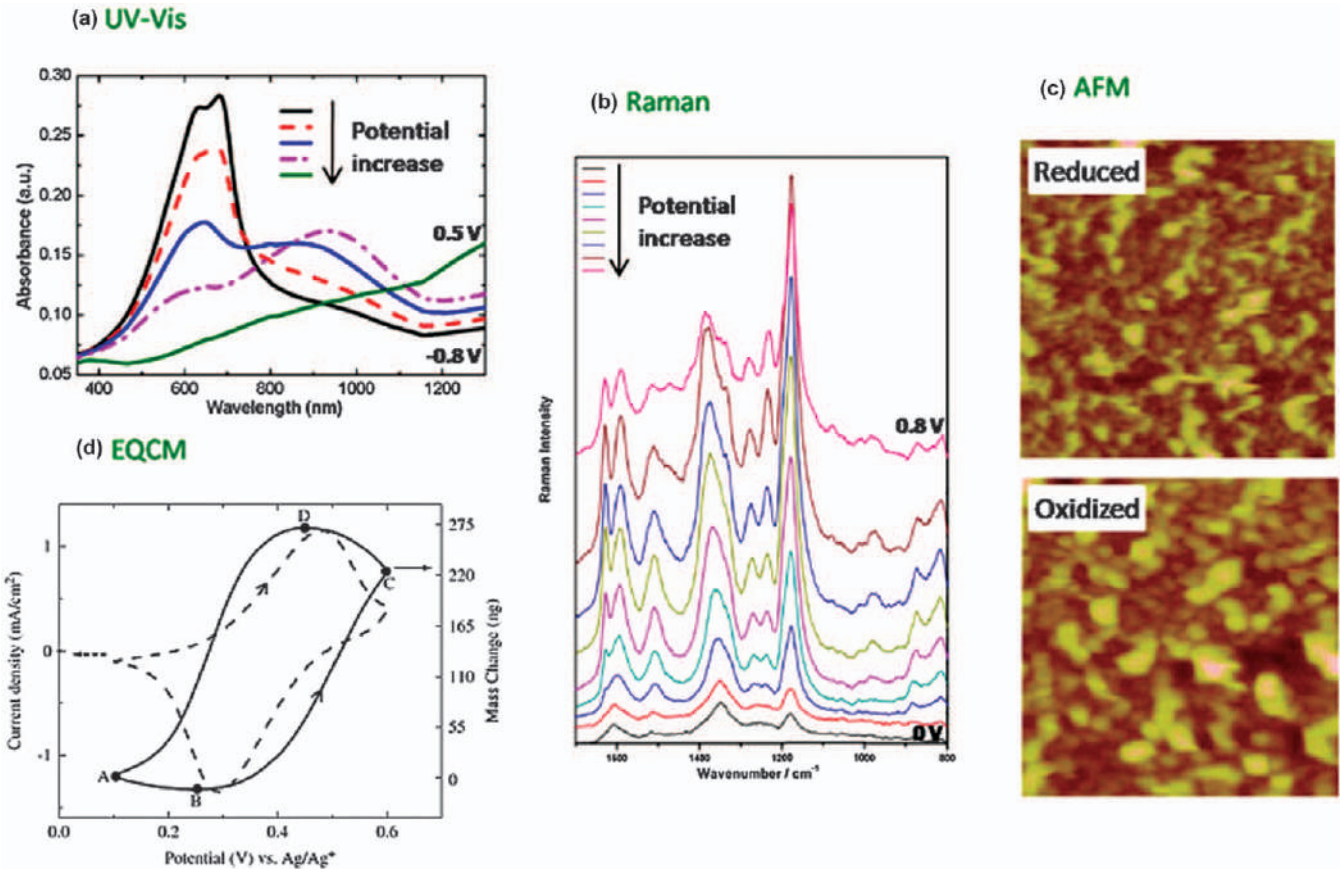


**Figure 1.6** Examples of characterization techniques coupled with electrochemical methods. (a) UV–Vis spectrum of PEDOT:PSS film; (b) Raman spectrum of polyaniline oxidation; (c) AFM images of reduced and oxidized states of PEDOT; and (d) EQCM graph of a poly(amine-imide).
Reproduced from ref. 3 with permission from Elsevier, Copyright 2016.

and bioelectronic devices. In the following sections, we will review the most important advances in the application of redox polymers in energy and medicine technologies.

### 1.4.1 Applications in Energy Conversion and Storage Devices

Energy has become one of the key issues of this century due to the growing population and the technological development. For this reason, the development of sustainable and green energy technologies has become of great importance in our society. New clean technologies which are able to create electricity from the natural abundant energy from the sun, waves or wind as well as to store that electricity are actively being searched. Redox polymers are playing an important role in the development of some of these technologies as will be highlighted in this section.

The most popular use of redox polymers nowadays is in electrochemical energy storage devices such as batteries, supercapacitors or flow cells. This will be extensively discussed in several chapters throughout this book, and due to its importance, we will dedicate a special subsection to this next. However, there are other technologies which are still in their infancy that are expected to have rapid development in the coming years. This is the case of the biofuel cells, where naturally occurring sugars are converted into electricity through an enzymatic process similar to the electrochemical biosensors using a redox polymer as the key ingredient.[87]

Two important types of devices that make use of similar redox polymers are thermoelectric cells and solar cells.[98,99] However, those devices that convert heat or light into electricity, respectively, are not discussed in this book. The reason behind this is that the polymers used in these cases, although they present redox type activity, are mostly known as (semi)-conducting, semiconjugated or optoelectronic polymers (Figure 1.7).

#### *1.4.1.1 Batteries and Supercapacitors*

Redox polymers are actively being investigated in several electrochemical energy storage or battery technologies. Back in the 1980s there was a great deal of hype about the use of conducting polymers in batteries. However, the expectations did not became reality due to the stability issues of the batteries and supercapacitors based on most conducting polymers at that time. Nowadays there is renewed interest in the use of redox polymers in several emerging battery technologies, such as flexible thin batteries, fast-charging batteries, organic batteries, metal-air, redox-flow batteries or aqueous batteries. In these technologies, redox polymers can play a different role, for example, as active materials in the cathode or anode, as a redox-active binder or mediator, or as soluble catholyte or anolyte in aqueous redox flow batteries.

Through the chapters of this book, the authors will discuss the challenges and characteristics of the most important redox polymers in battery

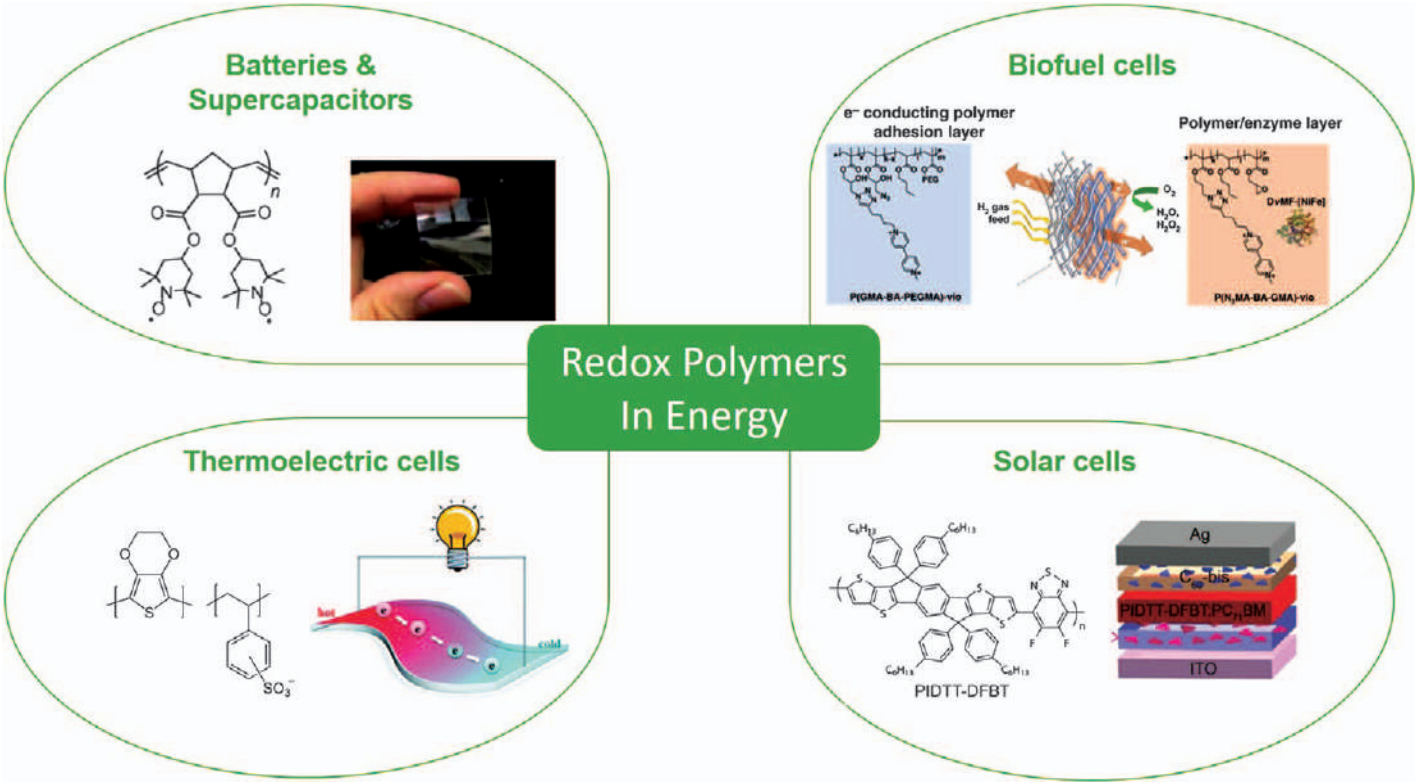


**Figure 1.7** Examples of main applications of redox polymers in the energy field. (a) Batteries and supercapacitors. Adapted from ref. 22 with permission from the Royal Society of Chemistry. (b) Biofuel cells. Adapted from ref. 100 https://doi.org/10.1038/s41467-018-07137-6, under the terms of the CC BY 4.0 licence, http://creativecommons.org/licenses/by/4.0/. (c) Thermoelectric cells. Adapted from ref. 98 with permission from the Royal Society of Chemistry. (d) Solar cells. Adapted from ref. 99 with permission from John Wiley and Sons, © 2014 WILEY-VCH Verlag GmbH & Co. KGaA, Weinheim.

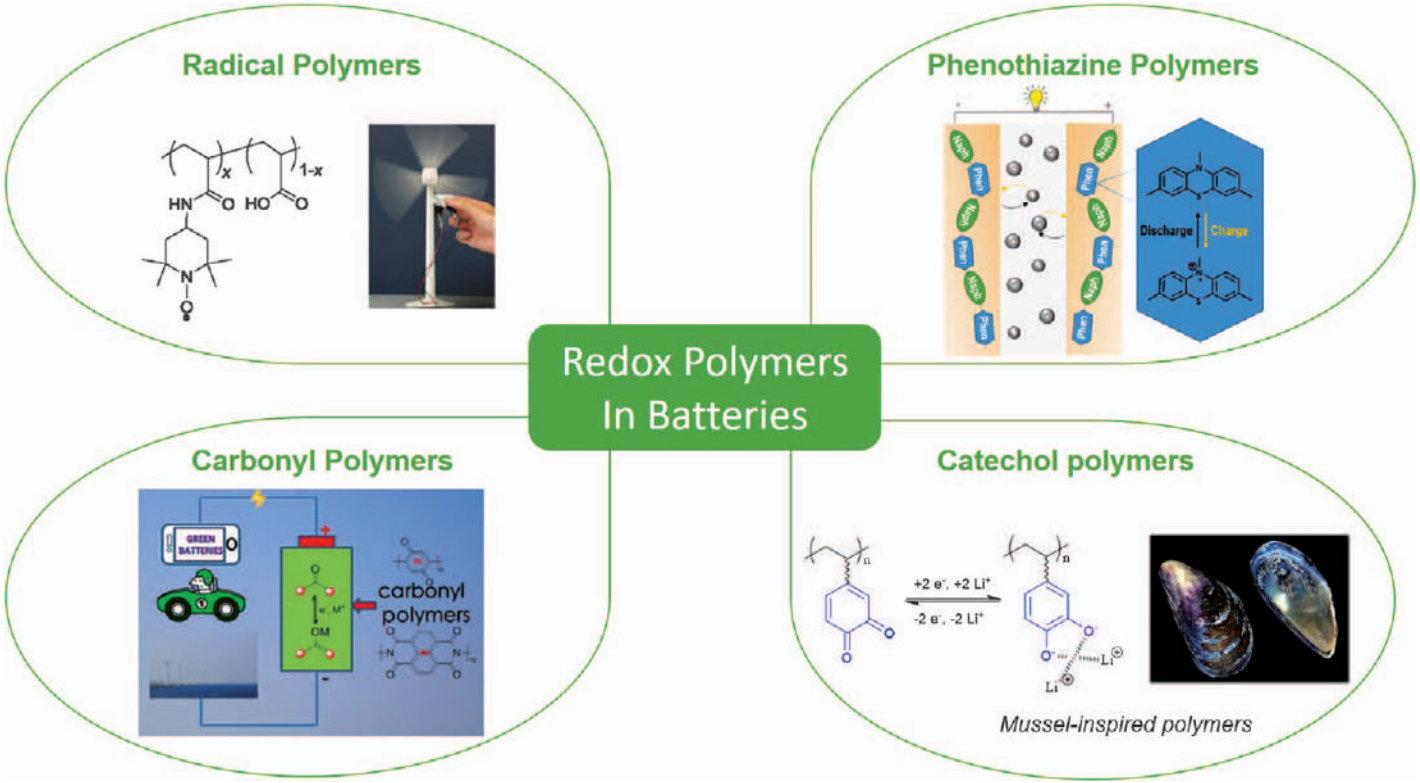


**Figure 1.8** Examples of the main types of redox polymers actually investigated in batteries and discussed in the chapters of this book: (a) Radical polymers. Adapted from ref. 101 with permission from John Wiley and Sons, © 2018 Wiley-VCH Verlag GmbH & Co. KGaA, Weinheim. (b) Phenothiazine polymers. Adapted from ref. 58 with permission John Wiley and Sons, © 2019 Wiley-VCH Verlag GmbH & Co. KGaA, Weinheim. (c) Carbonyl polymers. Reproduced from ref. 103, with permission from Elsevier, Copyright 2017. (d) Catechol polymers.

technologies. In other words, how the different polymers families such as radical polymers, phenothiazine-type polymers, carbonyl polymers or catechol polymers are used in emerging battery technologies.[44,101–104] Chapter 8 is devoted to discussing the new battery configurations led by the use of redox polymers (Figure 1.8).

### 1.4.2 Applications in Medicine

Although energy is the most popular field of use of redox polymers, medicine is expected to be the most important one in the coming decades. Historically, the most important application of redox polymers has been in the area of electrochemical biosensors such as glucose or other types of bioactive compounds. However, as will be discussed in this book, there is a high demand for new materials such as redox polymers in emerging healthcare technologies which are specially important nowadays.

For instance, in tissue engineering redox polymers are very popular in the development of conducting scaffolds for the growth or sensing of tissues based on electrically sensitive cells such as neurons or cardiomyocytes.[105] In Chapter 10, the use of redox-sensitive polymers presenting mostly disulfide cleavable bonds in drug delivery will be discussed. These new redox-sensitive drug-delivery vectors are becoming very important nowadays due to their sensitiveness to reactive oxygen species (ROS). ROS are key intermediates in a number of biological mechanisms and their role and high concentration in different diseases are important factors. In Chapter 13, it will be discussed how through the use of redox polymers electric signals can be transformed in movement through devices such as electromechanical actuators.[106] Those devices are part of the global development of bioinspired devices known as artificial muscles of importance in a number of new technologies in the robotics or microelectronics areas. Last but not least, the use of redox polymers such as PEDOT in different bioelectronic devices such as biosensors or electrodes to interface with the biological signals will be discussed (Figure 1.9).

## 1.5 Conclusions

Through this chapter, the field of redox polymers and the topics that will be more deeply discussed in the different chapters of this book are introduced. First, the different types of redox polymers and their classification are presented based on the chemical nature and how the redox-active site is distributed within the polymer. Next, the main characterization methods used for assessing the properties of redox polymers are introduced. Finally, the main applications of redox polymers in energy and medicine are indicated as they will be discussed in depth through the different chapters of the book.

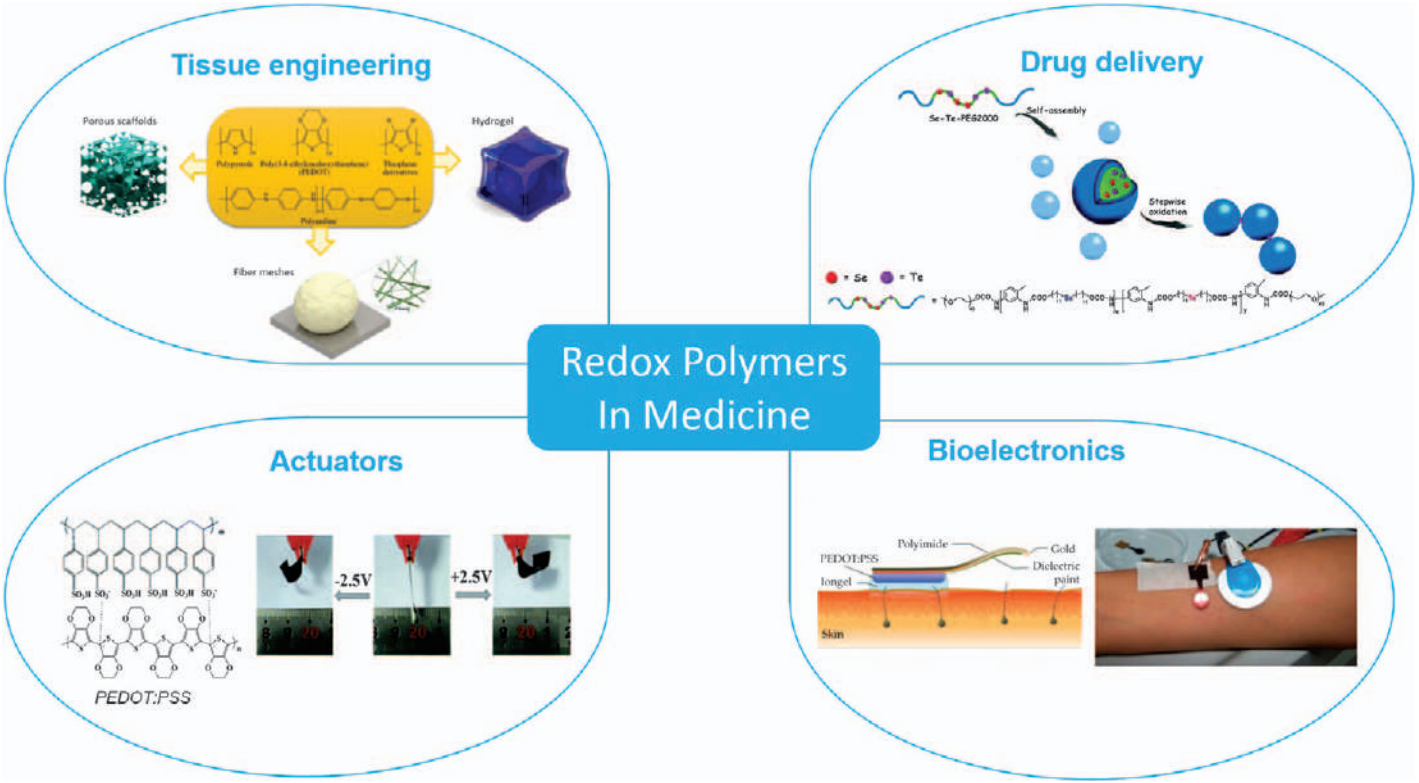


**Figure 1.9** Examples of the main applications of redox polymers in medicine and discussed in the chapters of this book. (a) Tissue engineering. Reproduced from ref. 105 with permission from the American Chemical Society, Copyright 2019. (b) Drug delivery. Reproduced from ref. 107 with permission from the Royal Society of Chemistry. (c) Actuators. Adapted from ref. 108 with permission from the Royal Society of Chemistry. (d) Bioelectronics. Adapted from ref. 109, https://doi.org/10.3390/polym10090989, under the terms of the CC BY 4.0 licence, https://creativecommons.org/licenses/by/4.0/.

## References


1. A. G. MacDiarmid, *Angew. Chem., Int. Ed.*, 2001, **40**, 2581–2590.
2. R. Pietschnig, *Chem. Soc. Rev.*, 2016, **45**, 5216–5231.
3. N. Casado, G. Hernández, H. Sardon and D. Mecerreyes, *Prog. Polym. Sci.*, 2016, **52**, 107–135.
4. C.-T. Chen, *Chem. Mater.*, 2004, **16**, 4389–4400.
5. X. Zhang, L. Han, M. Liu, K. Wang, L. Tao, Q. Wan and Y. Wei, *Mater. Chem. Front.*, 2017, **1**, 807–822.
6. M. Huo, J. Yuan, L. Tao and Y. Wei, *Polym. Chem.*, 2014, **5**, 1519–1528.
7. T. Abidin, Q. Zhang, K.-L. Wang and D.-J. Liaw, *Polymer*, 2014, **55**, 5293–5304.
8. R. Schroot, M. Jäger and U. S. Schubert, *Chem. Soc. Rev.*, 2017, **46**, 2754–2798.
9. H. Shirakawa, E. J. Louis, A. G. MacDiarmid, C. K. Chiang and A. J. Heeger, *J. Chem. Soc., Chem. Commun.*, 1977, 578–580.
10. J. Ouyang, C. W. Chu, F. C. Chen, Q. Xu and Y. Yang, *Adv. Funct. Mater.*, 2005, **15**, 203–208.
11. P. Sen, A. De, A. D. Chowdhury, S. K. Bandyopadhyay, N. Agnihotri and M. Mukherjee, *Electrochim. Acta*, 2013, **108**, 265–273.
12. H.-P. Cong, X.-C. Ren, P. Wang and S.-H. Yu, *Energy Environ. Sci.*, 2013, **6**, 1185–1191.
13. Y. Xia and J. Ouyang, *J. Mater. Chem.*, 2011, **21**, 4927–4936.
14. A. Elschner, F. Bruder, H. W. Heuer, F. Jonas, A. Karbach, S. Kirchmeyer, S. Thurm and R. Wehrmann, *Synth. Met.*, 2000, **111–112**, 139–143.
15. T. J. Simons, M. Salsamendi, P. C. Howlett, M. Forsyth, D. R. MacFarlane and C. Pozo-Gonzalo, *ChemElectroChem*, 2015, **2**, 2071–2078.
16. H. Varela and R. M. Torresi, *J. Electrochem. Soc.*, 2000, **147**, 665–670.
17. Y. Ishiguro, S. Inagi and T. Fuchigami, *Langmuir*, 2011, **27**, 7158–7162.
18. K. Nakahara, S. Iwasa, M. Satoh, Y. Morioka, J. Iriyama, M. Suguro and E. Hasegawa, *Chem. Phys. Lett.*, 2002, **359**, 351–354.
19. H. Nishide, S. Iwasa, Y.-J. Pu, T. Suga, K. Nakahara and M. Satoh, *Electrochim. Acta*, 2004, **50**, 827–831.
20. T. Janoschka, M. D. Hager and U. S. Schubert, *Adv. Mater.*, 2012, **24**, 6397–6409.
21. K. Oyaizu and H. Nishide, *Adv. Mater.*, 2009, **21**, 2339–2344.
22. T. Suga, H. Konishi and H. Nishide, *Chem. Commun.*, 2007, 1730–1732.
23. H. Fu, D. M. Policarpio, J. D. Batteas and D. E. Bergbreiter, *Polym. Chem.*, 2010, **1**, 631–633.
24. G. Hauffman, J. Rolland, J.-P. Bourgeois, A. Vlad and J.-F. Gohy, *J. Polym. Sci., Part A: Polym. Chem.*, 2013, **51**, 101–108.
25. T. Suga, M. Sakata, K. Aoki and H. Nishide, *ACS Macro Lett.*, 2014, **3**, 703–707.
26. M. Aydın, B. Esat, Ç. Kılıç, M. E. Köse, A. Ata and F. Yılmaz, *Eur. Polym. J.*, 2011, **47**, 2283–2294.

27. N. Casado, G. Hernández, A. Veloso, S. Devaraj, D. Mecerreyes and M. Armand, *ACS Macro Lett.*, 2016, **5**, 59–64.
28. K. Zhang, M. J. Monteiro and Z. Jia, *Polym. Chem.*, 2016, **7**, 5589–5614.
29. T. Jähnert, M. D. Hager and U. S. Schubert, *Macromol. Rapid Commun.*, 2016, **37**, 725–730.
30. T. Jähnert, B. Häupler, T. Janoschka, M. D. Hager and U. S. Schubert, *Macromol. Rapid Commun.*, 2014, **35**, 882–887.
31. J. T. Price, J. A. Paquette, C. S. Harrison, R. Bauld, G. Fanchini and J. B. Gilroy, *Polym. Chem.*, 2014, **5**, 5223–5226.
32. B. Häupler, A. Wild and U. S. Schubert, *Adv. Energy Mater.*, 2015, **5**, 1402034.
33. Z. Song, H. Zhan and Y. Zhou, *Chem. Commun.*, 2009, 448–450.
34. G. Hernández, N. Casado, R. Coste, D. Shanmukaraj, L. Rubatat, M. Armand and D. Mecerreyes, *RSC Adv.*, 2015, **5**, 17096–17103.
35. G. Hernández, M. Salsamendi, S. M. Morozova, E. I. Lozinskaya, S. Devaraj, Y. S. Vygodskii, A. S. Shaplov and D. Mecerreyes, *J. Polym. Sci., Part A: Polym. Chem.*, 2018, **56**, 714–723.
36. W. Deng, Y. Shen, J. Qian and H. Yang, *Chem. Commun.*, 2015, **51**, 5097–5099.
37. G. Hernández, N. Lago, D. Shanmukaraj, M. Armand and D. Mecerreyes, *Mater. Today Energy*, 2017, **6**, 264–270.
38. G. Hernández, N. Casado, A. M. Zamarayeva, J. K. Duey, M. Armand, A. C. Arias and D. Mecerreyes, *ACS Appl. Energy Mater.*, 2018, **1**, 7199–7205.
39. B. Baumgartner, M. J. Bojdys and M. M. Unterlass, *Polym. Chem.*, 2014, **5**, 3771–3776.
40. F. N. Ajjan, D. Mecerreyes and O. Inganäs, *Biotechnol. J.*, 2019, **14**, 1900062.
41. G. Milczarek and O. Inganäs, *Science*, 2012, **335**, 1468.
42. F. N. Ajjan, N. Casado, T. Rębiś, A. Elfwing, N. Solin, D. Mecerreyes and O. Inganäs, *J. Mater. Chem. A*, 2016, **4**, 1838–1847.
43. N. Casado, M. Hilder, C. Pozo-Gonzalo, M. Forsyth and D. Mecerreyes, *ChemSusChem*, 2017, **10**, 1783–1791.
44. N. Patil, C. Jérôme and C. Detrembleur, *Prog. Polym. Sci.*, 2018, **82**, 34–91.
45. N. Patil, A. Aqil, F. Ouhib, S. Admassie, O. Inganäs, C. Jérôme and C. Detrembleur, *Adv. Mater.*, 2017, **29**, 1703373.
46. N. Patil, A. Mavrandonakis, C. Jérôme, C. Detrembleur, J. Palma and R. Marcilla, *ACS Appl. Energy Mater.*, 2019, **2**, 3035–3041.
47. K. Pirnat, N. Casado, L. Porcarelli, N. Ballard and D. Mecerreyes, *Macromolecules*, 2019, **52**, 8155–8166.
48. L. Wang, J. Ding, S. Sun, B. Zhang, X. Tian, J. Zhu, S. Song, B. Liu, X. Zhuang and Y. Chen, *Adv. Mater. Interfaces*, 2018, **5**, 1701679.
49. C. Zhang, X. Yang, W. Ren, Y. Wang, F. Su and J.-X. Jiang, *J. Power Sources*, 2016, **317**, 49–56.
50. J. Ding, C. Zheng, L. Wang, C. Lu, B. Zhang, Y. Chen, M. Li, G. Zhai and X. Zhuang, *J. Mater. Chem. A*, 2019, **7**, 23337–23360.

51. J. Kim, H.-S. Park, T.-H. Kim, S. Yeol Kim and H.-K. Song, *Phys. Chem. Chem. Phys.*, 2014, **16**, 5295–5300.
52. M. Frank, J. Ahrens, I. Bejenke, M. Krick, D. Schwarzer and G. H. Clever, *J. Am. Chem. Soc.*, 2016, **138**, 8279–8287.
53. X. Kong, A. P. Kulkarni and S. A. Jenekhe, *Macromolecules*, 2003, **36**, 8992–8999.
54. M. Kolek, F. Otteny, P. Schmidt, C. Mück-Lichtenfeld, C. Einholz, J. Becking, E. Schleicher, M. Winter, P. Bieker and B. Esser, *Energy Environ. Sci.*, 2017, **10**, 2334–2341.
55. P. Acker, L. Rzesny, C. F. N. Marchiori, C. M. Araujo and B. Esser, *Adv. Funct. Mater.*, 2019, **29**, 1906436.
56. J. D. Milshtein, A. P. Kaur, M. D. Casselman, J. A. Kowalski, S. Modekrutti, P. L. Zhang, N. Harsha Attanayake, C. F. Elliott, S. R. Parkin, C. Risko, F. R. Brushett and S. A. Odom, *Energy Environ. Sci.*, 2016, **9**, 3531–3543.
57. A. Wild, M. Strumpf, B. Häupler, M. D. Hager and U. S. Schubert, *Adv. Energy Mater.*, 2017, **7**, 1601415.
58. N. Casado, D. Mantione, D. Shanmukaraj and D. Mecerreyes, *ChemSusChem*, n/a.
59. H.-D. Lim, B. Lee, Y. Zheng, J. Hong, J. Kim, H. Gwon, Y. Ko, M. Lee, K. Cho and K. Kang, *Nat. Energy*, 2016, **1**, 16066.
60. F. S. Arimoto and A. C. Haven, *J. Am. Chem. Soc.*, 1955, **77**, 6295–6297.
61. M. Gallei and C. Rüttiger, *Chem. – Eur. J.*, 2018, **24**, 10006–10021.
62. C. Tonhauser, M. Mazurowski, M. Rehahn, M. Gallei and H. Frey, *Macromolecules*, 2012, **45**, 3409–3418.
63. R. H. Staff, M. Gallei, M. Mazurowski, M. Rehahn, R. Berger, K. Landfester and D. Crespy, *ACS Nano*, 2012, **6**, 9042–9049.
64. M. A. Hempenius, C. Cirmi, F. L. Savio, J. Song and G. J. Vancso, *Macromol. Rapid Commun.*, 2010, **31**, 772–783.
65. C. Rüttiger, H. Hübner, S. Schöttner, T. Winter, G. Cherkashinin, B. Kuttich, B. Stühn and M. Gallei, *ACS Appl. Mater. Interfaces*, 2018, **10**, 4018–4030.
66. V. Bellas and M. Rehahn, *Angew. Chem., Int. Ed.*, 2007, **46**, 5082–5104.
67. J. Zhang, L. Ren, C. G. Hardy and C. Tang, *Macromolecules*, 2012, **45**, 6857–6863.
68. G.-A. Yu, Y. Ren, J.-T. Guan, Y. Lin and S. H. Liu, *J. Organomet. Chem.*, 2007, **692**, 3914–3921.
69. Z. Chen, H. Lemke, S. Albert-Seifried, M. Caironi, M. M. Nielsen, M. Heeney, W. Zhang, I. McCulloch and H. Sirringhaus, *Adv. Mater.*, 2010, **22**, 2371–2375.
70. J. Hollinger, A. A. Jahnke, N. Coombs and D. S. Seferos, *J. Am. Chem. Soc.*, 2010, **132**, 8546–8547.
71. A. A. Jahnke, B. Djukic, T. M. McCormick, E. Buchaca Domingo, C. Hellmann, Y. Lee and D. S. Seferos, *J. Am. Chem. Soc.*, 2013, **135**, 951–954.

72. H.-S. Na, Y. Morisaki, Y. Aiki and Y. Chujo, *J. Polym. Sci., Part A: Polym. Chem.*, 2007, **45**, 2867–2875.
73. M. Sebastian, M. Hissler, C. Fave, J. Rault-Berthelot, C. Odin and R. Réau, *Angew. Chem. Int. Ed.*, 2006, **45**, 6152–6155.
74. H. Xu, W. Cao and X. Zhang, *Acc. Chem. Res.*, 2013, **46**, 1647–1658.
75. N. Ma, Y. Li, H. Xu, Z. Wang and X. Zhang, *J. Am. Chem. Soc.*, 2010, **132**, 442–443.
76. A. Erxleben, *Coord. Chem. Rev.*, 2003, **246**, 203–228.
77. H. Li and L. Wu, *Soft Matter*, 2014, **10**, 9038–9053.
78. G. R. Whittell, M. D. Hager, U. S. Schubert and I. Manners, *Nat. Mater.*, 2011, **10**, 176–188.
79. G.-Q. Kong and C.-D. Wu, *Crystal Growth Design*, 2010, **10**, 4590–4595.
80. A. Valente, M. H. Garcia, F. Marques, Y. Miao, C. Rousseau and P. Zinck, *J. Inorg. Biochem.*, 2013, **127**, 79–81.
81. B. Askari, H. A. Rudbari, A. Valente, G. Bruno, N. Micale, N. Shivalingegowda and L. N. Krishnappagowda, *ChemistrySelect*, 2020, **5**, 810–817.
82. R. Antiochia and L. Gorton, *Biosens. Bioelectron.*, 2007, **22**, 2611–2617.
83. R. Ramya, R. Sivasubramanian and M. V. Sangaranarayanan, *Electrochim. Acta*, 2013, **101**, 109–129.
84. R. Kerr, C. Pozo-Gonzalo, M. Forsyth and B. Winther-Jensen, *Electrochim. Acta*, 2015, **154**, 142–148.
85. J. M. Saveant, in *Elements of Molecular and Biomolecular Electrochemistry*, DOI: 10.1002/0471758078.ch1, 2006, pp. 1–77.
86. J. M. Saveant, in *Elements of Molecular and Biomolecular Electrochemistry*, DOI: 10.1002/0471758078.fmatter, 2006, pp. i–xviii.
87. D. Ohayon, G. Nikiforidis, A. Savva, A. Giugni, S. Wustoni, T. Palanisamy, X. Chen, I. P. Maria, E. Di Fabrizio, P. M. F. J. Costa, I. McCulloch and S. Inal, *Nat. Mater.*, 2020, **19**, 456–463.
88. M. Levi and A. Doron, in *Solid State Electrochemistry I*, DOI: 10.1002/9783527627868.ch11, 2009, pp. 365–396.
89. S. Bilal, A.-U.-H. Ali Shah and R. Holze, *Electrochim. Acta*, 2011, **56**, 3353–3358.
90. L. Dunsch, *J. Solid State Electrochem.*, 2011, **15**, 1631–1646.
91. F. Tavoli and N. Alizadeh, *J. Electroanal. Chem.*, 2014, **720–721**, 128–133.
92. X. Zhang, T. T. Steckler, R. R. Dasari, S. Ohira, W. J. Potscavage, S. P. Tiwari, S. Coppée, S. Ellinger, S. Barlow, J.-L. Brédas, B. Kippelen, J. R. Reynolds and S. R. Marder, *J. Mater. Chem.*, 2010, **20**, 123–134.
93. P. Damlin, C. Kvarnström, H. Kulovaara and A. Ivaska, *Synth. Met.*, 2003, **135–136**, 309–310.
94. A. Vizintin, J. Bitenc, A. Kopač Lautar, K. Pirnat, J. Grdadolnik, J. Stare, A. Randon-Vitanova and R. Dominko, *Nat. Commun.*, 2018, **9**, 661.
95. K. Wagner, R. Byrne, M. Zanoni, S. Gambhir, L. Dennany, R. Breukers, M. Higgins, P. Wagner, D. Diamond, G. G. Wallace and D. L. Officer, *J. Am. Chem. Soc.*, 2011, **133**, 5453–5462.

96. A. I. Melato, A. S. Viana and L. M. Abrantes, *J. Solid State Electrochem.*, 2010, **14**, 523–530.
97. D. Plausinaitis, V. Ratautaite, L. Mikoliunaite, L. Sinkevicius, A. Ramanaviciene and A. Ramanavicius, *Langmuir*, 2015, **31**, 3186–3193.
98. M. He, F. Qiu and Z. Lin, *Energy Environ. Sci.*, 2013, **6**, 1352–1361.
99. K. Yao, M. Salvador, C.-C. Chueh, X.-K. Xin, Y.-X. Xu, D. W. deQuilettes, T. Hu, Y. Chen, D. S. Ginger and A. K.-Y. Jen, *Adv. Energy Mater.*, 2014, **4**, 1400206.
100. J. Szczesny, N. Marković, F. Conzuelo, S. Zacarias, I. A. C. Pereira, W. Lubitz, N. Plumeré, W. Schuhmann and A. Ruff, *Nat. Commun.*, 2018, **9**, 4715.
101. K. Hatakeyama-Sato, H. Wakamatsu, R. Katagiri, K. Oyaizu and H. Nishide, *Adv. Mater.*, 2018, **30**, 1800900.
102. F. Otteny, G. Studer, M. Kolek, P. Bieker, M. Winter and B. Esser, *ChemSusChem*, 2020, **13**, 2232–2238.
103. M. Tang, H. Li, E. Wang and C. Wang, *Chin. Chem. Lett.*, 2018, **29**, 232–244.
104. Z. Song, Y. Qian, M. L. Gordin, D. Tang, T. Xu, M. Otani, H. Zhan, H. Zhou and D. Wang, *Angew. Chem., Int. Ed.*, 2015, **54**, 13947–13951.
105. N. Alegret, A. Dominguez-Alfaro and D. Mecerreyes, *Biomacromolecules*, 2019, **20**, 73–89.
106. K. Rohtlaid, G. T. M. Nguyen, C. Soyer, E. Cattan, F. Vidal and C. Plesse, *Adv. Electron. Mater.*, 2019, **5**, 1800948.
107. L. Wang, W. Wang, W. Cao and H. Xu, *Polym. Chem.*, 2017, **8**, 4520–4527.
108. D. Wang, C. Lu, J. Zhao, S. Han, M. Wu and W. Chen, *RSC Adv.*, 2017, **7**, 31264–31271.
109. A. Y. Yuen, L. Porcarelli, R. H. Aguirresarobe, A. Sanchez-Sanchez, I. Del Agua, U. Ismailov, G. G. Malliaras, D. Mecerreyes, E. Ismailova and H. Sardon, *Polymers*, 2018, **10**, 989.

CHAPTER 2

# *Synthetic Strategies and Methods for Redox Polymers*

YANLIN SHI,[a] MICHAEL J. MONTEIRO[a] AND ZHONGFAN JIA*[b,c]

[a] Australian Institute for Bioengineering and Nanotechnology, The University of Queensland, Brisbane QLD 4072, Australia; [b] College of Science and Engineering, Flinders University, Sturt Road, Bedford Park, South Australia 5042, Australia; [c] Institute for NanoScale Science and Technology, Flinders University, Sturt Road, Bedford Park, South Australia 5042, Australia
*Email: zhongfan.jia@flinders.edu.au

## 2.1 Introduction

One-electron oxidation and reduction reactions of organic compounds with closed-shell electron configuration generate highly reactive cation and anion radicals, respectively.[1] Such reactions on stable organic radicals also produce reactive cations or anions.[2] These redox reactions are very common in many chemically driven life processes, and can also be used to create new synthetic molecules and materials. Many different types of organic groups that can undergo reversible redox reactions have been classified into organic redox systems. Tuning the redox properties of organic compounds provides an opportunity to develop new organic materials designed for various applications, including transistors,[3] organic magnetics,[4] organic catalysts,[5–7] energy conversion,[8–10] energy storage,[11–13] biomedicine,[14,15] and many others.[16] This chapter aims to summarize a few of the most studied redox-active groups, the strategies and methodologies to synthesize and incorporate

Polymer Chemistry Series No. 34
Redox Polymers for Energy and Nanomedicine
Edited by Nerea Casado and David Mecerreyes

Published by the Royal Society of Chemistry, www.rsc.org

these chemical groups into polymers, and thus provide a comprehensive overview on application-directed design and synthesis of redox polymers. Their applications in biomedicine and energy storage will be discussed in the later chapters.

## 2.2 Design, Synthesis and Characterization of Redox Polymers

So far, organic redox-active groups mainly include open-shell organic radicals, closed-shell neutral or ionic compounds, and organometallics.[1] The very different (electro)chemical reactivities and redox behaviours dictate which synthetic method should be used in the synthesis of their polymer counterparts.[12] For instance, free-radical polymerization (FRP) techniques cannot be used to polymerize monomers consisting of persistent organic radicals due to their rapid radical termination reactions with other free-radicals. Different synthetic strategies are often required to design redox polymers with distinct chemical compositions and architectures to meet demands for diverse applications. The chemical structures and physical properties of redox polymers can be characterized by conventional polymer characterization techniques, including size exclusion chromatography (SEC), matrix-assisted laser desorption ionization–time of flight (MALDI-ToF) mass spectrometry, nuclear magnetic resonance (NMR), differential scanning calorimetry (DSC), and many more. Some redox groups and their further intermediates are radicals, which require further identification and quantification using electron spin resonance (ESR).

Redox polymers are functional polymers consisting of redox-active functionalities. Like many other functional polymers, redox polymers are mainly synthesized through the three following approaches: (i) direct polymerization of monomers consisting of redox-active groups; (ii) post-polymerization conversion of polymer precursors to redox polymers; and (iii) post-modification of reactive polymers with functional redox molecules.[17]

Techniques for direct polymerization of redox-active monomers include radical polymerization, ionic polymerization, step or condensation polymerization and metathesis polymerization, *etc.*[18] This direct monomer approach is versatile and straightforward, particularly for the synthesis of redox polymers with controlled molecular weight and architecture; this can be accomplished using living radical polymerization (LRP). When monomers are not compatible with these polymerization conditions, post-polymerization conversion or post-modification can be used. These latter approaches avoid the side reactions from the redox groups during polymerization, but still provide control over the chemical composition and architecture. Among the different polymerization techniques, LRP such as reversible addition–fragmentation chain transfer (RAFT) polymerization,[19] atom transfer radical polymerization (ATRP)[20] and single-electron transfer living radical polymerization (SET-LRP)[21] can control both the molecular

weight and polymer structure, affording polymers with diverse chemical compositions, physical properties, and the ability to be self-assembled into nanostructures and organic–inorganic hybrid materials with redox properties. Owing to their specific chemical properties, the content of this chapter is thus organized according to the type of redox groups. It should be noted that most of the synthetic work on redox polymers summarized in this chapter is for nonconjugated polymers. The synthesis of conjugated polymers consisting of redox groups is only briefly mentioned and reviewed more comprehensively elsewhere.[11,22] In addition, synthetic methods for some redox groups that have been well documented previously will be introduced here but will not be comprehensively covered.

### 2.2.1 Redox Reaction of Nitroxide Radicals

Nitroxide radicals, first isolated in Russian in 1959,[23] are a class of stable radicals with an open-shell electron configuration. This type of radical possesses extremely high stability in oxygen and under heat. Also, the nitroxide radical is different from carbon-centred radicals as the nitroxide radical stability stems from the resonance delocalization of the unpaired electron across the N–O bond, as shown in Scheme 2.1.

In addition, the absence of an α-H is also critical to prevent disproportionation and degradation of the nitroxide. A typical example of a nitroxide radical is 2,2,6,6-tetramethylpiperidine-1-oxy (TEMPO). Theoretically, TEMPO and most of its derivatives or analogues can undergo an oxidation reaction to oxoammonium cations ($TEMPO^+$) and a reduction reaction to aminoxy anions ($TEMPO^-$). These redox reactions can, in principle, be carried out under chemical or electrochemical conditions, forming a reversible two-electron redox process. However, in many cases, the aminoxy anion can be rapidly protonated at the ambient condition to form a more stable hydroxylamine (*i.e.*, TEMPOH). TEMPOH is difficult to be electrochemically oxidized back to the TEMPO radical, but easily oxidized in the presence of weak oxidants such as oxygen or metal oxides (Scheme 2.2). The properties and applications of nitroxide radicals are determined by their single-electron spin and reversible redox properties. Since their discovery, a tremendous number of nitroxide radical derivatives have been reported, as summarized by Rozantsev.[23] The redox potential of nitroxide radicals is dictated by their inherent chemical structure, which has been well understood both theoretically and experimentally.[24,25] Recently, Jia and Coote[26] reported that both functional groups and heteroatom substitution on TEMPO have a great impact on the oxidation potentials, which range from 0.6 to 1.0 V *vs.* SHE (*i.e.*, standard hydrogen electrode).

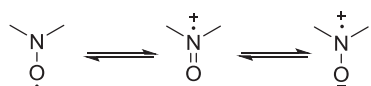

**Scheme 2.1** Resonance structures of nitroxide radicals.

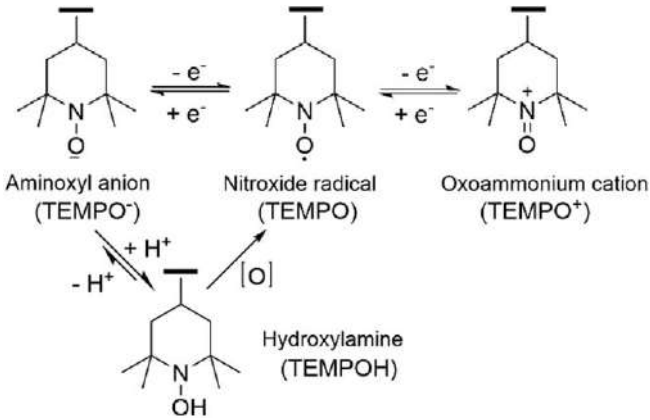


**Scheme 2.2** Proton-coupled two-electron redox reaction of TEMPO radical.

### 2.2.2 Redox Polymers Consisting of Nitroxide Radicals

Due to the potential widespread applications of nitroxide radical polymers (NRPs), they have been one of the most studied classes of redox polymers.[27] So far, most polymerization methods can be applied to produce NRPs, yielding abundant chemical compositions and physical architectures. Previous reviews have summarized the synthetic progress and applications for NRPs.[17,28] Therefore, we will provide a concise summary of the synthetic strategies and some recent progress.

In 1967, Griffith[29] first reported an anionic polymerization of TEMPO methacrylate M1 by using a Grignard reagent as initiator. Originally, the polymerization only produced oligomers, but later, Komaba[30] found this condition also led to gelation. Sukegawa[31] proposed that the carbanions in such aggressive organometallic initiators may attack the nitroxide radicals, resulting in cross-linking. To avoid this side reaction, the initiator was first capped with methyl methacrylate (MMA) and converted to a less reactive carbanion ($MMA^{-}Li^{+}$), which then allowed for the controlled polymerization of M1, producing the well-defined P1 with a number average molecular weight ($M_n$) up to 20 kDa and with a low dispersity ($Đ < 1.10$) (see Scheme 2.3).

TEMPO and other nitroxide radicals have been converted to monomers with epoxide functionality, which can then be polymerized through an anionic ring-opening polymerization (AROP) by using an organic base. Compared to a carbanion, the alkoxide is a much weaker base and is therefore often used as an initiator in the synthesis of polyethers. 4-Glycidyl-TEMPO (GTEMPO) M2 was one of the most studied monomers due to its ease of both synthesis and purification.[32,33] Several different initiators have been used to initiate the polymerization of M2 to give a polyether-based NRP (see Scheme 2.4).[34] Attempts using AROP of GTEMPO initiated by diethyl zinc/water ($Et_2Zn/H_2O$) resulted in polymers with high dispersity ($Đ \sim 1.7$–$2.1$),

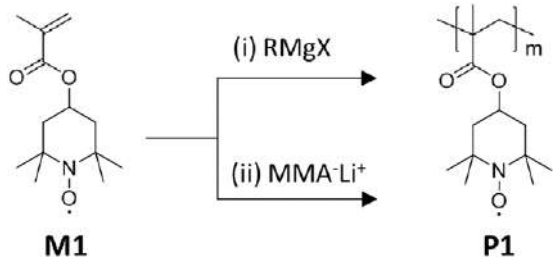


**Scheme 2.3** Synthesis of poly(TEMPO methacrylate) by anionic polymerization. Adapted from ref. 17 with permission from the Royal Society of Chemistry.

and in particular, it was found that there was a decrease in the radical number per repeating unit (*i.e.*, 0.62 spins/unit). Using a solid alkoxide, such as $^{t}$BuOK as the initiator, the resulting polymers showed broad dispersity ($Đ \sim 1.3$–$1.7$) due to the heterogeneous initiation, but with nearly quantitative retention of radicals.[35,36] Recently, Nishide and Oyaizu[37] reported the AROP of M2 initiated by using a strong organic base (*i.e.*, $^{t}$Bu-P$_4$, a phosphazene) together with alcohol. This system successfully produced a polymer from M2 at room temperature with high retention of the radical groups, critical for applications. Huang[32,33] reported the anionic copolymerization of M2 with ethylene oxide M3 in THF, producing the copolymer P3 with a $Đ$ of 1.10. Similarly, Wang[38] synthesized hyperbranched nitroxide radical copolymers, P4, by using glycidol M4 as a comonomer. Endo[36] used $^{t}$BuOK as an initiator for the copolymerization of M2 with M5, resulting in the copolymer P5. From this body of work, the density of nitroxide radicals in NRPs can be controlled by varying the molar ratio of M2 to the comonomers as found by electron paramagnetic resonance (EPR). Precise control over the radical density dictated whether they could be used as a macroinitiator to make highly dense bottlebrush polymers or directly applied in biomedicine and energy applications in which an appropriate nitroxide density gave better *in vivo* imaging and greater energy storage.[32,33,39–41]

In addition, AROP of other nitroxide radicals such as 2,2,5,5-tetramethyl-2,5-dihydro-1*H*-pyrrol-1-oxy and 2,2,5,5-tetramethylpyrrolidin-1-oxy (PROXYL) with oxirane or oxetane were unsuccessful. Even the less studied cationic polymerization of these and other nitroxide radical monomers was also not successful since the nitroxide radicals were prone to degradation by the Lewis acid or tin catalyst complexes.[36] In an example, Nakahara[42] carried out a cationic polymerization of 4-vinyloxyl-TEMPO with $BF_3 \cdot Et_2O$ as catalyst in DCM at $-25$ °C. The polymerization yielded a TEMPO-containing poly(vinyl ether) gel, indicating an unavoidable side reaction with the nitroxide radicals.

Olefin metathesis polymerization using transition metals, especially rhodium (Rh) complexes, as a catalyst has been widely explored for the polymerization of radical-containing olefins such as alkene and acetylene.[43,44]

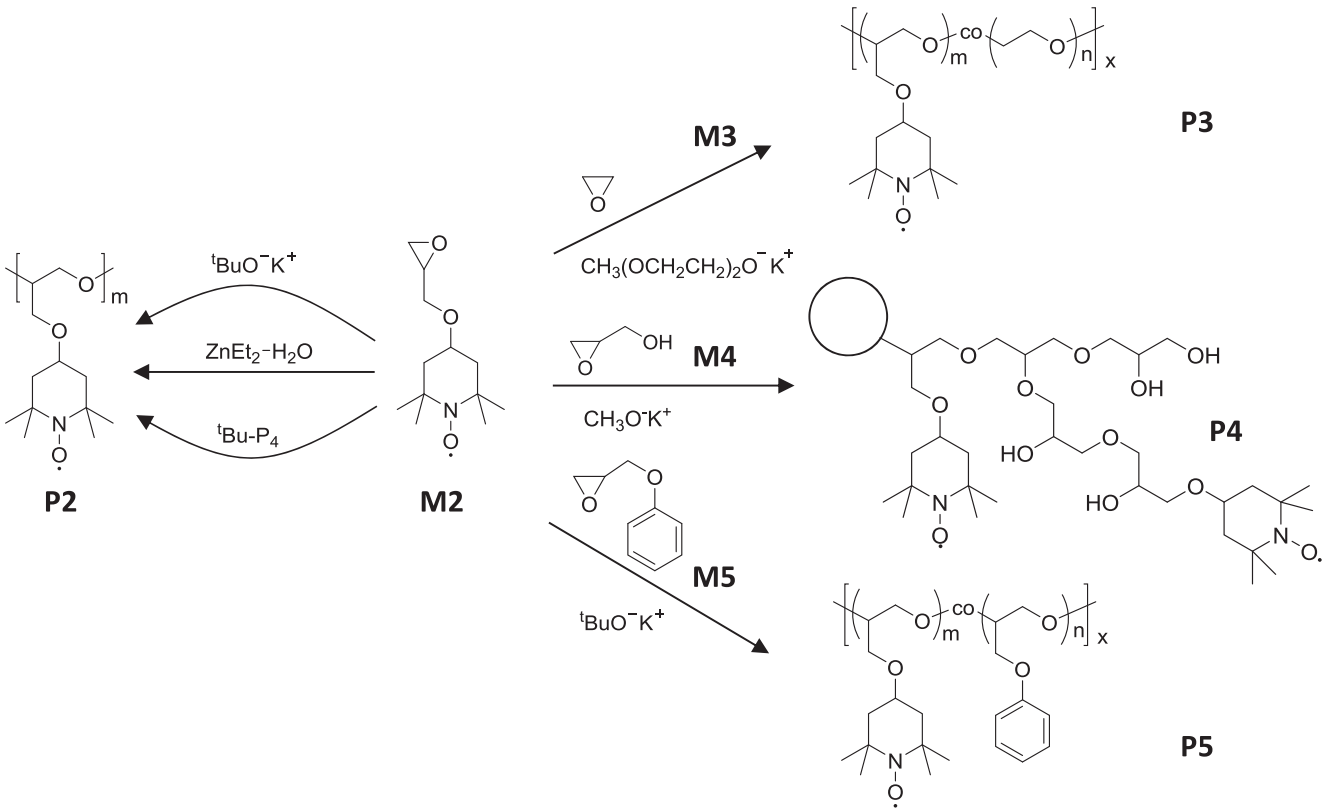


**Scheme 2.4** Anionic ring-opening (co)polymerization of GTEMPO to produce TEMPO-containing polyether. Reproduced from ref. 17 with permission from the Royal Society of Chemistry.

Fujii *et al.*[45] reported the synthesis of poly(phenylacetylene) consisting of nitronyl nitroxide radicals through an olefin polymerization of M6 with the rhodium catalyst, Rh(cod)($NH_3$)Cl (see Scheme 2.5). Nishide[46] used polymer P6 in applications such as organic magnetic materials and an electrochemical active component in the electrode. Based on the successful synthesis of such conjugated polymers, Masuda and co-workers[47–49] studied chiral effects on the electrochemical properties of NRPs through a series of acetylene functional nitroxide radical monomers (M7–M11) with different chiral centres. The polymerization was carried out at 30 °C using Rh catalysts (nbd)$Rh^+[\eta^6$-$C_6H_5B$-$(C_6H_5)_3]$ or $[(nbd)RhCl]_2$-$Et_3N$, resulting in polymers P7–P11 with $M_n$ greater than 10 KDa but high dispersity (*i.e.*, $Đ \sim 1.5$–11.5). To determine the effect of bulky or steric effects from the nitroxide radical on the electrochemical properties, they prepared a library of NRPs (P12–P19) with a polyacetylene backbone but with different densities of nitroxide side groups (M12–M19). Among these polymers (P10, P11 and P19), the side groups with chiral centres formed a helical conformation and enhanced the

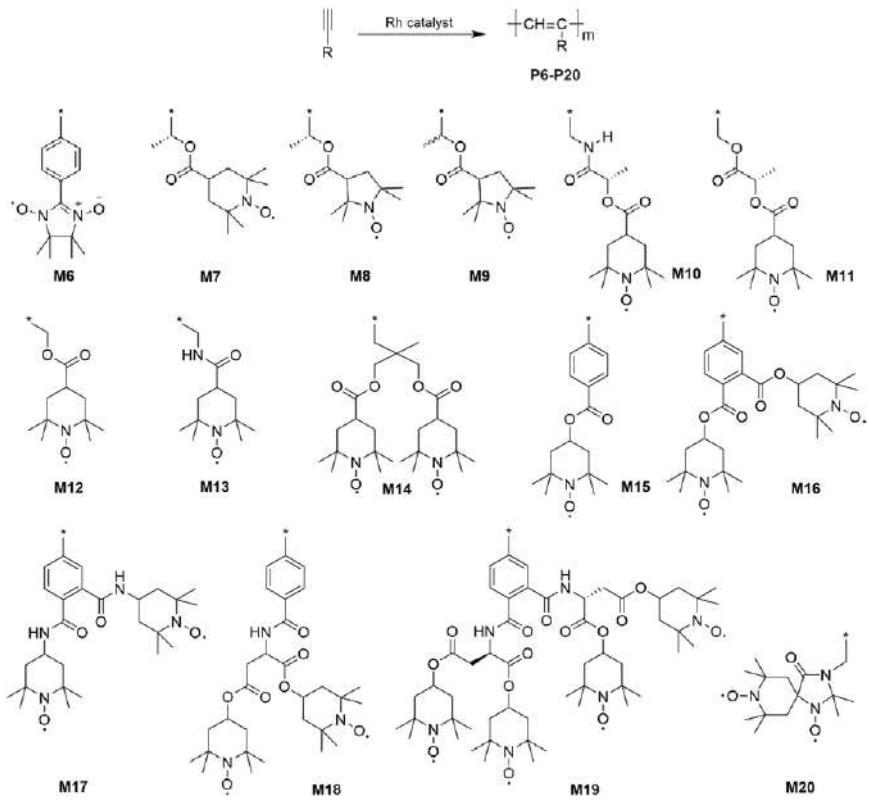


**Scheme 2.5** Olefin metathesis polymerization of acetylene functional nitroxide radical monomers to produce nitroxide-containing polyacetylenes. Reproduced from ref. 17 with permission from the Royal Society of Chemistry.

electrochemical properties.[49] For other NRPs, having multiple-radical side groups did not necessarily increase the electrochemical performance of polymers, and the underlying mechanism requires more research. Nesvadba[50] sought to increase the electrochemical performance through the polymerization of an acetylene functionalized spirobisnitroxide monomer, M20. Although the polymerization gave a polymer with an $M_n$ up to 42 kDa, the anticipated unique architecture of the spironitroxide radical to provide a high energy density and voltage due to their double radicals and constrained ring structure did not eventuate. In fact, P20 formed a cross-linked gel upon polymerization and showed poor electrochemical redox stability, with side reactions stemming from the oxidation of the backbone, whereas bulky side groups prevent free rotation of the nitroxide radicals and inhibit the electron transfer efficiency.

Ring-opening metathesis polymerization (ROMP) is the most used metathesis polymerization technique specifically suitable for cyclic alkene monomers. Using the Grubbs catalyst, control over the molecular weights and structures of norbornene polymers could be obtained, demonstrating its living polymerization behavior.[44] Masuda[47,51,52] pioneered the synthesis of a series of TEMPO-containing norbornene or oxanorbornene monomers M21–M29, and their corresponding polymers using the 2nd-generation Grubbs catalyst (see Scheme 2.6). Compared to the metathesis polymerization of acetylene-based monomers as discussed before, ROMP usually had much shorter polymerization times even under mild conditions (*e.g.* completed in 45 min in $CH_2Cl_2$, at 30 °C). However, the polymers reported by Masuda had high dispersity ($Đ > 3.5$) and in many cases formed gels with no explanation for their observation.[47,51] It was noted that these NRPs were thermally stable at temperatures up to 220 °C due to the stable polynorbornene backbone, a distinct advantage for high-temperature applications over other polymer types. In addition, the radical–radical distance obtained by X-ray crystallographic data showed that the endo/endo (P22) or exo/exo (P23) orientation was 10 Å, a value smaller than endo/exo (P21)-orientation. Although these isomers possess the same radical density, P21 demonstrated a much higher charge/discharge capacity than P22 and P23, suggesting the importance of the spatial configuration of TEMPO moieties.[51]

Nishide[53] subsequently synthesized a densely grafted NRP brush through a combination of AROP and ROMP. A nitroxide radical macromonomer with a norbornene chain-end was prepared *via* AROP and further polymerized using 2nd- or 3rd-generation Grubbs catalyst, producing P1 bottlebrushes with molecular weights from 32 to 230 kDa and the lowest dispersity of 1.17. Atomic force microscopy (AFM) characterization revealed the size of the rod-like polymer brushes was 5–6 nm in width and 30–40 nm in length. This was consistent with the theoretical size of fully stretched bottlebrush polymers. A thin-film electrode fabricated of the P1 bottlebrush demonstrated quantitative redox of all TEMPO radicals, indicating excellent electron hopping between the interchain radicals on the polymer side chains as supported by molecular dynamic simulation.[54] Johnson[55] further reported the synthesis of

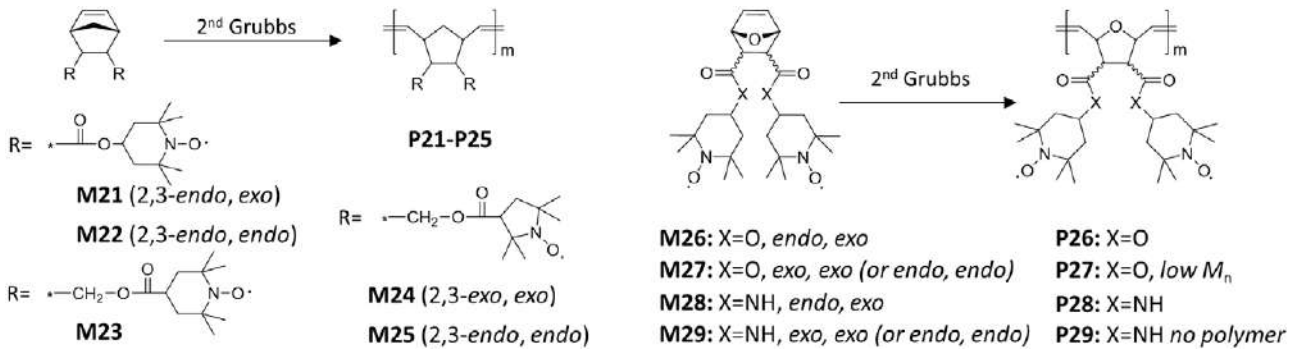


**Scheme 2.6** ROMP of norbornene and oxonorbornen functional nitroxides to produce nitroxide-containing polymers. Reproduced from ref. 17 with permission from the Royal Society of Chemistry.

norbornene-based macromonomer consisting of nitroxide radical and poly(ethylene glycol) (PEG) (M30) after copolymerization, resulting in a PEG bottlebrush (P30) with both nitroxide radicals and fluorescent probes (see Scheme 2.7). This polymer was then used as a redox-responsive dual-imaging agent.

Recently, Delaittre[56] reported a ROMP-induced self-assembly (ROMPISA) technique to synthesize NRP nanoparticles with a core–shell structure. By changing the solvent from THF in the first step to the EtOH/THF mixture in the second, a linear poly(norbornene) block P31 self-assembled into core–shell nanostructures. Such NRP self-assembled nanoparticles could oxidize alcohols when used as a polymer-supported catalyst and with excellent recycling capability (see Scheme 2.8).

During the last decade, the Grubbs 3rd-generation catalyst has been used for the cyclopolymerization of 1,6-heptdiyne and its derivatives.[57] Utilizing this key feature, Jia[58] recently designed a 1,6-heptadiyne functional TEMPO M32 and successfully converted it to a conjugated NRP, P32 (see Scheme 2.9). The polymerization reached a near quantitative monomer conversion within a few minutes at $-15$ °C. The resultant polymer P32 had an $M_n$ up to 27 kDa and a dispersity of 1.13. This is a new method to prepare conjugated NRPs. P32 showed great film-formation properties, potentially useful for film-based energy storage devices.

Turning our attention to the formation of NRP film, Nishide[59] reported the first NRP network with a polyester backbone using stepwise Michael polyaddition. An acetylacetone-functionalized TEMPO M33 was reacted with a multiacrylate cross-linker using 1,8-diazabicyclo undec-7-ene (DBU) as a catalyst, producing a cross-linked poly(β-ketoester) film P33 (see Scheme 2.10). This work provided a straightforward strategy to prepare thin-film electrodes *in situ* with good mechanical properties and thermal stability.

Seeking a well-defined NRP polyester, Barner-Kowollik and Fairfull-Smith[60] recently reported the preparation and ring-opening polymerization of a nitroxide containing carbonate M34. Using DBU and thiourea as the catalyst system, they found that radicals have no influence on the ring-opening copolymerization with D/L-lactide in a wide range of compositions between 10% and 80% of M34. This work demonstrates the synthesis of biocompatible and biodegradable NRPs, which is of great interest in biological applications (see Scheme 2.11).

Some other methods, such as an oxidation polymerization, have also been applied for the synthesis of NRPs. The most common monomer is thiophene, to which nitroxide radicals couple through different linkages. TEMPO functional thiophene M35 was synthesized *via* esterification or etherification. Chemical oxidation of this type of monomers by $FeCl_3$ formed polymers along with some side reactions.[61] Lutkenhaus[62–64] reported the electrochemical oxidation polymerization and directly coated the corresponding NRPs on the electrode surface for further electrochemical studies (see Scheme 2.12).

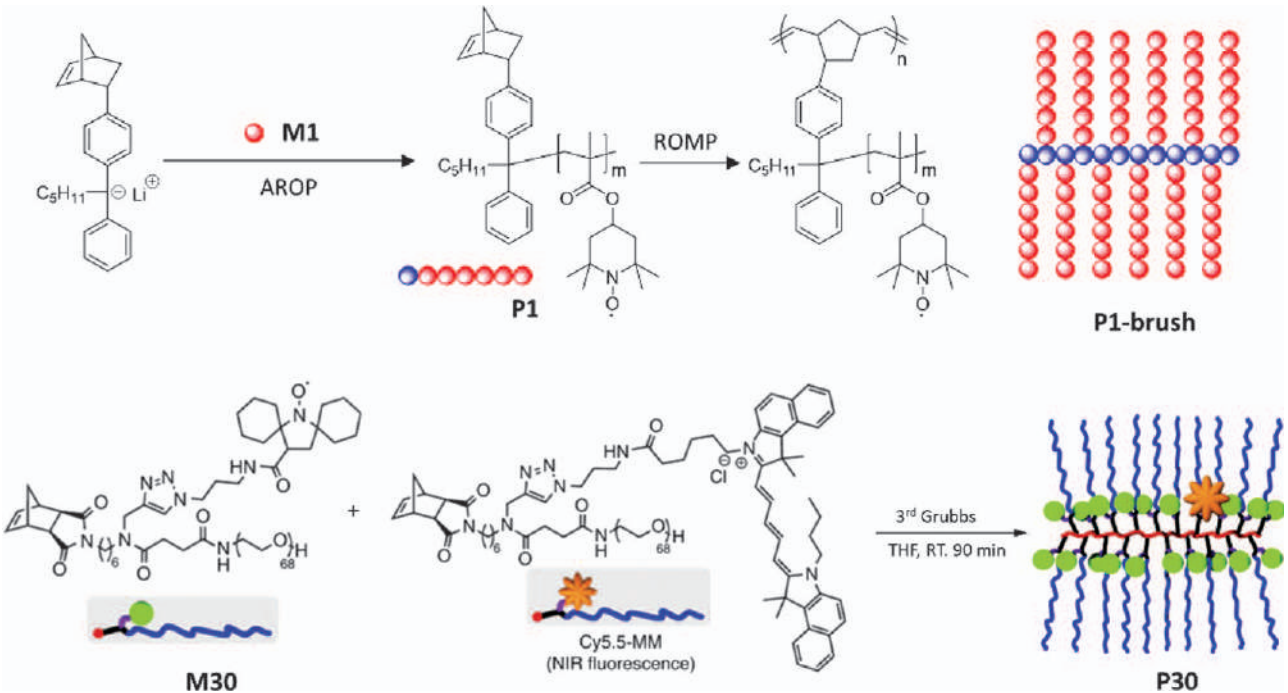


**Scheme 2.7** ROMP of norbornene-functional macromonomers to produce nitroxide-containing bottlebrush polymers. Reproduced from ref. 17 with permission from the Royal Society of Chemistry, from ref. 53 with permission from the American Chemical Society, Copyright 2014, and from ref. 55 with permission from Springer Nature, Copyright 2014.

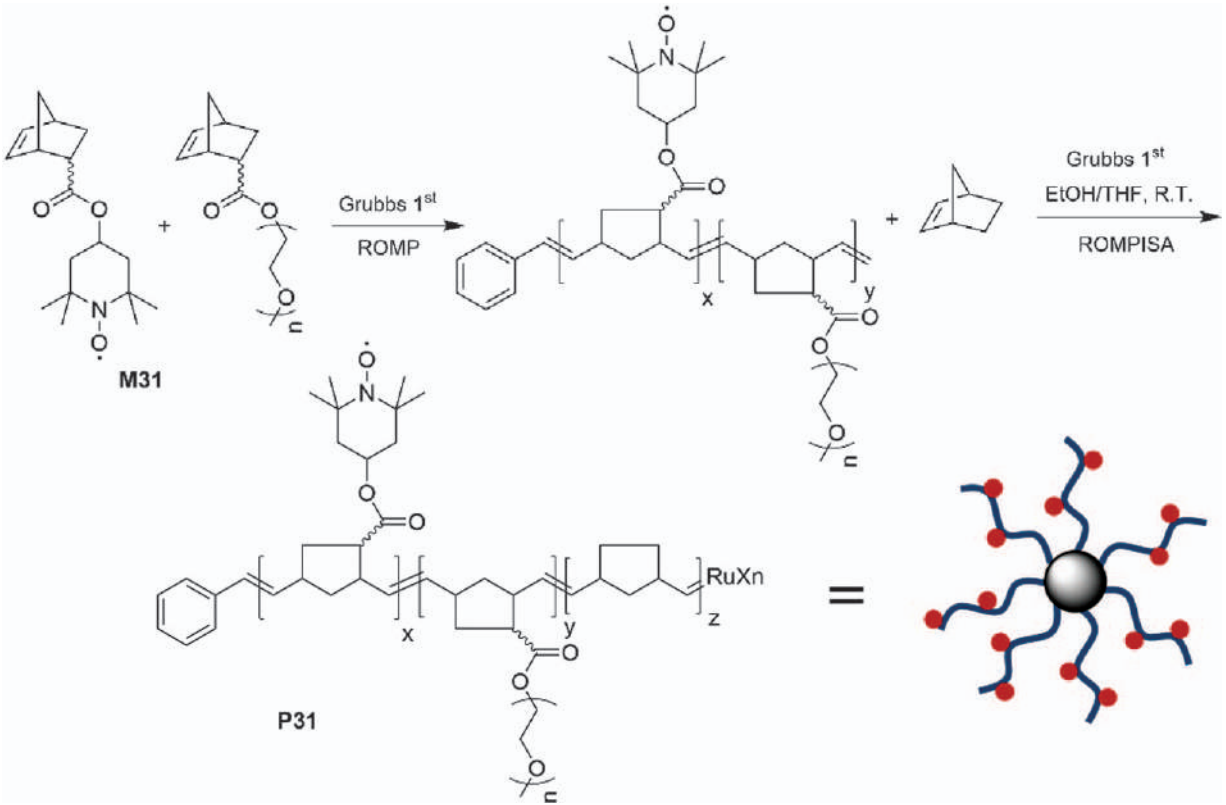


**Scheme 2.8** ROMPISA technique for the preparation of NRP nanoparticles.
Reproduced from ref. 56 with permission from John Wiley and Sons, © 2019 Wiley-VCH Verlag GmbH & Co. KGaA, Weinheim.

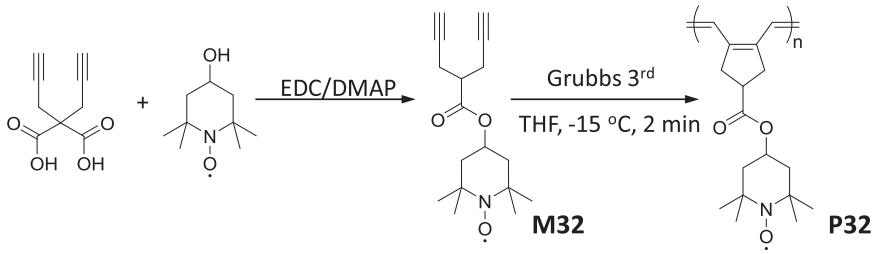


**Scheme 2.9** Ring-closure olefin metathesis polymerization of 1,6-heptadiyne functional TEMPO to produce TEMPO-containing conjugated polyacetylene. Adapted from ref. 58 with permission from the American Chemical Society, Copyright 2019.

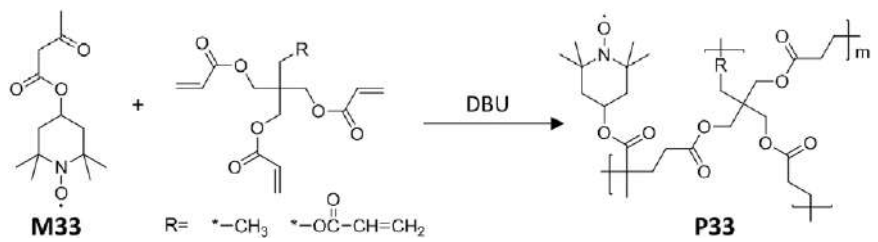


**Scheme 2.10** Michael polyaddition polymerization to synthesize a NRP network with polyester backbone.
Reproduced from ref. 59 with permission from the Royal Society of Chemistry.

Inspired by the adhesive mussel and taking advantage of the auto-oxidation polymerization of dopamine, Barner-Kowollik and Fairfull-Smith[65] recently designed a dopamine functional TEMPO derivative M36. In a basic buffer solution, the dopamine moiety in M36 polymerized to a polydopamine (P36) film coating on the substrate. The hydroxylamine salt was converted to nitroxide radicals through aerobic oxidation under basic condition (see Scheme 2.13). This polydopamine-coated surface with nitroxide radicals has potential antibacterial applications and in preventing initial biofilm formation.[66]

Many NRPs can be prepared through the post-polymerization conversion of precursor polymers to NRPs. This strategy allows the design of a variety of nitroxide radical precursor monomers [*i.e.*, (meth)acrylate, (meth)acrylamide and styrene] and the polymerization by both FRP and LRP techniques[17] (see Scheme 2.14). However, due to the basic secondary amine, aminolysis of the RAFT agent occurred during polymerization and required acidic conditions to obtain controlled molecular weight distributions.[67] ATRP of these monomers produced polymers with molecular weights only up to 30 kDa.[67] To overcome these limits, Gohy[68] reported the synthesis of NRP P37 through a SET-LRP process followed by oxidation, in which M37 was polymerized with copper (0)/PMDETA (*N,N,N′,N″,N″*-pentamethyldiethylenetriamine) as a

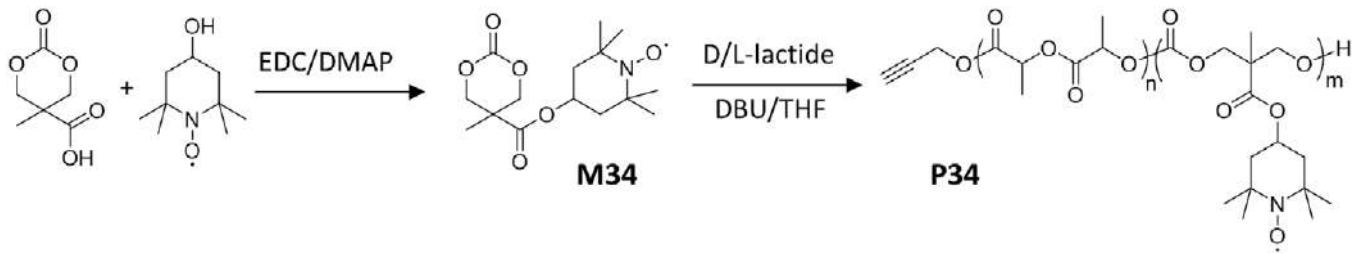


**Scheme 2.11** Ring-opening polymerization of cyclic carbonate to prepare NRP with polycarbonate backbone. Reproduced from ref. 60 with permission from the Royal Society of Chemistry.

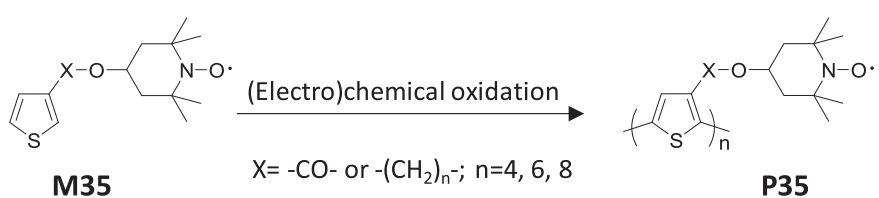


**Scheme 2.12** (Electro)chemical oxidation polymerization of thiophene functional TEMPO to prepare NRP with conjugated polythiophene backbone.

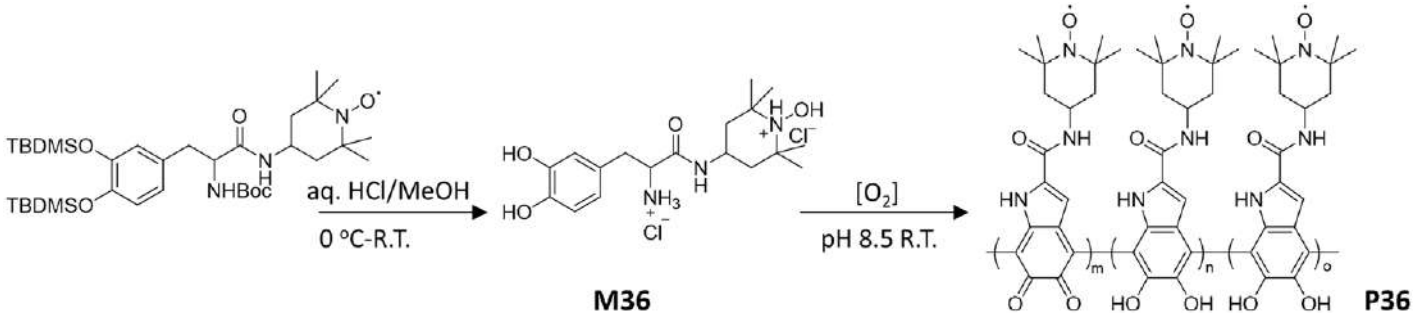


**Scheme 2.13** Oxidation polymerization of dopamine functional TEMPO to prepare surface-immobilized NRP.
Reproduced from ref. 65 with permission from the American Chemical Society, Copyright 2018.

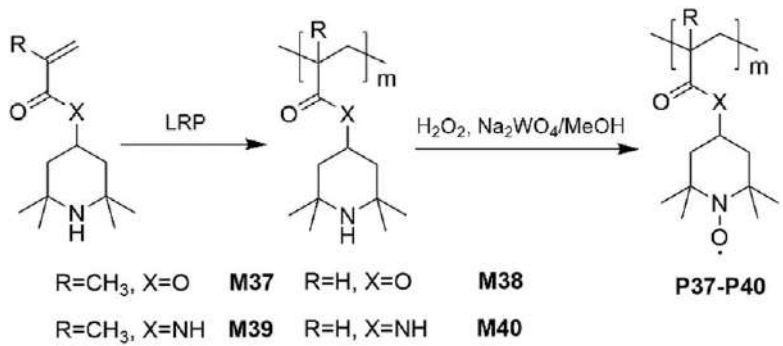


**Scheme 2.14** Synthesis of NRPs through LRP of 2,2,6,6-tetramethylpiperidine functional (meth)acrylate or (meth)acrylamide followed by oxidation.
Reproduced from ref. 17 with permission from the Royal Society of Chemistry.

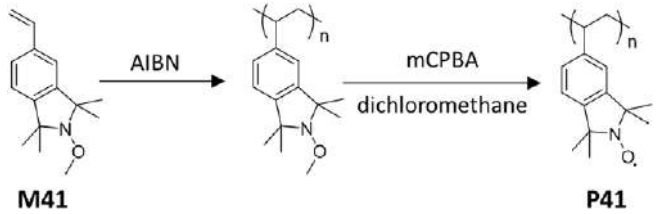


**Scheme 2.15** Synthesis of TMIO polymer through FRP followed by oxidation deprotection.
Reproduced from ref. 74 with permission from the American Chemical Society, Copyright 2018.

catalyst at 40 °C with an apparent propagation rate constant $k_{p,app}$ of $1.557\times10^{-4}$ $s^{-1}$ and $M_n$ up to 11 kDa. Jia[69] further modified the polymerization condition by replacing PMDETA with $Me_6$TREN (tris[2-(dimethylamino)ethyl]amine), a ligand more efficient for SET-LRP. The polymerization was much faster with a $k_{p,app}$ of $8.1\times10^{-4}$ $s^{-1}$ at 25 °C. More importantly, this condition produced NRPs (P37) with an $M_n$ up to 169 kDa, which possessed very low solubility in commonly used organic electrolytes and showed a more stable electrochemical performance when used as cathode materials. LRP can also grow NRPs (P37–P40) from functional surfaces through surface-initiated ATRP followed by oxidation, producing patterned films that can be used for transparent devices.[70–72]

1,1,3,3-Tetramethylisoindolin-2-yloxyl (TMIO) is another nitroxide structure which has been well-studied by Bottle.[73] The redox potential of TMIO was higher than TEMPO derivatives. Recently, Blinco[74] designed a methyl-protected TMIO with a vinyl group M41. After FRP, the polymer was deprotected by *meta*-chloroperbenzoic acid (*m*CPBA) to convert it to a TMIO radial polymer P41 (see Scheme 2.15). P41 showed a redox potential of about 1.2 V *vs.* SHE, having great potential in a high-voltage polymer battery.

Another approach to protect nitroxide radicals is through a nitroxide radical coupling (NRC) reaction.[75,76] Ecker and co-workers[77] reported the ATRP of an alkoxyamine methacrylate M42, producing protected NRP P42. Comparing with monomer M37, ATRP of M42 produced the precursor polymer P42 with a much narrower dispersity ($Đ = 1.1$) due to no interference from the secondary amine. The alkoxyamine moieties on P42 can be decomposed upon heating in the presence of oxygen, regenerating nitroxide radicals with an efficiency of 93% (see Scheme 2.16).

Apart from cyclic nitroxide radicals, Suga *et al.*[78] designed noncyclic nitroxide radicals such as 4-(*N*-tert-butyl-*N*-doxylamine)benzene and its derivatives. To make polymer counterparts using FRP, this nitroxylstyrene was protected by tert-butyldimethylsilyl (TBDMS) to form monomers M43 with different substitutions. Polymer P43 was obtained through FRP followed by the successive deprotection of TBDMS groups and the oxidation of hydroxylamine. Redox potentials of this type of radicals were greatly influenced by R substituents (see Scheme 2.17). Where there was no substitution on the

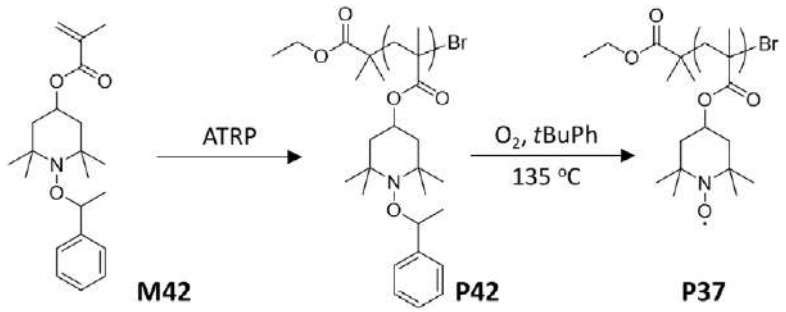


**Scheme 2.16** Synthesis of poly(TEMPO methacrylate) through ATRP of alkoxyamine functional monomer followed by thermal deprotection.
Reproduced from ref. 77 with permission from the American Chemical Society, Copyright 2013.

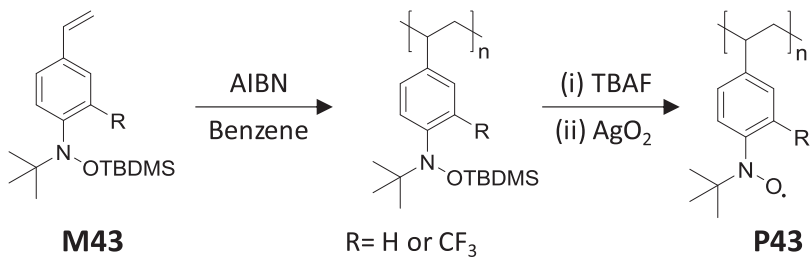


**Scheme 2.17** Synthesis of phenyl nitroxide polymer through FRP followed by successive deprotection and oxidation.
Reproduced from ref. 78 with permission from the American Chemical Society, Copyright 2007.

phenyl ring (*i.e.*, R=H), the radical showed a reversible oxidation reaction (*i.e.*, $NO^{\bullet}/NO^{+}$) with potential of 0.83 V (*vs.* Ag/AgCl). When R was switched to $CF_3$, the oxidation reaction was no longer reversible, but a reversible reduction couple (*i.e.*, $NO^{-}/NO^{\bullet}$) was observed with a potential of −0.92 V. This work suggests redox potentials of phenyl nitroxide radicals can be easily altered through the electronic inductive effect on the phenyl ring.

When NRPs were used as redox-active materials for biological applications or organic catalysts, they may not require having very high radical densities. In these cases, post-modification would be a simple way to make redox-active NRPs. Poly(*N*-acryloxysuccinimde) (PNAS) as one of the most used functional polymers has been employed to prepare functional NRPs. Bergbreiter[79] reported the post-modification of PNAS with both 2-propanamine and small-molecule nitroxide radical M44, which produced a random copolymer comprised of thermal-responsive poly(*N*-isopropyl acrylamide) segments and pendent nitroxide radicals (see Scheme 2.18). Upon the redox reaction of nitroxide radicals, the lower critical solution temperature (LCST) of P44 changed accordingly, demonstrating both redox- and

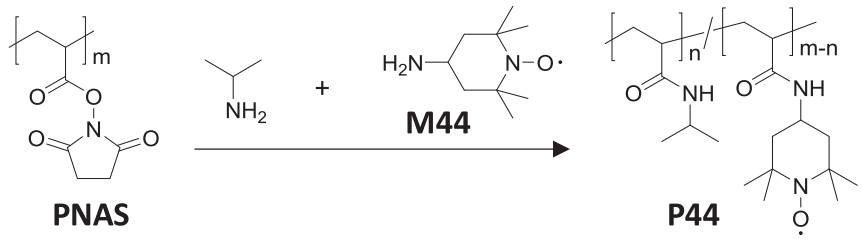


**Scheme 2.18** Post-modification of PNAS with 4-amino-TEMPO and isopropylamine to prepare thermo- and redox-responsive NRP.
Reproduced from ref. 79 with permission from the Royal Society of Chemistry.

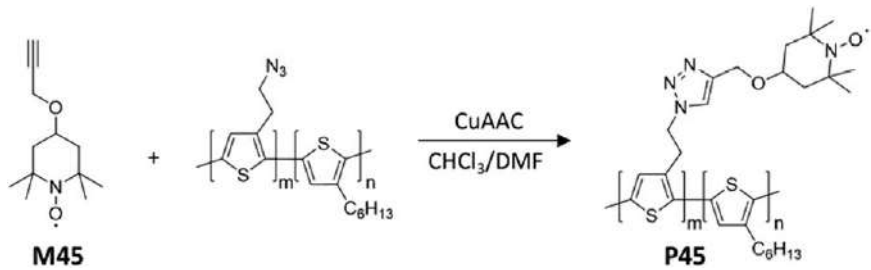


**Scheme 2.19** Post-modification of azide-functional polythiophene with 4-propargyl-TEMPO to produce NRP with polythiophene backbone.
Reproduced from ref. 82 with permission from the Royal Society of Chemistry.

thermal-responsive properties. Similarly, Theato[80] employed poly(pentafluorophenyl acrylate) as a reactive functional polymer precursor and through introducing an additional amine-functionalized azobenzene produced a triple responsive random copolymer that possessed thermal-, light- and redox-responsive features.

Previous work has proved that the existence of nitroxide radicals does not influence a copper-catalysed alkyne-azide cycloaddition (CuAAC) 'click' reaction, which provides great opportunities for the synthesis of NRPs *via* post-modification.[81] For example, to synthesize polythiophene-based NRP avoiding the (electro)chemical oxidation, Wolf[82] synthesized polythiophene with azide functionalities and coupled it with alkyne functional nitroxide radical M45 to produce NRP P45 (see Scheme 2.19). CuAAC chemistry was also applied for making NRP-coated silica nanoparticles as a recyclable catalyst for the oxidation reaction.[83]

Post-modification also allows to prepare NRPs with some unusual backbone that is not accessible through common polymerization techniques. For instance, Suguro[84] synthesized NRPs with polysiloxane backbone through hydrosilylation of poly(methylhydrosiloxane) (PMHS) with 4-allyl-TEMPO

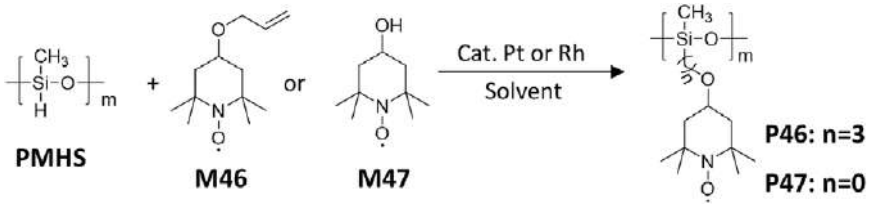


**Scheme 2.20** Synthesis of NRP with poly(methylsiloxane) backbone through hydrosilylation reaction with functional TEMPO radicals.
Reproduced from ref. 17 with permission from the Royal Society of Chemistry.

M46 or 4-hydroxyl-TEMPO M47 in toluene using Pt or Rh complex as catalyst (see Scheme 2.20). The highest reaction efficiency was about 76%, which strongly depended on the selection of catalysts. P47 demonstrated higher discharge capacity and electrochemical redox stability than P46 primarily due to the lower molecular weight per radical and more flexible siloxane backbone for P47 than P46.

Other post-modification methods include esterification, etherification, and amination reactions between functional polymers and nitroxide radicals. Masuda[85] reported the synthesis of cellulose-based NRPs by coupling the carboxylic acid functional nitroxide radicals with cellulous. The cellulose-based backbone allowed the preparation of paper-like or fibre-like electrochemical materials. Nagasaki[40] prepared diblock NRPs through the etherification or amination reactions of poly(4-chloromethyl styrene) (PCMS) with M43 or M46, respectively. These pH-sensitive or pH-insensitive linkages between the radical groups and the backbone dictated their self-assembly properties and applications as a scavenger for reactive oxygen species *in vivo*.[39]

### 2.2.3 Redox Reaction of Phenoxyl Radicals

Phenoxyl radical is an oxygen-centred radical which exists in many natural products and is involved in many biological processes.[86] Although first introduced in 1914, it was not until the 1960s that the existence of phenoxyl radical was evidenced by EPR spectroscopy.[87] One of the typical phenoxyl radicals is called galvinoxyl, named after Galvin who first reported the stable phenoxyl radicals.[88] Phenoxyl radicals can be obtained through oxidation of phenol by weak oxidants such as lead oxide and silver oxide. Phenoxyl radicals like galvinoxyl are stable in air over a few months. The stability of galvinoxyl is attributed to the delocalization of electrons over the conjugated aromatic system and the bulky tert-butyl groups that prevent the side reactions and the termination. The redox reaction of this phenoxyl radical relies on gaining one electron to form a phenolate anion. However, this redox process is often coupled with protons which strongly depend on the pH of the solution[89,90] (Scheme 2.21).

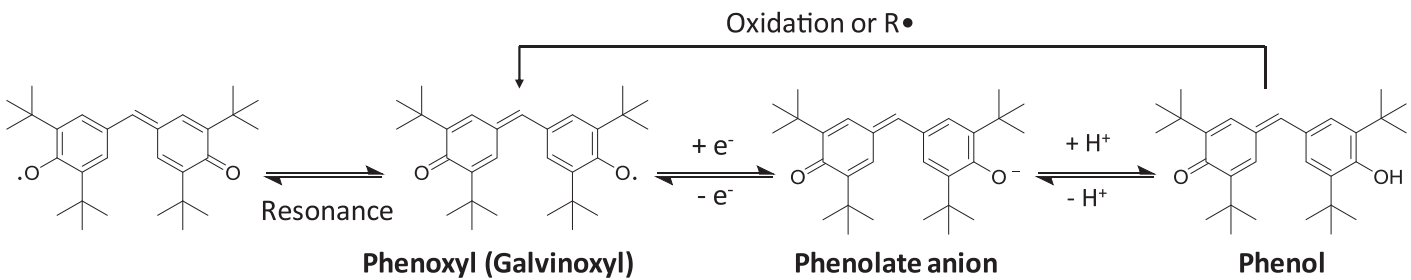


**Scheme 2.21** Resonance structures and proton-coupled one-electron redox reaction of galvinoxyl radical.

### 2.2.4 Redox Polymers Consisting of Phenoxyl Radicals

Phenoxyl radicals act as radical scavengers in many biological processes. They have also been used as inhibitors, such as butylated hydroxytoluene (BHT), to prevent the FRP of monomers. Like nitroxide radicals, the synthetic strategies for phenoxyl-containing polymers should avoid a radical process. Nishide[91] reported the synthesis of phenoxyl radical polymers with a polystyrene backbone. Monomers consisting of phenol groups M48 and M49 were polymerized by FRP. Oxidation of these precursor polymers by a lead oxide or potassium ferrocyanide produced phenoxyl radical polymers P48 and galvinoxyl radical polymer P49 with $M_n$ of 31 kDa (see Scheme 2.22). It was found that the bulky phenol structure had less interference on FRP. The group later designed similar polymers with a conjugated polythiophene backbone to study their magnetic property.[92]

Recent research on phenoxyl radical polymers focuses on applications in energy storage. For this purpose, Nishide[91] prepared polymer gels consisting of galvinoxyl radicals using monomer M49 and a cross-linker. The corresponding polymer gel was used as an anode and paired with P21 to fabricate an organic polymer battery. To explore the direct polymerization of phenoxyl radical monomers, Schubert[93] deigned 2,6-di-tert-butyl-phenoxyl-containing norbornene monomers M50 and M51. For a comparison, a 2,6-dimethyl-phenoxyl analogue M52 was also synthesized. ROMP of these monomers using 3rd-generation Grubbs catalyst produced polymers with very high molecular weights and low dispersity. Instead, using 2nd-generation Grubbs catalyst led to the gel formation due to the relatively low initiating activity. These polymers that were insoluble in many common solvents still found applications as electrode materials for energy storage (see Scheme 2.23).

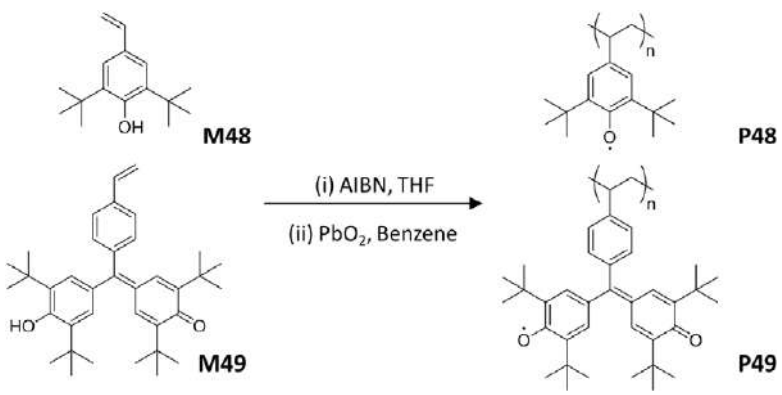


**Scheme 2.22** Synthesis of phenoxyl- or galvinoxyl-containing polymers through FRP followed by oxidation.
Reproduced from ref. 17 with permission from the Royal Society of Chemistry.

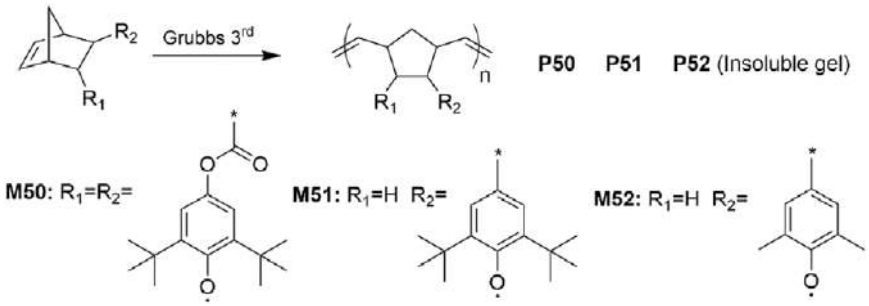


**Scheme 2.23** ROMP of norbornene functional phenoxyl radicals with different substituents.
Reproduced from ref. 17 with permission from the Royal Society of Chemistry.

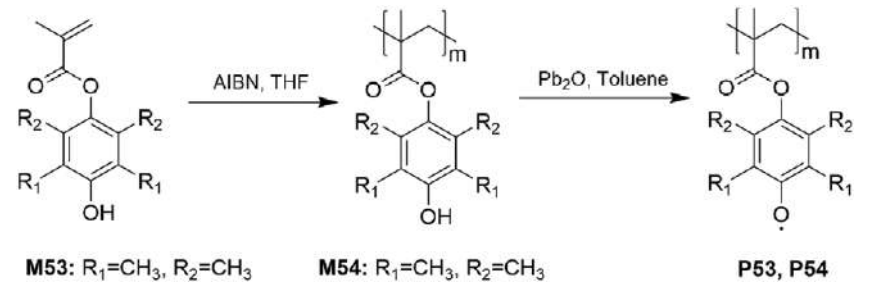


**Scheme 2.24** Synthesis of phenoxyl PMMA through FRP of phenol functional methacrylate followed by oxidation.
Reproduced from ref. 17 with permission from the Royal Society of Chemistry.

Schubert has also prepared phenol-containing methacrylates M53 and M54.[94] These monomers were polymerized through FRP, followed by oxidation resulting in phenoxyl radical polymers P53 and P54 (see Scheme 2.24). EPR characterization of these polymers P50–P54 revealed that polymers P49–P52 obtained by ROMP possessed higher radical concentration (91%) than those, P53–P54, through post-polymerization oxidation (73%), again suggesting the unavoidable side reactions to phenol groups. Electrochemical performance indicated P49 had great potential to be a redox polymer anode material for energy storage.

## 2.2.5 Redox Reaction of Verdazyl Radicals

Verdazyl is a nitrogen-centred radical in which the stability is originated from the delocalization of the unpaired electron on the six-membered ring and the sterically hindered structure. Verdazyl is very stable in an air and water environment. The redox behaviour of the verdazyl radical and its substituted derivatives has been systematically studied.[95] The verdazyl is a

7-π-electron neutral radical, which forms a 6-π-electron cation after oxidation by losing one electron or an 8-π-electron anion after reduction by gaining one electron (see Scheme 2.25). The redox potential and reversibility of this two-electron redox reaction strongly depends on its structure. Hicks[95] found that the potentials for the reduction of verdazyls (*i.e.*, redox couple of 8-$\pi^-$/7-$\pi^\bullet$) were relatively constant (*i.e.*, $\sim -1.25$ V *vs.* Fc/$Fc^+$). The oxidation potentials (*i.e.*, redox couple of 7-$\pi^\bullet$/6-$\pi^+$), on the other hand, increased from about $-0.3$ to 0.2 V *vs.* Fc/$Fc^+$ when the X changed from $CH_2$ to C=O. Although studies on verdazyl radicals have been focused on magnetic properties and coordination chemistries, their reversible two-electron redox makes them a promising material for electrochemical energy storage.

## 2.2.6 Redox Polymers Consisting of Verdazyl Radicals

So far, there have not been many reports on the synthesis of verdazyl radical polymers. In limited examples, Gilroy[96] designed norbornene functional verdazyl M55 through esterification of hydroxyl functional norbornene and carboxylic acid functional verdazyl with an overall yield of 62%. Further ROMP by Grubbs 3rd-generation catalyst produced 6-oxoverdazyl polymer P55 with $M_n$ of 46 kDa and a very low dispersity $Đ$ of 1.07. Electrochemical characterization of polymer P55 demonstrated a reversible two-electron redox process like monomer M55 (see Scheme 2.26). However, if this polymer is used as electrode materials, the theoretical capacity will be only 103 mAh $g^{-1}$ even with two-electron storage, primarily due to its high molecular weight per radical (*i.e.*, 506 g $mol^{-1}$). Therefore, the design of verdazyl-containing monomers with low molecular weight would be more attractive for energy storage applications.

Fanchini and Gilroy[97] reported the synthesis of a 6-oxoverdazyl radical methacrylate P56. First, a verdazyl radical precursor, (4-tetrazanyl)-phenyl methacrylate M56 was synthesized. FRP of M56 produced the tetrazane polymer, which after oxidation by *p*-benzoquinone formed the verdazyl radical polymer P56 (see Scheme 2.27). Electrochemical characterization indicated by switching the isopropyl to phenyl in P56, the redox potentials for 7-$\pi^\bullet$/6-$\pi^+$ and 8-$\pi^-$/7-$\pi^\bullet$ increased by 0.22 V and 0.53V, respectively.

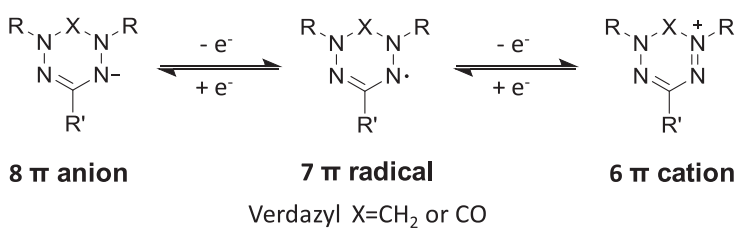


**Scheme 2.25** Two-electron redox reaction of verdazyl radical.
Reproduced from ref. 95 with permission from the American Chemical Society, Copyright 2007.

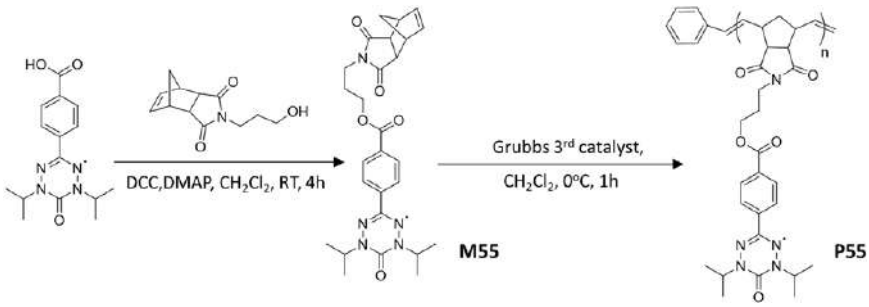


**Scheme 2.26** Synthesis of verdazyl-containing polymer through ROMP of norbornene functional radical monomer.
Reproduced from ref. 17 with permission from the Royal Society of Chemistry.

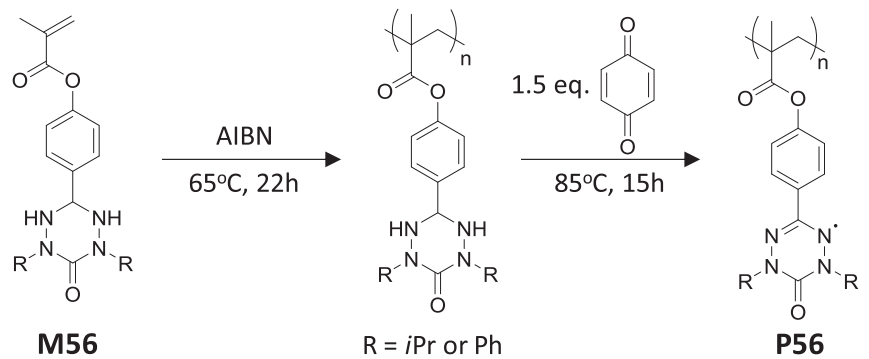


**Scheme 2.27** Synthesis of verdazyl-containing PMMA through FRP followed by oxidation.
Reproduced from ref. 17 with permission from the Royal Society of Chemistry.

Moreover, the theoretical capacity of P56 is 155 mAh $g^{-1}$, much higher than P55. This work showed the capability of structure design on tuning the electrochemical properties of the verdazyl radical.

Chahma[98] reported the successful electrochemical polymerization of both verdazyl functional terthiophene M57 and its tetrazane precursor to produce the verdazyl radical containing polythiophene P57 (see Scheme 2.28). M57 can be obtained through either chemical oxidation by *p*-benzoquinone or electrochemical oxidation at 1.0 V (*vs.* Ag/AgCl) and was further electrochemically oxidized to produce P57 under 1.3 V potential. Alternatively, a 1.3 V potential was directly applied to the tetrazane precursor to polymerize terthiophene and simultaneously oxidize tetrazane to verdazyl radical. This was, for the first time, the synthesis of a radical conjugated polymer through one-step electrochemical oxidation and polymerization of radical precursor monomer.

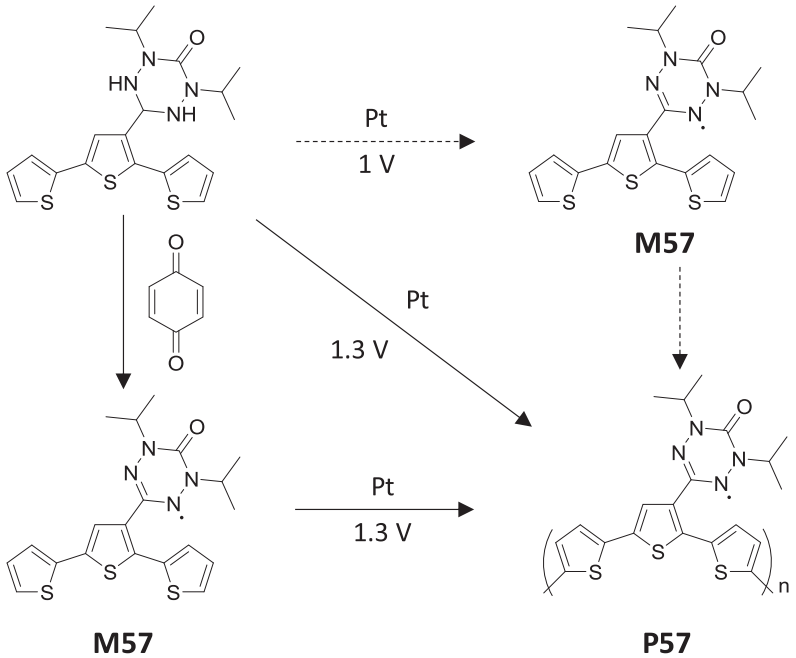


**Scheme 2.28** Electrochemical polymerization of verdazyl functional terthiophene to produce conjugated verdazyl radical polymer.
Reproduced from ref. 17 with permission from the Royal Society of Chemistry.

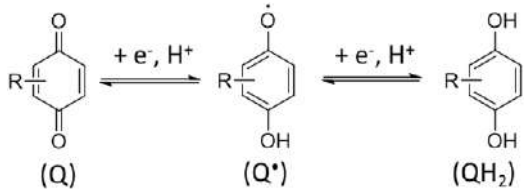


**Scheme 2.29** Proton-coupled two-electron redox reaction of benzoquinone.

## 2.2.7 Redox Reaction of Benzoquinone

Quinone and its derivatives can be found in nature and play a variety of important roles in living organisms (*i.e.*, enzyme NADH). Their critical functions stem from the redox property that involved in many biological processes.[99] Upon a proton-coupled electron transfer, benzoquinone (Q) is reduced to semiquinone ($Q^{\bullet}$) and further to hydroquinone ($QH_2$) (see Scheme 2.29). In the presence of oxygen, $Q^{\bullet}$ and $QH_2$ are oxidized back to Q, while oxygen is reduced to a superoxide anion radical ($O_2^{\bullet -}$).[100] Electrochemically, quinone can also undergo this overall reversible two-electron redox reaction, which has made quinone into one of the prevalent organic

materials for energy storage. The redox potentials of benzoquinone derivatives can be altered by introducing different substituents to the phenyl ring, providing great opportunities for designed quinones for diverse applications.

## 2.2.8 Redox Polymers Consisting of Quinone

Hydroquinone has three isomers: hydroquinone (1,4-hydroquinone), resorcinol (1,3-hydroquinone), and catechol (1,2-hydroquinone). The redox of resorcinol was not reversible and has been rarely studied. Polymers consisting of catechols are mostly made from dopamine and its analogues, which have been extensively studied and reviewed,[101] and will not be discussed here. In this section, we will focus on the synthesis of polymers consisting of 1,4-benzoquinone, 1,4-hydroquinone and their derivatives.

Some of the early quinone polymers were quinone-amine additives, namely poly(aminoquinone) or PAQ, which were synthesized through a 1,4-addition reaction of a diamine with benzoquinone, a similar reaction to quinone amination with proteins and peptides.[102] In the 1980s, Erhan[103] was the pioneer in using different diamine M58 to react with quinone. First the addition of amine generated a hydroquinone chain end, which was oxidized by another quinone molecule to form a quinone chain end. Repeating this reaction cycle produced oligomer P58 (see Scheme 2.30). The disadvantage of this reaction was the low atom efficiency with a large amount of hydroquinone by-product. PAQ has found great affinity to metal surfaces and is widely used as a coating to remain dry and prevent rust. Using a similar reaction, Armand[104] recently prepared PAQ/nanocarbon composite as electrode materials for aqueous-based energy storage.

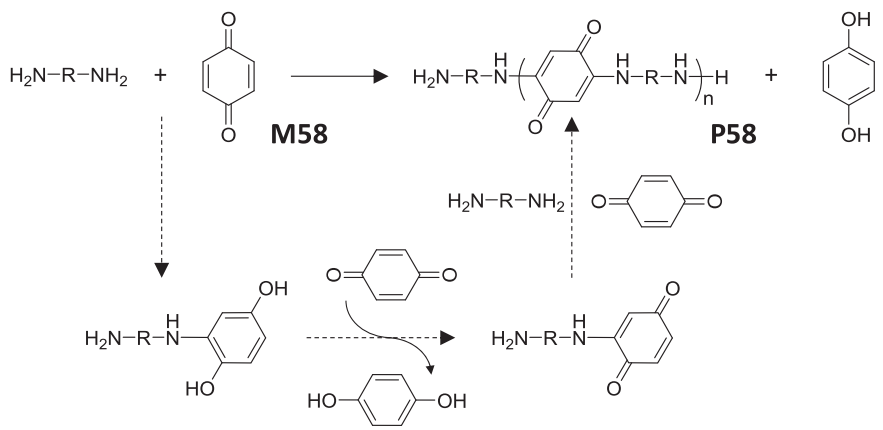


**Scheme 2.30** Synthesis of poly(aminoquinone) through aza-Michael addition step polymerization.
Reproduced from ref. 103 with permission from Elsevier, Copyright 1998.

As quinones usually act as radical scavengers (although not as efficient as nitroxide radical), FRP of quinone-based monomers could be challenging. To explore this, Schubert[94] designed two benzoquinone-based methacrylates, in which one was unsubstituted M59 and the other had methyl groups on 2-, 3-, and 5-position of benzoquinone M60. Polymerization of M59 was unsuccessful due to a severe radical termination reaction as expected, whereas methyl substitution can significantly prevent side reactions of quinone with radicals, hence producing the corresponding polymer P60 (see Scheme 2.31). However, the ester bonds in P60 may be hydrolysed when applied in aqueous electrolyte at the base condition.

Polymers consisting of benzoquinone can also be achieved through post-polymerization conversion. In this case, hydroxyl groups of hydroquinone were protected, and the corresponding monomers can be polymerized through either radical or electrochemical polymerization. For instance, a mesogen-jacketed liquid crystalline monomer M61 was polymerized by nitroxide-mediated radical polymerization (NMRP).[105] Hydrolysis of the corresponding liquid crystalline polymer produced poly(vinylhydroquinone), which can be further converted to poly(vinyl benzoquinone) P61 upon oxidation (see Scheme 2.32). The low molecular weight of repeating units (134 $g\,mol^{-1}$) together with two-electron redox afforded P61 with a theoretical capacity of 400 $mAh\,g^{-1}$, much higher than current lithium composite cathodes.

Alternatively, a library of pyrrole functional 1,4-dimethoxybenzene monomers with different linkage (M62) was prepared.[106,107] After electrochemical polymerization, a series of conducting redox polymers based on polypyrrole with hydroquinone pendant groups were obtained (P62) (see Scheme 2.33). It seems the longest linker would be beneficial for energy storage applications since the highly efficient utilization of pendant quinone groups with less internal charge transfer to the conjugated polypyrrole backbone.

From the above examples, the synthesis of well-defined benzoquinone polymers has been very challenging due to the high reactivity of the quinone ring to many functional groups and radicals. In contrast, anthraquinone has no protons on the quinone ring and thus eliminates the possible side reactions. Polymers with pendant anthraquinone possess highly stable redox activity and show great potential as polymer electrode materials.

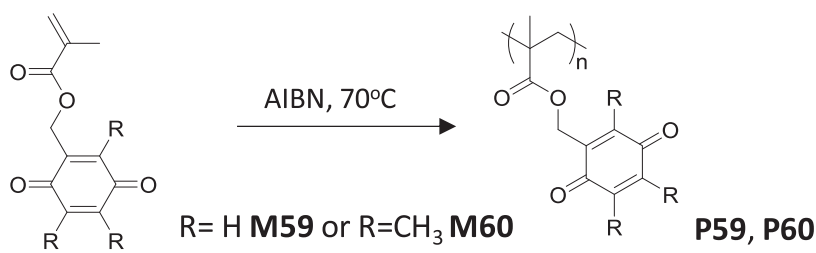


**Scheme 2.31** Synthesis of substituted poly(benzoquinone methacrylate) through FRP. Reproduced from ref. 94 with permission from John Wiley and Sons, © 2014 Wiley-VCH Verlag GmbH & Co. KGaA, Weinheim.

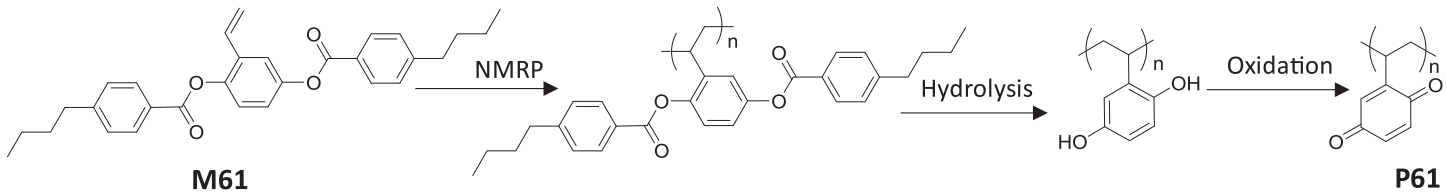


**Scheme 2.32** Synthesis of poly(vinyl benzoquinone) through NMRP of protected benzoquinone monomer followed by successive deprotection and oxidation.
Reproduced from ref. 105 with permission from the American Chemical Society, Copyright 2001.

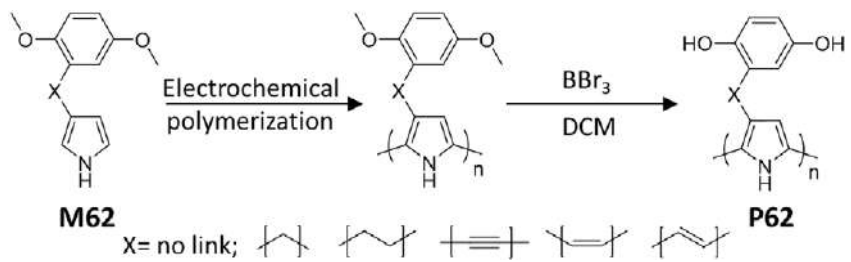


**Scheme 2.33** Synthesis of benzoquinone-containing polymers with conjugated polypyrrole backbone and different linkers.
Reproduced from ref. 107 with permission from the Royal Society of Chemistry.

Weddell[108] reported the synthesis of 2-acrylamidoantraquinone M63 from 2-aminoanthraquinone, and *via* FRP they obtained poly(2-acrylamidoantraquinone) P63. This polymer was originally used as a photosensitizer for cross-linking of nylon-6,6 fibre and film. With more attention on organic energy storage, polymers with pendent anthraquinone or its derivatives were continuously developed as electrode-active materials. For instance, Nishide[109] converted 2-aminoanthraquinone to 2-vinylanthraquinone M64 through a two-step modification. FRP of M64 produced P64 as an anode for a high-density and rechargeable polymer/air battery. Thanks to the absence of any hydrolysable ester or amide linkages, P64 demonstrated a nearly 100% Coulombic efficiency at a strong base condition (*i.e.*, pH 14). Schubert[110] further modified M64 to tetracyano-9,10-anthraquinonedimethane (TCAQ) functional monomer, M65. Polymerization of M65 produced polyTCAQ, P65, with Mn = 26.4 kDa and $Đ$ of 1.87 (see Scheme 2.34). This modification significantly increased redox potential from about −0.6 V for P64 to −0.2 V (*vs.* SHE) for P65. Whereas the theoretical capacity of the materials decreased

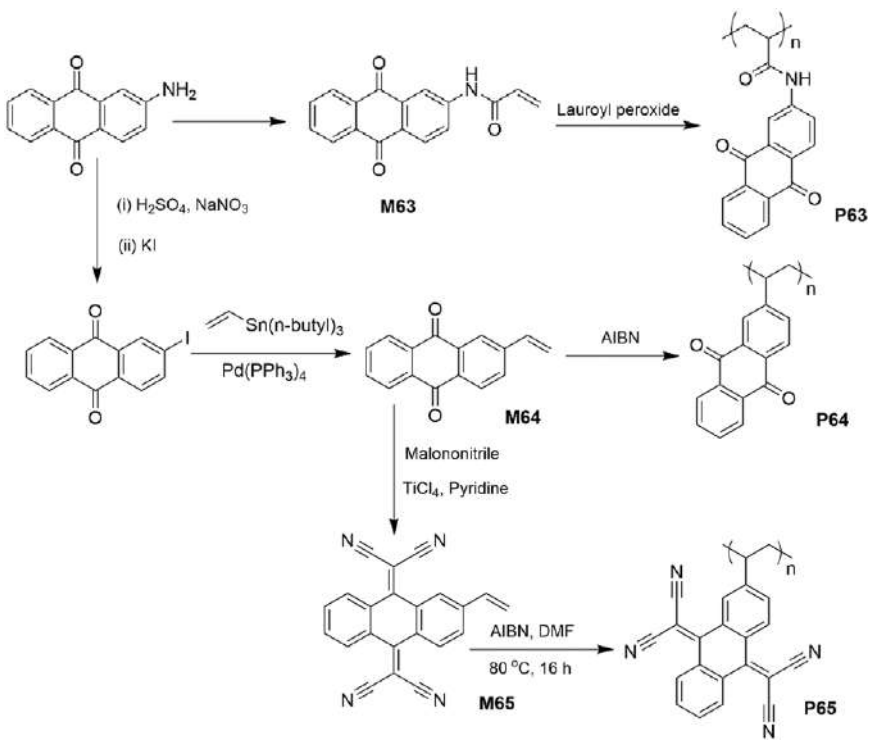


**Scheme 2.34** Synthesis of anthraquinone-containing polymers through modification of 2-amino-anthraquinone to different monomers followed by FRP. Reproduced from ref. 108 with permission from Elsevier, Copyright 1993, from ref. 109 with permission from the American Chemical Society, Copyright 2011, and from ref. 110 with permission from the Royal Society of Chemistry.

from 229 to 162 mAh $g^{-1}$ due to the increased molecular weight of repeating units. Later, the group designed some anthraquinone analogue monomers, dithiophenedione[111] and naphthotriazolequinonestyrene (NTQS),[112] and converted them to polymers. Poly(NTQS) had similar theoretical capacities as P63, but when used as a cathode in lithium-ion batteries (LIBs), they showed continuous fading of the capacity over cycles due to their unstable redox species.[111]

Taking the advantages of ROMP for its tolerance on functional groups, Nishide[113] designed a norbornene functional anthraquinone M66. Synthesis of M66 can be achieved through Suzuki coupling of two functional anthraquinone precursors with 2,5-norbornadiene (see Scheme 2.35). ROMP of M66 by using Grubbs 2nd-generation catalyst resulted in P66 with a molecular weight of 600 kDa, much higher than that of P64 (*i.e.*, 78 kDa).[109] When both P64 and P66 were used as an anode for a polymer/air battery, P66 exhibited greater stable cycling property (*i.e.*, 95% after 500 cycles) than P64 (*i.e.*, 91% after 300 cycles) possibly due to the lower solubility of P66 than P64 in electrolytes.

Similarly, the Pd catalyst was also used to polymerize the olefin functional anthraquinone. Schubert[114] designed 1,6-heptadiene functional monomer M67 through esterification between 2,2-diallylmalonic acid and 2-(hydroxymethyl)-anthraquinone. Owing to the decarboxylation as proved in a later report,[58] only mono-anthraquinone functional M67 was obtained with a yield of 85%. Compared to the cyclopolymerization of 1,6-heptadiyne, polymerization of M67 required a more complex catalyst system including a Pd catalyst and a co-catalyst $NaB[C_6H_3\text{-}3,5\text{-}(CF_3)_2]_4$ (NaBARF) (see Scheme 2.36). The polymerization took 5–20 h to reach a molecular weight of 53 kDa with a $Đ$ of 1.36–1.66. Unlike the polymerization of 1,6-heptadiyne which formed a conjugated backbone, cyclopolymerization of 1,6-heptadiene produced saturated backbone which had no interference with the redox of anthraquinone units.

Utilizing the reactivity of quinone with radical, Moulay[115] reported a direct conjugation of 1,3-benzoquinone (M68) and 1,4-benzoquinone (M58) to water-soluble polyacrylic acid (PAA). In the presence of $K_2S_2O_8$ and $AgNO_3$, PAA underwent an oxidation decarboxylation reaction and formed ethyl radical on the backbone which then added to the quinone and yielded hydroquinone polymer (PAA-HQ), which after oxidation by ceric ammonium nitrate formed poly(vinylbenzoquinone) P68 (see Scheme 2.37). This method was very straightforward, but only reached a maximum grafting efficiency of 35%.

Funt[116] reported the Friedel–Craft acylation reaction for the synthesis of anthraquinone-based polystyrene. Anthraquinone 2-carbonyl chloride M69 was reacted with polystyrene in the presence of $AlCl_3$. The corresponding product consisted of less than 49% of anthraquinone units. Later, Nishide[117] modified the procedure by using anthraquinone 2-carboxylic acid M70 and PCMS as polymer scaffold. This esterification reaction was catalysed by organic base DBU and resulted in the polymer P70 with nearly quantitative functionalization through NMR characterization (see Scheme 2.38). A high content of anthraquinone in these polymers is critical to delivering high capacity when used as electrode materials.

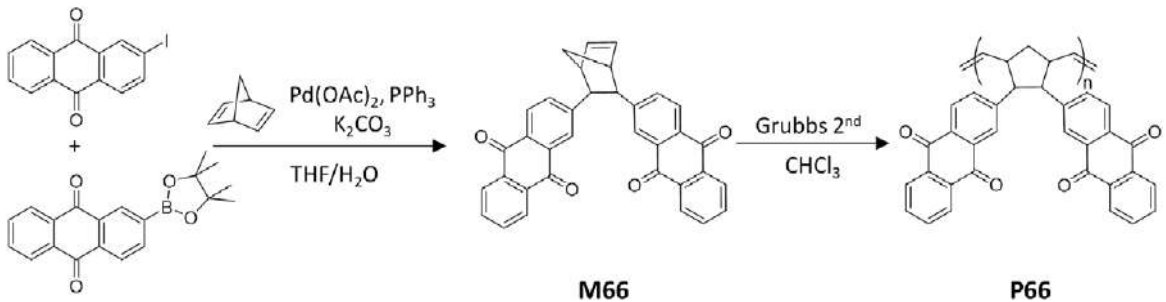


**Scheme 2.35** Direct synthesis of anthraquinone-containing polymers through ROMP of norbornene functional monomer. Reproduced from ref. 113 with permission from the American Chemical Society, Copyright 2015.

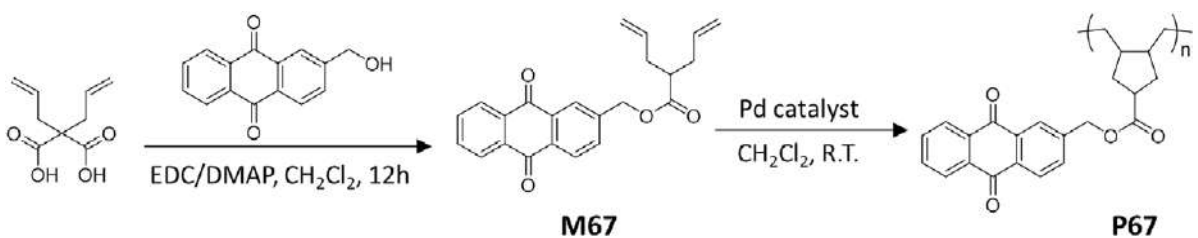


**Scheme 2.36** Synthesis of benzoquinone-containing polymers through cyclopolymerization of 1,6-heptadene functional monomer. Reproduced from ref. 114 with permission from John Wiley and Sons, © 2016 Wiley Periodicals, Inc.

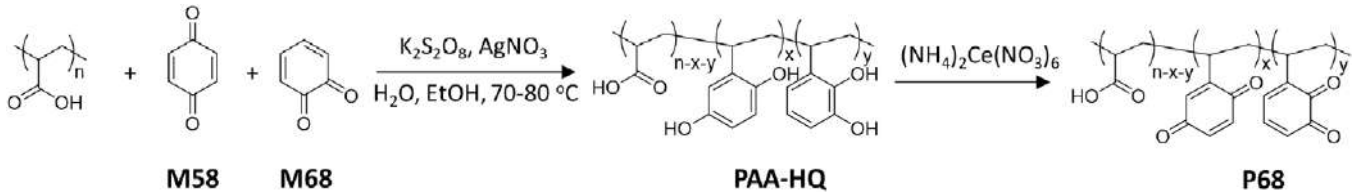


**Scheme 2.37** Synthesis of quinone-containing polymers with pendant 1,3- and 1,4-benzoquinone through a radical-quinone addition reaction. Reproduced from ref. 115 with permission from Elsevier, Copyright 2004.

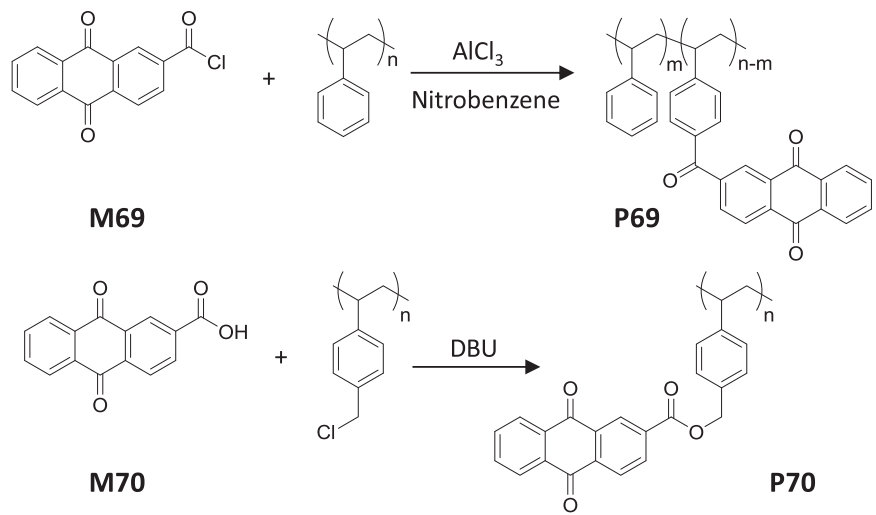


**Scheme 2.38** Synthesis of anthraquinone pendant polystyrene through post-modification *via* either Friedel–Craft or esterification reactions. Reproduced from ref. 116 with permission from The Electrochemical Society, Copyright 1984 and from ref. 117 with permission from John Wiley and Sons, © 2011 John Wiley & Sons, Ltd.

Recently, Minteer[118] designed epoxide functional o- and p-naphthoquinone molecules. M71 and M72 were reacted with polyethyleneimine (PEI) (see Scheme 2.39), respectively, through a ring-opening amination reaction, resulting in an extra hydroxyl group affording polymers with improved water solubility. It was also found that the epoxide substitution can significantly alter the redox potential of naphthoquinone by 100 mV. Using PEI as parent polymer allowed the further conjugation of glucose dehydrogenase (GDH), leading to a series of hydrogel consisting of GDH that can oxidize glucose, in which naphthoquinone played a role as redox mediate for electron transfer. Such a combination was used as an enzyme fuel cell anode to couple with biocathode for high power density biofuel cells.[118]

### 2.2.9 Redox Reaction of Viologen

Viologen, a bipyridinium derivative, and its derivatives have attracted increasing attention due to their interesting properties upon redox reaction. Viologen was first named by Michaelis in 1932 because of the unique violet colour of its reduced form.[119] Viologens are usually synthesized through quaternization of 4,4′-bipyridyl with an alkyl halide. Due to the formation of pyridinium salts, some viologens with short alkyl groups, such as methyl viologen ($MV^{2+}$), possess good water solubility. Viologens can undergo a sequential two-electron redox reaction accompanied by remarkable colour change (see Scheme 2.40).[120] The first reduction converts dication form to a radical cation ($MV^{\bullet+}$) with the colour changed to blue. Further reduction affords a neutral form ($MV^0$) and loses the water solubility. To maintain the water solubility of all three redox species, water-soluble alkyl halides were used to synthesize the viologen derivative.[121] The redox potentials for $MV^{2+}/MV^{\bullet+}$ and $MV^{\bullet+}/MV^0$ were $-0.78$ and $-1.19$ V *vs.* Ag/AgCl, respectively. The electron transfer is fast because the redox process results in little structural change. Owing to its reversible and rapid redox kinetics, dramatic colour and solubility changes, viologens, especially their polymers, have found broad applications spanning from electrochromic display devices, transistors, memory devices, molecular machines, molecular muscles and energy storage systems.[119,122]

### 2.2.10 Redox Polymers Consisting of Viologen

Synthesis of viologen is mainly through the quaternization of 1,4-bipyridyl. Therefore, the most straightforward method to synthesize viologen-containing polymers is through stepwise quaternization polymerization. This method usually generates polyviologen main chain polymers. Barnes[123] demonstrated the reaction process through a stepwise addition quaternization reaction as illustrated in Scheme 2.41. A bifunctional halide (*i.e.*, Cl, Br or I) can react with 1,4-bipyridyl M73 following the step polymerization mechanism. In this case, oligomers like P73 were obtained. This versatile procedure can also be used to prepare viologen-based dendrimers.[124]

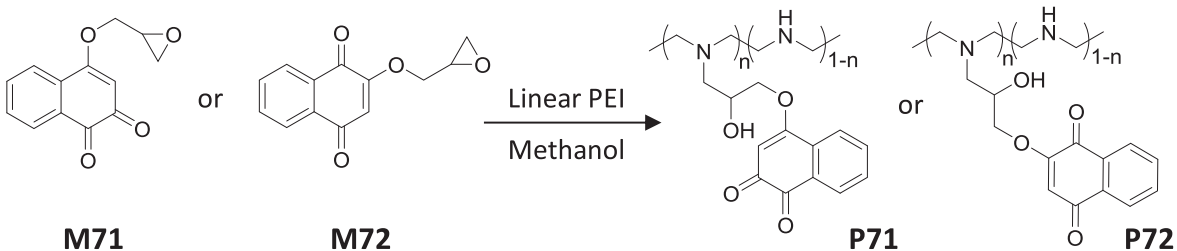


**Scheme 2.39** Synthesis of o- and p-naphthoquinone-containing polymers through amination reaction between the PEI and epoxy group. Reproduced from ref. 118 with permission from the Royal Society of Chemistry.

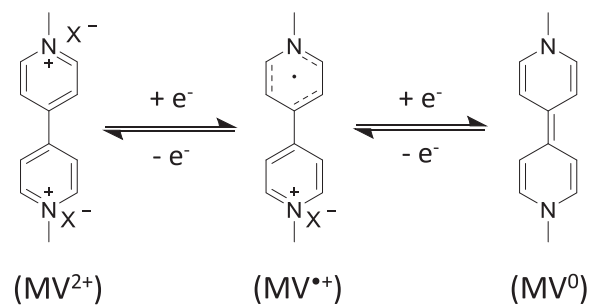


**Scheme 2.40** Two-electron redox reaction of methyl viologen.

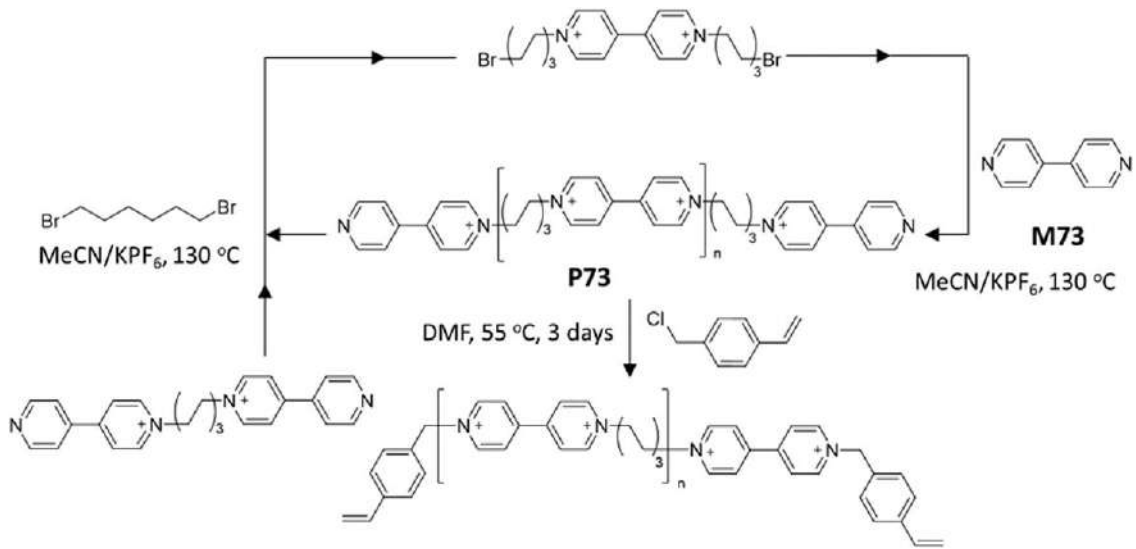


**Scheme 2.41** Synthesis of viologen polymers through step polymerization *via* the quaternization reaction. Reproduced from ref. 123 with permission from Taylor & Francis, Copyright 2019.

While FRP of viologen-based monomers can create polymers with viologen side groups, it requires careful design of asymmetric viologen where only one side is polymerizable. To this end, Rau and Schubert[6] designed methacrylate-functionalized viologen monomers. First, 1-methyl-4-(4′-pyridyl)-pyridinium (MPP) salt was synthesized through monomethylation of M73. MPP was reacted with either 3-bromo-1-propanol followed by reacting with methacryloyl chloride, or directly with 2-bromoethyl methacrylate through quaternization, both of which yielded a methacrylate-functional viologen monomer M74. After copolymerization with other monomers by a RAFT process, a random copolymer P74 consisting of viologen was obtained and used for photocatalysis (see Scheme 2.42).

However, methylation of only one of the pyridine rings in M73 by methyl iodide was a real challenge and often resulted in a low yield of MPP with the major product of viologen. Later, Schubert[125] improved the synthesis by using chloromethane to react with M73 in a MeCN/toluene mixture. Once formed, MPP precipitated from the solvent mixture, which prevented the second quaternization from forming viologen. The much higher isolated yield (~93%) of MPP would be more useful in terms of energy applications. MPP was further reacted with CMS, producing a styryl viologen monomer M75. FRP of M75 with acrylamide resulted in water-soluble viologen polymer P75 (see Scheme 2.42), which was employed as an anolyte for a redox flow battery.[125]

Alternatively, using post-modification strategy a copolymer precursor consisting of PCMS M76 was reacted with MPP, and the resulting polymer P76 (see Scheme 2.43) was demonstrated as the very first application in a polymer-based aqueous redox flow battery.[41] As aforementioned, the one-electron reduction of viologen produces a radical cation ($MV^{\bullet+}$), which can form a stable dimer through charge transfer complexation (CTC) and affect their electrochemical properties. Being interested in how the spatial arrangement of viologen affects the CTC formation during the redox, Moore and Rodríguez-López[126,127] designed viologen polymers in which viologen moieties were conjugated to different positions on the phenyl ring on a polystyrene backbone. They first synthesized two functional polystyrene precursors: poly(o-dichloromethylstyrene) or poly(m-dichloromethylstyrene). Post-modification of M77 and M78 with EPP (1-ethyl-4-(4′-pyridyl)-pyridinium) salt through a quaternization reaction resulted in two constitutional isomers, P77 and P78 (see Scheme 2.43).

As a symmetric structure, M73 is easily converted to a bifunctional viologen monomer. Yan[128] prepared an allyl functional viologen M79 by using an excess of allyl bromide. M79 was copolymerized with *N*-isopropylacrylamide (NIPAM), and the resulting cross-linked polymer P79 exhibited both temperature and redox responsiveness (see Scheme 2.44). This polymer gel has found application as a coating for the smart window. A similar work was reported by Ho[129] and Barnes[130] recently that demonstrated that the polymer gels based on viologen cross-linker possessed a reversible transmittance change and photo-written property

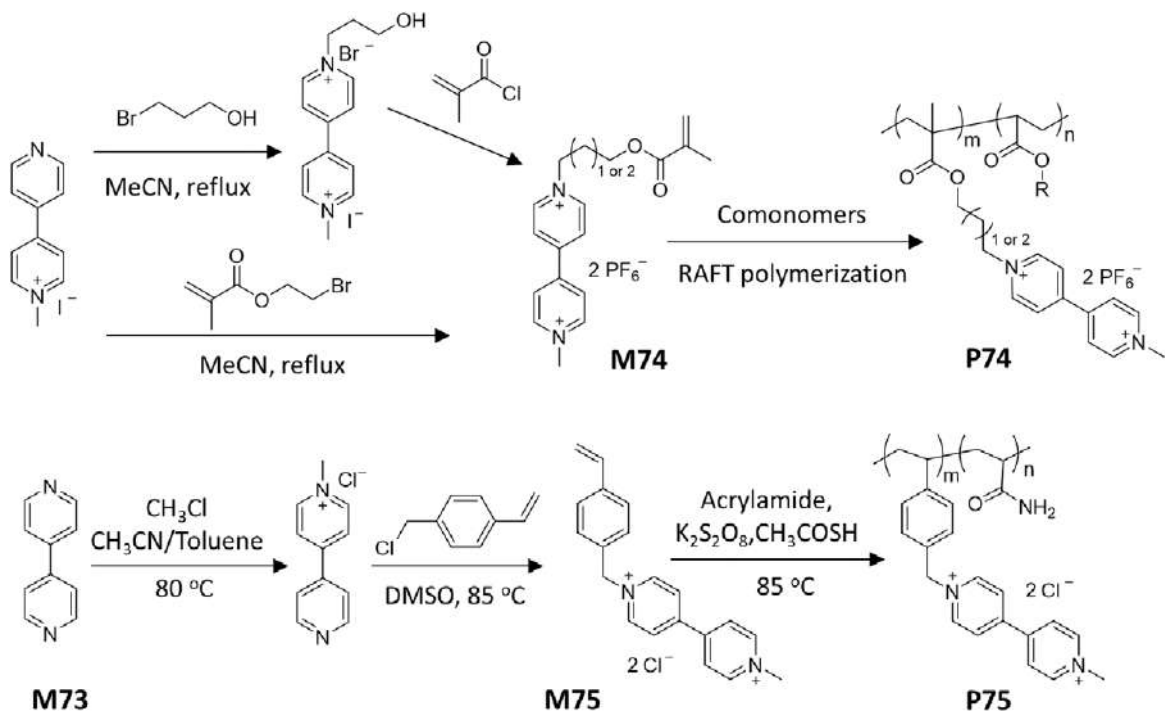


**Scheme 2.42** Synthesis of viologen polymers through FRP of viologen functional methacrylate of styrene monomers. Reproduced from ref. 6 with permission from John Wiley and Sons, © 2015 Wiley-VCH Verlag GmbH & Co. KGaA, Weinheim.

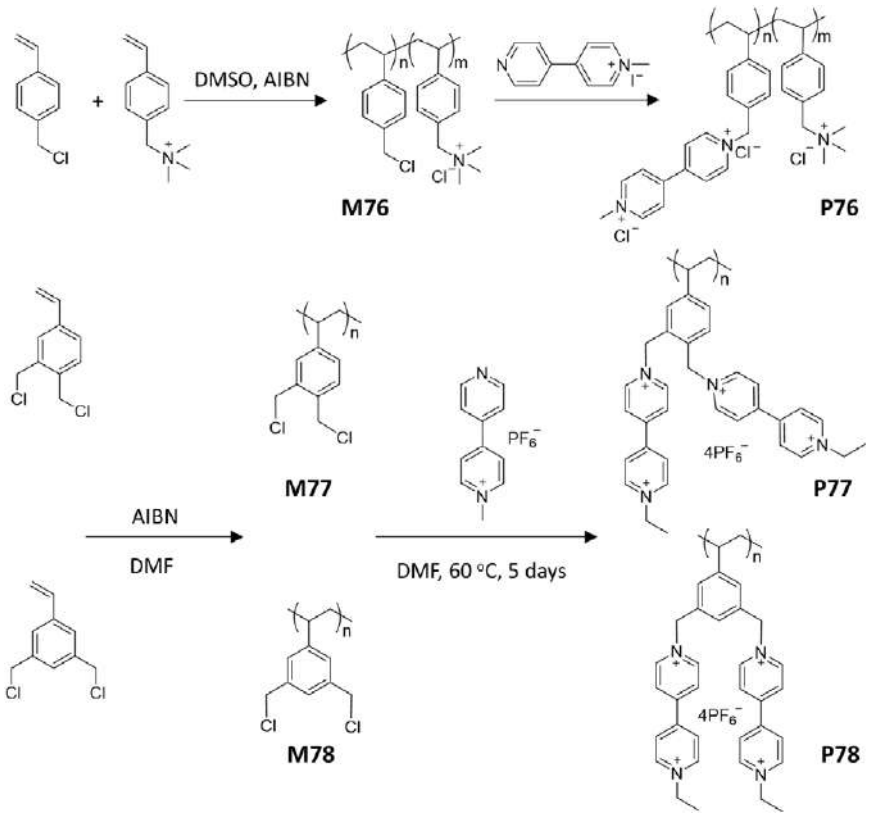


**Scheme 2.43** Synthesis of viologen-based polystyrene with different spatial control of viologen functionalities through post-modification with PCMS. Reproduced from ref. 41 with permission from Nature Publishing Group, Copyright 2015, and from ref. 127 with permission from the American Chemical Society, Copyright 2016.

(see Scheme 2.44) upon applying different potential bias. These viologen-based cross-linked polymer networks have demonstrated great applications as electrochromic devices.[122]

## 2.2.11 Redox Reaction of Tetrathiafulvalene

Tetrathiafulvalene (TTF) is another prevalent redox molecule having similar structure and properties to viologen. The oxidation of TTF by losing one electron produces $TTF^{\bullet+}$ radical cation, a stable radical due to the resonance equilibrium. Losing a second electron results in a dication $TTF^{2+}$ (see Scheme 2.45).[131] This two-electron transfer process is fully reversible owing to the stability of all redox species, exhibiting oxidation potentials of 0.37 and 0.74 V *vs.* Ag/AgCl, respectively. Over the decades, TTF has been widely used as a synthetic block to build molecular machines in which TTFs

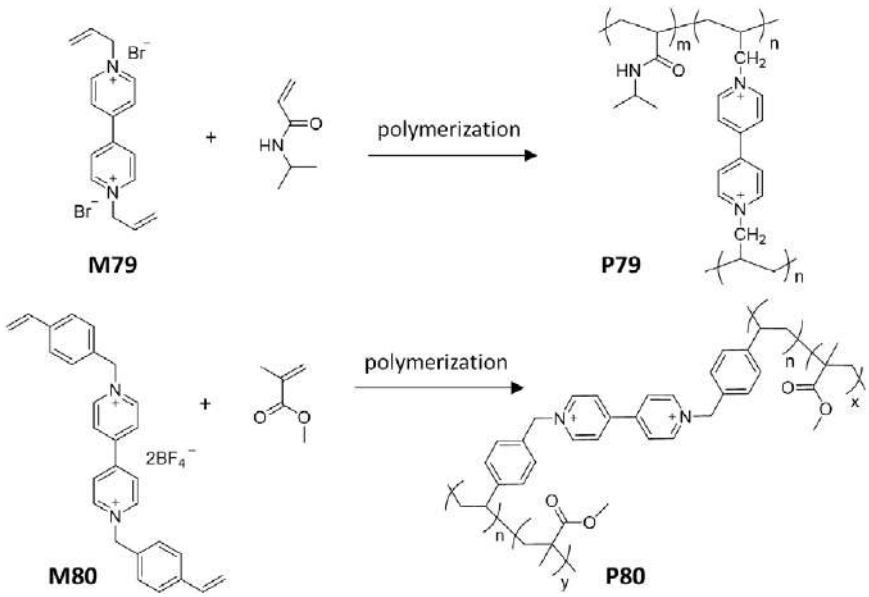


**Scheme 2.44** Synthesis of viologen-based polymer gel using bifunctional viologen monomers.
Reproduced from ref. 128 with permission from the Royal Society of Chemistry, and from ref. 129 with permission from the American Chemical Society, Copyright 2016.

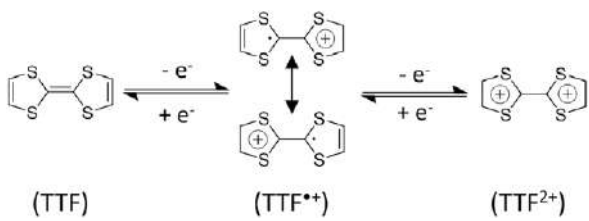


**Scheme 2.45** Two-electron redox reaction of tetrathiafulvalene (TTF).

can control the mechanical motion of interlocked molecules.[132] The driving force is originated from the changes in electronic structures, polarity and molecular conformations between those redox species. Meanwhile, such reversible redox reactions and high redox potentials also make TTF an attractive organic cathode material for energy storage applications.

## 2.2.12 Redox Polymers Consisting of Tetrathiafulvalene

In 1978, Kaplan[133] reported the synthesis of (*p*-vinylphenyl)tetrathiafulvalene and its polymerization. This could be one of the earliest reports on TTF polymers. Scheme 2.46 details the synthetic procedure which

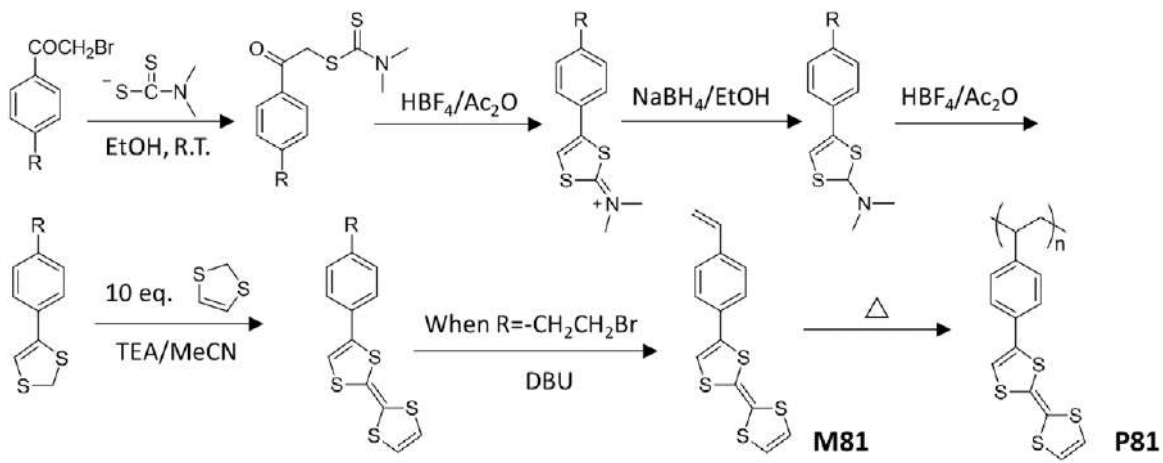


**Scheme 2.46** Stepwise synthesis of styrene functional TTF and its thermal polymerization.
Reproduced from ref. 133 with permission from the American Chemical Society, Copyright 1978.

also involved the synthesis of functional TTF. When the para-R was a bromoethyl group (see Scheme 2.46), it was further converted to a styryl TTF M81 by elimination of HBr using DBU as a base. M81 was polymerized by heat initiation to afford TTF polymer P81 with polystyrene as the backbone. Although it was a long procedure, it provided important information for the design of TTF with the desired chemical structures and functionalities.

In the early 1980s, the synthesis of TTF-based polymers was driven by interest in understanding their charge transfer properties in a thin polymer film. Koβmehl[134] prepared a redox polymer with TTF on the main chain. A TTF-dicarboxylic dichloride was reacted with α,ω-diols consisting of 2–16 methylene groups through polyesterification. The electrical conductivity of these polymers was found to be enhanced by $10^1$–$10^5$ after forming CTC with TCNQ (tetracyano-*p*-quinodimethane). Later, Schoeder and Kaufman[135] prepared TTF polymers with a polystyrene backbone through post-modification. They used metal salts of functional TTF, such as potassium TTF-carboxylate M82 and potassium TTF-phenolate M83, to react with PCMS through esterification and etherification, respectively, resulting in corresponding random copolymers P82 and P83 (see Scheme 2.47). The ratio of TTF in the final copolymers ranged from 0.15 to 0.85 by changing the molar ratio of the reactants. This was a great model to study the charge transfer mechanism with different TTF densities.

When CuAAC 'click' chemistry was applied for the synthesis of TTF polymers, TTFS with either azide M84 or alkyne M85 functionalities were synthesized from 2-hydroxymethyl TTF. Chujo[136] synthesized alkyne functional polymer scaffold, to which M84 was coupled using CuI and DBU as the catalyst. However, the coupling efficiency was only 59% even with an azide/alkyne ratio of 1.1 : 1, because of unavoidable Glaser coupling between the alkyne functionalities and subsequent gel formation. Alternatively,

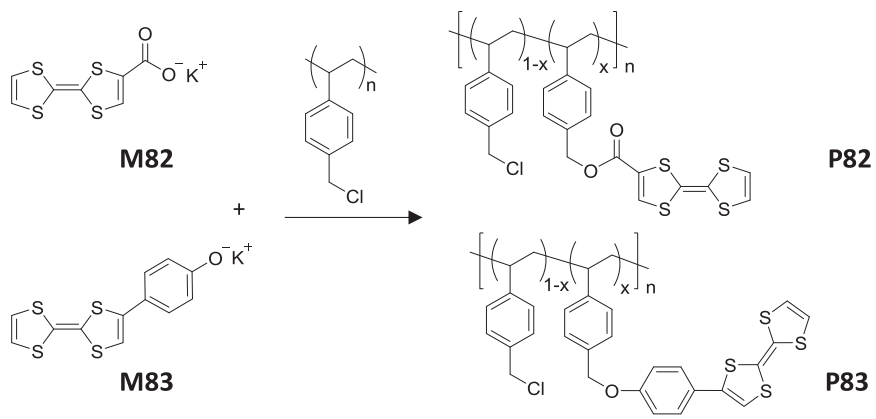


**Scheme 2.47** Synthesis of TTF-containing polystyrene through post-modification of PCMS with TTF-phenolate and -carboxylate.
Reproduced from ref. 135 with permission from Elsevier, Copyright 1980.

Emrick[137] reported a similar procedure by using M85 to click with azido-functional polymer precursors. Although copolymer P85 contained 35 mol% of TTF, no gel was formed using this method (see Scheme 2.48).

Also, some TTF-containing triple-bond monomers have been designed and polymerized by metal coordinate polymerization. Yamamoto[138] synthesized 2-ethynyl-TTF which was polymerized by Rh-complex catalyst. However, the resulting poly(arylacetylene) with conjugated backbone and TTF side groups did not provide any better electrochemical performance than a nonconjugated one, which has been found in many other redox polymers as discussed previously. Being interested in the impact of the chiral conformation on the redox behaviour, Amabilino[139] designed a chiral TTF-substituted poly(isocyanide). The formamide functional TTF was converted to isocyanide functional monomer M86, which was polymerized by using a $NiCl_2 \cdot 6H_2O$ as catalyst (see Scheme 2.49). This coordination-insertion polymerization resulted in P86 with $M_w$ of 33.8 kDa and a high dispersity $Đ$ of 2.33. The chiral conformation of P86 was evidenced by the circular dichroism (CD) spectrum. Interestingly, the redox reaction of P86 generated mixed-valence redox states due to its helical structure and CTC formation, exhibiting different chiroptical properties. This polymer had potential application in multistate optoelectrochemical devices.

Recently, Emrick[137] designed a norbornene functional TTF monomer M87. Like many other norbornene-based redox monomers, ROMP of M87 with another norbornene comonomer by Grubbs 1st-generation catalyst produced well-defined TTF-consisting polynorbornene with estimated molecular weights from 20 to 60 KDa and $Đ$ of 1.1–1.3 (see Scheme 2.50). P87 showed a slightly different redox behaviour to TTF. The two-electron oxidation was not observed in all the prepared polymers primarily due to the CTC formation (*i.e.*, $TTF/TTF^{\bullet+}$ dimer), which is then oxidized to dimer dications at a relatively broad potential window. Conceptually, in parallel with the graphene–pyrene interaction, P87 demonstrated robust, non-covalent interactions with $MoS_2$ nanosheets, providing great stability and band structure modulation for the $MoS_2$ nanosheets.[137]

### 2.2.13 Redox Reaction of Ferrocene

Ferrocene is one of the most classic organometallic compounds that possess a reversible one-electron redox reaction. The discovery and studies on ferrocene have greatly promoted the development of organometallic chemistry. Due to its simple structure, great redox stability and reversibility, so far ferrocene has been one of the most studied organometallic compounds and is often used as an internal standard in nonaqueous electrochemistry with a redox couple of $Fc^+/Fc$ at 0.4 V *vs.* SHE (see Scheme 2.51).[140] It is known that substituents on ferrocene can alter its redox potential. An electron-withdrawing group on cyclopentadiene increases the oxidation potential, while an electron-donating group decreases it. Furthermore, oxidation of ferrocene (Fc) to ferricenium ion ($Fc^+$) dramatically changes the molecule

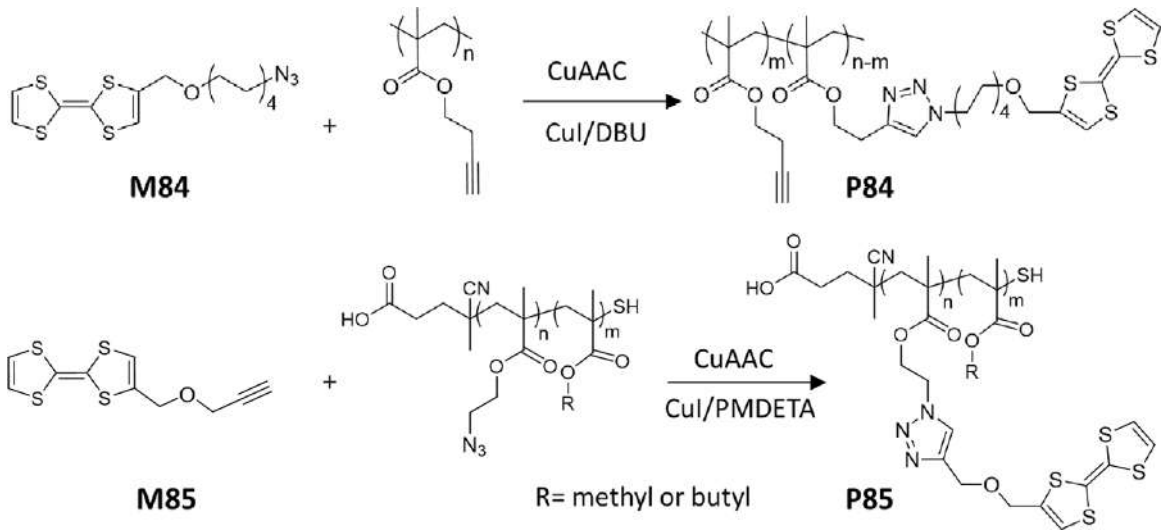


**Scheme 2.48** Synthesis of TTF-containing PMMA through post-modification *via* CuAAC click reaction. Reproduced from ref. 136 with permission from Elsevier, Copyright 2013 and from ref. 137 with permission from the Royal Society of Chemistry.

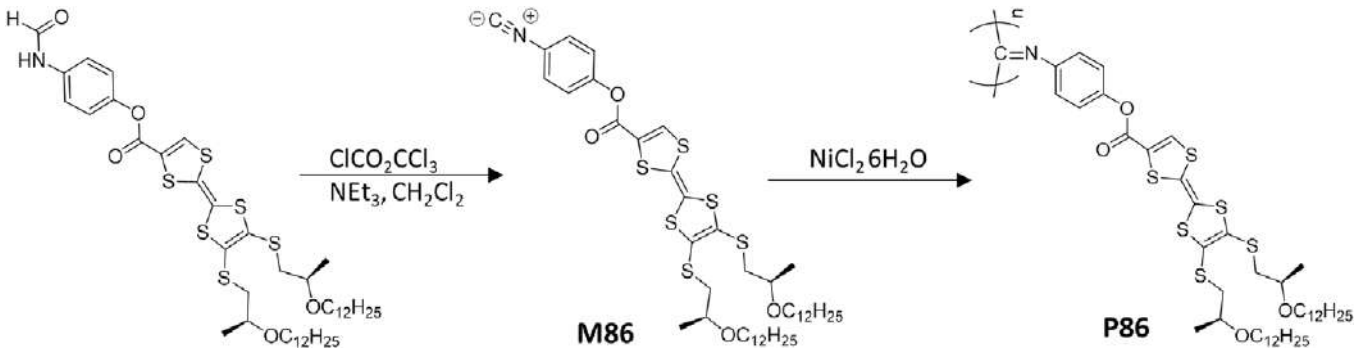


**Scheme 2.49** Synthesis of a chiral TTF polymer through coordination-insertion polymerization of a TTF functional isocyanide. Reproduced from ref. 139 with permission from John Wiley and Sons, © 2005 Wiley-VCH Verlag GmbH & Co. KGaA, Weinheim.

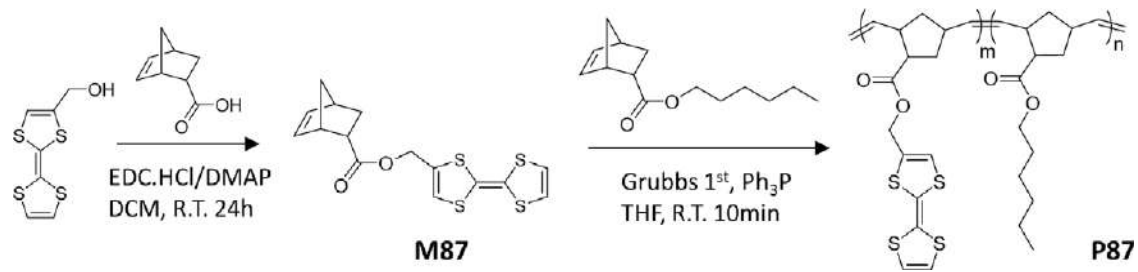


**Scheme 2.50** Synthesis of TTF-containing copolymer through ROMP of norbornene functional monomers. Reproduced from ref. 137 with permission from the Royal Society of Chemistry

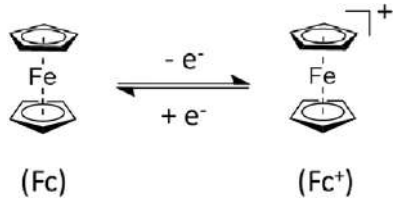


**Scheme 2.51** One-electron redox reaction of ferrocene.

from hydrophobic to hydrophilic. These characteristics provide ferrocene with great potential for wide applications including functional materials, biomedicine and so on.[141]

## 2.2.14 Redox Polymers Consisting of Ferrocene

Different from other redox polymers that are purely organic, polymers consisting of ferrocene are one of most common metallopolymers. Due to the aromaticity of cyclopentadiene ligands, ferrocene can undergo diverse chemical reactions and be modified with a range of functionalities, enabling the synthesis of ferrocene-based polymers with various chemical compositions and physical architectures.[142] Ferrocene is compatible with radical, ionic and many other types of polymerization techniques. The synthesis and polymerization of ferrocene functional monomers are a straightforward strategy. Vinylferrocene, the simplest monomer, can be directly polymerized through either anionic or radical processes. Gallei[143] reported anionic polymerization of vinylferrocene M88 by nBuLi to give poly(vinylferrocene) (PVFc) oligomer P88, and the living chain end was converted to a siloxane group for further immobilization to a surface. The wettability of the surface was modulated through the redox reaction of ferrocene. In another work,[144] the chain end of P88 was converted to hydroxyl groups which then can initiate the polymerization of L-lactide by $Sn(Oct)_2$, forming a PVFc-*b*-PLA. Due to the aromaticity of cyclopentadienyl rings, M88 was also well copolymerized with glycidol methacrylate M89 through FRP, as reported by Maltas.[145] The epoxy group enabled further modification with an amine on xanthine oxidase (see Scheme 2.52). The enzyme coupled with ferrocene polymer formed a catalytic electron transfer complex for electrochemical detection of xanthine.

To prepare a ferrocene-containing polyether, Wurm[146] designed a glycidol functional ferrocene M90 and copolymerized with allyl glycidyl ether M91 using an anionic ring-opening copolymerization technique. Even with the bulky ferrocene group in M90, the polymerization resulted in a random copolymer which was evidenced by quantitative $^{13}C$ NMR spectroscopy. The pendant allyl groups provide an opportunity for further modification *via* thiol–ene chemistry. A *N*-acetyl-L-cysteine methyl ester as a model biomolecule was reacted with P90 through a radical process. It was found that the functionalization efficiency was nearly 90% with no impact on ferrocene groups.


**Scheme 2.52** Synthesis of poly(vinyl ferrocene) *via* both anionic and FRP for surface modification.
Reproduced from ref. 143 with permission from the American Chemical Society, Copyright 2013, and from ref. 145 with permission from Elsevier, Copyright 2014.

The same group further designed a Janus monomer M92 which consisted of a glycidyl and a vinyl functionality on each cyclopentadiene ring.[147] FRP of the vinyl group produced a PVFc P91 with epoxy functionalities ($M_n = 6$ kDa and $Đ = 1.83$). Subsequently, the pendant glycidol moieties were reacted with amine groups of bovine serum albumin (BSA). The idea was to create a redox polymer/protein hybrid nanoparticle with potential application in biomedicine. The polymerization of glycidol produced a ferrocene-based polyether with vinyl functionalities P92. Different to P91, the copolymer P92 consisted mainly of EO units (*i.e.*, 85–90 mol%) and had low dispersities with $Đ$ of 1.09–1.14. Like P90, P92 can be further modified with functional thiol compounds (*i.e.*, 3-mercaptopropionic acid) and the resulting polymer demonstrated a thermo-responsive property, in which the lowest critical solution temperature (LCST) was determined by their composition and pH values (see Scheme 2.53).

To use LRP techniques to produce ferrocene polymers or copolymers, ferrocene was converted to its (meth)acrylate or (meth)acrylamide monomers. Gonsalves[148] prepared ferrocenemethyl methacrylate M93 and copolymerized with 4-(methacryloyloxyphenyl)dimethylsulfonium triflate (MAPDST) at different monomer ratios. Further work indicated that the incorporation of the ferrocene unit into the polymer backbone resulted in better thermal stability of the copolymer P93 compared to the poly(MAPDST). Tao[149] recently synthesized a new ferrocene monomer M94 through multicomponent Biginelli reaction using ferrocenecarboxaldehyde. M94 was copolymerized with PEG methacrylate (PEGMA) to produce a water-soluble redox polymer P94 (see Scheme 2.54). Interestingly, using this polymer for *in vivo* treatment of oxidative stress damage demonstrated a

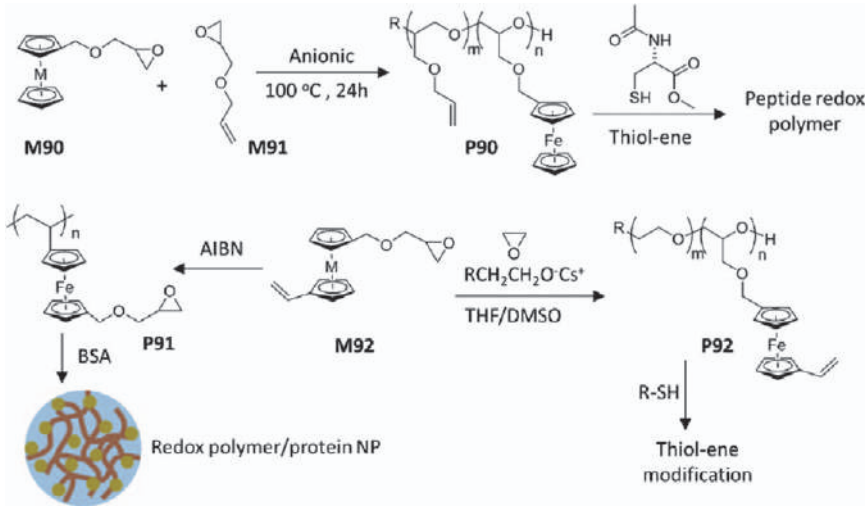


**Scheme 2.53** Synthesis of ferrocene-containing polymers with functionalities for post-modification.
Reproduced from ref. 146 with permission from the American Chemical Society, Copyright 2014, and from ref. 147 with permission from the Royal Society of Chemistry.

clear synergistic effect of the redox ferrocene group and the dihydropyrimidin-2(H)-one (DHPM) group from the Biginelli reaction.

Alternatively, ferrocenecarboxylic acid was reacted with 2-hydroxyethyl (meth)acrylate to give monomer M95 by an esterification reaction. M95 has been polymerized *via* either RAFT or surface-initiated ATRP (SI-ATRP) (see Scheme 2.55).[143] Through varying the monomer to initiator ratio and reaction time, the thickness of the surface-grafting polymers can be adjusted. To make a multiple-responsive polymer that incorporated with ferrocene, Huang[150] used acrylate analogue of M95 to react with *N*,*N*-diethylethylenediamine through an aza-Michael addition reaction, and the resulting secondary amine adduct was further converted to acrylamide monomer M96. RAFT polymerization of M96 created ferrocene polymer P96 with both redox- and pH-responsive properties (see Scheme 2.55).

To the best of our knowledge, some special polymerization techniques have been only employed to make ferrocene-based redox polymers. For example, Hey-Hawkins[151] reported the synthesis of ferrocenyl phosphine-borane M97 through the reaction of ferrocenyl phosphine with $BH_3$(THF). M97 was polymerized through a catalytic dehydro-coupling reaction (see Scheme 2.56). The resulting polymers with a phosphorus–boron backbone had an MW of up to 16 kDa. Due to the thermal stability of both the ferrocenyl side group and phosphorous–boron backbone, these polymers demonstrated excellent thermal stability with only 5% weight loss at 320 °C.

When post-modification was applied, it also allowed for the preparation of ferrocene-based polymers with an unusual backbone (see Scheme 2.57).

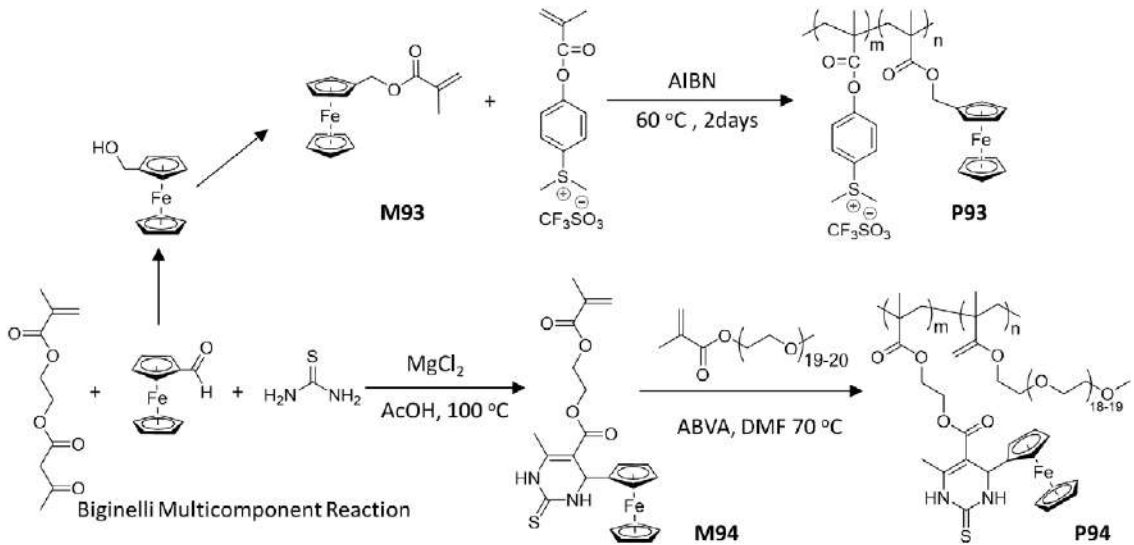


**Scheme 2.54** Synthesis of ferrocene-based copolymers through radical copolymerization of ferrocenyl methacrylate and Biginelli reaction generated ferrocenyl methacrylate.
Reproduced from ref. 149 with permission from the American Chemical Society, Copyright 2019.

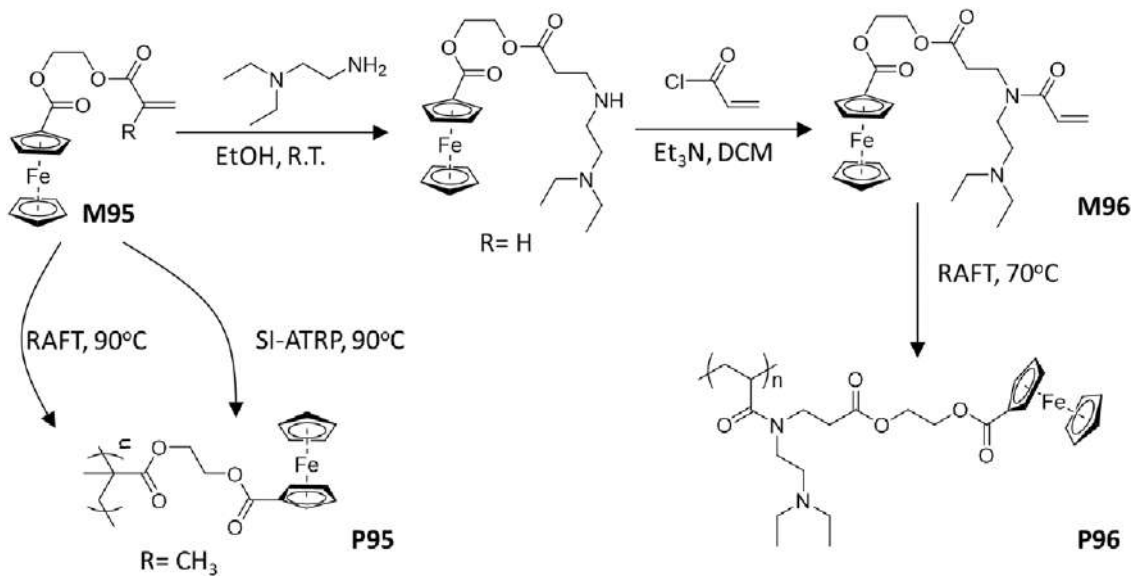


**Scheme 2.55** Synthesis of ferrocene-based PMMA and polyacrylamide through ATRP or RAFT polymerization. Reproduced from ref. 150 with permission from the Royal Society of Chemistry.

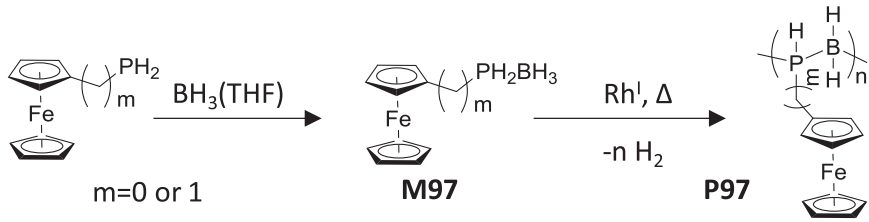


**Scheme 2.56** Synthesis of ferrocene-based polymer with a phosphorous–boron backbone through Rh-catalysed dehydro-coupling reaction.
Reproduced from ref. 151 with permission from John Wiley and Sons, © 2014 Wiley-VCH Verlag GmbH & Co. KGaA, Weinheim.

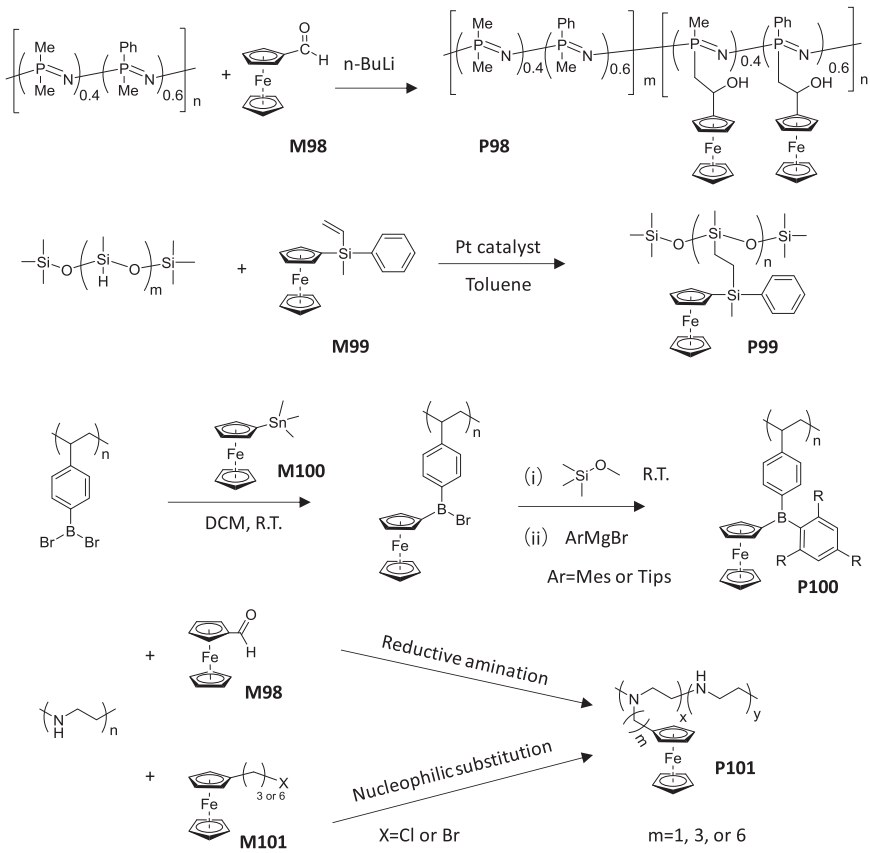


**Scheme 2.57** Post-modification of functional parent polymers with functional ferrocene to generate ferrocene-based polymers with unusual chemical compositions.
Reproduced from ref. 152–155 with permission from the American Chemical Society, Copyright 2009–2012.

For example, Crumbliss[152] used phosphazene polymers as a precursor, and after treating with *n*BuLi, the resulting methylene lithium further reacted with ferrocene carboxaldehyde M98 and formed redox polymers with pendant ferrocene and phosphazene backbone. To make a ferrocene polymer with polysiloxane as a backbone, Guadrado[153] carried out Karstedt-catalyzed hydrosilylation reactions between the commercially available Si–H-polyfunctionalized copolymer with vinyl functional ferrocene M99 using Pt catalyst. Ferrocenes were linked to polysiloxane to produce the final polymer P99. The group of Jakle[154] modified poly(trimethylsilyl styrene) with $BBr_3$, and the resulting poly(dibromoborostyrene) was readily reacted with trimethylsilyl ferrocene M100. The intermediate polymer was further converted to triarylborane polymers consisting of redox-active ferrocene. The polymer demonstrated two pairs of redox peaks from both ferrocene and boron functionalities. In another example, linear PEIs were used as parent polymers, the secondary amines were able to react with either M98 or halide functional ferrocene M101 through reductive amination and nucleophilic substitution, respectively.[155] These two reactions produced similar polymers P101 with different linkages between ferrocene and polyimine backbone.

In the family of ferrocene polymers, polyferrocenylsilane is a well-established metallopolymer with alternative ferrocene and organosilane units on the backbone. Such polymers were first reported in the 1990s by ring-opening polymerization of silicon-bridged ferrocenophanes. Since then, different polymerization techniques have been developed to synthesize polyferrocenylsilanes, including thermal, transition metal-catalysed and AROP methods. One typical polymerization process is shown in Scheme 2.58. Monomer M102 and its analogues were polymerized by using a carbanion initiator, which allowed further modification of the chain end for different application purposes. For details of poly(ferrocenylsilane), readers are referred to recent reviews.[156,157]

Apart from ROP, step polymerization was also applied for the synthesis of redox polymers with ferrocene in the backbone. A very early example of this type of reaction was reported by Neuse in 1964.[158] Ferrocene was reacted with both aromatic and aliphatic aldehyde M103 through a condensation reaction, and in the latter case, a closed reaction system was required (see Scheme 2.59). However, in many cases, the reactions resulted in polymers P103 with low yields (*i.e.*, 20–30%) and some cross-linked by-products involving the olefinic double bond were observed. While CuAAC was applied for the synthesis of linear redox polymer with ferrocene units in the main chain, well-defined structures were obtained. Tang[159] reported the synthesis of diazido-ferrocene M104 and the further CuAAC click with various dialkyne molecules (see Scheme 2.59). The click polymerization was carried out under 80 °C to minimize the side reactions. All the reactions produced polymers P104 with molecular weights of about 13 kDa and a dispersity of about 1.5. The pyrolysis of these polymers readily

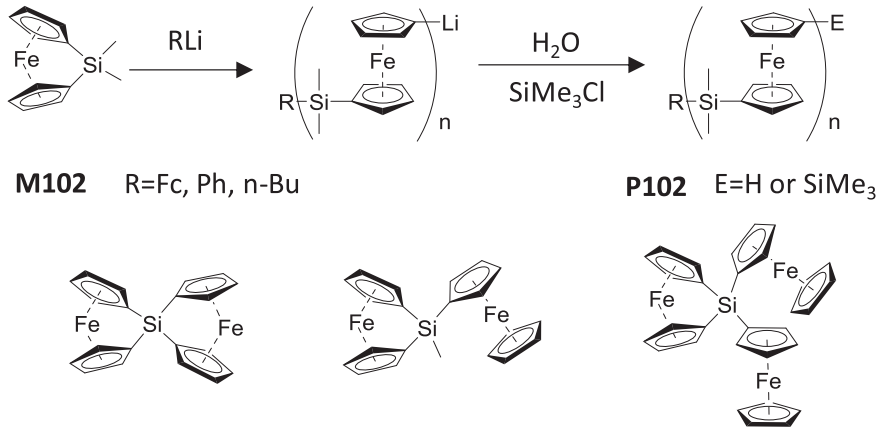


**Scheme 2.58** Synthesis of polyferrocenylsilanes through ring-opening polymerization of cyclic ferrocenylsilanes.
Reproduced from ref. 156 with permission from John Wiley and Sons, © 2007 Wiley-VCH Verlag GmbH & Co. KGaA, Weinheim, and from ref. 157 with permission from the Royal Society of Chemistry.

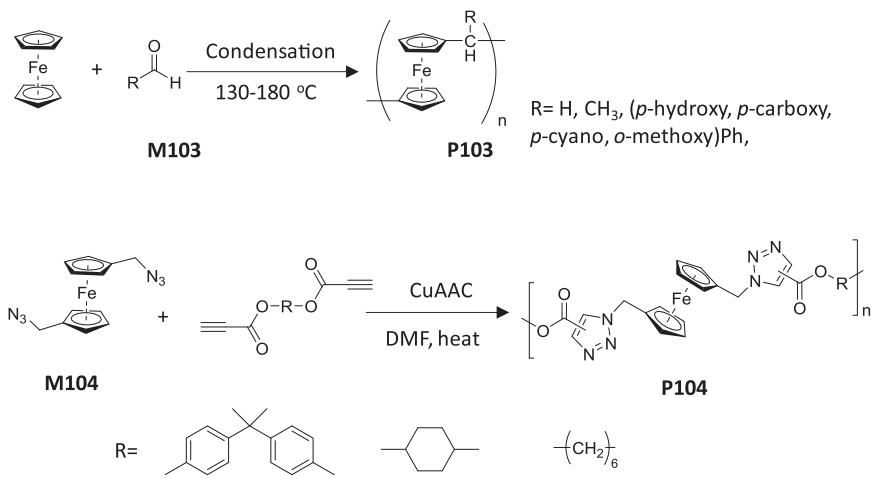


**Scheme 2.59** Redox polymers with ferrocene on backbone synthesized through condensation polymerization or step polymerization *via* CuAAC click chemistry.
Reproduced from ref. 158 with permission from Springer Nature, Copyright 1964, and from ref. 159 with permission from the Royal Society of Chemistry.

generated ceramics with high magnetizability and low coercivity as soft magnetic materials. This method was later applied for the synthesis of a hyperbranched polymer analogue of P104.[160]

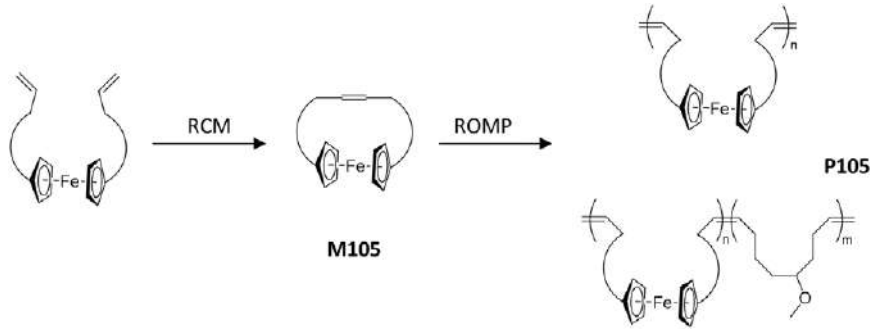


**Scheme 2.60** Synthesis of cyclic ferrocenyl olefins *via* ring-close metathesis and further polymerization through ROMP.
Reproduced from ref. 161 with permission from the American Chemical Society, Copyright 2018.

Recently, Tang[161] reported a ROMP strategy for the synthesis of redox polymers with ferrocene units on the backbone. To achieve this, a series of ferrocenyl dienes were synthesized and cyclized through ring-close metathesis to form cyclic ferrocenyl olefins M105. These olefins were then polymerized *via* a ROMP process by using Grubbs 2nd catalyst in dichloromethane at room temperature, producing main-chain ferrocene-containing homopolymers or copolymers P105 (see Scheme 2.60). The polymerization capability was determined by the functionality and size of the ring. Generally, the monomer conversions were over 70% with a molecular weight of 25 kDa and $Đ$ of 1.68–1.79. These monomers were also applied to generate nanostructured organometallics through a ROMPI-CDSA process, a ring-opening metathesis polymerization-induced crystallization-driven self-assembly strategy.[162]

## 2.2.15 Redox Reaction of Phenothiazine

Phenothiazine (PTZ) is a thiazine-class heterocyclic compound consisting of an amine and a thioether. Derivatives of PTZ are highly bioactive and have been widely used in medicinal and analytic chemistry. PTZ possesses a bent conformation which changes to a more plane one after one-electron oxidation with the formation of a radical cation $PTZ^{\bullet+}$. Recent work by Brushett and Odom[163] demonstrated a stable two-electron redox of PTZ to $PTZ^{2+}$ in nonaqueous electrolyte by introducing different functionalities and their redox potentials were also affected by those substituents (see Scheme 2.61). $PTZ^{2+}$ is not stable in aqueous media in which it converts to a sulfoxide analogue. The oxidation potential for $PTZ/PTZ^{\bullet+}$ was about 0.05–0.3 V and the second one for $PTZ^{\bullet+}/PTZ^{2+}$ was about 0.65–0.95 V *vs.* $Fc/Fc^{+}$. Realizing this reversible two-electron redox makes PTZ and its derivative of great potential in energy storage applications.

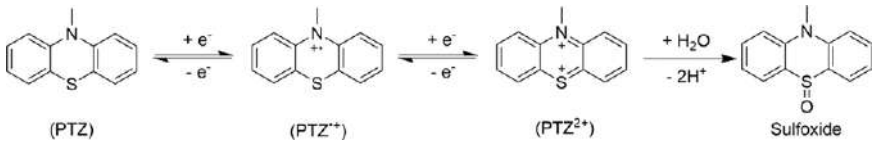


**Scheme 2.61** Two-electron redox reaction of phenothiazine (PTZ).

### 2.2.16 Redox Polymer Consisting of Phenothiazine

The structure of phenothiazine provides many opportunities for the functionalization of PTZ, including the design of different types of monomers. As early as 1970, Gipstein *et al.*[164] reported the synthesis of 3-vinyl-*N*-methylphenothiazine monomer M106 through Wittig reaction and its FRP to polymer P106. In the same work, monomer M107 and polyacrylamide with PTZ moieties were also prepared. Unfortunately, no further electrochemical redox properties have been tested. Long after, Crivello[165] used PTZ as the parent molecule and developed three different monomers M108–M110, mainly through alkylation of the secondary amine of PTZ. These epoxy or vinyl functional monomers were polymerized through cationic polymerization using, for example, $BF_3(Et_2O)$ as the initiator. These polymers P108–P110 were studied as a photosensitizer for photopolymerization. Golriz *et al.*[166] reported the synthesis of styryl functional PTZ M111 with a different number of carbons between styryl and PTZ. FRP of M111 produced polymer P111 and was used as a cathode material in LIB. Compared to the small molecular PTZ that can achieve two-electron storage,[163,167] P111 only demonstrated one-electron redox in LIB system (Scheme 2.62).

### 2.2.17 Redox Polymers Consisting of Other Types of Functionalities

Apart from those classic organic redox groups discussed above, some special organic functionalities possessing stable redox reaction have also been studied, particularly for energy-storage applications. For instance, 2,5-disubstituted 1,4-dimethoxybenzene can undergo one-electron oxidation, forming a radical cation stabilized by dimethoxy groups. The substitution on the benzene ring is of key importance for the stability of the oxidized product.[168] This reversible redox potential is found to be 3.85 V *vs.* $Li^+/Li$ and is often used as redox shuttle molecules for LIBs. Nesvadba[169] designed a methacrylate with 2,5-di-*t*-butyl-1,4-dialkoxybenzene functionality M112. Using FRP, P112 was obtained with $M_n$ of 8.2 kDa and $M_w$ of 32 kDa. When P112 was used as cathode materials, its high solubility in a common electrolyte solution (*i.e.*, DMC/EC) caused a continuous decrease in the capacity (Scheme 2.63).

Triarylamine can also undergo one-electron oxidation, forming an *N*-centred radical cation. Triarylamine and its derivatives have found applications in organic photoelectronic devices such as OLED, organic solar cells

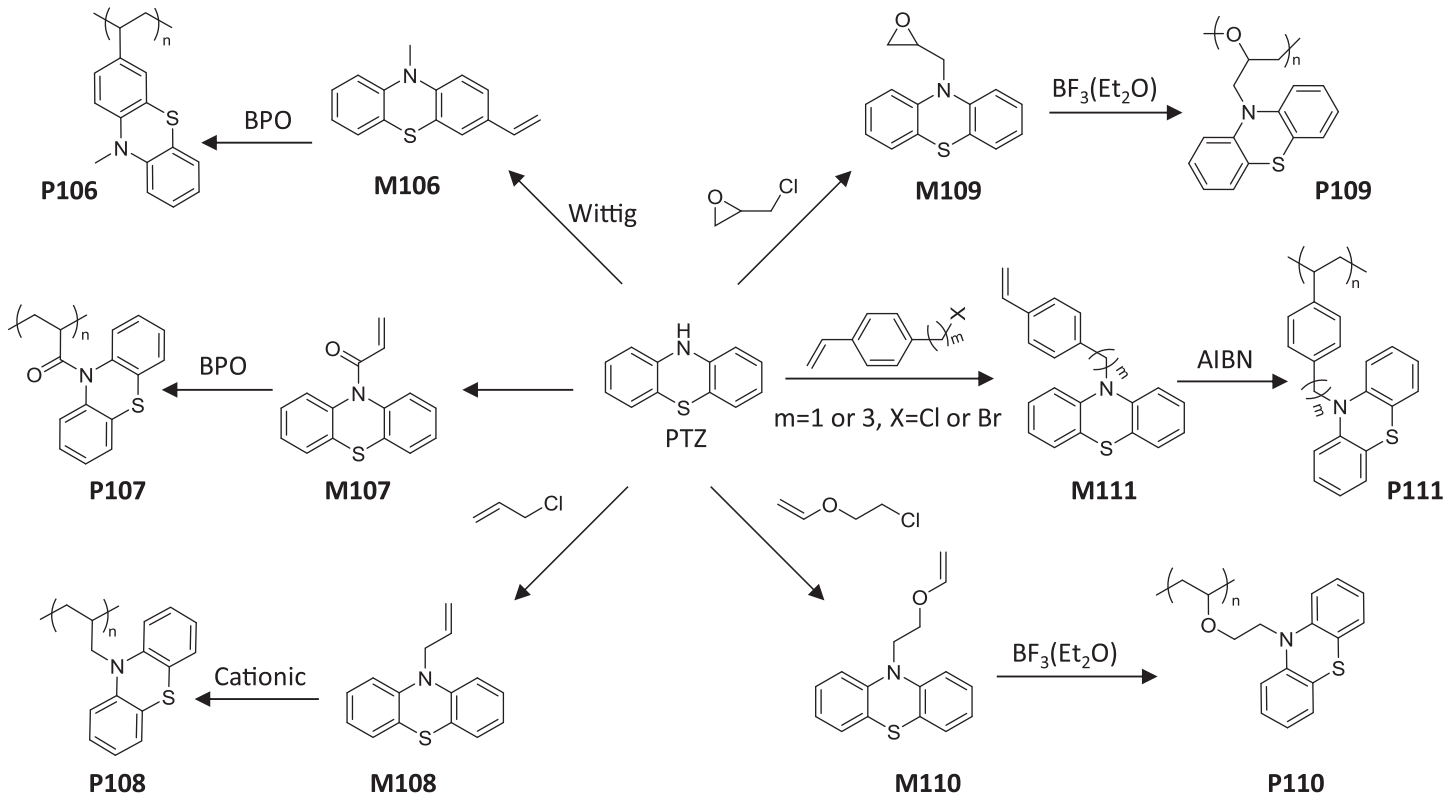


**Scheme 2.62** Synthesis of PTZ functional monomers and their polymerization to PTZ-containing polymers with different backbones. Reproduced from ref. 164 with permission from John Wiley and Sons, © 1970 John Wiley & Sons, Inc., from ref. 165 with permission from the American Chemical Society, Copyright 2002, and from ref. 166 with permission from the Royal Society of Chemistry.

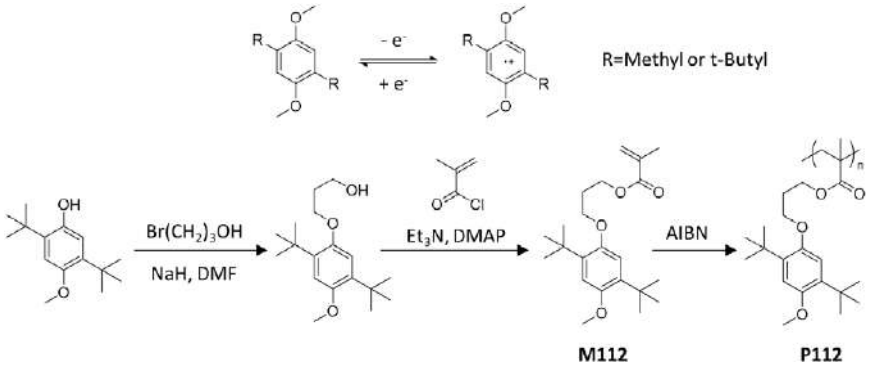


**Scheme 2.63** One-electron redox reaction of 2,5-dialkyl-1,4-dialkoxybenzene and the synthesis of the corresponding polymer through FRP.
Reproduced from ref. 169 with permission from Elsevier, Copyright 2011.

and so on.[170] Synthesis of triarylamine is easily achieved through Ullmann coupling or Buchwald–Hartwig coupling.[171] Moreover, its aromatic structure enables tuning the redox potential through the para-substitution on phenyl rings, which can be predicted through a linear relationship between the redox potentials and Hammett constants.[172] In terms of a polymer comprising of triarylamine, Yang[173] reported the synthesis of conjugated polymer poly(triphenylamine) through oxidation of triphenylamine, which was used as cathode materials for a total polymer battery. Very recently, Schubert[174] designed a styrene version of triphenylamine with different substituents on the phenyl ring. Through anionic polymerization, oligomers and polymers were obtained with very low dispersity ($Đ = 1.02$–$1.11$), enabling in-depth studies on the effect of chain length impacts on electrochemical properties (Scheme 2.64).

In the last decade, conjugated dicarboxylates have been widely explored as organic anode materials for energy storage. One typical example is terephthalate, whose redox reaction involves two-electron transfer coupled with metal ion association. So far, many different dicarboxylates have been widely employed as anode materials in $Li^+$, $Na^+$ and $K^+$ ion batteries.[175–177] However, there is very little work on the synthesis and application of dicarboxylate-containing polymers. Sjodin[178] synthesized a thiophene functional dicarboxylate M114 and through electrochemical polymerization produced corresponding polymer P114 with polythiophene backbone and dicarboxylate as pendant groups (Scheme 2.65). In his work, many other analogues to M114 were prepared in which different linkers were introduced between thiophene or ethylenedioxythiophene and the terephthalate. After electrochemical polymerization, the monomer with methyl-linker showed lower molecular weight than that with ethyl-linker due to the higher steric hindrance of the former. Further studies on these polymers demonstrated that the electrochemical stability was strongly dependent on the linkers.

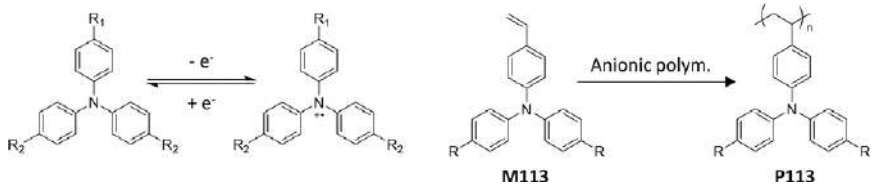


**Scheme 2.64** One-electron redox reaction of triarylamine and the synthesis of poly(vinyl triphenylamine) *via* anionic polymerization.
Reproduced from ref. 174 with permission from the American Chemical Society, Copyright 2019.

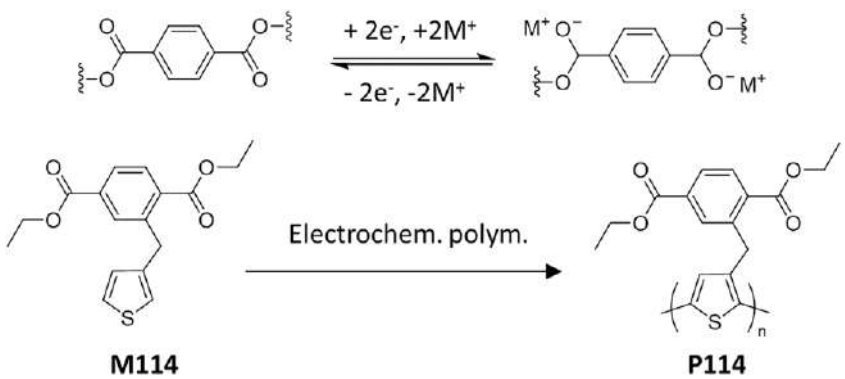


**Scheme 2.65** Metal-ion coupled two-electron redox reaction of conjugated dicarboxylate and the synthesis of terephthalate-containing polythiophene *via* electrochemical polymerization.
Reproduced from ref. 178 with permission from the Royal Society of Chemistry.

In those well-studied redox groups discussed above, only a few of them possess negative redox potential and are suitable as anode materials. Very recently, Nishide[179] reported a new redox-active molecule, dibenzothiophenesulfone, which can undergo a stable and reversible two-electron redox in an aprotic solution. This reduction took place at the very negative potential of −1.8 V *vs.* Ag/AgCl. It was found that the heterogeneous electron-transfer rate constant and diffusion coefficient for dibenzothiophenesulfone was even higher than for anthraquinone.[179] The only disadvantage is that the reaction became irreversible in a protic solution. This new compound had great potential to be an organic anode material. They further modified dibenzothiophenesulfone with a vinyl group M115, and through FRP, poly(vinyldibenzothiophenesulfone) P115 was obtained with a molecular weight of 14 kDa (Scheme 2.66). P115 demonstrated similar thermostability to polystyrene. When used as an anode material, it can deliver a capacity of 211 mAh $g^{-1}$ (221 mAh $g^{-1}$ in theory) at the high current density of 10–120 C.

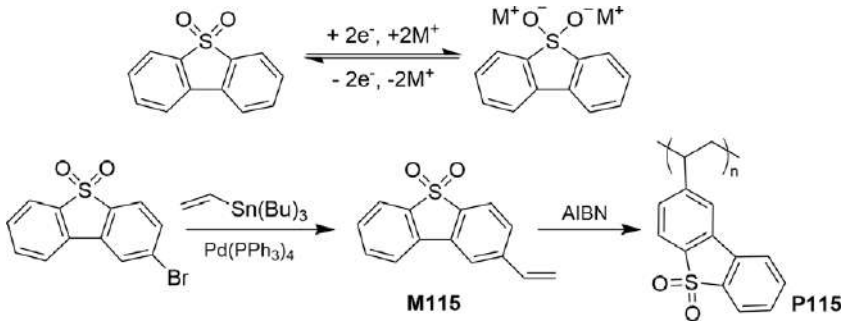


**Scheme 2.66** Two-electron redox reaction of dibenzothiophenesulfone and the synthesis of poly(vinyldibenzothiophenesulfone) through FRP. Reproduced from ref. 179 with permission from John Wiley and Sons, © 2018 Wiley-VCH Verlag GmbH & Co. KGaA, Weinheim.

## 2.3 Conclusion

The development of new methods and strategies for the synthesis of redox polymers has been driven by the revival of their applications in biomedicine and energy storage over the past two decades. This chapter has summarized the most studied organic redox molecules and more importantly the synthetic advances of the corresponding polymers, in which some of the newly developed methods have been detailed. However, these previous studies mainly focus on the synthesis and/or application performance of redox polymers with different types of redox groups and backbones. There have been only a few scattered studies investigating the impact of chemical composition (*i.e.*, backbone and side group). In particular there is a lack of understanding on how polymer architectures of redox polymers affect their physical properties and the redox performance in different application aspects. Furthermore, many redox-active molecules have biological activity and could be used in biomedicine. Therefore, biocompatible and biodegradable polymers consisting of redox groups may be further developed. Finally, developing environmentally friendly redox polymers and applying them for energy storage are expected to minimize the environmental impacts when the devices come to the end of their life.

## References

1. T. Nishinaga, in *Organic Redox Systems*, ed. T. Nishinaga, John Wiley & Sons, Inc., 2016, pp. 1–12.
2. R. G. Hicks, in *Stable Radicals*, John Wiley & Sons, Ltd, 2010, pp. i–xviii.
3. B. Zhang, F. Fan, W. Xue, G. Liu, Y. Fu, X. Zhuang, X. H. Xu, J. Gu, R. W. Li and Y. Chen, *Nat. Commun.*, 2019, **10**, 736.
4. A. Rajca, J. Wongsriratanakul and S. Rajca, *Science*, 2001, **294**, 1503–1505.

5. Z. Li, T. Konno, M. Takai and K. Ishihara, *Biosens. Bioelectron.*, 2012, **34**, 191–196.
6. B. Happ, J. Kubel, M. G. Pfeffer, A. Winter, M. D. Hager, B. Dietzek, S. Rau and U. S. Schubert, *Macromol. Chem. Phys.*, 2015, **36**, 671–677.
7. A. Dijksman, I. W. C. E. Arends and R. A. Sheldon, *Chem. Commun.*, 2000, 271–272.
8. K. Kawashima, Y. Tamai, H. Ohkita, I. Osaka and K. Takimiya, *Nat. Commun.*, 2015, **6**, 10085.
9. C. Friebe and U. S. Schubert, *Adv. Energy Mater.*, 2015, **5**, 1500858.
10. S. M. Swick, W. Zhu, M. Matta, T. J. Aldrich, A. Harbuzaru, J. T. Lopez Navarrete, R. Ponce Ortiz, K. L. Kohlstedt, G. C. Schatz, A. Facchetti, F. S. Melkonyan and T. J. Marks, *Proc. Natl. Acad. Sci. U. S. A.*, 2018, **115**, E8341–E8348.
11. J. Kim, J. H. Kim and K. Ariga, *Joule*, 2017, **1**, 739–768.
12. M. Burgess, J. S. Moore and J. Rodriguez-Lopez, *Acc. Chem. Res.*, 2016, **49**, 2649–2657.
13. W. Waskitoaji, T. Suga and H. Nishide, *AIP Conf. Proc.*, 2009, **1169**, 13–18.
14. H. Nakagawa, Y. Matsumoto, Y. Matsumoto, Y. Miwa and Y. Nagasaki, *Biomaterials*, 2015, **69**, 165–173.
15. N. Casado, G. Hernández, H. Sardon and D. Mecerreyes, *Prog. Polym. Sci.*, 2016, **52**, 107–135.
16. R. Gracia and D. Mecerreyes, *Polym. Chem.*, 2013, **4**, 2206–2214.
17. K. Zhang, M. J. Monteiro and Z. Jia, *Polym. Chem.*, 2016, **7**, 5589–5614.
18. S. Muench, A. Wild, C. Friebe, B. Häupler, T. Janoschka and U. S. Schubert, *Chem. Rev.*, 2016, **116**, 9438–9484.
19. S. Perrier, *Macromolecules*, 2017, **50**, 7433–7447.
20. K. Matyjaszewski and N. V. Tsarevsky, *Nat. Chem.*, 2009, **1**, 276–288.
21. A. Anastasaki, V. Nikolaou and D. M. Haddleton, *Polym. Chem.*, 2016, **7**, 1002–1026.
22. J. F. Mike and J. L. Lutkenhaus, *J. Polym. Sci., Part B: Polym. Phys.*, 2013, **51**, 468–480.
23. E. G. Rozantsev, *Free Nitroxide Radicals*, Springer, New York, 1970.
24. J. L. Hodgson, M. Namazian, S. E. Bottle and M. L. Coote, *J. Phys. Chem. A*, 2007, **111**, 13595–13605.
25. J. P. Blinco, J. L. Hodgson, B. J. Morrow, J. R. Walker, G. D. Will, M. L. Coote and S. E. Bottle, *J. Org. Chem.*, 2008, **73**, 6763–6771.
26. K. Zhang, B. B. Noble, A. C. Mater, M. J. Monteiro, M. L. Coote and Z. Jia, *Phys. Chem. Chem. Phys.*, 2018, **20**, 2606–2614.
27. T. Janoschka, M. D. Hager and U. S. Schubert, *Adv. Mater.*, 2012, **24**, 6397–6409.
28. K.-A. Hansen and J. P. Blinco, *Polym. Chem.*, 2018, **9**, 1479–1516.
29. O. H. Griffith, J. F. Keana, S. Rottschaefer and T. Warlick, *J. Am. Chem. Soc.*, 1967, **89**, 5072.
30. S. Komaba, T. Tanaka, T. Ozeki, T. Taki, H. Watanabe and H. Tachikawa, *J. Power Sources*, 2010, **195**, 6212–6217.

31. T. Sukegawa, H. Omata, I. Masuko, K. Oyaizu and H. Nishide, *ACS Macro Lett.*, 2014, **3**, 240–243.
32. Z. F. Jia, Q. Fu and J. L. Huang, *J. Polym. Sci., Part A: Polym. Chem.*, 2006, **44**, 3836–3842.
33. Z. F. Jia, Q. Fu and J. L. Huang, *Macromolecules*, 2006, **39**, 5190–5193.
34. K. Oyaizu, T. Suga, K. Yoshimura and H. Nishide, *Macromolecules*, 2008, **41**, 6646–6652.
35. Y. Joo, V. Agarkar, S. H. Sung, B. M. Savoie and B. W. Boudouris, *Science*, 2018, **359**, 1391–1395.
36. T. Endo, K. Takuma, T. Takata and C. Hirose, *Macromolecules*, 1993, **26**, 3227–3229.
37. T. Sukegawa, K. Sato, K. Oyaizu and H. Nishide, *RSC Adv.*, 2015, **5**, 15448–15452.
38. J. Zhang, H. Shen, W. Song and G. Wang, *Macromolecules*, 2017, **50**, 2683–2695.
39. T. Yoshitomi, A. Hirayama and Y. Nagasaki, *Biomaterials*, 2011, **32**, 8021–8028.
40. T. Yoshitomi, D. Miyamoto and Y. Nagasaki, *Biomacromolecules*, 2009, **10**, 596–601.
41. T. Janoschka, N. Martin, U. Martin, C. Friebe, S. Morgenstern, H. Hiller, M. D. Hager and U. S. Schubert, *Nature*, 2015, **527**, 78–81.
42. M. Suguro, S. Iwasa, Y. Kusachi, Y. Morioka and K. Nakahara, *Macromol. Rapid Commun.*, 2007, **28**, 1929–1933.
43. H. K. Lee, K. T. Bang, A. Hess, R. H. Grubbs and T. L. Choi, *J. Am. Chem. Soc.*, 2015, **137**, 9262–9265.
44. O. M. Ogba, N. C. Warner, D. J. O'Leary and R. H. Grubbs, *Chem. Soc. Rev.*, 2018, **47**, 4510–4544.
45. A. Fujii, T. Ishida, N. Koga and H. Iwamura, *Macromolecules*, 1991, **24**, 1077–1082.
46. K. Oyaizu, T. Sukegawa and H. Nishide, *Chem. Lett.*, 2011, **40**, 184–185.
47. J. Qu, T. Katsumata, M. Satoh, J. Wada and T. Masuda, *Macromolecules*, 2007, **40**, 3136–3144.
48. J. Qu, T. Katsumata, M. Satoh, J. Wada, J. Igarashi, K. Mizoguchi and T. Masuda, *Chem. – Eur. J.*, 2007, **13**, 7965–7973.
49. J. Qu, T. Fujii, T. Katsumata, Y. Suzuki, M. Shiotsuki, F. Sanda, M. Satoh, J. Wada and T. Masuda, *J. Polym. Sci., Part A: Polym. Chem.*, 2007, **45**, 5431–5445.
50. P. Nesvadba, L. Bugnon, P. Maire and P. Novák, *Chem. Mater.*, 2009, **22**, 783–788.
51. T. Katsumata, J. Qu, M. Shiotsuki, M. Satoh, J. Wada, J. Igarashi, K. Mizoguchi and T. Masuda, *Macromolecules*, 2008, **41**, 1175–1183.
52. T. Katsumata, M. Satoh, J. Wada, M. Shiotsuki, F. Sanda and T. Masuda, *Macromol. Rapid Commun.*, 2006, **27**, 1206–1211.
53. T. Sukegawa, I. Masuko, K. Oyaizu and H. Nishide, *Macromolecules*, 2014, **47**, 8611–8617.

54. T. W. Kemper, T. Gennett and R. E. Larsen, *J. Phys. Chem. C*, 2016, **120**, 25639–25646.
55. M. A. Sowers, J. R. McCombs, Y. Wang, J. T. Paletta, S. W. Morton, E. C. Dreaden, M. D. Boska, M. F. Ottaviani, P. T. Hammond, A. Rajca and J. A. Johnson, *Nat. Commun.*, 2014, **5**, 5460.
56. D. Le, M. Dilger, V. Pertici, S. Diabaté, D. Gigmes, C. Weiss and G. Delaittre, *Angew. Chem., Int. Ed.*, 2019, **58**, 4725–4731.
57. E. H. Kang, S. Y. Yu, I. S. Lee, S. E. Park and T. L. Choi, *J. Am. Chem. Soc.*, 2014, **136**, 10508–10514.
58. Y. Xie, K. Zhang, M. J. Monteiro and Z. Jia, *ACS Appl. Mater. Interfaces*, 2019, **11**, 7096–7103.
59. T. Ibe, R. B. Frings, A. Lachowicz, S. Kyo and H. Nishide, *Chem. Commun.*, 2010, **46**, 3475–3477.
60. C. Lang, L. Barner, J. P. Blinco, C. Barner-Kowollik and K. E. Fairfull-Smith, *Polym. Chem.*, 2018, **9**, 1348–1355.
61. M. Aydın, B. Esat, Ç. Kılıç, M. Köse, A. Ata and F. Yılmaz, *Eur. Polym. J.*, 2011, **47**, 2283–2294.
62. F. Li, Y. Zhang, S. R. Kwon and J. L. Lutkenhaus, *ACS Macro Lett.*, 2016, **5**, 337–341.
63. F. Li, D. N. Gore, S. Wang and J. L. Lutkenhaus, *Angew. Chem., Int. Ed.*, 2017, **56**, 9856–9859.
64. F. Li, S. Wang, Y. Zhang and J. L. Lutkenhaus, *Chem. Mater.*, 2018, **30**, 5169–5174.
65. H. Woehlk, J. Steinkoenig, C. Lang, L. Michalek, V. Trouillet, P. Krolla, A. S. Goldmann, L. Barner, J. P. Blinco, C. Barner-Kowollik and K. E. Fairfull-Smith, *Langmuir*, 2018, **34**, 3264–3274.
66. S.-A. Alexander, C. Kyi and C. H. Schiesser, *Org. Biomol. Chem.*, 2015, **13**, 4751–4759.
67. T. Janoschka, A. Teichler, A. Krieg, M. D. Hager and U. S. Schubert, *J. Polym. Sci., Part A: Polym. Chem.*, 2012, **50**, 1394–1407.
68. O. Bertrand, B. Ernould, F. Boujioui, A. Vlad and J.-F. Gohy, *Polym. Chem.*, 2015, **6**, 6067–6072.
69. K. Zhang, Y. Hu, L. Wang, J. Fan, M. J. Monteiro and Z. Jia, *Polym. Chem.*, 2017, **8**, 1815–1823.
70. M.-K. Hung, Y.-H. Wang, C.-H. Lin, H.-C. Lin and J.-T. Lee, *J. Mater. Chem.*, 2012, **22**, 1570–1577.
71. H.-C. Lin, C.-C. Li and J.-T. Lee, *J. Power Sources*, 2011, **196**, 8098–8103.
72. Y.-H. Wang, M.-K. Hung, C.-H. Lin, H.-C. Lin and J.-T. Lee, *Chem. Commun.*, 2011, **47**, 1249–1251.
73. J. P. Blinco, B. A. Chalmers, A. Chou, K. E. Fairfull-Smith and S. E. Bottle, *Chem. Sci.*, 2013, **4**, 3411–3414.
74. K.-A. Hansen, J. Nerkar, K. Thomas, S. E. Bottle, A. P. O'Mullane, P. C. Talbot and J. P. Blinco, *ACS Appl. Mater. Interfaces*, 2018, **10**, 7982–7988.
75. J. Kulis, C. A. Bell, A. S. Micallef, Z. Jia and M. J. Monteiro, *Macromolecules*, 2009, **42**, 8218–8227.

76. Z. F. Jia, C. A. Bell and M. J. Monteiro, *Macromolecules*, 2011, **44**, 1747–1751.
77. F. Behrends, H. Wagner, A. Studer, O. Niehaus, R. Pöttgen and H. Eckert, *Macromolecules*, 2013, **46**, 2553–2561.
78. T. Suga, Y.-J. Pu, S. Kasatori and H. Nishide, *Macromolecules*, 2007, **40**, 3167–3173.
79. H. Fu, D. M. Policarpio, J. D. Batteas and D. E. Bergbreiter, *Polym. Chem.*, 2010, **1**, 631–633.
80. P. Schattling, F. D. Jochum and P. Theato, *Chem. Commun.*, 2011, **47**, 8859–8861.
81. Z. F. Jia, C. A. Bell and M. J. Monteiro, *Chem. Commun.*, 2011, **47**, 4165–4167.
82. T. K. Kunz and M. O. Wolf, *Polym. Chem.*, 2011, **2**, 640–644.
83. K. Saito, K. Hirose, T. Okayasu, H. Nishide and M. T. W. Hearn, *RSC Adv.*, 2013, **3**, 9752–9756.
84. M. Suguro, A. Mori, S. Iwasa, K. Nakahara and K. Nakano, *Macromol. Chem. Phys.*, 2009, **210**, 1402–1407.
85. J. Qu, F. Z. Khan, M. Satoh, J. Wada, H. Hayashi, K. Mizoguchi and T. Masuda, *Polymer*, 2008, **49**, 1490–1496.
86. Y. Wang, J. L. DuBois, B. Hedman, K. O. Hodgson and T. D. P. Stack, *Science*, 1998, **279**, 537–540.
87. G. M. Coppinger, *Tetrahedron*, 1962, **18**, 61–65.
88. G. M. Coppinger, *J. Am. Chem. Soc.*, 1957, **79**, 501–502.
89. F. G. Bordwell and J. Cheng, *J. Am. Chem. Soc.*, 1991, **113**, 1736–1743.
90. R. D. Webster, *Electrochem. Commun.*, 2003, **5**, 6–11.
91. T. Suga, H. Ohshiro, S. Sugita, K. Oyaizu and H. Nishide, *Adv. Mater.*, 2009, **21**, 1627–1631.
92. M. Miyasaka, T. Yamazaki, E. Tsuchida and H. Nishide, *Macromolecules*, 2000, **33**, 8211–8217.
93. T. Jahnert, M. D. Hager and U. S. Schubert, *Macromol. Chem. Phys.*, 2016, **37**, 725–730.
94. B. Häupler, A. Ignaszak, T. Janoschka, T. Jähnert, M. D. Hager and U. S. Schubert, *Macromol. Chem. Phys.*, 2014, **215**, 1250–1256.
95. J. B. Gilroy, S. D. J. McKinnon, B. D. Koivisto and R. G. Hicks, *Org. Lett.*, 2007, **9**, 4837–4840.
96. J. A. Paquette, S. Ezugwu, V. Yadav, G. Fanchini and J. B. Gilroy, *J. Polym. Sci., Part A: Polym. Chem.*, 2016, **54**, 1803–1813.
97. J. T. Price, J. A. Paquette, C. S. Harrison, R. Bauld, G. Fanchini and J. B. Gilroy, *Polym. Chem.*, 2014, **5**, 5223–5226.
98. S. Almubayedh and M. h. Chahma, *New J. Chem.*, 2015, **39**, 7738–7741.
99. M. A. Colucci, G. D. Couch and C. J. Moody, *Org. Biomol. Chem.*, 2008, **6**, 637–656.
100. P. S. Guin, S. Das and P. C. Mandal, *Int. J. Electrochem.*, 2011, **2011**, 1–22.
101. Y. Liu, K. Ai and L. Lu, *Chem. Rev.*, 2014, **114**, 5057–5115.
102. M. Morrison, W. Steele and D. J. Danner, *Arch. Biochem. Biophys.*, 1969, **134**, 515–523.

103. V. S. Nithianandam and S. Erhan, *Polymer*, 1998, **39**, 4095–4098.
104. A. M. Navarro-Suárez, J. Carretero-González, T. Rojo and M. Armand, *J. Mater. Chem. A*, 2017, **5**, 23292–23298.
105. K. Takada, P. Gopalan, C. K. Ober and H. D. Abruna, *Chem. Mater.*, 2001, **13**, 2928–2932.
106. C. Karlsson, H. Huang, M. Strømme, A. Gogoll and M. Sjödin, *J. Phys. Chem. C*, 2014, **118**, 23499–23508.
107. C. Karlsson, H. Huang, M. Stromme, A. Gogoll and M. Sjodin, *RSC Adv.*, 2015, **5**, 11309–11316.
108. N. S. Allen, J. P. Hurley, A. Rahman, G. W. Follows and I. Weddell, *Eur. Polym. J.*, 1993, **29**, 1155–1160.
109. W. Choi, D. Harada, K. Oyaizu and H. Nishide, *J. Am. Chem. Soc.*, 2011, **133**, 19839–19843.
110. B. Haupler, R. Burges, T. Janoschka, T. Jahnert, A. Wild and U. S. Schubert, *J. Mater. Chem. A*, 2014, **2**, 8999–9001.
111. B. Haupler, T. Hagemann, C. Friebe, A. Wild and U. S. Schubert, *ACS Appl. Mater. Interfaces*, 2015, **7**, 3473–3479.
112. S. Muench, J. Winsberg, C. Friebe, A. Wild, J. C. Brendel, A. Lex-Balducci and U. S. Schubert, *ACS Appl. Energy Mater.*, 2018, **1**, 3554–3559.
113. T. Kawai, K. Oyaizu and H. Nishide, *Macromolecules*, 2015, **48**, 2429–2434.
114. K. Motokuni, B. Häupler, R. Burges, M. D. Hager and U. S. Schubert, *J. Polym. Sci., Part A: Polym. Chem.*, 2016, **54**, 2184–2190.
115. S. Moulay and R. Mehdaoui, *React. Funct. Polym.*, 2004, **61**, 265–275.
116. B. L. Funt and P. M. Hoang, *J. Electrochem. Soc.*, 1984, **131**, 2295–2298.
117. K. Oyaizu, W. Choi and H. Nishide, *Polym. Adv. Technol.*, 2011, **22**, 1242–1247.
118. R. D. Milton, D. P. Hickey, S. Abdellaoui, K. Lim, F. Wu, B. Tan and S. D. Minteer, *Chem. Sci.*, 2015, **6**, 4867–4875.
119. J. Ding, C. Zheng, L. Wang, C. Lu, B. Zhang, Y. Chen, M. Li, G. Zhai and X. Zhuang, *J. Mater. Chem. A*, 2019, **7**, 23337–23360.
120. Q. Sui, X. T. Ren, Y. X. Dai, K. Wang, W. T. Li, T. Gong, J. J. Fang, B. Zou, E. Q. Gao and L. Wang, *Chem. Sci.*, 2017, **8**, 2758–2768.
121. W. Wang and V. Sprenkle, *Nat. Chem.*, 2016, **8**, 204–206.
122. K. Madasamy, D. Velayutham, V. Suryanarayanan, M. Kathiresan and K.-C. Ho, *J. Mater. Chem. C*, 2019, **7**, 4622–4637.
123. A. O. Delawder, A. Natraj, N. D. Colley, T. Saak, A. F. Greene and J. C. Barnes, *Supramol. Chem.*, 2019, **31**, 523–531.
124. K. Murugavel, *Polym. Chem.*, 2014, **5**, 5873–5884.
125. T. Janoschka, S. Morgenstern, H. Hiller, C. Friebe, K. Wolkersdorfer, B. Haupler, M. D. Hager and U. S. Schubert, *Polym. Chem.*, 2015, **6**, 7801–7811.
126. G. Nagarjuna, J. Hui, K. J. Cheng, T. Lichtenstein, M. Shen, J. S. Moore and J. Rodríguez-López, *J. Am. Chem. Soc.*, 2014, **136**, 16309–16316.

127. M. Burgess, E. Chénard, K. Hernández-Burgos, G. Nagarjuna, R. S. Assary, J. Hui, J. S. Moore and J. Rodríguez-López, *Chem. Mater.*, 2016, **28**, 7362–7374.
128. F. Chen, Y. Ren, J. Guo and F. Yan, *Chem. Commun.*, 2017, **53**, 1595–1598.
129. S. Y. Kao, H. C. Lu, C. W. Kung, H. W. Chen, T. H. Chang and K. C. Ho, *ACS Appl. Mater. Interfaces*, 2016, **8**, 4175–4184.
130. F. Amir, K. P. Liles, A. O. Delawder, N. D. Colley, M. S. Palmquist, H. R. Linder, S. A. Sell and J. C. Barnes, *ACS Appl. Mater. Interfaces*, 2019, **11**, 24627–24638.
131. H. V. Schroder and C. A. Schalley, *Beilstein J. Org. Chem.*, 2018, **14**, 2163–2185.
132. A. Jana, S. Bähring, M. Ishida, S. Goeb, D. Canevet, M. Sallé, J. O. Jeppesen and J. L. Sessler, *Chem. Soc. Rev.*, 2018, **47**, 5614–5645.
133. M. L. Kaplan, R. C. Haddon, F. Wudl and E. D. Feit, *J. Org. Chem.*, 1978, **43**, 4642–4646.
134. G. Koßmehl and M. Rohde, *Makromol. Chem. Rapid Comm.*, 1982, **183**, 2077–2084.
135. A. H. Schroeder, F. B. Kaufman, V. Patel and E. M. Engler, *J. Electroanal. Chem. Interf. Electrochem.*, 1980, **113**, 193–208.
136. K. Tanaka, T. Matsumoto and Y. Chujo, *Synth. Met.*, 2013, **163**, 13–18.
137. R. C. Selhorst, E. Puodziukynaite, J. A. Dewey, P. Wang, M. D. Barnes, A. Ramasubramaniam and T. Emrick, *Chem. Sci.*, 2016, **7**, 4698–4705.
138. T. Shimizu and T. Yamamoto, *Chem. Commun.*, 1999, 515–516.
139. E. Gomar-Nadal, J. Veciana, C. Rovira and D. B. Amabilino, *Adv. Mater.*, 2005, **17**, 2095–2098.
140. D. Astruc, *Eur. J. Inorg. Chem.*, 2017, **2017**, 6–29.
141. K. Heinze and H. Lang, *Organometallics*, 2013, **32**, 5623–5625.
142. J. Wu, L. Wang, H. Yu, A. Zain ul, R. U. Khan and M. Haroon, *J. Organomet. Chem.*, 2017, **828**, 38–51.
143. J. Elbert, M. Gallei, C. Ruttiger, A. Brunsen, H. Didzoleit, B. Stuhn and M. Rehahn, *Organometallics*, 2013, **32**, 5873–5878.
144. J. Morsbach, A. Natalello, J. Elbert, S. Winzen, A. Kroeger, H. Frey and M. Gallei, *Organometallics*, 2013, **32**, 6033–6039.
145. S. Z. Bas, E. Maltas, B. Sennik and F. Yilmaz, *Colloid. Surf. A Physicochem. Eng. Asp.*, 2014, **444**, 40–47.
146. A. Alkan, A. Natalello, M. Wagner, H. Frey and F. R. Wurm, *Macromolecules*, 2014, **47**, 2242–2249.
147. A. Alkan, L. Thomi, T. Gleede and F. R. Wurm, *Polym. Chem.*, 2015, **6**, 3617–3624.
148. V. S. V. Satyanarayana, V. Singh, V. Kalyani, C. P. Pradeep, S. Sharma, S. Ghosh and K. E. Gonsalves, *RSC Adv.*, 2014, **4**, 59817–59820.
149. T. Mao, L. Yang, G. Liu, Y. Wei, Y. Gou, J. Wang and L. Tao, *ACS Macro Lett.*, 2019, **8**, 639–645.
150. X. Jiang, R. Li, C. Feng, G. Lu and X. Huang, *Polym. Chem.*, 2017, **8**, 2773–2784.

151. S. Pandey, P. Lonnecke and E. Hey-Hawkins, *Eur. J. Inorg. Chem.*, 2014, **2014**, 2456–2465.
152. D. C. Kraiter, P. Wisian-Neilson, C. P. Zhang and A. L. Crumbliss, *Macromolecules*, 2012, **45**, 3658–3668.
153. M. Zamora, S. Bruna, B. Alonso and I. Cuadrado, *Macromolecules*, 2011, **44**, 7994–8007.
154. K. Parab and F. Jäkle, *Macromolecules*, 2009, **42**, 4002–4007.
155. S. A. Merchant, M. T. Meredith, T. O. Tran, D. B. Brunski, M. B. Johnson, D. T. Glatzhofer and D. W. Schmidtke, *J. Phys. Chem. C*, 2010, **114**, 11627–11634.
156. V. Bellas and M. Rehahn, *Angew. Chem., Int. Ed.*, 2007, **46**, 5082–5104.
157. R. L. Hailes, A. M. Oliver, J. Gwyther, G. R. Whittell and I. Manners, *Chem. Soc. Rev.*, 2016, **45**, 5358–5407.
158. E. W. Neuse, *Nature*, 1964, **204**, 179–180.
159. H. Li, L. Li, H. Wu, J. W. Y. Lam, J. Z. Sun, A. Qin and B. Z. Tang, *Polym. Chem.*, 2013, **4**, 5537–5541.
160. H. Li, W. Chi, Y. Liu, W. Yuan, Y. Li, Y. Li and B. Z. Tang, *Macromol. Chem. Phys.*, 2017, **38**, 1700075.
161. Y. Sha, Y. Zhang, T. Zhu, S. Tan, Y. Cha, S. L. Craig and C. Tang, *Macromolecules*, 2018, **51**, 9131–9139.
162. Y. Sha, M. A. Rahman, T. Zhu, Y. Cha, C. W. McAlister and C. Tang, *Chem. Sci.*, 2019, **10**, 9782–9787.
163. N. H. Attanayake, J. A. Kowalski, K. V. Greco, M. D. Casselman, J. D. Milshtein, S. J. Chapman, S. R. Parkin, F. R. Brushett and S. A. Odom, *Chem. Mater.*, 2019, **31**, 4353–4363.
164. E. Gipstein, W. A. Hewett and O. U. Need, *J. Polym. Sci., Part A: Polym. Chem.*, 1970, **8**, 3285–3294.
165. Z. Gomurashvili and J. V. Crivello, *Macromolecules*, 2002, **35**, 2962–2969.
166. A. A. Golriz, T. Suga, H. Nishide, R. Berger and J. S. Gutmann, *RSC Adv.*, 2015, **5**, 22947–22950.
167. J. A. Kowalski, M. D. Casselman, A. P. Kaur, J. D. Milshtein, C. F. Elliott, S. Modekrutti, N. H. Attanayake, N. Zhang, S. R. Parkin, C. Risko, F. R. Brushett and S. A. Odom, *J. Mater. Chem. A*, 2017, **5**, 24371–24379.
168. J. Huang, B. Pan, W. Duan, X. Wei, R. S. Assary, L. Su, F. R. Brushett, L. Cheng, C. Liao, M. S. Ferrandon, W. Wang, Z. Zhang, A. K. Burrell, L. A. Curtiss, I. A. Shkrob, J. S. Moore and L. Zhang, *Sci. Rep.*, 2016, **6**, 32102.
169. P. Nesvadba, L. B. Folger, P. Maire and P. Novák, *Synth. Met.*, 2011, **161**, 259–262.
170. J. Wang, K. Liu, L. Ma and X. Zhan, *Chem. Rev.*, 2016, **116**, 14675–14725.
171. T. Liu, J. Sun, R. Li and X. Tao, *Chin. J. Org. Chem.*, 2011, **31**, 1799–1810.
172. X. Wu, A. P. Davis, P. C. Lambert, L. Kraig Steffen, O. Toy and A. J. Fry, *Tetrahedron*, 2009, **65**, 2408–2414.
173. W. Deng, X. Liang, X. Wu, J. Qian, Y. Cao, X. Ai, J. Feng and H. Yang, *Sci. Rep.*, 2013, **3**, 2671.

174. R. Schroot, M. Jäger and U. S. Schubert, *Macromolecules*, 2019, **52**, 4673–4685.
175. W. Deng, J. Qian, Y. Cao, X. Ai and H. Yang, *Small*, 2016, **12**, 583–587.
176. M. Armand, S. Grugeon, H. Vezin, S. Laruelle, P. Ribiere, P. Poizot and J. M. Tarascon, *Nat. Mater.*, 2009, **8**, 120–125.
177. C. Li, J. Xue, J. Ma and J. Li, *J. Electrochem. Soc.*, 2018, **166**, A5221–A5225.
178. L. Yang, X. Huang, F. Mamedov, P. Zhang, A. Gogoll, M. Stromme and M. Sjodin, *Phys. Chem. Chem. Phys.*, 2017, **19**, 25052–25058.
179. K. Oka, R. Kato, K. Oyaizu and H. Nishide, *Adv. Funct. Mater.*, 2018, **28**, 1805858.

CHAPTER 3

# *Atomic-scale Modelling of Redox-active Organic Molecules and Polymers for Energy Applications*

RODRIGO P. CARVALHO,[a] CLEBER F. N. MARCHIORI,[b] C. MOYSES ARAUJO[a] AND DANIEL BRANDELL*[b]

[a] Materials Theory Division, Department of Physics and Astronomy, Uppsala University, Box 516, 75120 Uppsala, Sweden; [b] Department of Chemistry – Ångström Laboratory, Uppsala University, Box 538, 75121 Uppsala, Sweden
*Email: Daniel.Brandell@kemi.uu.se

## 3.1 Introduction

The classical use of modelling techniques in materials science has been to reach an in-depth *understanding* of relevant structures and processes. The molecular, atomic and electronic scales are all difficult to assess even with the best experimental techniques, and modelling has for many decades been shown to assist in the interpretation of a large range of chemical and physical phenomena. The reliability of these computational techniques, which often by necessity have had to employ vast approximations, has on the other hand been rightfully questioned at times. Presently, however, we are experiencing a rapid development of computer power to a degree where we can much better use these methodologies in a trustworthy way. These tools

Polymer Chemistry Series No. 34
Redox Polymers for Energy and Nanomedicine
Edited by Nerea Casado and David Mecerreyes

Published by the Royal Society of Chemistry, www.rsc.org

are becoming good enough to use for problems that seemed too complex just years ago. Nowadays, chemical reactions and mass transport phenomena in complex composites with components in different phases and with advanced interfacial structures can be explored through multiscale techniques. This also means that computational techniques can be used for *prediction* in a different sense than they were previously normally applied for. This might indeed constitute a disruptive moment for the employment of computational materials science: when large numbers of components, chemistries and structures can be explored reliably by the means of computers, this will save large costs and at the same time render better materials. Using machine-learning approaches, intelligent screening studies can be performed. The larger the structural variations of the system, the more effective will this methodology be as compared to the traditional experimental counterparts. In the context of organic redox-active materials, where the structural variation is large, there will surely be a lot to gain from modelling.

The traditional framework for materials modelling spans several computational techniques. The more refined the approximations, the more expensive the technique becomes. Advanced electronic structure calculations generally require *ab initio* techniques and the solution of the appropriate Hartree–Fock equation. This is demanding, and thereby limits the system size. For most materials science problems, density functional theory (DFT) serve the same purpose, but often with lower computational costs. These techniques can explore the electronic structures of the materials, redox reactions, electron transport, *etc.* Electronic structure is also necessary for most problems involving coordination chemistry. Mass transport – diffusion, migration, convection – on the one hand, requires less refined electronic structure estimations, but on the other hand needs a larger system size to accurately capture the structure and dynamics of the system. For these problems, force-field methods, where the interactions are described through analytical expressions, are adequate. For larger morphologies, coarse-graining of the molecular components might be necessary, which increase the level of approximation further but allow for even larger structures. At the system level, materials modelling is generally of little use, and modelling requires an analytical description of the relevant processes, instead of the materials *per se*. With the advent of multiscale modelling tools, however, there are presently much better possibilities to resolve questions which appear over several length and time scales, as well as exploring how microscopic and macroscopic phenomena are interrelated. This is also highly relevant for organic redox-active materials, which often display complex macroscopic structures which control the microscopic redox activity – and *vice versa*.

In particular, there are a number of problems and issues for electroactive organic materials which can be addressed by different computational techniques. DFT or *ab initio* calculations are highly useful to model the kinetics of redox reactions, electrochemical potentials, defect energies, dissociation

energy, adsorption energy, energy barriers and general chemical stability *vs.* other compounds. The thermodynamics of different redox processes can also be estimated accurately through DFT calculations. These are often vital processes and phenomena for organic electroactive materials. Furthermore, there are ample opportunities for comparison with experimental data from organic redox materials, not least spectroscopy, using electronic structure calculations. If the system is small enough, these electronic structure calculations can also be used for estimating interacting forces between the particles, and are thereby useful for investigation of the dynamics of the redox processes. If the system is large, on the other hand, molecular dynamics (MD) simulations or kinetic Monte Carlo (kMC) methods are more useful to employ. Here, diffusivities and a range of structure-dynamic properties can be analysed. Especially for nonperiodic structures or liquid–solid interfaces, which are often the case for many organic devices employed for energy storage and conversion, these methods are highly useful for exploration of both macromolecular structure and ionic or solvent transport. Similar methodologies but with more severe approximation are then necessary to explore the meso-scale (above the nanometer level), where the true morphology of these materials is captured.

In this chapter, we exemplify through a number of relevant examples in recent literature how different modelling approaches are used to gain insights into different electroactive organic materials, spanning over organic solar cells, organic semiconductors, organic battery electrodes and organic supercapacitors. The chapter is focused on different key methodologies, and how these are utilized to gain insights into fundamental properties of this rich category of materials and devices.

## 3.2 Electronic Structure and Optical Properties from Oligomeric Models

As already mentioned, DFT is nowadays both a versatile and important tool in computational materials science. This is indeed a very powerful method to describe the electronic structure of multi-electronic systems such as molecules and solids.

The pillar of the DFT methodology is the Hohenberg–Kohn theorems.[1] The first one states that there is a one-to-one correspondence between the ground-state density, $\rho(r)$, of an interacting-particle system and the external potential that it is subjected to. As a consequence, the ground-state expectation value of any observable can be written a functional of the ground-state density. Thus, the latter becomes the main entity to describe the physical properties of a given system. Furthermore, the second theorem states that for any external potential, $V_{\text{ext}}$, applied to the interacting-particle system it is possible to define a universal total energy functional, written as:

$$E[\rho(\boldsymbol{r})] = E_{HK}[\rho(\boldsymbol{r})] + \int V_{\text{ext}}(\boldsymbol{r})\rho(\boldsymbol{r})\mathrm{d}\boldsymbol{r} \tag{3.1}$$

where $E_{HK}[\rho(r)]$ is the term including all internal interactions of the system. By using the variational theorem, the ground-state total energy of the system is obtained by finding the electronic density that minimizes eqn (3.1).

Moreover, the DFT framework is based on the Kohn–Sham ansatz,[2] which essentially assumes that the actual interacting many-body system is equivalent to a noninteracting system submitted to an external effective potential. The resulting energy functional is:

$$E[\rho(r)] = T[\rho(r)] + \int V_{\text{ext}}(r)\rho(r)\mathrm{d}r + \frac{1}{2}\iint \frac{\rho(r)\rho(r')}{|r-r'|} + E_{xc}[\rho(r)], \qquad (3.2)$$

where $E_{xc} = E_x[\rho(r)] + E_c[\rho(r)]$ are the exchange and correlation terms. The exchange–correlation functional can be considered as the core of this methodology. This term gives rise to a set of different classes of functionals which use different approximations to compute this quantity. For instance, the local density approximation (LDA), the simplest way to calculate the exchange and correlation, considers that the exchange–correlation density of energy $\varepsilon_{xc}$ is approximated as a uniform electron gas at each point in space. In the so-called generalized gradient approximation (GGA), this is improved by considering $\varepsilon_{xc}$ dependent on the electronic density and on the gradient of the electronic energy in each point in space. Many different functionals have been proposed, for example, Becke[3] and Lee, Parr and Yang.[4]

Some extensions to the GGA approach are largely employed in DFT calculations. Not least are those which include a percentage of exact exchange from the Hartree–Fock approach, as is the well-known B3LYP functional,[3] which is the most widely used functional for calculations related to organic molecular systems. Another example of hybrid functionals is the Minnesota series – M06,[5] M08HX[6] and MN15[7] – which is suitable for investigation of thermochemistry, thermochemical kinetics and noncovalent interactions. Using one of these functionals, *viz.* the M06 [more precisely, M06/6-311G(d,p)[8,9] theory level], some examples of calculations of the electronic structures and optical properties (UV–vis absorption) illustrate well how the properties of organic materials can be calculated using DFT and the Gaussian16 code.[10]

DFT calculations have been widely used for many years in the field of organic photovoltaics. For instance, the benchmark system consisting of the polymer poly-3-hexylthiophene (P3HT) as the electron donor and the fullerene $C_{60}$ as electron-acceptor materials was explored by means of DFT calculations, aiming to gain insights into the physics underlying the electron–hole pair (usually called an exciton) dissociation. By using solid-state calculations and periodic boundary conditions,[11] the molecular level[12,13] electronic structure of P3HT:fullerene complexes was explored, shedding light on the energy-level alignments and the hybridization of the electronic states on the exciton dissociation at the donor:acceptor heterostructure. These studies described how the coupling of the donor electronic structure with the acceptor is related to the exciton dissociation process.

In particular, the ground state charge transfer in donor–acceptor complexes gives rise to a local dipole moment, which might assist the exciton dissociation.[12–15]

Recently, with the advent of novel electron acceptors, the field experienced a new stage of development with devices reaching previously unprecedented photovoltaic power conversion efficiencies of up to 17%.[16,17] These new 'nonfullerene' electron acceptors[18] display much higher absorption coefficients in the visible range in comparison to fullerene and its derivatives. Thanks to this feature, these materials can be designed to form donor–acceptor heterojunctions with suitable energy-level alignments for the electron–hole transfer, resulting in exciton dissociation. Furthermore, a complementary absorption profile can be achieved if the donor and acceptor materials display absorptions peaks in different ranges of the visible spectrum.[19,20] Additionally, by properly combining electron-donating and electron-withdrawing building blocks, it is possible to design molecules with an intrinsic spatial separation of the frontier orbitals Highest Occupied Molecular Orbital (HOMO) and Lowest Unoccupied Molecular Orbital (LUMO) which can favour the electron–hole separation and thereby enhance the excited state lifetime.

Figure 3.1 depicts the spatial distribution of the HOMO and LUMO orbitals of three nonfullerene acceptors, calculated by DFT calculations. It is possible to see that for the DCAO3T(BDT)3T molecule,[21] the HOMO orbital is delocalized over the central benzodithiophene (BDT) unit as well as over the neighbouring thiophene rings (T), while the LUMO is mainly distributed over the thiophene units and the ending groups which have electron-withdrawing characteristics. This indicates that instantaneously after the absorption of one photon, an exciton with a spatial separation of the electron and the hole can be formed, resulting in a long-lived excited state unless the structural relaxation in the excited state assists the recombination process. On the other hand, for the other two acceptors, that is, FDICTF and FDNCTF, both HOMO and LUMO are delocalized over the whole molecule, indicating that these molecules do not display internal charge transfer character.

Troisi *et al.* performed an extensive study of the electronic and geometric structure of nonfullerene acceptors for organic solar cells. By using DFT calculations, they investigated a set of 80 high-performing materials in a search for descriptors which can be used to design new materials. They discovered that all high-performing materials display a very low gap between LUMO and LUMO + 1 orbitals.[22] This feature may be responsible for the ability of the material to withdraw electrons from the excited donor molecule.

Conjugated polymers are another class of materials that has been intensively explored for many energy-related applications. In particular, in the field of organic photovoltaics, there is a vast literature regarding these materials as promising candidates for solar energy conversion. In particular, donor–acceptor copolymers have been largely explored for solar cells[23–26]

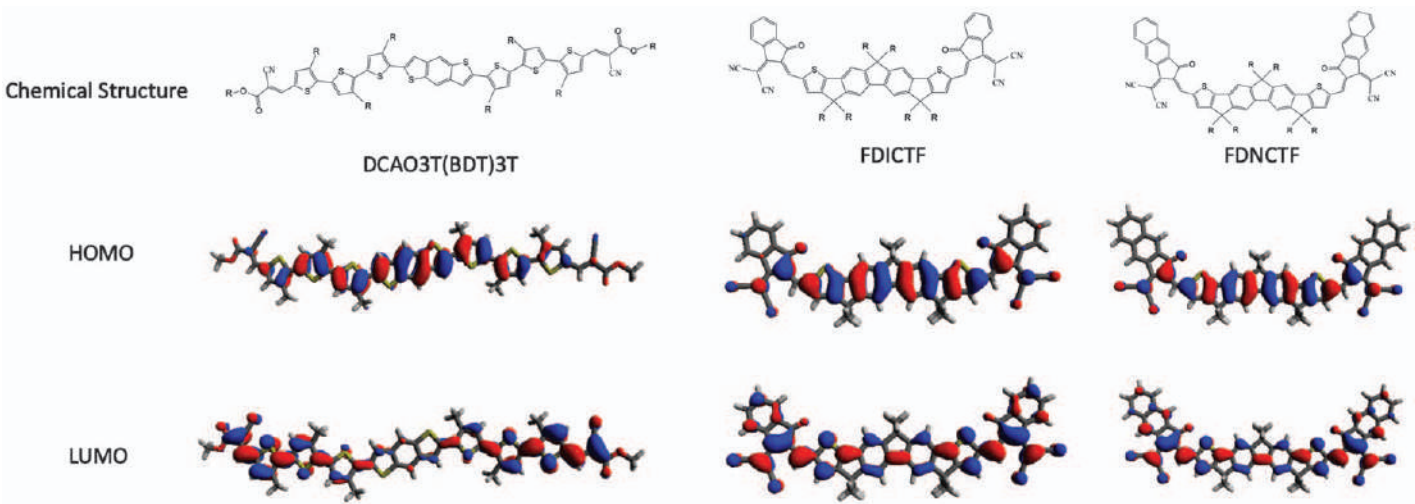


**Figure 3.1** Chemical structure and spatial distribution of HOMO and LUMO orbitals (isovalue: 0.02) for three nonfullerene acceptors. The orbitals were obtained from calculation at M06/6-311G(d,p) theory level.

and more recently as photocatalysts for hydrogen production.[27–30] Besides the energy-generation applications, some of these polymers are also considered as candidates for application as electrodes in Li-ion or Na-ion batteries.[31–33] From a computational point of view, modelling a polymeric material demands a systematic study in order to get the correct description of the desired properties. For instance, when using molecular calculation (*i.e.*, without using periodic boundary conditions) the first step is to build a proper oligomeric model that is able to describe the properties of the polymeric material fairly. Usually this is a compromise between the accuracy and the computational power demanded for the calculations.

One possible way to proceed beyond this compromise is to perform a convergency study of the energy levels, aiming to find the size of the chain needed to describe the energy levels or redox potentials. As shown in Figure 3.2, conjugated polymers, exemplified by polythiophene (PT), and conventionally nonredox-active polymers such as poly(ethylene oxide) (PEO) display a very distinct behaviour. The evolution of the redox potentials when increasing the number of monomers in PT displays a convergence tendency (see Figure 3.2a), reaching an almost stationary value after six units. The main reason behind this effect is that a minimum size of the chain is necessary to reproduce the conjugation length, enabling the orbital delocalization and minimizing the confinement effect due to the finite size of the chain. By plotting the redox potential *versus* the inverse of the number of units (Figure 3.2b), the value of the potential for an 'infinite' chain can be estimated. The nonconjugated polymer, on the other hand, has a completely different behaviour, as can be observed in Figures 3.2c and d. Since there is no conjugation, the orbitals consequently tend to be more localized and there is a weak dependence of the redox potentials with the chain length.

Figure 3.3 displays the orbitals for both conjugated and nonconjugated polymers. As expected for a nonconjugated polymer, the PEO backbone is prone to having more localized orbitals. It can be seen from Figure 3.3 that even for a straight polymer conformation, the orbitals keep the p-like character of the atomic orbitals with a small superposition, clearly characteristic of nonconjugated systems. If considering a twisted conformer, the orbital localization becomes even more evident. PT, which is conjugated, displays the fully delocalized HOMO and LUMO orbitals characteristic of $\pi$ states. The same is observed for F8T2 in Figure 3.3.

For the PFO-DBT polymer (Figure 3.3), the HOMO is again delocalized, as expected for a conjugated polymer. However, the LUMO is mainly localized at the benzothiadiazole (BT) unit. This occurs thanks to the electron acceptor nature of the BT unit. The insertion of such a kind of acceptor unit in the polymer backbone generates a so-called donor–acceptor copolymer.[34,35] This has as its main signature, besides the localized nature of the LUMO orbital, a double peak in the absorption profile.

In order to get information about the absorption profile of the materials, it is necessary to calculate the electronic transition within the framework of time-dependent DFT (TD-DFT). One alternative is to use a semiempirical

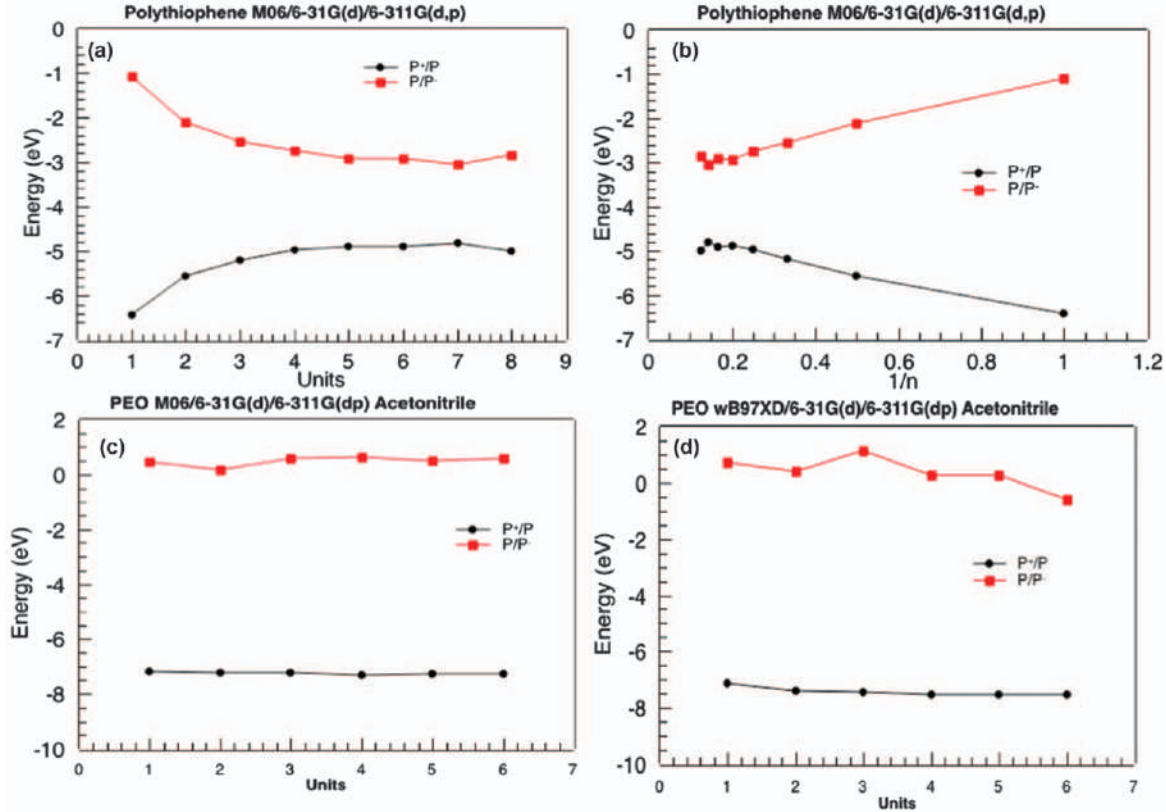


**Figure 3.2** (a) Redox potentials for different oligothiophene models *versus* the number of units. (b) Redox potentials for different oligothiophene models *versus* the inverse on the number of units. (c) Redox potentials for different PEO model oligomers with different numbers of repeating units. The redox potentials were calculated at M06/6-31G(d) theory level for geometry optimization and frequency calculations and M06/6-311G(d,p) for total electronic energy and solvation calculations. (d) Redox potentials for different PEO model oligomers with different numbers of repeating units at wB97XD/6-31G(d)/6-311G(d,p). The solvent used in all cases was acetonitrile in a PCM model.

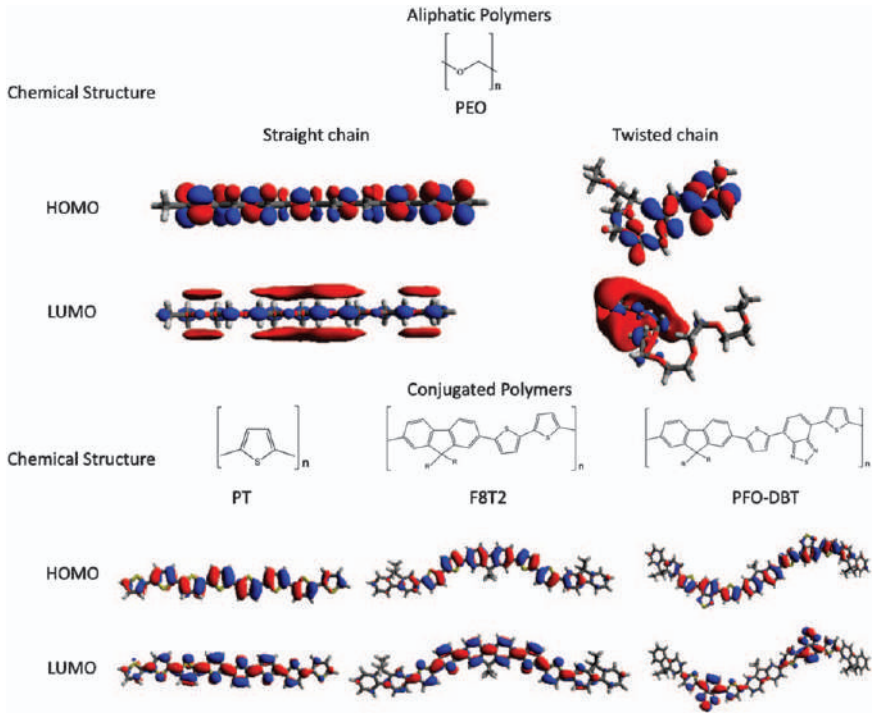


**Figure 3.3** Chemical structures and spatial distribution of HOMO and LUMO orbitals (isovalue: 0.02) for the nonconjugated polymer poly(ethylene oxide) (PEO) on top and at the bottom for three conjugated polymers, polythiophene (PT), [poly(9,9-dioctylfluorenyl-2,7-diyl)-cobithiophene)] (F8T2) and poly(2,7-(9,9-dioctylfluorene)-*alt*-4,7-bis(thiophen-2-yl)benzo-2,1,3-thiadiazole) (PFO-DBT). The orbitals were obtained from calculations using oligomer with six units at the M06/6-311G(d,p) theory level. Reproduced from ref. 36 with permission from the American Chemical Society, Copyright 2018.

method such as ZINDO,[37,38] which is incomparably less computationally expensive than TD-DFT, but on the other hand is associated with all the drawbacks of semiempirical strategies, not least the need for extensive parametrization or, alternatively, a poor description of the system.

Figure 3.4 shows a comparison between the experimental and calculated UV–vis spectra for the materials discussed earlier. Additionally, two different theoretical approaches are compared: TD-DFT and ZINDO. It is here possible to see that, apart from that the semiempirical approach overestimates the position of the absorption peak, there is generally a good agreement between the two computational methods. In most cases, both TD-DFT and ZINDO tend to underestimate the position of the absorption peak (as in Figure 3.4b and c) due to the calculations being performed in a vacuum. The use of an implicit solvation model (see Section 3.3) can significantly improve the agreement with experimental data.

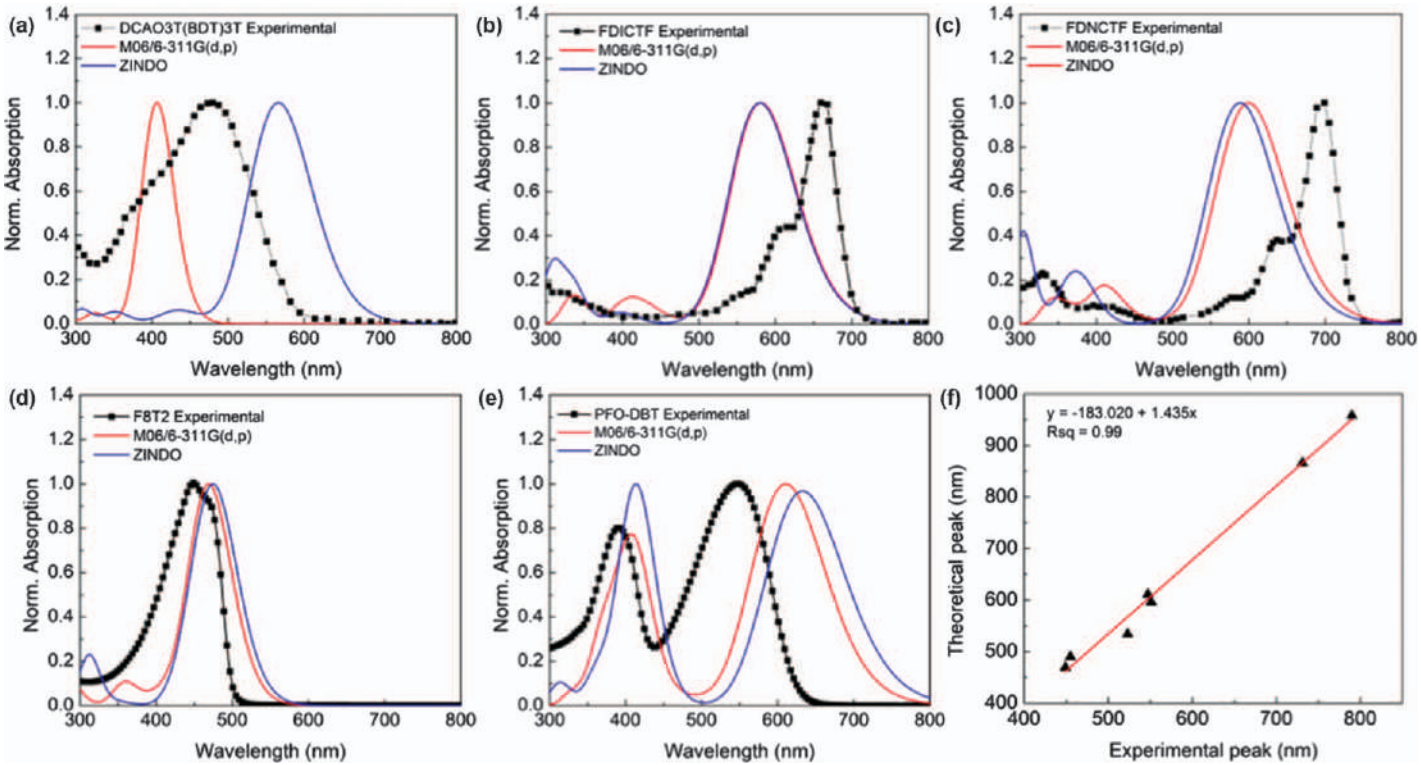


**Figure 3.4** (a–c) Comparison between the experiential and calculated absorption spectra for the molecules shown in Figure 3.1; (d, e) for the polymers F8T2 and PFO-DBT (shown in Figure 3.4f) shows the correlation between the first absorption peaks and their respective experimental reported values for all polymers. The linear equation and the squared correlation coefficient are shown in detail. (a) Reproduced from ref. 21 with permission from John Wiley and Sons, © 2011 Wiley-VCH Verlag GmbH & Co. KGaA, Weinheim. (b) and (c) Reproduced from ref. 39 with permission from the American Chemical Society, Copyright 2017. (d–f) Reproduced from ref. 36 with permission from the American Chemical Society, Copyright 2018.

For the conjugated polymers discussed here, the calculated spectra for F8T2 display an impressive agreement with the experimental data, while for PFO-DTBT, both calculated spectra are more red-shifted than the experimental counterpart. It is worth highlighting that the M06 functional succeeds in reproducing not only the typical double-peak profile of donor–acceptor copolymers but also the relative intensity of the peaks, which is not well reproduced by the ZINDO calculation. Thereby, M06 seems to be a good choice for TD-DFT calculations. As shown in Figure 3.4f, there is a very good correlation between experimental and calculated positions of the absorption peak when using the M06/6-311G(d,p) theory level.[36] This result allows one to use this kind of methodology as a predictive tool when aiming to anticipate the absorption properties in the design of novel organic materials. Recently, Damas *et al.* applied this methodology to evaluate a set of donor–acceptor copolymers used as photocatalysts for hydrogen evolution reactions.[36] Through a careful description of the electronic structure, redox potentials and optical properties, they could provide guidance for the design of novel organic materials, both polymerics[40] and small molecules.[41]

In the field of dye-sensitized solar cells (DSSCs), both DFT and TD-DFT calculations have been extensively used to design new materials for energy conversion.[42–45] For instance, Lu and co-workers reported a DFT-based prediction of photoelectric properties of five novel D–A–π–A metal-free organic dyes.[46] They showed that an improved coplanarity and enhanced conjugation promoted the transfer of intramolecular charges of the designed dyes. The calculated electronic structures revealed a great charge transfer capability, which results in improved energy conversion efficiency.[46]

The calculated electronic structures of organic materials can unveil important aspects of charge transfer and/or redox process that are difficult to assess experimentally. Regarding the performance of redox-active polymers as electrode material for Li-ion batteries, Esser and co-workers reported a promising cathode battery material in the form of a π-conjugated copolymer, enabling ultra-high rate capability and cycling stability.[31] By comparing a set of phenothiazine-based copolymers, they could demonstrate that the best performance was achieved by a copolymer possessing alternating phenothiazine and bithiophene units. By means of DFT calculations, it was shown that, despite the conjugated structure, the localized phenothiazine redox centre was maintained along the polymer chain, which resulted in well-defined plateau potentials on both charge and discharge at 3.6 V *vs.* $Li/Li^+$. The calculations also showed that the presence of an aryl ether substituent was responsible for the well-localized redox centre within the phenothiazine group.

In the case of crystalline organic electrode materials based on small molecules, DFT calculations allow following of both the changes in crystal structure as well as in the electronic structure induced by the reduction process and its corresponding process of insertion of an Li-ion. This kind of study has proven to be a powerful tool to understand the electrochemistry of this category of battery materials and has given guidance on how to improve

their performance. A number of studies have reported on this kind of approach to understand the redox process taking place in organic redox-active materials, which are highly challenging to investigate experimentally.[48–53] For example, Banerjee and co-workers reported a detailed DFT study of the lithiation process for one of the most studied organic electroactive materials, the dilithium terephthalate (TP) and its derivatives.[54] The goal was to evaluate the impact of small modifications on the TP electrochemistry, *viz.* the insertion of a diethyl group. They observed a distinct redox mechanisms, where $Li_2TP$ displayed a disproportionation reaction, while $Et_2Li_0TP$ showed stepwise redox reactions.

Sun *et al.* reported a theoretical methodology to predict the performance of new organic electrode materials for Na-ion batteries.[47] They computationally evaluated five carbonyl-containing materials (shown in Figure 3.5a) by calculating the voltage by determining the Gibbs free energy before and after sodiation (see the structures shown in Figure 3.5b). By calculating the electronic structure for each sodiation state, *i.e.*, before sodiation and after sodiation, it is possible to have a better understanding of the reduction process which is accompanied by $(Na^+ + e^-)$ insertion. It is possible to see from the density of states (DOS), depicted in Figure 3.5c, that the first unoccupied band becomes completely populated in the second sodiation step. From the DOS, the energy gap for the $Na^+$ insertion/extraction could be evaluated, and thereby insights into the electronic conductivity of these materials were gained. This methodology can likely be a good approach when screening for new electroactive materials.

## 3.3 Electrochemical Properties – Thermodynamics Assessment

Ultimately, to describe the electrochemical properties of active materials participating in the redox reactions, their redox potentials need to be determined, where electronic structure calculations are highly useful. To obtain the redox potentials thermodynamically, one strategy is to break it down into the oxidation (3.3) and reduction (3.4) reactions of a given active specie, *M*:

$$M \rightarrow M^+ + e^- \tag{3.3}$$

$$M + e^- \rightarrow M^- \tag{3.4}$$

The oxidation and reduction potentials ($E^0_{oxd}$ and $E^0_{red}$, respectively) can then be computed from the changes in the Gibbs free energy $\Delta G_r$ of the respective reduction reaction (3.3/3.4) through the Nernst equation:

$$E^0_r = \frac{-\Delta G_r}{n\mathrm{F}} \tag{3.5}$$

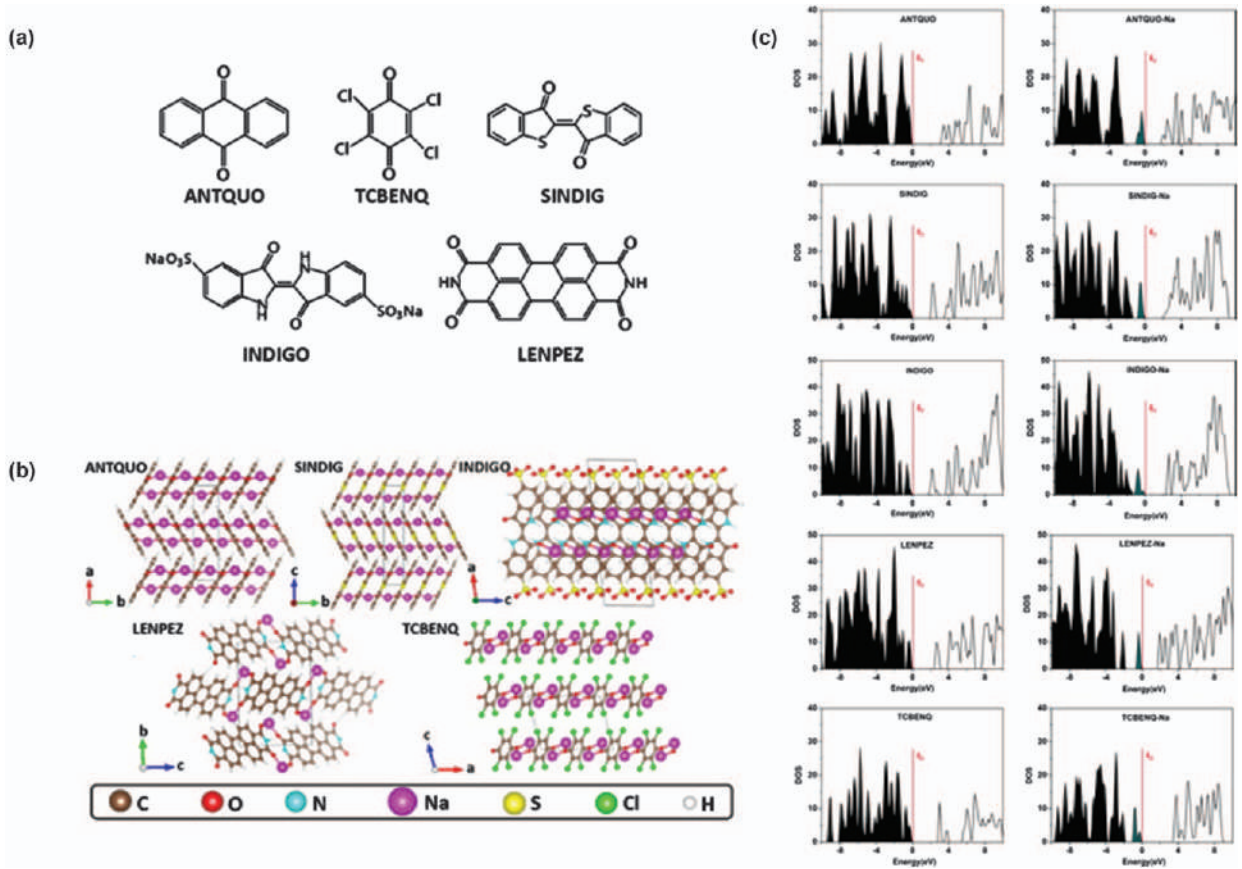


**Figure 3.5** (a) Chemical structures for the five organic materials, (b) crystal structures after the NA insertion and (c) density of states before and after Na insertion.
Reproduced from ref. 47 with permission from Elsevier, Copyright 2017.

where $n$ is the number of electrons transferred on the reaction and F is the Faraday constant. The Gibbs free energy in the gas phase is given as follows:

$$G = H - T(S_{\text{vib}} + S_{\text{trans}} + S_{\text{rot}}) \tag{3.6}$$

where

$$H = E_{\text{elect}} + E_{ZPE} + U_{\text{vib}} + U_{\text{trans}} + U_{\text{rot}} + PV \tag{3.7}$$

with $E_{\text{elect}}$ being the electronic total energy, $E_{ZPE}$ the zero-point energy, $U_{\text{vib}}$ the thermal vibrational energy, $U_{\text{trans}} = \frac{3}{2}k_bT$ and $U_{\text{rot}} = \frac{3}{2}k_bT$ are the thermal translational and rotational energies, respectively, $PV$ represents the pressure–volume product energy and $S$ is the entropic contributions to the free energy. For redox-active molecules and polymers, all these contributions to the Gibbs free energy play an important role in describing their redox properties.

In solution, the redox potentials can be evaluated following a free energy cycle (the Born–Harber thermodynamic cycle), as described in Figure 3.6 and eqn (3.8). These solvation effects are important to achieve an appropriate description of the electrochemical reactions, as such processes usually involve interactions with liquid electrolyte solvents. This methodology has been extensively applied to study several organic moieties,[55] *e.g.*, ketones,[56–59] quinones,[60–63] carboxylates,[62,64] organosulphur,[65,66] nitroxide radicals,[67,68] PEDOTs[69–71] and several polymeric systems,[27,30,72–75] in the context of batteries, solar cells, fuel cells and electrocatalysis. The solvation energy of solvated species has then been calculated using theoretical solvation models.

$$\Delta G_{(\text{solvent})}(\text{Red}) = \Delta G_{(\text{gas})}(\text{Red}) + \Delta G_{(\text{solvation})}(\text{Red}) - \Delta G_{(\text{solvation})}(\text{Ox}) \tag{3.8}$$

The use of the full Gibbs free energy, and hence the complete thermodynamic cycle, in describing electrochemical properties is of relevance for the correct description of electrochemical properties. For instance, the HOMO–LUMO orbital energies as obtained in quantum mechanical calculations[76] are commonly employed to assess several types of properties, such

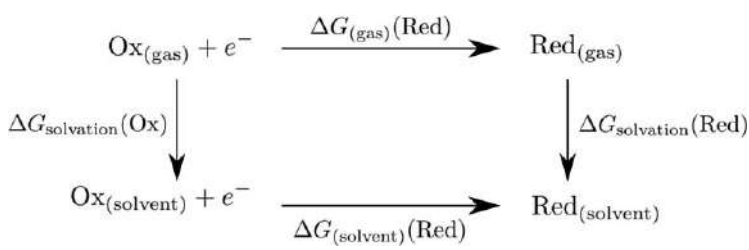


**Figure 3.6** Free energy cycle for the redox reaction $M \rightarrow M^+ + \text{e}^-$. The subscripts (gas) and (solvent) represent the moiety in the gas phase and in solvation, respectively.

as the electrochemical stability window of electrolytes in lithium-ion batteries[77–79] or possible reaction pathways in (photo)electrocatalysis. However, these energy levels are generally not sufficient for the energetic estimation of species participating in redox reactions, considering HOMO–LUMO are ultimately derivations from approximated electronic structure theory, as pointed out in the recent work of Peljo and Girault.[80] In Figure 3.7, an example is shown of how the electrochemical stability window (ESW) can be misjudged if only these orbital levels are considered. The water thermodynamic potential window is limited to 1.23 V by the redox couple $H_2O/H_2$ for the reduction and $O_2/H_2O$ for oxidation, in total discordance with that suggested by HOMO–LUMO levels – Figure 3.7a. Likewise, as shown in Figure 3.7b, the ESW for electrolytes in batteries can be erratically estimated by only judging orbital energies, thereby failing to identify redox reactions happening on the system.

Moreover, even when the HOMO–LUMO levels present a good correlation with the redox potentials, the discrepancy when using these to represent electrochemical reactions can be off by several eVs, particularly when considering solvation effects.[80] In Figure 3.8, the correlation between changes in Gibbs free energy for the oxidation reaction and the HOMO energy level is illustrated in (a) and for the reduction reaction and LUMO energy level in (b) for the polymers poly(ethylene oxide) (PEO), poly(ethylene carbonate) (PEC), poly(trimethylene carbonate) (PTMC), poly(ε-caprolactone) (PCL), poly(vinyl alcohol) (PVA), polyethylenimine (PEI), polyacrylonitrile (PAN) and the Li-salts lithium bis(trifluoromethanesulphonyl)imide (LiTFSI), lithium bis(fluorosulphonyl)imide (LiFSI) and lithium trifluoromethanesulphonate ($LiCF_3SO_3$). It is worth noting the poor correlation for this set of species, widely aimed for Li-ion batteries, especially between the LUMO and $\Delta G(P/P^-)$, displaying an offset of approximately 4 eV ($\sim$92 kcal mol$^{-1}$). This shows that a complete thermodynamic analysis instead is necessary to obtain a good description of the redox reactions and, therefore, their electrochemical properties.

Combined with quantum mechanical calculations, such as DFT, a thermodynamic assessment can aid in the understanding of different aspects of electroactive compounds. When screening a set of carbocyclic and heterocyclic molecules for organic fuel cells, Araujo *et al.*[55] applied this methodology to assess the open circuit potential (OCP). They could then show a very good agreement with experimental results from the NIST database,[81] as presented in Figure 3.8c. In another example, Renault *et al.*,[64] in a joint experimental-computation study, investigated dilithium benzenedipropiolate ($Li_2BDP$) as a high-capacity electrode for Li-ion batteries. For a low current, they could show that this electrode material could present a capacity as high as 1363 mAh g$^{-1}$ in a process coined 'superlithiation'. The corresponding thermodynamic assessment based on DFT calculation could support this finding, by showing that a lithiation up to 16 $Li^+$ per BDP molecule could be favourably inserted, thereby significantly contributing to understanding this extreme lithiation mechanism. Furthermore, the redox

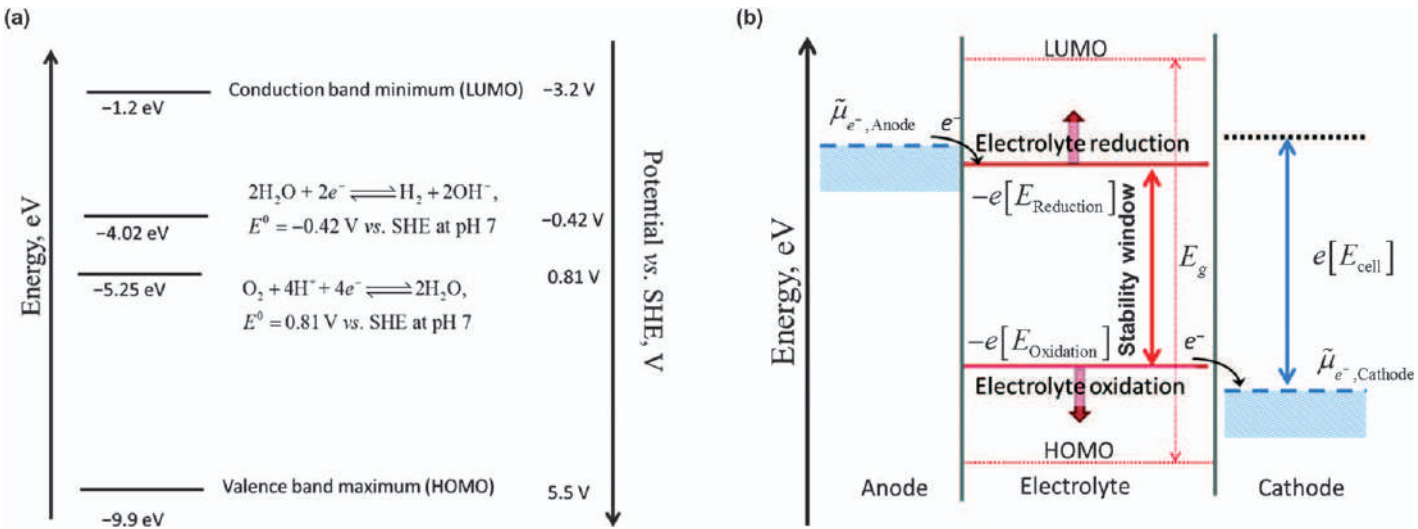


**Figure 3.7** (a) HOMO–LUMO energy levels and electrochemical stability window of water at pH 7; (b) a comparison between the electrolyte stability window and the energy levels of HOMO–LUMO.
Reproduced from ref. 80 with permission from the Royal Society of Chemistry.

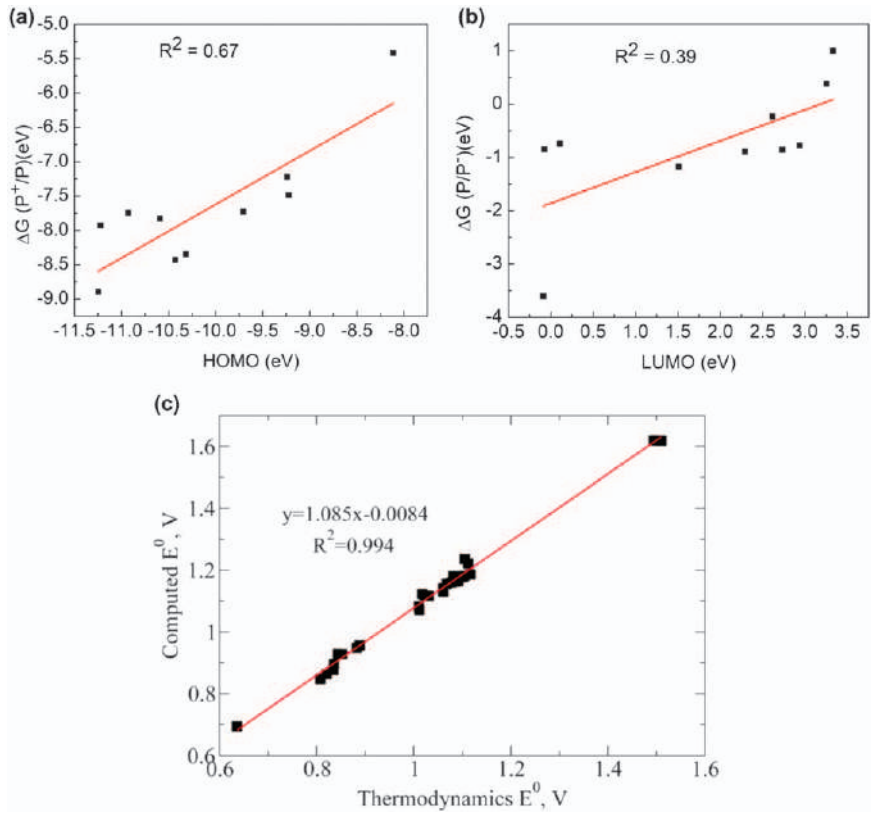


**Figure 3.8** Correlation between (a) the changes in Gibbs free energy for the oxidation reaction and HOMO energy level and (b) the changes in Gibbs free energy for the reduction reaction and LUMO energy level for the polymers poly(ethylene oxide) (PEO), poly(ethylene carbonate) (PEC), poly(trimethylene carbonate) (PTMC), poly(ε-caprolactone) (PCL), poly(vinyl alcohol) (PVA), polyethylenimine (PEI), polyacrylonitrile (PAN) and the Li-salts lithium bis(trifluoromethanesulphonyl)imide (LiTFSI), lithium bis(fluorosulphonyl)imide (LiFSI) and lithium trifluoromethanesulphonate ($LiCF_3SO_3$). The HOMO/LUMO energies were obtained from DFT calculations. (c) Correlation between open-circuit voltages from the theoretical thermodynamics analysis and data from the NIST database for different organic fuel cell compounds. The different filled squares represent the group of investigated carbocyclic and heterocyclic molecules. (c) Reproduced from ref. 55 with permission from the Royal Society of Chemistry.

potentials of nitroxide radicals have also been computationally analysed[68] to understand their role in catalytic reactions. Hodgson *et al.*[67] have seen from their thermodynamics assessment how the addition of different functional groups induces changes in the redox potentials of nitroxides, with electron-donating groups helping to stabilize oxidized species and electron-withdrawing groups stabilizing the reduced species when the substitution

occurs within a ring unit. Similarly, Park *et al.*[56] have evaluated the redox potentials for a group of ketone derivatives as potential positive electrodes for lithium-ion batteries, while Kim *et al.*[61] and Bachman *et al.*[60] have assessed the electrochemical properties for a large number of quinone derivates. Thereby, they could shed light on the interactions between organic moieties and Li ions, observing how the number of carbonyls as active units can alter the redox properties of compounds, as it is possible to see in Figure 3.9a for phenanenyl and anthracene. In Figure 3.9b, the redox potentials for a set of quinone derivatives is presented (*vs.* $Li/Li^+$), as obtained from the thermodynamics analysis, also showing a good agreement when compared with experimental findings. In addition, the functionalization effects on the anthraquinone (AQ) are shown in Figure 3.9c. By changing the character of the functional group – from electron donating to electron withdrawing – and the number of added units, Bachman *et al.*[60] have estimated these effects on the reduction window and oxidative stability of the AQ, proposing a theoretical platform to further study new quinone molecules for energy-storage materials.

Solvation is an important aspect of determining the redox potential of active materials participating in electrochemical reactions. Several different approaches have been developed in the past years to deal with solvent effects in a desired solute. Among these, three major categories can be identified: (i) explicit methods, where the solvent molecules and their interactions with the solute are explicitly taken into consideration; (ii) implicit methods, in which the solvent is represented by a continuum medium and parametrized by a set of properties, *e.g.*, its bulk dielectric constant; and (iii) hybrid methods, where the implicit method is used combined with a few molecules of the solvent around the solute to better represent the first solvation shell effects. All methods have strengths and drawbacks, but the implicit solvation generally offers a fast assessment of the solvation properties with a reasonable computation cost and accuracy. It is possible to find several implicit solvation models in the literature, *e.g.*, PCM[82] (polarizable continuum model), PBF[83] (Poisson–Boltzmann finite elements model), COSMOS[84] (conductor-like screening model) and SMD[85] (solvation model density). PCM is one of the most widely used implicit solvation methods and has been extensively applied to assess the solvation effects in polymers. In one illustrative example for redox-active organic compounds, Kim *et al.*[61] investigated the effects of solvation in the thermodynamics properties for a set of quinone derivatives, varying the number of Li atoms bounded to the moiety. They noticed how the presence of Li atoms can affect the thermodynamics properties and the presence of a solvent with a high dielectric constant can increase the redox potentials of these quinone derivatives.

When characterizing molecules and polymers, the determination of their dielectric constant is relevant for assessing several electronic properties. Combined with the implicit solvation approaches, the dielectric constant can be applied to model a target specie into a solvent, which can be useful in different ways: (1) in the cases where the moieties are rather complex to

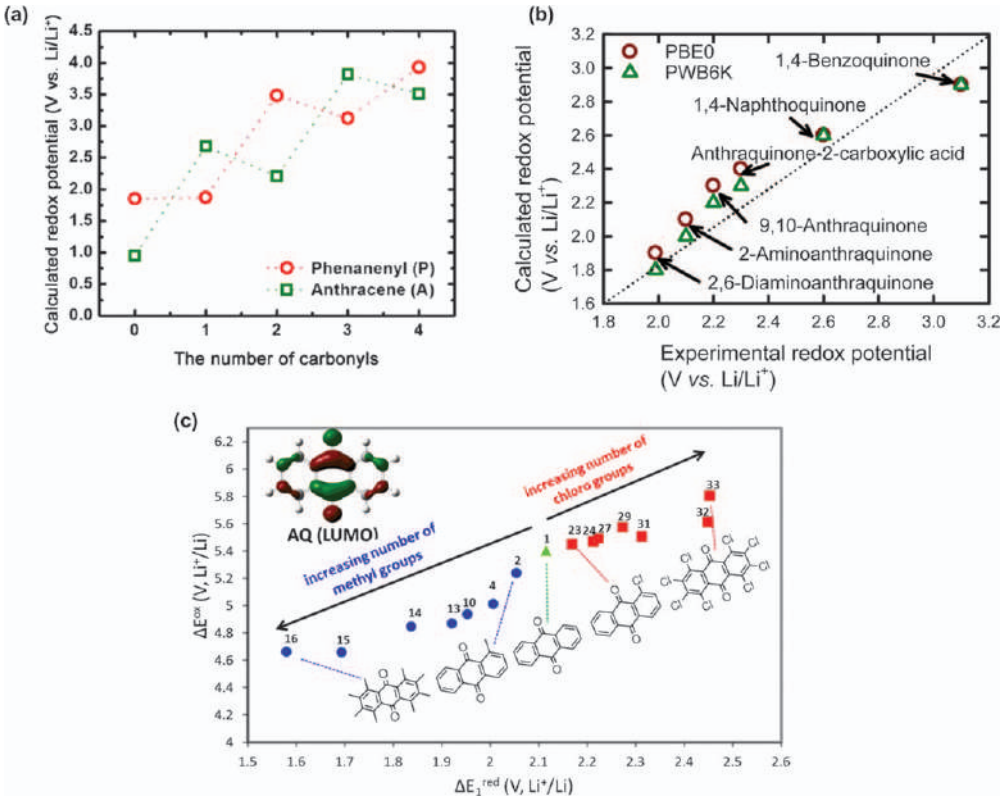


**Figure 3.9** (a) Calculated redox potentials for phenanenyl and anthracene for different numbers of carbonyl units; (b) experimental and calculated redox potentials (*vs.* $Li/Li^+$) for the moieties 1,4-benzoquinone, 1,4-naphthoquinone, 9,10-anthraquinone, 2-aminoanthraquinone, 2,6-diaminoanthraquinone and anthraquinone-2-carboxylic acid; (c) calculated oxidation and reduction potentials (*vs.* $Li/Li^+$) for a set of anthraquinone derivatives.
(a) Reproduced from ref. 56 with permission from John Wiley and Sons, © 2017 Wiley-VCH Verlag GmbH & Co. KGaA, Weinheim. (b) Reproduced from ref. 61 with permission from the American Chemical Society, Copyright 2016. (c) Reproduced from ref. 60 with permission from the American Chemical Society, Copyright 2014.

be modelled in a solid-state phase, they can be treated simultaneously as solute and solvent, leading to a bulk-like effect. This has been shown to be helpful in studies of several redox-active polymers, for instance, poly(3,4-ethylenedioxythiophene) (PDMcT), poly(2,2,6,6-tetramethylpiperidinyloxy methacrylate) (PTMA), poly(2,2,5,5-tetramethyl-3-oxiranyl-3-pyrrolin-1-oxyl ehtylene oxide) (PTEO), poly(benzobisimidazobenzophenanthroline) (BBL), *etc*.; (2) in electrolyte-salt systems, the polymer dielectric constant can be used as implicit solvent to the salt, *e.g.*, $LiPF_6$ salt being solvated by ethylene carbonate/dimethyl carbonate (EC/DMC).

To calculate the dielectric constant based on DFT calculations, the Clausius–Mossotti equation can be employed:[86]

$$\frac{\varepsilon - 1}{\varepsilon + 2} = \frac{4\pi}{3}\frac{\rho}{M}N_A\alpha \tag{3.9}$$

where $\rho$, $M$, $N_A$ and $\alpha$ are the material's density and molecular mass, Avogadro's constant and the electronic polarizability for the considered specie. These quantities can be obtained through DFT calculations, with $\rho N_A/M$ being the inverse of the molecular volume after geometry optimization and $\alpha$, as a first response of the electronic density to an external electric field, being straightforwardly computed from the converged electronic structure. It is important to stress that, in this approach, it is possible to consider both frequency-independent (static)[87] and frequency-dependent (dynamic)[88] electronic polarizabilities. However, the static polarizability is generally satisfactory for several energy-related purposes. For electroactive organic species, this has been particularly relevant for the solvation effects of different electrolytes and to model a bulk-like effect in a more complex system. Nayak *et al.*[89] and Schwenn *et al.*[90] have, for example, employed this methodology to assess the thermodynamic properties for a set of redox-active organic compounds, *e.g.*, tetracyanoquinodimethane (TCNQ), difluoro-tetracyanoquinodimethane (F2TNCQ), tetrafluoro-tetracyanoquinodimethane (F4TCNQ), tetracyanonaphthoquinodimethane (TNAP), perylenetetracarboxylic acid dianhydride (PTCDA), poly-(3-methyl-thiophene) (P3MT), N-methyl perylene tetracarboxylic diimide (mPTCDI) and naphthalene tetracarboxylic dianhydride (NTCDA). They could achieve good agreement with experimental findings and, moreover, Nayak *et al.* were able to further extend their results to grasp charge transfer properties.[90]

## 3.4 Dynamic Properties – Classical Force Field MD

If size and time restrictions become too severe and computationally expensive for *ab initio* and DFT approaches, but the electronic structure does not necessarily need to be resolved for the problem at hand, *force field* methods can be a fruitful strategy. Here, the atom rather than the electron is generally the smallest unit simulated, and the atoms interact through specifically and analytically described atom–atom forces, which are either attractive or

repulsive. The perhaps most well-known and versatile force field methodology in materials science is molecular dynamics (MD) simulations.[91] MD allows us to simulate the dynamics of the particles in a well-defined system to gain insights into local structure and local dynamics, and how these properties are intrinsically coupled. In an MD simulation, atomic motion in a chemical system is described in classical mechanics terms by solving Newton's equations of motion:

$$\vec{F}_i = m_i \vec{a}_i \tag{3.10}$$

for each atom $i$ in a system of $N$ atoms; $m_i$ is their respective atomic mass; $a_i = \mathrm{d}^2 r_i / \mathrm{d}t^2$ is their acceleration; and $F_i$ is the force acting upon atom $i$ by all other particles in the system. By repeatedly solving this equation for all particles in the system, its evolution in time can be captured. The forces, in turn, are generated from an energy potential $E$:

$$\frac{-\mathrm{d}E}{\mathrm{d}\vec{r}_i} = \vec{F}_i = m_i \frac{\mathrm{d}^2 \vec{r}_i}{\mathrm{d}t^2} \tag{3.11}$$

In a conventional MD simulation, around 100 000 atoms can straightforwardly be simulated; *i.e.*, it is possible to sequentially calculate the locations and velocities of all particles in the system for a time-frame in the nanosecond to microsecond regime. This simulation thus generates a sequence of snapshots which constitutes a ''movie'' of the modelled system on the atomic scale, and which can be analyzed using statistical tools. For example, structural properties are straightforwardly achieved through radial distribution functions (RDFs), while dynamic processes can be approximated through the mean-square-displacement (MSD) of different species. Moreover, the main strength of MD simulations is perhaps the possibility to explore the interdependence of structural properties and dynamic events, which can be analyzed through correlation functions. Thereby, a proper understanding of which atomic and molecular configurations that give rise to the desired – or undesired – properties of the material can be obtained, and in turn provide a basis for optimizing and tailoring the chemical system further.

All the input parameters needed to solve the equations of motion are the masses of the particles and a description of the potentials, $E$. While the treatment of atomic masses is unproblematic, an appropriate description of $E$, however, is nontrivial, and often large amounts of time and effort are necessary to develop a specific force field for the system under study – generally requiring extensive electronic structure calculations such as DFT. While there exists a number of force field libraries, their quality can often be considered limited, especially for more complex materials. For molecular systems, also bonding forces, angular bonding forces, dihedral forces, *etc.*, are necessary to generate with great care. The quality of the force field is generally the most critical factor for the validity of the MD simulation and also where the results are easily criticized and need to be treated with care.

In electrochemical systems, electrolyte materials constitute the components which have been most vastly explored by MD simulations.[92] This is not strange, considering that MD is highly useful for investigating mass transport processes, while redox activity is beyond the framework of standard MD methodologies. Nevertheless, mass transport and solid-state diffusion and migration are key properties also for electrodes in electrochemical devices, and there is now a rich literature where these phenomena are researched using MD for a large number of materials. These examples are, however, generally focused on the inorganic materials which are also being found in most technical applications (*e.g.*, inorganic electrodes for Li-ion batteries), but MD techniques are perhaps – as will be discussed – especially useful for exploring the organic counterparts. The structures in this latter category of materials are often disordered, amorphous, or at least have a great tendency to not form highly symmetrical and periodic structures. This renders them problematic for straightforward exploitation by electronic structure calculations that rely on periodicity. If instead using MD, the macromolecular structure can be obtained also for highly complex systems. On the other hand, for the vital redox processes which necessarily determine the functionality of any organic electrode material, electron transfer ultimately needs to be implemented into the model. Thus, MD often constitutes a *complimentary tool* in the modelling of redox-active organic materials rather than a stand-alone methodology.

There are several key relationships between MD and electronic structure calculations when implemented for organic electroactive materials. As stated above, electronic structure calculations are generally used for generating the force field necessary for conducting high-quality MD simulations, while MD can provide useful starting structures for materials where large-scale systems are necessary, and the space becomes too complex to map with other techniques. MD can also be used to validate structures generated by first-principles calculations, as for example in a study of the organic Li-ion and K-ion battery terephtalate electrode materials.[93] When exploring the lithiation and potassiation processes and diffusion paths in the crystalline structures, annealing MD simulations were helpful to reduce the number of possible structures to explore, since these could confirm that the true energy minima in the configurational space had actually been reached. The amount of possible Li or K trajectories mapped is much higher in MD than if using DFT calculations, and can thereby cover a correspondingly larger phase space.

One promising category of organic electroactive materials is the polymeric nitroxyl-radicals, which can be utilized as cathodes in all-organic batteries.[94] One of the most well-studied materials in this class of material is poly(2,2,6,6-tetramethylpipridinyloxy methacrylate) (PTMA; see Figure 3.10), which incorporates the neutral radical 2,2,6,6-tetramethyl-1-piperidinyloxy (TEMPO) unit. There exist, however, large uncertainties in the structure of these polymers, their electronic transport paths, how solvent and ion interactions with the polymer determine the conductivity, how ion mobility

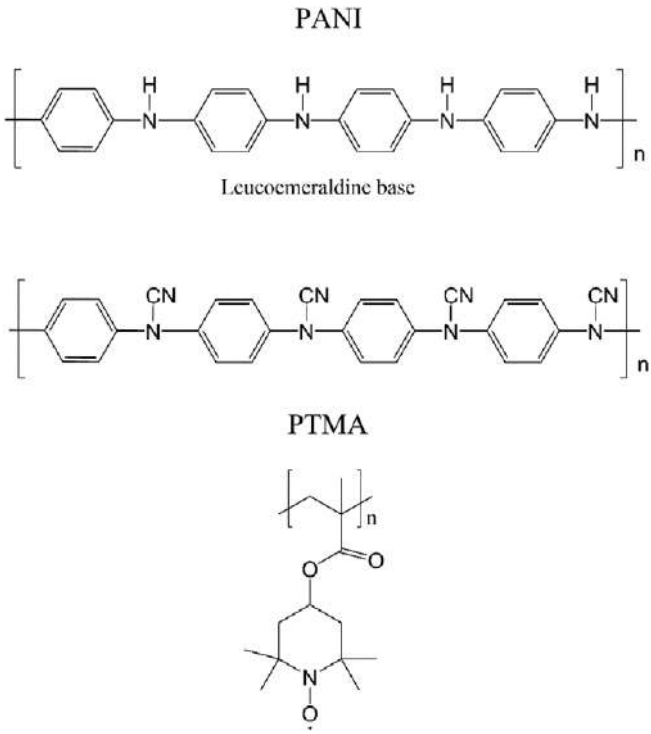


**Figure 3.10** Lewis structures of redox-active polymers subjected to MD simulations.

in the polymer matrix occurs, *etc.* These are typical properties which can be elucidated computationally – as has been done by Kemper *et al.* Considering the complexity of the system, MD simulations are a natural starting point to generate the fundamental morphologies in order to understand its amorphous structure and assess the morphological polymer-structure features associated with electron transport.[95] In the solvent-free PTMA system, it was found in these simulations that the radical electron primarily occupied the oxygen–nitrogen bond in the TEMPO ring of the polymer. The methyl–methyl interactions of the TEMPO groups then control the inter-nitroxyl distances, and induce a series of packing structures of different molecular motifs in the polymers. By calculating the electronic coupling, a strong intergroup coupling between TEMPO rings on different chains was found. Thereby, the favourable stacking motif allowed for charge transport over much larger distances than what is envisioned if the electron is merely transported to the adjacent coupled TEMPO rings.

By adding acetonitrile solvent and $BF_4^-$ counterions to the PTMA system, both its structure and the possible electron pathways change to some degree.[96] At the same time, the inclusion of anions makes it possible to simulate the material under a different state of charge (SOC), by removing electrons from a corresponding number of TEMPO groups. However, the

main structural features were seen to remain intact in MD simulations of the swelled system, and the packing likewise remained with incorporation of the solvent. The solvent molecules instead occupied voids in the structure, while the intersite coupling was generally left undisturbed. The $BF_4^-$ counterions, on the other hand, were seen to bind strongly to the charged TEMPO motifs, irrespective of SOC, indicating difficulties in fully discharging the resulting electrode. The strong anion–cation bonding will also likely influence the electronic transport through that particular molecular unit, since there are limited possibilities for electrons to occupy the corresponding orbital. Interestingly, however, this did not seem to strongly influence the total electronic conductivity through the polymer matrix for a low degree of anionic doping, since enough neutral groups remained and were largely unaffected by the ion pairing occurring in other parts of the material. The influence of ion pairing was thus merely local at low SOC levels, but will on the other hand have serious implications for the rate performance at high SOC. The MD simulations thereby gave strong implications in how to tailor the system further: by choosing salt anions with lower coordination strength to the TEMPO cationic groups.

Polyaniline (PANI; Figure 3.10) and its cyano-group functionalized counterpart is another promising organic cathode material for energy storage, studied computationally by Chen *et al.*[97,98] These investigations highlighted the shortcomings of simply relying on DFT calculations solely, which were shown to be too limited to capture the aggregated state of the polymeric material. For PANI, which comprises a substantial degree of disorder and several co-existing local energy minima and different coordination environments, the system becomes too large for making predictions of voltage–capacity curves through DFT optimizations. Moreover, computing the oxidation potential using DFT becomes numerically difficult for materials where the counterion is necessary to implement, since this requires several specific large-scale simulation cells employing different concentrations of counterions. Thus, resorting to MD simulation to map the configurational space provided a route forward to deal with the large size of the simulation cell and the multitude of potential structures. By preoptimizing the possible structures, and then reoptimizing them using DFT-B (a semiempirical version of DFT with higher speed), a clear short-cut could be taken to obtain the desired properties, and the results displayed good agreement with experimental data. DTF-B moreover was shown to be highly useful for materials which operated by oxidation, since the notoriously difficult cationic interactions did not need to be parametrized (as would be the case for materials operating by reduction).

One of the most well-studied organic electroactive materials is poly(3,4-ethylenedioxythiophene) (PEDOT), which due to its high conductivity has shown high versatility in a number of different applications and devices, including for energy storage and conversion.[99] PEDOT is generally doped with a molecular counterion, most often polystyrene sulphonate (PSS), although in recent years tosylate (TOS) has emerged as a popular alternative.

Much attention has been directed towards understanding the interplay between polymer structure, redox mechanisms and electronic transport in PEDOT and related materials, and computational efforts have here played a significant role. PEDOT constitutes a truly *multiscale problem*: the nature of the charged state (polarons, bipolarons, *etc.*), electronic conductivity, mass transport and morphology all exist on different length and time scales. MD is here a crucial technique to capture the more large- and long-scale phenomena. In this context, Zozoulenko and co-workers have performed pioneering work in recent years,[100–102] with the aim of moving from oversimplified models such as periodic crystals and single oligomers. By including the molecular TOS counterion and solvent water in the MD simulations, a more advanced structural model can be constructed which can be used to explore crystallization processes, swelling, degree of crystallinity, *etc.* Using an all-atom force field, a structure where the PEDOT arranges in small crystallites with 3–6 π–π stacked chains could be determined for the polymer in the dry state (Figure 3.11). These crystallites are surrounded by an amorphous matrix, but interlinked through a percolating network of π–π stacked units, which appear irrespective of chain length. The crystallites swell and bend when water is added, but the π–π stacked

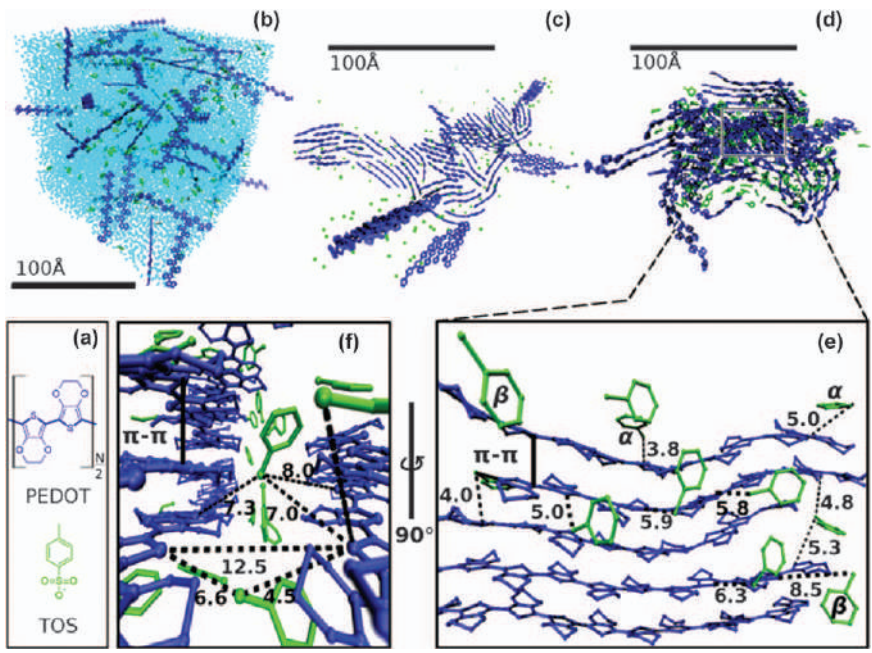


**Figure 3.11** (a) Molecular structures of PEDOT and TOS. (b–e) MD snapshots of the structure of PEDOT (blue) and TOS (green) either in water (b, c) or dry (d–f) on different length scales or perspectives.
Reproduced from ref. 100 with permission from the American Chemical Society, Copyright 2017.

distances appeared to remain unaffected by changes in solvent content or charge concentration. The TOS counterions, in turn, were primarily located at the top of the chains or on the side of the PEDOT crystallites.

In order to achieve an even more realistic picture of the PEDOT morphology, above a length scale of tens of nanometers, further approximations beyond all-atom MD are necessary. This is necessary to capture some of the key electrochemical parameters, which are strongly dependent on the material morphology in highly doped conducting polymers. One method within the general MD framework to reach this so-called *mesoscale* is through *coarse-graining* of the model. Here, molecular units are summarized as beads, and a novel force field is constructed describing the bead–bead interactions. A coarse-grained model of PEDOT was thereby constructed by Modarresi *et al.*, which could correctly reproduce the formation of π–π crystallites.[103] The coarse-graining allowed simulations of 400 PEDOT chains in a cubic box, also containing 52 000 water molecules and up to 1600 TOS molecular ions depending on oxidation. NaCl, a common electrolyte salt in PEDOT-based electrochemical devices, was added at different concentrations. It was then found that the ionic diffusion, as expected, decreased with doping level, when the TOS counterions enter the polymer matrix. The ionic diffusion coefficients on the other hand increased exponentially with water level, and experienced a dramatic decrease in conductivity when the percolating water network in the structure was disrupted at very low water levels (10 wt.%). Moreover, most ions at low water levels are confined in close coordination with the polymer, where their diffusivity is lower than the detection limit. This clearly controls the electrochemical performance of the material. This coarse-grained model developed was later utilized in an analysis of the PEDOT/TOS system at exceptionally high doping levels, which were experimentally achieved through vapour phase polymerization.[104] The MD simulations could help in explaining the experimental findings of an increased capacity in the absence of nonionic ether-based triblock copolymers, where it could be seen that the nearest neighbour π–π stacking was lost at *ca.* 75% of doping, while a PEDOT–TOS–PEDOT stacking started to emerge at higher doping levels – thereby providing a conjugated network.

MD simulations have also been used to explore the thermal transport in PEDOT materials.[105] A low thermal conductivity is, for example, useful for attaining high energy conversion efficiency in thermoelectric devices, while thermal transport is highly desired in most organic electronic applications with high power capabilities. MD simulations can effectively be used to model thermal transport in anharmonic materials. A force field needs then to be implemented which can take the anharmonic vibrations into account, using high-order terms or cross-terms for the intramolecular interactions. For PEDOT, it could then be observed that while the thermal transport is anisotropic, doping decreases its thermal conductivity. Primarily, doped PEDOT experiences a negative temperature dependence of the thermal conductivity along the polymer chains. Especially low-frequency phonon

lifetimes were affected by the doping level, most likely due to PEDOT–TOS interactions.

Another intriguing example of the use of MD for organic electroactive materials is that of the donor–acceptor interface in organic solar cells. Han *et al.* studied this system by atomistic simulations using a copolymer that included a donor unit of benzo(1,2-*b*-4,5-b′)ditiophene (BDT) – a donor–acceptor (D–A) copolymer – and an organic acceptor of indacenodithieno(2,3-b)thiophene (IT), *i.e.*, an A–D–A structured acceptor.[106] MD simulation of the resulting polymer blend (see Figure 3.12) could generate a structural prediction of the steric hindrance in the structure, which primarily exposed the acceptor units in the structure, and it became clear that π–π interactions are crucial for the exciton dissociation, which could be confirmed by DFT calculations. Such structures are thereby vital for dissociating excitons, and provide an important means for electron transport in the material. This was also compared to a system using fullerenes instead of the A–D–A acceptor, where the superiority of the organic counterpart was confirmed. Similarly, Medina *et al.* combined MD with DFT calculations to investigate how molecular orientations influence electronic transport in an organic semiconductor for optoelectronic applications.[107] The charge migration in the 2D covalent organic framework under study relies mainly on

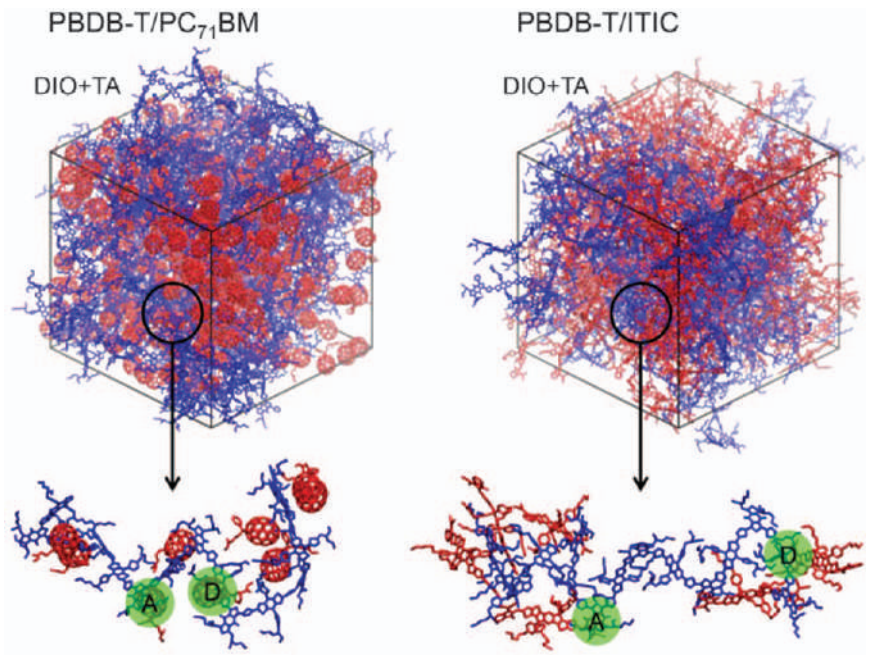


**Figure 3.12** MD generation of a representative structure for donor–acceptor redox-active polymers intended for organic solar cells.
Reproduced from ref. 106 with permission from John Wiley and Sons, © 2018 Wiley-VCH Verlag GmbH & Co. KGaA, Weinheim.

the interaction with adjacent layers in these 2D structures. The MD simulations showed that just a minor displacement (1–2 Å) led to significant stabilization, and is thereby likely highly correlated to electron transport in the system. Movement of the planes horizontally relative to each other could relieve any electrostatic repulsion. In conclusion, MD is a powerful tool for exploring exotic structures in organic electronics, and the structural background to electronic conductance and its temperature dependence can be assessed directly.

Finally, an interesting example of employing MD simulations to investigate a complete fully organic and biodegradable supercapacitor device was recently shown by Colherinhas *et al.*[108] Since the entire simulation cell is a few tens of nanometers, and lacks crucial components (such as a separator), the approximations made are obviously unrealistic, but the example still shows the strength of the MD methodology and that the simulations can still provide vital insights. The system in question was composed of self-organizing peptides as electrodes, and an amino-acid (cholinium)-based ionic liquid as electrolyte. It was seen that the interaction between the polar surface groups and the electrolyte was highly beneficial and generated a semipermeation of ions inside the nanosheet electrode surface, thereby contributing to a very high capacitance as compared to planar metallic electrodes. The MD simulations could also provide a direct insight into the variation of the electrostatic potential across the electrochemical cell, based on the concentration profile throughout the entire cell. Thereby, estimation of electrochemical properties is directly accessible from the MD simulations, since they are interdependent on the localization of the electrolyte ions in the system.

## 3.5 Dynamical Properties – *Ab Initio* MD

Despite all aforementioned advantages of classical force field MD techniques to investigate larger and more complex systems, the methodology is by principle insufficient to describe electrochemical processes that involve chemical bonding breaking/reconstruction, *e.g.*, the redox process of metal–organic molecules, polymer degradation process at electrochemical interfaces or polymerization mechanisms. Here, the description of the interatomic interactions needs to go beyond the analytical parametrized force fields. Such scientific challenges can be resolved by molecular dynamics simulation approaches based on first-principles theory, which have recently undergone significant advances thanks to developments in both theoretical methodologies and computational facilities.[109] These methods are usually termed *ab initio* MD (AIMD), or sometimes also *quantum* MD (QMD; which should not be confused with quantum dynamics where the states of the atoms are described by wavefunction in the Hilbert space). Using AIMD, the interatomic forces are determined directly from the solution of the quantum mechanical problem of electrons without any adjustment of parameters, while the nuclei are still treated as classical objects with their dynamics governed by eqn (3.11).

There are two main approaches for the computational implementation of AIMD simulations. One divides the problem into two parts: (a) the motion of the nuclei and (b) the quantum mechanics solution for the many-body problem. Within the DFT formalism, the latter corresponds to achieving the self-consistent solution of Kohn–Sham equations for the electrons. This methodology is called Born–Oppenheimer molecular dynamics (BOMD). The alternative approach is the so-called Car–Parinello molecular dynamics (CPMD). Here, the dynamics of nuclei and the quantum electronic problem are solved within the same algorithm.[109]

While primarily constituting a redox process which is a side reaction, AIMD simulations have been employed in battery systems to investigate polymer degradation at the polymer–Li metal interface. This has shed light on the early stage of solid electrolyte interphase (SEI) formation in solid-state batteries.[110] A large set of different ion-coordinating and ion-transporting polymers has been investigated: poly(ethylene oxide) (PEO), poly(ethylene carbonate) (PEC), poly(trimethylene carbonate) (PTMC), poly(caprolactone) (PCL), poly(vinyl alcohol) (PVA), polyethyleneimine (PEI) and polyacrylonitrile (PAN) using BOMD simulations. The simulation time amounts to only 15 ps, but was still enough to target polymer reduction reactions. Although there are limitations in the simulation time and the size of the system, it is thus possible to obtain significant insights into the stability of the systems. In the case of PEO, PVA and PEI, no chemical bond breaking occurred, indicating higher stability of these polymers as compared to PEC, PTMC, PCL and PAN. For PEC and PTMC, the $C_{carbonyl}$–$O_{ethereal}$ bond breaks, producing CO and alkoxides. PCL follows a similar degradation pathway with $C_{carbonyl}$–$O_{ethereal}$ bond cleavage, but with formation of only alkoxides. For PAN, the main outcome is the C–C bond formation, which stabilizes the interaction with the Li metal surface. The final snapshots of the simulations are shown in Figure 3.13. The insights obtained from these simulation runs could thereafter be used to create models where the reaction pathways are investigated in further detail. This latter-stage analysis was achieved using first-principles thermodynamics calculations.

AIMD has been also used to investigate the early stages of polymerization reactions. For instance, Röthlisberger *et al.* have investigated the anionic polymerization of isoprene induced by ethyl lithium using CPMD.[111] It was possible within the simulation time to identify a high stereoselectivity favouring the *cis*-product, which displays good agreement with the experimental findings. Following a similar strategy, AIMD simulations have been used to shed light on the possible reaction pathways, which are then investigated in more detail to assess the thermodynamics and kinetics. The isomerization occurring is proposed as the rate-determining step. Such results could certainly not be obtained by employing force-field MD simulations, which shows the advantage of using electronic structure calculations for dynamic simulations.

Furthermore, AIMD techniques have also been successfully used to unveil the underlying structural and dynamical properties of lithium-rich

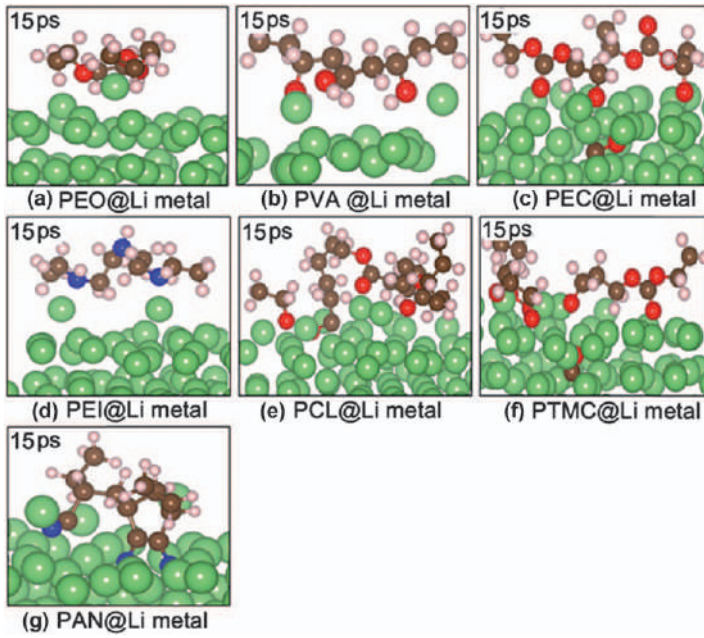


**Figure 3.13** Final snapshots of AIMD simulations of different polymers of a Li–metal surface: (a) PEO, (b) PVA, (c), PEC, (d) PEI, (e) PCL, (f) PTMC, (g) PAN. Reproduced from ref. 110 with permission from the Royal Society of Chemistry.

organic compounds. In particular, $Li_2NH$ displays a superionic-like state that controls the crystal structure at a finite temperature.[112] AIMD has then been able to describe the temperature-induced structural phase transition that occurs at around 400 K, in excellent agreement with experimental findings. This is indeed a very intriguing transition, which is associated with a melting of the cation sublattice composed of Li ions, giving rise to a 'superionic' phase. This transition is accompanied by an order–disorder transition of the N–H bond orientation. Only through taking such dynamical properties into account can the correct crystal structure be obtained from DFT calculations.

## 3.6 Final Remarks – Emerging Methodologies

Apart from the above-employed methods, spanning from *ab initio* methods to coarse-grain MD mesoscale modelling, which essentially are *materials modelling* methodologies, there is also an emerging literature on *electrochemical modelling* where the resulting cell device is in focus. Here, instead of simulating atomic and molecular components, the fundamental differential equations governing the chemical system are solved simultaneously, not rarely using finite element methodology (FEM). Through this approach,

electrochemical device data (*e.g.*, voltage curves, capacity fade, *etc.*) can be generated computationally, and directly compared to experimental device data. One illustrative example for redox-active organic species is the simulation of a polypyrrole/nanocellulose energy storage device, based on Ohm's law and Fickian diffusion models, whereby electrode kinetics, nonlinear interfacial interactions, and mass transport inside the porous electrode structure could be implemented.[113] The morphological properties of the electrode were implemented using scanning electrode microscopy (SEM). Through simulation of electrochemical impedance data using a description of the relevant Faradaic and non-Faradaic processes in the cell, a direct comparison could be made with experimental counterparts. Thereby, the effect of electrode porosity and the electrochemically limiting processes could be elucidated. It was clear that the charge transport was mainly controlled by the diffusion of counter ions in the electrolyte matrix within the electrode, and the onset frequency for the pseudocapacitance was found to be dependent on the sluggish diffusion kinetics. Similar tools will certainly be highly useful to explore a vast range of organic electrochemistry systems, but will also require highly time-consuming parameterization of all relevant materials properties in the system. Most commercial software materials' libraries have so far only rudimentary descriptions of the parameters governing the well-established Li-ion battery systems, and the situation for organic electronics is – naturally – much worse.

Another emerging trend in the scientific literature is associated with the use of data-driven methods, or so-called machine-learning (ML) techniques. Their application in materials and molecular science is increasing at a fast rate.[114] The trained ML algorithms allow addressing fundamental questions on complex systems that are unfeasible, or very difficult, to tackle with standard methods. ML has been applied, for instance, to bypass fundamental quantum mechanics calculations in the description of interatomic interactions or in the prediction of the materials' properties.[115,116]

In short, ML techniques employ statistical algorithms that are trained in a given dataset to build up models able to unveil underlying rules and make predictions. The implementation of ML approaches relies heavily on the amount and quality of available data. In this context, materials modelling and simulations based on first-principles theory are serving a potentially prominent role in systematically constructed databases with specific properties. For instance, such an approach has been employed in the design of ML methods to search for redox-active molecular materials for Li-ion batteries[117] and to predict the properties of copolymers.[118] The latter comprises a significant amount of redox-active polymers, where it could be determined that the DFT calculations provide the needed high-quality data for the algorithm training.

A second relevant component in the implementation of ML techniques is the representation of the data, *i.e.*, the conversion of the data into something

that is more appropriate for the algorithms. It consists actually in finding fingerprints for each molecular or crystalline system. This could have a significant impact on the learning process and the best choices depend on the investigated properties. While a coulomb matrix[119] constitutes the common representation for molecular systems, Wilbraham *et al.* have demonstrated that the use of trimers to generate molecular 'descriptors' of oligomeric chains, in the form of *fixed-dimensional bit vectors*, significantly reduces the computational time and provides excellent results in the prediction of the optoelectronic properties of the copolymers.[118] This has been shown to be highly useful to assess the properties of a wide library of polymeric materials what would not be feasible through computationally demanding DFT calculations. Alternative formalisms to represent the one-dimensional polymeric structures have also been developed by Pilania *et al.*,[120] which are based on the compositional and configurational information. Such molecular representations are generally not transferable for the investigation of solid-state systems. The periodicity of the solids poses additional challenges for the use of ML techniques due to the lattices being able to be represented in a wide range of ways. Different representations have been developed to overcome such hurdles, which are based on radial distribution functions,[121] Voronoi tessellations[122] and property-labelled materials fragments.[123] Through these approaches, unique representations of crystalline systems can be achieved.

The final step in the implementation of ML approaches is to choose the statistical algorithms to build up the desired models. This is also associated with the learning methods that may be supervised, semisupervised or unsupervised depending on the amount of data and the scientific problem. There are currently a wide range of such methods, *e.g.* artificial neural networks.[124] These have been demonstrated to be capable of accurately predicting the optical and thermodynamic properties of conjugated copolymers, including a diversity of redox-active polymers,[118] which could be useful to explore large databases in the search for materials with specific properties. The neural network algorithms are very versatile, allowing the modelling of more complicated nonlinear structure–properties relationships.

Another active area of investigation is the use of ML techniques to solve inverse design problems. The task here is to search for the right materials given the desirable properties. Tagade *et al.*[125] have developed a deep learning inverse prediction framework for molecular design. This approach has been successfully applied to design organic molecules for different applications, *e.g.*, organic semiconductors for thin-film transistors, small organic acceptors for solar cells and electrolyte additives with high redox stability.

More recently, evolutionary algorithms have been successfully employed to resolve the structure of redox-active organic materials. In particular, it has allowed the prediction of the crystal structures of organic battery materials, composed of small redox-active molecules, obtained entirely from

first-principles theory without any experimental input.[50,51,54] Such predictive theoretical approaches have been shown to be useful for advancing our fundamental understanding of the electrochemistry of organic electrode materials. In short, the method selects crystalline structures in a free energy landscape only based on the chemical composition of the system, and then aim at approaching the global minimum. Starting from a random generation of a set of structures (first population), subsequent generations evolve by applying three different variation operators: heredity, soft mutation and permutation. This is carried out until a selection criterion is satisfied (usually the system free energy), resulting in the final structure being chosen.[126] The experimental characterization of these crystalline structures of highly reactive organic materials during battery operation is a challenging task, which requires the employment of sophisticated operando spectroscopy and/or diffraction techniques. Thus, methodologies based on first-principles theory interplayed with an evolutionary algorithm can provide key complementary contributions in this research field.

Finally, significant predictive power has also been demonstrated by recent developments in so-called *high-throughput computational materials design* (HCMD),[127] which is an emerging field of materials science. The idea is simple: to use supercomputers to virtually study hundreds or thousands of chemical compounds at a time, quickly and efficiently looking for the best building blocks for a new material. This is particularly useful for the design of redox organic molecules with a given target property (*e.g.*, combinations of redox potential and capacity) due to the extremely wide range of chemical compositions and structures. To give an idea of such versatility, 166 billion organic structures have recently been enumerated by considering only small molecules up to 17 atoms of C, N, O, S and halogens.[128] To tap into this huge materials reservoir, rational design methodologies using high-throughput screening techniques are necessary. A great share of HCMD work has been oriented to study redox-active organic molecules for application in aqueous flow batteries, which has culminated with the proposal for a number of novel compounds. For instance, Er *et al.*[129] have proposed novel quinone-based electroactive molecules for the positive and negative sides of the flow battery, inspired by biological processes. Flores *et al.*[130] have been able to explore a new class of materials, based on thiophenoquinones, including a large combination of functional groups (∼10 611 compounds). They could thereby identify a large number of potential materials having redox potentials within a desired range. Other studies have also contributed to this research domain using similar methodologies, which have greatly contributed to the development of this relevant area of stationary electrochemical energy storage.[131–134] The bottom line is that the synthesis of such an enormous amount of compounds is most likely impossible. Therefore, the aforementioned techniques of ML, evolutionary algorithms and HCMD are opening new horizons in materials science by accelerating the discovery of novel compounds while unveiling fundamental structure–property relationships.

## References


1. P. Hohenberg and W. Kohn, Inhomogeneous electron gas, *Phys. Rev.*, 1964, **136**, B864–B871.
2. W. Kohn and L. J. Sham, Self-consistent equations including exchange and correlation effects, *Phys. Rev.*, 1965, **140**, A1133.
3. A. D. Becke, Density-functional thermochemistry. III. The role of exact exchange, *J. Chem. Phys.*, 1993, **98**, 5648–5652.
4. C. Lee, W. Yang and R. G. Parr, Development of the Colle-Salvetti correlation-energy formula into a functional of the electron density, *Phys. Rev. B*, 1988, **37**, 785–789.
5. Y. Zhao and D. G. Truhlar, The M06 suite of density functionals for main group thermochemistry, thermochemical kinetics, noncovalent interactions, excited states, and transition elements: Two new functionals and systematic testing of four M06-class functionals and 12 other function, *Theor. Chem. Acc.*, 2008, **120**, 215–241.
6. Y. Zhao and D. G. Truhlar, Exploring the limit of accuracy of the global hybrid meta density functional for main-group thermochemistry, kinetics, and noncovalent interactions, *J. Chem. Theory Comput.*, 2008, **4**, 1849–1868.
7. H. S. Yu, X. He, S. L. Li and D. G. Truhlar, MN15: A Kohn-Sham global-hybrid exchange-correlation density functional with broad accuracy for multi-reference and single-reference systems and noncovalent interactions, *Chem. Sci.*, 2016, **7**, 5032–5051.
8. W. J. Hehre, K. Ditchfield and J. A. Pople, Self-consistent molecular orbital methods. XII. Further extensions of gaussian-type basis sets for use in molecular orbital studies of organic molecules, *J. Chem. Phys.*, 1972, **56**, 2257–2261.
9. M. M. Francl, W. J. Pietro, W. J. Hehre, J. S. Binkley, M. S. Gordon, D. J. DeFrees and J. A. Pople, Self-consistent molecular orbital methods. XXIII. A polarization-type basis set for second-row elements, *J. Chem. Phys.*, 1982, **77**, 3654–3665.
10. M. J. Frisch, G. W. Trucks, H. B. Schlegel, G. E. Scuseria, M. A. Robb, J. R. Cheeseman, G. Scalmani, V. Barone, G. A. Petersson, H. Nakatsuji, X. Li, M. Caricato, A. V. Marenich, J. Bloino, B. G. Janesko, R. Gomperts, B. Mennucci, H. P. Hratchian, J. V. Ortiz, A. F. Izmaylov, J. L. Sonnenberg, D. Williams-Young, F. Ding, F. Lipparini, F. Egidi, J. Goings, B. Peng, A. Petrone, T. Henderson, D. Ranasinghe, V. G. Zakrzewski, J. Gao, N. Rega, G. Zheng, W. Liang, M. Hada, M. Ehara, K. Toyota, R. Fukuda, J. Hasegawa, M. Ishida, T. Nakajima, Y. Honda, O. Kitao, H. Nakai, T. Vreven, K. Throssell, J. J. A. Montgomery, J. E. Peralta, F. Ogliaro, M. J. Bearpark, J. J. Heyd, E. N. Brothers, K. N. Kudin, V. N. Staroverov, T. A. Keith, R. Kobayashi, J. Normand, K. Raghavachari, A. P. Rendell, J. C. Burant, S. S. Iyengar, J. Tomasi, M. Cossi, J. M. Millam, M. Klene, C. Adamo, R. Cammi,

J. W. Ochterski, R. L. Martin, K. Morokuma, O. Farkas, J. B. Foresman, D. J. Fox, *Gaussian 16*, Gaussian Inc., Wallingford, CT, 2016.
11. Y. Kanai and J. C. Grossman, Insights on interfacial charge transfer across P3HT/fullerene photovoltaic heterojunction from ab initio calculations, *Nano Lett.*, 2007, **7**, 1967–1972.
12. C. F. N. Marchiori and M. Koehler, Dipole assisted exciton dissociation at conjugated polymer/fullerene photovoltaic interfaces: A molecular study using density functional theory calculations, *Synth. Met.*, 2010, **160**, 643–650.
13. C. F. N. Marchiori and M. Koehler, Density functional theory study of the dipole across the P3HT: PCBM complex: The role of polarization and charge transfer, *J. Phys. D: Appl. Phys.*, 2014, **47**, 215104.
14. V. I. Arkhipov, P. Heremans and H. Bässler, Why is exciton dissociation so efficient at the interface between a conjugated polymer and an electron acceptor?, *Appl. Phys. Lett.*, 2003, **82**, 4605–4607.
15. M. Wiemer, A. V. Nenashev, F. Jansson and S. D. Baranovskii, On the efficiency of exciton dissociation at the interface between a conjugated polymer and an electron acceptor, *Appl. Phys. Lett.*, 2011, **99**, 013302.
16. X. Xu, K. Feng, Z. Bi, W. Ma, G. Zhang and Q. Peng, Single-Junction Polymer Solar Cells with 16.35% Efficiency Enabled by a Platinum(II) Complexation Strategy, *Adv. Mater.*, 2019, **31**, 1901872.
17. L. Zhan, S. Li, T. K. Lau, Y. Cui, X. Lu, M. Shi, C. Z. Li, H. Li, J. Hou and H. Chen, Over 17% efficiency ternary organic solar cells enabled by two non-fullerene acceptors working in an alloy-like model, *Energy Environ. Sci.*, 2020, **13**, 635–645.
18. Y. Lin and X. Zhan, Non-fullerene acceptors for organic photovoltaics: An emerging horizon, *Mater. Horizons*, 2014, **1**, 470–488.
19. M. E. Ziffer, S. B. Jo, H. Zhong, L. Ye, H. Liu, F. Lin, J. Zhang, X. Li, H. W. Ade, A. K. Y. Jen and D. S. Ginger, Long-Lived, Non-Geminate, Radiative Recombination of Photogenerated Charges in a Polymer/Small-Molecule Acceptor Photovoltaic Blend, *J. Am. Chem. Soc.*, 2018, **140**, 9996–10008.
20. K. Cnops, B. P. Rand, D. Cheyns, B. Verreet, M. A. Empl and P. Heremans, 8.4% Efficient Fullerene-Free Organic Solar Cells Exploiting Long-Range Exciton Energy Transfer, *Nat. Commun.*, 2014, **5**, 3406.
21. Y. Liu, X. Wan, F. Wang, J. Zhou, G. Long, J. Tian and Y. Chen, High-performance solar cells using a solution-processed small molecule containing benzodithiophene unit, *Adv. Mater.*, 2011, **23**, 5387–5391.
22. A. Kuzmich, D. Padula, H. Ma and A. Troisi, Trends in the electronic and geometric structure of non-fullerene based acceptors for organic solar cells, *Energy Environ. Sci.*, 2017, **10**, 395–401.
23. C. D. Canestraro, P. C. Rodrigues, C. F. N. Marchiori, C. B. Schneider, L. Akcelrud, M. Koehler and L. S. Roman, The role of the double peaked absorption spectrum in the efficiency of solar cells based on donor-acceptor-donor copolymers, *Sol. Energy Mater. Sol. Cells*, 2011, **95**, 2287–2294.

24. F. Zhang, O. Inganäs, Y. Zhou and K. Vandewal, Development of polymer-fullerene solar cells, *Natl. Sci. Rev.*, 2016, **3**, 222–239.
25. J. Liu, S. Chen, D. Qian, B. Gautam, G. Yang, J. Zhao, J. Bergqvist, F. Zhang, W. Ma, H. Ade, O. Inganäs, K. Gundogdu, F. Gao and H. Yan, Fast charge separation in a non-fullerene organic solar cell with a small driving force, *Nat. Energy*, 2016, **1**, 16089.
26. K. Vandewal, K. Tvingstedt, A. Gadisa, O. Inganäs and J. V. Manca, On the origin of the open-circuit voltage of polymer-fullerene solar cells, *Nat. Mater.*, 2009, **8**, 904–909.
27. P. B. Pati, G. Damas, L. Tian, D. L. A. Fernandes, L. Zhang, I. B. Pehlivan, T. Edvinsson, C. M. Araujo and H. Tian, An experimental and theoretical study of an efficient polymer nano-photocatalyst for hydrogen evolution, *Energy Environ. Sci.*, 2017, **10**, 1372–1376.
28. Y. Xu, N. Mao, C. Zhang, X. Wang, J. Zeng, Y. Chen, F. Wang and J. X. Jiang, Rational design of donor-Π-acceptor conjugated microporous polymers for photocatalytic hydrogen production, *Appl. Catal. B Environ.*, 2018, **228**, 1–9.
29. D. J. Woods, R. S. Sprick, C. L. Smith, A. J. Cowan and A. I. Cooper, A Solution-Processable Polymer Photocatalyst for Hydrogen Evolution from Water, *Adv. Energy Mater.*, 2017, DOI: 10.1002/aenm.201700479.
30. G. Zhang, Z. A. Lan and X. Wang, Conjugated Polymers: Catalysts for Photocatalytic Hydrogen Evolution, *Angew. Chemie - Int. Ed.*, 2016, **55**, 15712–15727.
31. P. Acker, L. Rzesny, C. F. N. Marchiori, C. M. Araujo and B. Esser, π-Conjugation Enables Ultra-High Rate Capabilities and Cycling Stabilities in Phenothiazine Copolymers as Cathode-Active Battery Materials, *Adv. Funct. Mater.*, 2019, **29**, 1906436.
32. N. Casado, D. Mantione, D. Shanmukaraj and D. Mecerreyes, Symmetric All-Organic Battery Containing a Dual Redox-Active Polymer as Cathode and Anode Material, *ChemSusChem*, 2019, DOI: 10.1002/cssc.201902856.
33. G. Dai, Y. Gao, Z. Niu, P. He, X. Zhang, Y. Zhao and H. Zhou, Dilution of the Electron Density in the π-Conjugated Skeleton of Organic Cathode Materials Improves the Discharge Voltage, *ChemSusChem*, 2020, DOI: 10.1002/cssc.201903502.
34. H. Zhou, L. Yang, S. Stoneking and W. You, A weak donor-strong acceptor strategy to design ideal polymers for organic solar cells, *ACS Appl. Mater. Interfaces*, 2010, **2**, 1377–1383.
35. H. Zhou, L. Yang and W. You, Rational design of high performance conjugated polymers for organic solar cells, *Macromolecules*, 2012, **45**, 607–632.
36. G. Damas, C. F. N. Marchiori and C. M. Araujo, On the Design of Donor-Acceptor Conjugated Polymers for Photocatalytic Hydrogen Evolution Reaction: First-Principles Theory-Based Assessment, *J. Phys. Chem. C*, 2018, **122**, 26876–26888.

37. J. Ridley and M. Zerner, An intermediate neglect of differential overlap technique for spectroscopy: Pyrrole and the azines, *Theor. Chim. Acta*, 1973, **32**, 111–134.
38. M. C. Zerner, Semiempirical Molecular Orbital Methods, *Rev. Comput. Chem.*, 2007, 313–365.
39. H. Feng, N. Qiu, X. Wang, Y. Wang, B. Kan, X. Wan, M. Zhang, A. Xia, C. Li, F. Liu, H. Zhang and Y. Chen, An A-D-A Type Small-Molecule Electron Acceptor with End-Extended Conjugation for High Performance Organic Solar Cells, *Chem. Mater.*, 2017, **29**, 7908–7917.
40. G. B. Damas, C. F. N. Marchiori and C. M. Araujo, Tailoring the Electron-Rich Moiety in Benzothiadiazole-Based Polymers for an Efficient Photocatalytic Hydrogen Evolution Reaction, *J. Phys. Chem. C*, 2019, **123**, 25531–25542.
41. G. B. Damas, F. Von Kieseritzky, J. Hellberg, C. F. N. Marchiori and C. M. Araujo, Symmetric Small-Molecules with Acceptor-Donor-Acceptor Architecture for Efficient Visible-Light Driven Hydrogen Production: Optical and Thermodynamic Aspects, *J. Phys. Chem. C*, 2019, **123**, 30799–30808.
42. Y. H. Cui, Y. Tong, L. Han, J. Gao and J. K. Feng, Design and photoelectric properties of D-A-π-A carbazole dyes with different π-spacers and acceptors for use in solar cells: a DFT and TD-DFT investigation, *J. Mol. Model.*, 2019, **25**, 249.
43. J. Preat, D. Jacquemin and E. A. Perpète, Design of new triphenylamine-sensitized solar cells: A theoretical approach, *Environ. Sci. Technol.*, 2010, **44**, 5666–5671.
44. H. Bin Li, J. Zhang, Y. Wu, J. L. Jin, Y. A. Duan, Z. M. Su and Y. Geng, Theoretical study and design of triphenylamine-malononitrile-based p-type organic dyes with different π-linkers for dyes-sensitized solar cells, *Dye. Pigment.*, 2014, **108**, 106–114.
45. Y. Guo, X. Lu, G. Li, L. Zhao, S. Wei and W. Guo, Theoretical design of push-pull porphyrin dyes with π-bridge modification for dye-sensitized solar cells, *J. Photochem. Photobiol. A Chem.*, 2017, **332**, 232–240.
46. Y. Xu, X. Xu, M. Li and W. Lu, Prediction of photoelectric properties, especially power conversion efficiency of cells, of IQ1 and derivative dyes in high-efficiency dye-sensitized solar cells, *Sol. Energy*, 2020, **195**, 82–88.
47. W. Zhang, P. Sun and S. Sun, A theoretical method to predict novel organic electrode materials for Na-ion batteries, *Comput. Mater. Sci.*, 2017, **134**, 42–47.
48. R. B. Araujo, A. Banerjee, P. Panigrahi, L. Yang, M. Strømme, M. Sjödin, C. M. Araujo and R. Ahuja, Designing strategies to tune reduction potential of organic molecules for sustainable high capacity battery application, *J. Mater. Chem. A*, 2017, **5**, 4430–4454.
49. L. Miao, L. Liu, K. Zhang and J. Chen, Molecular Design Strategy for High-Redox-Potential and Poorly Soluble n-Type Phenazine Derivatives as Cathode Materials for Lithium Batteries, *ChemSusChem*, 2020, **13**, 2337–2344, DOI: 10.1002/cssc.202000004.

50. C. F. N. Marchiori, D. Brandell and C. M. Araujo, Predicting Structure and Electrochemistry of Dilithium Thiophene-2,5-Dicarboxylate Electrodes by Density Functional Theory and Evolutionary Algorithms, *J. Phys. Chem. C*, 2019, **123**, 4691–4700, DOI: 10.1021/acs.jpcc.8b11341.
51. R. P. Carvalho, C. F. N. Marchiori, D. Brandell and C. M. Araujo, Tuning the electrochemical properties of organic battery cathode materials: Insights from evolutionary algorithm DFT calculations, *ChemSusChem*, 2020, **13**, 2402, DOI: 10.1002/cssc.201903450.
52. Y. Chen, S. Sun, X. Wang and Q. Shi, Study of Lithium Migration Pathways in the Organic Electrode Materials of Li-Battery by Dispersion-Corrected Density Functional Theory, *J. Phys. Chem. C*, 2015, **119**, 25719–25725.
53. S. J. Yang, X. Y. Qin, R. He, W. Shen, M. Li and L. Bin Zhao, A density functional theory study on the thermodynamic and dynamic properties of anthraquinone analogue cathode materials for rechargeable lithium ion batteries, *Phys. Chem. Chem. Phys.*, 2017, **19**, 12480–12489.
54. A. Banerjee, R. B. Araujo, M. Sjödin and R. Ahuja, Identifying the tuning key of disproportionation redox reaction in terephthalate: A Li-based anode for sustainable organic batteries, *Nano Energy*, 2018, **47**, 301–308.
55. C. M. Araujo, D. L. Simone, S. J. Konezny, A. Shim, R. H. Crabtree, G. L. Soloveichik and V. S. Batista, Fuel selection for a regenerative organic fuel cell/flow battery: Thermodynamic considerations, *Energy Environ. Sci.*, 2012, **5**, 9534–9542.
56. J. H. Park, T. Liu, K. C. Kim, S. W. Lee and S. S. Jang, Systematic Molecular Design of Ketone Derivatives of Aromatic Molecules for Lithium-Ion Batteries: First-Principles DFT Modeling, *ChemSusChem*, 2017, **10**, 1584–1591.
57. Y. Hu, B. Zhou, H. Chen and C. Wang, Manganese-Catalyzed Redox-Neutral C − H Olefination of Ketones with Unactivated Alkenes, *Angew. Chemie - Int. Ed.*, 2018, **57**, 12071–12075.
58. Q. L. Xu, H. Gao, M. Yousufuddin, D. H. Ess and L. Kürti, Aerobic, transition-metal-free, direct, and regiospecific mono-α-arylation of ketones: Synthesis and mechanism by DFT calculations, *J. Am. Chem. Soc.*, 2013, **135**, 14048–14051.
59. C. Pejo, H. Pardo, A. Mombrú, M. F. Cerdá, J. S. Gancheff, R. Chiozzone and R. González, Re(v) complexes formed by metal-assisted solvolysis of di-(2-pyridyl) ketone: Synthesis, X-ray studies, redox behavior and DFT calculations, *Inorganica Chim. Acta*, 2011, **376**, 105–111.
60. J. E. Bachman, L. A. Curtiss and R. S. Assary, Investigation of the redox chemistry of anthraquinone derivatives using density functional theory, *J. Phys. Chem. A*, 2014, **118**, 8852–8860.
61. K. C. Kim, T. Liu, S. W. Lee and S. S. Jang, First-Principles Density Functional Theory Modeling of Li Binding: Thermodynamics and Redox Properties of Quinone Derivatives for Lithium-Ion Batteries, *J. Am. Chem. Soc.*, 2016, **138**, 2374–2382.

62. K. Hernández-Burgos, S. E. Burkhardt, G. G. Rodríguez-Calero, R. G. Hennig and H. D. Abruña, Theoretical studies of carbonyl-based organic molecules for energy storage applications: The heteroatom and substituent effect, *J. Phys. Chem. C*, 2014, **118**, 6046–6051.
63. M. Yao, H. Senoh, S. I. Yamazaki, Z. Siroma, T. Sakai and K. Yasuda, High-capacity organic positive-electrode material based on a benzoquinone derivative for use in rechargeable lithium batteries, *J. Power Sources*, 2010, **195**, 8336–8340.
64. S. Renault, V. A. Oltean, C. M. Araujo, A. Grigoriev, K. Edström and D. Brandell, Superlithiation of Organic Electrode Materials: The Case of Dilithium Benzenedipropiolate, *Chem. Mater.*, 2016, **28**, 1920–1926.
65. J. VandeVondele, R. Ayala, M. Sulpizi and M. Sprik, Redox free energies and one-electron energy levels in density functional theory based ab initio molecular dynamics, *J. Electroanal. Chem.*, 2007, **607**, 113–120, DOI: 10.1016/j.jelechem.2007.01.009.
66. G. G. Rodríguez-Calero, M. A. Lowe, Y. Kiya and H. D. Abruña, Electrochemical and computational studies on the electrocatalytic effect of conducting polymers toward the redox reactions of thiadiazole-based thiolate compounds, *J. Phys. Chem. C*, 2010, **114**, 6169–6176.
67. J. L. Hodgson, M. Namazian, S. E. Bottle and M. L. Coote, One-electron oxidation and reduction potentials of nitroxide antioxidants: A theoretical study, *J. Phys. Chem. A*, 2007, **111**, 13595–13605.
68. M. Shibuya, F. Pichierri, M. Tomizawa, S. Nagasawa, I. Suzuki and Y. Iwabuchi, Oxidation of nitroxyl radicals: Electrochemical and computational studies, *Tetrahedron Lett.*, 2012, **53**, 2070–2073.
69. S. K. Singh, X. Crispin and I. V. Zozoulenko, Oxygen Reduction Reaction in Conducting Polymer PEDOT: Density Functional Theory Study, *J. Phys. Chem. C*, 2017, **121**, 12270–12277.
70. Y. Kiya, G. R. Hutchison, J. C. Henderson, T. Sarukawa, O. Hatozaki, N. Oyama and H. D. Abruña, Elucidation of the redox behavior of 2,5-dimercapto-1,3,4-thiadiazole (DMcT) at poly(3,4-ethylenedioxythiophene) (PEDOT)-modified electrodes and application of the DMcT – PEDOT composite cathodes to lithium/lithium ion batteries, *Langmuir*, 2006, **22**, 10554–10563.
71. I. Zozoulenko, A. Singh, S. K. Singh, V. Gueskine, X. Crispin and M. Berggren, Polarons, Bipolarons, And Absorption Spectroscopy of PEDOT, *ACS Appl. Polym. Mater.*, 2019, **1**, 83–94.
72. Y. Zhou, W. A. Saidi and K. A. Fichthorn, Comparison of the binding of polyvinylpyrrolidone and polyethylene oxide to Ag surfaces: Elements of a successful structure-directing agent, *J. Phys. Chem. C*, 2013, **117**, 11444–11448.
73. J. R. Smith, P. A. Cox, S. A. Campbell and N. M. Ratcliffe, Application of density functional theory in the synthesis of electroactive polymers, *J. Chem. Soc., Faraday Trans.*, 1995, **91**, 2331–2338.
74. P. Guiglion, A. Monti and M. A. Zwijnenburg, Validating a density functional theory approach for predicting the redox potentials

associated with charge carriers and excitons in polymeric photocatalysts, *J. Phys. Chem. C*, 2017, **121**, 1498–1506.
75. K. Tasaki, Solvent decompositions and physical properties of decomposition compounds in Li-ion battery electrolytes studied by DFT calculations and molecular dynamics simulations, *J. Phys. Chem. B*, 2005, **109**, 2920–2933.
76. E. J. Baerends, O. V. Gritsenko and R. Van Meer, The Kohn-Sham gap, the fundamental gap and the optical gap: the physical meaning of occupied and virtual Kohn-Sham orbital energies, *Phys. Chem. Chem. Phys.*, 2013, **15**, 16408–16425.
77. J. B. Goodenough, Electrochemical energy storage in a sustainable modern society, *Energy Environ. Sci.*, 2014, **7**, 14–18.
78. J. B. Goodenough and K. S. Park, *J. Am. Chem. Soc.*, 2013, **135**, 1167–1176.
79. B. C. Melot and J. M. Tarascon, Design and preparation of materials for advanced electrochemical storage, *Acc. Chem. Res.*, 2013, **46**, 1226–1238.
80. P. Peljo and H. H. Girault, Electrochemical potential window of battery electrolytes: The HOMO-LUMO misconception, *Energy Environ. Sci.*, 2018, **11**, 2306–2309.
81. N. I. of S. and Technology, NIST Standard Reference Database Number 101.
82. G. Scalmani and M. J. Frisch, Continuous surface charge polarizable continuum models of solvation. I. General formalism, *J. Chem. Phys.*, 2010, **132**, 114110.
83. S. R. Edinger, C. Cortis, P. S. Shenkin and R. A. Friesner, Solvation free energies of peptides: Comparison of approximate continuum solvation models with accurate solution of the Poisson-Boltzmann equation, *J. Phys. Chem. B*, 1997, **101**, 1190–1197.
84. A. Klamt and G. Schüürmann, COSMO: A new approach to dielectric screening in solvents with explicit expressions for the screening energy and its gradient, *J. Chem. Soc., Perkin Trans. 2*, 1993, 799–805.
85. A. V. Marenich, C. J. Cramer and D. G. Truhlar, Universal solvation model based on solute electron density and on a continuum model of the solvent defined by the bulk dielectric constant and atomic surface tensions, *J. Phys. Chem. B*, 2009, **113**, 6378–6396.
86. E. Talebian and M. Talebian, A general review on the derivation of Clausius-Mossotti relation, *Optik (Stuttg.)*, 2013, **124**, 2324–2326.
87. D. Hait and M. Head-Gordon, How accurate are static polarizability predictions from density functional theory? An assessment over 132 species at equilibrium geometry, *Phys. Chem. Chem. Phys.*, 2018, **20**, 19800–19810.
88. S. J. A. Van Gisbergen, J. G. Snijders and E. J. Baerends, A density functional theory study of frequency-dependent polarizabilities and Van der Waals dispersion coefficients for polyatomic molecules, *J. Chem. Phys.*, 1995, **103**, 9347–9354.

89. P. K. Nayak and N. Periasamy, Calculation of electron affinity, ionization potential, transport gap, optical band gap and exciton binding energy of organic solids using ''solvation'' model and DFT, *Org. Electron.*, 2009, **10**, 1396–1400.
90. P. E. Schwenn, P. L. Burn and B. J. Powell, Calculation of solid state molecular ionisation energies and electron affinities for organic semiconductors, *Org. Electron.*, 2011, **12**, 394–403.
91. M. P. Allen, D. J. Tildesley and J. R. Banavar, Computer Simulation of Liquids, *Phys. Today*, 1989, **42**, 105–106.
92. A. A. Franco, A. Rucci, D. Brandell, C. Frayret, M. Gaberscek, P. Jankowski and P. Johansson, Boosting Rechargeable Batteries R&D by Multiscale Modeling: Myth or Reality?, *Chem. Rev.*, 2019, **119**, 4569–4627.
93. Y. Y. Zhang, Y. Y. Sun, S. X. Du, H. J. Gao and S. B. Zhang, Organic salts as super-high rate capability materials for lithium-ion batteries, *Appl. Phys. Lett.*, 2012, **100**, 091905.
94. H. Nishide and K. Oyaizu, Toward flexible batteries, *Science*, 2008, **319**, 737–738.
95. T. W. Kemper, R. E. Larsen and T. Gennett, Relationship between molecular structure and electron transfer in a polymeric Nitroxyl-radical energy storage material, *J. Phys. Chem. C*, 2014, **118**, 17213–17220.
96. T. W. Kemper, T. Gennett and R. E. Larsen, Molecular Dynamics Simulation Study of Solvent and State of Charge Effects on Solid-Phase Structure and Counterion Binding in a Nitroxide Radical Containing Polymer Energy Storage Material, *J. Phys. Chem. C*, 2016, **120**, 25639–25646.
97. Y. Chen and S. Manzhos, Voltage and capacity control of polyaniline based organic cathodes: An ab initio study, *J. Power Sources*, 2016, **336**, 126–131.
98. Y. Chen, J. Lüder, M. F. Ng, M. Sullivan and S. Manzhos, Polyaniline and CN-functionalized polyaniline as organic cathodes for lithium and sodium ion batteries: A combined molecular dynamics and density functional tight binding study in solid state, *Phys. Chem. Chem. Phys.*, 2017, **20**, 232–237.
99. H. Shi, C. Liu, Q. Jiang and J. Xu, Effective Approaches to Improve the Electrical Conductivity of PEDOT:PSS: A Review, *Adv. Electron. Mater.*, 2015, **1**, 1500017.
100. J. F. Franco-Gonzalez and I. V. Zozoulenko, Molecular Dynamics Study of Morphology of Doped PEDOT: From Solution to Dry Phase, *J. Phys. Chem. B*, 2017, **121**, 4299–4307.
101. S. Rudd, J. F. Franco-Gonzalez, S. Kumar Singh, Z. Ullah Khan, X. Crispin, J. W. Andreasen, I. Zozoulenko and D. Evans, Charge transport and structure in semimetallic polymers, *J. Polym. Sci., Part B: Polym. Phys.*, 2018, **56**, 97–104.
102. N. Rolland, J. F. Franco-Gonzalez, R. Volpi, M. Linares and I. V. Zozoulenko, Understanding morphology-mobility dependence in PEDOT:Tos, *Phys. Rev. Mater.*, 2018, **2**, 045605.

103. M. Modarresi, J. F. Franco-Gonzalez and I. Zozoulenko, Morphology and ion diffusion in PEDOT:Tos. A coarse grained molecular dynamics simulation, *Phys. Chem. Chem. Phys.*, 2018, **20**, 17188–17198.
104. J. Rehmen, K. Zuber, M. Modarresi, D. Kim, E. Charrault, P. Jannasch, I. Zozoulenko, D. Evans and C. Karlsson, Structural Control of Charge Storage Capacity to Achieve 100% Doping in Vapor Phase-Polymerized PEDOT/Tosylate, *ACS Omega*, 2019, **4**, 21818–21826.
105. X. Yu, R. Li, T. Shiga, L. Feng, M. An, L. Zhang, J. Shiomi and N. Yang, Hybrid Thermal Transport Characteristics of Doped Organic Semiconductor Poly(3,4-ethylenedioxythiophene):Tosylate, *J. Phys. Chem. C*, 2019, **123**, 26735–26741.
106. G. Han, Y. Guo, X. Ma and Y. Yi, Atomistic Insight Into Donor/Acceptor Interfaces in High-Efficiency Nonfullerene Organic Solar Cells, *Sol. RRL*, 2018, **2**, 1800190.
107. D. D. Medina, M. L. Petrus, A. N. Jumabekov, J. T. Margraf, S. Weinberger, J. M. Rotter, T. Clark and T. Bein, Directional Charge-Carrier Transport in Oriented Benzodithiophene Covalent Organic Framework Thin Films, *ACS Nano*, 2017, **11**, 2706–2713.
108. G. Colherinhas, T. Malaspina and E. E. Fileti, Storing Energy in Biodegradable Electrochemical Supercapacitors, *ACS Omega*, 2018, **3**, 13869–13875.
109. R. M. Martin, *Electronic Structure: Basic Theory and Practical Methods*, Cambridge University Press, Cambridge, 2004.
110. M. Ebadi, C. Marchiori, J. Mindemark, D. Brandell and C. M. Araujo, Assessing structure and stability of polymer/lithium-metal interfaces from first-principles calculations, *J. Mater. Chem. A*, 2019, **7**, 8394–8404.
111. U. Röthlisberger, M. Sprik and M. L. Klein, Living polymers: Ab initio molecular dynamics study of the initiation step in the polymerization of isoprene induced by ethyl lithium, *J. Chem. Soc. – Faraday Trans.*, 1998, **94**, 501–508.
112. C. M. Araújo, A. Blomqvist, R. H. Scheicher, P. Chen and R. Ahuja, Superionicity in the hydrogen storage material Li2 NH: Molecular dynamics simulations, *Phys. Rev. B – Condens. Matter Mater. Phys*, 2009, **79**, 172101.
113. S. Srivastav, P. Tammela, D. Brandell and M. Sjödin, Understanding Ionic Transport in Polypyrrole/Nanocellulose Composite Energy Storage Devices, *Electrochim. Acta*, 2015, **182**, 1145–1152.
114. K. T. Butler, D. W. Davies, H. Cartwright, O. Isayev and A. Walsh, *Nature*, 2018, **559**, 547–555.
115. F. Brockherde, L. Vogt, L. Li, M. E. Tuckerman, K. Burke and K. R. Müller, Bypassing the Kohn-Sham equations with machine learning, *Nat. Commun.*, 2017, **8**, 1–10.
116. J. Behler, First Principles Neural Network Potentials for Reactive Simulations of Large Molecular and Condensed Systems, *Angew. Chem., Int. Ed.*, 2017, **56**, 12828–12840.

117. O. Allam, B. W. Cho, K. C. Kim and S. S. Jang, Application of DFT-based machine learning for developing molecular electrode materials in Li-ion batteries, *RSC Adv.*, 2018, **8**, 39414–39420.
118. L. Wilbraham, R. S. Sprick, K. E. Jelfs and M. A. Zwijnenburg, Mapping binary copolymer property space with neural networks, *Chem. Sci.*, 2019, **10**, 4973–4984.
119. M. Rupp, A. Tkatchenko, K.-R. Müller and O. A. von Lilienfeld, Fast and accurate modeling of molecular atomization energies with machine learning, *Phys. Rev. Lett.*, 2012, DOI: 10.1103/PhysRevLett.108.058301.
120. G. Pilania, C. Wang, X. Jiang, S. Rajasekaran and R. Ramprasad, Accelerating materials property predictions using machine learning, *Sci. Rep.*, 2013, **3**, 1–6.
121. K. T. Schütt, H. Glawe, F. Brockherde, A. Sanna, K. R. Müller and E. K. U. Gross, How to represent crystal structures for machine learning: Towards fast prediction of electronic properties, *Phys. Rev. B - Condens. Matter Mater. Phys*, 2014, **89**, 205118.
122. L. Ward, R. Liu, A. Krishna, V. I. Hegde, A. Agrawal, A. Choudhary and C. Wolverton, Including crystal structure attributes in machine learning models of formation energies via Voronoi tessellations, *Phys. Rev. B*, 2017, **96**, 024104.
123. O. Isayev, C. Oses, C. Toher, E. Gossett, S. Curtarolo and A. Tropsha, Universal fragment descriptors for predicting properties of inorganic crystals, *Nat. Commun.*, 2017, **8**, 1–12.
124. J. Schmidhuber, Deep learning in neural networks: An overview, *Neural Networks*, 2015, **61**, 85–117.
125. P. M. Tagade, S. P. Adiga, S. Pandian, M. S. Park, K. S. Hariharan and S. M. Kolake, Attribute driven inverse materials design using deep learning Bayesian framework, *npj Comput. Mater.*, 2019, **5**, 1–14.
126. C. W. Glass, A. R. Oganov and N. Hansen, USPEX-Evolutionary crystal structure prediction, *Comput. Phys. Commun.*, 2006, **175**, 713–720.
127. S. Curtarolo, G. L. W. Hart, M. B. Nardelli, N. Mingo, S. Sanvito and O. Levy, The high-throughput highway to computational materials design, *Nat. Mater.*, 2013, DOI: 10.1038/nmat3568.
128. L. Ruddigkeit, R. Van Deursen, L. C. Blum and J. L. Reymond, Enumeration of 166 billion organic small molecules in the chemical universe database GDB-17, *J. Chem. Inf. Model.*, 2012, **52**, 2864–2875.
129. S. Er, C. Suh, M. P. Marshak and A. Aspuru-Guzik, Computational design of molecules for an all-quinone redox flow battery, *Chem. Sci.*, 2015, DOI: 10.1039/c4sc03030c.
130. S. D. Pineda Flores, G. C. Martin-Noble, R. L. Phillips and J. Schrier, Bio-Inspired Electroactive Organic Molecules for Aqueous Redox Flow Batteries. 1. Thiophenoquinones, *J. Phys. Chem. C*, 2015, **119**, 21800–21809.

131. C. S. Sevov, D. P. Hickey, M. E. Cook, S. G. Robinson, S. Barnett, S. D. Minteer, M. S. Sigman and M. S. Sanford, Physical Organic Approach to Persistent, Cyclable, Low-Potential Electrolytes for Flow Battery Applications, *J. Am. Chem. Soc.*, 2017, **139**, 2924–2927.
132. L. Cheng, R. S. Assary, X. Qu, A. Jain, S. P. Ong, N. N. Rajput, K. Persson and L. A. Curtiss, Accelerating Electrolyte Discovery for Energy Storage with High-Throughput Screening, *J. Phys. Chem. Lett.*, 2015, **6**, 283–291.
133. H. G. Roth, N. A. Romero and D. A. Nicewicz, Experimental and Calculated Electrochemical Potentials of Common Organic Molecules for Applications to Single-Electron Redox Chemistry, *Synlett*, 2016, **27**, 714–723.
134. K. Wedege, E. Dražević, D. Konya and A. Bentien, Organic Redox Species in Aqueous Flow Batteries: Redox Potentials, Chemical Stability and Solubility, *Sci. Rep.*, 2016, **6**, 39101.

CHAPTER 4

# *Radical Polymers for Rechargeable Batteries*

KOUKI OKA AND HIROYUKI NISHIDE*

Department of Applied Chemistry, Research Institute for Science and Engineering, Waseda University, 3-4-1 Okubo, Shinjuku, Tokyo 169-8555, Japan
*Email: nishide@waseda.jp

## 4.1 General Introduction

The Nobel Prize in Chemistry 2019 recognized ''The development of the lithium-ion battery. This lightweight, rechargeable and powerful battery is now used in everything from mobile phones to laptops and electric vehicles. It can also store significant amounts of energy from solar and wind power, making possible a fossil fuel-free society''.[1] While the conventional rechargeable batteries, including Li-ion batteries, are considered to comprise a ''green energy'' technology for our society, a great risk lies in the electrode-active inorganic materials, such as the scarcity of sources, energy-consuming production processes, problematic recycling and their toxicity and biohazardous nature. Organic batteries using organic electrode-active materials have inherent advantages that overcome the above risk, and the properties of the organic materials can be tailored through chemical synthesis.

The search for organic batteries began with the discovery of the electric conductivity of doped polyacetylene in the late 1970s.[2] However, early attempts using polyacetylene and other π-conjugated polymers did not prove fruitful because of the insufficient doping level or the low charging capacity of the material used, the drifting output voltage being dependent on the

Polymer Chemistry Series No. 34
Redox Polymers for Energy and Nanomedicine
Edited by Nerea Casado and David Mecerreyes

Published by the Royal Society of Chemistry, www.rsc.org

doping level, and the chemical instability of the doped polymers.[3] Several other avenues toward fabricating such batteries have been explored for these two decades by targeting redox-active organic compounds. A breakthrough was achieved using radical polymers, or organic polymers composed of robust but redox-active radical moieties in their repeating unit.

Some of the radical polymers are characterized by the rapid and reversible one-electron redox ability of the radical sites. A typical example is poly(2,2,6,6 tetramethylpiperidinyloxy methacrylate), which has a very positive redox potential. The combination of the high density of radical redox sites and the amorphous plasticized state coexisting with a small quantity of electrolytes allows for a rapid self-exchange reaction among the sites driven by a steep concentration gradient, which leads to efficient charge transport and storage throughout the polymers. The chemical bistability of the reduced and oxidized species of radical polymers permits an ultimate energy density and durable cyclability during charging and discharging. Lithium-ion and all-organic batteries have thus been fabricated using radical polymers as electrode-active materials. The output voltage of the batteries is constant, corresponding to their redox potential difference, and can be tuned by the molecular design. The batteries provide burst power, which also allows instant full charging in a few seconds.

This chapter describes organic radical polymers by focusing on their design, syntheses and electrochemical properties and, in the latter half, their performances as electrode-active materials employed in rechargeable batteries. The practical examples of radical batteries mentioned in this chapter could open up new dimensions for rechargeable power sources beyond those presented by conventional batteries, such as installation in the device or instrument through a facile printing process, fabrication of a thin, flexible, or even stretchable battery, and human skin-adherable or body-implantable batteries composed of biocompatible or biodegradable polymers.

This chapter also describes the redox-reaction-based electron (charge) transport and storage behavior of these materials, demonstrated for the first time by analyzing the very high reactivity of the radical sites condensed in the bulk radical polymers.

## 4.2 Radical Molecules

Radicals are defined as organic molecules that have one or more unpaired electron(s) and an open-shell electronic configuration.[4–6] They are usually intractable, often appear as intermediates in photochemical and combustion reactions, and initiate and terminate the polymerization of olefins. However, organic radical molecules are converted to their robust derivatives or materials with sufficient lifetimes even in the open atmosphere to be easily managed through incorporating a sterically protected and/or π-conjugated chemical structure. Robust radical molecules reported include nitroxide radicals such as 2,2,6,6-tetramethylpiperidinyloxyl (TEMPO), nitrogen- and oxygen-centered radicals such as 1,1-diphenyl-2-picrylhydrazyl[7]

and 2,4,6-tri-*t*-butylphenoxy radical,[8] and π-conjugated radicals such as tris(pentachlorophenyl)methyl radical.[9] They are studied and utilized in biomedical applications[10] and organic-based magnets,[11,12] which are ascribed to their unpaired electrons.

Some radical molecules have reversible redox abilities.[13] For example, TEMPO is reversibly one-electron oxidized to its oxoammonium cation and is reduced with one electron to regenerate the original TEMPO radical (Figure 4.1). This redox reaction is rapid, with an electron self-exchange rate constant of $10^9$ $M^{-1}s^{-1}$ determined by electron spin resonance spectroscopy.[14] The one-electron oxidized TEMPO molecule or the salt of TEMPO oxoammonium with counter anions, such as hexafluorophosphate ($PF_6^-$), is isolated as a crystal. The crystal structures of the TEMPO derivative and the oxidized TEMPO derivative[15] are shown in Figure 4.1; there are no structural changes such as the formation and breakage of a chemical bond that results in a very rapid and simple one-electron transfer reaction. The crystalline isolation of the TEMPO cation salt means that not only the starting robust TEMPO radical but also the oxidized TEMPO cation are chemically stable, indicating ''bistability'' of the starting (reduced) radical and the oxidized cation. The bistability is established with a small difference in the Gibbs free energy and a small activation energy between the reduced and oxidized states that enables a rapid electron-exchange reaction between them. The crystalline isolation of TEMPO and its cation also indicates a high density of the redox-active species in the neat materials.

Viologens exhibit a reversible one-electron redox reaction between the dications and the radical cations (Scheme 4.1). Salts of viologen cation radicals are isolated as robust, deep blue-violet crystals (the starting viologens are almost colorless).[16] They are known electrochromic materials with high cyclability. The redox couple of viologen and its reduced form are also representative examples of electrochemical ''bistability.'' Commercial

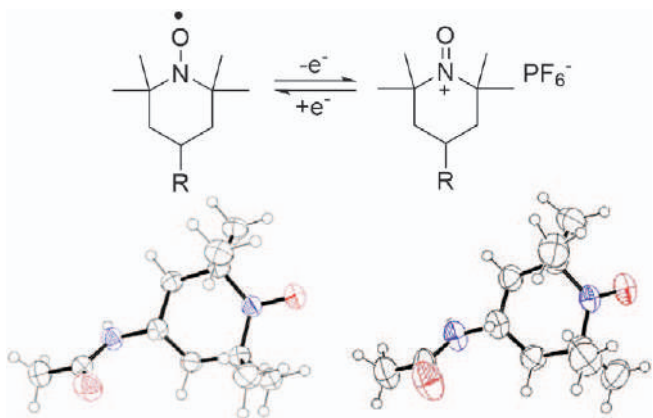


**Figure 4.1** Bistability: nitroxide radical and oxoammonium cation and their crystallographic structures.

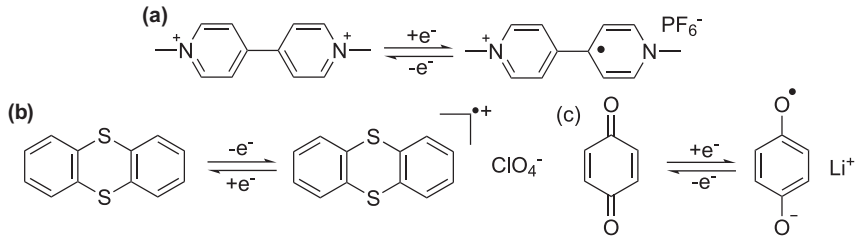


**Scheme 4.1** One-electron redox reaction of (a) viologen, (b) thianthrene and (c) benzoquinone.

applications include production of an antiglare rear-view mirror and an auto-dimming smart window installed on Boeing 787 aircraft.[16]

Thianthrene is one electron oxidized to its cation radical. The perchlorate ($ClO_4^-$) salt of the latter is isolated and robust.[17] Benzoquinone is one electron reduced to form the lithium salt of its anion radical.[18] These are also examples of electrochemical bistable redox couples. It could be noted that coexistent counterions often affect the bistability behavior of redox couples.

## 4.3 Redox-active Radical Molecules as Electrode-active Materials

Portable electrical equipment such as mobile phones, personal computers, robots and electric vehicles require power sources that are rechargeable. A rechargeable battery is a cell that converts chemical energy into electrical energy. The battery consists of two electrodes, an anode and a cathode, in contact with an electrolyte solution and a porous separator film (Figure 4.2). The anode-active material is associated with its oxidative chemical reaction that releases electrons into an external circuit during discharging. The cathode-active material gains electrons from the external circuit with its reductive chemical reaction. The charging process occurs with opposite electron flow, and reductive and oxidative reactions. Reversible redox reactions at both electrode-active materials store electrons or charges as energy together with counterion compensation from the electrolyte solution.

The electrode-active materials of conventional rechargeable batteries are composed of metals and metal oxides such as zinc, lead and cadmium, and manganese-, nickel- and cobalt-oxides, respectively.[19] Rechargeable batteries are characterized by high energy density, constant output voltage and inability to self-discharge. They are regarded as mature technologies. However, there remain unsolved issues, such as the poor power performance or a long charging time of >1 h for full charging. For example, the intercalation and elimination of lithium ions into and from the lattice of cobalt oxide in the cathode is a rate-determining step in the charging–discharging process of lithium-ion battery electrodes.[20] The inherent limitations of metal-based batteries are attributed to their toxicity, biohazard, overheating, tedious recycling and limited metal resources.[21]

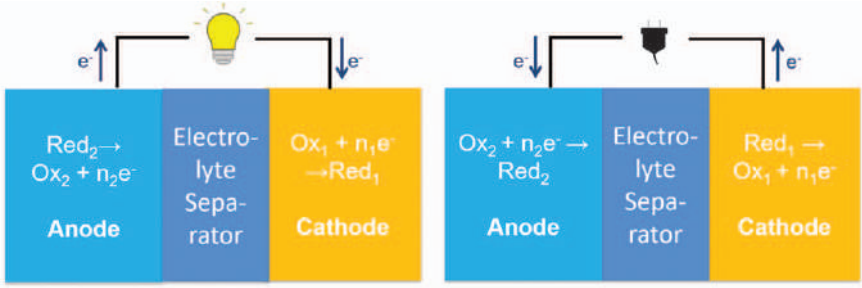


**Figure 4.2** Cell configuration of a rechargeable battery.

Considering the counter part of metal-based electrodes, there are investigations on using organic electrode-active materials for rechargeable batteries.

Organic compounds such as conjugated carbonyl compounds[22–25] and conjugated carboxylates[26–29] are extensively studied as promising organic electrode-active materials. Typical examples are crystals of rhodizonic acid and terephthalic acid. They are reversibly redoxed with multiple electrons through the lithiation of their phenolic alcohols and aromatic carboxylic acids.[30,31] They are expected to have a high theoretical capacity of 200–600 Ah $kg^{-1}$ owing to their compact molecular structures. However, analogous to the redox of inorganic electrode-active materials, an incorporation of lithium-ions in organic crystals and slow lithiation reaction significantly restrict the power rate performance as an electrode. The output voltage *vs.* $Li/Li^+$ of these organic compounds also remains very low at $<2.0$ V because of their negative redox potentials.

Polycyclic π-conjugated molecules[32,33] such as trioxotriangulene are expected to have a high theoretical redox capacity of >200 Ah $kg^{-1}$ *via* multiple redox reactions. However, multiple reactions provide low power rates, drifting output voltage, and often chemical instability of the molecules. These organic compounds for the electrode-active materials were tested as their crystals or solid powders, which lack electric conductivity in the fabricated electrode and require addition of a significant quantity of conductive carbon, as a result, to tremendously reduce the practical energy capacity as the electrode.

Organosulfur compounds, such as tetraethyl thiuram disulfide and diphenyl disulfide, have been studied as cathode-active materials to give a voltage of 2.0–2.3 V *vs.* $Li/Li^+$.[34–36] Although they have a very high capacity of >800 Ah $kg^{-1}$, the redox reaction between the disulfides and the thiols (or the lithium thiolates) is very slow, with an electron-transfer rate constant of $10^{-8}$ cm $s^{-1}$.[37] There have been investigations into modifying the molecular sulfur structure and compositing with conductive additives to improve the low power rate performance, however, the poor order of the sulfur fragments remains a problematic subject.

Nitroxide radical molecules, represented by TEMPO, show an electrochemically reversible redox ability at very positive potentials (>3.5 V *vs.*

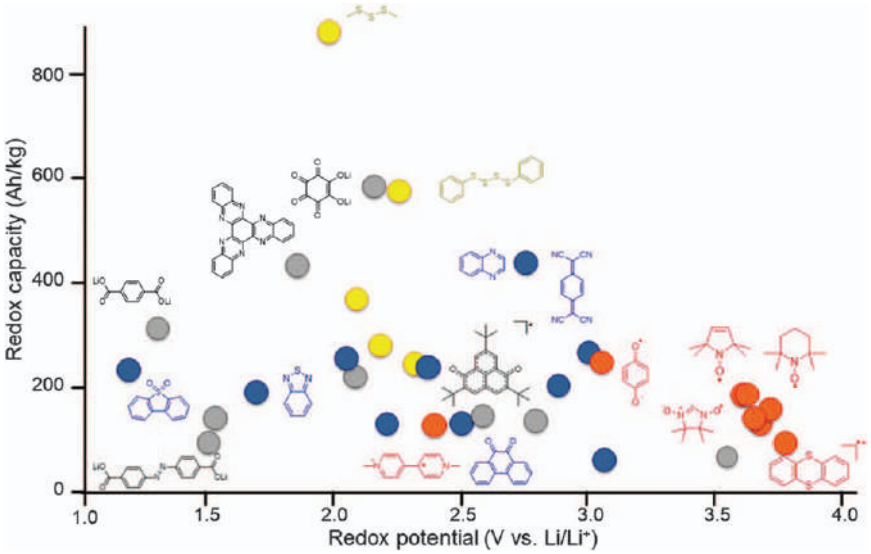


**Figure 4.3** Redox-active organic molecules projected on redox potential and capacity axes.

$Li/Li^+$) (Figure 4.3), while its capacity is not high. An output voltage of 3.7 V was recorded for a rechargeable beaker cell of the TEMPO solution with a $LiPF_6$ electrolyte.[38] The redox reaction of TEMPO did not interfere with oxygen in the air because of its positive potential position, which is advantageous for battery applications. The TEMPO redox reaction occurs on conventional current collectors such as a glassy carbon plate, an indium tin oxide (ITO) plastic film and an aluminum foil with a tremendously high heterogeneous electron-transfer rate constant of $10^{-1}$ cm $s^{-1}$,[38] which is ascribed to the very rapid electron-exchange reaction (mentioned above) to yield an excellent high power rate performance. These superior redox behaviors of TEMPO and chemical bistability between TEMPO and its cation ensure quasi-solidification of TEMPO with the guarantee of counterion mobility, which can result in an excellent cathode-active material for practical rechargeable batteries. The authors have successfully extended TEMPO to its polymeric analogues.[39–42]

## 4.4 Radical Polymers and Their Syntheses

Polymers of TEMPO had been studied as metal-free or environmentally benign catalysts for the oxidative reactions of organic compounds, such as the oxidation of alcohols to aldehydes and carboxylic acids.[43,44] The cross-linked polymers function as heterogeneous catalysts for substrates in solution and are easily separated by filtration, just as an ion-exchanging resin does. However, they had not received any attention as an electrode-active material. The authors focused, for the first time, on polymers of the redox-active

radical molecules including TEMPO, called them ''radical polymers,'' and applied them an electrode-active material.[39–41,45]

Radical polymers as electrode-active materials require: (1) Solvophilic or well-solvation with the electrolyte to ensure counterion mobility in the polymer. (2) An appropriately swollen but insoluble in the electrolyte solution to impede self-discharging. Dissolution of the polymer or elution out of the redox-active fragment into the electrolyte solution works as a charge-carrier shuttle between the cathode and anode and causes a fatal phenomenon of self-discharging. The immobilization of radical polymers in the fabricated electrode is caused by the formation of very high-molecular-weight polymers and/or slight cross-linking of polymer chains. (3) Compact structure of the repeating or monomer unit of the radical site. The formed polymer backbone sacrifices the values of the redox capacity or energy density of the radical polymers. (4) The flexibility of the polymer backbone and the linker group between the backbone and the radical moiety often facilitates electron exchange or charge propagation in the radical polymer.

Several combinations of monomers bearing robust radical moieties, polymerization mechanisms and catalysts have been extensively investigated to yield the radical polymers. Here, the radical polymer syntheses bearing the TEMPO derivatives are mainly described.

Conventional radical polymerization of the vinyl monomers bearing the TEMPO moiety does not yield the corresponding polymers because the redox activity of the TEMPO moiety reacts with the initiating and propagating radical, and terminates the polymerization. Anionic polymerization of the vinyl monomers bearing TEMPO moiety is the most precise way to obtain the radical polymer, for example, with controlled and high molecular weight, although anionic polymerization requires well-dried glass vessels and careful experimental skill. TEMPO methacrylate[46] is the representative vinyl monomer; for example, it is anionically polymerized with methyl methacrylate-capped diphenylhexyl lithium as an initiator, wherein the nucleophilicity is moderate to suppress the side reaction between the nitroxide radical of the TEMPO moiety and the carbanion of diphenylhexyl lithium, to yield poly(TEMPO methacrylate) with well-controlled molecular weight, narrow polydispersity index, high yield, and an accurate 1.0 radical per monomer unit[47] (Scheme 4.2a). Anionic ring-opening polymerization of the epoxide bearing TEMPO was reported using potassium *t*-butoxide as the catalyst to yield poly(TEMPO-substituted glycidyl ether)[48] (Scheme 4.2b). The flexible and ionophilic polyether backbone enabled a polymer with high redox performance in the electrolyte solution.

Cationic polymerization of the TEMPO-bearing vinyl monomer with the electron-donating ether linkage or TEMPO-substituted vinyl ether yielded the corresponding TEMPO polymer using boron trifluoride etherate as the initiator[49,50] (Scheme 4.2c). The polymer has a high theoretical capacity (135 $Ah\,kg^{-1}$), provided flexibility and ionophilicity, and eliminated any bond cleavage such as hydrolysis.

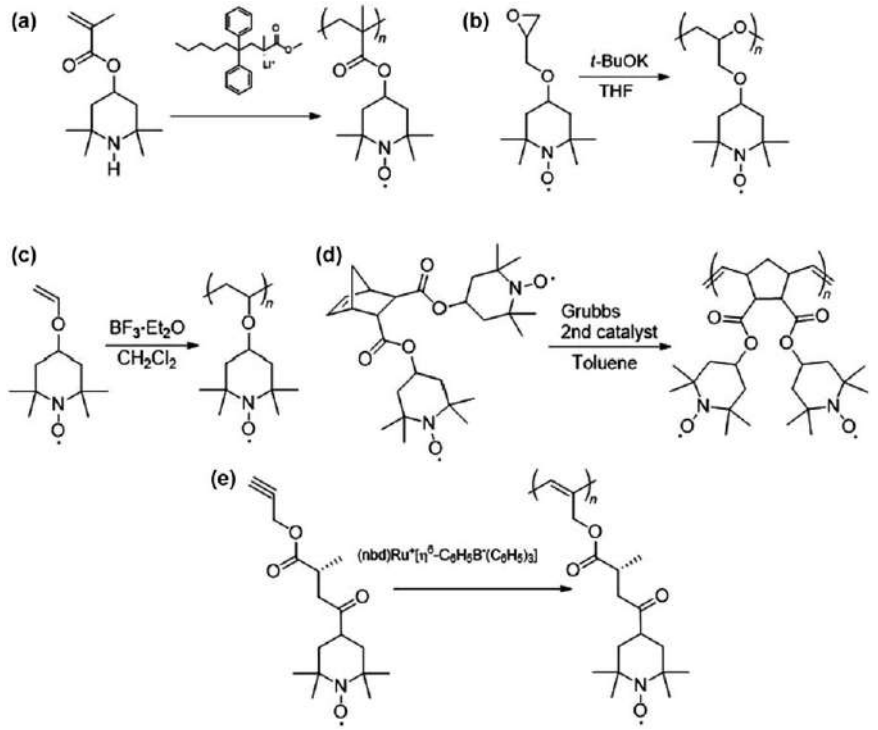


**Scheme 4.2** Polymerization of the monomers bearing TEMPO: (a) anionic polymerization of the methacrylate, (b) anionic polymerization of the epoxide, (c) cationic polymerization of the vinyl ether, (d) ring-open metathesis polymerization of the norbornene and (e) coordination polymerization of the acetylene. nbd: norbornadiene.

Ring-opening metathesis polymerization of TEMPO-substituted norbornene derivatives using the second-generation Grubbs catalyst was performed to yield the corresponding poly(TEMPO-substituted norbornene) without any side reactions[51] (Scheme 4.2d). The Grubbs catalysts have high tolerance to both redox-active species and bulky substituents. Copolymerization with a small quantity of bis(norbornene) derivatives gave a TEMPO polymer that is cross-linked and insoluble but still swelled with electrolytes (Scheme 4.3a). The polynorbornene backbone involves unsaturated olefin residues that act as the cross-linking sites with, for example, a bis(azide) cross-linker *via* a simple photoinitiated reaction after coating the polymer and the cross-linker upon a current collector[51] (Scheme 4.3b).

Acetylene monomers bearing TEMPO were polymerized *via* ruthenium norbornadiene-catalyzed coordination polymerization to give high-molecular-weight polymers. However, the higher structure of the polyacetylene formed in the electrolyte was unfavorable for efficient redox activity of the TEMPO residues[52,53] (Scheme 4.2e).

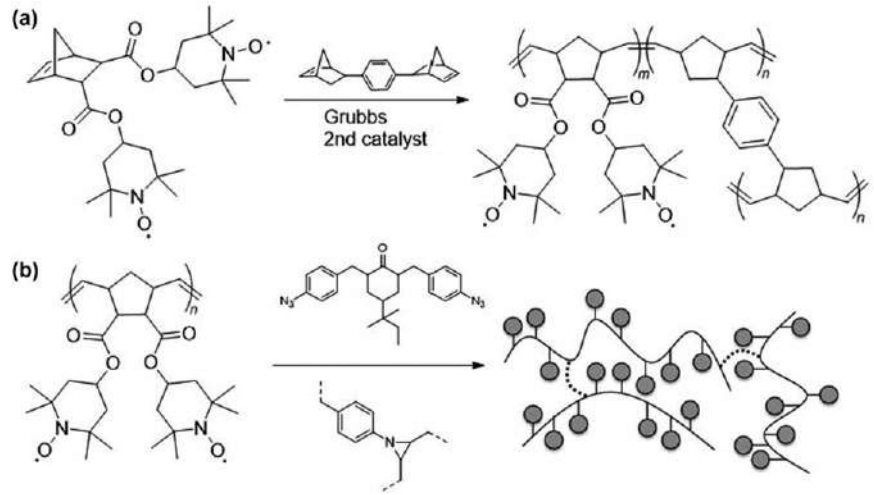


**Scheme 4.3** Examples of the cross-linking TEMPO polymers: (a) copolymerization with a small quantity of bifunctional monomer and (b) photo-cross-linking of poly(TEMPO-substituted norbornene) with a bisazido.

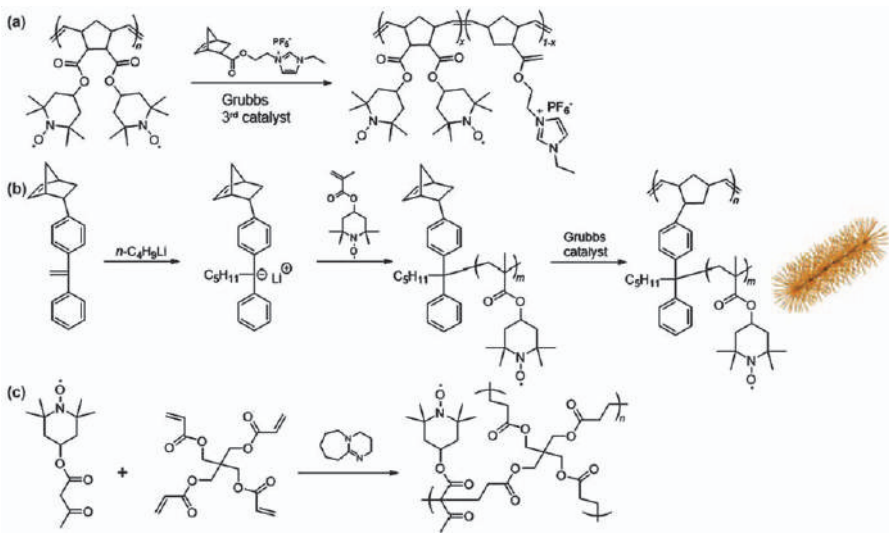


**Scheme 4.4** Examples of the TEMPO polymers: (a) block copolymer of imidazolium-containing norbornene, (b) bottle-brush-structured TEMPO polymer, and (c) networked TEMPO polymer *via* click polycondensation reaction.

TEMPO has also been incorporated into block, brush and network polymers (Scheme 4.4). Successive addition of the imidazolium-containing norbornene monomer in the ring-open metathesis polymerization of TEMPO-substituted norbornene yielded a TEMPO and imidazolium-containing block copolymer.[54] The radical and ion segment ratio in the

block copolymers was tuned with the monomer feed ratio to provide a new combination of the redox-active and ionic liquid moieties.

TEMPO bottle-brushes were prepared *via* a grafting-through approach. Anionic polymerization of TEMPO methacrylate using a norbornene-substituted diphenylhexyl lithium yielded a norbornene-functionalized macromonomer, and subsequent ring-opening metathesis polymerization of the macromer using a Grubbs third-generation catalyst prevented critical side reactions involving the TEMPO radical moiety.[55] A bottle-brush polymer was formed, which was characterized by the defined molecular dimension, persistent shape, peripherally extended TEMPO chains (as illustrated in Scheme 4.4b), and low solution viscosity compared to the corresponding linear polymer.

Polyaddition *via* the Michael reaction of the acetoacetate and acryloyl derivatives directly yielded a TEMPO polymer network.[56] The step-growth mechanism of the Michael polyaddition of multifunctional monomers formed a geometrically homogeneous network structure that led to an appropriate cross-linking density and high adhesion on any type of current collectors.

Polycondensation or oxidative polymerization of 3,4-ethylenedioxythiophene (EDOT) bearing TEMPO moiety yielded a TEMPO-substituted PEDOT.[57,58] Electrochemical oxidation of the monomer by tuning the applied potential yielded a polymer upon a current collector. The formed PEDOT polymer displayed an electronic conductivity of 0.06 $S\,cm^{-1}$ according to the π-conjugated polymer structure and the charge storage capability of the TEMPO redox moiety (Scheme 4.5).

Polymerization of the monomer bearing a TEMPO precursor or bearing a TEMPO modified with a protecting group, and subsequent oxidation of the precursor or removal of the protective group, are facile approaches to obtaining the TEMPO radical-containing polymers. For example, 2,2,6,6-tetramethylpiperidine methacrylate was polymerized with a radical initiator, and the precursor was treated with oxidizing reagents such as peroxybenzoic acid and hydrogen peroxide to yield poly(TEMPO methacrylate).[39] However, in the polymer reaction, the reaction yield ($x$ in Scheme 4.6) remained at *ca.* 90%.

Grafting of the TEMPO polymers from and onto conductive additives or current collectors are important syntheses for molecular-level composite

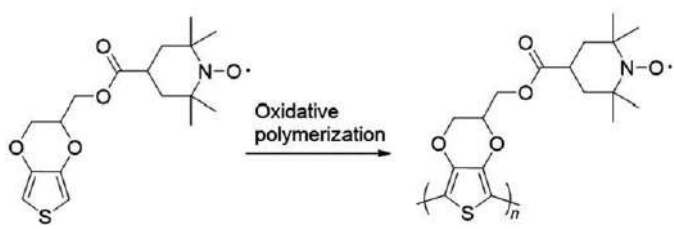


**Scheme 4.5** Oxidative polymerization of TEMPO-bearing thiophene *via* electrolysis.

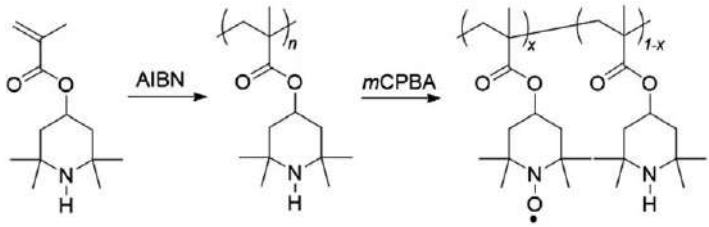


**Scheme 4.6** Synthesis of the TEMPO radical polymer by a polymer reaction: facile radical polymerization of the vinyl precursor monomer and the subsequent oxidation. AIBN: 2,2′-azobis(isobutyronitrile) and *m*CPBA: *m*-chloroperoxybenzoic acid.

fabrication of effective electrodes. A multiwalled carbon nanotube surface was functionalized with norbornene-methanol and then the TEMPO-substituted norbornene was grafted from with the Grubbs 2nd catalyst.[59] Block copolymers of TEMPO methacrylate and glycidyl methacrylate were grafted onto an ITO glass substrate through the reaction of the hydroxy group of the substrate surface with the epoxy group of the polymer to form a redox-active layer with thicknesses of up to 5 μm[60] (Scheme 4.7).

Being apart from the TEMPO structure, the synthesis of nitroxide polymers along with the molecular design to significantly enhance the redox capacity was challenged (Scheme 4.8). However, it failed because the compact molecular structures of nitroxide radicals relinquished their chemical stability.

The following are noted at the end of the TEMPO polymer section. TEMPO is produced from acetone as the starting material *via* its dehydration to form the dimer, the amination and ring formation in liquid ammonia, reduction with hydrazine to form tetramethylpiperidine and oxidation with peroxide. TEMPO is an inexpensive organic compound. Although TEMPO and its oxidized derivative, oxoammonium cation, are chemically stable in organic and aqueous solvents, the latter suffers degradation reactions in strong acidic and alkaline aqueous solutions to yield nitrone derivatives.[61,62] The oxoammonium cation of TEMPO operates as a strong oxidizing catalyst for organic compounds (as described at the beginning of this section; for example, the TEMPO cation is practically utilized for the oxidation of cellulose to produce cellulose nanofibers[63]) that is ascribed to its extremely positive redox potential. In other words, one should pay attention to the very strong oxidizing power of TEMPO cation, which may trigger oxidative decomposition of the organic components of a battery such as the separator film.

Vinyl and norbornene derivatives bearing thianthrene and galvinohydroxy were polymerized with a radical initiator or a Grubbs catalyst, and the resultant polymers were oxidized to the corresponding cation radical and oxyl radical, respectively, through a polymer reaction with the appropriate oxidizing reagents.[64–66]

Poly(hydroxybenzoquinone) was synthesized *via* facile addition condensation with formaldehyde and converted to its anion radical polymer (Scheme 4.9).[67]

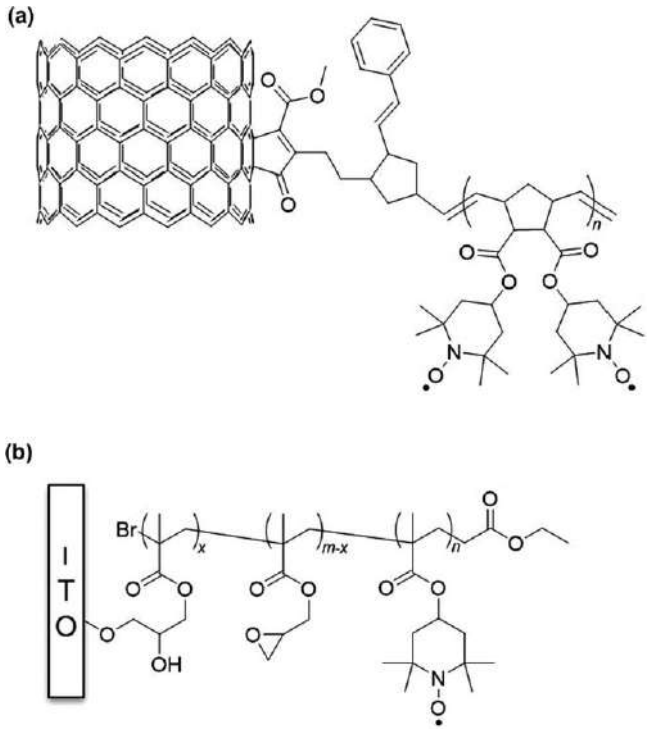


**Scheme 4.7** Examples of (a) grafting-from- and (b) grafting-onto-preparation of the TEMPO polymer from a carbon nanotube and onto an ITO substrate.

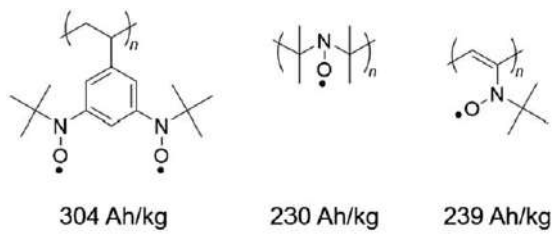


**Scheme 4.8** Nitroxide polymers with an ultra-high capacity.

Synthesis of polyviologens *via* a polycondensation reaction are often studied for their electrochromic applications. Condensation of the nitrogen of pyridine with an alkylhalide (Menshutkin reaction) forms a quaternized pyridium cation. This reaction was extended to 4,4′-bipyridine with α,ω-alkene dihalide to yield corresponding polyviologen and its cation radical[68] (Scheme 4.10a). The polycondensation of bipyridine with xylene dihalide yielded a polymer with high molecular weight and hydrophobic properties. The reductive coupling reaction of the 4-cyclopyridinium moiety of 1,3,5-mesitylene gave a cross-linking polyviologen[69] (Scheme 4.10b). Electrolytic

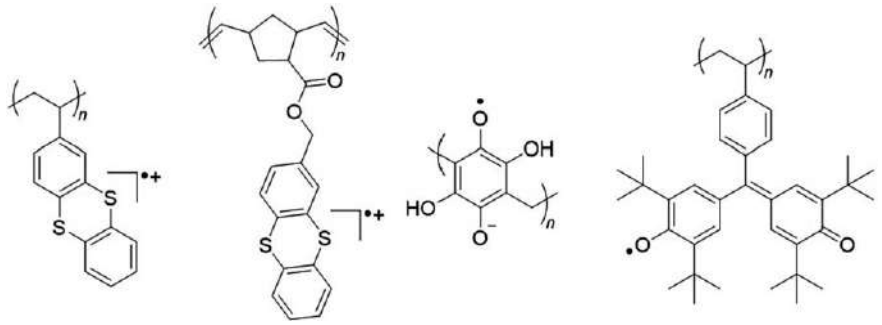

**Scheme 4.9** Examples of the radical polymers: (a) the polymer bearing thianthrene cation radical, (b) polynorbornene bearing thianthrene cation radical, (c) poly(2,5-dihydroxy-1,4-benzoquinone-3,6-methylene) anion radical, and (d) poly(galvinoxyl styrene).

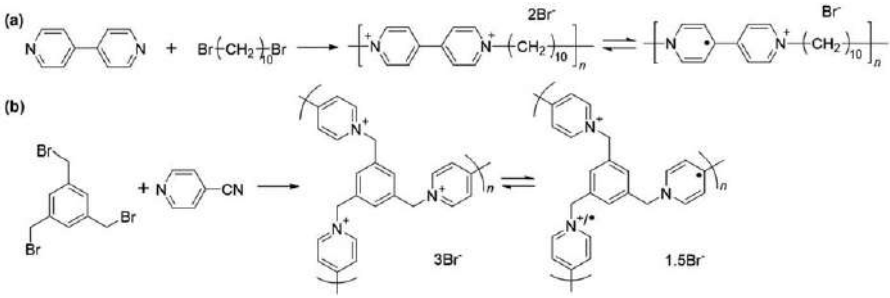

**Scheme 4.10** Synthesis of polyviologens: (a) condensation of 4,4′-bipyridine with α,ω-alkane dihalide, and (b) reductive coupling reaction of 4-cyclopyridinium moiety of 1,3,5-mesitylene.

reduction was applied to this reaction to immobilize the polyviologen onto a current collector. Polyviologens as a polycation were also deposited on a current collector as the electrode-active material through a layer-by-layer assembly or a polyion complex formation with an anionic polymer. However, in this procedure, the redox capacity and rate of the polyviologen layer were reduced.[16]

TEMPO radical molecules are widely used as spin labels and radical scavengers in biological systems.[10] Viologens are one of the classical dyes and are often used as an activator of redox enzymes.[16] Precursors of the radical polymers and oligomers, hindered polyamines and polyphenols, are produced in ton-level quantities as antioxidants and photostabilizers for plastics and commonly used materials.[70] They reductively remove oxygen and peroxide radicals with their convention to the corresponding robust radicals. That is, many organic radical polymers and their precursors have been examined and guaranteed as less-toxic materials.

## 4.5 Charge Transport and Storage in the Radical Polymers

The radical polymers have the following advantages as electrode-active materials (some are described in Section 4.6):

1. Surprisingly high power rate performance as an electrode-active material
2. High energy density ascribed to the redox ability at positive potentials (>3.5 V *vs.* $Li/Li^+$)
3. Appropriate capacity of 100–150 $Ah\,kg^{-1}$ according to the compact molecular structure per redox site
4. High cyclability attributed to the amorphous state without any large deformation and heat generation during the redox process
5. Good adhesion to current collectors and conducting additives resulting in low interface resistance

Lightweight, flexible, moldable, and simple wet fabrication are inherent advantages of organic polymers.

The TEMPO radical polymers are swollen or solvated with electrolytes, plasticized and coated upon current collectors. In the plasticized polymer layers, the radical sites are densely packed with very high concentrations (several M) that is significantly higher than the solubility limits of organic molecules in solutions. Electron spin resonance spectroscopy and electrochemical analyses have indicated that the radical sites of polymers maintained high electron-exchange activity and electron-transfer reactivity even in the plasticized or quasi-solid state.

Electrochemical studies, such as chronoamperometry after a pulse potential application on the TEMPO radical polymer layers with different thicknesses, yielded a (apparent) charge diffusion constant of $10^{-8}\,cm^2\,s^{-1}$.[71] This charge diffusivity is not high; however, the diffusion front of charge reaches 1 μm for 1 s, which is rapid enough for the charging process of a battery electrode. Fast electron transport or charge propagation at a finite distance of the radical polymer layer upon a current collector is illustrated in Figure 4.4. It begins with a very rapid heterogeneous electron-transfer reaction upon the current collector with the attached radical moiety of the polymer. The electron is rapidly transported to the neighboring redox site of the polymer, followed by the next neighboring and successive electron self-exchange reaction. Efficient electron exchange is caused by a high collision frequency in the reaction according to the ultra-high density of the radical redox site or a short distance of less than 10 Å between them. The rapid reaction obeys an electron-hopping model along the Marcus–Hush theory and segmental motion of the radical sites. The latter is dominated by the physical mobility of the radical sites that is related to the flexibility of the polymer backbone and the pendant spacer group.[72] The mobility of the counterions in the polymer domain often influences the rate of charge-exchange reactions. After the voltage application, the

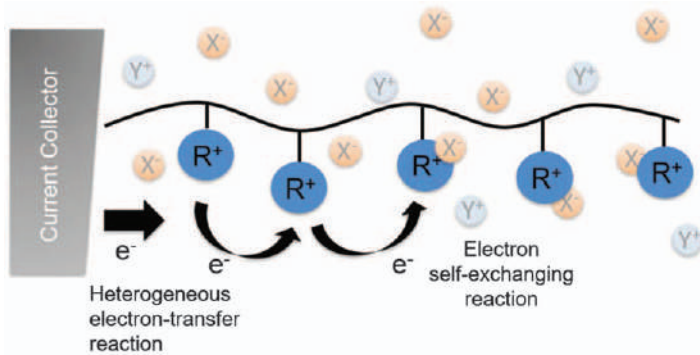


**Figure 4.4** Electron exchanging and transfer reactions in a radical polymer.

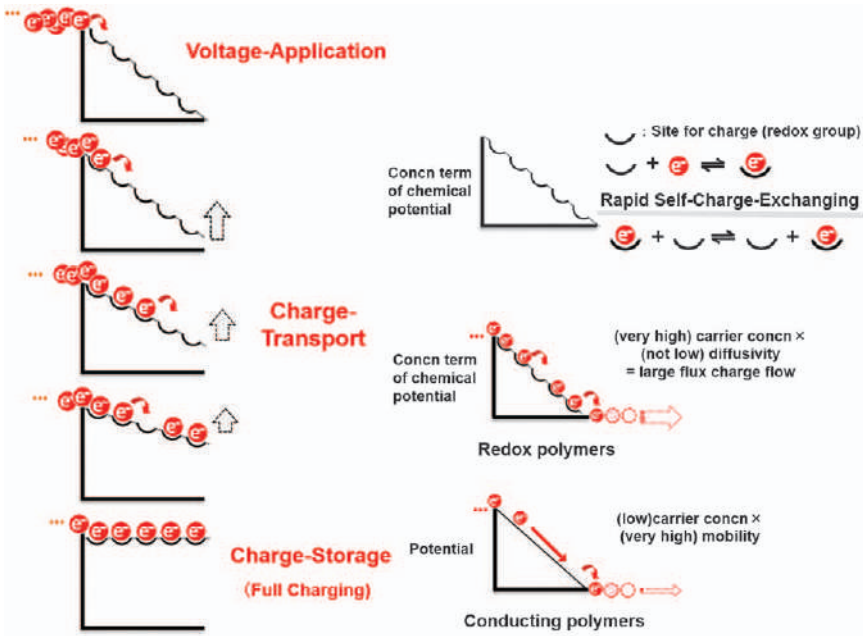


**Figure 4.5** Electron- or charge-transport and charge-storage with the driving force of concentration gradient in the radical polymer.

charge propagates through the polymer and is finally stored in the whole of the radical polymer.

The driving force for charge transport and storage is the concentration gradient of electrons or charges (Figure 4.5). The self-exchange reaction occurs very rapidly, as illustrated in the upper right scheme in Figure 4.5. There, the concentration term of the chemical potential of the radical redox site is represented as the vertical axis. Redox sites are accumulated on the polymer chain, and the gradient is steep. The self-electron- or (charge-

**Table 4.1** Charge-transport in the radical polymers *vs.* the conducting polymers.

| Polymer | Driving force | Exchange reaction rate constant | Diffusion coefficient carrier mobility | Current density (thickness 1 μm) | Carrier concn. |
|---|---|---|---|---|---|
| Radical polymers | Concentration gradient | $10^{6\sim8}$ M s$^{-1}$ | $10^{-7\sim-9}$ cm$^2$ s$^{-1}$ | 20 mA cm$^{-2}$ | $10^{21\sim22}$ cm$^{-3}$ |
| π-Conjugated polymers (organic semiconductor) | Potential gradient | — | $10^{-4\sim1}$ cm$^2$ V$^{-1}$S$^{-1}$ | (Application 1 V) $10^{-1\sim3}$ A cm$^{-2}$ | $10^{20}$ cm$^{-3}$ |

)exchange is still rapid despite their immobilization on the polymer. Upon voltage application, the injected electrons hop through the redox sites toward the area of lower charge concentration or the unoccupied sites, and finally the redox sites are fully charged with electrons or full-charge states, as illustrated on the left side of Figure 4.5.

Conducting π-conjugated organic polymers are actively studied and applied in electronic and photoelectronic devices.[73] Here their electronic function is expressed by mobile π-electrons. Although the flux of the electron or current density is small, the mobility of electrons is very fast (but the electron or carrier concentration is low) (bottom right of Figure 4.5). This is suitable, for example, in transistor applications. For the radical polymers, although diffusivity of the carrier is not as high as the high mobility in the conducting polymers, the carrier concentration is very high. Consequently, a large charge flow flux or a high current density is observed for the radical polymers. This is advantageous for applications in charge-storable battery electrodes.

Table 4.1 summarizes the features of radical polymers in charge transport and storage. In the radical polymer plasticized with a small quantity of electrolyte, the redox site is highly condensed in the quasi-solid state, but still it maintains its high reactivity comparable to that in solution. The driving force of charge propagation is the concentration gradient of charge, and almost all redox sites are fully charged up in the bulk polymer, as in the solution.

## 4.6 Performance of the Radical Polymers as Electrode-active Materials

The electrode preparation and charging and discharging performance of the radical polymers are described using Li/Li$^+$ as a counter electrode and a lithium salt/carbonate electrolyte solution (Figure 4.6a). Li is one of the smallest elements that yields a large specific capacity and electromotive force, which results in a high energy density and the highest output voltage as the anode-active material.[19]

The radical polymer itself does not possess sufficient electrical conductivity. Fast and quantitative charge-propagation and -storage or

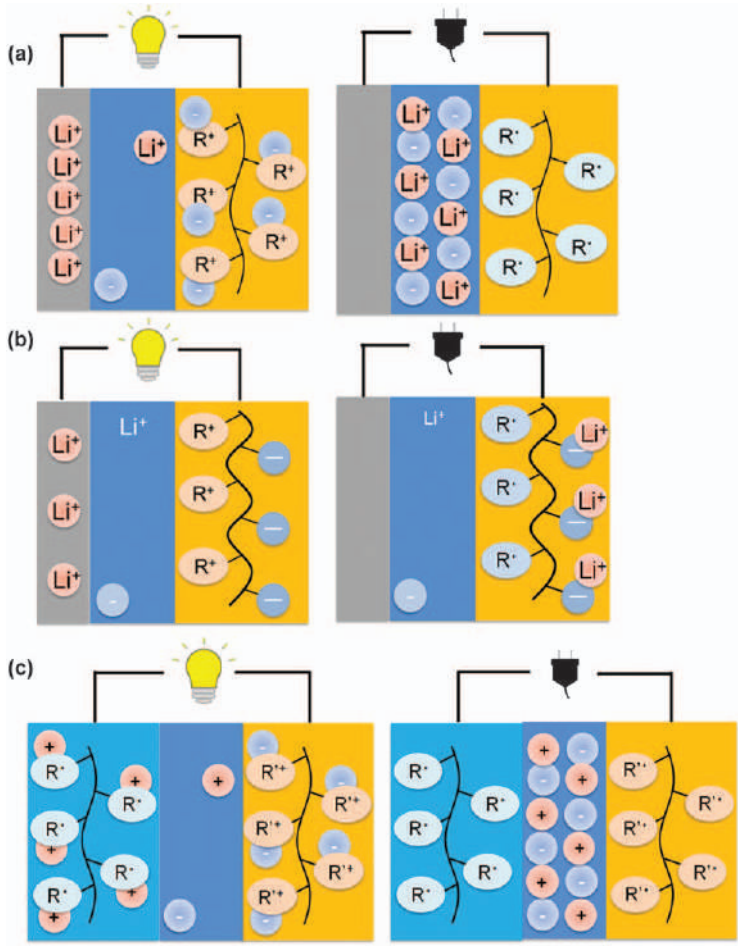


**Figure 4.6** Schematic images of rechargeable batteries fabricated with the radical polymers: (a) battery with a lithium metal or a lithium-ion-intercalated carbon anode, (b) battery with a cathode of the TEMPO copolymer to form a zwitterion and (c) an all-organic battery with the radical polymers for both the anode and cathode. R: radical unit.

electrochemically reversible redox behaviors (as described in Section 4.5) are observed for the genuine radical polymer layer thickness up to *ca.* 1 μm upon a current collector, so that the radical polymers are often mixed with 5–70 wt.% (*vs.* the radical polymer) carbon additives, such as carbon fibers, to create electrodes. Recently, the authors demonstrated that the single-walled carbon nanotubes with high aspect ratio and crystallinity form a well-percolated current collection network with only 1–5 wt.% addition.[74] The radical polymer swollen with the electrolyte fulfills the remaining major space to yield an outstanding power rate performance. Molecular-level compositing of carbon additive with radical polymer is crucial to form an

effective electrode by modifying the mixing process and, especially, the solvent in the mixing. Good adhesion or covering of the polymer with or around the carbon additive current collector reduces their interfacial resistance, resulting in the high charging–discharging rate performance of the radical polymer electrode.

The charging–discharging curves of the electrode composed of the poly(TEMPO methacrylate) radical polymer (containing 20 wt.% vapor-phase grown carbon fiber) electrode with a lithium metal counter in the $LiPF_6$ ethylene carbonate electrolyte display a plateau voltage at 3.6 V, which is consistent with the redox potential of poly(TEMPO methacrylate) *vs.* $Li/Li^+$ (or 0.7 V *vs.* $Ag/Ag^+$) determined by cyclic voltammetry.[39,42,75] The charging–discharging capacities are consistent with each other (coulomb efficiency *ca.*100%) at *ca.* 110 Ah $kg^{-1}$ (polymer). This almost coincides with the loaded quantity of the radical moiety of polymer upon the current collector (an aluminum plate), or with the theoretical capacity of the polymer (111 Ah $kg^{-1}$). The most important feature of the electrode is that it exhibits a surprisingly high current density or energy power performance, enabling tremendously fast charging within a few seconds (360 C), or supplying burst discharging power with a large discharging current without any substantial loss of output voltage (Figure 4.7), in contrast to those of conventional lithium-ion batteries. The cycle performance in charging and discharging of the electrode is extremely stable, and no

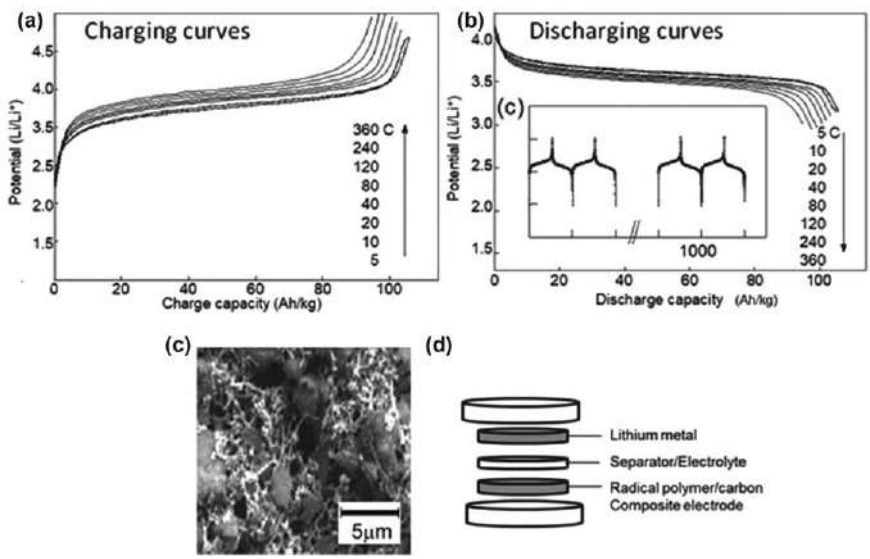


**Figure 4.7** (a) Charging and (b) discharging curves of the poly(TEMPO methacrylate)/carbon composite electrode. 1C is defined as the current density wherein the charging and discharging of the battery takes 1 hour. (c) Scanning electron microscopy (SEM) image of poly(TEMPO methacrylate)/carbon composite electrode (the materials and composition given in Figure 4.8). (d) Configuration of the coin-cell.

significant deterioration in the capacity was observed for more than 1000 cycles. Temperature elevation is not detected in the electrode in the rapid charging and discharging process. This surprisingly high current ability and long cyclability is attributed to the rapid and reversible one-electron transfer reaction of the radical, to no significant structural change of the plasticized radical polymer during the redox reaction and to the amorphous electrode structure.[40,45]

## 4.7 Radical Polymers in Lithium-ion Batteries

The prototype lithium-ion battery cell was developed by laminating the TEMPO radical polymer electrode with a separator film and graphite carbon as the anode, using ethylene carbonate-containing $LiPF_6$ as the electrolyte[42] (Figure 4.8). The lithium-ion battery (cell thickness of 100 μm) was fabricated with the TEMPO radical polymer composite cathode (70 μm thickness), the lithium-ion-intercalated graphite anode (10 μm thickness), the porous polyethylene separator holding the 1.5 M $LiPF_6$ electrolyte in ethylene carbonate/dimethyl carbonate and aluminum foils as the current collector. It displayed an energy density of 120 $Wh\,L^{-1}$ (battery) and a power density of 11 $kW\,L^{-1}$. The battery is characterized by a high output voltage of 3.7 V and very high power density according to the high cathode current density of $>100\ Ah\,kg^{-1}$. A smart card (0.3 mm thickness) installed with this battery was distributed as test samples among customers.[75] The card was bendable, and the 3 $cm^2$ battery provided a capacity of 3 mAh and a power density of 5 $kW\,L^{-1}$ that enabled radio-pulsed communication with the card more than $10^4$ times after full charging.

The reversible one-electron oxidation to produce the TEMPO cations in the polymer changes the salt concentration in charging–discharging owing to anion migration for charge neutralization. The change in salt concentration makes an excess quantity of electrolyte salt necessary for ionic conduction and might cause safety problems of lithium deposition.

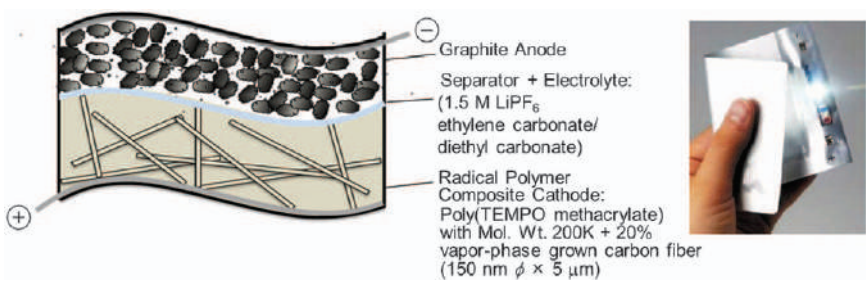


**Figure 4.8** The laminated battery cell fabricated with aluminum foils, TEMPO radical polymer composite electrode with a carbon fiber as the cathode, lithium-incorporated graphite carbon as the anode, and a porous polyolefin separator film holding the $LiPF_6$ carbonate electrolyte.

Lithium-ion migration along a rocking-chair type in the conventional lithium-ion batteries was taken in a TEMPO-based battery. Rocking-chair lithium-ion migration ensures a constant concentration of the electrolyte in the charging–discharging process that enables a significant reduction in the quantity of electrolyte, preventing precipitation and lake of the electrolyte salts (Figure 4.6b). The reduction of the electrolyte consequently improves the energy density in an overall lithium-ion battery cell. A zwitterionic design of the polymer accomplishes the rocking-chair-type charging–discharging characteristics, maintaining the redox feature of the TEMPO radical. Sulfonate, benzenesulfonate and trifluoromethanesulfonyl imide (TFSI) were incorporated into the radical polymers as counter anions of the oxidized TEMPO oxoammonium moiety.[77–79] A test cell fabricated with the poly(-TEMPO methacrylate-*co*-TFSI styrene; Scheme 4.11) cathode exhibited a high discharging voltage of 3.7 V and high charging–discharging rate at 30 C (or a full charging in 2 min) with a small quantity of electrolyte.

A highly flexible, paper-like lithium-ion battery with reasonably high energy density is an important challenge to be a suitable power source installed in bendable and wearable electronic devices and electric equipment. The intrinsic brittleness of the inorganic cathode material is a crucial difficulty, and the relationship between mechanical flexibility or toughness and the appropriate energy density of the battery are a trade-off. The TEMPO-substituted polyether (Figure 4.9a) functioned as a redox-active and highly adhesive binder of lithium cobalt oxide ($LiCoO_2$) particles as the cathode-active material and a small quantity of carbon nanotubes.[80] The synergistic effect of the radical polymer binder (5–20 wt.%) and the carbon nanotube networks enabled both mechanical toughness and high bendability of the composite (as illustrated in Figure 4.9b) and the high energy density of the electrode. The paper-like lithium-ion battery with a total thickness (including the total sealings) of 0.5 mm exhibited a constant output voltage of 3.8 V and the highest volumetric cathode capacity was beyond 300 mAh $cm^{-3}$ (because of the very low porosity of $<20\%$). The battery can operate under rapid bending (with a curvature radius of 1 mm) of over $10^4$ without any cracking and peeling of the electrode active material from the aluminum current collector foil.[79]

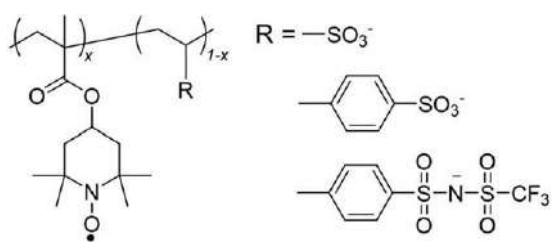


**Scheme 4.11** Poly(TEMPO methacrylate) copolymerized with the monomer to form zwitterions.

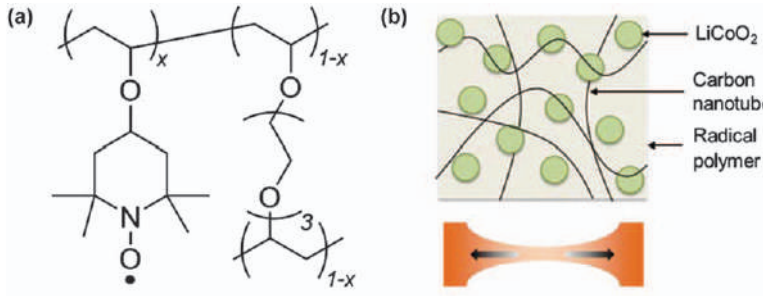


**Figure 4.9** A flexible and highly bendable lithium-ion battery composed of (a) TEMPO-substituted polyether and (b) a scheme with mechanical toughness in the cathode.

Composites of the conventional lithium-ion phosphate ($LiFePO_4$) and the TEMPO radical polymer were studied to accelerate rapidly the charging process while maintaining a high energy density. The radical polymer functions as a charge-transporting mediator according to its rapid charge diffusivity and heterogeneous rate constant, along the redox potential cascade from the $LiFePO_4$ particle *via* the TEMPO moiety to a current collector. Although charging with a low rate of 1 C occurred stepwise at 3.4 and 3.6 V ascribed to the oxidation of $LiFePO_4$ and TEMPO, respectively, fast charging with the current density of 60 C proceeded with a one-step flat potential without any overvoltage.[81]

A redox couple of thianthrene and its cation radical locates at a more positive potential (4.1 V *vs.* $Li/Li^+$) than that of TEMPO:[65] It was investigated to fabricate an organic lithium-ion battery with an output voltage of >4.0 V (Figure 4.3). Poly(thianthrene-substituted norbornene) and poly(2-vinylthianthrene) were synthesized (Scheme 4.9), and their test cells yielded a high voltage of 3.9–4.1 V and moderate discharge capacity of *ca.* 100 Ah $kg^{-1}$.[65,66] A 5 V-Class cathode-active polymer will be a challenging target.

Lithium-ion batteries were researched and developed by accompanying exploitation of the electrolytes with a wide electrochemical window and chemical stability, especially using organic solvents. Organic electrolyte solvents are flammable and harmful, although the polymer electrolytes partially reduce these negative issues. The history of batteries began with Volta and Daniel batteries that use nonflammable, inexpensive and plentiful aqueous electrolytes.[19] However, their output voltages are limited to a narrow potential window of 1.23 V provided by the aqueous electrolyte. Recently, an aqueous electrolyte containing large quantities of lithium salts (≥21 M) has extended the potential window up to 3.0 V because of the almost total disappearance of free water in the so-called water-in-salt electrolyte.[82–84] A 4.0 V aqueous lithium-ion battery with high efficiency has been recently demonstrated using a water-in-salt electrolyte and a lithium anode modified with a strongly hydrophobic fluorinated additive.[84] Recently, researchers including the authors reported the redox ability of organic radical polymers with a lithium-ion

metal anode in a lithium electrolyte in water-in-salt.[58] This suggests that a rechargeable battery from the water-in-salt system could be one of the best candidates for the next generation of lithium-ion batteries.

## 4.8 All-organic Rechargeable Devices Fabricated with Radical Polymers

A pair of radical polymers with different redox potentials was sandwiched with the thin separator film holding an appropriate electrolyte to provide an all-organic rechargeable device. The combination of the galvinoxyl radical polymer, poly(galvinoxylstyrene) (in Scheme 4.9d) (but slightly cross-linked with diacrylate comonomer) as an anode-active material, and the photo-cross-linked poly(TEMPO-substituted norbornene) (in Scheme 4.3b) as a cathode-active material was the first demonstration of all-organic devices by utilizing the acetonitrile solution of alkylammonium perchlorate as an electrolyte salt and of a small quantity of alkylammonium hydroxide (the last was added to keep the solution basic for the simultaneous redox on both electrodes).[64] The device exhibited a plateau potential of 0.66 V, which co-incided with the redox potential difference of each polymer, and operated at a very high rate performance of 360 C. The paper-like device was transparent and turned bluish after full charging owing to the formation of galvinoxy anions that served as an indicator of the charging degree of the device.

To achieve a higher energy density, especially a higher voltage, some couples of the redox polymers were examined. For example, a device consisting of poly[bis(dicyanomethylene) anthracenylmethacrylamide] as an anode and poly(vinylthianthrene) as a cathode exhibited an output voltage of 1.4 V using lithium perchlorate in ethylene carbonate and dimethyl carbonate as an electrolyte.[66]

Anode-active organic polymers were further investigated to achieve a higher output-voltage of >2.0 V as an all-organic rechargeable device. Dibenzothiophenesulfone has a redox ability at a very negative potential of −1.8 V (*vs.* Ag/AgCl) in an organic electrolyte that is ascribed to the electron-withdrawing sulfone group. An all-organic device was fabricated with poly(vinyldibenzothiophenesulfone) (Figure 4.10a), poly(TEMPO methacrylate), and tetraethylammonium percolate acetonitrile solution, as an anode-active material, a cathode-active material and an electrolyte, respectively.[85] This device yielded a maximum output voltage of 2.6 V, and the active component of the anode had a very high energy density of >500 Wh $kg^{-1}$ (Figure 4.10b). Further molecular design of organic redox polymers for a higher energy density may be anticipated from these examples.[86]

The nitroxylnitroxide radical is stabilized by the symmetrically conjugated structure of two nitroxide sites and reversibly turned to both its cation at 0.72 V *vs.* Ag/AgCl and anion at −0.6 V through one-electron oxidation and reduction, respectively. Nitroxylnitroxide was extended to its styrene- and norbornene-based polymers.[87,88] An all-organic rechargable device with a

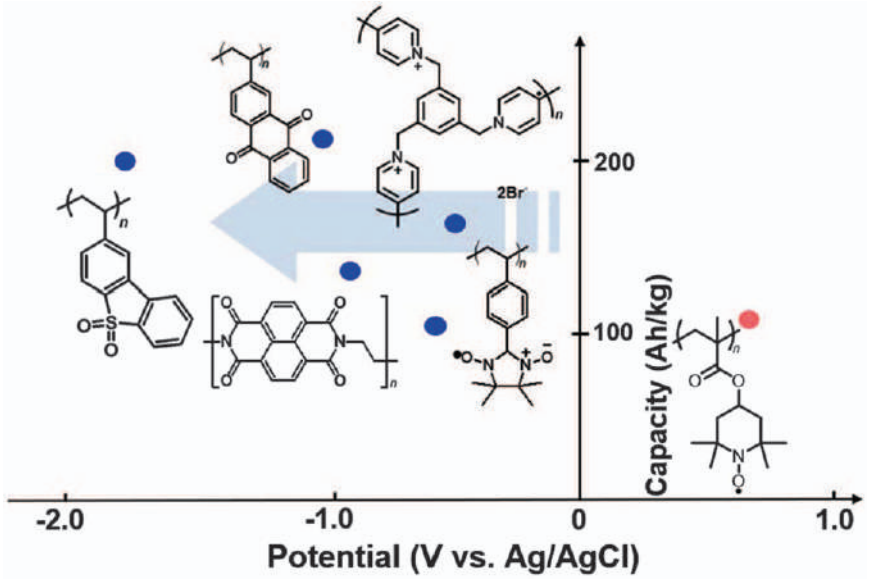


**Figure 4.10** Negative redox potential of poly(vinyldibenzothiophenesulfone) (a) as an anode-active material and (b) charging–discharging behavior of its all-organic rechargeable device with a poly(TEMPO methacrylate) cathode.

symmetric configuration consisting of the same nitroxylnitroxide polymer for both electrodes was fabricated. The charging and discharging curves gave a plateau of 1.3 V, consistent with the potential gap for concurrent reduction and oxidation of the same nitronylnitroxide at the anode and cathode, respectively (Figure 4.11), and the device exhibited high power ability and cyclability. In Figure 4.11, another plateau of −1.3 V indicated a dual function of the radical polymer as a cathode and an anode. That is, the reversed bias also enabled charging of this device, and the device direction was reversible, leading to a curious poleless battery.

An aqueous electrolyte is expected to maximize the rate performance of all-organic rechargeable devices with a high ionic conductivity on the order of $10^{2-3}$ S cm$^2$ mol$^{-1}$. A cross-linked polyviologen hydrogel, poly(tripyridiniomesitylene), as an anode-active material displayed an output voltage of 1.1 V and fast charging–discharging characteristics for 3 s (1200 C) with the combination of the hydrophilic TEMPO-substituted polymer cathode.[68,69]

Very recently, Evonik Creavis GmbH advertised a fully printable and flexible rechargeable device composed of TEMPO, viologen polymer derivatives, an ionic liquid as the nonvolatile and highly conductive electrolyte.[89]

The hydrophilic poly(TEMPO acrylamide) yielded a dense hydrogel with the addition of 5 wt.% single-walled carbon nanotubes. The nanotube formed a 3D current collection network with an electric conductivity of *ca.* 500 S cm$^{-1}$ that was fulfilled with the radical polymer swollen with the aqueous brine electrolyte. The radical polymer hydrogel was mechanically

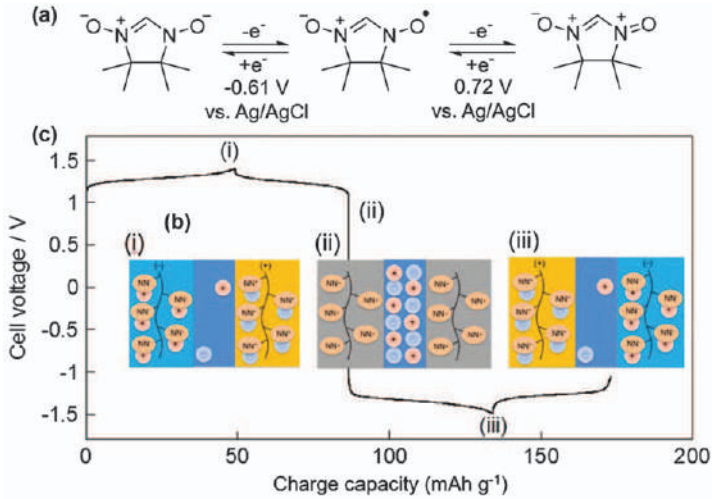


**Figure 4.11** (a) Bipolar redox reactions of nitronylnitroxyl polymers to form its cation and anion, (b) a symmetric pole-less battery fabricated with the same radical polymer, and (c) its charging and discharging behavior.

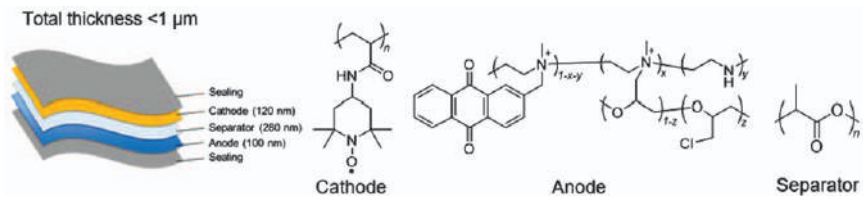


**Figure 4.12** Configuration of an organic polymer-based rechargeable nanosheet.

tough (strain resistance up to 18%) and the polymer worked as an elastic binder. The TEMPO hydrogel was applied as a cathode in conjunction with poly(anthraquinone-substituted ethyleneimine).[74] The device does reversible charging–discharging characteristics at 1.1 V, corresponding to the potential difference between the two polymers, with a capacity of 80 Ah $kg^{-1}$ at a rate of 10 C. The device does not require any metal-foil substrate as a current collector (because of the sufficient electric conduction with the carbon nanotube network), a metal foil-free, bendable device that significantly reduces the total cell volume and the fabrication process.

An ultrathin and stretchable organic redox polymer nanosheet recently demonstrated was rechargeable and conformable to the skin surface (Figure 4.12).[90] The rechargeable nanosheet was fabricated by sandwiching a biodegradable and porous poly(lactate) separator film holding an aqueous brine solution with the 5 wt.% carbon nanotube-containing layers of the poly(TEMPO acrylamide) cathode and the poly(anthraquinone-substituted polyethylamine) anode, and laminating styrene-butadiene rubber films as a

sealing, to give a nanosheet with a large area and a total thickness of less than 1 μm. The sheet was stretchable over 700% in length with a Young's modulus of 10 Pa, and was sufficiently sticky to be adhesive to and peal from human skin. The sheet device provided a moderately large current density of 0.4 $mA\,cm^{-2}$ that satisfies the requirements for radio-wave emission and light-flashing. Conventional batteries are too thick (>1 mm) for even so-called thin batteries and lack flexibility owing to the intrinsic brittleness of conventional electrodes. Harsh, flammable and toxic components limit their direct application to the skin and inside the body. For example, TEMPO-substituted lactide polymers were synthesized, and their biodegradability and electroactivity were successfully examined in *in vitro* and *ex vivo* experiments.[91] These organic and rechargeable devices may lead to new fields of power sources in the medical field.

## 4.9 Conclusions

This chapter has discussed the successive and geared redox reaction of radical sites present in high numbers in polymer that could facilitate efficient electron (charge) transport and storage and consequently produce new organic-based electrode materials with burst power supplying or instant full charging. A cyclohexanediamine derivative bearing the TEMPO group was gelated to form its supramolecular chain. The charge diffusion coefficient obtained *via* hopping through the pendant TEMPO moieties along the chain was nearly $10^{-6}$ $cm\,s^{-1}$, comparable to that of the homogeneous solution. A very large current density of 1 $mA\,cm^{-2}$ was observed for the specimen of the purely organic TEMPO supramolecular gel in a quasi-solid state with a thickness greater than 50 μm.[92] These results conclude that radical polymers and supramolecular species work as electrically conducting materials without any help from metal additives, and that the concept for conduction is totally different from that of metallic conduction or mobile π-electron conduction for organic semiconductors. The electric conduction and very efficient charge transport based on the long sequence of the rapid chemical reaction described in this chapter may stimulate the development of new electric and ionic functions in soft organic matter, including biological systems.

Organic electrodes are intrinsically bulkier or have a lower volumetric energy density than those of conventional batteries. However, they are plastic and can be molded to varied shapes such as those of the mechanical or flexible parts of devices and instruments, and bulkiness may not be a problem in such a case. They can be easily adapted to roll-to-roll and inkjet printing processes for use in various electr(on)ic equipment, such as battery-on-a-chip, battery-on-a-package, battery-in-intelligent card and portable instruments. Radical polymers are produced *via* general chemical manufacturing processes as an inexpensive material from a nonlimited resource, and after their service life they can undergo thermal runaway without any odor or ash formation. The radical polymer rechargeable batteries appear to

fulfill these demands for current IoT tags and portable instruments and meet environmental and safety standards.

## References


1. https://www.nobelprize.org/prizes/chemistry/2019/press-release/.
2. H. Shirakawa, A. McDiarmid and A. Heeger, *Chem. Commun.*, 2003, **1**, 1.
3. P. Novak, K. Muller, K. S. Santhanam and O. Haas, *Chem. Rev.*, 1997, **97**, 207.
4. W. A. Waters, *The Chemistry of Free Radicals*, Clarendon Press, Oxford, 1948.
5. C. Walling, *Free Radicals in Solution*, John Wiley & Sons, New York, 1957.
6. E. G. Rozantsev and V. O. Sholle, *Synthesis*, 1971, **1971**, 190.
7. J. Heidberg and J. A. Weil, *J. Am. Chem. Soc.*, 1964, **86**, 5173.
8. M. A. DaRooge and L. R. Mahoney, *J. Org. Chem.*, 1967, **32**, 1.
9. C. Trapp, C. S. Wang and R. Filler, *J. Chem. Phys.*, 1966, **45**, 3472.
10. C. Chatgilialoglu and A. Studer, *Encyclopedia of Radicals in Chemistry, Biology, and Materials*, John Wiley & Sons, New York, 2012.
11. P. M. Lahti, *Magnetic Properties of Organic Materials*, CRC Press, Boca Raton, 1999.
12. T. Makarova and F. Palacio, *Carbon Based Magnetism: An Overview of the Magnetism of Metal Free Carbon-based Compounds and Materials*, Elsevier, Amsterdam, 2006.
13. R. Hicks, *Stable Radicals: Fundamentals and Applied Aspects of Odd-electron Compounds*, John Wiley & Sons, New York, 2011.
14. K. Oyaizu and H. Nishide in *Chapter 71 of Encyclopedia of Radicals in Chemistry, Biology and Materials*, ed. C. Chatgilialoglu and A. Studer, John Wiley & Sons, New York, 2012.
15. Y. Yonekuta, K. Oyaizu and H. Nishide, *Chem. Lett.*, 2007, **36**, 866.
16. K. W. Shah, S. X. Wang, D. X. Y. Soo and J. Xu, *Polymers*, 2019, **11**, 1839.
17. B. Boduszek and H. J. Shine, *J. Org. Chem.*, 1988, **53**, 5142.
18. K. J. Stutts and G. W. Eastland, *J. Electroanal. Chem.*, 1987, **235**, 357.
19. T. B. Reddy, *Linden's Handbook of Batteries*, Mcgraw-hill, New York, 2011.
20. M. S. Whittingham, *Chem. Rev.*, 2004, **104**, 4271.
21. R. A. Meyers, *Encyclopedia of Sustainability Science and Technology*, Springer, New York, 2012.
22. J. M. Tarascon and M. Armand, *Nature*, 2001, **414**, 359.
23. M. Armand and J. M. Tarascon, *Nature*, 2008, **451**, 652.
24. H. Chen, M. Armand, M. Courty, M. Jiang, C. P. Grey, F. Dolhem, J. M. Tarascon and P. Poizot, *J. Am. Chem. Soc.*, 2009, **131**, 8984.
25. Z. Luo, L. Liu, J. Ning, K. Lei, Y. Lu, F. Li and J. Chen, *Angew. Chem., Int. Ed.*, 2018, **57**, 9443.
26. M. Armand, S. Grugeon, H. Vezin, S. Laruelle, P. Ribiere, P. Poizot and J. M. Tarascon, *Nat. Mater.*, 2009, **8**, 120.
27. X. Han, G. Qing, J. Sun and T. Sun, *Angew. Chem., Int. Ed.*, 2012, **51**, 5147.

28. S. Renault, V. A. Oltean, C. M. Araujo, A. Grigoriev, K. Edström and D. Brandell, *Chem. Mater.*, 2016, **28**, 1920.
29. P. Poizot, F. Dolhem and J. Gaubicher, *Curr. Opin. Electrochem.*, 2018, **9**, 70.
30. H. Chen, M. Armand, G. Demailly, F. Dolhem, P. Poizot and J. M. Tarascon, *ChemSusChem*, 2008, **1**, 348.
31. A. Jouhara, N. Dupre, A. C. Gaillot, D. Guyomard, F. Dolhem and P. Poizot, *Nat. Commun.*, 2018, **9**, 4401.
32. Y. Morita, S. Nishida, T. Murata, M. Moriguchi, A. Ueda, M. Satoh, K. Arifuku, K. Sato and T. Takui, *Nat. Mater.*, 2011, **10**, 947.
33. Y. Morita, T. Murata, A. Ueda, C. Yamada, Y. Kanzaki, D. Shiomi, K. Sato and T. Takui, *Bull. Chem. Soc. Jpn.*, 2018, **91**, 922.
34. N. Oyama, T. Tatsuma, T. Sato and T. Sotomura, *Nature*, 1995, **373**, 598.
35. W. J. Chung, J. J. Griebel, E. T. Kim, H. Yoon, A. G. Simmonds, H. J. Ji, P. T. Dirlam, R. S. Glass, J. J. Wie, N. A. Nguyen, B. W. Guralnick, J. Park, A. Somogyi, P. Theato, M. E. Mackay, Y. E. Sung, K. Char and J. Pyun, *Nat. Chem.*, 2013, **5**, 518.
36. N. Casado, G. Hernández, H. Sardon and D. Mecerreyes, *Prog. Polym. Sci.*, 2016, **52**, 107.
37. S. J. Visco, C. C. Mailhe, L. C. De Jonghe and M. B. Armand, *J. Electrochem. Soc.*, 1989, **136**, 661.
38. T. Suga, Y.-J. Pu, K. Oyaizu and H. Nishide, *Bull. Chem. Soc. Jpn.*, 2004, **77**, 2203.
39. H. Nishide, S. Iwasa, Y.-J. Pu, T. Suga, K. Nakahara and M. Satoh, *Electrochim. Acta*, 2004, **50**, 827.
40. H. Nishide and T. Suga, *Electrochem. Soc. Interface*, 2005, **14**, 32.
41. H. Nishide and K. Oyaizu, *Science*, 2008, **319**, 737.
42. K. Nakahara, K. Oyaizu and H. Nishide, *Chem. Lett.*, 2011, **40**, 222.
43. T. Miyazawa, T. Endo, S. Shiihashi and M. Okawara, *J. Org. Chem.*, 1985, **50**, 1332.
44. T. Endo, K. Takuma, T. Takata and C. Hirose, *Macromol.*, 1993, **26**, 3227.
45. K. Oyaizu and H. Nishide, *Adv. Mater.*, 2009, **21**, 2339.
46. https://www.tcichemicals.com/eshop/en/jp/commodity/M1531/.
47. T. Sukegawa, H. Omata, I. Masuko, K. Oyaizu and H. Nishide, *ACS Macro Lett.*, 2014, **3**, 240.
48. T. Suga, K. Yoshimura and H. Nishide, *Macromol. Symp.*, 2006, **245–246**, 416.
49. M. Suguro, S. Iwasa, Y. Kusachi, Y. Morioka and K. Nakahara, *Macromol. Rapid Commun.*, 2007, **28**, 1929.
50. K. Koshika, N. Sano, K. Oyaizu and H. Nishide, *Chem. Commun.*, 2009, 836.
51. T. Suga, H. Konishi and H. Nishide, *Chem. Commun.*, 2007, 1730.
52. J. Qu, T. Fujii, T. Katsumata, Y. Suzuki, M. Shiotsuki, F. Sanda, M. Satoh, J. Wada and T. Masuda, *J. Polym. Sci., Part A*, 2007, **45**, 5431.
53. J. Q. Qu, T. Katsumata, M. Satoh, J. Wada and T. Masuda, *Macromol.*, 2007, **40**, 3136.
54. T. Suga, M. Sakata, K. Aoki and H. Nishide, *ACS Macro Lett.*, 2014, **3**, 703.

55. T. Sukegawa, I. Masuko, K. Oyaizu and H. Nishide, *Macromol.*, 2014, **47**, 8611.
56. T. Ibe, R. B. Frings, A. Lachowicz, S. Kyo and H. Nishide, *Chem. Commun.*, 2010, **46**, 3475.
57. N. Casado, G. Hernandez, A. Veloso, S. Devaraj, D. Mecerreyes and M. Armand, *ACS Macro Lett.*, 2016, **5**, 59.
58. K. Oka, C. Strietzel, R. Emanuelsson, H. Nishide, K. Oyaizu, M. Strømme and M. Sjödin, *Electrochem. Commun.*, 2019, **105**, 106489.
59. W. Choi, S. Endo, K. Oyaizu, H. Nishide and K. E. Geckeler, *J. Mater. Chem. A*, 2013, **1**, 2999.
60. K. Takahashi, K. Korolev, K. Tsuji, K. Oyaizu, H. Nishide, E. Bryuzgin, A. Navrotskiy and I. Novakov, *Polymer*, 2015, **68**, 310.
61. V. A. Golubev and V. D. Sen', *Russ. Chem. Bull.*, 2009, **58**, 1824.
62. V. A. Golubev and V. D. Sen', *Russ. J. Org. Chem.*, 2011, **47**, 869.
63. A. Isogai, T. Saito and H. Fukuzumi, *Nanoscale*, 2011, **3**, 71.
64. T. Suga, H. Ohshiro, S. Sugita, K. Oyaizu and H. Nishide, *Adv. Mater.*, 2009, **21**, 1627.
65. M. E. Speer, M. Kolek, J. J. Jassoy, J. Heine, M. Winter, P. M. Bieker and B. Esser, *Chem. Commun.*, 2015, **51**, 15261.
66. A. Wild, M. Strumpf, B. Häupler, M. D. Hager and U. S. Schubert, *Adv. Energy Mater.*, 2017, **7**, 1601415.
67. K. Oka, S. Furukawa, S. Murao, T. Oka, H. Nishide and K. Oyaizu, *Chem. Commun.*, 2020, **56**, 4055.
68. K. Koshika, N. Chikushi, N. Sano, K. Oyaizu and H. Nishide, *Green Chem.*, 2010, **12**, 1573.
69. N. Sano, W. Tomita, S. Hara, C. M. Min, J. S. Lee, K. Oyaizu and H. Nishide, *ACS Appl. Mater. Interfaces*, 2013, **5**, 1355.
70. L. Packer, *Handbook of Antioxidants*, CRC Press, Boca Raton, 2001.
71. K. Oyaizu, Y. Ando, H. Konishi and H. Nishide, *J. Am. Chem. Soc.*, 2008, **130**, 14459.
72. K. Sato, R. Ichinoi, R. Mizukami, T. Serikawa, Y. Sasaki, J. Lutkenhaus, H. Nishide and K. Oyaizu, *J. Am. Chem. Soc.*, 2018, **140**, 1049.
73. T. A. Skotheim and J. Reynolds, *Conjugated Polymers: Theory, Synthesis, Properties, and Characterization*, CRC Press, Boca Raton, 2006.
74. K. Hatakeyama-Sato, H. Wakamatsu, R. Katagiri, K. Oyaizu and H. Nishide, *Adv. Mater.*, 2018, **30**, e1800900.
75. K. Nakahara, S. Iwasa, M. Satoh, Y. Morioka, J. Iriyama, M. Suguro and E. Hasegawa, *Chem. Phys. Lett.*, 2002, **359**, 351.
76. http://www.nec.co.jp/press/en/0512/0701.html.
77. I. S. Chae, M. Koyano, K. Oyaizu and H. Nishide, *J. Mater. Chem. A*, 2013, **1**, 1326.
78. I. S. Chae, M. Koyano, T. Sukegawa, K. Oyaizu and H. Nishide, *J. Mater. Chem. A*, 2013, **1**, 9608.
79. H. Tokue, T. Murata, H. Agatsuma, H. Nishide and K. Oyaizu, *Macromol.*, 2017, **50**, 1950.

80. K. Hatakeyama-Sato, R. Mizukami, T. Serikawa, K. Oyaizu and H. Nishide, *Energy Tech*, 2019, 1901159.
81. A. Vlad, N. Singh, J. Rolland, S. Melinte, P. M. Ajayan and J. F. Gohy, *Sci. Rep.*, 2014, **4**, 4315.
82. L. M. Suo, O. Borodin, T. Gao, M. Olguin, J. Ho, X. L. Fan, C. Luo, C. S. Wang and K. Xu, *Science*, 2015, **350**, 938.
83. L. Suo, O. Borodin, W. Sun, X. Fan, C. Yang, F. Wang, T. Gao, Z. Ma, M. Schroeder, A. von Cresce, S. M. Russell, M. Armand, A. Angell, K. Xu and C. Wang, *Angew. Chem., Int. Ed.*, 2016, **55**, 7136.
84. C. Yang, J. Chen, T. Qing, X. Fan, W. Sun, A. von Cresce, M. S. Ding, O. Borodin, J. Vatamanu, M. A. Schroeder, N. Eidson, C. Wang and K. Xu, *Joule*, 2017, **1**, 122.
85. K. Oka, R. Kato, K. Oyaizu and H. Nishide, *Adv. Funct. Mater.*, 2018, **28**, 1805858.
86. R. Kato, K. Oka, K. Yoshimasa, M. Nakajima, H. Nishide and K. Oyaizu, *Macromol. Rapid Commun.*, 2019, e1900139.
87. T. Suga, S. Sugita, H. Ohshiro, K. Oyaizu and H. Nishide, *Adv. Mater.*, 2011, **23**, 751.
88. T. Sukegawa, A. Kai, K. Oyaizu and H. Nishide, *Macromol.*, 2013, **46**, 1361.
89. https://www.taettooz.com/product/taettooz/en/technology/.
90. K. Hatakeyama-Sato, H. Wakamatsu, K. Yamagishi, T. Fujie, S. Takeoka, K. Oyaizu and H. Nishide, *Small*, 2019, **15**, e1805296.
91. X. Zhuang, H. Zhang, N. Chikushi, C. Zhao, K. Oyaizu, X. Chen and H. Nishide, *Macromol. Biosci.*, 2010, **10**, 1203.
92. Y. Sasada, R. Ichinoi, K. Oyaizu and H. Nishide, *Chem. Mater.*, 2017, **29**, 5942.

CHAPTER 5

# *Phenothiazine-based Redox Polymers for Energy Storage*

FABIAN OTTENY,[a] GAUTHIER DESMAIZIERES[a] AND BIRGIT ESSER*[a,b,c]

[a] Institute for Organic Chemistry, University of Freiburg, Albertstr. 21, 79104 Freiburg, Germany; [b] Freiburg Materials Research Center, University of Freiburg, Stefan-Meier-Str. 21, 79104 Freiburg, Germany; [c] Cluster of Excellence livMatS @ FIT—Freiburg Center for Interactive Materials and Bioinspired Technologies, University of Freiburg, Georges-Köhler-Allee 105, 79110 Freiburg, Germany
*Email: besser@oc.uni-freiburg.de

## 5.1 Introduction

Phenothiazine has gained increasing attention since its first synthesis reported by Bernthsen in 1883.[1] Its derivatives for dye chemistry[2–4] and its biological activity[5,6] have fascinated scientists and inspired them to gain a deeper knowledge of its physical and chemical properties.[7,8] Interestingly, most of the properties of phenothiazine derivatives are based on its redox properties.[9–11] The first systematic electrochemical investigations into phenothiazine were performed by Billon (Figure 5.1).[12,13] The voltammetric curves showed two distinct redox processes. Oxidation of phenothiazine (PT) at $E_1 = 270$ mV *vs.* $Ag/Ag^+$ led to the stable radical cation $PT^{\bullet +}$, illustrated by the subsequent flat plateau. The second oxidation to the dication $PT^{2+}$ occurred at potentials above 700 mV *vs.* $Ag/Ag^+$. However, the asymptotic behaviour and the thereafter less defined plateau indicate a reduced stability of this second process.

Polymer Chemistry Series No. 34
Redox Polymers for Energy and Nanomedicine
Edited by Nerea Casado and David Mecerreyes

Published by the Royal Society of Chemistry, www.rsc.org

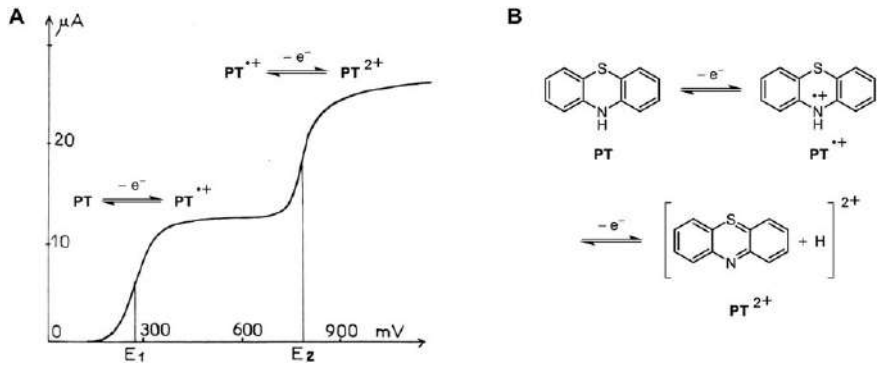


**Figure 5.1** (A) Oxidation curve of phenothiazine (2 mM in acetonitrile with 0.1 M $LiClO_4$, 0.4% water and 0.1 M $HClO_4$; working electrode: Pt; reference electrode: $Ag/Ag^+$) with (B) assigned redox states.
Reproduced from ref. 13 with permission from the Societé Chimique de France.

Since then, phenothiazine derivatives have been used in many biological and optoelectronic applications, including energy storage. Small-molecule derivatives have been used as redox shuttles for overcharge protection in lithium-ion batteries[14–16] or as catholytes in redox-flow batteries.[17,18] Phenothiazine-containing polymers have been known for more than 50 years. They were first investigated in the form of nonconjugated structures using the phenothiazine moiety as electron donor.[19] In 1983, Morishima *et al.* published a fundamental study focusing on the electrochemical behaviour of one of these polymers.[20] In this study they compared electroactive poly(vinyl-*N*-methylphenothiazine) (PVMPT) with a monomeric model compound and with copolymers containing *N*-methylphenothiazine (MPT) units. Interestingly, they could show that the phenothiazine moieties in PVMPT were not the noninteracting redox centres they expected from theory.[21] In contrast, interactions between the MPT units led to enhanced electronic conductivity up to the order of $10^{-5}$ S cm$^{-1}$, which is in the range of semiconductors, despite the aliphatic nature of the polymer backbone.[22] It can therefore be expected that the observed interactions between phenothiazine units have an enormous impact on the electrochemical properties of this and other phenothiazine-based polymers and play a crucial role in the application of such redox polymers in energy storage, as will be shown later.

Despite this early investigation, the first successful application of a phenothiazine-based redox polymer as battery electrode material was reported in 2015.[23] This is partly due to the fact that the research area of redox polymers as battery electrode materials only successfully took off between 2005 and 2010. However, using polymers as battery electrode materials had been attempted before – after the discovery of conducting polymers. With the rise of the polymer sciences, the electrochemical activity and electronic conductivity of organic compounds, especially those of conjugated polymers,

gained increasing interest. Based on the seminal work of Shirakawa, MacDiarmid and Heeger,[24] for which they were awarded the Nobel Prize in 2000, presented the first approach for an organic battery using doped poylacetylene.[25] Although later developed conducting polymers based on heteroaromatics were used in commercially available batteries, a real breakthrough was not achieved due to their intrinsic sloping redox potentials and, as a result, their low cycling performance.[26–28]

In 1991, the first commercially available lithium-ion battery was launched by Sony – based on the studies of Whittingham, Goodenough and Yoshino, who received the Nobel Prize for Chemistry in 2019.[29,30] In the same year, Nishio *et al.* resumed research on conductive polymers and examined several polymers for their suitability as cathode materials for secondary lithium-ion batteries.[31] One of these was poly(phenothiazine), synthesized by oxidative polymerization. Unfortunately, poly(phenothiazine) showed almost no activity under the applied conditions, and the authors explained this result with a low achievable doping level of the polymer. It would take more than 10 years until the first battery – with stable and discrete redox potential – using an organic cathode material was reported.[32] After this pioneering work by Nakahara in 2002, groups all over the world started to work in this field, encouraged by the need for more sustainable energy storage technologies.[32–38] In recent years, phenothiazine as a redox-active compound with high radical cation stability has gained increasing interest in this regard. Due to its high solubility in organic-based electrolytes, immobilization by embedding phenothiazine into a polymeric structure is the most prominent approach to achieving good cycling performance in solid-state batteries. All reported examples of phenothiazine-based polymers used for energy storage as well as their specific properties are discussed in the following.

## 5.2 Overview of Phenothiazine-based Redox Polymers Used as Battery Electrode Materials

Phenothiazine-based polymers for energy storage can be broken down into two structural types: (A) Polymers that contain phenothiazine moieties as side groups attached to a polymeric backbone and (B) polymers, where phenothiazine units are embedded into the main chain.[39] Both types are illustrated in Figure 5.2, including the respective examples reported in the literature.

Up to 2019, eight studies on phenothiazine-containing redox polymers for application as organic electrode materials in batteries were published. These polymers reach redox potentials from 3.5 to 3.7 V *vs.* $Li/Li^+$, reflecting the first and reversible oxidation of the phenothiazine group to a radical cation.[23,40–46] To give the best possible overview, the results obtained from these studies are summarized and presented together with information on the experimental battery cell setup in Table 5.1. The ordering of the polymers in Table 5.1 corresponds to that in Figure 5.2. PVBPT and PVPPP were the

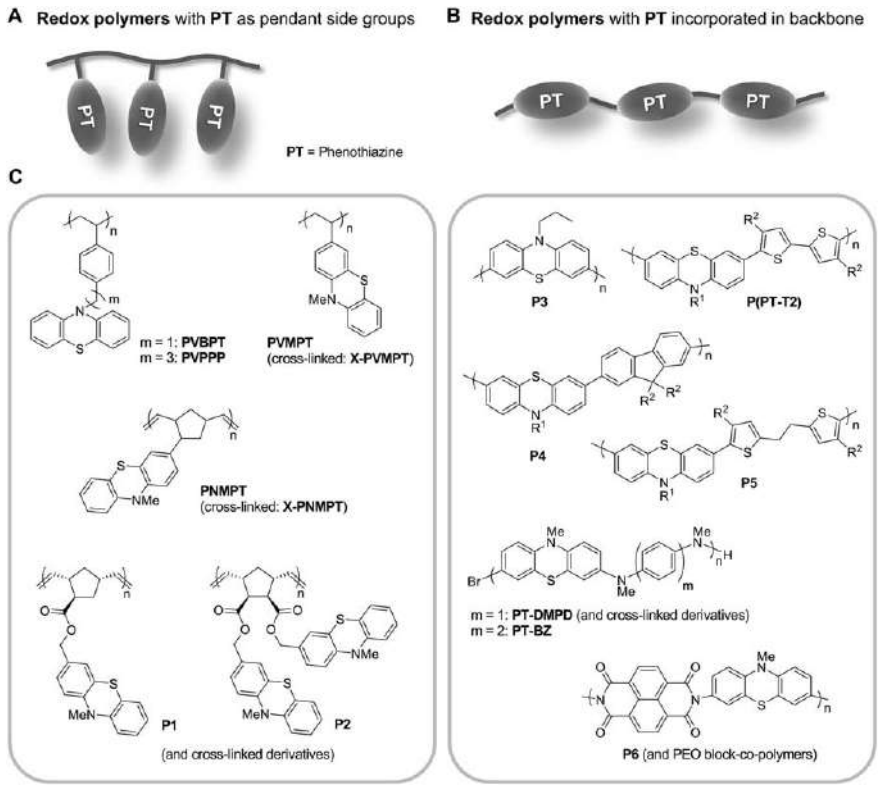


**Figure 5.2** Schematic of possible redox polymer structures with (A) phenothiazine as a pendant side group or (B) incorporated into the polymer backbone. (C) Phenothiazine-based redox polymers used for energy storage and their association to both types of polymers [$R^1 = 4$-((2-ethylhexyl)oxy)-benzene, $R^2 = C_6H_{13}$].[23,40–46]

first aliphatic polymers of type (A) to be tested as cathode-active battery materials by Suga, Nishide, Gutman and co-workers in 2015.[23] Structurally these are poly(styrene)s with phenothiazine groups attached *via* an alkyl spacer to the phenyl groups. Noteworthy is the high cycling stability and rate capability, in particular of PVPPP with the longer alkyl connector. The performance of these polymers will be discussed later in the context of stabilizing interactions and charge mobility. PVMPT, initially reported by Morishima (see above), and its cross-linked derivative X-PVMPT were used as cathode-active materials by Esser, Bieker and co-workers, published in 2017 and 2018.[41,42] The cycling stabilities of both polymers were excellent. While PVMPT showed outstanding rate performance and provided half of its theoretical specific capacity, for X-PVMPT the full theoretical specific capacity could be accessed at a reduced but still respectable rate performance. The reasons for these different performances were investigated in detail and are discussed below in the context of stabilizing interactions and charge

**Table 5.1** Phenothiazine-containing redox polymers with respective data from test cell measurements. For each polymer the acronyms from Figure 5.2 were used. Polymers without acronyms were labelled P1–P6, and for clarification the abbreviation used in the reference is given in brackets (VGCF = vapour-grown carbon fibres, PVdF = polyvinylidene difluoride, CL = cross-linker).

| Polymer | Theor. spec. capacity ($mAh\,g^{-1}$) | Discharge capacity ($mAh\,g^{-1}$) | Cycling stability (% retention) | Rate capability | Electrode composition (wt%) | Electrolyte/counter electrode/type of cell | Ref. |
|---|---|---|---|---|---|---|---|
| PVBPT | 85 | 61 (at 10C) | 73% at 10C (500 cycles)[a] | — | Polymer/VGCF/PVdF 10/80/10 | EC/DEC (1 : 1) + 1 M $LiPF_6$/Coin cell | 23 |
| PVPPP | 78 | 72 (at 10C) | 88% at 10C (500 cycles)[a] | 56 $mAhg^{-1}$ at 50C (75% retention)$_a$ | Polymer/VGCF/PVdF 10/80/10 | EC/DEC (1 : 1) + 1 M $LiPF_6$/Coin cell | 23 |
| PVMPT | 112 | 50 (at 1C) | 94% at 10C (10 000 cycles)[a] | 26 $mAh\,g^{-1}$ at 100 C (46% retention)$_a$ | Polymer/Super C65/PVdF 50/47/3 | EC/DMC (1 : 1) + 1 M $LiPF_6$/Li/ Swagelok T-cell | 41 |
| X-PVMPT | 112 | 107 (at 1C) | 95% at 1C (1000 cycles),[a] 100% at 10C (1000 cycles)[a] | 96 $mAh\,g^{-1}$ at 10C (94% retention)$_a$ | Polymer/Super C65/PVdF 50/40/10 | EC/DMC (1 : 1) + 1 M $LiPF_6$/Li/ Swagelok T-cell | 42 |
| PNMPT | 88 | 69 (at 1C) | 69% at 10C (1000 cycles)[b] | 58 $mAh\,g^{-1}$ at 20 C (73% retention)$_a$ | Polymer/Super C65/PVdF 50/45/5 | EC/DMC (1 : 1) + 1 M $LiPF_6$/Li/ Swagelok T-cell | 46 |
| X-PNMPT | 85 | 62 (at 10C) | 73% at 10C (1000 cycles),[b] 55% at 100C (10 000 ycles)[b] | 47 $mAh\,g^{-1}$ at 100 C (75% retention)$_a$ | Polymer/Super C65/PVdF 50/45/5 | EC/DMC (1 : 1) + 1 M $LiPF_6$/Li/ Swagelok T-cell | 46 |
| P1 | 74 | 62 (at 1C) | 45% at 1C (300 cycles)[a] | — | Polymer/Super C65/PVdF 50/45/5 | EC/DMC + 1 M $LiPF_6$/Li/ Swagelok T-cell | 46 |
| P2 | 86 | 73 (at 1C) | 45% at 1C (300 cycles)[a] | — | Polymer/Super C65/PVdF 50/45/5 | EC/DMC + 1 M $LiPF_6$/Li/ Swagelok T-cell | 46 |
| P3 (Poly3) | 112 | 80 (at 0.1C) | 98% at 0.1C (10 cycles)[a] | — | Polymer/Carbon C65/VGCF/PVdF 65/20/5/10 | EC/DMC + 1 M $LiPF_6$/Li/Swagelok cell | 40 |

| | | | | | | | |
|---|---|---|---|---|---|---|---|
| P(PT-T2) (P1a) | 36.4 | 33.7 (at 1C) | 95% at 1C (100 cycles)[b], 98% at 100C (30 000 cycles)[b] | 32.7 mAh $g^{-1}$ at 100 C (90% retention) | Polymer/Super C65/PVdF 60/35/5 | EC/DMC + 1 M $LiPF_6$/Li/ Swagelok T-cell | 44 |
| P4 (P2) | 36.4 | 33.7 (at 1C) | 92% at 1C (100 cycles)[b] | 30.9 mAh $g^{-1}$ at 100 C (85% retention) | Polymer/Super C65/PVdF 60/35/5 | EC/DMC + 1 M $LiPF_6$/Li/ Swagelok T-cell | 44 |
| P5 (P3) | 35.1 | 28.8 (at 1C) | 88% at 1C (100 cycles)[b] | 10 mAh $g^{-1}$ at 10 C (33% retention) | Polymer/Super C65/PVdF 60/35/5 | EC/DMC + 1 M $LiPF_6$/Li/ Swagelok T-cell | 44 |
| PT-DMPD | 156[c] | 128 (at 1C) | 65% at 5C (50 cycles)[b] | — | Polymer/Super P/PVdF 30/60/10 | EC/DEC (1 : 1) + 1 M $LiPF_6$/Li/Coin cell | 43 |
| PT-DMPD (10% CL) | — | 150 | 74% at 5C (50 cycles)[b] | 122 mAh $g^{-1}$ at 120 C (82% retention) | Polymer/Super P/PVdF 30/60/10 | EC/DEC (1 : 1) + 1 M $LiPF_6$/Li/Coin cell | 43 |
| PT-BZ | 127[c] | 97 (at 1C) | 66% at 1C (50 cycles)[b] | — | Polymer/Super P/PVdF 30/60/10 | EC/DEC (1:1) + 1 M $LiPF_6$/Li/Coin cell | 43 |
| P6 (PI1) | 169.1[d] | 160 (at 25 mA $g^{-1}$) with discharge potentials of 3.6 V (PT part) and 2.4 V (NDI part) | — | 107 mAh $g^{-1}$ at 800 mA $g^{-1}$ (63%) | Polymer/Ketjen Black/PVdF 40/40/20 | EC/DMC (1 : 1) + 1 M $LiPF_6$ + 2wt% vinylene carbonate/ Li/Coin cell | 45 |

[a]Percentage of initial discharge capacity;
[b]Percentage of theoretical capacity;
[c]Calculated for a one-electron oxidation of the phenothiazine moiety and a two-electron oxidation of the diamine moiety;
[d]Calculated for a one-electron oxidation of the phenothiazine moiety and a two-electron reduction of the naphthalene bisimide moiety.

mobility as well as electrolyte (in)solubility issues and cross-linking. As a third class of aliphatic phenothiazine polymer, poly(norbornene)s were reported by Esser, Kolek and co-workers in 2020.[46] Between the directly backbone-linker PNMPT and the ester-linked derivatives P1 and P2, PNMPT showed the best performance. Its cross-linked derivative X-PNMPT performed even better and demonstrated outstanding rate performance and long-term cycling stability at high C-rates. More details on the performance of these two poly(norbornene)s can be found below in the section on stabilizing interactions and charge mobility as well as electrolyte (in)solubility issues and cross-linking.

Concerning phenothiazine-based polymers of type (B) for battery applications, the first example, P3, was reported by Godet-Bar and co-workers in 2015.[40] The initial tests concerning its battery cycling stability look promising, however, only 10 charge/discharge cycles were reported. The strong conjugation within the backbone is clearly visible in the absence of plateaus in the charge/discharge curves. This behaviour is discussed in more detail below in the section on internal resistance and conductivity. Different types of conjugated phenothiazine-based co-polymers were investigated by Esser and co-workers in 2019.[44] The bithiophene co-polymer P(PT-T2) was compared to its fluorene analogue P4, and P5 with interrupted conjugation used for comparison. The conjugated co-polymers P(PT-T2) and P4 outperformed P5 regarding cycling stability, even at a 1C rate. With increasing C-rate, the influence of conjugation had a larger effect. Both P(PT-T2) and P4 demonstrated excellent rate performance up to 100C, and P(PT-T2) could even be cycled at this rate with full retention of the initial capacity for 30 000 cycles. The bithiophene co-monomer in P(PT-T2) was superior to fluorene in P4, likely due to its better charge-stabilizing properties. This is discussed in more detail below in the context of internal resistance and conductivity as well as tailoring π-conjugation in phenothiazine-based polymers. As partly conjugated polymers of type B, PT-DMPD and BT-BZ were investigated in batteries by Fors and co-workers in 2018.[43] Due to the redox activity of both the phenothiazine and the 1,4-diamine groups, the specific capacities of these polymers were high. However, this mixing of redox-active sites can also be seen in the absence of clear plateaus in the charge/discharge curves. High rate performance was reported, in particular for PT-DMPD, due to a low charge transfer resistance, which allowed for the fabrication of electrodes with a high active material ratio of 75%. This will be brought into context below in the sections on electrolyte (in)solubility issues and cross-linking as well as tailoring π-conjugation in phenothiazine-based polymers. As a final example, phenothiazine-naphthalene bisimide (NDI)-*co*-polymer P6 and PEO-block co-polymers thereof were reported by Mecerreyes and co-workers in 2019.[45] Due to the n-type redox activity of the NDI units, they could be used as both positive and negative electrode materials in an all-organic battery. This is the first report on an all-organic battery using a phenothiazine-based cathode. The cell showed stable cycling performance and an average discharge potential of 0.8 V. These results are discussed in

more detail below in the context of tailoring π-conjugation and the section on all-organic batteries using phenothiazine-based redox polymers.

The structure–property relationship of the presented polymers, however, is not only determined by the above-mentioned classification into side-chain and main-chain phenothiazine-containing redox polymers. Many different design principles can be used to affect their behaviour during charging and discharging of the battery cell. In the following, the main characteristics based on the uniqueness of phenothiazine as well as important coherences to understand the effects and challenges are addressed.

## 5.3 Specific Properties in Phenothiazine-based Redox Polymers for Energy Storage

### 5.3.1 Stabilizing Interactions and Charge Mobility

Phenothiazine units can undergo strong interactions with each other when one or both groups are oxidized to a radical cation. This type of interaction has been investigated in detail for many redox-active groups, and it can lead to bonding shorter than typical van der Waals distances.[47]

In 2004, Kochi and co-workers investigated this effect using small-molecule phenothiazine derivatives including bridged compounds with two PT units (*e.g.*, Figure 5.3A).[48] They described these interactions in detail and rationalized their occurrence by the energy gain resulting from the charge delocalization over both PT units. The delocalization results in a split of energy levels (Figure 5.3B), and the charge resonance (CR) band of the

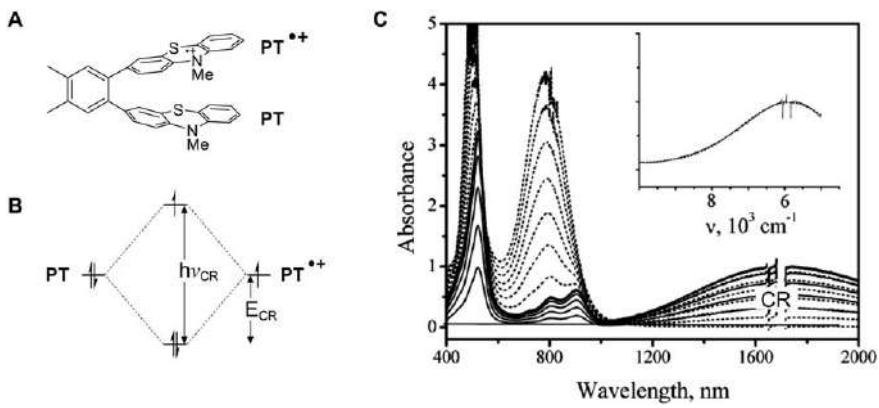


**Figure 5.3** (A) Structure of 1,2-bis(*N*-phenothiazinyl)4,5-dimethylbenzene in the mixed valent oxidized state. (B) Schematic split-up of energy levels based on MO theory. (C) Spectral changes in the NIR region upon addition of an oxidant to a solution of 1,2-bis(*N*-phenothiazinyl)4,5-dimethylbenzene [concentrations: 2 mm; oxidant (from bottom to top at 800 nm) 0, 0.4, 0.8, 1.2, 1.6, 2.0, 2.4, 2.8, 3.2, 3.6, 4.0, 4.4, 5.0 mm]. Adapted from ref. 48 with permission from the American Chemical Society, Copyright 2004.

formed complex can be detected by spectral analysis (broad band in the near-IR region, Figure 5.3C).[49,50] Kochi established the term ''π-mer'' or ''pimer'' to describe such interacting species, since ''π-dimer'' is reserved for the respective dicationic complexes, and to distinguish them from classical π-donor/acceptor pairs.

Morishima *et al.* investigated these interactions in phenothiazine-based polymers and observed a shift of the redox potential towards lower values in comparison to MPT or MPT-containing co-polymers with enhanced distance between the redox-active centres.[20] They also proved the existence of such interactions in the polymer by absorption spectroscopy. Besides the band for the literature-known radical cation of the MPT group at about 530 nm,[8] two more absorption bands at around 820 nm and 1400 nm (broad band) appeared (Figure 5.4).[22] He assigned the band at 820 nm to the dimer of two oxidized species (''π-dimer'') and the band in the near-IR region to a dimer of one neutral and one oxidized phenothiazine (''pimer''), both stabilized by π-interactions and in accordance with the studies by Kochi, mentioned above.

Esser, Bieker and co-workers discovered that these interactions were also at work in composite electrodes of PVMPT as organic cathode material for batteries.[41] In the battery electrode, these π-interactions between two phenothiazine units of the polymer led to a stabilization of oxidized states. To better understand the charge and discharge mechanism of the electrodes, the redox mechanism between the neutral and oxidized states in PVMPT can be split into two processes (Figure 5.5).

The intensity of charge delocalization, described by Kochi, could also be seen in these studies.[41] Chemically oxidized samples of PVMPT were

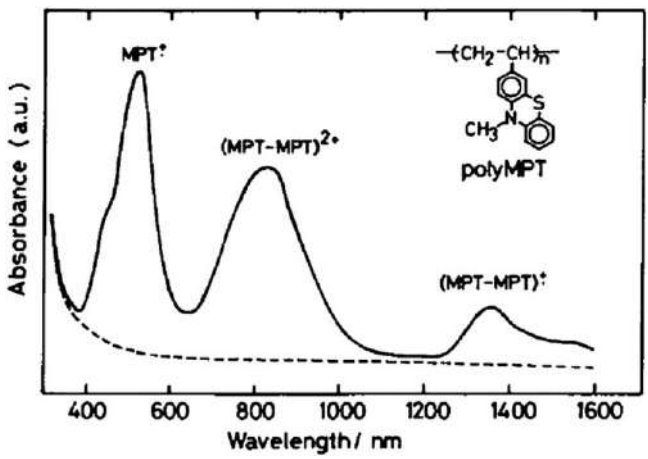


**Figure 5.4** Absorption spectra of a PVMPT (here labelled as polyMPT) film before (dashed line) and after (solid line) electrochemical oxidation, showing the bands for the radical cation $MPT^{\bullet+}$, the ''π-dimer'' $(MPT\text{-}MPT)^{2+}$ and the ''pimer'' $(MPT\text{-}MPT)^{\bullet+}$.
Reproduced from ref. 22 with permission from John Wiley and Sons, © 1985 Wiley-VCH Verlag GmbH & Co. KGaA, Weinheim.

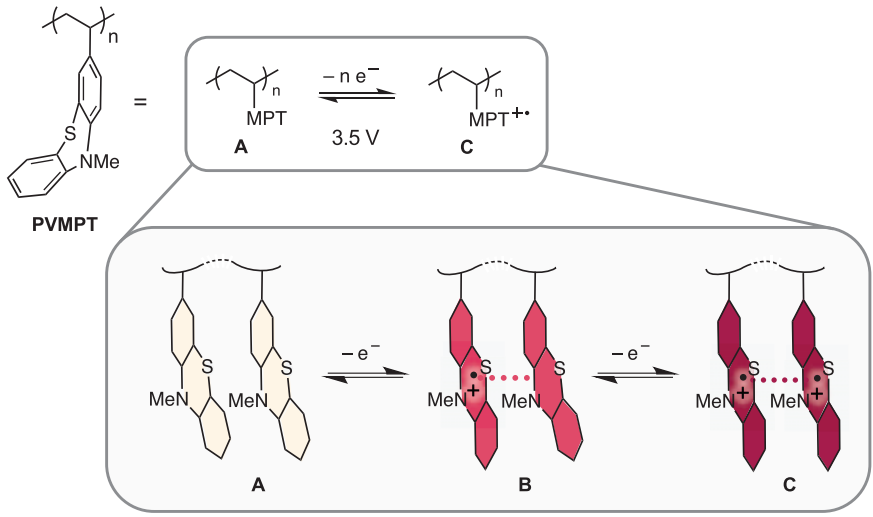


**Figure 5.5** π-Interactions between phenothiazine units, leading to a split-up of the redox mechanism in PVMPT.
Adapted from ref. 41 with permission from the Royal Society of Chemistry.

investigated by pulsed EPR spectroscopy. Most revealing was the result obtained for the fully oxidized sample (depicted as state C in Figure 5.5). Although this sample contained many paramagnetic centres, no EPR signal was detected, demonstrating the strong interactions between the radical cation centres (Figure 5.6A).[41] DFT calculations reinforced this observation. The HOMOs calculated for a dimeric model compound in each oxidation state clearly show significant orbital overlap for the fully oxidized as well as the semi-oxidized form (Figure 5.6B). The split-up of energy levels, shown in Figure 5.6C, schematically illustrates the energy gain resulting from the π-interactions and explains the diamagnetic (EPR-silent) state of the dicationic "π-dimer".

Up to now, such strong interactions within a redox polymer seem to be a special feature of phenothiazine in PVMPT. However, "pimer"-formation has also been observed for other redox centres in dimeric compounds[51] and oligomers.[52] Hence, it might be an interesting design principle for future redox polymers. The uniqueness of phenothiazine in this respect becomes apparent when comparing its electrochemical and battery performance with those of very similar heteroaromatics, namely thianthrene[53,54] and *N*-methylphenoxazine[55] attached to poly(vinylene)s (Figure 5.7). The redox-active groups herein showed much weaker π-interactions and hence a cycling behaviour significantly different from PVMPT. Furthermore, the relative intensity of "pimer"-formation in PVMPT and poly(vinyl-*N*-methylphenoxazine) (PVMPO) was compared using UV/Vis/NIR-spectroscopic measurements.[55] Chemically oxidized samples of both polymers showed significantly different behaviour in solution. While all three bands (free radical cation,

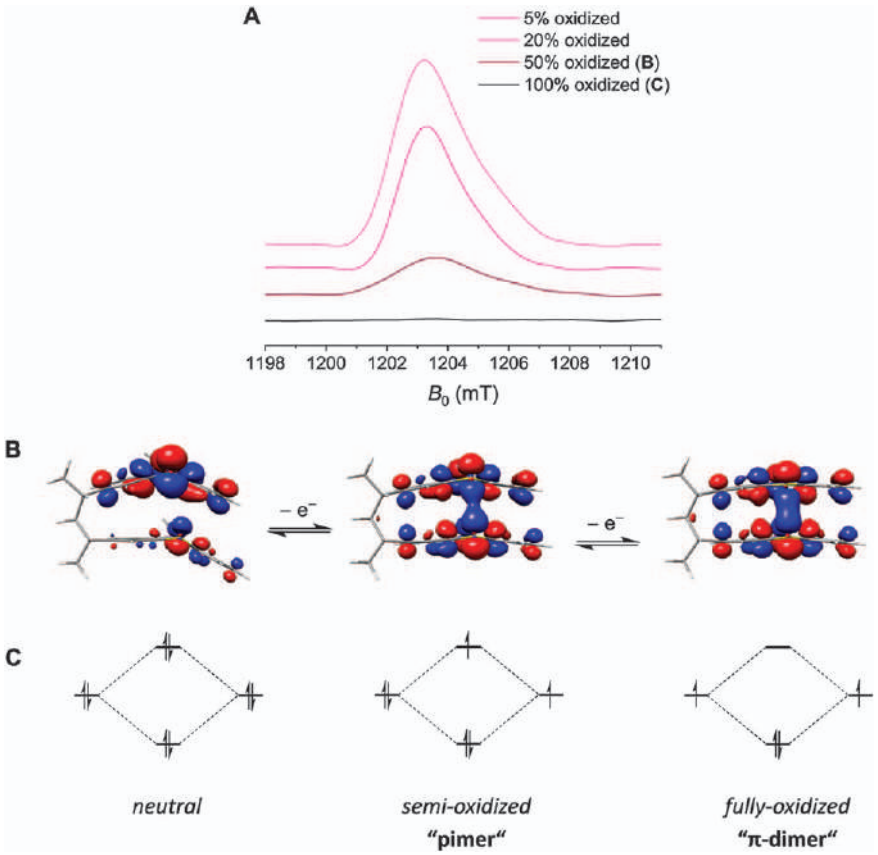


**Figure 5.6** (A) Pulsed Q-band EPR spectrum (80 K) of a $CH_2Cl_2$ solution of PVMPT in different oxidation states. Adapted from ref. 41 with permission from the Royal Society of Chemistry. (B) Highest occupied molecular orbitals (B3LYP-D3/def2-TZVP+COSMO) of the dimeric model compound in the respective oxidation state with (C) a schematic split-up of energy levels based on the MO theory.

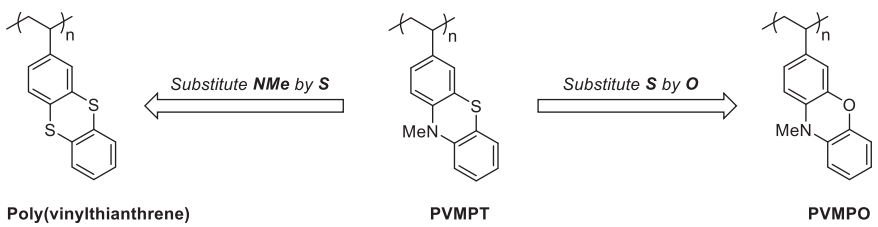


**Figure 5.7** Structures of poly(vinylene)s similar to PVMPT: poly(vinylthianthrene) (left) and poly(vinyl-*N*-methylphenoxazine) (PVMPO, right).

''π-dimer'' and ''pimer'') could be observed for PVMPT, the ''π-dimer'' band was absent in the spectra of PVMPO, showing the limited ability of phenoxazine to exhibit such interactions.[55]

The stabilization through the ''pimer'' and ''π-dimer'' formation in PVMPT led to a charge and discharge mechanism in the battery electrode that switched between these two forms. Full discharging to the neutral form was not achieved. Hence a specific capacity of 56 $mAh\,g^{-1}$ was accessible, which corresponded to half of the theoretical value for the redox pair PVMPT/PVMPT$^{\bullet+}$. In spite of this capacity loss, these interactions led to a highly stable system, where the battery could be cycled 10 000 times at a 10C rate without significant capacity loss.[41]

Another benefit of these π-interactions was that the charge-transfer process not only occurred between redox-active groups and the conductive carbon additive but also between the phenothiazine units themselves, allowing for supramolecular hole transport. This additional charge transport was one of the main reasons for the high rate capability obtainable in PVMPT. The degree of π-interactions, and *vice versa* that of supramolecular hole transport, depends on the intra- or intermolecular distances between two redox groups.[56–58] Because segmental motions of the redox centres are necessary for the phenothiazine units to arrange themselves into a face-to-face orientation, which enables effective electron self-exchange, energy has to be spent to achieve this juxtaposition (in connection with a loss of entropy due to the more highly ordered structure). This means that site-to-site electron transfer between neighbouring groups would strongly be favoured by a close proximity of the redox-active centres, requiring less organization.

Suga, Nishide, Gutmann and co-workers used this design principle to influence π-interactions and synthesized two poly(styrene)s side group-functionalized with phenothiazine groups, connected by an alkyl spacer between its nitrogen atom and the styrene backbone (Figure 5.8).[23] Varying the spacer length resulted in an increased rotational freedom of the redox centres. Indeed, they observed significant differences in the electrochemical behaviour of the two polymers. The additional rotational freedom due to the longer spacer in PVPPP led to lower electron self-exchange rates compared to PVBPT. This was explained by the reduced tendency of PVPPP to undergo π-interactions because the rotational freedom would be limited by forming a π-dimer complex. The relative amount of π-dimers inside the polymer could also be visualized by *in situ* electrochemical UV/Vis spectra. The absorption bands of the phenothiazine radical cation and the π-dimer can be found in the ranges of 400–600 nm and 650–950 nm, respectively (Figure 5.8).

The lowered self-exchange rates achieved by impeding the formation of π-dimers in PVPPP had a positive effect on its charge storage ability in test cells. In contrast, the enhanced electron-transfer caused by the π-interactions led to an increased self-discharge in PVBPT. This was shown most expressively by the difference in Coulombic efficiencies,

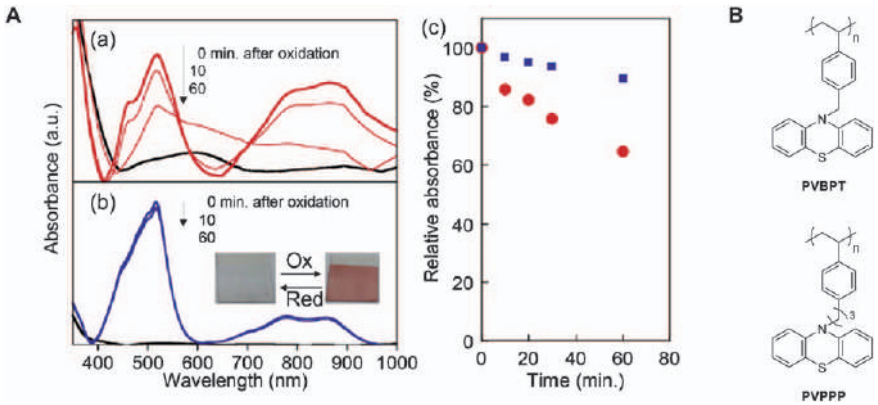


**Figure 5.8** (A) *In situ* electrochemical UV/Vis spectra of (a) PVBPT and (b) PVPPP on an ITO electrode. The neutral polymers are shown in black, and the corresponding oxidized forms under the applied potential of 1.1 V in red and blue, respectively. (c) Time decay of the relative absorbance at 518 nm ascribed to the radical cations for PVBPT (red) and PVPPP (blue). (B) Molecular structures of the respective polymers.
Reproduced from ref. 23 with permission from the Royal Society of Chemistry.

being 77% for PVBPT and 97% for PVPPP, making the latter polymer superior. Also worth mentioning is that the authors obtained up to 92% of the theoretical discharge capacity for PVPPP showing reduced π-complex formation. The long-term cycling stability, however, was only moderate, which might be explained by solubility issues of the polymer in the battery electrolyte.

Another strategy to influence the mobility and distance of neighbouring redox centres inside a polymer can be achieved by changing the polymer backbone. Esser, Kolek and co-workers realized this approach by attaching phenothiazine to poly(norbornene)s through ester groups or direct linkages.[46] All tested polymers showed decreased π-interactions, as seen from UV/Vis/NIR measurements in comparison with PVMPT (Figure 5.9A). The esters P1 and P2 (for structures see Figure 5.9B) showed a moderate cycling performance, which could be explained by the limited stability of the ester functionality suffering from traces of hydrogen fluoride or other decomposition products of the electrolyte or the polymer itself. PNMPT, on the other hand, as well as its cross-linked derivative X-PNMPT, were highly stable and showed excellent cycling performance, reaching a specific capacity of 69 and 62 mAh $g^{-1}$, respectively. This corresponded to a theoretical capacity of 78% for PNMPT and of 73% for X-PNMPT. As discussed for the polymers in the previous paragraph, this underlines the lowered ability of these polymers to undergo π-interactions.

Another strategy to influence π-stacking is to prevent it completely, for instance by cross-linking the redox polymers, which is discussed in the context of polymer solubility in the next section.

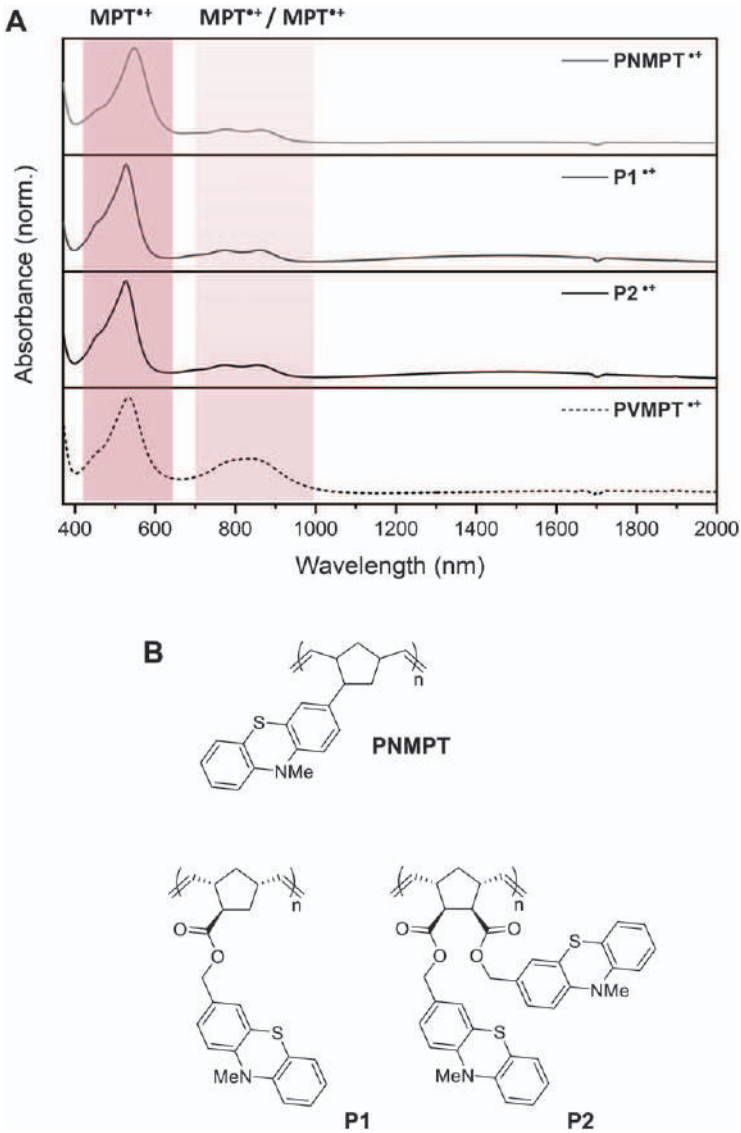


**Figure 5.9** (A) UV/Vis/NIR spectra of oxidized PNMPT, P1, P2 and PVMPT in $CH_2Cl_2$ and (B) structures of the respective poly(norbornene)s.
Reproduced from ref. 46 with permission from John Wiley and Sons, © 2020 Wiley-VCH Verlag GmbH & Co. KGaA, Weinheim.

## 5.3.2 Electrolyte (in)solubility Issues and Cross-linking

Insolubility in the battery electrolyte is usually a crucial property for high cycling stability of redox polymers as electrode materials.[39,59] In most cases dissolution over time leads to capacity fading. It is important to consider insolubility both

in the neutral and charged states. For phenothiazine polymers, interestingly, electrolyte solubility was not in all cases fatal for battery performance. This has been studied in detail by Esser, Bieker and co-workers for PVMPT.[41,60] They found that this polymer dissolved in the electrolyte [EC/DMC (1 : 1) with 1 M $LiPF_6$] in its fully oxidized state (state C, Figure 5.5), but was insoluble in the neutral or semi-oxidized form. In spite of this solubility, the cycling stability of PVMPT was outstanding, and cycling over 10 000 cycles at a 10C rate proceeded without significant capacity loss, but at half of the theoretical specific capacity (see above).[41] The reason for this outstanding cycling stability was that the dissolution of PVMPT in its oxidized form allowed for a rearrangement of the phenothiazine redox-active group to achieve a high number of π-stacked dimers. This happened during charging, when PVMPT was dissolved out of the composite electrode. Upon discharging, the insoluble semi-oxidized form was redeposited onto the electrode surface, maintaining the π-stacked "pimer" complexes (see Figure 5.10). This process and the formation of a polymer layer on top of the conductive carbon could clearly be seen in micrographs, especially in cross-sectional scanning electron microscopy (SEM).

Interestingly, even though oxidized PVMPT was soluble in the electrolyte no considerable traces of the polymer or its degradation products were found on the surface of the lithium electrode. Three possible reasons to explain this observation are: (1) Repulsion of the positively charged polymer by the lithium cations on the lithium surface, (2) a kinetically favoured decomposition of the electrolyte instead of the polymer and (3) prevention of polymer degradation by the already-formed solid electrolyte interphase on the lithium surface.[60]

Having in mind that solubility is essential for the rearrangement process to achieve π-stacking of the phenothiazine units, cross-linking was applied to achieve complete insolubility of the polymer in both its neutral and oxidized

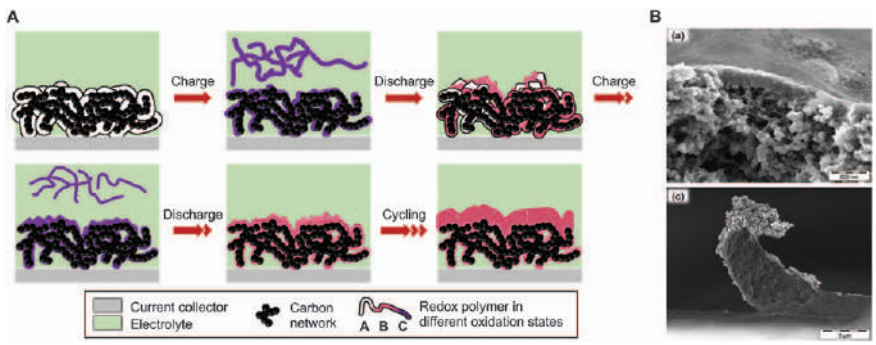


**Figure 5.10** (A) Mechanism of charge/discharge of a PVMPT-based electrode and (B) cross-sectional SEM micrographs of PVMPT-based electrodes in the discharged state after 1000 cycles. (a) Surface layer on top of the electrode (40 000× magnification); (c) peeled-off surface layer (5000× magnification).
Reproduced from ref. 60 with permission from the American Chemical Society, Copyright 2018.

form. Indeed, with the cross-linked derivative X-PVMPT Esser, Bieker and co-workers obtained the full theoretical capacity of up to 112 mAh $g^{-1}$ by reducing the polymer mobility.[42] However, preventing the π-interactions also lowered the ability for supramolecular hole transport, which could be seen in the limited rate capability compared to noncross-linked PVMPT – still, a stable specific capacity of 85 mAh $g^{-1}$ was accessible for 1000 cycles at 10C rate. A benefit of the reduced conductivity and polymer mobility was the remarkably low self-discharge rate of 2% within 3 days for X-PVMPT.

As a consequence, the question whether π-interactions are beneficial in phenothiazine-based polymers depends on the requirements of the application. The effect of these interactions on the battery performance can be significant and varies with the polymer structure. Hence the extent of π-interactions needs to be tailored for each polymer, and sometimes it might be even preferential to completely suppress π-interactions.

Cross-linking was also applied for various poly(norbornene)s functionalized with phenothiazine units.[46] In this case, due to the higher molecular weight of the poly(norbornene)s, PNMPT as well as its cross-linked congener X-PNMPT were both insoluble in the battery electrolyte (for structures see Figure 5.11). Linear PNMPT possessed good rate capability up

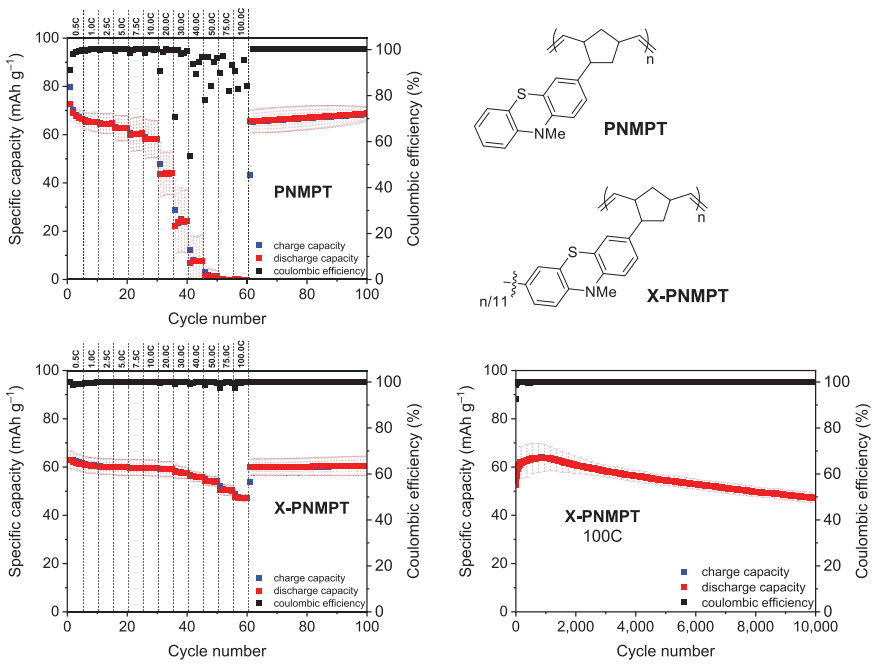


**Figure 5.11** Rate capability of PNMPT- and X-PNMPT-based composite electrodes and constant current cycling measurement of X-PNMPT-based composite electrodes at 100C rate (average of three different cells).
Adapted from ref. 46 with permission from John Wiley and Sons, © 2020 Wiley-VCH Verlag GmbH & Co. KGaA, Weinheim.

to 10C, while cross-linked X-PNMPT showed excellent cycling stability even at a rate of 100C (Figure 5.11; specific capacity of 47 $mAh\,g^{-1}$ after 10 000 cycles, corresponding to 75% of the initial charge capacity and 55% of the theoretical value). These results are surprising with regard to the lack of hole-transport, since π-interactions were absent, and illustrate that more effects, such as for instance counter ion mobility, have to be taken into account to describe reasons for rate capability.

To prevent its dissolution in the electrolyte, Fors and co-workers applied cross-linking to a partially conjugated system based on a phenothiazine co-polymer with phenylenediamine units, and, in addition, obtained improved conductivity similar to that observed in X-PNMPT.[43] The largest impact could be seen by comparing linear PT-DMPD with its cross-linked derivatives (for structures see Figures 5.2 and 5.12A). The cycling stability markedly increased with the degree of cross-linkage, resulting in enhanced capacity retentions of 65%, 73%, 74% and 82% for cross-linker percentages of 0%, 5%, 10% and 33%, respectively, after 50 cycles at 5C (Figure 5.12B).

Particularly noteworthy is the authors' study on the effect of the cross-linkage degree on the battery performance. Varying the cross-linker ratio affected the morphology of the polymer in the composite and led to higher rigidity. The composite structure is important for the ion mobility inside the framework. A higher rigidity can lead to reduced ion mobility within the electrode. To take these important factors into account the next section focuses on these issues.

### 5.3.3 Internal Resistance and Conductivity

The internal resistance (and thereby conductivity) of a polymer is an important parameter for the final battery. The higher the conductivity of a polymer, the less conductive additive will be required for the electrode composition, leading to a higher amount of active material. The electron or hole conductivity within the composite electrode can be influenced through the charge carrier mobility within the redox polymer. The electron or hole transport can occur *via* hopping processes or delocalization along the polymeric chain, if the structure allows for conjugation. In the case of an aliphatic polymer backbone (Figure 5.13A), the electrons will move through the structure from one redox-active unit to the next *via* a hopping mechanism. This is the favoured electron-transport mechanism in most phenothiazine-based polymers, partly because of the strong π-interactions between the redox-active units (see above), but also due to their usually aliphatic backbone. On the other hand, within a conjugated polymer backbone (Figure 5.13B) the charge carriers should be able to move along the polymer backbone through delocalization in addition to the hopping mechanism.

Two examples of conjugated phenothiazine-based polymers were reported in the literature: Godet-Bar and co-workers synthesized and investigated a conjugated homo-polymer based on phenothiazine (P3 in Figure 5.2), and

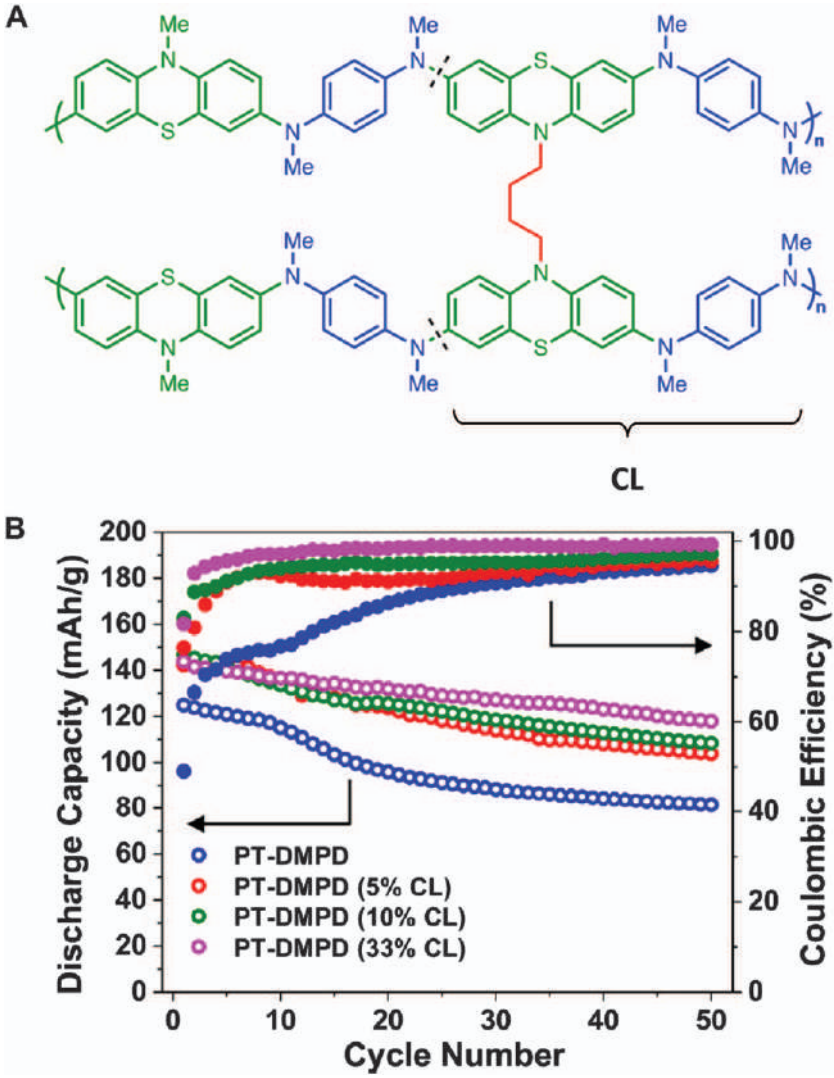


**Figure 5.12** (A) Structure of cross-linked PT-DMPD (cross-linked segment marked with CL), and (B) cycling performance of coin cells with 0.55 mg cm$^{-2}$ mass loading of PT-DMPD and its cross-linked derivatives at 5C. Reproduced from ref. 43 with permission from the American Chemical Society, Copyright 2018.

more recently Esser and co-workers synthesized and investigated conjugated phenothiazine co-polymers [P(PT-T2) and P4 in Figure 5.2].[40,44] The first polymer type (Figure 5.13A) should exhibit a well-defined and stable redox potential at each charging state of the battery, while the conductivity of the polymer is relatively low due to the presence of the nonconjugated backbone. The π-conjugated polymer type (Figure 5.13B), on the other hand,

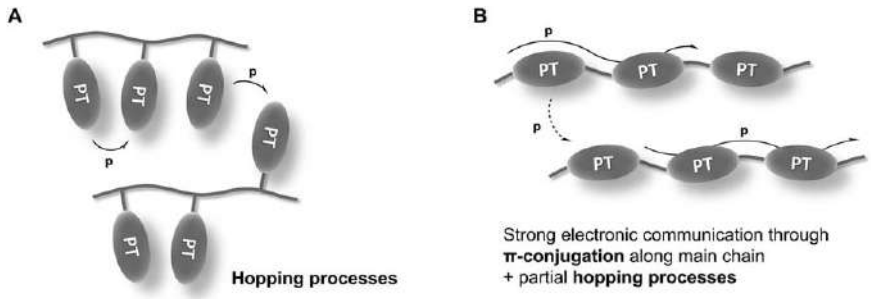


**Figure 5.13** Possible charge transport mechanisms occurring in (A) an aliphatic polymer backbone with the phenothiazine units attached as side groups and (B) a π-conjugated polymer with the redox centres implemented in the main chain.

could be expected to show less well-defined redox peaks (see also below) but good conductivity (in the doped state). Indeed, this was observed by Godet-Bar and co-workers for P3. The CVs for this conjugated polymer showed broad peaks (Figure 5.14A), as expected for this type of polymer.[40,61,62] On the contrary, the co-polymers P(PT-T2) and P4 by Esser and co-workers showed narrow and well-defined redox peaks (Figure 5.14B). This was due to the co-polymer structure, which left the defined phenothiazine redox centres intact. These co-polymers all showed highly stable cycling behaviour, in particular bithiophene-based P(PT-T2).[44] Flat plateaus resulted during charge and discharge, demonstrating the localization of redox events onto the phenothiazine units.

Conductive polymers become unstable when the doping level is too high, which is caused by a repulsion of charges (Figure 5.15).[34] The open-circuit voltage of the resulting battery also depends on the doping level of the polymer. When synthesized, the polymer is in state B and can be charged (state D) or discharged (state A). The conductivity during this procedure will change and, as a result, a sloping cell voltage will be obtained from the measurement.[36]

Using electrochemical impedance spectroscopy (EIS) it is possible to determine the resistance of a polymer in different states of charge. Depending on the polymer type, the resistance will change with the state of charge. The influence of conjugation along the polymer chain and the internal resistance were investigated by Esser and co-workers in the case of the phenothiazine-based co-polymers P(PT-T2) and P5 (for structures see Figure 5.2). For the conjugated polymer P(PT-T2) (Figure 5.16A), the resistance was smaller by one order of magnitude compared to polymer P5 with interrupted π-conjugation (Figure 5.16B). Furthermore, the resistance of P(PT-T2) decreased with increasing state of charge, indicating good hole conduction of the material. On the contrary, with interrupted conjugation along the polymer backbone, such as for polymer P5 (Figure 5.16B), the resistance increased with the state of charge due to the poor hole conduction.[44]

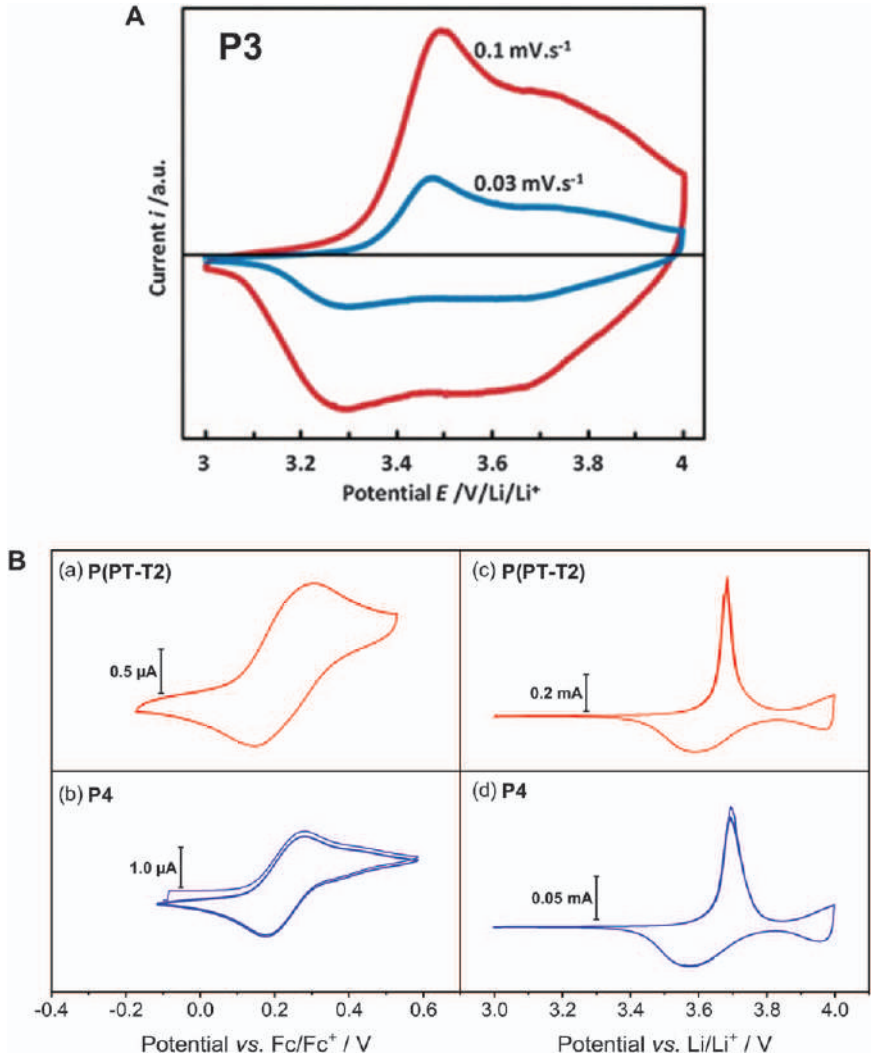


**Figure 5.14** (A) CV of the fully conjugated phenothiazine homo-polymer P3 (for structure see Figure 5.2). Reproduced from ref. 40 with permission from the Royal Society of Chemistry. (B) CV of the conjugated phenothiazine co-polymers P(PT-T2) and P4 in solution (a, b) and composite electrode (c, d).
Reproduced from ref. 44 with permission from John Wiley and Sons, © 2019 Wiley-VCH Verlag GmbH & Co. KGaA, Weinheim.

A good conductivity of the polymer-composite electrode is an essential requirement to manufacture a well-performing battery. Usually, even in the case of the phenothiazine co-polymer P(PT-T2) above, the polymer itself is not conductive enough and is therefore mixed with a conductive additive. However, within the organic materials, it is also possible to manipulate the

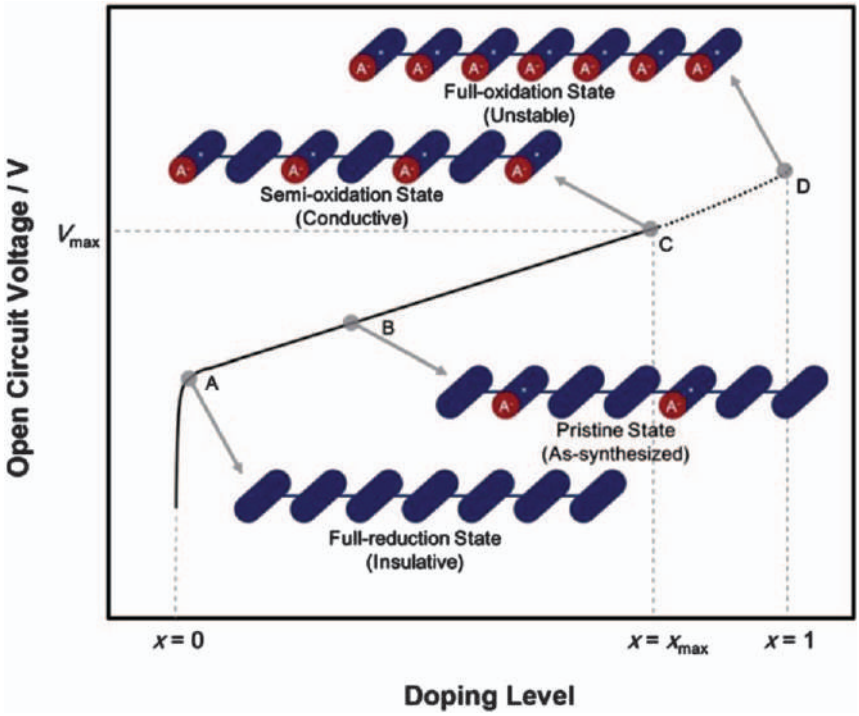


**Figure 5.15** Electrochemical behaviour of a p-type conductive polymer. Reproduced from ref. 34 with permission from the Royal Society of Chemistry.

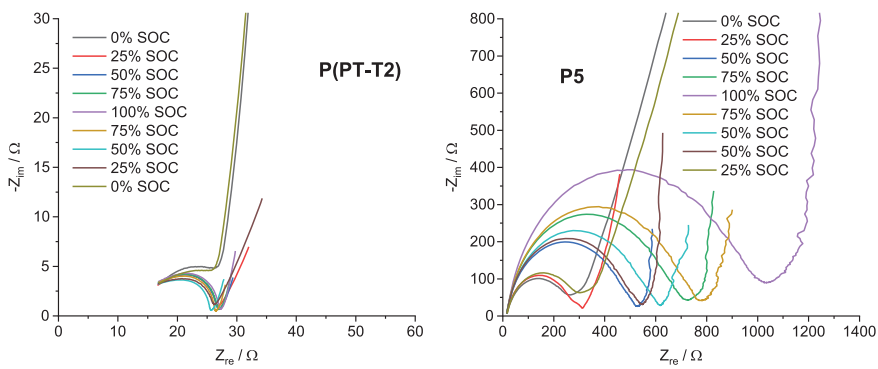


**Figure 5.16** Nyquist plots from electrochemical impedance spectroscopy measurements of composite electrodes of conjugated polymer P(PT-T2) (left) or polymer P5 with interrupted conjugation (right). Reproduced from ref. 44 with permission from John Wiley and Sons, © 2019 Wiley-VCH Verlag GmbH & Co. KGaA, Weinheim.

conductivity through structural modifications, also known as tailoring, which is discussed in the next section for phenothiazines.

### 5.3.4 Tailoring π-Conjugation

Tailoring an organic polymer through a structural modification leads to a tuning of its properties. This could, for example, enhance π-interactions, charge transport or ionic conductivity.[63] The chemical structure of phenothiazine allows for different modifications, in particular substitution at the nitrogen atom and at the 3- and 7-positions of the aromatic rings.

#### *5.3.4.1 Nitrogen Substitution*

A substitution at nitrogen can increase the reversibility of the redox process. This was studied by Godet-Bar and co-workers, who compared phenothiazine with several of its *N*-alkyl derivatives (methyl, ethyl and *n*-propyl substituent).[40] Furthermore, the geometrical conformation of the phenothiazine core depends on the nitrogen substituent. The so-called butterfly angle is the dihedral angle formed between the two planes defined by the two aromatic rings of the phenothiazine core (Figure 5.17). This angle significantly differs in the neutral and charged states of phenothiazine and depends on the substituent. While phenothiazine is usually bent in its neutral state, it almost completely planarizes in the oxidized state. Without a substituent on the nitrogen atom, the butterfly angle of phenothiazine switches from 158.5° in the neutral form to 179.1° in the oxidized state, while this change is often smaller in *N*-substituted derivatives. Hence it is beneficial for a reversible and fast redox process to add a nitrogen substituent.[64,65] The butterfly conformation in the ground state of phenothiazine is also able to prevent π–π-aggregation, this topic will be treated in more detail below.[66,67]

#### *5.3.4.2 Carbon Substitution*

A substitution at C-atoms 3 and 7 of the phenothiazine core is synthetically favourable due to its location *para* to the nitrogen atom. Hence through electrophilic aromatic substitution a variety of substituents can be introduced at these positions. The electrochemical properties of the phenothiazine core can be influenced depending on the electronic nature of the substituent. It was shown, for instance, that it is possible to stabilize the second (and normally irreversible) oxidation of phenothiazine by introducing electron-rich methoxy substituents in these positions.[68]

Both Fors and co-workers,[43] as well as Mecerreyes and co-workers,[45] synthesized polymers with nitrogen substituents at the 3- and 7-positions, however, with a different goal. Fors and co-workers synthesized co-polymers PT-DMPD and PT-BT (for structures see Figure 5.2) based on phenothiazine and phenylenediamine.[43] They used the advantages of phenothiazine, such as stable cycling and a high redox potential, and combined these with the

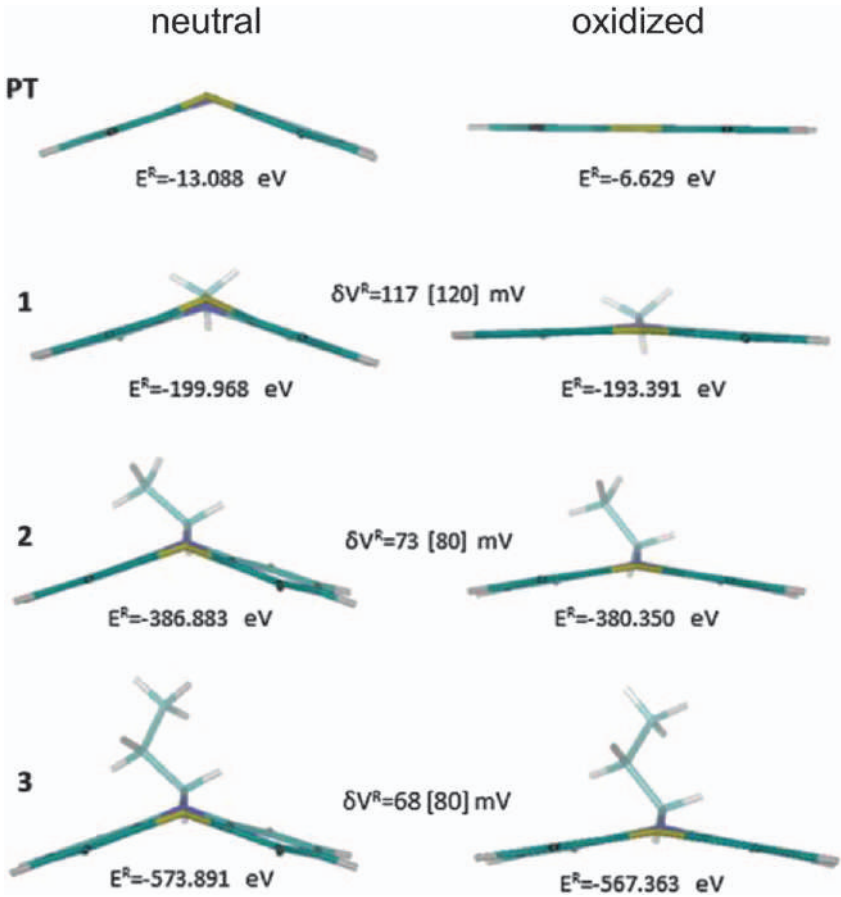


**Figure 5.17** Calculated geometry, total energy and gain in the oxidation potential of different nitrogen-substituted phenothiazines: methyl (1), ethyl (2), propyl (3).
Reproduced from ref. 40 with permission from the Royal Society of Chemistry.

redox activity of phenylenediamine moieties. The final co-polymer showed a high specific capacity of 150 mAh $g^{-1}$ and was capable of good capacity retention on cycling at high discharge rates. Mecerreyes and co-workers presented a co-polymer based on naphthalene bisimide (NDI) as n-type and phenothiazine as p-type redox-active group (P6 in Figure 5.2). Hence this polymer could be used as both anode and cathode material. When tested as cathode material the authors obtained a reversible two-electron redox reaction from the NDI moiety and a one-electron process from the phenothiazine moiety, resulting in a high specific capacity.[45] In constructing the full cell they could use the benefits of both units: phenothiazine for the fast charge transport and polyimide as the anode material capable of a two-electron redox reaction (see also below).

Esser and co-workers synthesized and investigated π-conjugated co-polymers based on phenothiazine and either bithiophene or fluorene as neighbouring molecules [P(PT-T2) and P4, see Figure 5.2 for structures], as mentioned above in the context of intrinsic conductivity.[44] As the specific capacities of the co-polymers were similar, the influence of the co-monomers was investigated. All co-polymers showed stable cycling behaviour with a maximal 2% capacity loss after 100 cycles at 1C for the fluorene-containing co-polymer. The flat plateau visible during charge and discharge for both co-polymers indicated that π-conjugation did not influence the redox potential of phenothiazine. Long-term measurements showed the best results for the conjugated bithiophene-containing co-polymer, which lost less than 3% of its initial capacity after 30 000 cycles at 100C. An explanation of these promising results could be the electron-donating and charge-stabilizing effect of the bithiophene in comparison to the fluorene units, enforcing the concept that electron-rich substituents are beneficial for the electrochemical properties of phenothiazine.

### 5.3.5 Processability

After the synthesis of phenothiazine-based redox polymers, the next step to test them in a battery is to prepare the electrode, which usually contains a composite. A conductive carbon additive is mixed with the polymer to ensure the conductivity of the electrode. This is often done by mixing a slurry, consisting of redox polymer, conductive carbon and binder, in a high-boiling solvent, which is then applied to a foil, and electrodes are punched out after drying of the film. Depending on the polymer type (see previous section), the electrode composition can change. A π-conjugated polymer has a better intrinsic conductivity, and hence it is possible to reduce the amount of carbon black and thereby increase the amount of active material in the electrode. In order to prepare a good slurry, the polymer should have a decent solubility in the chosen solvent (often NMP), otherwise the composite will not be homogeneous, resulting in polymer agglomeration. The surface of the electrode can be characterized using scanning electron microscopy (SEM). Comparison of electrodes based on PVMPT or the cross-linked derivative X-PVMPT, for instance, each containing 50 wt.% active polymer, proved that the soluble PVMPT gave a more homogeneous electrode surface (Figure 5.18, left), whereas X-PVMPT partly formed polymer agglomerates (Figure 5.18, right).[42]

Furthermore, using energy-dispersive X-ray (EDX) spectroscopy, it is possible to target specific atoms on the electrode surface. As carbon atoms are contained in each component of the electrode (active material, carbon black and binder additive), the sulphur atoms of the phenothiazine units are particularly useful to obtain information about the homogeneity of the composite (Figure 5.19). Fluorine atoms can be targeted to obtain information on the distribution of the binder in the case of the commonly used polyvinylidene fluoride (PVdF).

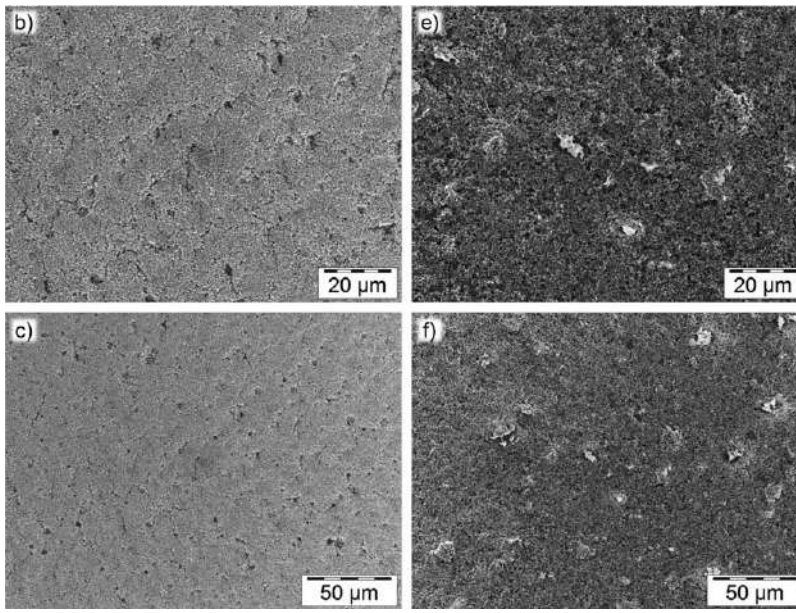


**Figure 5.18** SEM micrographs of pristine electrodes containing 50 wt.% redox polymer: unpressed electrode with PVMPT (b and c) and unpressed electrode with X-PVMPT (e and f).
Reproduced from ref. 42 with permission from John Wiley and Sons, © 2018 Wiley-VCH Verlag GmbH & Co. KGaA, Weinheim.

In order to increase the polymer solubility to obtain more homogeneous slurries and electrodes, alkyl side chains can be added. These, however, will reduce the specific capacity of the material (as the molecular weight of the polymer will increase) and in some cases the Coulombic efficiency of the electrode (long alkyl chains will enhance the solubility in the electrolyte and therefore the degradation of the material), so a balance has to be found between processability and battery performance.[44,69] The polymer backbone can also be tuned, as shown by Mecerreyes and co-workers, through incorporation of polyether blocks (PEO) in the co-polymer structure to improve its processability and avoid the use of binder in the electrode composition.[45]

### 5.3.6 All-organic Batteries Using Phenothiazine-based Redox Polymers

As electronic devices, such as cell phones and laptop computers, are becoming more powerful, there is a strong demand for new energy storage devices powering different types of technologies. These should be nontoxic, safe and recyclable. The necessity to find nontoxic and sustainable materials to build new batteries is crucial. To this aim, in all-organic batteries both electrodes are replaced with organic redox polymers.[70,71] As the properties of such organic redox polymers are tuneable, it is possible to increase

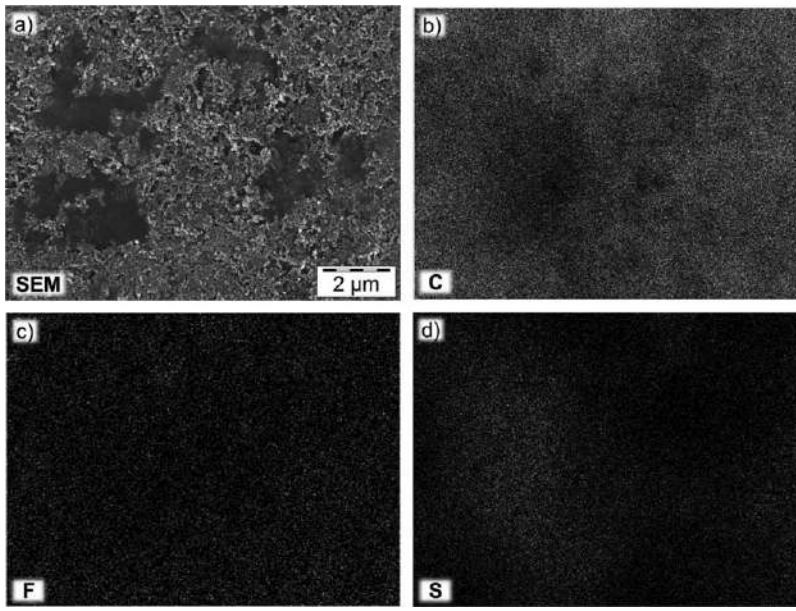


**Figure 5.19** SEM/EDS mapping of a pristine X-PVMPT-based (pressed) electrode at 10 000× magnification: (a) SEM micrograph, (b) carbon map, (c) fluorine map, (d) sulphur map.
Reproduced from ref. 42 with permission from John Wiley and Sons, © 2018 Wiley-VCH Verlag GmbH & Co. KGaA, Weinheim.

(decrease) the potential of the cathode (anode, respectively) and therefore theoretically control (and enhance) the output voltage of the final battery. Furthermore, the use of polymers allows for the resulting composite electrodes and batteries to be mechanically flexible, which leads to a large degree of freedom for the design of the final device.

All-organic batteries are divided into three cell categories as described by Poizot and co-workers: The cation rocking-chair cell containing n-type electrode materials, the anion rocking-chair cell containing p-type electrode materials and the dual-ion cell with an n-type material as anode and a p-type material as cathode (Figure 5.20).[70] Note that the battery can be symmetric or asymmetric depending on whether both polymer electrodes are the same or not.

The main challenge to building an all-organic battery is to find two redox-active polymers with significantly large potential difference, which are compatible with the same electrolyte.[45] As all-organic polymer, the synthetic process should also be as short as possible for both environmental reasons and a potential large-scale application. In 1981, MacDiarmid built the first all-organic battery.[25] The bipolar nature of polyacetylene was used, since it can be both n- and p-doped and thereby serve as cathode or anode material.[24] In the last 10 years, several further examples of all-organic batteries have been reported, as discussed in recent review articles.[70,71]

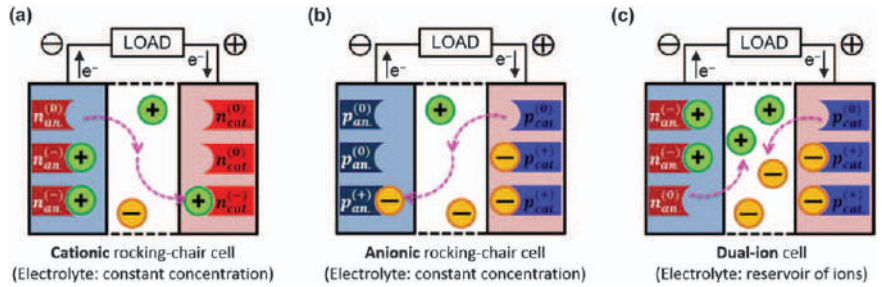


**Figure 5.20** Scheme of three different configurations of all-organic batteries: (a) with n-type materials; (b) with p-type materials; (c) with n- and p-type materials.
Reproduced from ref. 70 with permission from Elsevier, Copyright 2018.

Using a phenothiazine-based redox polymer, the first study of an all-organic battery was reported by Mecerreyes and co-workers in 2019. Polymer P6 (see Figure 5.2 for structure), which showed good cycling behaviour in a half cell *versus* lithium (see Figure 5.21), was used as both cathode- and anode-active material based on the redox activity of the phenothiazine and NDI units, respectively.[45] The symmetric battery composed of this polymer (both in the neutral state) as cathode and anode did not need a prelithiation step to be usable, which is an advantage for large-scale applications. The battery showed a good rate capability up to 1000 mA $g^{-1}$ at an average charge/discharge potential of 0.9 V, corresponding to a one-electron redox reaction of the methylphenothiazine groups on the cathode side and a reduction of the NDI units on the anode side. The cell showed a Coulombic efficiency of 97% at a high current density of 800 mA $g^{-1}$ and lost only 6% of its initial specific capacity after 1000 cycles at the same rate, which indicated a high cycling stability.

As can be seen in this example, the cell voltage of 0.9 V of the full-organic cell is high, but is not comparable with the lithium-ion technology, which can achieve a cell voltage of around 4 V.[72] In order to compete with this technology in the future, it will be necessary to develop anode materials with lower redox potential. On the other hand p-type materials could be developed with higher redox potential, but only a few electrolytes are stable under such high voltage oxidation.[73] Regardless, all-organic batteries are of interest for a range of applications, where the voltage is of lesser importance, related to the Internet of Things and the medical market, among others.

### 5.3.7 Ongoing Challenges

Although a variety of different redox polymers using phenothiazine as redox-active group have been synthesized, an unmet challenge is still to enable a two-electron redox process. This would double the specific capacity of the redox polymer and lead to a higher cell voltage associated with the second

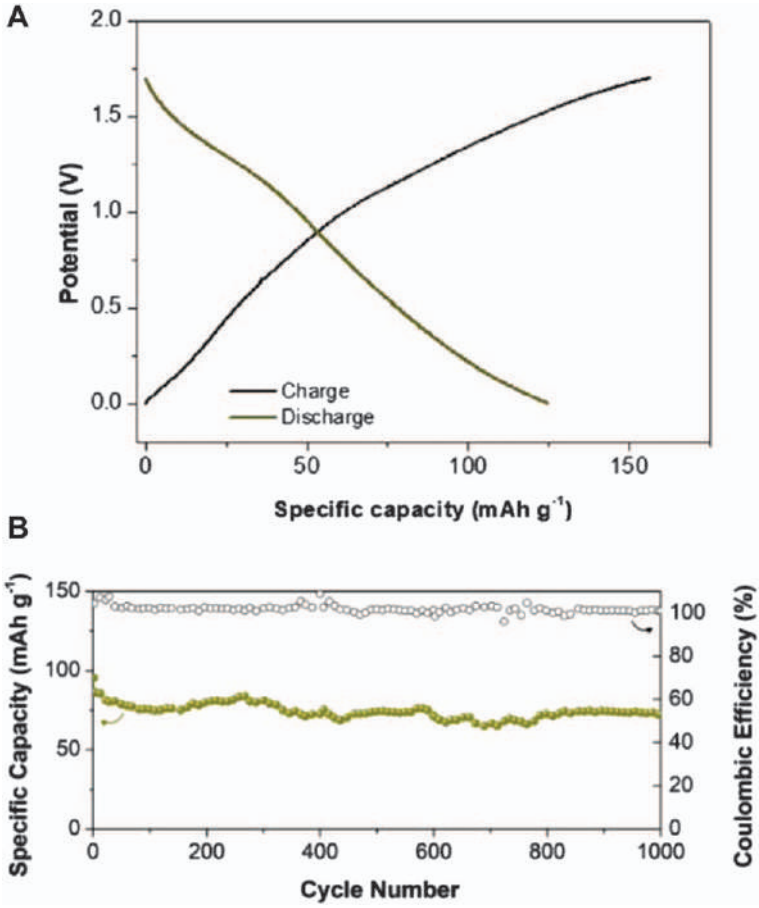


**Figure 5.21** Symmetric polymer battery with P6 as cathode and anode. (a) Charge and discharge voltage profiles at a current density of 100 $mA\,g^{-1}$ between 0.0 and 1.7 V. (b) Cycling stability at 800 $mA\,g^{-1}$ between 0.005 and 1.65 V.
Reproduced from ref. 45 with permission from John Wiley and Sons, © 2019 Wiley-VCH Verlag GmbH & Co. KGaA, Weinheim.

oxidation step. The most promising approach seems to be the attachment of electron-donating methoxy groups, as demonstrated by Odom and co-workers. *N*-ethyl-3,7-dimethoxyphenothiazine was tested as the catholyte for redox flow batteries, and the second oxidation step could be stabilized by the electron-donating methoxy groups.[68] However, in the solid state and especially in a composite electrode, this might still be more challenging to achieve. In addition, a suitable polymer design has to be identified.

Another approach to enhancing the energy density of the electrode can be achieved by increasing the redox potential of the polymer and, as a result, the output voltage of the battery. This can be obtained by similar design

principles *via* attaching electron-withdrawing substituents to the phenothiazine core.[14] Raising the electron deficiency of the formed radical cation leads to an increased redox potential.

Furthermore, using existing phenothiazine-based redox polymers, the energy density can also be enhanced by increasing the relative amount of redox-active material in the composite electrode or, *vice versa*, lowering the amount of conductive carbon and binder additives. If the polymer itself is predominantly insulating and the effect of doping is limited, a significant amount of carbon additive is needed. The amount of carbon additives used in the literature is widespread and varies between 15–80 wt.%. Regarding design principles, the best phenothiazine-based redox polymers allowing for a low amount of conductive carbon additives are the π-conjugated ones. Due to their intrinsic conductivity Godet-Bar and co-workers,[40] as well as Esser and co-workers,[44] could reduce the conductive carbon amount to 25 and 35 wt.%, respectively, for homopolymer P3 and co-polymers P(PT-T2) and P4. However, as mentioned above, processing is also crucial to achieving a uniform distribution of the material and increasing the contact of the redox polymer with the conductive additive. This was demonstrated for X-PVMPT. By optimizing the processing, even X-PVMPT with moderate conductivity could be used with merely 20 wt.% carbon additive, still showing good cyclability.[42] Another remarkable strategy was used by Mecerreyes and co-workers.[45] In this work, discussed in the all-organics chapter above, they used PEO block-*co*-polymers of the investigated phenothiazine-based redox polymer. This way the composites did not need binder, and by using a high surface area carbon additive they could reduce its amount to 15 wt.%. Furthermore, the processability of the polymer was facilitated by the solubility-promoting part of the PEO block, increasing the uniformity of the composite. However, by implementing such additional subunits into the redox polymer, the specific capacity significantly decreases, and the advantages and disadvantages have to be precisely balanced.

## 5.4 Conclusions

To conclude, phenothiazine-based polymers are highly promising for battery applications due to their reversible redox chemistry, among others. Several aspects were discussed in this chapter, including the ability of the phenothiazine unit to undergo mutual π-interactions and its effects on battery performance. A number of high-performing phenothiazine-based polymers have been developed for battery applications, as discussed above. However, there remains room for further developments, for instance by tuning the redox potential, specific capacity or processability of such polymers. This requires the creativity of organic chemists, polymers chemists and electrochemists as well as a detailed knowledge of battery manufacturing.

## References


1. A. Bernthsen, *Ber. Deut. Chem. Ges.*, 1883, **16**, 2896–2904.
2. R. Pummerer and S. Gaßner, *Ber. Deut. Chem. Ges.*, 1913, **46**, 2310–2327.
3. C. O. Okafor, *Dye. Pigment.*, 1985, **6**, 405–415.
4. J.-S. Luo, Z.-Q. Wan and C.-Y. Jia, *Chin. Chem. Lett.*, 2016, **27**, 1304–1318.
5. F. Mietzsch, *Angew. Chem.*, 1954, **66**, 363–371.
6. A. Jaszczyszyn, K. Gąsiorowski, P. Świątek, W. Malinka, K. Cieślik-Boczula, J. Petrus and B. Czarnik-Matusewicz, *Pharmacol. Reports*, 2012, **64**, 16–23.
7. S. P. Massie, *Chem. Rev.*, 1954, **54**, 797–833.
8. C. Bodea and I. Silberg, *Adv. Heterocycl. Chem.*, 1968, **9**, 321–460.
9. F. Kehrmann and L. Diserens, *Ber. Deut. Chem. Ges.*, 1915, **45**, 318–328.
10. L. Michaelis, S. Granick and M. P. Schubert, *J. Am. Chem. Soc.*, 1941, **63**, 351–355.
11. C. M. Murphy, H. Ravner and N. L. Smith, *Ind. Eng. Chem.*, 1950, **42**, 2479–2489.
12. J. P. Billon, *Bull. Soc. Chim. Fr.*, 1960, 1784–1785.
13. J. P. Billon, *Bull. Soc. Chim. Fr.*, 1961, 1923–1929.
14. S. Ergun, C. F. Elliott, A. P. Kaur, S. R. Parkin and S. A. Odom, *Chem. Commun.*, 2014, **50**, 5339–5341.
15. K. A. Narayana, M. D. Casselman, C. F. Elliott, S. Ergun, S. R. Parkin, C. Risko and S. A. Odom, *ChemPhysChem*, 2015, **16**, 1179–1189.
16. M. D. Casselman, A. P. Kaur, K. A. Narayana, C. F. Elliott, C. Risko and S. A. Odom, *Phys. Chem. Chem. Phys.*, 2015, **17**, 6905–6912.
17. C. Zhang, Z. Niu, S. Peng, Y. Ding, L. Zhang, X. Guo, Y. Zhao and G. Yu, *Adv. Mater.*, 2019, **31**, 1901052.
18. N. H. Attanayake, J. A. Kowalski, K. V. Greco, M. D. Casselman, J. D. Milshtein, S. J. Chapman, S. R. Parkin, F. R. Brushett and S. A. Odom, *Chem. Mater.*, 2019, **31**, 4353–4363.
19. W. Klöpffer and W. Willicks, *Die Makromol. Chemie*, 1968, **115**, 156–177.
20. Y. Morishima, Y. Itoh and A. Koyagi, *J. Polym. Sci., Polym. Chem. Ed.*, 1983, **21**, 953–960.
21. J. B. Flanagan, S. Margel, A. J. Bard and F. C. Anson, *J. Am. Chem. Soc.*, 1978, **100**, 4248–4253.
22. Y. Morishima, I. Akihara and S.-I. Nozakura, *J. Polym. Sci., Polym. Lett. Ed.*, 1985, **23**, 651–653.
23. A. A. Golriz, T. Suga, H. Nishide, R. Berger and J. S. Gutmann, *RSC Adv.*, 2015, **5**, 22947–22950.
24. H. Shirakawa, E. J. Louis, A. G. MacDiarmid, C. K. Chiang and A. J. Heeger, *J. Chem. Soc., Chem. Commun.*, 1977, 578–580.
25. D. MacInnes, M. A. Druy, P. J. Nigrey, D. P. Nairns, A. G. MacDiarmid and A. J. Heeger, *J. Chem. Soc., Chem. Commun.*, 1981, 317–319.
26. R. Bittihn, G. Ely, F. Woeffler, H. Münstedt, H. Naarmann and D. Naegele, *Makromol. Chemie. Macromol. Symp.*, 1987, **8**, 51–59.

27. D. Naegele, *Solid State Ionics*, 1988, **28–30**, 983–989.
28. T. Matsunaga, H. Daifuku and T. Kawagoe, *Nippon Kagaku Kaishi*, 1990, **1990**, 1–11.
29. M. S. Whittingham, *Science*, 1976, **192**, 1126–1127.
30. K. Mizushima, P. C. Jones, P. J. Wiseman and J. B. Goodenough, *Mater. Res. Bull.*, 1980, **15**, 783–789.
31. K. Nishio, M. Fujimoto, N. Yoshinaga, N. Furukawa, O. Ando, H. Ono and T. Suzuki, *J. Power Sources*, 1991, **34**, 153–160.
32. K. Nakahara, S. Iwasa, M. Satoh, Y. Morioka, J. Iriyama, M. Suguro and E. Hasegawa, *Chem. Phys. Lett.*, 2002, **359**, 351–354.
33. H. Nishide, S. Iwasa, Y.-J. Pu, T. Suga, K. Nakahara and M. Satoh, *Electrochim. Acta*, 2004, **50**, 827–831.
34. Z. Song and H. Zhou, *Energy Environ. Sci.*, 2013, **6**, 2280–2301.
35. D. Larcher and J.-M. Tarascon, *Nat. Chem.*, 2015, **7**, 19–29.
36. S. Muench, A. Wild, C. Friebe, B. Häupler, T. Janoschka and U. S. Schubert, *Chem. Rev.*, 2016, **116**, 9438–9484.
37. T. B. Schon, B. T. McAllister, P.-F. Li and D. S. Seferos, *Chem. Soc. Rev.*, 2016, **45**, 6345–6404.
38. S. Lee, G. Kwon, K. Ku, K. Yoon, S.-K. Jung, H.-D. Lim and K. Kang, *Adv. Mater.*, 2018, **30**, 1704682.
39. B. Esser, *Org. Mater.*, 2019, **01**, 63–70.
40. T. Godet-Bar, J.-C. Leprêtre, O. Le Bacq, J.-Y. Sanchez, A. Deronzier and A. Pasturel, *Phys. Chem. Chem. Phys.*, 2015, **17**, 25283–25296.
41. M. Kolek, F. Otteny, P. Schmidt, C. Mück-Lichtenfeld, C. Einholz, J. Becking, E. Schleicher, M. Winter, P. Bieker and B. Esser, *Energy Environ. Sci.*, 2017, **10**, 2334–2341.
42. F. Otteny, M. Kolek, J. Becking, M. Winter, P. Bieker and B. Esser, *Adv. Energy Mater.*, 2018, **8**, 1802151.
43. B. M. Peterson, D. Ren, L. Shen, Y.-C. M. Wu, B. Ulgut, G. W. Coates, H. D. Abruña and B. P. Fors, *ACS Appl. Energy Mater.*, 2018, **1**, 3560–3564.
44. P. Acker, L. Rzesny, C. F. N. Marchiori, C. M. Araujo and B. Esser, *Adv. Funct. Mater.*, 2019, **29**, 1–12.
45. N. Casado, D. Mantione, D. Shanmukaraj and D. Mecerreyes, *ChemSusChem*, 2020, **13**, 2464–2470.
46. F. Otteny, G. Studer, M. Kolek, P. Bieker, M. Winter and B. Esser, *ChemSusChem*, 2020, 2232–2238.
47. M. Kertesz, *Chem. – Eur. J.*, 2019, **25**, 400–416.
48. D. Sun, S. V. Rosokha and J. K. Kochi, *J. Am. Chem. Soc.*, 2004, **126**, 1388–1401.
49. J. K. Kochi, R. Rathore and P. Le Maguères, *J. Org. Chem.*, 2000, **65**, 6826–6836.
50. P. Le Maguères, S. V. Lindeman and J. K. Kochi, *J. Chem. Soc. Perkin Trans*, 2001, **2**, 1180–1185.
51. T. Suzuki, W. Nojo, Y. Sakano, R. Katoono, Y. Ishigaki, H. Ohno and K. Fujiwara, *Chem. Lett.*, 2016, **45**, 720–722.

52. W. Nojo, Y. Ishigaki, T. Takeda, T. Akutagawa and T. Suzuki, *Chem. – Eur. J.*, 2019, **25**, 7759–7765.
53. M. E. Speer, M. Kolek, J. J. Jassoy, J. Heine, M. Winter, P. M. Bieker and B. Esser, *Chem. Commun.*, 2015, **51**, 15261–15264.
54. A. Wild, M. Strumpf, B. Häupler, M. D. Hager and U. S. Schubert, *Adv. Energy Mater.*, 2017, **7**, 1601415.
55. F. Otteny, V. Perner, D. Wassy, M. Kolek, P. Bieker, M. Winter and B. Esser, *ACS Sustain. Chem. Eng.*, 2020, **8**, 238–247.
56. H. Dahms, *J. Phys. Chem.*, 1968, **72**, 362–364.
57. I. Ruff and V. J. Friedrich, *J. Phys. Chem.*, 1971, **75**, 3297–3302.
58. Y. Morishima, I. Akihara, H. S. Lim and S. Nozakura, *Macromolecules*, 1987, **20**, 978–983.
59. M. E. Bhosale, S. Chae, J. M. Kim and J.-Y. Choi, *J. Mater. Chem. A*, 2018, **6**, 19885–19911.
60. M. Kolek, F. Otteny, J. Becking, M. Winter, B. Esser and P. Bieker, *Chem. Mater.*, 2018, **30**, 6307–6317.
61. T. J. J. Müller, A. W. Franz, C. S. Barkschat, M. Sailer, K. Meerholz, D. Müller, A. Colsmann and U. Lemmer, *Macromol. Symp.*, 2010, **287**, 1–7.
62. M. Sailer, A. W. Franz and T. J. J. Müller, *Chem. – Eur. J.*, 2008, **14**, 2602–2614.
63. M. Tang, S. Zhu, Z. Liu, C. Jiang, Y. Wu, H. Li, B. Wang, E. Wang, J. Ma and C. Wang, *Chem*, 2018, **4**, 2600–2614.
64. J. J. H. McDowell, *Acta Crystallogr., Sect. B: Struct. Crystallogr. Cryst. Chem.*, 1976, **32**, 5–10.
65. S. V. Rosokha and J. K. Kochi, *J. Am. Chem. Soc.*, 2007, **129**, 3683–3697.
66. Z. Wan, C. Jia, Y. Duan, L. Zhou, Y. Lin and Y. Shi, *J. Mater. Chem.*, 2012, **22**, 25140–25147.
67. W. Wu, J. Yang, J. Hua, J. Tang, L. Zhang, Y. Long and H. Tian, *J. Mater. Chem.*, 2010, **20**, 1772–1779.
68. J. A. Kowalski, M. D. Casselman, A. P. Kaur, J. D. Milshtein, C. F. Elliott, S. Modekrutti, N. H. Attanayake, N. Zhang, S. R. Parkin, C. Risko, F. R. Brushett and S. A. Odom, *J. Mater. Chem. A*, 2017, **5**, 24371–24379.
69. A. Robitaille, A. Perea, D. Bélanger and M. Leclerc, *J. Mater. Chem. A*, 2017, **5**, 18088–18094.
70. P. Poizot, F. Dolhem and J. Gaubicher, *Curr. Opin. Electrochem.*, 2018, **9**, 70–80.
71. C. Friebe, A. Lex-Balducci and U. S. Schubert, *ChemSusChem*, 2019, **12**, 4093–4115.
72. A. E. Lakraychi and P. L. Pasteur, *Chimie Nouvelle*, 2018, **127**, 1–9.
73. B. Flamme, G. Rodriguez Garcia, M. Weil, M. Haddad, P. Phansavath, V. Ratovelomanana-Vidal and A. Chagnes, *Green Chem.*, 2017, **19**, 1828–1849.

CHAPTER 6

# *Carbonyl-containing Polymers for Organic Batteries*

ZHIPING SONG

Hubei Key Laboratory of Electrochemical Power Sources, College of Chemistry and Molecular Sciences, Wuhan University, Wuhan, Hubei 430072, China
Email: zpsong@whu.edu.cn

## 6.1 Introduction to Organic Electrode Materials

In the past decades, the state-of-the-art Li-ion batteries have made great commercial strides in powering our consumer electronics and electric vehicles. However, the ever-growing markets of these fields combined with the emerging development of energy storage stations created greater requirements from rechargeable batteries, for not only electrochemical performance (energy density, power density, cycle life, *etc.*), but also safety, cost, sustainability and even recyclability. In particular, the conventional inorganic cathode materials are now facing both electrochemical performance limitations and concerns about resource sustainability of metal elements including Li, Co and Ni, which may be exhausted in the coming decades if battery technologies remain predominantly relying on them. Therefore, in recent years, scientists have focused increasingly on electrode materials and battery technologies based on abundant elements, such as rechargeable Na/K/Mg/Zn batteries, Li–S batteries and Li–air batteries. Another rising topic is organic electrode materials (OEMs) consisting of elements like C, H, O, N, S, *etc.*, which have shown not only huge potential in electrochemical performance, but also great versatility to various battery chemistries.[1–6]

Polymer Chemistry Series No. 34
Redox Polymers for Energy and Nanomedicine
Edited by Nerea Casado and David Mecerreyes

Published by the Royal Society of Chemistry, www.rsc.org

Unlike transition-metal-based inorganic electrode materials (IEMs, *e.g.*, $LiCoO_2$ and $LiFePO_4$), the electrochemical redox reaction of an OEM is based on the reversible charge state change of the electroactive organic group or moiety, instead of the valence change of the transition metal. Generally, an organic molecule is pristinely in a neutral state, and can be first reduced (in discharge process) to a negatively charged state or oxidized (in charge process) to a positively charged state. Accordingly, it is defined as n-type or p-type material, respectively (see Figure 6.1). While the redox reaction occurs in the electrode, cations ($M^+ = Li^+$, $Na^+$, $K^+$, $Mg^{2+}$, $Zn^{2+}$, *etc.*) or anions ($A^- = ClO_4^-$, $PF_6^-$, $TFSI^-$, *etc.*) of the electrolyte have to transport into the electrode to neutralize the charge of n-type or p-type material, respectively. In the reverse charge or discharge process, the organic molecule is recovered to a neutral state, accompanied by $M^+$ or $A^-$ transferring back into the electrolyte. Thanks to the great structural diversity, the redox potentials of OEMs are widely distributed within 0–4.5 V *vs.* $Li^+/Li$ (see Table 6.1), and thus they can play the role of either cathode or anode, in either aprotic or aqueous electrolytes. A rough rule is that n-type reaction usually occurs below 3 V, while p-type reaction mostly occurs above 3 V. Although there is not a strict definition, the name ''organic batteries'' has been frequently used to catalogue rechargeable batteries involving organic cathode or/and anode materials in recent years, to distinguish them from conventional

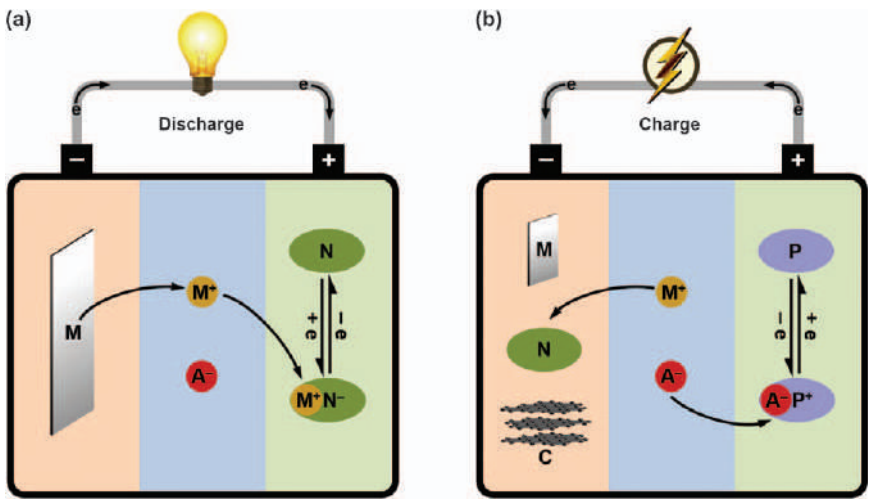


**Figure 6.1** The cell configurations and operating mechanisms of the two main types of organic batteries. M = Li, Na, K, Mg, Zn (for divalent metal, $M^+$ should be modified to $M^{2+}$ with the number halved for the reaction); $A^- = ClO_4^-$, $PF_6^-$, $TFSI^-$ (bis(trifluoromethanesulfonyl)imide), *etc.*; N = n-type molecule in neutral state; P = p-type molecule in neutral state; C = carbon anode material (*e.g.*, graphite for $Li^+$ or hard carbon for $Na^+$). For (b), M plays the role of substrate or current collector rather than active material, which is usually used for laboratory half-cell tests.

**Table 6.1** The typical material, redox mechanism and redox potential of the five types of OEMs.

| Type | Typical material | Redox mechanism | Redox potential[a] |
|---|---|---|---|
| Conducting polymer | Polyaniline (PAni) | 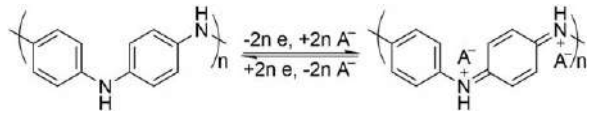 | $3.5 \pm 0.7$ |
| | Polythiophene (PTh) | 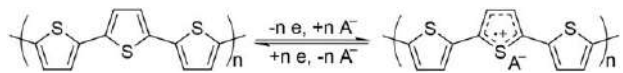 | $3.8 \pm 0.6$ |
| Organodisulfide | Poly(2,5-dimercapto-1,3,4-thiadiazole) (PDMcT) | 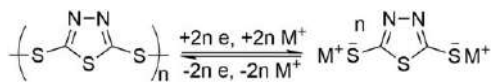 | $2.7 \pm 0.2$ |
| Nitroxyl radical | Poly(2,2,6,6-tetramethylpiperidine-1-oxyl-4-yl methacrylate) (PTMA) | 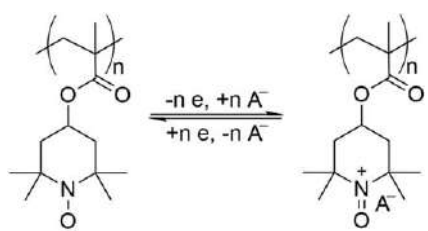 | $3.6 \pm 0.1$ |
| Carbonyl | Anthraquinone (AQ) | 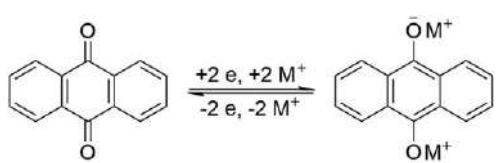 | $2.3 \pm 0.1$ |

| | | | |
|---|---|---|---|
| | 1,4,5,8-Naphthalenetetracarboxylic dianhydride (NTCDA) | 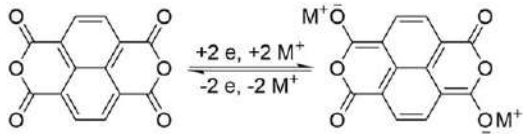 | $2.4 \pm 0.3$ |
| | Terephthalate ($M_2TP$) | 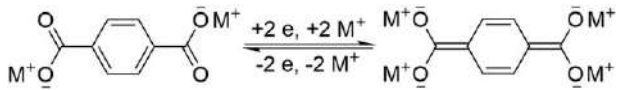 | $0.9 \pm 0.1$ |
| Pyrazine | Triquinoxalinylene (TQY) | 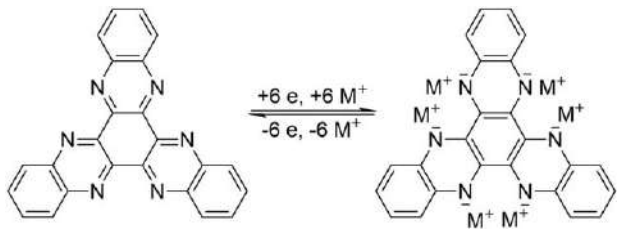 | $1.9 \pm 0.7$ |

[a]The redox potential (V *vs.* $Li^+/Li$, M = Li) is denoted by the average value for evaluating the energy density followed by (using ±) the deviation range for evaluating the shape of the charge–discharge curve (plateau or slope). The value is comprehensively estimated from previous references and the author's experiments, which may remain an error within 0.2 V due to different testing conditions.

batteries containing only IEMs. In most cases, OEMs are tested in the laboratory and may be practically applied as cathodes to couple with metal anodes including Li, Na, K, Mg and Zn.

In fact, OEM is not a fresh concept. Organic molecules have long been known for their electroactivity, and electrochemically investigated as redox couples in solution phase. The first attempt at using them as a solid electrode in batteries can be traced back to 1969 (as early as the birth of the lithium battery), when dichloroisocyanuric acid was applied as a cathode for a primary Li battery.[7] According to the redox mechanisms and roughly ordered by the timeline, we can summarize the history of OEMs into the following five stages (see Table 6.1).

1. Conducting polymer. Since the discovery of conducting polymers, scientists have found that they can achieve high redox activity in addition to the high electronic conductivity. Then they were widely studied as electrode materials for rechargeable batteries since 1981,[8] among which polyaniline (PAni), polypyrrole (PPy) and polythiophene (PTh) are the most famous.[2] In spite of some n-type properties, they are mostly regarded as p-type cathode materials with pseudocapacitive behavior. Unfortunately, their reversible capacity is significantly restricted by the large size of the doping anion ($A^-$), structure instability of overoxidized polymer and possible side reactions between electrolytes and active material (AM) under high potential. Therefore, they can only achieve one-third to one-half of their theoretical capacity ($C_t = 300–400\ mAh\,g^{-1}$, supposing that each monomer unit transfers one electron without taking the weight of $A^-$ into account) and unsatisfactory cycling stability. Then in recent years they have mainly played a subsidiary role in the electrode, to enhance the electronic conductivity and/or immobilization of other AMs.
2. Organodisulfide. The organic S–S bond is known for its redox reversibility, like elemental sulfur cathode, providing a much larger capacity than conducting polymers by the two-electron (2e) reaction. Since 1988, many organic dimers and polymers containing disulfide bonds[9,10] have been reported, among which poly(2,5-dimercapto-1,3,4-thiadiazole) (PDMcT) is the most anticipated one due to its high $C_t$ ($362\ mAh\,g^{-1}$), high discharge voltage (~2.7 V *vs.* $Li^+/Li$) and low cost. However, the reaction kinetics of the single-bond breaking/rebuilding mechanism is intrinsically much slower than the double-bond/single-bond conversion mechanism of other types of OEMs. Furthermore, the discharge products (*e.g.*, $DMcT^{2-}$) are easily dissolved in the aprotic electrolytes, resulting in poor cycling stability. Then, after the intensive researches in 1990s and 2000s, organodisulfides received negligible attentions.
3. Nitroxyl radical. Nitroxyl radicals, especially the 2,2,6,6-tetramethylpiperidine-1-oxyl (TEMPO), have been recognized as one of the few types of stable radicals. Since 2002, a TEMPO-based polymer, namely poly(2,2,6,6-tetramethylpiperidine-1-oxyl-4-yl methacrylate) (PTMA),[11]

has been intensively studied as p-type cathode materials, regardless of its unremarkable n-type behavior like conducting polymers. A great strength of PTMA is the ultrafast charge–discharge ability, benefitting from the rapid electron self-exchange between adjacent TEMPO radicals. However, the limited $C_t$ (*e.g.*, 112 mAh $g^{-1}$ for PTMA) seriously restricts the practical application of nitroxyl radical electrode materials.

4. Carbonyl. The above-mentioned first OEM, dichloroisocyanuric acid,[7] can be assigned to carbonyl compounds although the rechargeability was not tested at that time (1969). Actually, during the next four decades, there has sporadically appeared about 10 reports on carbonyl-based electrode materials for rechargeable batteries, including quinones and dianhydrides. All these early attempts failed to achieve acceptable reversible capacity and cycling performance, which can be ascribed to the serious dissolution, imperfect synthesis (of polymers) and unoptimized test conditions. However, they revealed the huge structural designability and performance possibility of carbonyl compounds as OEMs. Thus, after 2007, marked by the report of dilithium rhodizonate ($Li_2C_6O_6$)[12] and 3,4,9,10-perylentetracarboxylic dianhydride (PTCDA),[13] more and more successful examples appeared with satisfactory electrochemical performance, making carbonyl compounds the mainstream of today's research on OEMs.[14,15]
5. Pyrazine. The redox mechanism of pyrazine compounds is similar to carbonyl compounds, except that the exocyclic C=O bond is replaced by a heterocyclic C=N bond. Since triquinoxalinylene (TQY)[16] was reported as a cathode material in 2011, such types of large π-conjugated molecules containing pyrazine rings have been regarded as an emerging type of OEM because of their high $C_t$ (*e.g.*, 418 mAh $g^{-1}$ for TQY). However, the practical energy density as a cathode is limited by the relatively low redox potential (on average below 2.0 V) and incomplete utilization.

To sum up, carbonyl compounds stand out from various types of OEMs for the following reasons: (1) p-type OEMs including conducting polymers and nitroxyl radicals suffer from low reversible capacity (<150 mAh $g^{-1}$) and can be only applied as cathodes for dual-ion batteries (see Figure 6.1b, in which $A^-$ participates in the cathode reaction but $M^+$ participates in the anode reaction) with less practicability than conventional metal-ion or metal batteries involving only $M^+$ as the charge carrier; (2) among n-type OEMs, carbonyl compounds show the best prospect of comprehensive electrochemical performance including energy density, cycling stability and rate capability; and (3) compared to organodisulfides and pyrazines, there is much more room to design the chemical structure of carbonyl-type OEMs for required voltage, capacity and stability, with lower cost and easier synthesis.

The biggest challenge to n-type OEMs, including carbonyl compounds, is dissolution of AM in the electrolyte (either aprotic or aqueous) during the charge–discharge process. Unlike IEMs, almost all small-molecule OEMs

(or their discharged phases) are soluble in aprotic electrolytes, leading to AM loss from the electrode, self-discharge, shuttle effect, side reactions with the anode and electrode structure degradation that finally result in low capacity utilization, fast capacity fading and poor Coulombic efficiency. Many strategies[5] have been attempted to solve this problem but mostly have failed to achieve satisfactory long-term cycling performance. For example, immobilizing AM in conductive carbon matrix (*e.g.*, mesoporous carbon, carbon nanotube, graphene), preventing dissolved species from migrating to the anode through cation selective separators (solid-state electrolyte or Nafion film), optimizing the electrolyte composition and converting organics to Li/Na salt for lower solubility. Up to now, the most reliable approach has been developing carbonyl-containing polymers (CCPs) with inherent insolubility in the electrolyte. Nevertheless, it is also a huge challenge for the CCPs to simultaneously achieve good cycling stability as well as high energy density. This chapter focuses on this interdisciplinary topic and elaborates the principles, synthesis, performance and applications of CCPs, aiming at attracting more research interests and efforts toward practical organic batteries.

## 6.2 Electroactive Carbonyl Units

To construct a high-performance CCP, the first step is to select an appropriate electroactive carbonyl unit (ECU) as monomer. Generally, the structure is composed of coupled carbonyl groups (usually 2 or 4) adjoining to an aromatic ring core, sometimes with additional substituent groups. The coupled carbonyl groups are reduced to stable dianion products rather than unstable anion radicals for a single carbonyl group, while the conjugacy between carbonyl groups and aromatic ring delocalizing the negative charge, together facilitating the redox reversibility of ECU (see Table 6.1). Based on the above principle, many ECUs have been discovered over the past decades, and the typical examples can be assigned into four types as summarized in Scheme 6.1, including para-quinone, para-quinone derivative, ortho-quinone/diketone and tetracarboxylic diimide. Note that dicarboxylate (see Table 6.1) is not involved herein because it can be only applied as anode in salt form rather than polymer form.

As cathode materials, CCPs are expected to possess as high energy density as possible on the basis of guaranteed cycling stability. Therefore, ECU with higher redox potential and higher $C_t$ is preferred because the former can be well maintained by the polymer and the latter determines the maximum capacity of the polymer. As shown in Scheme 6.1, the approximately average redox potentials range from 2.0 to 3.0 V *vs.* $Li^+$/Li. The different redox potential can be intuitively explained by their relative oxidizability, *e.g.*, BQ (2.7 V) is more oxidative than AQ (2.3 V) but less oxidative than oBQ (3.0 V). To quantifiably understand or compare the redox potential of unfamiliar ECUs, DFT (density functional theory) calculation is a powerful means. One way is by calculating the Gibbs free energy change ($\Delta G$) between the reaction product (the Li/Na salt of dianion) and the

reactant (Li/Na atom and the pristine molecule), and obtaining the voltage ($E$) according to the equation,

$$\Delta G\ (\mathrm{J\,mol^{-1}}) = n \times E\ (\mathrm{V}) \times F\ (\mathrm{C\,mol^{-1}})$$

where $n$ means the electron transfer number and $F$ is the Faraday constant (96 485 $\mathrm{C\,mol^{-1}}$). Another way is to calculate the electron configuration of the molecules and evaluate the redox potential by comparing their LUMO (lowest unoccupied molecular orbital) energy level (eV), according with the rule that lower LUMO means larger electron affinity or higher oxidizability, and thus higher reduction potential. The two methods can be also applied to calculate the voltage plateau of each single-electron process of the whole multielectron discharge reaction and predict the voltage profile. It is worth noting that the above calculations are mostly done at a molecular level and neglect the effect of crystalline structure and electrolyte, and thus they are more suitable to compare a series of analogues.

Theoretical capacity ($C_t$) is another key parameter to evaluate an ECU and even more crucial to energy density due to the wide range from 100 to 500 $\mathrm{mAh\,g^{-1}}$. According to Faraday's law, it can be calculated by the formula,

$$C_t(\mathrm{mAh\,g^{-1}}) = \frac{n \times F(\mathrm{C\,mol^{-1}})}{M_w(\mathrm{g\,mol^{-1}})} = \frac{n \times 96485\ (\mathrm{C})}{M_w(\mathrm{g})} = \frac{n \times 96485(\mathrm{A} \times \mathrm{s})}{M_w(\mathrm{g})}$$

$$= \frac{n \times 96485 \times 1000/3600(\mathrm{mA} \times \mathrm{h})}{M_w(\mathrm{g})} = \frac{26801 \times n}{M_w}(\mathrm{mAh\ g^{-1}})$$

where $M_w$ is the molecular weight of the ECU. Obviously, there are two ways of enlarging $C_t$: increasing the density of usable carbonyl groups or reducing the $M_w$ of ECU. For the former, it is worth noting that not all carbonyl groups are contributive, especially when $n > 2$. For example, only a 2e reaction can reversibly occur for many ECUs containing four carbonyl groups such as TKP, PMDI, NTCDI and PTCDI, because the subsequent 2e reduction (at $<1.0$ V) may lead to unstable product and serious capacity fading. For the latter, extra electroinactive groups are never suggested. Although electron-withdrawing substituents (*e.g.*, –CN, –F, –Cl) are proposed to improve the discharge voltage, the increment (0.05–0.2 V per substituent)[5] can hardly offset the capacity loss.

Besides the voltage and capacity, we should also consider the affordability of the monomer and difficulty of the polymerization for designing a CCP. For instance, although BQ and oBQ have the highest voltages (2.7 V and 3.0 V) and capacity (496 $\mathrm{mAh\,g^{-1}}$) among all ECUs, successful examples of their polymers with ideal structure and energy density have been rarely reported because of their difficult synthesis. In contrast, although with moderate voltage and capacity, AQ- and NTCDI-based polymers have received wider attention because of their cost-effective performance.

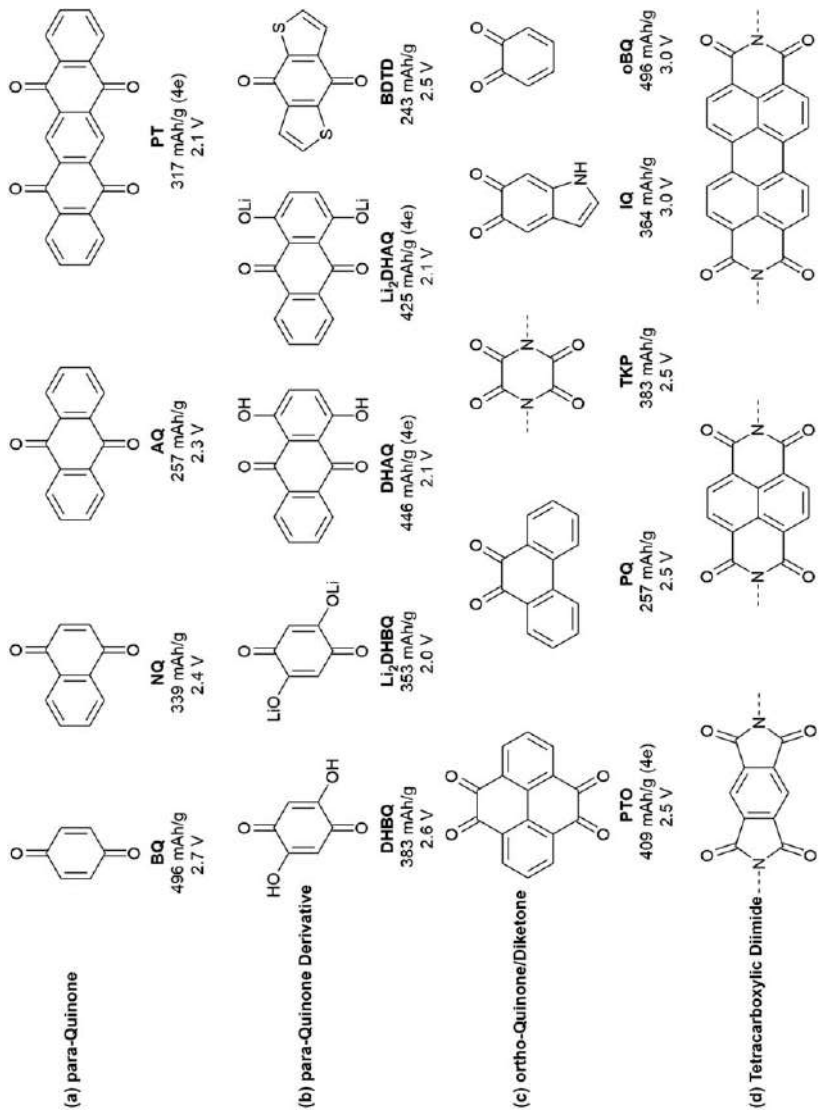
(a) para-Quinone
BQ
496 mAh/g
2.7 V
NQ
339 mAh/g
2.4 V
AQ
257 mAh/g
2.3 V
PT
317 mAh/g (4e)
2.1 V
(b) para-Quinone Derivative
DHBQ
383 mAh/g
2.6 V
Li2DHBQ
353 mAh/g
2.0 V
DHAQ
446 mAh/g (4e)
2.1 V
Li2DHAQ
425 mAh/g (4e)
2.1 V
BDTD
243 mAh/g
2.5 V
(c) ortho-Quinone/Diketone
PTO
409 mAh/g (4e)
2.5 V
PQ
257 mAh/g
2.5 V
TKP
383 mAh/g
2.5 V
IQ
364 mAh/g
3.0 V
oBQ
496 mAh/g
3.0 V
(d) Tetracarboxylic Diimide
PMDI
250 mAh/g
2.1 V
NTCDI
203 mAh/g
2.4 V
PTCDI
138 mAh/g
2.5 V

Keeping in mind the above factors, we can comprehensively recognize the merits and drawbacks of the four series of ECUs, and thus select the most appropriate one for an identified target or discover new ECUs inspired by them.

1. para-Quinone. For ordinary para-quinones, we can find a discipline in which both potential and capacity decline as the aromatic ring extends, *i.e.*, BQ > NQ > AQ. Compared to AQ, PT possesses higher capacity due to doubled carbonyl groups but lower average voltage because of the charge repulsion effect of $PT^{2-}$ intermediate to the subsequent 2e reduction. Taking the availability of the derivative monomer into account, BQ and AQ are more promising for practical use among these four.
2. para-Quinone derivative. Regardless that most substituents make no sense in improving the energy density, the effect of –OH and –OLi substituents are more complicated (see Scheme 6.2). For BQ derivatives, the reversible reaction between $Li_2$DHBQ and $Li_4$DHBQ is similar to that between BQ and $Li_2$BQ, except for a much lower voltage (2.0 *vs.* 2.7 V) due to the electron-donating effect of phenolate anions. The attempt at electrooxidizing $Li_2$DHBQ into 4-carbonyl form (oDHBQ) for doubled capacity failed due to the instability of the fully oxidized structure. The behavior of DHBQ is similar to $Li_2$DHBQ, except that the electron-withdrawing –OH groups can elevate the redox potential while the gradually generated –OLi by ion-exchange counteracts the elevating effect. The released protons are likely reduced into $H_2$ or participate side reactions of electrolyte under low potential (probably $<1.5$ V), which has not been clearly understood yet but is definitely harmful to the cycling stability. For AQ derivatives, $Li_2$DHAQ and DHAQ show similar behavior to the BQ counterpart when the redox reaction occurs between them and the fully reduced product ($Li_4$DHAQ). In contrast, their initial electrooxidation into 4-carbonyl form (oDHAQ) is feasible, and then the $C_t$ is doubled to above 400 mAh $g^{-1}$ by the subsequent 4e

**Scheme 6.1** The typical ECUs to construct polymer electrode materials, together with their theoretical capacity (based on a 2e reaction, or 4e reaction if specified) and roughly average redox potential (*vs.* $Li^+$/Li). (a) para-*Q*uinone: BQ, benzoquinone;[17–23] NQ, naphthoquinone;[24] AQ, anthraquinone;[25–34] PT, 5,7,12,14-pentacenetetrone.[35–37] (b) para-Quinone derivative: DHBQ, 2,5-dihydroxy-1,4-benzoquinone;[38] $Li_2$DHBQ, dilithium salt of 2,5-dihydroxy-1,4-benzoquinone;[39] DHAQ, 1,4-dihydroxyanthraquinone (quinizarin);[40] $Li_2$DHAQ, dilithium salt of 1,4-dihydroxyanthraquinone;[41] BDTD, benzo[1,2-b:4,5-b′]dithiophene-4,8-dione.[42,43] (c) ortho-Quinone/diketone: PTO, pyrene-4,5,9,10-tetraone;[44,45] PQ, phenanthraquinone;[46] TKP, 2,3,5,6-tetraketopiperazine;[47] IQ, 5,6-indolequinone;[48] oBQ, ortho-benzoquinone.[49] (d) Tetracarboxylic diimide: PMDI, pyromellitic diimide;[50–56] NTCDI, 1,4,5,8-naphthalenetetracarboxylic diimide;[52–54,57–61] PTCDI, 3,4,9,10-perylentetracarboxylic diimide.[57,62]

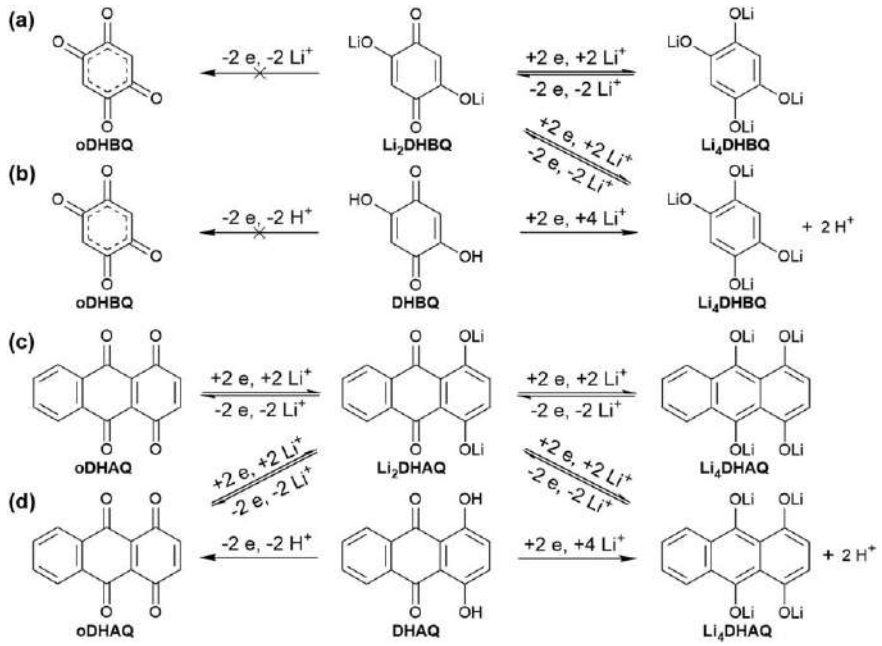


**Scheme 6.2** The proposed electrochemical reactions of –OLi and –OH substituted benzoquinone and anthraquinone: (a) $Li_2$DHBQ, (b) DHBQ, (c) $Li_2$DHAQ, (d) DHAQ. Note that the ion-exchange reaction of –OH to –OLi may only partially occur in a discharge process.

reaction. Although the pristine half-reduced phase ($Li_2$DHAQ and DHAQ) is inappropriate for practical batteries, it encourages us to develop other multicarbonyl ECUs and CCPs with higher capacity. Besides substituting, another orientation of derivatization is introducing a heterocyclic ring (*e.g.*, pyrrole, pyridine, furan, thiophene) into the aromatic structure. For example, BDTD containing a thiophene ring exhibits higher voltage and energy density than AQ.

3. ortho-Quinone/diketone. It was mentioned that oBQ has higher voltage than BQ. In fact, many other ortho-quinones or diketones also exhibit relatively higher voltage. Benefiting from the 4e reaction, PTO is a good candidate for high energy density, but the expensive synthesis of PTO monomer is a serious obstacle to its practical application. As an isomer of AQ, PQ has higher voltage but fewer derivative monomers for polymerization. TKP has an attractive $C_t$ based on 2e reaction, but the synthesis of both TKP monomers and polymers retaining high capacity is challenging. As the oxidized structure of dopamine, IQ may be a cost-effective ECU with high energy density. However, it is difficult to synthesize a fully oxidized polydopamine containing completely IQ units. Instead, IQ and its reduction form (5,6-hydroxyindole) coexist in the product and the abundant hydrogen bonds seriously inhibit the revealing of the expected

electroactivity of IQ at high potential (3.0 V). oBQ faces similar problems that the synthesis of fully oxidized oBQ polymer is difficult and the residual phenol groups is a big hazard to battery stability.

4. Tetracarboxylic diimide. As the derivative structure of tetracarboxylic dianhydride when it is polycondensed with diamine, tetracarboxylic diimide inherits the electrochemical property of the corresponding dianhydride. As the aromatic ring extends, PMDI, NTCDI and PTCDI follow the discipline that the capacity decreases but the voltage increases. Regardless that the 2e reaction limits energy density, they have been widely studied as ECU of various polyimides (PIs) due to their low cost and mass producibility. It should be noted that although many reports claim that they have successfully synthesized PIs based on PTCDI, the characterization results are never as convincing because the poor solubility and strong interlayer interaction make it difficult to form a long polymer chain.

## 6.3 Polymerization Methods

For the selected ECU, choosing the right polymerization method becomes the next challenge. Unlike other function polymers for optoelectronic, semiconductor and medical applications, there is an important restriction for designing CCPs for organic batteries. The desired carbonyl density or $C_t$ requires the electroinactive moiety to link ECUs to be as less as possible. Regardless that dozens of CCPs have been synthesized in the past decades, the polymerization methods never have been summarized in published review papers. Therefore, this topic will be emphasized in this chapter as a guide to design and synthesize novel CCPs.

### 6.3.1 Hanging on a Polymer Chain

Hanging the ECU as a pendant on a robust polymer backbone is a universal polymerization method for various types of ECUs, which can be classified into four specified synthetic routes.

1. Grafting the ECU to a polymer backbone (see Scheme 6.3a, b).[29,44] Typical polymer backbones include poly(4-chloromethylstyrene) (**2**) and polymethacryloyl chloride (**5**) with high reactivity to the ECU monomer to form an ester or amide bond. A drawback of this method is that the grafting yield may be less than 100% if the steric hindrance is significant between adjacent pendants, resulting in reduced $C_t$.
2. Alkenyl polymerization (see Scheme 6.3c, d).[28,42] ECU monomer containing an alkenyl group such as vinyl or allyl can be polymerized by introducing an initiator like AIBN or TBPB, obtaining a robust polymer with slightly reduced $C_t$.
3. Ring-opening metathesis polymerization (ROMP, see Scheme 6.3e).[33] A typical example is derivating two AQ units on a norbornadiene

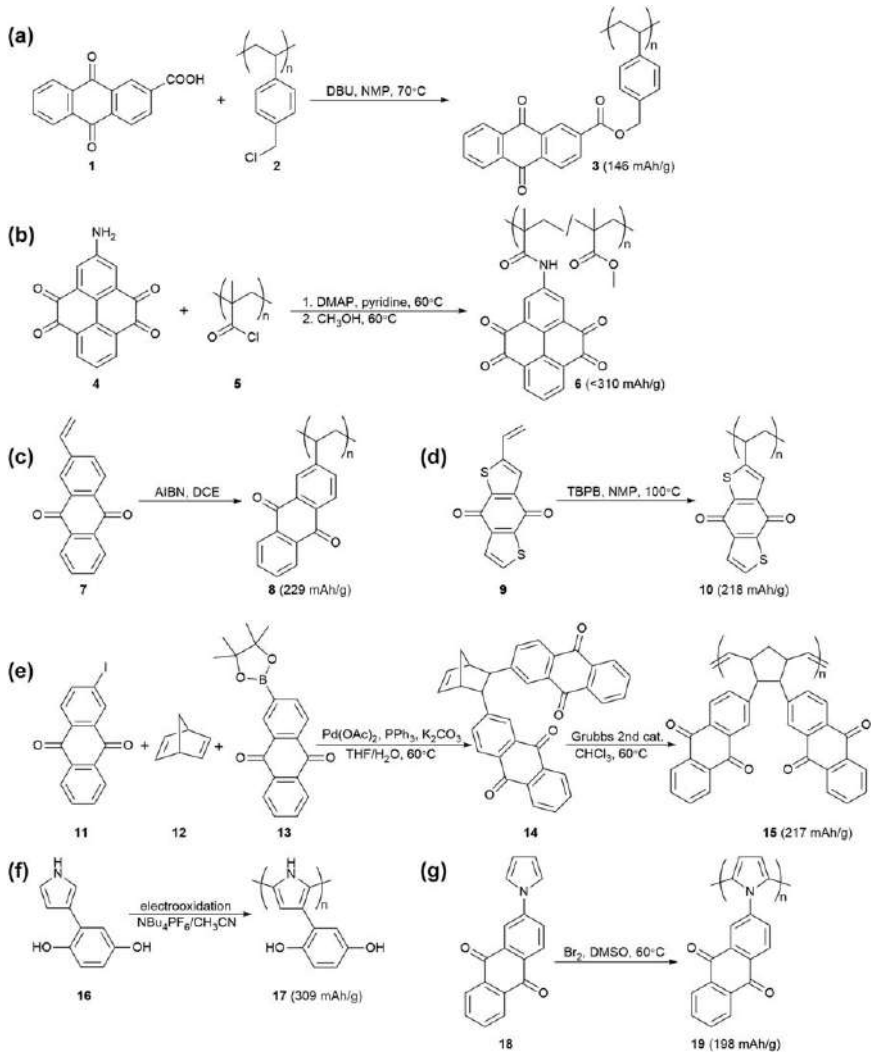


**Scheme 6.3** The typical synthesis routes for hanging the ECU on a polymer chain. The full names of the compounds are listed below: **1**, anthraquinone-2-carboxylic acid;[29] **2**, poly(4-chloromethylstyrene); DBU, 1,8-diazabicyclo [5.4.0]undec-7-ene; **4**, 2-aminopyrene-4,5,9,10-tetraone;[44] **5**, polymethacryloyl chloride; DMAP, 4-dimethylaminopyridine; **7**, 2-vinylanthraquinone; **8**, poly(vinylanthraquinone);[28] AIBN, 2,2′-azobisisobutyronitrile; DCE, 1,2-dichloroethane; **9**, 2-vinylbenzo[1,2-b:4,5-b′]-dithiophene-4,8-dione; **10**, poly(2-vinylbenzo[1,2-b:4,5-b′]-dithiophene-4,8-dione);[42] TBPB, tert-butylperoxybenzoate; **11**, 2-iodoanthraquinone; **12**, 2,5-norbornadiene; **13**, 2-pinacolboronanthraquinone; **14**, dianthraquinone-substituted norbornene; **15**, poly(dianthraquinone-substituted norbornene);[33] **16**, 2-(1-*H*-pyrrol-3-yl)-1,4-hydroquinone; **17**, poly(pyrrol-3-ylhydroquinone);[18] **18**, 2-pyrrol-1-ylanthraquinone; **19**, poly(*N*-anthraquinonyl pyrrole).[34]

molecule by tandem Suzuki coupling reaction, followed by a ROMP using the Grubbs second-generation catalyst.

4. Conducting polymer derivatization (see Scheme 6.3f, g).[18,34] The first step is linking an ECU on a monomer of conducting polymer (*e.g.*, aniline, pyrrole, thiophene), and the next step is chemical or electrochemical oxidative polymerization to form a conducting polymer chain. It is proposed that the high electronic conductivity of the conducting polymer chain may facilitate the redox kinetics of ECUs.

We can find some common merits and drawbacks of the above synthetic routes: (1) the ECU pendant has little effect on the polymerization of backbone and thus the method is universally applicable to different ECUs; (2) the $M_w$ is usually high enough to prevent the dissolution for long cycle life; and (3) the difficult synthesis of the ECU monomer may be a major obstacle for the further development of this method.

### 6.3.2 Linking through a Thioether Group (–S–)

Inspired by the Phillips method to synthesize poly(p-phenylene sulfide) (PPS, a famous engineering plastic) from dichlorobenzene and $Na_2S$, it was proposed linking ECUs through a thioether bond (–S–) in the main chain from the polycondensation of dihalogenated monomer and $Na_2S$ or $Li_2S$ (see Scheme 6.4). Necessary polymerization conditions include strong polar organic solvent such as NMP or DMF, anhydrous sulfide salts and high reaction temperature (>150 °C). The mild reaction in addition to commercial availability of various dihalogenated ECUs provide this method with remarkable mass producibility. However, due the side reactions brought by different monomers, the reaction mechanism and condition are more complicated than expected.

Scheme 6.4a, b[27,32,36] shows the simplest situation that only the polycondensation reaction occurs between equivalent mole of dihalogenated ECU (**20** or **22**) and sulfide salt. Scheme 6.4c, d[39,41] shows the second situation when the monomer contains phenol groups. Besides polycondensation, the acid–base reaction between phenol and sulfide consumes an extra equivalent of sulfide to generate phenolate and $H_2S$. Scheme 6.4e[20] shows the third situation when the monomer has a relatively high redox potential (*e.g.*, BQ). The side reaction between oxidative carbonyl and reductive sulfide consumes extra sulfide (0.5 equivalent for BQ) until the oxidizability declines to the level of elemental S, generating phenolate and elemental S as byproducts. The phenolate-containing product needs to be further oxidized (*e.g.*, by DDQ) to the full-carbonyl state. Scheme 6.4f[22] shows the fourth situation when the monomer is tetrahalogenated, *e.g.*, tetrafluorobenzoquinone was proposed to synthesize a ladder-like CCP with thianthrene moiety. The high conjugacy may be beneficial to improve the electronic conductivity and thus the redox kinetics.

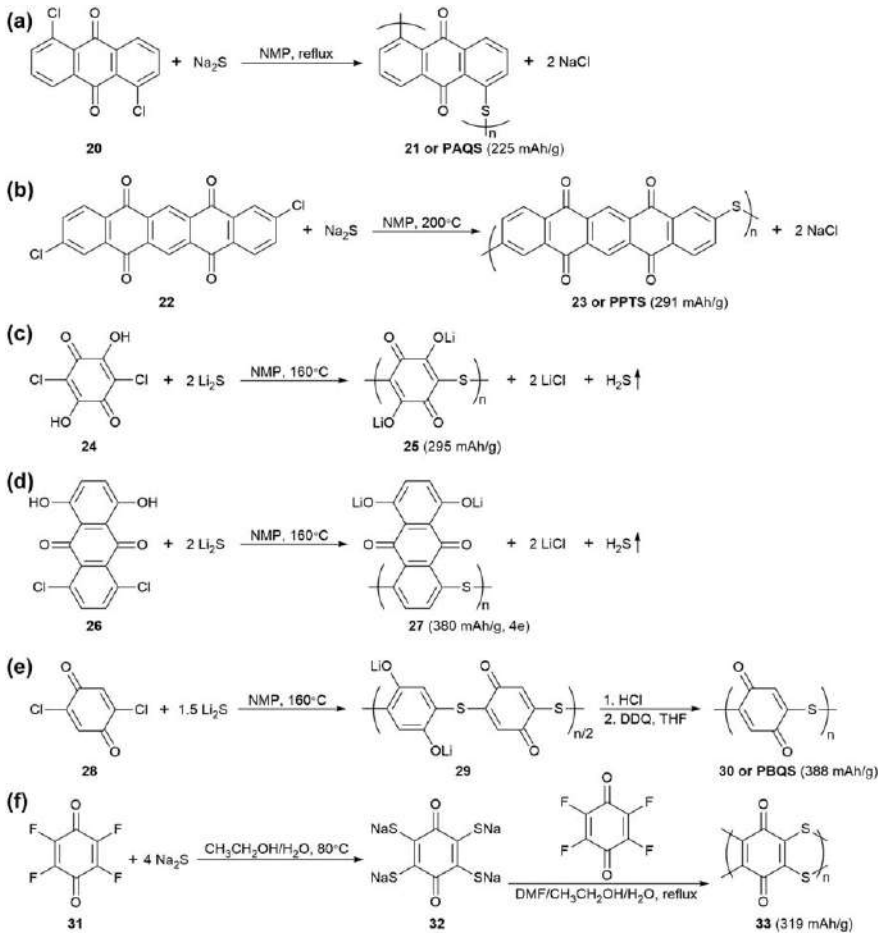


**Scheme 6.4** The typical synthesis routes for linking the carbonyl units through a thioether group. The full names of the compounds are listed below: **20**, 1,5-dichloroanthraquinone; **21**, poly(anthraquinonyl sulfide), PAQS;[27,32] **22**, 2,9-dichloropentacene-5,7,12,14-tetrone; **23**, poly(pentacenetetrone sulfide), PPTS;[36] **24**, chloranilic acid; **25**, dilithium salt of poly(2,5-dihydroxy-*p*-benzoquinonyl sulfide);[39] **26**, 5,8-dichloro-1,4-dihydroxyanthraquinone; **27**, dilithium salt of poly(dihydroxyanthraquinonyl sulfide);[41] **28**, 2,5-dichlorobenzoquinone; **30**, poly(benzoquinonyl sulfide), PBQS;[20] DDQ, 2,3-dicyano-5,6-dichlorobenzoquinone; **31**, fluoranil; **33**, poly(2,3-dithiino-1,4-benzoquinone).[22]

### 6.3.3 Linking through an Imino Group (–NH–)

Inspired by the synthesis of polyaniline, imino group (–NH–) was introduced to connect ECUs in the main chain (see Scheme 6.5). Both chemical or electrochemical oxidation can be applied for the polymerization of quinone monomers containing single or double amino groups. This approach shows several merits including the mild synthesis conditions, little capacity loss

because of the low $M_w$ of –NH–, and possible enhanced electronic conductivity from the polyaniline backbone. However, the precise structure of the polymer product still has some indeterminacy that on one hand the doping degree is unclear, on another hand the side reaction between

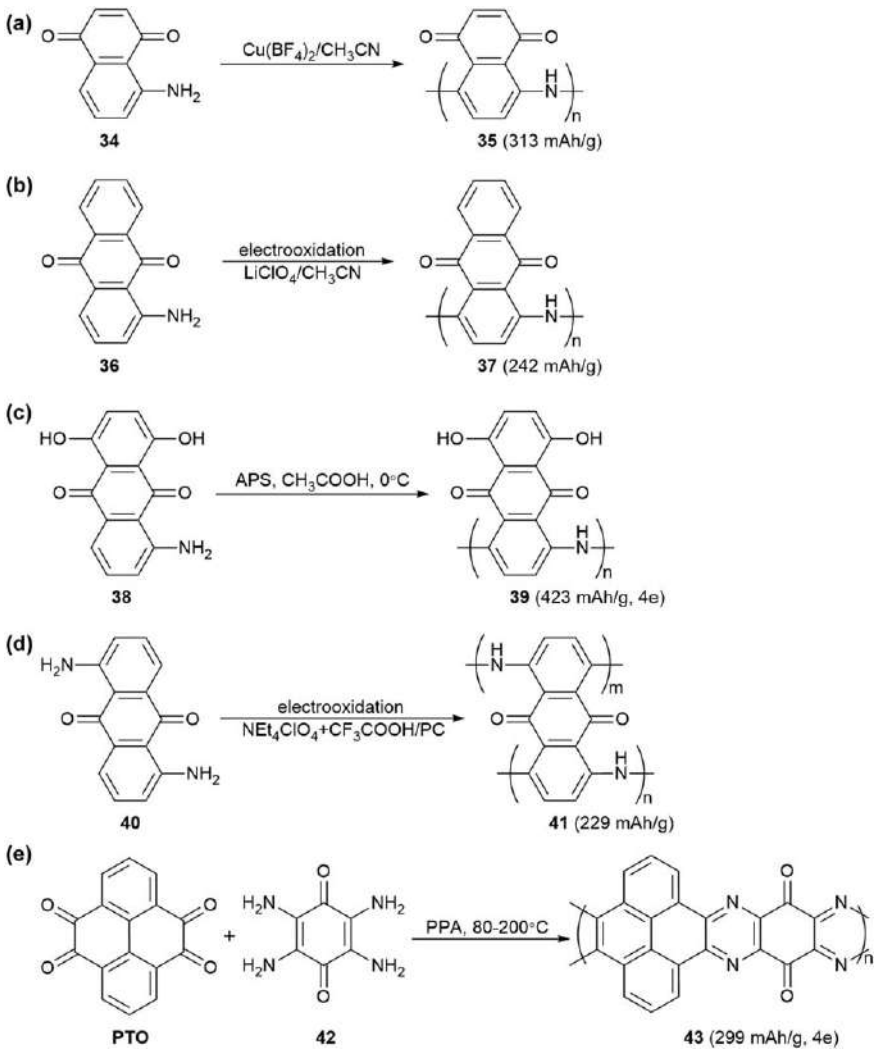


**Scheme 6.5** The typical synthesis routes for linking the carbonyl units through an imino group. The full names of the compounds are listed below: **34**, 5-aminonaphthoquinone; **35**, poly(5-aminonaphthoquinone);[24] **36**, 1-aminoanthraquinone; **37**, poly(1-aminoanthraquinone);[26] **38**, 5-amino-1,4-dihydroxyanthraquinone; **39**, poly(5-amino-1,4-dihydroxyanthraquinone);[40] APS, ammonium persulfate; **40**, 1,5-diaminoanthraquinone; **41**, poly(1,5-diaminoanthraquinone);[25] PC, propylene carbonate; **42**, tetraaminobenzoquinone;[23] PPA, polyphosphoric acid.

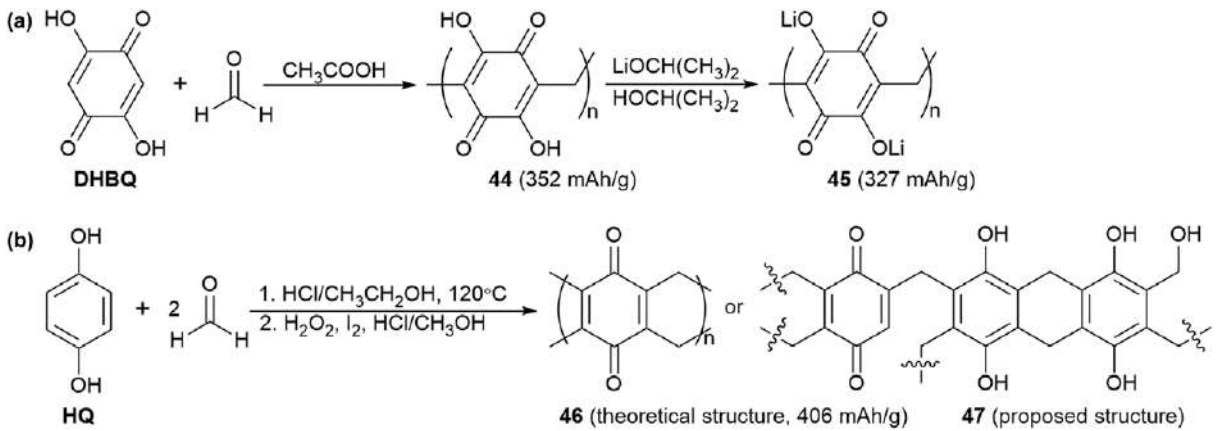


**Scheme 6.6** The typical synthesis routes for linking the carbonyl units through a methylene group. The full names of the compounds are listed below: **44**, poly(2,5-dihydroxybenzoquinone-3,6-methylene);[38] HQ, hydroquinone.[21]

carbonyl and amino to form imine group (=N–) cannot be excluded. Furthermore, how the electroactive polyaniline backbone influence the electrochemical behavior of ECU is to be further studied.

An extended application of the nitrogen-linking approach is synthesizing a ladder-like polymer containing ECUs linked by pyrazine rings. As shown in Scheme 6.5e,[23] ECU containing two pairs of ortho-diamine (*e.g.*, tetraaminobenzoquinone) can react with reagent containing two pairs of orthoquinone (*e.g.*, PTO), generating a polymer containing adjoining quinone and pyrazine moieties. The synergistic electroactivity of carbonyl and pyrazine provide extra n-type capacity and more sloping charge–discharge curves.

### 6.3.4 Linking through a Methylene Group (–$CH_2$–)

Inspired by the synthesis of phenol-formaldehyde resin, methylene group (–$CH_2$–) was introduced to link ECUs in the main chain (see Scheme 6.6). Monomers containing para-diphenol group (*e.g.*, DHBQ[38] and HQ[21]) have been applied for polycondensation with formaldehyde in a mild acidic or alkaline solution. The robust structure, mass producibility and low capacity loss (due to the low $M_w$ of –$CH_2$–) make it a promising approach for practical CCPs. However, there are still some issues to be addressed for expected electrochemical performance. First, the product is actually in fully reduced (with complete diphenol moieties) or half-reduced state (with equivalent diphenol and quinone moieties) of the proposed CCP. It is necessary but difficult to convert them into fully oxidized state by chemical oxidation or Li/Na salts by acid–base neutralization (see Scheme 6.6a),[38] otherwise the electroactivity cannot be sufficiently revealed because of the strong hydrogen-bond interaction and the released protons will harm the cycling stability. Second, the accurate polymer structure at different synthetic conditions should be further studied in regard to all possible moieties including cyclohexane ring, methylol and ether (see Scheme 6.6b).[21] There remains significant room to discover the huge potential of this route in synthesis optimization and structure–performance relationship understanding.

### 6.3.5 Linking through Cross Coupling (C–C)

All the above linking methods will more or less reduce the $C_t$ due to increased $M_w$ from inactive linkers. Fortunately, there is a method of linking ECUs directly by a C–C bond called cross coupling (see Scheme 6.7), which will not decrease but instead increase the $C_t$ slightly. The most popular reaction is Yamamoto coupling[32,43] using $Ni(COD)_2$ as a coupling agent of the dihalogenated ECU (*e.g.*, dichloroanthraquinone). Although the one-step polymerization seems simple, there are two drawbacks to this reaction. First, the expensive $Ni(COD)_2$ must be added at a reactant amount rather than a catalyst amount, making it hard to come out of the laboratory. Second, high-voltage ECUs (approximately $>2.5$ V) will make $Ni(COD)_2$ deactivated by oxidizing the Ni(0) and thus the applicability of the reaction is

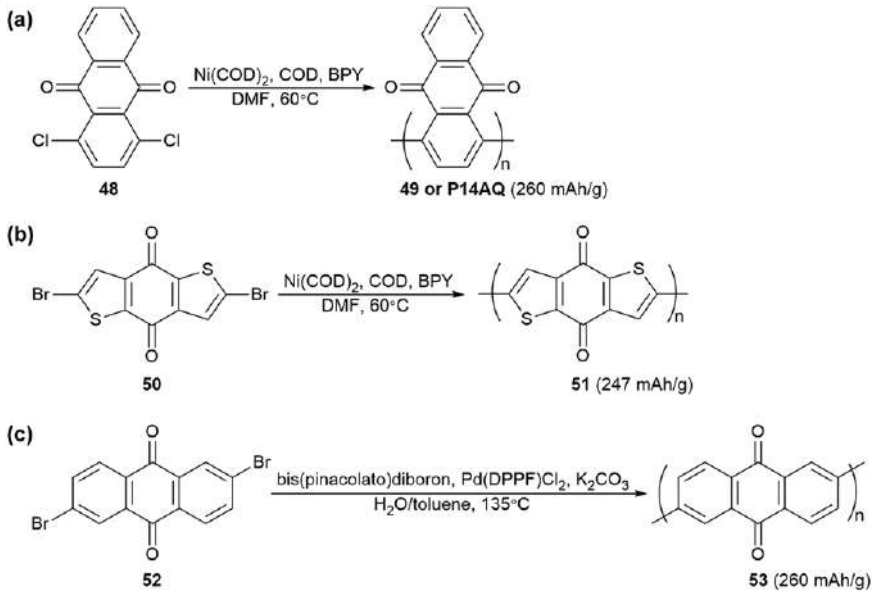


**Scheme 6.7** The typical synthesis routes for linking the carbonyl units through cross coupling. The full names of the compounds are listed below: **48**, 1,4-dichloroanthraquinone; **49**, poly(1,4-anthraquinone), P14AQ;[32] $Ni(COD)_2$, bis(1,5-cyclooctadiene)nickel(0); COD, 1,5-cyclooctadiene; BPY, 2,2′-bipyridine; **50**, 2,6-dibromobenzo[1,2-b:4,5-b′]dithiophene-4,8-dione; **51**, poly(benzo[1,2-b:4,5-b′]dithiophene-4,8-dione-2,6-diyl;[43] **52**, 2,6-dibromoanthraquinone; **53**, poly(2,6-anthraquinone);[31] $Pd(DPPF)Cl_2$, [1,1′-bis(diphenylphosphino)ferrocene]dichloropalladium(II).

limited. Another famous reaction is Suzuki coupling[31] using palladium-catalyst [$Pd(DPPF)Cl_2$] to polymerize dihalogenated ECU in the presence of bis(pinacolato)diboron (similar to the synthesis of **14**, see Scheme 6.3e). It is more cost-effective than Yamamoto coupling but the selectivity on monomer is still to be studied. Of course, there remain many other cross-coupling methods to be discovered for the efficient synthesis of high-capacity CCPs.

### 6.3.6 Carbonyl Protection–Deprotection

As mentioned above, many ECUs, especially those with high oxidizability (*e.g.*, BQ, oBQ, PQ, PTO) are difficult to directly polymerize due to serious side reactions. A carbonyl protection–deprotection strategy is then proposed for the synthesis of some CCPs with high energy density (see Scheme 6.8).[17,19,45,46,49] Usually, there are three steps to this strategy: acylation or etherification, phenolation and reoxidation. Carbonyl or phenol is firstly converted to acetate ester or ether of methyl, benzyl or ethylene glycol (only for ortho-quinone), *etc.* After polymerization, the protecting group is removed to recover phenol, usually in an acidic solution. Then the phenol is

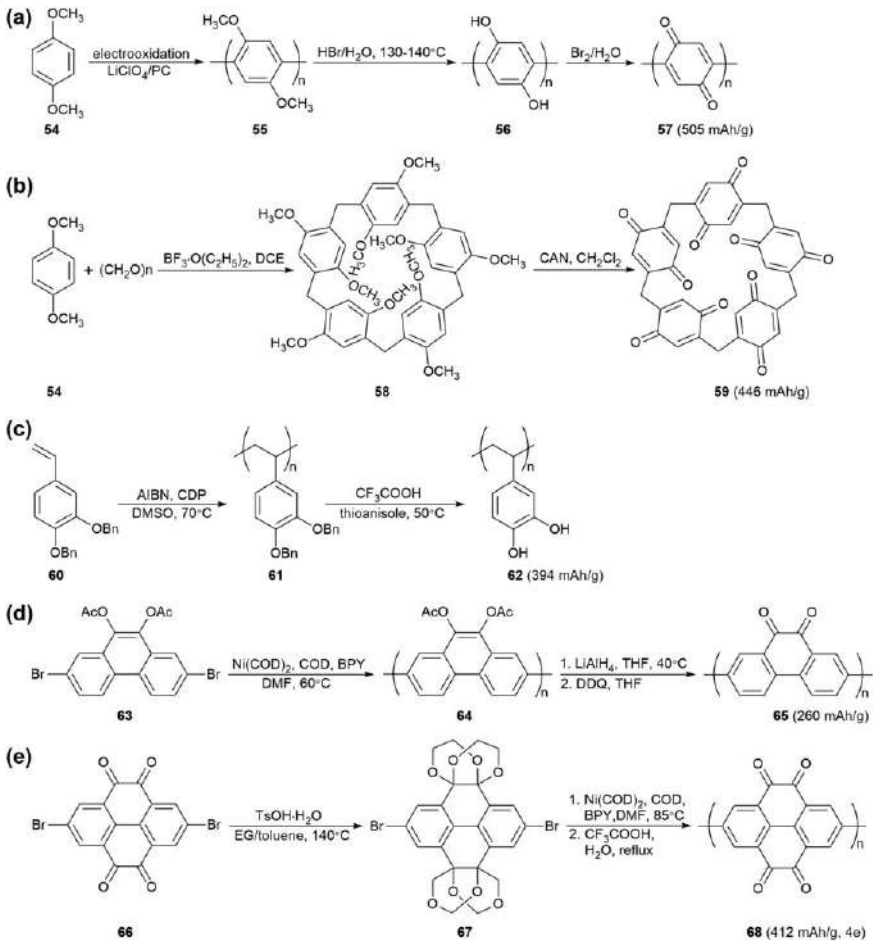


**Scheme 6.8** The typical synthesis routes for carbonyl protection–deprotection. The full names of the compounds are listed below: **54**, 1,4-dimethoxybenzene; **55**, poly(1,4-dimethoxybenzene); **56**, poly(hydroquinone); **57**, poly(benzoquinone);[17] **58**, 1,4-dimethoxypillar[5]arene; **59**, pillar[5]quinone;[19] CAN, ceric ammonium nitrate; **60**, (((4-vinyl-1,2-phenylene)bis(oxy))bis(methylene))dibenzene; **62**, poly(4-vinyl catechol);[49] Bn, benzyl; CDP, 4-cyano-4-(((dodecylthio)carbonothioyl)thio)pentanoic acid; **63**, 9,10-diacetoxy-2,7-dibromophenanthrene; **64**, poly(9,10-diacetoxyphenanthrene); **65**, poly(9,10-phenanthraquinone);[46] **66**, 2,7-dibromopyrene-4,5,9,10-tetraone; **68**, poly(pyrene-4,5,9,10-tetraone);[45] TsOH, p-toluenesulfonic acid; EG, ethylene glycol.

reoxidized into carbonyl by an oxidant such as $Br_2$, ceric ammonium nitrate (CAN), DDQ and $O_2$ in the air. For dimethoxy-containing polymers, the CAN can also simultaneously complete the two steps of phenolation and reoxidation (see Scheme 6.8b).[19] The carbonyl protection–deprotection strategy will increase the complexity of synthesis. An even greater problem is

incomplete phenolation and reoxidation due to the poor solubility or swellability of the polymer in the required solvent.

### 6.3.7 Aldehyde–Amino Polycondensation for Covalent Organic Frameworks

The covalent organic framework (COF) is an emerging topic receiving wide interest in many fields including gas storage and separation, heterogeneous catalysis, sensing, drug delivery and energy storage. The concept of COF, especially that with a 2D crystalline structure, has been also introduced to OEMs (especially CCPs) since 2013.[30] It is assumed that the electronic conduction and ionic diffusion can be facilitated by the high surface area, large planar π-conjugated systems and uniform nanometer pores. The most popular synthetic route is an aldehyde-amino polycondensation between diamino-substituted ECU and triformylphloroglucinol (TFP) as a triple linker in a molar ratio of 3 : 2 (see Scheme 6.9). Such a cross-linking method is beneficial to obtaining polymers with insolubility and higher surface area (typically several hundred $m^2 g^{-1}$) compared to previous linear polymers. Unfortunately, the successful synthesis of uniformly hexagonal COF structure still needs to be confirmed. In regard to the current low capacity utilization and the high cost of TFP, the practical advantage of COF should be further proved. The aldehyde–amino

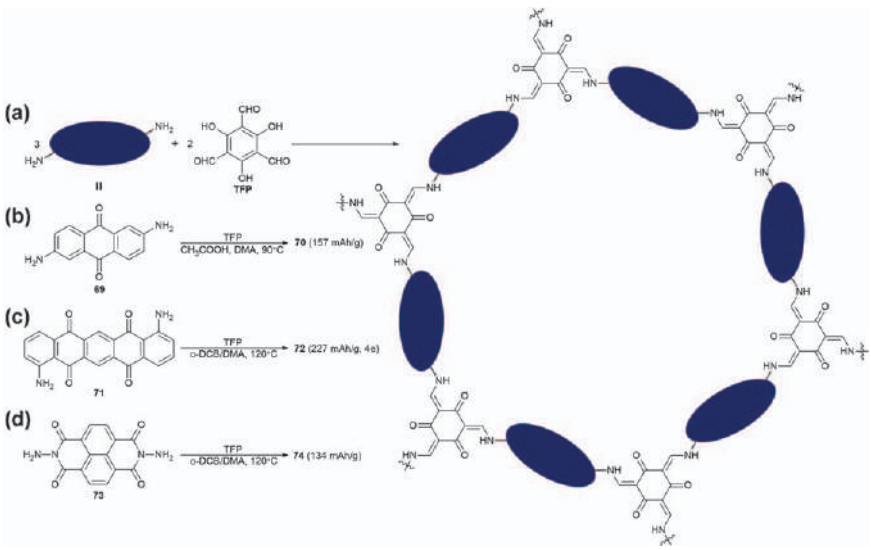


**Scheme 6.9** The typical synthesis routes for aldehyde-amino polycondensation to form COFs. The full names of the compounds are listed below: TFP, 1,3,5-triformylphloroglucinol; **69**, 2,6-diaminoanthraquinone;[30] DMA, dimethylacetamide; **71**, 1,8-diaminopentacene-5,7,12,14-teraone;[37] o-DCB, 1,2-dichlorobenzene; **73**, *N,N′*-diamino-1,4,5,8-naphthalenetetracarboxylic diimide.[58]

polycondensation may be migrated as a simple but effective synthetic route for other CCPs.

### 6.3.8 Anhydride–Aamino Polycondensation for Polyimides

Polyimide (PI) is a famous engineering plastic with high mechanical strength and thermal stability. Little attention has been focused on the electrochemistry of PI until 2010.[50–52] PI is mainly synthesized from the polycondensation of dianhydride and diamine or multiamine, and thus retains the essential structure and electroactivity of dianhydride monomers in a corresponding tetracarboxylic diimide form (see Scheme 6.10). The detailed synthetic route contains two steps: polymerization in strong polar solvent (typically NMP) to generate polyamic acid and heat treatment (>300 °C) for full imidization. The different combinations of abundant anhydride and amine monomers lead to a variety of polymers named in the manner of PI-anhydride-amine.

PMDA and NTCDA are the most commonly used dianhydrides, showing advantages in capacity and voltage, respectively. As previously mentioned, PTCDA is not an appropriate monomer for the synthesis of PI due to its poor solubility and the product is likely to be diimide monomer, dimer and so on. BPDA and OPDA with phthalic anhydride moiety are also electroactive, but have received little attention due to the inappropriate redox potential (~1.5 V) for either cathode or anode.

Amine plays a role of linker of ECUs in PI, which shows little effect on the voltage but much on the capacity and reaction kinetics. The most popular ones are damines such as hydrazine, ethylene diamine and phenylenediamine. Electroactive damines including diaminoanthraquinone (**69**[53] and **78**[54]) are also introduced for higher $C_t$. Along with the rise of the COF concept, damines were extended to triamines (*e.g.*, melamine[56]) or tetraamines (*e.g.*, tetraaminobenzoquinone[55]), and then the linear PIs were extended to cross-linked PIs with hexagonal or tetragonal networks, respectively. However, as discussed in Section 6.3.7, the COF-type PIs need to prove their exact structure and actual superiorities to linear ones (note that the improved performance of PI-PMDA-42[55] mainly comes from the electroactive tetraaminobenzoquinone rather than the COF structure).

### 6.3.9 Other Methods

Besides the above classified routes, there have been sporadic reports on other polymerization methods as summarized in Scheme 6.11. For the synthesis of **83** based on TKP unit (Scheme 6.11a),[47] an acyclic diene metathesis (ADMET) polymerization was selected. It is similar to the ROMP reaction (see Scheme 6.3e) but is different as implied by the generation of ethylene as a by-product. The synthesis of polydopamine (**85**, Scheme 6.11b)[48] is similar to that of conducting polymers (*e.g.*, PAni), but it simultaneously completes the indole ring formation, partial oxidation of

catechol and the cross coupling. As previously discussed in Section 6.2, the existence of abundant phenol groups and hydrogen bonds restricts the full utilization of IQ units. Therefore, the structure stability and synthesis optimization of fully oxidized polydopamine should be further studied. Scheme 6.11c shows a Stille coupling method for the synthesis of NTCDI-based polymer (**88**).[59] The difference with other cross-coupling reactions is the introduction of vinyl between two ECUs.

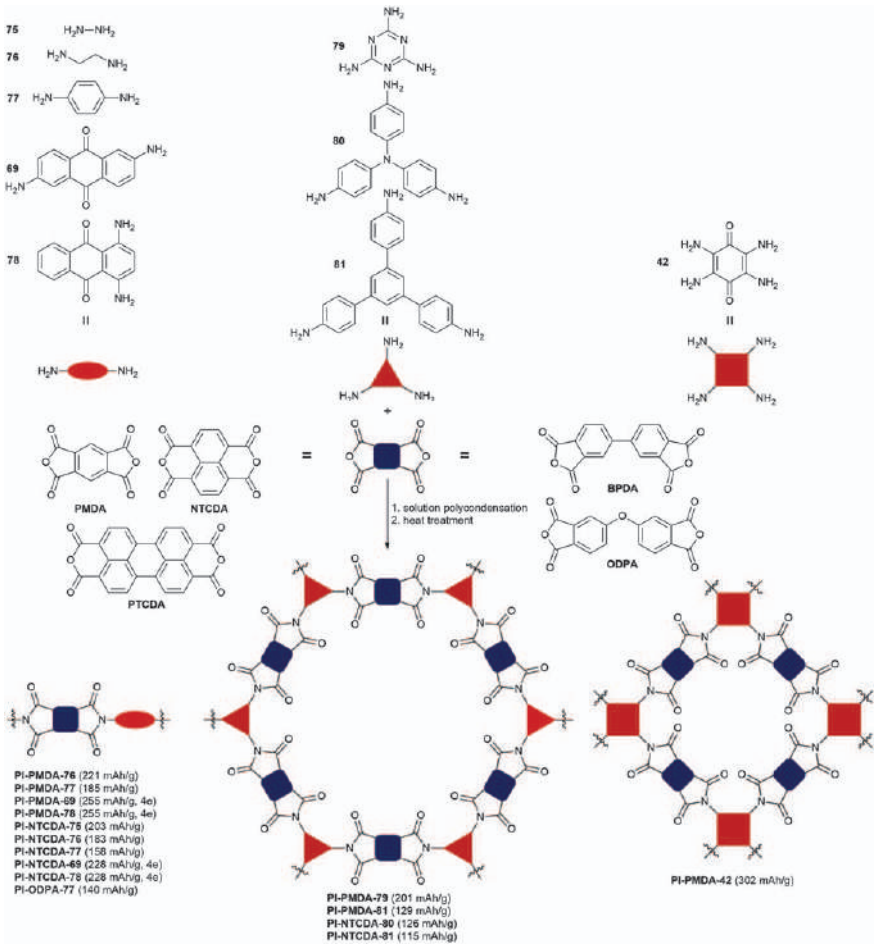


**Scheme 6.10** The typical synthesis routes for anhydride-amino polycondensation to form polyimides. The full names of the compounds are listed below: **75**, hydrazine;[52] **76**, ethylene diamine;[52,62] **77**, *p*-phenylenediamine;[50–52] **78**, 1,4-diaminoanthraquinone;[54] **79**, melamine;[56] **80**, tris(4-aminophenyl) amine;[60] **81**, 1,3,5-tris(4-aminophenyl)-benzene;[57] PMDA, pyromellitic dianhydride;[50–54,56] NTCDA, 1,4,5,8-naphthalenetetracarboxylic dianhydride;[52–54,57,60] PTCDA, 3,4,9,10-perylenetetracarboxylic dianhydride;[57,62] BPDA, 3,3′,4,4′-biphenyltetracarboxylic dianhydride;[63] ODPA, 4,4′-oxydiphthalic anhydride.[50,51]

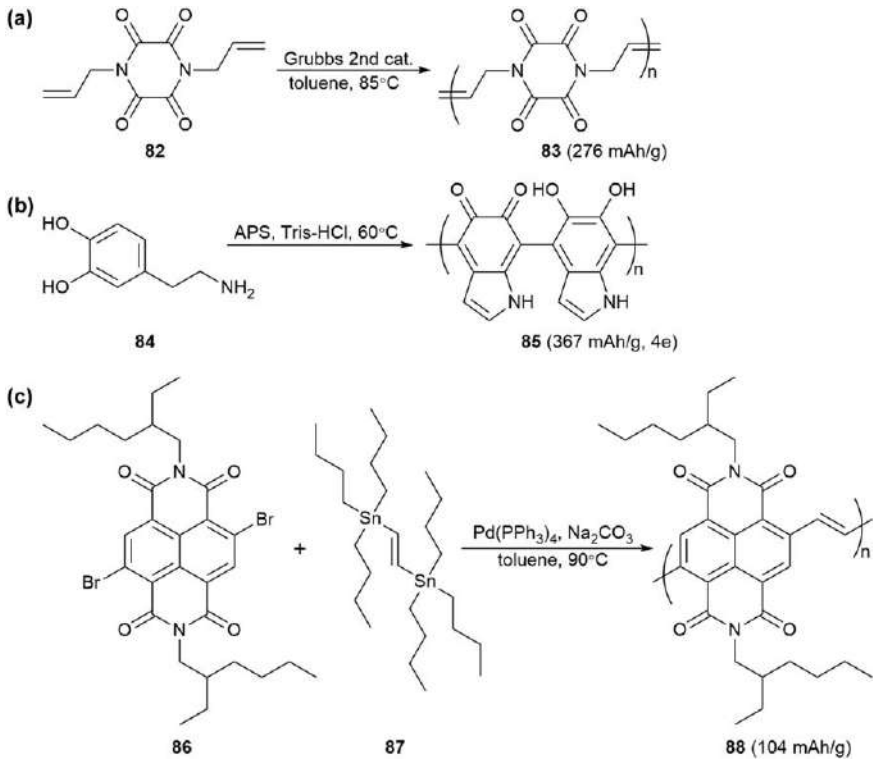


**Scheme 6.11** Some other synthesis routes for CCPs. The full names of the compounds are listed below: **82**, *N,N′*-diallyl-2,3,5,6-tetraketopiperazine;[47] **84**, dopamine; **85**, polydopamine;[48] Tris, tris(hydroxymethyl)aminomethane; **86**, 2,6-dibromo-*N,N′*-bis(2-ethylhexyl)-1,4,5,8-naphthalene diimide; **87**, bisbutylstannylethylene; **88**, poly[ethylene-*N,N′*-bis(2-ethylhexyl)-1,4,5,8-naphthalene diimide].[59]

## 6.3.10 Summary of Synthesis

The above elaborations and schemes summarize a majority of the polymerization methods and typical examples reported in recent years. A variety of novel CCPs can be developed by replacing the ECU and optimizing the conditions for each polymerization reaction. However, it must be clearly noted that many CCPs have not been rigorously characterized because of their insolubility in most organic solvents and the fact that most researchers in this field are battery experts rather than organic or polymer chemists. It is suggested to gather the structure information as much as possible because this is the basis for understanding the structure–performance relationship and further optimization of the synthesis. First, there is more or less a calculated capacity gap between the practical and ideal structure, on account of side reactions related to carbonyl, incomplete oxidation of phenol or phenolate, residual organic solvent or water in the polymer matrix, and other

impurities. Second, many polymerization products are, in fact, partially or fully oligomers, which is an important factor of the unsatisfactory cycling stability. Another point to be kept in mind is that we must evaluate the cost performance of each synthetic route, even in the basic research stage. It is suggested to use commercially available or easily synthesized monomers, adopt polymerization methods with one or two steps, mild conditions, and inexpensive reagents and catalyst, and avoid column chromatography throughout the entire process. CCPs with low $C_t$ (<100 mAh $g^{-1}$) are not recommended to be investigated unless they present unique superiority in other aspects such as high electronic conductivity[61] and film-forming ability.[32]

## 6.4 Electrochemical Performance

The successful synthesis of a CCP is just the beginning of achieving high battery performance. A rechargeable battery is a complicated system in which the cathode, anode, electrolyte, separator and even the current collector can influence the electrochemical performance. Generally, a novel CCP is at first evaluated in a half-cell with excess Li or Na metal anode, as a reference for predicting its suitability and performance in other novel battery systems (see Section 6.5). Table 6.2 summarizes the electrochemical parameters of typical CCPs listed in Schemes 6.3–6.11. Some materials are excluded because they were tested as a supercapacitor electrode, or the electrochemical behavior is distant from that of carbonyl due to inappropriate test conditions. Since the research into OEMs is still at a primary stage, there is a wide variety of test conditions for reported CCPs. This makes the comparison between different literatures less rigorous, because the influence of electrode composition and electrolyte on the electrochemical performance is much more remarkable than that for IEMs, and sometimes even as important as the synthesis of the CCP. Nevertheless, we can still obtain a general impression of the actual and prospective electrochemical performances of each CCP after understanding how it is affected by the exact polymer structure and different test conditions.

1. Actual carbonyl density. From Table 6.2 we can see that only a few CCPs can achieve a reversible capacity close to the $C_t$. An important reason for this is the gap between the actual and ideal polymer structure. For example, the $C_t$ of PBQS (see Scheme 6.4e)[20] is as high as 388 mAh $g^{-1}$, but the capacity calculated from the elemental analysis data (O content from carbonyl and phenol) is reduced to 307 mAh $g^{-1}$, which is closer to the measured reversible capacity of 275 mAh $g^{-1}$. The structure difference is sometimes as large as reducing the capacity by one-half or two-thirds, especially for BQ-based polymers with high $C_t$ but difficult synthesis.
2. Residual phenol groups. The influence of phenol groups is complicated. On one hand, they can be partially or completely electrooxidized to carbonyl in the charge process and contribute to the reversible

**Table 6.2** Electrochemical parameters of various CCPs listed in Schemes 6.3–6.11.

| Carbonyl unit | Polymer material | Electrode composition[a] | Electrolyte[b] | Voltage[cd] (average ± deviation) | Capacity[d] (reversible/ theoretical) | Cycling performance[d] (reversible capacity@current rate[e], capacity retention@cycle number) | Rate performance[d] (capacity retention@high *vs.* low current rate[e]) | Ref. |
|---|---|---|---|---|---|---|---|---|
| BQ | 30 or PBQS | AM : KB : PTFE = 6 : 3 : 1 | 1 M LiTFSI/ DOL + DME | 2.7 ± 0.6 V | 275/388 mAh $g^{-1}$ | 246 mAh $g^{-1}$@500 mA $g^{-1}$, 86%@1000 | 72%@5000 *vs.* 50 mA $g^{-1}$ | 20 |
| | 33 | AM : CNT : PVDF = 3 : 5 : 2 | 1 M LiTFSI/ DOL + DME | 2.6 ± 0.7 V | 237/319 mAh $g^{-1}$ | 196 mAh $g^{-1}$@1000 mA $g^{-1}$, 86%@500 | 76%@1000 *vs.* 20 mA $g^{-1}$ | 22 |
| | 43 | AM : rGO : PVDF = 6 : 3 : 1 | 1 M $NaPF_6$/ DME | 2.1 ± 1.1 V *vs.* $Na^+$/Na | 245/299 mAh $g^{-1}$ | 210 mAh $g^{-1}$@1000 mA $g^{-1}$, 98%@1400 | 58%@8000 *vs.* 200 mA $g^{-1}$ | 23 |
| | 47 | AM : PX : PTFE = 8 : 9 : 3 | 1 M LiTFSI/ DOL + DME | 2.3 ± 0.8 V | 149/406 mAh $g^{-1}$ | 149 mAh $g^{-1}$@50 mA $g^{-1}$, 98%@200 | 40%@1620 *vs.* 20 mA $g^{-1}$ | 21 |
| | 57 | AM : AB : C/PTFE = 4 : 4 : 2 | 1.5 M $LiAsF_6$/ THF | 2.8 ± 0.4 V | 144/505 mAh $g^{-1}$ | 144 mAh $g^{-1}$@5 mA $g^{-1}$, 33%@7 | | 17 |
| NQ | 35 | AM : CB : PIB = 49 : 49 : 2 | 0.75 M $LiClO_4$/ $CH_3CN$ | 2.5 ± 0.5 V | 250/313 mAh $g^{-1}$ | 250 mAh $g^{-1}$@20 mA $g^{-1}$, 80%@17 | | 24 |
| AQ | 3 | AM : VGCF : PVDF = 1 : 8 : 1 | 0.1 M NaCl/ $H_2O$ (pH = 13) | −0.7 ± 0.1 V *vs.* Ag/AgCl | 62/146 mAh $g^{-1}$ | 62 mA $g^{-1}$, 72%@50 | 88%@75 *vs.* 3 C | 29 |
| | 8 | AM Film (80 nm thick) | 30 wt% NaOH/ $H_2O$ | −0.8 ± 0.1 V *vs.* Ag/AgCl | 217/229 mAh $g^{-1}$ | 217 mAh $g^{-1}$@5000 mA $g^{-1}$, 91%@300 | | 28 |
| | 15 | AM Film (50 nm thick) | 10 M NaOH/ $H_2O$ | −0.8 ± 0.1 V *vs.* Ag/AgCl | 210/217 mAh $g^{-1}$ | 210 mAh $g^{-1}$, 95%@500 | 97%@600 *vs.* 10 C | 33 |
| | 21 or PAQS | AM : KB : PTFE = 6 : 3 : 1 | 1 M LiTFSI/ DOL + DME | 2.2 ± 0.2 V | 214/225 mAh $g^{-1}$ | 214 mAh $g^{-1}$@45 mA $g^{-1}$, 98%@100 | | 32 |
| | 49 or P14AQ | AM : KB : PTFE = 6 : 3 : 1 | 1 M LiTFSI/ DOL + DME | 2.2 ± 0.2 V | 263/260 mAh $g^{-1}$ | 248 mAh $g^{-1}$@260 mA $g^{-1}$, 98%@1000 | 69%@5200 *vs.* 52 mA $g^{-1}$ | 32 |
| PT | 23 or PPTS | AM : SP : PVDF = 4 : 5 : 1 | 1 M $NaPF_6$/ DME | 1.6 ± 0.8 V *vs.* $Na^+$/Na | 285/291 mAh $g^{-1}$ | 252 mAh $g^{-1}$@1000 mA $g^{-1}$, 91%@2000 | 86%@2000 *vs.* 100 mA $g^{-1}$ | 36 |
| | 72 | AM : SP : PVDF = 5 : 4 : 1 | 1 M $NaPF_6$/ DME | 1.6 ± 0.8 V *vs.* $Na^+$/Na | 168/227 mAh $g^{-1}$ | 168 mAh $g^{-1}$@100 mA $g^{-1}$, 86%@1000 | 72%@5000 *vs.* 100 mA $g^{-1}$ | 37 |
| DHBQ | 44 | AM : AB : PTFE = 13 : 10 : 2 | 1 M $LiPF_6$/ EC + DMC | 2.3 ± 0.6 V | 150/352 mAh $g^{-1}$ | 135 mAh $g^{-1}$@0.5 C, 78%@100 | | 38 |
| $Li_2$DHBQ | 25 | AM : KB : PTFE = 6 : 3 : 1 | 1 M LiTFSI/ DOL + DME | 2.0 ± 0.3 V | 268/295 mAh $g^{-1}$ | 239 mAh $g^{-1}$@500 mA $g^{-1}$, 90%@1500 | 83%@5000 *vs.* 50 mA $g^{-1}$ | 39 |

**Table 6.2** (*Continued*)

| Carbonyl unit | Polymer material | Electrode composition[a] | Electrolyte[b] | Voltage[cd] (average ± deviation) | Capacity[d] (reversible/ theoretical) | Cycling performance[d] (reversible capacity@current rate[e], capacity retention@cycle number) | Rate performance[d] (capacity retention@high *vs.* low current rate[e]) | Ref. |
|---|---|---|---|---|---|---|---|---|
| DHAQ | 39 | AM : AB : PVDF = 5 : 4 : 1 | 1 M $LiPF_6$/ EC + DEC | 2.3 ± 0.8 V | 143/423 mAh $g^{-1}$ | 143 mAh $g^{-1}$@400 mA $g^{-1}$, 90%@50 | 68%@1400 *vs.* 350 mA $g^{-1}$ | 40 |
| $Li_2$DHAQ | 27 | AM : SP : PTFE = 9 : 9 : 2 | 1 M LiTFSI/ DOL + DME | 2.5 ± 0.9 V | 330/380 mAh $g^{-1}$ | 330 mAh $g^{-1}$@0.5 C, 80%@400 | 81%@10 *vs.* 0.25 C | 41 |
| BDTD | 10 | AM : CNT : PVDF = 1 : 8 : 1 | 1 M $LiClO_4$/ EC + DMC | 2.2 ± 0.3 V | 230/218 mAh $g^{-1}$ | 230 mAh $g^{-1}$@1090 mA $g^{-1}$, 49%@100 | | 42 |
| | 51 | AM : CNT : SP : PTFE = 49 : 11 : 30 : 10 | 1 M $LiClO_4$/ DOL + DME | 2.5 ± 0.3 V | 214/247 mAh $g^{-1}$ | 180 mAh $g^{-1}$@1071 mA $g^{-1}$, 96%@250 | 88%@2142 *vs.* 214 mA $g^{-1}$ | 43 |
| PTO | 6[f] | AM : AB : PVDF = 3 : 8 : 2 | LiTFSI/G4 (1/1, m/m) | 2.5 ± 0.5 V | 231/262 mAh $g^{-1}$ | 231 mAh $g^{-1}$@1 C, 83%@500 | 90%@30 *vs.* 1 C | 44 |
| | 68 | AM : CNT : PVDF = 3 : 5 : 2 | 1 M LiTFSI/ DOL + DME | 2.5 ± 0.5 V | 215/412 mAh $g^{-1}$ | 215 mAh $g^{-1}$@20 mA $g^{-1}$, 75%@100 | 70%@100 *vs.* 20 mA $g^{-1}$ | 45 |
| PQ | 65 | AM : rGO : PX : PTFE = 47 : 13 : 30 : 10 | 1 M LiTFSI/ DOL + DME | 2.5 ± 0.4 V | 200/260 mAh $g^{-1}$ | 200 mAh $g^{-1}$@50 mA $g^{-1}$, 91%@500 | 51%@5000 *vs.* 50 mA $g^{-1}$ | 46 |
| TKP | 83 | AM : KB = 7 : 3 | 1 M $LiPF_6$/ EC + DMC | 2.4 ± 0.1 V | 160/276 mAh $g^{-1}$ | 160 mAh $g^{-1}$@69 mA $g^{-1}$, 69%@10 | | 47 |
| IQ | 85[g] | AM : AB = 8 : 2 | 1 M $LiPF_6$/ EC + DMC | 0.8 ± 0.8 V | 1818/367 mAh $g^{-1}$ | 1510 mAh $g^{-1}$@500 mA $g^{-1}$, 93%@580 | 62%@1600 *vs.* 50 mA $g^{-1}$ | 48 |
| oBQ | 62 | AM : CNT = 2 : 8 | 1.5 M LiTFSI/ G4 + EMC | 3.0 ± 1.0 V | 350/394 mAh $g^{-1}$ | 290 mAh $g^{-1}$@1860 mA $g^{-1}$, 99%@530 | 71%@3720 *vs.* 74 mA $g^{-1}$ | 49 |
| PMDI | PI-PMDA-76 | AM : PX : PTFE = 6 : 3 : 1 | 1 M LiTFSI/ DOL + DME | 2.1 ± 0.2 V | 220/221 mAh $g^{-1}$ | 206 mAh $g^{-1}$@89 mA $g^{-1}$, 83%@100 | | 52 |
| | PI-PMDA-69 | AM : KB : PVDF = 4 : 4 : 2 | 1 M $NaPF_6$/ DOL + DME | 1.9 ± 0.4 V *vs.* $Na^+$/Na | 180/255 mAh $g^{-1}$ | 180 mAh $g^{-1}$@50 mA $g^{-1}$, 92%@150 | | 53 |
| | PI-PMDA-78 | AM : KB : PVDF = 4 : 4 : 2 | 1 M $NaPF_6$/ DOL + DME | 1.9 ± 0.4 V *vs.* $Na^+$/Na | 201/255 mAh $g^{-1}$ | 201 mAh $g^{-1}$@50 mA $g^{-1}$, 81%@150 | 33%@500 *vs.* 50 mA $g^{-1}$ | 54 |
| | PI-PMDA-42 | AM : G : KB : PVDF = 32 : 8 : 5 : 5 | 1 M LiTFSI/ DOL + DME | 2.2 ± 0.4 V | 271/302 mAh $g^{-1}$ | 242 mAh $g^{-1}$@1 C, 86%@300 | 72%@10 *vs.* 0.1 C | 55 |

| | | | | | | | | |
|---|---|---|---|---|---|---|---|---|
| NTCDI | 74 | AM : SP : PVDF = 6 : 2 : 2 | 1 M $LiPF_6$/EC + DMC + EMC | 2.3 ± 0.4 V | 104/134 mAh $g^{-1}$ | 100 mAh $g^{-1}$@200 mA $g^{-1}$, 87%@200 | 64%@2000 *vs.* 50 mA $g^{-1}$ | 58 |
| | PI-NTCDA-75 | AM : KB : PTFE = 6 : 3 : 1 | 1 M LiTFSI/ EC + DEC | 2.5 ± 0.2 V | 200/203 mAh $g^{-1}$ | 200 mAh $g^{-1}$@203 mA $g^{-1}$, 92%@200 | 70%@20300 *vs.* 203 mA $g^{-1}$ | 64 |
| | PI-NTCDA-76 | AM : PX : PTFE = 6 : 3 : 1 | 1 M LiTFSI/ DOL + DME | 2.3 ± 0.3 V | 181/183 mAh $g^{-1}$ | 181 mAh $g^{-1}$@73 mA $g^{-1}$, 96%@100 | | 52 |
| | PI-NTCDA-69 | AM : KB : PVDF = 4 : 4 : 2 | 1 M $NaPF_6$/ DOL + DME | 1.9 ± 0.4 V *vs.* $Na^+$/Na | 197/228 mAh $g^{-1}$ | 197 mAh $g^{-1}$@50 mA $g^{-1}$, 95%@150 | | 53 |
| | PI-NTCDA-78 | AM : KB : PVDF = 4 : 4 : 2 | 1 M $NaPF_6$/ DOL + DME | 1.9 ± 0.4 V *vs.* $Na^+$/Na | 213/228 mAh $g^{-1}$ | 213 mAh $g^{-1}$@50 mA $g^{-1}$, 89%@150 | 70%@500 *vs.* 50 mA $g^{-1}$ | 54 |
| | PI-NTCDA-80 | AM : CNT : SP : NaAlg = 4 : 4 : 1 : 1 | 1 M LiTFSI/ DOL + DME | 2.4 ± 0.3 V | 104/126 mAh $g^{-1}$ | 100 mAh $g^{-1}$@500 mA $g^{-1}$, 100%@8000 | 91%@2000 *vs.* 200 mA $g^{-1}$ | 60 |
| | PI-NTCDA-81 | AM : AB : PTFE = 16 : 3 : 1 | 1 M $LiPF_6$/EC + DMC + EMC | 2.3 ± 0.2 V | 98/115 mAh $g^{-1}$ | 98 mAh $g^{-1}$@25 mA $g^{-1}$, 70%@30 | | 57 |
| | 88 | AM : AB : PVDF = 4 : 5 : 1 | 1 M $LiPF_6$/ EC + DMC | 2.2 ± 0.2 V | 65/104 mAh $g^{-1}$ | 65 mAh $g^{-1}$@20 mA $g^{-1}$, 58%@100 | 33%@404 *vs.* 20 mA $g^{-1}$ | 59 |

[a]The electrode is usually composed of active material (AM), conductive carbon, and binder with specified weight ratio. The conductive carbons include AB (acetylene black), CB (carbon black), SP (Super P), PX (Printex XE2), KB (Ketjenblack ECP-600JD), VGCF (vapor grown carbon fiber), CNT (carbon nanotube), G (graphene) and rGO (reduced graphene oxide). The binders include PTFE (polytetrafluoroethylene), PVDF (polyvinylidene fluoride), PIB (polyisobutylene) and NaAlg (sodium alginate).

[b]The electrolyte is usually composed of lithium or sodium salt and mixed solvents with specified molar concentration; LiTFSI = lithium bis(trifluoromethanesulfonyl)imide. The aprotic solvents include DOL (1,3-dioxacyclopentane), DME (1,2-dimethoxyethane), G4 (tetraglyme), THF (tetrahydrofuran), EC (ethylene carbonate), DMC (dimethyl carbonate), DEC(diethyl carbonate), EMC (ethyl methyl carbonate) and $CH_3CN$.

[c]The voltage (*vs.* $Li^+$/Li unless otherwise specified) is denoted in the same manner as for Table 6.1 and is adopted from the discharge curve under low current rate.

[d]The data are adopted from the text or measured from the figures following the same standards as far as possible, which may be somewhat different from the claimed data but more objective for comparing the electrochemical performance in different references. Especially, the reversible capacity is defined as the maximum discharge capacity after deducting the remarkable irreversible capacity in the initial one or several cycles.

[e]The unit of current rate is converted into mA $g^{-1}$ if the original unit "C" in the literature is clearly defined.

[f]The electrochemical performance was tested under 45 °C.

[g]The material was tested as an anode and the data cannot represent the electrochemical performance of carbonyl unit.

capacity (*e.g.*, PBQS,[20] **39**,[40] **62**[49]). On the other hand, the strong hydrogen-bonding between phenol and carbonyl may also hinder the redox reaction, resulting in charge–discharge curves with poor reversibility and greatly reduced capacity (*e.g.*, **39**,[40] **44**,[38] **47**,[21] **85**[48]). Furthermore, the negative impact of releasable protons on battery stability should be also taken into account. It is usually neglected in half-cell tests because they can be exhausted by side reactions with largely excess electrolyte and Li/Na anode without an obvious effect on the cycling stability. However, it is intolerable in practical batteries containing lean aprotic electrolyte and a matched amount of anode. Therefore, full oxidation of residual phenol groups in CCPs is desired for higher capacity and stable cycling.

3. Molecular weight. Molecular weight distribution or polymerization degree is an important parameter for the characterization of CCPs. As they are required to be completely insoluble in aprotic electrolytes, they are probably also insoluble or sparingly soluble in most organic solvents for $M_w$ tests (excluding a few soluble CCPs like **8**,[28] **15**,[33] **25**,[39] and P14AQ[32]). Then the measurement of $M_w$ is always difficult and this information is absent for most reported CCPs. It does not matter when the cycling stability is very good, but when it is unsatisfactory we should distinguish whether the reason is the gradual dissolution or swelling of a low-$M_w$ portion, or other factors like the electrode structure evolution. For example, the relatively poor cycling performance of P15AQ compared to P14AQ was ascribed to the relatively low $M_w$ (230 000 and 2300 Da for P14AQ and P15AQ, respectively) calculated from the C/Cl molar ratio (tested by elemental analysis).[32]
4. Electrolyte. From Table 6.2 we can see that the electrolytes for testing CCP are predominantly ether-type (typically 1 M LiTFSI/DOL + DME) and ester-type (typically 1 M $LiPF_6$/EC + DMC), which have been widely used for Li–S batteries and Li-ion batteries using IEMs, respectively. Generally, we find a rule that ether-type electrolyte is better than ester-type for taking full advantage of most CCPs in terms of redox reversibility and structure stability. It is well known that ester-type electrolyte is incompatible with Li–S batteries because of the serious nucleophilic reaction between the polysulfide anion ($S_n^{2-}$, $4 < n < 8$) and the carbonate ester molecule (*e.g.*, EC, DMC, DEC, EMC). Similarly, the side reaction probably also exists for CCPs in carbonate ester solvent, due to the generation of nucleophilic anion radical and dianion with approximate redox potential to $S_n^{2-}$. It is speculated to be the main reason for the poor battery performance of many well-synthesized CCPs (*e.g.*, **10**[42] and **83**[47]). It is also found that the side reaction may be negligible for some ECUs that NTCDI-based polymers (*e.g.*, **74**[58] and PI-NTCDA-75[64]) work well in ester-type electrolytes. The detailed mechanism is to be studied on how the ECU and carbonate ester structure influence the nucleophilic reaction. Ether-type electrolyte is preferred for most CCPs but may also have a bottleneck of low resistance to oxidation, *i.e.*, Coulombic

efficiency may obviously decline when charging to above 3.8 V for high-voltage CCPs (*e.g.*, **27**[41] and PBQS[20]).

5. Species and content of conductive carbon. Compared to IEMs, OEMs possess much lower electronic conductivity and mass density as well as higher surface area. This puts forward a higher requirement on the conductive carbon used to improve the electronic conduction in the electrode. In past years, a variety of conductive carbons have been applied in the electrode fabrication of CCPs, including acetylene black (AB), Super P (SP), Ketjenblack ECP-600JD (KB), carbon nanotube (CNT), graphene (G or rGO), and so on. Unlike IEMs using AB or SP (both with surface areas of $\sim$60 $m^2 g^{-1}$) in general, organic electrodes prefer carbon with higher electronic conductivity and surface area such as KB (1400 $m^2 g^{-1}$). Although many reports claimed that CNT and graphene can improve the battery performance, there is insufficient evidence to prove their advantage over KB under the same conditions. The mass ratio of conductive carbon in organic electrode is widely ranging from 10 to 80 wt.% (generally below 10 wt.% for IEMs), while the AM accounts for 80 to 10 wt.% (the binder content is usually 10 wt.%). The addition of a large amount of conductive carbon brings two contradictory effects. On one hand, it facilitates the capacity release of carbonyl and accelerates the charge–discharge kinetics. On another hand, it reduces the energy density of the whole electrode due to lowered AM proportion, which has been generally neglected in the literature but needs serious consideration in practical applications. Moreover, it may lead to overestimation of the actual capacity of AM because carbon also contributes reversible capacity as a capacitive material, but the specific capacity is calculated based on only the AM weight. Taking a recommended electrode composition, AM : KB : PTFE = 6 : 3 : 1, as an example, the specific capacity of sole KB is approximately 46 mAh $g^{-1}_{KB}$ within 1.5–3.5 V, which can be converted to an extra 23 mAh $g^{-1}_{AM}$ for AM. The contribution is more considerable if increasing the KB ratio or extending the voltage window. Therefore, it is suggested to be taken into account when analyzing the electrochemical data, otherwise an unfair comparison in the same work or between different literatures may lead to unreliable conclusions.
6. Polymer/carbon composite. To improve the high-rate performance or reduce carbon proportion, polymer/carbon composite is a widely used approach before electrode fabrication. The goal is to facilitate the homogeneous distribution of polymer and carbon, preferably at the molecular level, and thus the conductive carbon can be efficiently utilized. Popular techniques are ball milling, ultrasonic dispersion and *in situ* polymerization. The latter two methods using CNT[65,66] or graphene[67] and followed by a vacuum filtration have been also used to prepare a free-standing, binder-free and flexible electrode, which is a unique superiority of polymer electrode materials for flexible batteries (see Section 6.5.6).

7. Cutoff voltage. Because of the variety of redox potential and sloping charge–discharge curves of OEMs (see Figure 6.2a), the cutoff voltage becomes an important parameter to affect the reversible capacity, Coulombic efficiency, and even cycling stability. It should be carefully determined depending on both the charge–discharge voltage profiles and electrochemical window of the electrolyte. For example, 1 M LiTFSI/DOL + DME electrolyte is ensured for electrochemical stability within 1.3–3.8 V for typical organic electrodes. Such a narrow voltage window is not comparable to that of 1 M $LiPF_6$/EC + DMC electrolyte (approximately 0–4.4 V) used in Li-ion batteries. This is ascribed to the poorer electrochemical stability of ether solvent (especially in the charge process) and dramatically enlarged electrochemical surface of the organic electrode by orders of magnitude than Li, graphite and IEMs. Hence, there is a selection dilemma for CCPs with considerable electroactivity at lower voltage range (<1.3 V) or higher voltage range (>3.8 V): conservative cutoff voltage to sacrifice a part of reversible capacity (*e.g.*, **27**[41] and **43**[23]), or offensive cutoff voltage to sacrifice the Coulombic efficiency and cycling stability caused by electrolyte decomposition. In addition, when the cutoff voltage is lowered to 1.0 V, the discharge capacity will be dramatically increased by hundreds of mAh $g^{-1}$, indicating a serious reduction of electrolyte with possible participation of AM. This may persist for many cycles due to partial reversibility, causing difficulty in distinguishing the actual reversible capacity of AM.
8. Current rate. The influence of the current rate on the battery performance of CCPs exists in three aspects. First, reversible capacity definitely declines along with the current rate increasing (see Table 6.2), and thus a low current rate like 50 mA $g^{-1}$ or 0.2 C is recommended to explore the maximum reversible capacity. Second, a high current rate may lead to a capacity activation process for the initial several cycles in cycling test (see Figure 6.2), which can be ascribed to the slow infiltration of electrolyte into the AM. Third, a high current rate can improve the apparent cycling performance and Coulombic efficiency because of the suppression on side reactions with poorer kinetics than the redox reaction of AM. To objectively evaluate the long-term cycling stability, it is suggested to test at a moderate rate like 1 or 2 C for several months, rather than at an ultrahigh rate above 10 C for few days, regardless of the same cycle number.

It must be admitted that the systematic study and detailed understanding on the above issues is very lacking at present. In addition to these factors, it is also necessary to understand how the electrochemical performance is influenced by the electronic conductivity and surface area of the CCP, porous electrode structure formed by different electrode fabrication methods (rolling with PTFE binder or coating with PVDF binder), and electrode structure evolution during the charge–discharge process caused by polymer swelling and side reactions. To realize the ideal performance of a CCP, we must satisfy

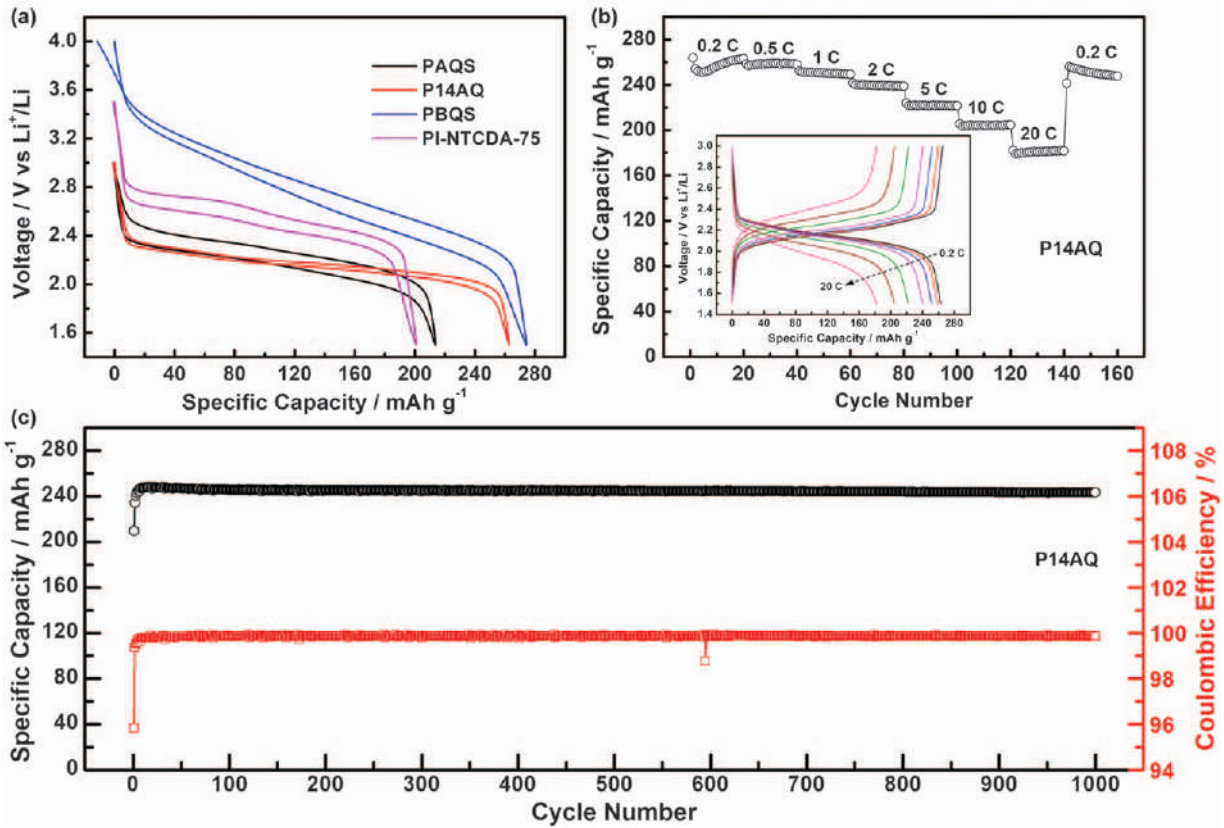


**Figure 6.2** Electrochemical performance of promising CCPs including PAQS, P14AQ, PBQS and PI-NTCDA-75: (a) typical charge–discharge voltage profiles of the four samples; (b) rate performance of P14AQ with inset showing the corresponding voltage profiles at different current rates (1 C = 260 mA $g^{-1}$); (c) long-term cycling performance of P14AQ at a current rate of 1 C. The data of PBQS and PI-NTCDA-75 are collected from ref. 20 and 64, respectively.
Reproduced from ref. 32 with permission from John Wiley and Sons, © 2015 Wiley-VCH Verlag GmbH & Co. KGaA, Weinheim.

simultaneously all of the following criteria: successfully synthesized polymer with high $M_w$ and purity, proper electrode composition and fabrication, and appropriate battery test conditions including electrolyte. P14AQ[32] is one of the few examples that achieves ideal comprehensive electrochemical performance (see Figure 6.2), including reversible capacity close to $C_t$ (260 mAh $g^{-1}$), small charge–discharge voltage gap (0.04 V), ultrastable cycling performance (99.4% capacity retention after 1000 cycles), high Coulombic efficiency (99.8% at 1 C), and excellent high-rate performance (69% capacity retention at 20 C *vs.* 0.2 C). This illustrates the huge performance potential of CCPs and encourages researchers to develop CCPs with higher energy density while keeping other superior properties. However, for practical application, there is still a long way to go in decreasing the conductive carbon proportion, increasing the AM loading (mg $cm^{-2}$) and using lean electrolyte.

## 6.5 Prospective Applications

As illustrated in Figure 6.1, the cation-independent n-type reaction with a moderate redox potential of 2.0–3.0 V provides CCPs with wide application prospects in all kinds of organic batteries, either as the cathode or anode, with aprotic or aqueous electrolyte. Specifically, they can play the role of a cathode for aprotic Li/Na/K/Mg batteries and aqueous Zn batteries, an anode for aqueous batteries and dual-ion batteries, as well as an electrode for flexible batteries. In addition, CCPs have been also investigated in aprotic Al batteries,[66] proton batteries[68] and solid-state batteries,[69] which are not discussed in detail due to their having received less attention. In many reports, they were also studied as electrode materials for supercapacitors or Li/Na-ion capacitors due to their pseudocapacitive behavior, however these devices can be also regarded as one of the above-mentioned batteries. One of the greatest strengths of CCPs is that the same materials can be applied in various battery systems, showing comparable or even exceeding the electrochemical performance of their inorganic counterparts. In addition to the common pursuit of energy density and cycling stability, these batteries also place special emphasis on other aspects including sustainability, safety, cost, environmental protection, fast kinetics and flexibility.

### 6.5.1 Organic Cathodes for Aprotic Li/Na/K Batteries

The most popular role of CCPs is as cathode material for aprotic Li batteries, which we have discussed in detail in Section 6.4. The scarcity and uneven distribution of Li resources has prompted researchers to explore more sustainable alternatives. Na and K are the most reasonable choices because of their resource abundance and similar properties to Li. Although it is said that the reaction feasibility of carbonyl is not relying on the cation, the replacement of anode and cation from Li to Na or K brings about non-negligible electrochemical performance variations in both thermodynamics and dynamics.

The relative potential of Na and K anodes compared to Li anodes in aprotic electrolytes is approximately 0.3 and −0.1 V (a comprehensive outcome of atom electronegativity and solvation effect),[70] respectively. It will reduce the voltage of an Na–organic battery by 0.3 V or enlarge the voltage of a K–organic battery by 0.1 V if the redox potential of the CCP cathode is constant. However, the experimental results do not support this assumption. From Figure 6.3 we can see a tendency of absolute voltage declining by 0.3–0.5 V along with replacing the charge carrier from $Li^+$ to $Na^+$ and $K^+$. This is probably because that the larger Shannon's ionic radius of $Na^+$ (1.02 Å) and $K^+$ (1.38 Å, *vs.* 0.76 Å of $Li^+$) leads to weaker ionic bonding between the cation ($M^+$) and enolate anion ($C–O^-$), resulting in smaller $\Delta G$ and thus lowered redox potential. The voltage variations of both anode and cathode cause a significant voltage decrease of the Na/K–organic battery using the same CCP cathode, usually in the order of Li > K > Na.

Moreover, the down-shift of absolute voltage may bring about incomplete releasing of the capacity, especially for low-voltage CCPs restrained by the electrochemical window of the electrolyte. For the influence on cycling stability and rate capability, a larger ionic radius of $Na^+$ and $K^+$ is also an adverse factor that decelerates the ion diffusion but accelerates the electrode structure evolution.

In conclusion, the battery performance, especially the energy density of an Na/K–organic battery, is inferior to that of an Li–organic battery. Nevertheless, an Na/K–organic battery may be superior to an Na/K–inorganic battery due to the lack of high-performance Na/K-storage inorganic cathodes. The

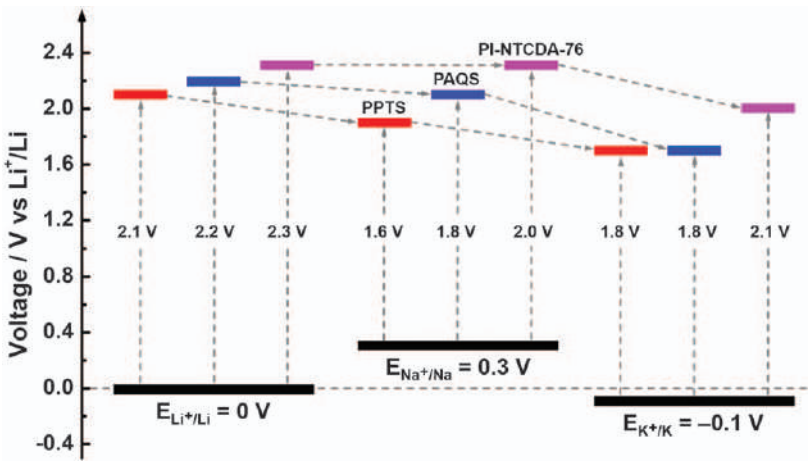


**Figure 6.3** Comparison of the absolute average voltage (*vs.* $Li^+$/Li) of typical CCPs including PAQS,[32,71,72] PPTS[36,73] and PI-NTCDA-76[52,74,75] in aprotic Li, Na and K batteries. The relative average voltage (*vs.* $Li^+$/Li, $Na^+$/Na or $K^+$/K) data are claimed by the references or measured from the discharge curve under low current rate. The data of PPTS in Li batteries is absent from the literature and thus reasonably replaced by that of PT monomer[35] as an approximation.

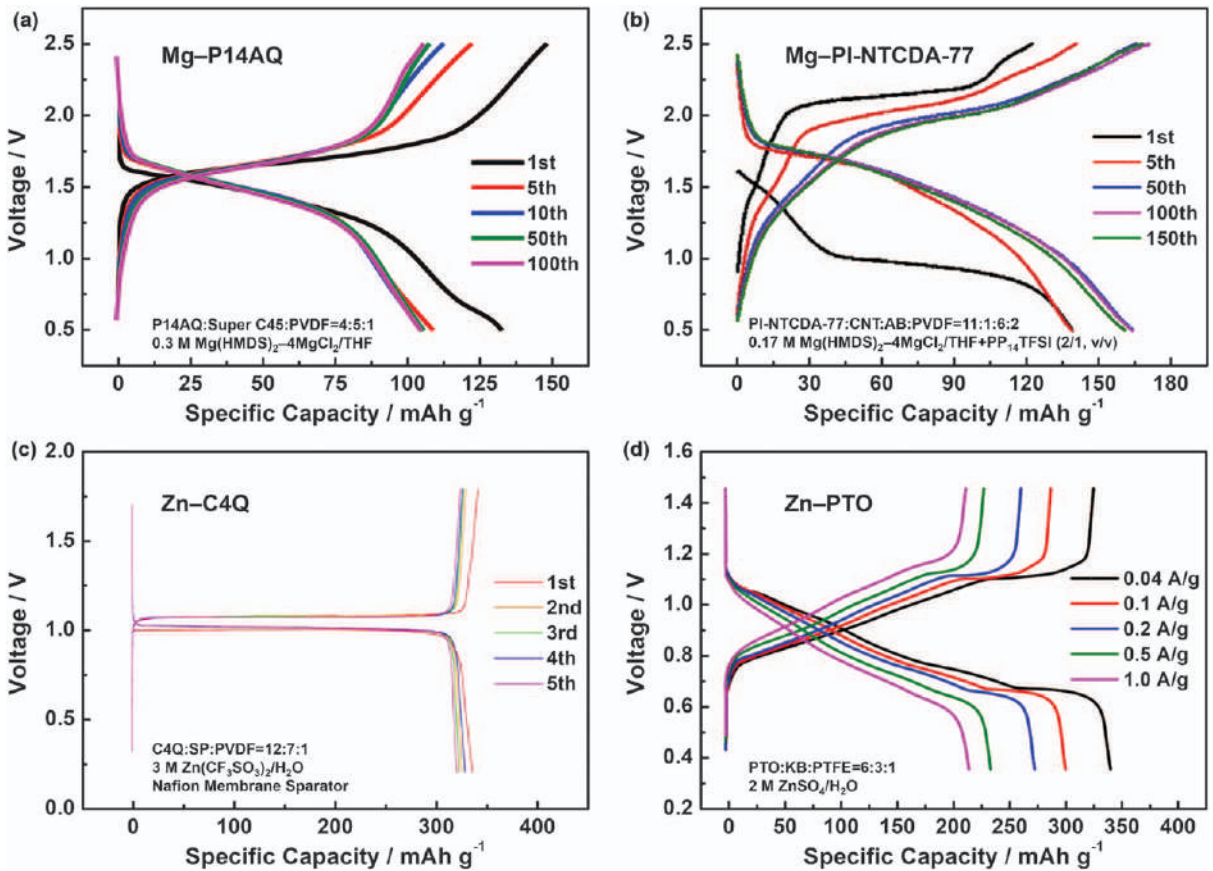
(a)
Mg–P14AQ
Voltage / V
Specific Capacity / mAh g-1
1st
5th
10th
50th
100th
P14AQ:Super C45:PVDF=4:5:1
0.3 M Mg(HMDS)2–4MgCl2/THF
(b)
Mg–PI-NTCDA-77
Voltage / V
Specific Capacity / mAh g-1
1st
5th
50th
100th
150th
PI-NTCDA-77:CNT:AB:PVDF=11:1:6:2
0.17 M Mg(HMDS)2–4MgCl2/THF+PP14TFSI (2/1, v/v)
(c)
Zn–C4Q
Voltage / V
Specific Capacity / mAh g-1
1st
2nd
3rd
4th
5th
C4Q:SP:PVDF=12:7:1
3 M Zn(CF3SO3)2/H2O
Nafion Membrane Sparator
(d)
Zn–PTO
Voltage / V
Specific Capacity / mAh g-1
0.04 A/g
0.1 A/g
0.2 A/g
0.5 A/g
1.0 A/g
PTO:KB:PTFE=6:3:1
2 M ZnSO4/H2O

independence on both Li and transition metals makes the Na/K–organic battery a promising candidate for sustainable battery technologies in the future.

### 6.5.2 Organic Cathode for Aprotic Mg Batteries

Rechargeable Mg batteries have received a great deal of attention because of the low cost, resource sustainability, as well as large volumetric capacity (3833 mAh $cm^{-3}$, *vs.* 2062 mAh $cm^{-3}$ of Li) and inherent safety of Mg compared to alkali metals. The potentially dendrite-free deposition in addition to less reactivity ($E_{Mg^{2+}/Mg} = 0.67$ V *vs.* $Li^+$/Li in aqueous electrolyte) of the Mg anode indicate that Mg metal batteries are more feasible than Li/Na/K metal batteries in terms of safety. Therefore, Mg–organic batteries seem more suitable for the practical use of an n-type CCP cathode (see Figure 6.1a).

The biggest challenge is the lack of appropriate electrolyte satisfying simultaneously the compatibility with Mg anode and the upper cutoff voltage of CCP cathode. Figure 6.4a, b demonstrates two examples showing the best electrochemical performance up to now. Non-nucleophilic electrolytes based on an $Mg(HMDS)_2$–$MgCl_2$ mixture were adopted for both Mg–P14AQ[76] and Mg–PI-NTCDA-77 cells,[77] to avoid serious side reactions between nucleophilic electrolytes (more compatible with Mg anode) and electrophilic carbonyl. The electrochemical performance including energy density is much superior to their inorganic counterparts (*e.g.*, $V_2O_5$, $MnO_2$, $Mo_6S_{8-x}Se_x$, $MgMnSiO_4$) suffering from the sluggish diffusion of divalent $Mg^{2+}$ in the crystalline particles. Unfortunately, it is still far from their performance in Li batteries. Especially, the utilization of reversible capacity remains very low (usually $<50\%$) despite the amorphous morphology and pseudocapacitive property. It is speculated that the actual charge carrier is solvated $Mg^{2+}$, partially desolvated $Mg^{2+}$ or solvated $MgCl^+$ complex with very large size rather than nude $Mg^{2+}$ (with even a smaller ionic radius of 0.72 Å than $Li^+$), due to the strong coordination ability of $Mg^{2+}$ with ether solvent molecules or halogen anions.[78] It causes either inadequate storage of these large cations or increased voltage polarization for further desolvation. Furthermore, the non-negligible voltage gap (usually above 0.2 V) between deposition and stripping of the Mg anode will

**Figure 6.4** The typical charge–discharge curves of high-performance Mg–organic and Zn–organic batteries (together with detailed electrode and electrolyte composition). (a) Mg–P14AQ, $Mg(HMDS)_2$ = magnesium bis(hexamethyldisilazide), 130 mA $g^{-1}$. Reproduced from ref. 76 with permission from John Wiley and Sons, © 2016 Wiley-VCH Verlag GmbH & Co. KGaA, Weinheim. (b) Mg–PI-NTCDA-77, $PP_{14}TFSI$ = *N*-butyl-*N*-methyl-piperidinium bis(trifluoromethanesulfonyl)imide, 158 mA $g^{-1}$. Reproduced from ref. 77 with permission from Elsevier, Copyright 2019. (c) Zn–C4Q, C4Q = calix[4]quinone, 20 mA $g^{-1}$. Reproduced from ref. 79 with permission from AAAS, Copyright 2018. (d) Zn–PTO. Reproduced from ref. 80 with permission from John Wiley and Sons, © 2018 Wiley-VCH Verlag GmbH & Co. KGaA, Weinheim.

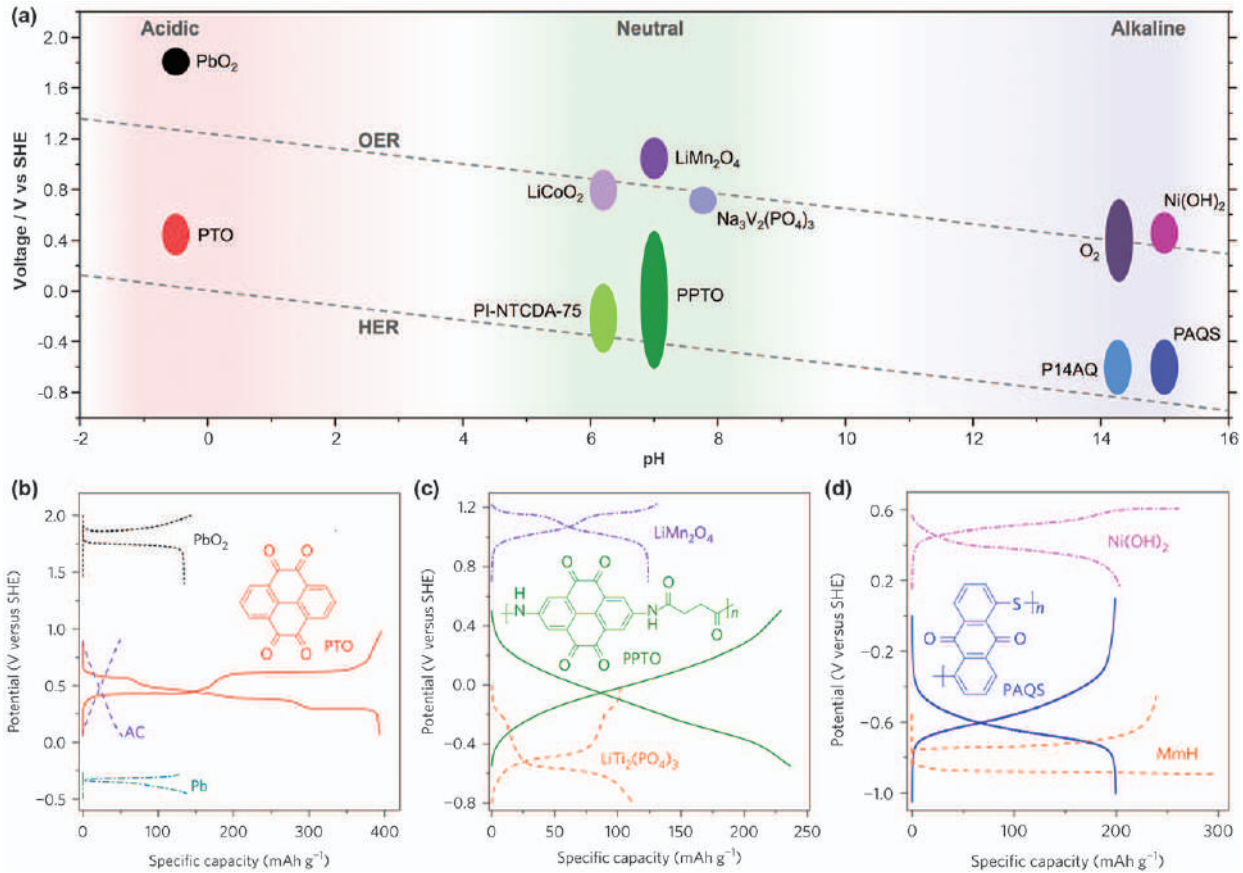
(a)
Acidic
Neutral
Alkaline
PbO2
OER
LiMn2O4
LiCoO2
Na3V2(PO4)3
Ni(OH)2
O2
PTO
PPTO
PI-NTCDA-75
HER
PAQS
P14AQ
Voltage / V vs SHE
pH
(b)
PbO2
PTO
AC
Pb
Potential (V versus SHE)
Specific capacity (mAh g−1)
(c)
LiMn2O4
PPTO
LiTi2(PO4)3
Potential (V versus SHE)
Specific capacity (mAh g−1)
(d)
Ni(OH)2
PAQS
MmH
Potential (V versus SHE)
Specific capacity (mAh g−1)

further reduce the discharge voltage and enlarge the voltage gap between the charge and discharge process. The comprehensive result is that the average discharge voltage of a CCP cathode in Mg batteries is approximately 0.8–1.0 V lower than that in Li batteries.

In summary, the performance improvement of Mg–organic batteries greatly depends on the understanding and exploration of magnesium electrolytes. Hybrid $Mg^{2+}/Na^{+}$ electrolyte may be a possible solution for the full utilization of carbonyl. Electrolyte with a larger voltage window (>3.0 V *vs.* Mg anode) is desired for the application of many high-voltage CCPs such as PBQS.

### 6.5.3 Organic Cathode for Aqueous Zn Batteries

Aqueous batteries are intrinsically safer than aprotic batteries, despite the lower working voltage (usually <1.5 V) limited by water electrolysis. Aqueous Zn batteries became promising candidates in this field very recently because zinc anode exhibits relatively low redox potential ($E_{Zn^{2+}/Zn} = -0.76$ V *vs.* SHE = 2.28 V *vs.* $Li^{+}/Li$), high capacity (820 mAh $g^{-1}$), large hydrogen evolution overpotential and low cost. Like aprotic Mg batteries, their development has been hindered by the shortage of high-performance Zn-storage cathode materials due to the sluggish diffusion of $Zn^{2+}$ in crystalline structures. Organic cathode materials, especially carbonyl-based ones, have shown significant advantages as alternatives to conventional inorganic cathodes (*e.g.*, $MnO_2$, $V_2O_5$, Prussian blue analogues).

Calix[4]quinone (C4Q)[79] and PTO[80] (see Figure 6.4c, d) are two examples showing high reversible capacity above 300 mAh $g^{-1}$. It is amazing that the experimental discharge voltage (1.0 and 0.8 V for C4Q and PTO, respectively) is about 0.6 V higher than prediction based on the voltage difference between them (2.7 and 2.5 V for C4Q and PTO, respectively) and Zn (2.28 V) anode *vs.* $Li^{+}/Li$. It is speculated that the voltage elevation is caused partially by solvation effect and partially by the strong ionic bonding between $Zn^{2+}$ and $C–O^{-}$. Another advantage is that $Zn^{2+}$ seems beneficial in preventing the small organic molecules (C4Q and PTO) from dissolving to some extent due to its strong coordination ability. However, the long-term cycling performance is still unsatisfactory, and thus it is anticipated that CCPs will show their superiority in aqueous Zn batteries.[81]

**Figure 6.5** The (a) voltage distribution of promising electrode materials and (b–d) electrochemical performances of aqueous rechargeable batteries using carbonyl-based organic anode at different pH values. (b) Typical voltage profiles of PTO (40 mA $g^{-1}$), AC (active carbon, 50 mA $g^{-1}$), Pb (10 mA $g^{-1}$) and $PbO_2$ (20 mA $g^{-1}$) in acidic electrolyte (4.4 M $H_2SO_4$). (c) Typical voltage profiles of PPTO (polymerized PTO, 280 mA $g^{-1}$), $LiTi_2(PO_4)_3$ (120 mA $g^{-1}$) and $LiMn_2O_4$ (140 mA $g^{-1}$) in neutral electrolyte (2.5 M $Li_2SO_4$). (d) Typical voltage profiles of PAQS (100 mA $g^{-1}$), MmH (mischmetal hydride,150 mA $g^{-1}$), and $Ni(OH)_2$ (40 mA $g^{-1}$) in alkaline electrolyte (10 M KOH). (b–d) Reproduced from ref. 82 with permission from Springer Nature, Copyright 2017.

### 6.5.4 Organic Anode for Aqueous Batteries

For the above systems, CCP plays the role of a cathode coupled with a low-voltage metal anode. Nevertheless, it can also play the role of an anode coupled with a high-voltage cathode pristinely in the reduction state. Theoretically, the moderate redox potential of CCPs promises their wide application in aqueous electrolyte with different pH from −1 to 15 (see Figure 6.5). For example, they can replace the Pb anode in lead-acid batteries,[82] the hydrogen storage alloy (MmH) anode in alkaline nickel–metal hydride batteries,[82] and the Zn anode in rechargeable alkaline air batteries,[28,33,83] as well as match Li/Na storage cathode materials [*e.g.*, $LiMn_2O_4$, $LiCoO_2$, $Na_3V_2(PO_4)_3$] in neutral electrolytes.[82,84] A general principle for selecting CCP anodes and matched cathodes is that their redox potential region must be located within the hydrogen evolution reaction (HER) potential to oxygen evolution reaction (OER) potential (slight excess is allowed by the overpotential), both of which proportionally decline along with increasing pH. It is remarkable that the redox potential of CCPs also shifts along with pH because the reaction participant is mainly $H^+$ in acidic electrolyte rather than $M^+$ ($Li^+$, $Na^+$, $K^+$) in neutral or alkaline electrolyte. Then lower pH or higher $H^+$ concentration will elevate the redox potential of the CCP anode based on the Nernst equation. As a result of the above two factors, PTO (2.5 V *vs.* $Li^+$/Li in aprotic electrolyte or 0.4 V *vs.* SHE in acidic electrolyte) and AQ (2.3 V $Li^+$/Li in aprotic electrolyte or −0.6 V *vs.* SHE in neutral or alkaline electrolyte) are two representative ECUs for acidic and alkaline batteries, respectively, exhibiting the lowest acceptable potential to maximize the full-cell voltage.

There are three main concerns for the electrochemical performance of CCP anodes in aqueous batteries. First, the HER is difficult to completely eliminate because of overlap of the reduction voltage region. The high surface area of conductive carbon reduces the HER overpotential and thus increases the irreversible capacity. Second, the discharged CCP is very sensitive to oxygen that can reoxidize it chemically, and thus it is necessary to eliminate the residual oxygen in the electrolyte before sealing the cell. Third, despite the insolubility of CCP itself in aqueous electrolyte, the salt phase after discharge is possibly soluble or swollen, especially when the $M_w$ is not high enough. The former two factors will reduce the Coulombic efficiency and the latter will hamper the cycling stability. Compared to the acidic battery with corrosive electrolyte and more serious HER, neutral and alkaline batteries are preferred for practical use, in which CCPs will show more superiorities to inorganic anodes.

### 6.5.5 Organic Anode for Dual-ion Batteries

In addition to the above batteries involving only cation as charge carrier for both anode and cathode, dual-ion battery has been also proposed by using cation for the anode and anion for the cathode, respectively (see

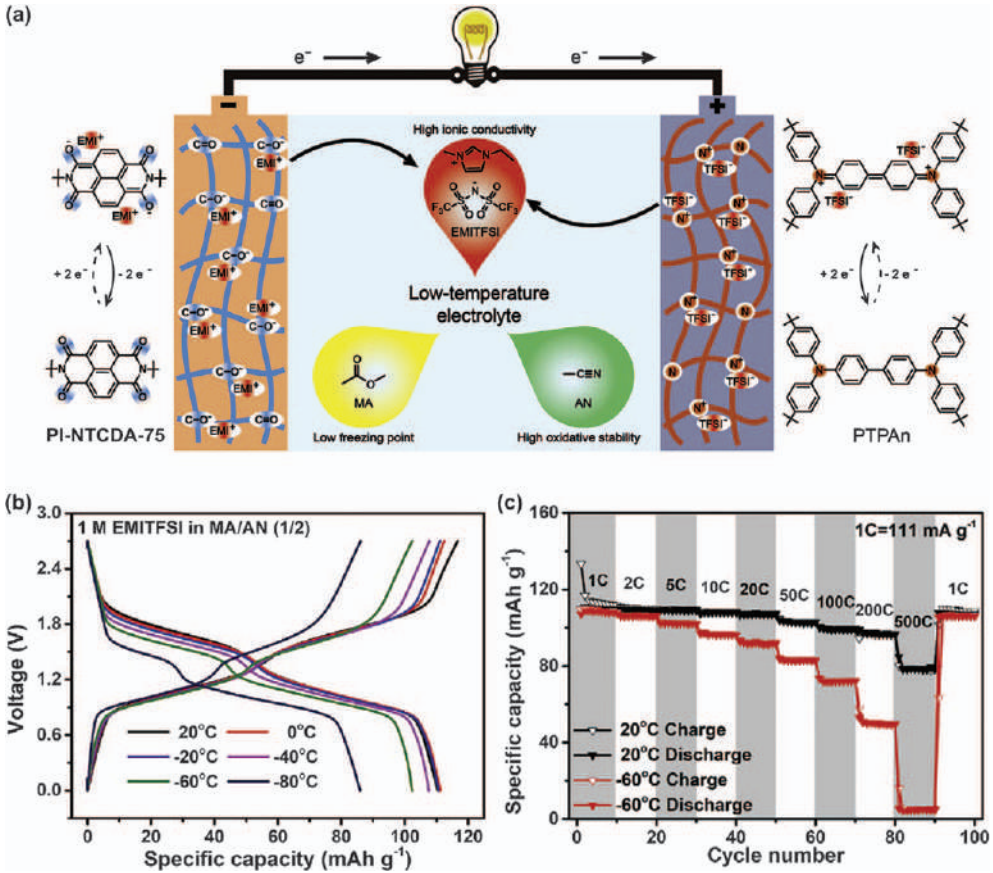


**Figure 6.6** The (a) cell configurations, redox chemistries and (b, c) electrochemical performances of a low-temperature, dual-ion, metal-free battery (PI-NTCDA-75//1 M EMITFSI in MA/AN (1/2, v/v)//PTPAn). PTPAn = polytriphenylamine, EMITFSI = 1-ethyl-3-methylimidazolium bis(trifluoromethylsulfonyl)imide, MA = methyl acetate, AN = acetonitrile. (b) Typical charge–discharge voltage profiles under 1 C (111 mA $g^{-1}$) at different temperatures. (c) Rate performance at 20 and −60 °C.
Reproduced from ref. 87 with permission from Elsevier, Copyright 2020.

Figure 6.1b). The most famous example is a dual-graphite battery using graphite as both the anode and cathode, based on the cation-insertion and anion-insertion ability of graphite.[85]

An all-organic battery adopting n-type organic anode and p-type organic cathode also attracted a great deal of attention due to some unique advantages rather than energy density.[8,64,71,86] Figure 6.6 exhibits an interesting metal-free battery using PI-NTCDA-75 as the anode, polytriphenylamine (PTPAn) as the cathode, and ionic liquid-based low-temperature electrolyte (1 M EMITFSI in MA/AN).[87] The results indicate that besides various metal ions and proton, organic cations ($C^+$) can also participate in the redox reaction of CCPs. The weak ionic bonding between large $C^+$ and $C–O^-$ is also beneficial in improving the reaction kinetics, helping the battery to achieve excellent performance at an ultralow temperature of $-80$ °C. If removing the solvent, this battery can still work well with pure ionic liquid electrolyte,[64] which ensures excellent safety from the nonvolatile and nonflammable ionic liquid. Unlike in an aqueous battery, the redox potential of an organic anode in aprotic electrolyte is not limited by the HER potential, and so there is lots of room to improve the energy density of the dual-ion battery based on a CCP anode.

### 6.5.6 Organic Electrodes for Flexible Batteries

The rapid development of flexible and wearable electronic devices has motivated researchers to explore flexible batteries as power sources. At the current start-up stage, there is no strict standard of flexibility and defined fabrication process to guide how to make a flexible battery. The dominant method is to obtain flexibility by structural engineering of inorganic electrodes.[88] The inherent rigidity of IEMs requires a large amount of substrate

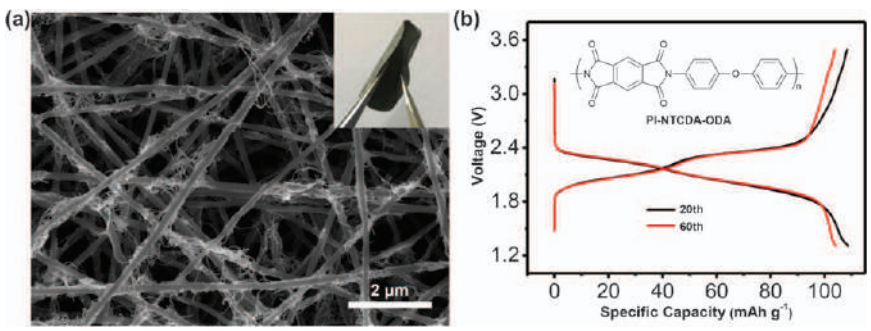


**Figure 6.7** An electrospun PI-PMDA-ODA/CNT (ODA = 4,4′-oxydianiline) composite electrode for a flexible battery. (a) SEM image showing the polyimide fibers (200 nm thick) intertwined by 20 wt.% CNT, with inset showing the photograph of the flexible electrode. (b) Typical charge–discharge voltage profiles of the electrode in Li batteries (1 M LiTFSI/DOL + DME, 28 mA $g^{-1}$).
Reproduced from ref. 89 with permission from the American Chemical Society, Copyright 2019.

and current collector materials to ensure flexibility, which will seriously reduce the energy density. The rising of organic, especially polymer, electrode materials provides possibilities to build a binder-free, free-standing and flexible electrode with high AM proportion. For example, a modified electrospinning approach was applied to construct a flexible PI-PMDA-ODA/CNT electrode with only 20 wt.% CNT (see Figure 6.7).[89] In the electrode, the robust polyimide fibers play a role of not only AM, but also electrode skeleton. Theoretically the CNT ratio can be further decreased without compromising the mechanical properties, which is much superior to other strategies using CNT as both conductive carbon and skeleton. Despite the current low capacity of PI-PMDA-ODA, it is believed that CCPs will show more advantages in flexible batteries due to their structural diversity and good processability.

## 6.6 Conclusions and Outlook

As the most intensively studied type of OEMs, electroactive carbonyl compounds have shown huge potential in the development of efficient and sustainable batteries beyond conventional Li-ion batteries. Compared to small organic molecules, synthesizing CCPs has been recognized as an essential strategy for most ECUs to prevent dissolution and guarantee long-term cycling stability. To realize the ideal electrochemical performance of a CCP, a series of challenges must be overcome in the whole process from polymer synthesis, electrode fabrication, to cell assembly and test.

First, although a variety of polymerization methods have been attempted for different ECUs, the successful synthesis of a CCP with high purity and $M_w$ is not easy. For battery use, it is not necessary to reach a purity of 100% and very high $M_w$, but it is suggested to remove all the reactive impurities, soluble oligomers, unoxidized phenol and residual solvent. These unfavorable factors will not only hamper the reversible capacity and cycling stability, but also cause misunderstanding of the electrochemical behavior. Keeping in mind practical applications, it is preferred to design a CCP with simple structure and easy synthesis, rather than a CCP with specious structure and complicated synthesis. BQ- and oBQ-based polymers may realize attractive energy density, for which we should pay more attention on the precise and cost-effective synthesis.

Second, the electrode fabrication must guarantee sufficient electronic conduction and ion diffusion to give full play to the CCP's electroactivity. Especially, the species and ratio of conductive carbon are crucial factors for the capacity utilization and rate capability. When analyzing the electrochemical data, it is necessary to distinguish the reversible capacity of AM from the capacity contribution of conductive carbon. A recommended electrode composition is AM : KB : PTFE = 6 : 3 : 1 at the current stage. As conductive carbon, the superiority of CNT and graphene to KB needs to be proved by more systematic studies. It is also required to further reduce the

carbon ratio by promoting the homogeneous mixing of AM and carbon, not only for higher energy density of the whole electrode, but also to minimize side reactions of the electrolyte.

Third, the perfect matching of anode, cathode and electrolyte is desired for the cell assembly. A novel CCP is suggested to be first investigated in the mature Li–organic battery system, for accurate understanding of its electrochemical behavior. Ether-type electrolyte (typically 1 M LiTFSI/DOL + DME) is preferred to ester-type electrolyte with reactivity to enolate anion. Beyond the Li–organic battery, CCPs can be widely applied as a cathode or anode, in aprotic or aqueous electrolytes with different charge carriers of $H^+$, $Li^+$, $Na^+$, $K^+$, $Mg^{2+}$, $Zn^{2+}$ and organic cations. In exploring these emerging battery technologies, the key point is matching the redox potential of the CCP and voltage window of the electrolyte, and understanding how different charge carriers influence the thermodynamics and dynamics of the electrochemical reaction.

It is difficult honestly to say whether OEMs will be commercially applied in the future. It is unlikely that they will compete with IEMs in conventional Li-ion batteries for consumer electronics and electric vehicles, because of the relatively lower volumetric energy density and dependence on Li metal anodes. It is more reasonable to expect their competitiveness in batteries focusing more on safety, cost, fast charge–discharge ability and flexibility. At the very least, the discovery of more high-performance OEMs and in-depth understanding of their electrochemical behavior will be beneficial to other fields such as electrocatalysis and electrosynthesis. From now on, we must improve our studies on OEMs step by step, from precise and cost-effective synthesis, sufficient optimization of electrode and electrolyte, to accurate evaluation of the electrochemical performance.

## References

1. Z. Song and H. Zhou, *Energy Environ. Sci.*, 2013, **6**, 2280.
2. S. Muench, A. Wild, C. Friebe, B. Häupler, T. Janoschka and U. S. Schubert, *Chem. Rev.*, 2016, **116**, 9438.
3. T. B. Schon, B. T. McAllister, P.-F. Li and D. S. Seferos, *Chem. Soc. Rev.*, 2016, **45**, 6345.
4. S. Lee, G. Kwon, K. Ku, K. Yoon, S.-K. Jung, H.-D. Lim and K. Kang, *Adv. Mater.*, 2018, **30**, 1704682.
5. Y. Lu, Q. Zhang, L. Li, Z. Niu and J. Chen, *Chem*, 2018, **4**, 2786.
6. Y. Liang and Y. Yao, *Joule*, 2018, **2**, 1690.
7. D. L. Williams, J. J. Byrne and J. S. Driscoll, *J. Electrochem. Soc.*, 1969, **116**, 2.
8. P. J. Nigrey, D. MacInnes, Jr., D. P. Nairns, A. G. MacDiarmid and A. J. Heeger, *J. Electrochem. Soc.*, 1981, **128**, 1651.
9. S. J. Visco and L. C. DeJonghe, *J. Electrochem. Soc.*, 1988, **135**, 2905.
10. M. Liu, S. J. Visco and L. C. De Jonghe, *J. Electrochem. Soc.*, 1991, **138**, 1891.

11. K. Nakahara, S. Iwasa, M. Satoh, Y. Morioka, J. Iriyama, M. Suguro and E. Hasegawa, *Chem. Phys. Lett.*, 2002, **359**, 351.
12. H. Chen, M. Armand, G. Demailly, F. Dolhem, P. Poizot and J.-M. Tarascon, *ChemSusChem*, 2008, **1**, 348.
13. X. Han, C. Chang, L. Yuan, T. Sun and J. Sun, *Adv. Mater.*, 2007, **19**, 1616.
14. B. Häupler, A. Wild and U. S. Schubert, *Adv. Energy Mater.*, 2015, **5**, 1402034.
15. K. Amin, L. Mao and Z. Wei, *Macromol. Rapid Commun.*, 2018, **40**, 1800565.
16. T. Matsunaga, T. Kubota, T. Sugimoto and M. Satoh, *Chem. Lett.*, 2011, **40**, 750.
17. J. S. Foos, S. M. Erker and L. M. Rembetsy, *J. Electrochem. Soc.*, 1986, **133**, 836.
18. C. Karlsson, H. Huang, M. Strømme, A. Gogoll and M. Sjödin, *J. Phys. Chem. C*, 2014, **118**, 23499.
19. Z. Zhu, M. Hong, D. Guo, J. Shi, Z. Tao and J. Chen, *J. Am. Chem. Soc.*, 2014, **136**, 16461.
20. Z. Song, Y. Qian, T. Zhang, M. Otani and H. Zhou, *Adv. Sci.*, 2015, **2**, 1500124.
21. K. Pirnat, G. Mali, M. Gaberscek and R. Dominko, *J. Power Sources*, 2016, **315**, 169.
22. J. Xie, Z. Wang, Z. J. Xu and Q. Zhang, *Adv. Energy Mater.*, 2018, **8**, 1703509.
23. Y. Chen, H. Li, M. Tang, S. Zhuo, Y. Wu, E. Wang, S. Wang, C. Wang and W. Hu, *J. Mater. Chem. A*, 2019, **7**, 20891.
24. D. Häringer, P. Novák, O. Haas, B. Piro and M.-C. Pham, *J. Electrochem. Soc.*, 1999, **146**, 2393.
25. K. Naoi, S. Suematsu and A. Manago, *J. Electrochem. Soc.*, 2000, **147**, 420.
26. K. M. Ismail, Z. M. Khalifa, M. A. Azzem and W. A. Badawy, *Electrochim. Acta*, 2002, **47**, 1867.
27. Z. Song, H. Zhan and Y. Zhou, *Chem. Commun.*, 2009, **45**, 448.
28. W. Choi, D. Harada, K. Oyaizu and H. Nishide, *J. Am. Chem. Soc.*, 2011, **133**, 19839.
29. K. Oyaizu, W. Choi and H. Nishide, *Polym. Adv. Technol.*, 2011, **22**, 1242.
30. C. R. DeBlase, K. E. Silberstein, T.-T. Truong, H. D. Abruña and W. R. Dichtel, *J. Am. Chem. Soc.*, 2013, **135**, 16821.
31. Y. Zhou, B. Wang, C. Liu, N. Han, X. Xu, F. Zhao, J. Fan and Y. Li, *Nano Energy*, 2015, **15**, 654.
32. Z. Song, Y. Qian, M. L. Gordin, D. Tang, T. Xu, M. Otani, H. Zhan, H. Zhou and D. Wang, *Angew. Chem., Int. Ed.*, 2015, **54**, 13947.
33. T. Kawai, K. Oyaizu and H. Nishide, *Macromolecules*, 2015, **48**, 2429.
34. J. Cao, F. Ding, H. Chen, H. Wang, W. Wang, Z. Chen and J. Xu, *J. Power Sources*, 2019, **423**, 316.
35. M. Yao, S.-i. Yamazaki, H. Senoh, T. Sakai and T. Kiyobayashi, *Mater. Sci. Eng., B*, 2012, **177**, 483.

36. M. Tang, S. Zhu, Z. Liu, C. Jiang, Y. Wu, H. Li, B. Wang, E. Wang, J. Ma and C. Wang, *Chem*, 2018, **4**, 2600.
37. H. Li, M. Tang, Y. Wu, Y. Chen, S. Zhu, B. Wang, C. Jiang, E. Wang and C. Wang, *J. Phys. Chem. Lett.*, 2018, **9**, 3205.
38. T. Le Gall, K. H. Reiman, M. C. Grossel and J. R. Owen, *J. Power Sources*, 2003, **119–121**, 316.
39. Z. Song, Y. Qian, X. Liu, T. Zhang, Y. Zhu, H. Yu, M. Otani and H. Zhou, *Energy Environ. Sci.*, 2014, **7**, 4077.
40. L. Zhao, W. Wang, A. Wang, K. Yuan, S. Chen and Y. Yang, *J. Power Sources*, 2013, **233**, 23.
41. A. Petronico, K. L. Bassett, B. G. Nicolau, A. A. Gewirth and R. G. Nuzzo, *Adv. Energy Mater.*, 2018, **8**, 1700960.
42. B. Häupler, T. Hagemann, C. Friebe, A. Wild and U. S. Schubert, *ACS Appl. Mater. Interfaces*, 2015, **7**, 3473.
43. Y. Jing, Y. Liang, S. Gheytani and Y. Yao, *Nano Energy*, 2017, **37**, 46.
44. T. Nokami, T. Matsuo, Y. Inatomi, N. Hojo, T. Tsukagoshi, H. Yoshizawa, A. Shimizu, H. Kuramoto, K. Komae, H. Tsuyama and J.-I. Yoshida, *J. Am. Chem. Soc.*, 2012, **134**, 19694.
45. J. Xie, W. Chen, G. Long, W. Gao, Z. J. Xu, M. Liu and Q. Zhang, *J. Mater. Chem. A*, 2018, **6**, 12985.
46. K. Pirnat, J. Bitenc, A. Vizintin, A. Krajnc and E. Tchernychova, *Chem. Mater.*, 2018, **30**, 5726.
47. J. Geng, J.-P. Bonnet, S. Renault, F. Dolhem and P. Poizot, *Energy Environ. Sci.*, 2010, **3**, 1929.
48. T. Sun, Z.-j. Li, H.-g. Wang, D. Bao, F.-l. Meng and X.-b. Zhang, *Angew. Chem., Int. Ed.*, 2016, **55**, 10662.
49. N. Patil, A. Aqil, F. Ouhib, S. Admassie, O. Inganäs, C. Jérôme and C. Detrembleur, *Adv. Mater.*, 2017, **29**, 1703373.
50. S. Mazur, P. S. Lugg and C. Yarnitzky, *J. Electrochem. Soc.*, 1987, **134**, 346.
51. K. Oyaizu, A. Hatemata, W. Choi and H. Nishide, *J. Mater. Chem.*, 2010, **20**, 5404.
52. Z. Song, H. Zhan and Y. Zhou, *Angew. Chem., Int. Ed.*, 2010, **49**, 8444.
53. F. Xu, J. Xia and W. Shi, *Electrochem. Commun.*, 2015, **60**, 117.
54. F. Xu, H. Wang, J. Lin, X. Luo, S.-A. Cao and H. Yang, *J. Mater. Chem. A*, 2016, **4**, 11491.
55. Z. Luo, L. Liu, J. Ning, K. Lei, Y. Lu, F. Li and J. Chen, *Angew. Chem., Int. Ed.*, 2018, **57**, 9443.
56. H. Duan, P. Lyu, J. Liu, Y. Zhao and Y. Xu, *ACS Nano*, 2019, **13**, 2473.
57. D. Tian, H.-Z. Zhang, D.-S. Zhang, Z. Chang, J. Han, X.-P. Gao and X.-H. Bu, *RSC Adv.*, 2014, **4**, 7506.
58. D.-H. Yang, Z.-Q. Yao, D. Wu, Y.-H. Zhang, Z. Zhou and X.-H. Bu, *J. Mater. Chem. A*, 2016, **4**, 18621.
59. H. Zhang, Y. Xie, X. Chen, T. Jia, W. Huang, S. Luo, Q. Hou, R. Zeng and Z. Sun, *J. Electrochem. Soc.*, 2017, **164**, A290.

60. H.-g. Wang, N. Chandrasekhar, B. P. Biswal, D. Becker, S. Paasch, E. Brunner, M. Addicoat, M. Yu, R. Berger and X. Feng, *Adv. Mater.*, 2019, **31**, 1901478.
61. Y. Liang, Z. Chen, Y. Jing, Y. Rong, A. Facchetti and Y. Yao, *J. Am. Chem. Soc.*, 2015, **137**, 4956.
62. H.-g. Wang, S. Yuan, D.-l. Ma, X.-l. Huang, F.-l. Meng and X.-b. Zhang, *Adv. Energy Mater.*, 2014, **4**, 1301651.
63. H. Yang, S. Liu, L. Cao, S. Jiang and H. Hou, *J. Mater. Chem. A*, 2018, **6**, 21216.
64. J. Qin, Q. Lan, N. Liu, F. Men, X. Wang, Z. Song and H. Zhan, *iScience*, 2019, **15**, 16.
65. H. Wu, S. A. Shevlin, Q. Meng, W. Guo, Y. Meng, K. Lu, Z. Wei and Z. Guo, *Adv. Mater.*, 2014, **26**, 3338.
66. X. Fan, F. Wang, X. Ji, R. Wang, T. Gao, S. Hou, J. Chen, T. Deng, X. Li, L. Chen, C. Luo, L. Wang and C. Wang, *Angew. Chem., Int. Ed.*, 2018, **57**, 7146.
67. Z. Song, T. Xu, M. L. Gordin, Y. B. Jiang, I. T. Bae, Q. Xiao, H. Zhan, J. Liu and D. Wang, *Nano Lett.*, 2012, **12**, 2205.
68. R. Emanuelsson, M. Sterby, M. Strømme and M. Sjödin, *J. Am. Chem. Soc.*, 2017, **139**, 4828.
69. W. Wei, L. Li, L. Zhang, J. Hong and G. He, *Electrochem. Commun.*, 2018, **90**, 21.
70. T. Hosaka, K. Kubota, A. S. Hameed and S. Komaba, *Chem. Rev.*, 2020, DOI: 10.1021/acs.chemrev.9b00463.
71. W. Deng, X. Liang, X. Wu, J. Qian, Y. Cao, X. Ai, J. Feng and H. Yang, *Sci. Rep.*, 2013, **3**, 2671.
72. Z. Jian, Y. Liang, I. A. Rodríguez-Pérez, Y. Yao and X. Ji, *Electrochem. Commun.*, 2016, **71**, 5.
73. M. Tang, Y. Wu, Y. Chen, C. Jiang, S. Zhu, S. Zhuo and C. Wang, *J. Mater. Chem. A*, 2019, **7**, 486.
74. L. Chen, W. Li, Y. Wang, C. Wang and Y. Xia, *RSC Adv.*, 2014, **4**, 25369.
75. Y. Hu, H. Ding, Y. Bai, Z. Liu, S. Chen, Y. Wu, X. Yu, L. Fan and B. Lu, *ACS Appl. Mater. Interfaces*, 2019, **11**, 42078.
76. B. Pan, J. Huang, Z. Feng, L. Zeng, M. He, L. Zhang, J. T. Vaughey, M. J. Bedzyk, P. Fenter, Z. Zhang, A. K. Burrell and C. Liao, *Adv. Energy Mater.*, 2016, **6**, 1600140.
77. Y. Wang, Z. Liu, C. Wang, Y. Hu, H. Lin, W. Kong, J. Ma and Z. Jin, *Energy Storage Mater.*, 2020, **26**, 494.
78. H. Dong, Y. Liang, O. Tutusaus, R. Mohtadi, Y. Zhang, F. Hao and Y. Yao, *Joule*, 2019, **3**, 782.
79. Q. Zhao, W. Huang, Z. Luo, L. Liu, Y. Lu, Y. Li, L. Li, J. Hu, H. Ma and J. Chen, *Sci. Adv.*, 2018, **4**, eaao1761.
80. Z. Guo, Y. Ma, X. Dong, J. Huang, Y. Wang and Y. Xia, *Angew. Chem., Int. Ed.*, 2018, **57**, 11737.
81. G. Dawut, Y. Lu, L. Miao and J. Chen, *Inorg. Chem. Front.*, 2018, **5**, 1391.
82. Y. Liang, Y. Jing, S. Gheytani, K.-Y. Lee, P. Liu, A. Facchetti and Y. Yao, *Nat. Mater.*, 2017, **16**, 841.

83. Y. Li, L. Liu, C. Liu, Y. Lu, R. Shi, F. Li and J. Chen, *Chem*, 2019, **5**, 2159.
84. H. Qin, Z. P. Song, H. Zhan and Y. H. Zhou, *J. Power Sources*, 2014, **249**, 367.
85. M. Wang and Y. Tang, *Adv. Energy Mater.*, 2018, **8**, 1703320.
86. X. Dong, Z. Guo, Z. Guo, Y. Wang and Y. Xia, *Joule*, 2018, **2**, 902.
87. J. Qin, Q. Lan, N. Liu, Y. Zhao, Z. Song and H. Zhan, *Energy Storage Mater.*, 2020, **26**, 585.
88. G. Qian, X. Liao, Y. Zhu, F. Pan, X. Chen and Y. Yang, *ACS Energy Lett.*, 2019, **4**, 690.
89. N. Liu, Y. Liu, Y. Zhao, Y. Liu, Q. Lan, J. Qin, Z. Song and H. Zhan, *ACS Appl. Mater. Interfaces*, 2019, **11**, 46726.

CHAPTER 7

# *Catechol-containing Polymers for Electrochemical Energy Storage*

NAGARAJ PATIL* AND REBECA MARCILLA*

Electrochemical Processes Unit, IMDEA Energy, Avda. Ramón de la Sagra 3, 28935, Móstoles, Madrid, Spain
*Emails: rebeca.marcilla@imdea.org; nagaraj.patil@imdea.org

## 7.1 Introduction

The quest to build safe, low-cost, scalable and sustainable electrochemical energy-storage (EES) systems is becoming more important than ever before, which feeds a growing interest in the substitution of some scarce metals such as cobalt, lithium or vanadium that are currently used as active materials in commercial batteries,[1] by nontoxic, abundant and less expensive organic electrode materials.[2] Specifically, the pursuit of novel redox-active polymer (RAP) to be used both as solid electrodes in supercapacitors and static batteries such as Li-ion batteries, Na-ion batteries, *etc.*, and as liquid redox electrolytes in redox flow batteries (RFBs) has been attracting increasing attention in recent years.[3–5] Among the vast variety of organic redox-active groups (carboxylates, imides, viologens, organosulfur, nitroxyl, *etc.*), polymers containing quinone-derivatives have been gathering renowned interest as high-performance electrodes for EES because of their high theoretical specific capacity, structural diversity, tunable redox potentials and fast kinetics.[6,7] In particular, within the family of quinones, *para*-quinone-based RAPs have received extensive research efforts for both capacitor and

Polymer Chemistry Series No. 34
Redox Polymers for Energy and Nanomedicine
Edited by Nerea Casado and David Mecerreyes

Published by the Royal Society of Chemistry, www.rsc.org

battery applications in recent years. However, very little attention has been dedicated to their sister compounds, poly(*ortho*-quinone)s, which show additional physicochemical and electrochemical features that might contribute to improve the performance of such devices.

The need for the development of *ortho*-quinone-based cathode materials in pseudocapacitors (based on 9,10-phenanthrenequinone and 4,5-pyrenedione) and lithium-ion batteries (based on pyrene-4,5,9,10-tetraone) was first recognized by Anjos *et al.*[8] and Yoshida *et al.*,[9] respectively. Indeed, *ortho*-quinones show a stronger aromaticity of the reduced form that not only increases the redox potentials (thus, energy density), but also improves the reaction reversibility (thus, long cycle life) as compared to their *para*-counterparts (Figure 7.1A).[8–10] Moreover, they offer a more favorable coordination of metal cations (charge carriers in the electrolyte) by the oxygen atoms suitably located

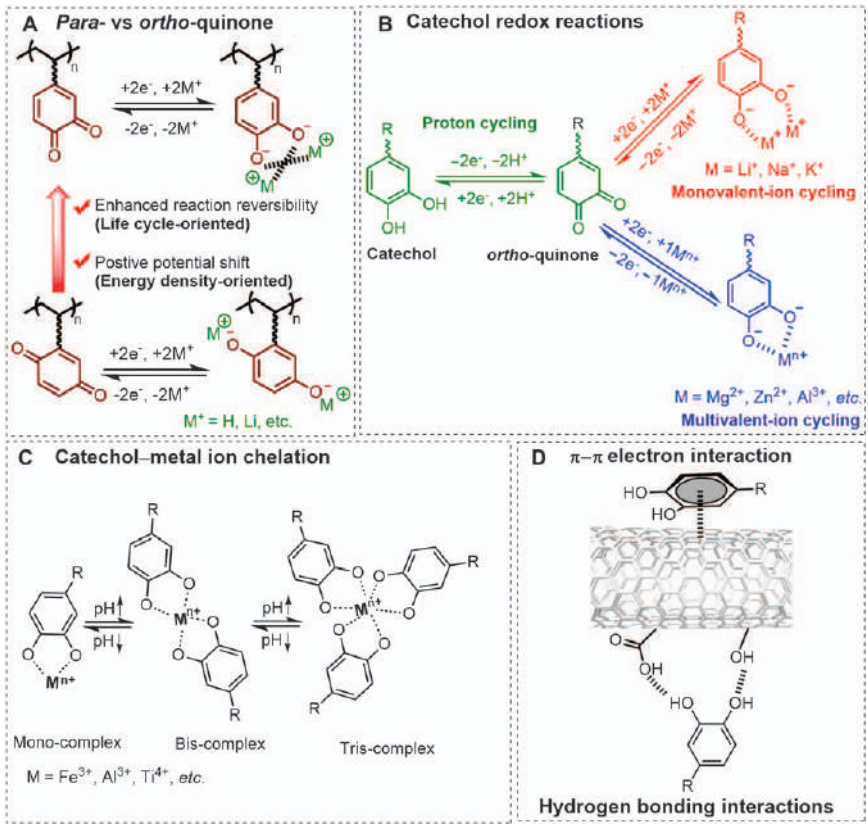


**Figure 7.1** Some of the most relevant physicochemical and electrochemical properties of catechols for energy storage.
(A) Adapted from ref. 28 with permission from John Wiley and Sons, © 2017 Wiley-VCH Verlag GmbH & Co. KGaA, Weinheim. (B) Adapted from ref. 83 with permission from the American Chemical Society, Copyright 2019.

in the 1,2-position endowing the coordination of both monovalent and multivalent cations (Figure 7.1B, C). Although, poly(*ortho*-quinone)s can be accessed through different synthetic routes, poly(catechol)s remain the first choice as *ortho*-quinone precursors owing to their several intriguing properties, which are discussed in the following sections.

Motivated by the aforementioned enhanced electrochemical features of *ortho*-quinones, in this chapter, first, we highlight the relevant physicochemical and electrochemical properties of catechols and their precursors. Moreover, different routes toward poly(catechol)s, including bioresources and synthetic strategies, will be reviewed. Lastly, their application as electrode materials in different electrochemical energy-storage devices will be discussed.

## 7.2 Relevant Physicochemical and Electrochemical Properties of Catechols for Energy Storage

Catechol compounds are ubiquitous to many natural systems, and play a pivotal role in a plethora of biological processes and functions. For instance, some important features associated with their versatile activities are potent antioxidant, antiinflammatory, antimicrobial and anticancer properties, redox abilities, metallic chelation and sequestration, adhesion to both organic and inorganic surfaces through the formation of reversible noncovalent or irreversible covalent interactions, *etc.*[11–13] From these examples, we can see that a single catechol functionality is capable of demonstrating diverse and fascinating properties ascribed to their flexibility in physicochemical properties. In light of these rich properties, we will elaborate some of the archetypal bioinspired catechol chemistries in this section, with a focus on energy-storage applications.

(1) Catechol can be easily oxidized to form *ortho*-quinone by a proton-coupled two-electron oxidation process (Figure 7.1B).[14] Indeed, these reversible redox couples of catechol/*ortho*-quinone ($QH_2$/Q) have been extensively applied to aqueous-based pseudocapacitors and proton batteries (*vide infra*). Furthermore, in order to expand the scope of catechols for other energy-storage systems, they are also used as parental molecules to produce *ortho*-quinone redox sites.

(2) Catechol also chelates metal ions to form strong, yet reversible complexes with various metal ions, including $Li^+$, $Zn^{2+}$, $Mg^{2+}$, $Fe^{3+}$, $V^{3+}$, $Ti^{4+}$, *etc.* (Figure 7.1C).[15] The stoichiometry of the metal–catechol bond is highly dependent on the valence of the metal ion, the catechol to metal ion molar ratios, and the pH. This propensity is highly desired for the design of catechol-based universal electrodes that are compatible with different battery chemistries, including mono- and multivalent cell configurations. For instance, Figure 7.1B shows that the *in situ* generated *ortho*-quinone further undergoes two-electron and two-monovalent cation (or one-multivalent cation) reversible redox conversions with the catecholate, which makes it a promising electrode candidate for various nonproton batteries.

(3) Catechol is capable of interacting with surfaces that are rich in aromatic compounds (*e.g.*, carbon nanotubes, graphene, *etc.*) through π–π interaction and hydrogen bonding (Figure 7.1D).[16–18] This mussel-inspired adhesion onto high-surface energy substrates enables them to be applied as both dual-functional binder and redox-active electrode materials. Excluding the use of an external binder is always an extra advantage to increase the energy density of the device and to ensure a long cycle life, by avoiding spurious reactions arising from the binder.[19]

Therefore, the wide breadth of bioinspired surface- and redox-active catechol chemistry, benefiting from the reversible redox activity of the $QH_2$/Q couple, followed by chelation/unchelation of metal ions is highly coveted for energy-storage applications, and will push forward the design of novel and advanced biomimetic poly(catechol) materials.

## 7.3 General Design Features Toward Catechol-containing Polymers

Generally, multiple catechol functionalities are incorporated into (bio)polymers as pendant groups or as part of the polymer backbone by employing various (semi)synthetic protocols summarized in Figure 7.2. Biopolymers such as lignin (Figure 7.2A), melanin (Figure 7.2B) and tannin (Figure 7.2C) are examples of poly(catechol)s featuring catechol moieties in their polymer backbone. Figure 7.2D shows a representative scheme of the oxidative polymerization of catechol monomers which typically provides polymers with catechols in the main chain. On the other hand, direct chemical conjugation of catechol synthons onto preformed (bio)polymers through post-polymerization procedure generally affords polymers with catechols as the side-chain derivatives (Figure 7.2E). Conducting polymers doped with anion-functionalized catechol small molecules are also reported. As a special case, the catechol moieties neither constitute the part of the polymer backbone nor present as the pendant groups, rather they are held with the polymeric host *via* electrostatic interactions (Figure 7.2F). Additionally, the polymerization of pendant catechol-containing monomers, protected or not, by different polymerization techniques also integrates catechol units as pendant groups (Figure 7.2G). In the following subsections, these main synthetic protocols are elaborated.

### 7.3.1 Catechol Biopolymers

#### *7.3.1.1 Lignin-based Biopolymers*

Lignin is a three-dimensional (3D) amorphous and highly branched polyphenolic biopolymer network which connects different kinds of methoxylated phenylpropanoid units (*p*-hydroxyphenyl, guaiacyl and syringyl) by ether bonds and carbon–carbon bonds.[20] Lignin structure is complicated

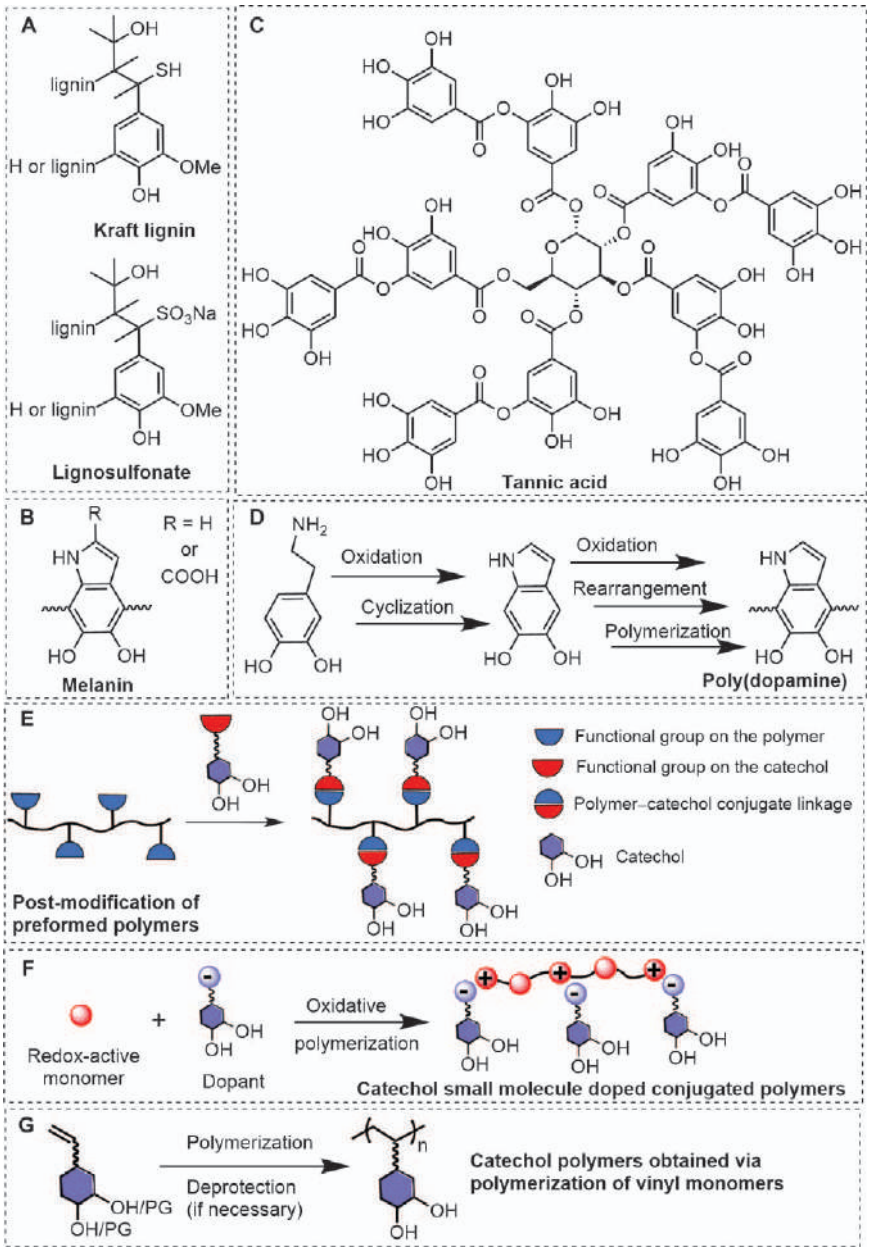


**Figure 7.2** Catechol biopolymers (A–C) and different design strategies toward catechol containing synthetic polymers (D–G).

compared with other polymers due to its random chemical bonding between various monolignols. The simplified chemical structure of the two most common lignins, kraft lignins (or alkaline lignins) and lignosulfonates

(which contain sulfonate groups) is shown in Figure 7.2A. Lignin, being the second most abundant naturally occurring biopolymer, and a by-product of the pulp and paper industry, produced at several millions of pounds per year, therefore holds a great prospect as a renewable ultralow-cost active material to fabricate large-scale energy-storage systems.

#### *7.3.1.2 Melanin-based Biopolymers*

Eumelanin is a disordered heteroaromatic polymeric pigment ubiquitous in flora and fauna.[21] It contains a high density of redox-active polyphenols in the form of catechols based on 5,6-dihydroxyindole and 5,6-dihydroxyindole carboxylic acid building blocks. The simplified chemical structure of melanin is given in Figure 7.2B, but different redox forms of the building blocks, hydroxyquinone, semiquinone and quinone moieties, also possibly coexist in the macromolecular structure.

#### *7.3.1.3 Tannin Biopolymers*

Tannic acid, one of the hydrolyzable tannins, is a natural polyphenolic biomass extensively found in woods and plant-derived feeds. They have molecular weights ranging from ~500 to 5000 Da, and are highly water-soluble.[22] Tannic acid possesses a unique polyphenol structure with a large number of redox centers consisting of a mixture of catechol and pyrogallol derivates and glucose (Figure 7.2C).

### 7.3.2 Synthetic Poly(catechol)s

#### *7.3.2.1 Catechol Polymers Obtained* via *Oxidative Polymerization of Redox-active Monomers*

The oxidative polymerization of catechol and its derivatives (L-3,4-dihydroxyphenylalanine, dopamine, *etc.*) has been widely practiced owing to the chemical reactivity of catechol precursors, ease of polymerization and polymerization-induced robust coating propensity.[23] Taking dopamine, commonly known as a neurotransmitter, as a model compound, its self-polymerization into poly(dopamine) *via* oxidation is shown in Figure 7.2D. In the presence of molecular oxygen or an external oxidizing agent, the catechol functional group oxidizes to *ortho*-quinone and further undergoes cyclization, rearrangement reactions and spontaneously polymerizes into poly(dopamine) under alkaline aqueous conditions, incorporating catechol, quinone and amine functionalities in the polymer structure.[23]

#### *7.3.2.2 Catechol-derived Polymers* via *Post-modification of Preformed Polymers*

Among different approaches, the chemical conjugation of catechols onto preformed (bio)polymer is a simple and straightforward route. Thanks to the

huge diversity of biopolymers that feature numerous reactive functional groups such as –$NH_2$, –COOH, –CHO, and –OH, *etc.*, catechol-derivatives bearing complementary functional groups can be readily ligated through the formation of amide, ester and miscellaneous linkages.[13] Additionally, such functional groups can also be easily installed on (semi)synthetic polymers, employing commonly practiced synthetic strategies. A schematic illustration of this approach is given in Figure 7.2E.

#### *7.3.2.3 Catechol Small-molecule Doped Conjugated Polymers*

Another interesting protocol to incorporate catechol groups into the polymer system is by doping of an anion-functionalized catechol small-molecule approach. During the (electro)chemical polymerization of redox-active monomer (pyrrole, aniline, *etc.*), the anion-functionalized catechol molecules act as the electroneutralizing dopants, eventually integrating into the conducting polymer matrix, held *via* electrostatic interactions with the host (Figure 7.2F).[24,25]

### 7.3.3 Catechol Polymers Obtained *via* Polymerization of Vinyl Monomers

One of the main limitations of the above-mentioned biopolymers (Section 7.3.1) in energy-related applications is their low phenolic content relative to their high molecular weights and complex structures of such biopolymers. Please note that the specific capacity of electrode materials directly depends on the content of these redox-active cores in the macromolecule. Moreover, post-modification of preformed polymers (Section 7.3.2.2) and incorporation of catechols as small counter-anions (Section 7.3.2.3), suffer from nonquantitative catechol incorporation, and even more importantly, lack of precise control over functional, spatial and compositional tunability. Therefore, to create poly(catechol)s with controlled structures and superior properties, the polymerization of pendant catechol-containing vinyl monomers, protected or not, by different polymerization techniques has become an intriguing platform (Figure 7.2G).[13] This approach not only provides a fundamental route toward such materials but also imparts numerous multifunctional properties inherent to this synthetic methodology (macromolecular engineering aspects).

For instance, Patil el al. reported the synthesis of well-defined poly(dopamine acrylamide) [$P(DA)_n$] homopolymers with different molar masses ranging from 5 to 35 kg mol$^{-1}$ and low dispersities (*ca.* <1.3) by the reversible addition–fragmentation chain transfer (RAFT) polymerization of acetonide-protected dopamine acrylamide (Figure 7.3A).[26] Post-polymerization acid-catalyzed hydrolysis cleaved acetonides, releasing free catechols in quantitative yields. The same group exploited a cobalt-mediated radical polymerization (CMRP) approach to develop inventive catechol-derived poly(ionic liquid)s, featuring different counteranions (*e.g.*, $Cl^-$, $PF_6^-$, $TFSI^-$, *etc.*) (Figure 7.3B).[27] Later, they extended the RAFT polymerization strategy for the preparation of poly(4-vinyl catechol) [$P(4VC)_n$] and

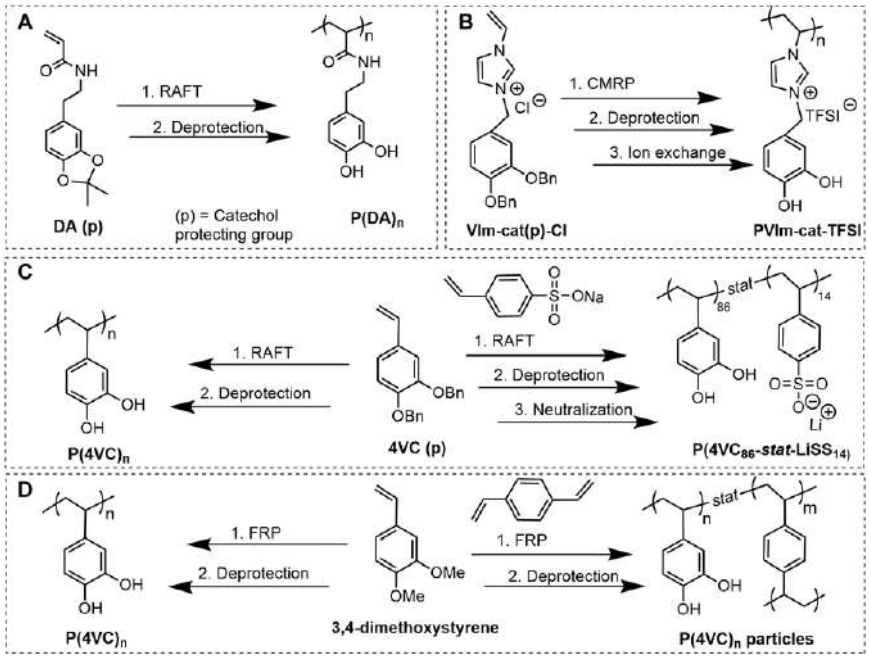


**Figure 7.3** Macromolecular engineering of catechol-bearing (co)polymers by radical polymerization of vinyl monomers.

their copolymer, poly(4-vinyl catechol-*stat*-lithium styrene sulfonate) [P($4VC_{86}$-*stat*-$LiSS_{14}$)] (Figure 7.3C).[28] Very recently, P(4VC)$_n$ homopolymers were also obtained through free-radical homopolymerization of 3,4-dimethoxystyrene (DMS) followed by a deprotection step.[29] In a pioneering work, Mecerreyes *et al.* reported the synthesis of P(4VC)$_n$ in the form of nanoparticles by cross-linking copolymerization of DMS with divinylbenzene *via* (mini)emulsion polymerization (Figure 7.3D).[30]

## 7.4 Application of Catechol Polymers in Electrochemical Energy Storage

Due to the interesting redox properties of poly(catechol)s, they have found application as active materials in different types of electrochemical energy storage devices. In this chapter, we discuss the electrochemical performance of such materials in different energy storage systems and report on the main challenges, opportunities and limitations faced by these materials. A basic description of the different electrochemical energy storage technologies represented in Figure 7.4 is included below.

(1) Electric double-layer capacitor (EDLC): This includes two symmetric electrodes based on high surface area conducting material (activated carbon, CNTs, graphene, *etc.*) (Figure 7.4A). EDLCs store the charge

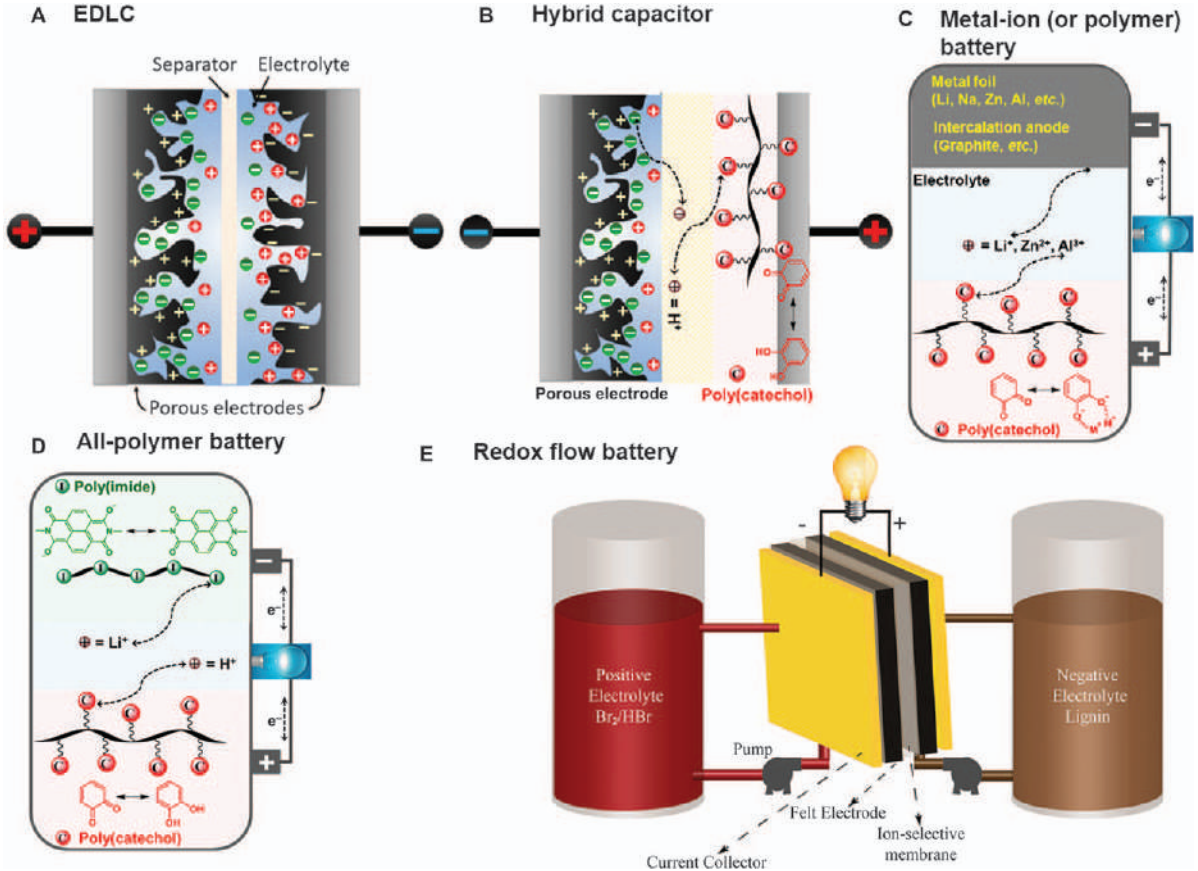


**Figure 7.4** Schematic illustration of different energy-storage devices described in this chapter. (A) Electric double-layer capacitor. (B) Hybrid capacitor. (A and B) Adapted from ref. 88 with permission from Elsevier, Copyright 2019. (C) Metal-ion (or polymer) battery. (D) All-polymer battery. (E) Redox flow battery. Reproduced from ref. 87 with permission from the American Chemical Society, Copyright 2017.

electrostatically using reversible electroadsorption of ions of the electrolyte onto polarized electrode materials in the form of the electrical double-layer. They possess many properties that are currently unattainable for batteries involving higher power density, subsecond charging, ultralong cycle life, and a very wide range of operational temperature, but store less energy than batteries.[31]

(2) Hybrid capacitor: This device comprises one capacitive electrode, typical from EDLC, which stores energy *via* the formation of an electric double-layer and one battery-like electrode whose energy storage mechanism is based on intercalation or conversion reactions (Figure 7.4B).[32,33] Since hybrid capacitors store both forms of energy (faradaic and capacitive), they exhibit compromised cell performances, effectively bridging the gap between batteries and EDLC. It is worth mentioning that the fast and reversible faradaic redox reactions undergone by some redox-active materials such as poly(catechol)s give sometimes a pseudocapacitive electrochemical response (still faradaic). Therefore, the devices containing these electrodes are sometimes classified either as hybrid capacitors or pseudocapacitors in the literature. In this chapter, we use the term ''hybrid capacitor'' for asymmetric designs and ''pseudocapacitor'' for devices with a symmetric design such as poly(catechol)/poly(catechol). As will be discussed later, some authors have recently demonstrated that poly(catechol)s can be employed as faradaic electrodes in high-performing hybrid capacitors and pseudocapacitors.

(3) Metal-ion (or polymer) battery: This typically consists of one metal anode (or intercalation anode) and one inorganic intercalation cathode, deposited onto a metallic current collector and separated by an insulating membrane. A liquid electrolyte impregnates both electrodes and provides media for the shuttling of ions between the electrodes (Figure 7.4C). Usually, batteries exhibit high specific capacity, and thus energy density, but often suffer from a lack of stability during cycling and slow charging/discharging rates. In metal–polymer batteries the intercalation cathode is substituted by a redox-active polymer such as poly(catechol).

(4) All-polymer battery: In this battery configuration, both cathode and anode are based on redox-active polymers (Figure 7.4D) having redox activity at different redox potentials. Such devices are particularly intriguing from the standpoint of availability, sustainability (metal-free) and cost but generally deliver lower energy density than conventional metal-ion batteries.

(5) Redox flow battery (RFB): Unlike the aforementioned devices that use active materials as solid electrodes stack to the current collectors in conventional static batteries, the redox flow battery utilizes the energy-bearing redox-active materials dissolved in liquid electrolytes which are stored in external reservoirs, as shown in Figure 7.4E. Energy conversion occurs when the redox-active electrolytes (containing

vanadium active species in the state-of-the-art RFB) are pumped into the electrochemical reactor to pass through porous electrodes. This unique battery design decouples the stored energy and power, which enables their independent scaling, leading to significant advantages such as excellent scalability, flexible design and long life. Therefore, RFBs employing nature-based redox organic molecules, instead of toxic and problematic vanadium compounds, are widely recognized to be suitable for large-scale, safe and sustainable storage applications.[34]

It is worth mentioning here that, similar to their inorganic counterparts, most of the redox polymers, including poly(catechol)s are not sufficiently conductive to be used as electrodes right away. Therefore, it is necessary to combine them with good electronic conductors in order to exploit their redox activity and obtain efficient charge transfer to and from the active sites. Most often, high surface area carbon-based inorganic materials, such as carbon black, carbon nanotubes or reduced graphene oxide are used as electric conductivity enhancers in the electrode. Lately, intrinsically conducting polymers such as poly(pyrrole), poly(aniline) and poly(3,4-ethylenedioxythiophene) were also found to be interesting electric conductivity-enhancing components for the fabrication of carbon-free electrodes (or fully polymeric electrodes).[35] The latter approach is particularly captivating from the perspective of material handling, processing, and manufacturing, benefiting from the superior dispersibility of conductive polymers in aqueous or organic solvents over the conventional carbon additives. Additionally, because of their soft, light-weight and flexible nature, they also bring about great opportunities to make wearable, flexible, foldable and printable advanced energy-storage systems.

## 7.4.1 Supercapacitors

### *7.4.1.1 Activated Carbon Electrodes* via *Carbonization of Catechol Polymers for EDLC*

Poly(catechol)s are promising bioinspired sources for preparing porous carbon materials *via* carbonization due to their excellent biocompatibility, high carbon yield, robust wetting and adhesion capabilities, and ability to dope heteroatoms (N, S, O, *etc.*), which might also contribute to energy storage *via* pseudocapacitance. Since this research topic has received extensive dissemination over recent years and poly(catechol)s are used here as carbon precursors but not as active-materials,[23,36,37] only one representative example is included in this chapter. In this selected example, Guo *et al.* reported a lignin-based three-dimensional (3D) hierarchical porous carbon with abundant interconnected large pores, prepared *via* hydrothermal carbonization and KOH activation processes (Figure 7.5).[38] The porous carbon electrode exhibited a high specific surface area of 1660 $m^2 g^{-1}$, good electrical conductivity of 5.4 $S cm^{-1}$ and a 3D hierarchical texture made up of abundant micropores, small mesopores and macropores. Consequently, this

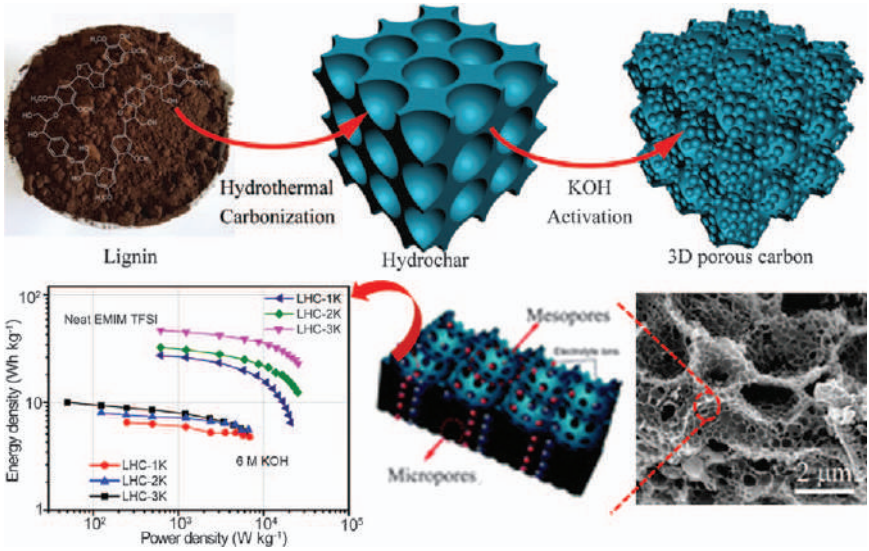


**Figure 7.5** Schematic illustration of the preparation of lignin-based 3D hierarchical porous carbon, along with an SEM image.
Adapted from ref. 38 with permission from the Royal Society of Chemistry.

electrode demonstrated a high specific capacitance (420 $F\,g^{-1}$), exceptional rate performance (67% retention when the current density increased 1000-fold from 0.1 $A\,g^{-1}$ to 100 $A\,g^{-1}$), and excellent cycle stability (99% capacitance retention after 10 000 cycles at 5 $A\,g^{-1}$) in 6 M KOH electrolyte. Moreover, the symmetric supercapacitor delivered an outstanding maximum energy/power density of 46.8 $Wh\,kg^{-1}$/25.4 $kW\,kg^{-1}$.

### *7.4.1.2 Composite Electrodes for Hybrid Capacitors and Pseudocapacitors*

**7.4.1.2.1 Lignin Electrodes.** Lignins are the most studied electrode materials among the different poly(catechol)s for hybrid capacitors (asymmetric designs) and pseudocapacitors (symmetric design). They are typically mixed with two types of conductivity-enhancing additives, *i.e.*, carbon additives (graphite, CNT, graphene, *etc.*) and conductive polymers [poly(pyrrole), *etc.*]. In some of those cases, the conducting additive is also used as a physical scaffold to mitigate one of the main issues of lignin electrodes which is the dissolution of lignin in the electrolyte during operation. This issue causes the loss of active material in the electrode and consequently a fast capacity decay with cycling.

Among the carbon conductive additives, graphite is one of the cheapest and is easily obtained from nature. Liu *et al.* emphasized the fabrication of lignosulfonate/graphite electrodes under a solvent-free mechanical milling method, without additional additives (Figure 7.6A).[39] The optimized composite

electrode having 20 wt.% graphite exhibited a conductivity of 280 $S\,m^{-1}$ and discharge capacity of 35 $mAh\,g^{-1}$. This approach is a promising direction toward scalable production of lignosulfonate organic electrodes, typically, whose commercialization is limited by the expensive conductive additives.

Liedel and co-workers observed that in the absence of external binder, low-molecular-weight lignin in composite electrodes containing activated carbon suffered from capacity decay due to the dissolution of part of the active material into the electrolyte during prolonged cycling.[40] To mitigate this, they proposed a glyoxal cross-linking approach, and optimized composite electrode fabrication through a two-step process; demonstrating how the different order of processing steps may influence the electrochemical performance.[41] The glyoxal cross-linking of lignin/active carbon (AB-520 with a specific surface area of 2000 $m^2\,g^{-1}$) deposited on the current collector was found to be the better approach [process (ii) in Figure 7.6B] than the prior cross-linking and subsequent processing with the active-carbon route [process (i)]. The former approach significantly improved both the specific capacity and cycling stability even in the binder-free configuration. Final electrodes which benefit from combined faradaic (derived from lignin) and non-faradaic charge storage (related to activated carbon) reached a capacity of 80 $mA\,h\,g^{-1}$ and exhibited a combination of battery-like and capacitor-like behaviors.

Carbon nanotubes are the preferred conductive additives for the fabrication of flexible electrodes in wearable/portable electronics. Peng *et al.* fabricated a flexible solid pseudocapacitor by using lignosulfonate/$HNO_3$-treated single-walled carbon nanotube (SWCNT) as the electrode and cellulose/$Li_2SO_4$ gel as the electrolyte.[42] The lightweight composite electrode exhibited a 3D network structure due to hydrogen and π–π interaction between lignin and SWCNT (Figure 7.6C). The assembled device not only achieved a high specific capacitance of 292 $F\,g^{-1}$, excellent rate capability and outstanding energy density of 17.1 $Wh\,kg^{-1}$ with a power density of 324 $W\,kg^{-1}$, but also retained them even after suffering 1000 bending cycles.

Graphene possesses high surface area, good chemical stability, flexibility and excellent mechanical strength, and also is a useful growth substrate that can anchor diversified active materials for electrochemical applications. Inspired by the Venus flytrap, Geng *et al.* designed a reconfigurable and 3D hierarchical graphene cage that provides a robust physical barrier against lignin dissolution into the electrolyte (Figure 7.6D).[43] The composite electrode delivered a high capacitance of 211 $F\,g^{-1}$ at 1.0 $A\,g^{-1}$ with 88% capacity retention after 15 000 cycles.

A pioneering work by Inganas *et al.* in 2012 has led to an important advancement in the field of carbon additives-free renewable electrode materials.[35] They designed lignosulfonate/poly(pyrrole)-based interpenetrating networks by the electrochemical polymerization of pyrrole in aqueous lignosulfonate solution that served as the redox-active electroneutralizing polyanion (Figure 7.7). *Ortho*-quinone functionalities generated *in situ* during oxidation processes were the major contributors to the overall stored energy [minor contribution also comes from poly(pyrrole)], and the

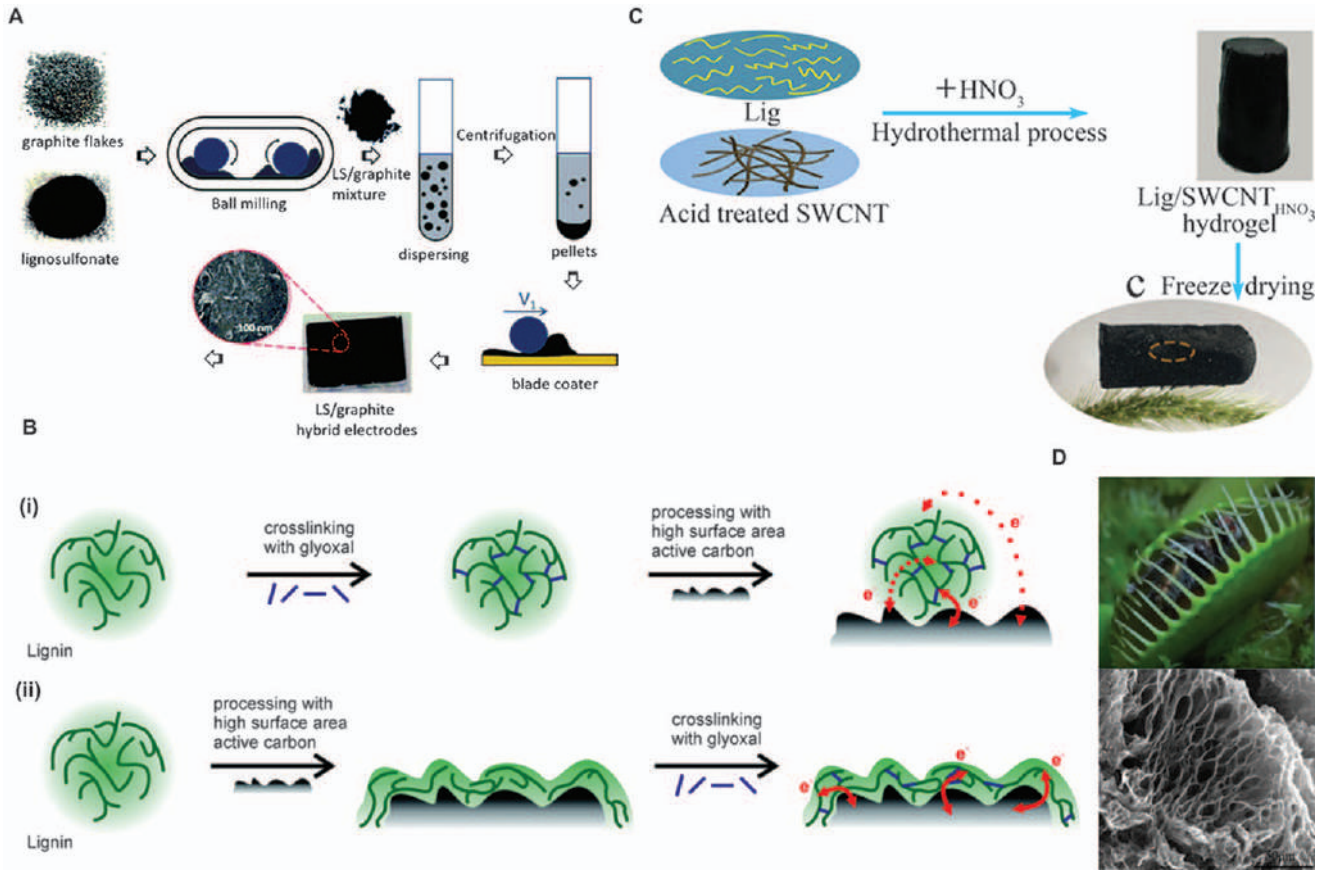
A
graphite flakes
lignosulfonate
Ball milling
LS/graphite mixture
Centrifugation
dispersing
pellets
blade coater
LS/graphite hybrid electrodes
C
Lig
Acid treated SWCNT
+HNO3
Hydrothermal process
Lig/SWCNT HNO3 hydrogel
Freeze drying
B
(i)
crosslinking with glyoxal
processing with high surface area active carbon
Lignin
(ii)
processing with high surface area active carbon
crosslinking with glyoxal
Lignin
D

capacitance values spanned from 1000 $F g^{-1}$ at low discharge rates (1 $A g^{-1}$) to a remarkable 900 $F g^{-1}$ at high discharge rates (16 $A g^{-1}$), with no diffusion limitations. Inspired by this approach, later, ternary composites were also designed and tested as electrodes in pseudocapacitors. The charge storage capacities of the binary composites [lignosulfonate/poly(pyrrole)] are significantly enhanced from 70 to 147 mAh $g^{-1}$ and from 69 to 128 mAh $g^{-1}$ by including two separate electroactive dopants, anthraquinone sulfonate[44] and phosphomolybdic acid,[45] respectively.

One of the disadvantages of a carbon-free electrode is the poor mechanical strength. In order to improve the mechanical integrity of such electrodes, Peng *et al.* designed lignosulfonate/poly(pyrrole) hydrogel by introducing functionalized porous carbon nanospheres as cross-linking sites.[46] These additional cross-linking sites not only improved the compressive strength of the composite electrode (9.3 *versus* 6.0 kPa) but also the electrochemical performance compared to the traditional lignosulfonate/poly(pyrrole) network. The assembled symmetric flexible pseudocapacitor with cellulose/$H_2SO_4$ hydrogel electrolyte demonstrated superior areal capacitance (522 mF $cm^{-2}$), good rate capability and outstanding energy density (72.5 μWh $cm^{-2}$), and remarkably, retained electrochemical stability even after suffering 1000 bending cycles.

Though poly(pyrrole)/lignin gained widespread attention for the design of carbon-free electrodes, fast degradation of poly(pyrrole) within the composite after cycling lead the researchers to investigate lignin blends with other conducting polymers, among them polyaniline (PANI) and poly(3,4-ethylenedioxythiophene) (PEDOT), to name only a few.

Ajjan *et al.* employed both chemical polymerization and electrochemical polymerization approaches to synthesize a highly stable lignosulfonate/PEDOT electrode that delivered specific capacitance of 170 $F g^{-1}$ and excellent capacitance retention of 83% after 1000 cycles (Figure 7.8A).[47] Once again, by introducing a third redox-active component [poly(aminoanthraquinone)], the same group reported a trihybrid electrode with specific capacitance of 418 $F g^{-1}$ that impressively retained more than 80% capacitance after 10 000 cycles.[48] Later, Mecerreyes' group went a step further by assembling asymmetric hybrid capacitors based on lignosulfonate/PEDOT and partially reduced graphite oxide as the positive and negative electrodes, respectively (Figure 7.8B).[49] The asymmetric device exhibited capacitance of 34.6 $F g^{-1}$ within an operational voltage window of 1 V, and capacitance retention up to

**Figure 7.6** The schematic illustration of the preparation of (A) lignosulfonate/graphite electrode. Reproduced from ref. 39 with permission from the Royal Society of Chemistry. (B) Lignin/active carbon composite electrode through two approaches. Reproduced from ref. 41 with permission from the Royal Society of Chemistry. (C) Lignosulfonate/$HNO_3$-treated SWCNT structural electrode. Reproduced from ref. 42 with permission from the American Chemical Society, Copyright 2018. (D) Venus flytrap-inspired lignin-based 3D hierarchical graphene, along with SEM image. Reproduced from ref. 43 with permission from the American Chemical Society, Copyright 2018.

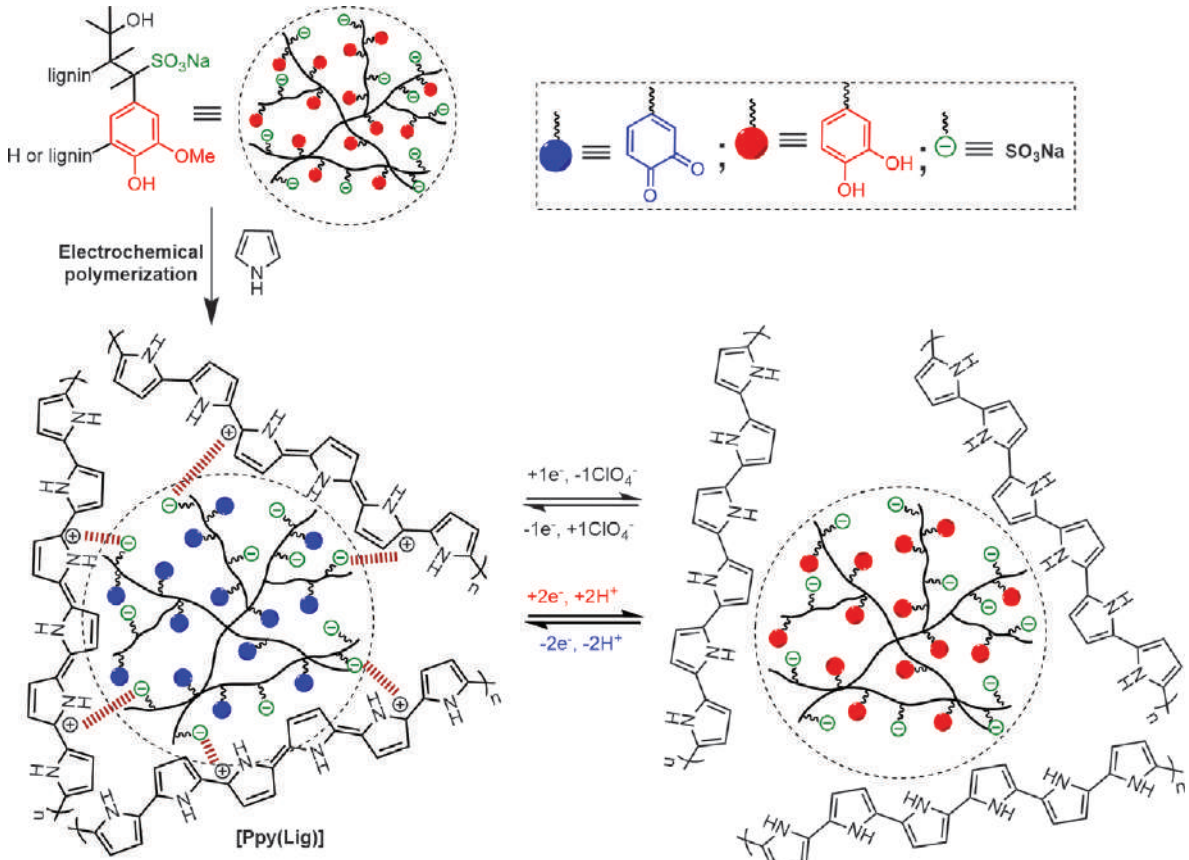


**Figure 7.7** Route toward renewable organic electrode materials based on lignosulfonate/poly(pyrrole) interpenetrating networks. Adapted from ref. 13 with permission from Elsevier, Copyright 2018.

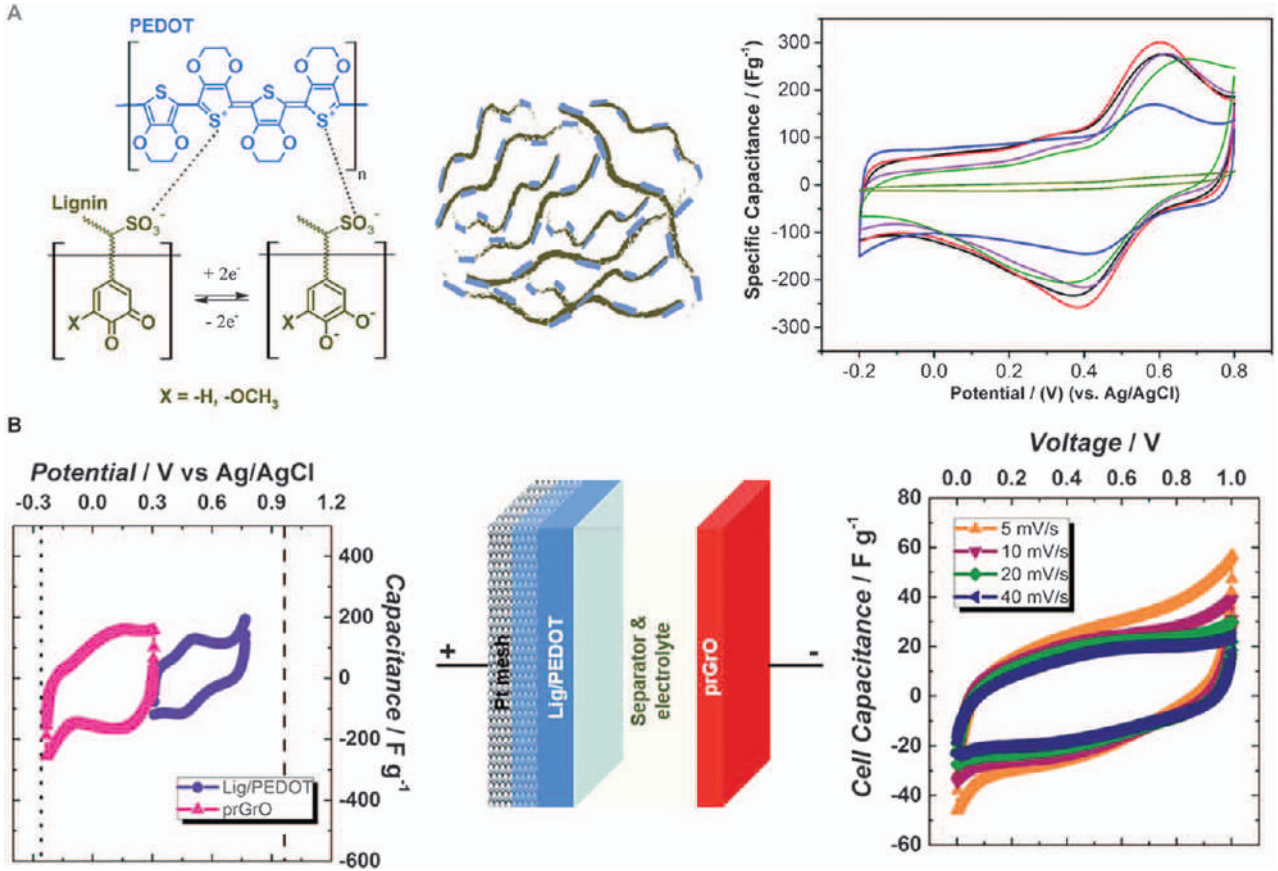


**Figure 7.8** (A) Schematic illustration of lignosulfonate/PEDOT, along with cyclic voltammograms. Reproduced from ref. 47 with permission from the Royal Society of Chemistry. (B) Asymmetric pseudocapacitor based on lignosulfonate/PEDOT and partially reduced graphite oxide. Reproduced from ref. 49 with permission from the Royal Society of Chemistry.

52.2% after 1000 cycles. Very recently, Che *et al.* simplified the redox-active polymer/conducting polymer electrode fabrication method.[50] Their approach is based on the spontaneous incorporation of lignosulfonate into PEDOT by means of counter-ion exchange *via* aqueous synthesis. This method offers the possibility for manufacturing of the lignosulfonate/PEDOT composite in an up-scaling effort toward large-scale electrical energy-storage technology. The electrode synthesized through an optimized strategy reached an improved charge capacity of 44.6 $mAh\,g^{-1}$, compared to the aforementioned one-pot (electro)chemical oxidative polymerization approaches (27.8 $mAh\,g^{-1}$).

Lately, PANI doped with lignosulfonate interpenetrating networks were also reported. Wu *et al.* demonstrated an interconnected 3D porous conductive network by attaching functionalized graphene hydrogel in chemically oxidized carbon cloth *via* a one-step hydrothermal process, with subsequent chemical deposition of the lignosulfonate/PANI hydrogel, resulting in complete coverage of the functionalized carbon cloth by the functionalized graphene hydrogel (Figure 7.9).[51] The binder- and metal current collector-free, self-standing composite electrode was assembled into a symmetric pseudocapacitor using 1 M $H_2SO_4$ electrolyte. This device demonstrated superior areal capacitance of 1.2 $F\,cm^{-2}$ and an energy density of 0.17 $mWh\,cm^{-2}$ at a power density of 1 $W\,cm^{-1}$ that outperformed most of the conventional supercapacitors in aqueous electrolytes. Furthermore, they also fabricated a flexible all-solid-state pseudocapacitor with $H_2SO_4$/poly(vinyl alcohol) gel electrolyte that exhibited excellent flexibility, despite a lower specific capacitance value of 1.15 $F\,cm^{-2}$.

**7.4.1.2.2 Eumelanin Electrodes.** Eumelanin-based electrodes assembled into aqueous pseudocapacitors have been also reported in the literature. Kumar *et al.* demonstrated a binder-free flexible micro-pseudocapacitor fabricated on polyethylene terephthalate substrate by unconventional lithography based on ParyleneC patterning.[52] This device showed a power density of 5.24 $mW\,cm^{-2}$ at an energy density of 0.44 $mJ\,cm^{-2}$, a specific capacitance of 10.8 $F\,g^{-1}$, and also operated at fast electrode potential scan rates (up to 10 $V\,s^{-1}$). Since Eumelanin exhibits broadband absorption in the UV–Vis region, Xu *et al.* exploited solar light as an external trigger to enhance the storage performance of pseudocapacitors.[53] Under solar light conditions, the resistance of the symmetric device decreased significantly and the capacitance increased by 39%, from 3.8 to 5.3 $mF\,cm^{-2}$ with respect to the dark conditions (after 2000 cycles in Figure 7.10A). Moreover, the device operated over 5000 cycles after prolonged illumination without capacitance decay. The authors hypothesized that supramolecular rearrangements, involving covalent and noncovalent interactions, improved reticulation and presumably improved the performance under prolonged illumination. However, further works are needed to confirm this.

**7.4.1.2.3 Tannin Electrodes.** Oh *et al.* developed a free-standing flexible pseudocapacitor composed of metal ion-assisted tannins and SWCNT

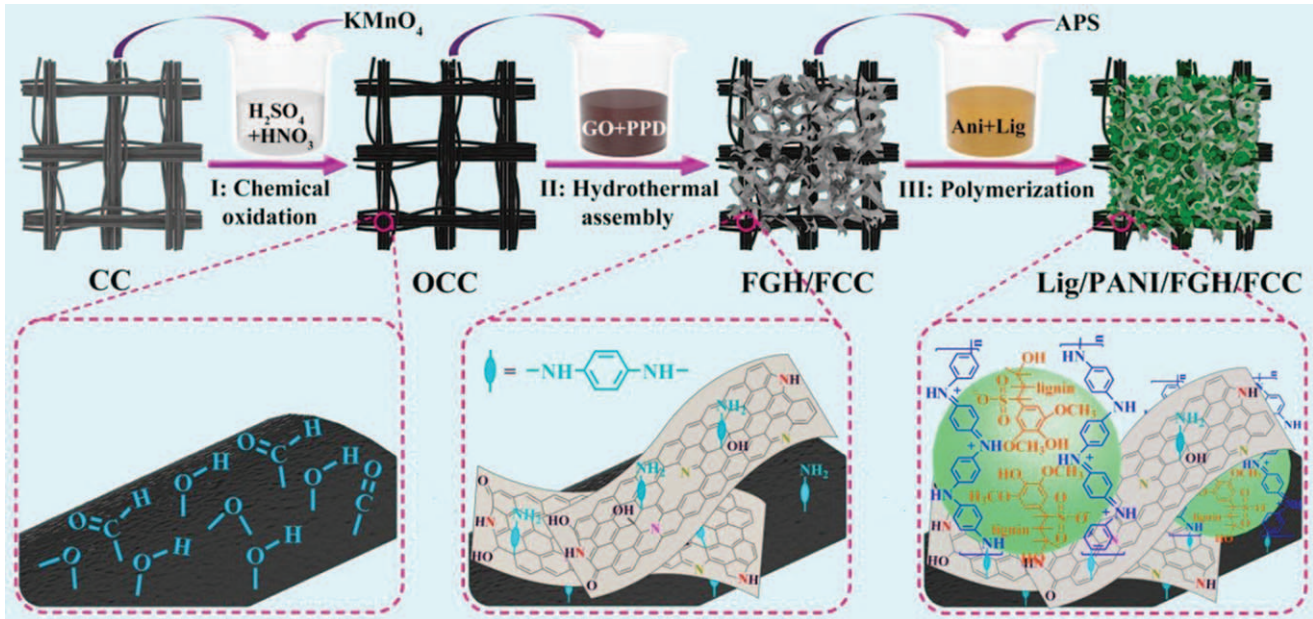


**Figure 7.9** Schematic illustration of the preparation process of lignosulfonate/PANI/functionalized graphene hydrogel/carbon cloth electrode.
Reproduced from ref. 51 with permission from the Royal Society of Chemistry.

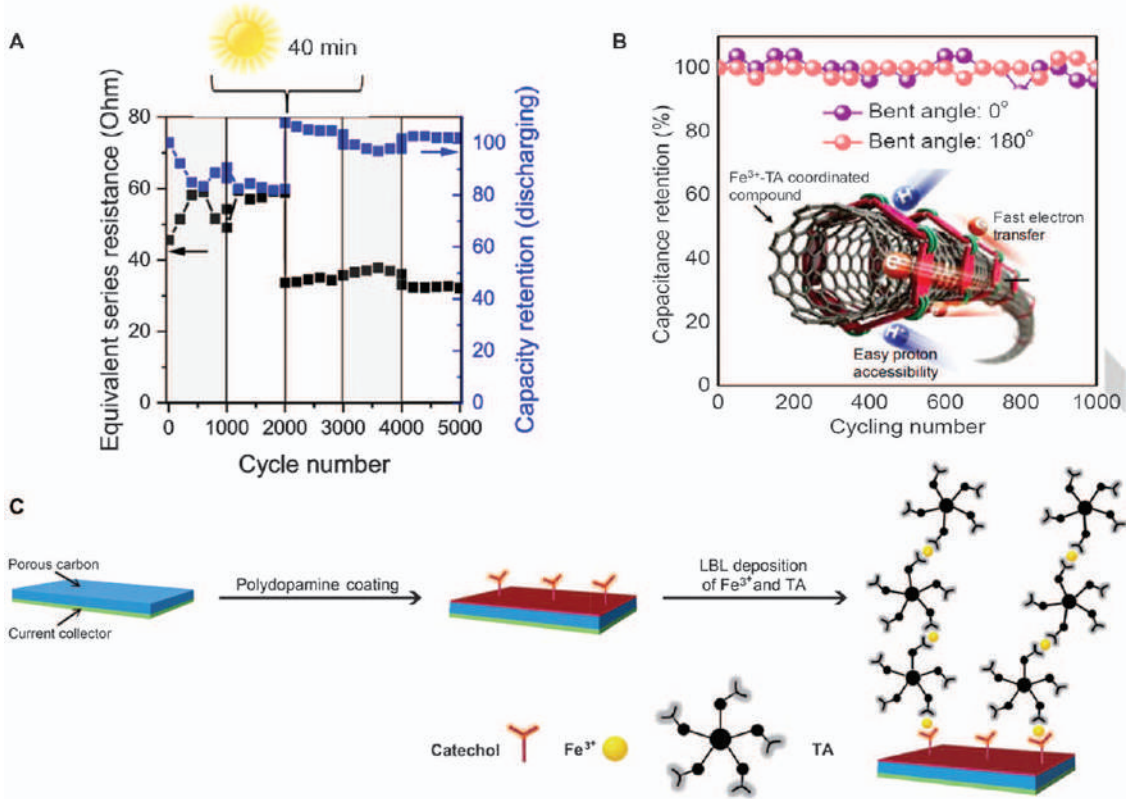


**Figure 7.10** (A) Electrochemical performance (equivalent series resistance and capacity retention) of eumelanin-based pseudocapacitor in both dark and light conditions. Reproduced from ref. 53 with permission from the American Chemical Society, Copyright 2019. (B) Robust and flexible pseudocapacitor based on metal-phenolic self-assembly from Fe-tannic acid on SWCNTs. Reproduced from ref. 54 with permission from John Wiley and Sons, © 2017 Wiley-VCH Verlag GmbH & Co. KGaA, Weinheim. (C) Schematic representation of carbon nanosheet surface modification by poly(dopamine) and subsequent Fe–tannic acid layer-by-layer deposition. Reproduced from ref. 55 with permission from the Royal Society of Chemistry.

electrodes.[54] Tannins formed a stable iron-phenolic coordination complex that self-assembled on the SWCNTs, producing robust and flexible film that maintains stable capacitance retention upon deformation, even after 1000 cycles (Figure 7.10B), along with a high volumetric capacitance of 107.8 $F\,cm^{-3}$ and energy density of 5.8 $mW\,h\,cm^{-3}$. In another work, Lee *et al.* fabricated iron-tannic acid films by layer-by-layer deposition of ferric ions ($Fe^{3+}$) and tannic acid using an aqueous-based process on poly(dopamine)-modified interconnected porous carbon nanosheets (Figure 7.10C).[55] The poly(dopamine) coating not only increased specific capacitance to 244 $F\,g^{-1}$ (83% higher than that of the unmodified electrode) through the pseudocapacitance induced by the catechol groups, but also improved capacitance retention by 7% even after 1000 cycles. Further work with metal ion ($Ni^{2+}$, $Cu^{2+}$or $Fe^{3+}$)-tannin coordination electrodes was performed by Xiong *et al.* who developed 3D porous tannic acid/graphene composites through a hydrothermal assembly.[56] The $Ni^{2+}$-, $Cu^{2+}$- and $Fe^{3+}$-coordinated single electrodes exhibited higher specific capacitance (and energy density based on symmetric device) of 412.4 (16.76 $Wh\,kg^{-1}$), 460.4 (19.13 $Wh\,kg^{-1}$) and 429.4 $F\,g^{-1}$ (17.6 $Wh\,kg^{-1}$) than the pristine tannic acid/graphene (373.6 $F\,g^{-1}$ and 14.76 $Wh\,kg^{-1}$).

Mukhopadhyay *et al.* used tannins extracted from bark of the chestnut tree to fabricate tannin/poly(pyrrole) electroactive electrodes by oxidative electropolymerization on sustainable carbonized wood in order to prepare a free-standing cathode entirely from biomass.[57] The electrode exhibited a discharge capacity of ~370 $F\,g^{-1}$ at 0.5 $A\,g^{-1}$ and still retained 196 $F\,g^{-1}$ at a high current rate of 25 $A\,g^{-1}$. Moreover, the high porosity and the large surface area offered by the hierarchical anisotropic structure of carbonized wood enabled high mass loaded electrodes with thicknesses up to 4.5 μm. Consequently, this biohybrid electrode achieved an areal capacitance value of 4.6 $F\,cm^{-2}$ at 0.5 $mA\,cm^{-2}$ with capacity retention of 2.6 $F\,cm^{-2}$ at the higher current rate of 10 $mA\,cm^{-2}$, which is 1.5 times higher than conventional activated wood carbon.

**7.4.1.2.4 Synthetic Poly(catechol) Electrodes.** In this subsection, we discuss the electrochemical properties of poly(catechol)s that were not obtained by bioresources but by means of different synthetic routes. Kim *et al.* compared the electrochemical performance of electrosynthesized poly(pyrrole-*co*-catechol), a mesostructured composite electrode obtained *via* a colloidal templating strategy using polystyrene opal (Figure 7.11A, B) with a randomly structured copolymer electrode (obtained without polystyrene opal template) and poly(pyrrole).[58] The well-structured (pCy) and randomly structured (Cy) copolymer electrodes delivered superior volumetric capacitance (~138 and ~117 $F\,cm^{-3}$, respectively, *versus* ~106 $F\,cm^{-3}$) than the poly(pyrrole) (PPy; Figure 7.11C). Moreover, the presence of macropores in the pCy electrode facilitated electron/ion transport, which rendered enhanced rate capability compared to the Cy electrode. Furthermore, both these electrodes demonstrated excellent cycling performance, which retained more than 75% capacitance over an extended 10 000 cycles.

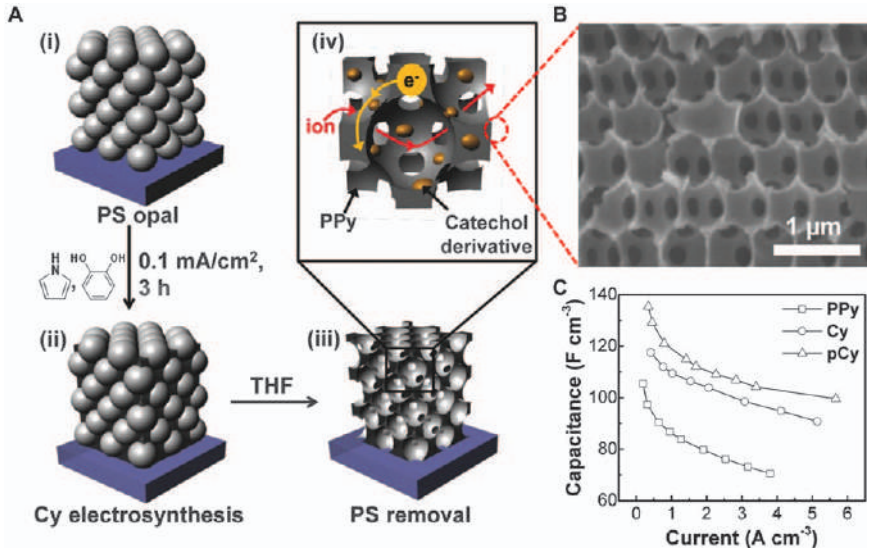


**Figure 7.11** (A) Process flow for the fabrication of a well-structured mesoporous poly(pyrrole-*co*-catechol) electrode that possesses fast and facile ion and electron transport pathways, along with its cross-sectional SEM image (B). (C) Rate capability of PPy, Cy and pCy electrodes at different current densities.
Adapted from ref. 58 with permission from John Wiley and Sons, © 2015 Wiley-VCH Verlag GmbH & Co. KGaA, Weinheim.

Benoit *et al.* proposed a dual-functional binder- and redox-active catechol polymer that was obtained through diazotization of methoxy-protected 3,4-dimethoxybenzenediazonium ions and polystyrene, followed by *in situ* electrochemical oxidative removal of methoxy protecting groups to release *ortho*-quinone moieties (Figure 7.12A, right-half).[16] For comparison they also fabricated 3,4-dihydroxybenzene-modified activated carbon with polystyrene (Figure 7.12A, left-half) and unmodified activated carbon with polystyrene electrodes. The dual-functional polymer/activated carbon electrode not only demonstrated a higher specific charge of 188 $C\,g^{-1}$ *versus* 123 and 76 $C\,g^{-1}$, but also a superior rate performance, retaining 86% *versus* 82 and 77% at 100 $mV\,s^{-1}$ (compared to that at 1 $mV\,s^{-1}$) compared to catechol-modified activated carbon and unmodified electrodes. Furthermore, these modified electrodes showed ~90% of the capacitance retention upon cycling over 5000 CVs at 10 $mV\,s^{-1}$.

Milroy *et al.* reported pseudocapacitive hydrogel electrode based on electropolymerization of dopamine-conjugated hyaluronic acid which was obtained *via* one-step carbodiimide chemistry (Figure 7.12B).[59] This biopolymer electrode exhibited high pseudocapacitance (up to ~900 $F\,g^{-1}$) and discharge capacity (~130 $mAh\,g^{-1}$ at 10 $A\,g^{-1}$), while maintaining long-term electroactivity over 400 CV cycles. Another example of catechol precursor-modified biopolymer was demonstrated by Liedel and co-workers.[60] They

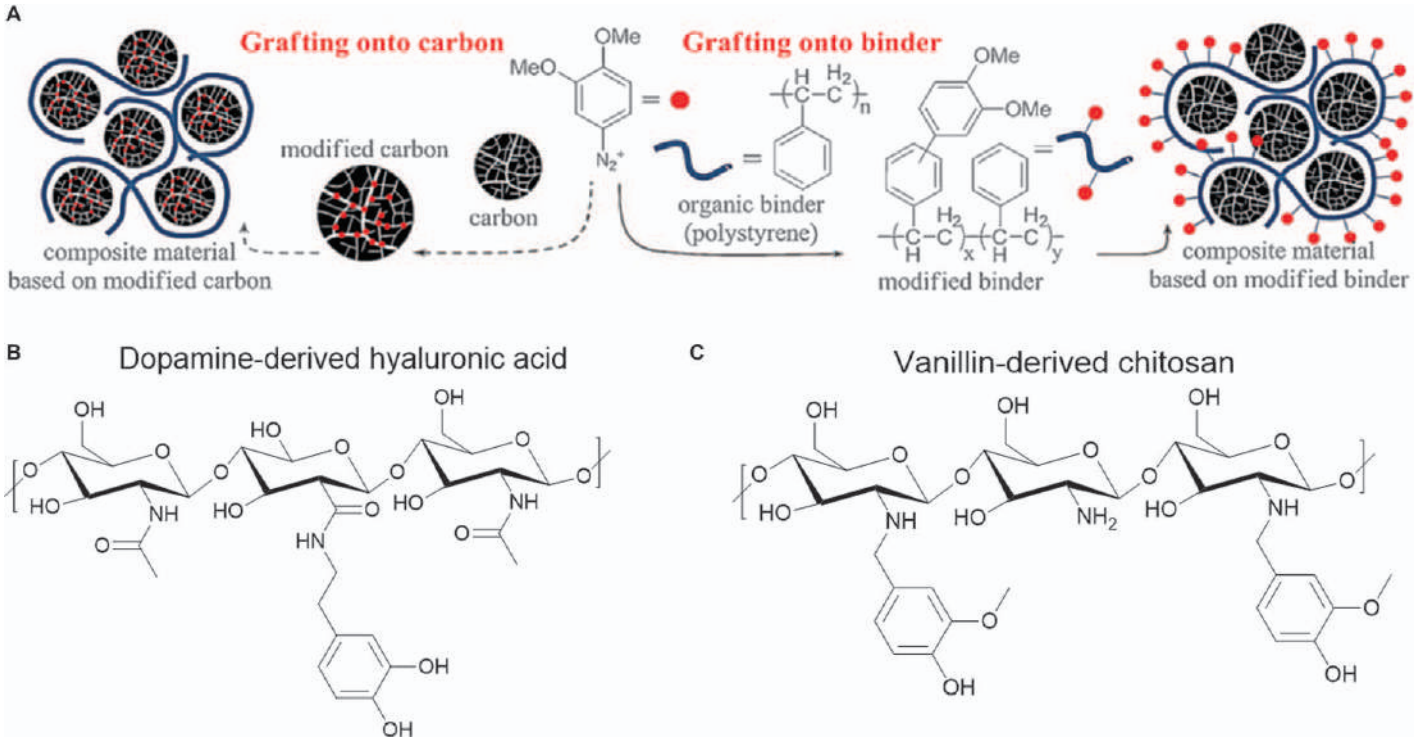


**Figure 7.12** (A) Schematic representation for the preparation of catechol-modified activated carbon (left-half) and catechol-modified polystyrene binder/activated carbon (right-half) electrodes. Reproduced from ref. 16 with permission from John Wiley and Sons, © 2016 Wiley-VCH Verlag GmbH & Co. KGaA, Weinheim. Chemical structure of dopamine-derived hyaluronic acid (B) and vanillin-derived chitosan (C) biopolymers.

derivitized primary amine-rich chitosan with vanillin by successive imine formation and imine reduction reactions (Figure 7.12C). This biocomposite with carbon black electrode in a binder-free configuration showed reversible charge storage up to 80 mAh $g^{-1}$ (respective to the total electrode material) and good stability (68% capacity retention over 100 cycles at 0.1 A $g^{-1}$).

Inganas and co-workers developed an electrochemical doping of poly(1-aminoanthraquinone) (PAAQ) strategy with three structurally different phenolic acids (sinapic, ferulic and syringic acid), which were selected due to their resemblance to redox-active groups found in lignin (Figure 7.13A).[24] The sinapic, ferulic and syringic acid-doped PAAQ electrodes delivered higher specific capacitances of 171, 186 and 210 F $g^{-1}$, respectively,

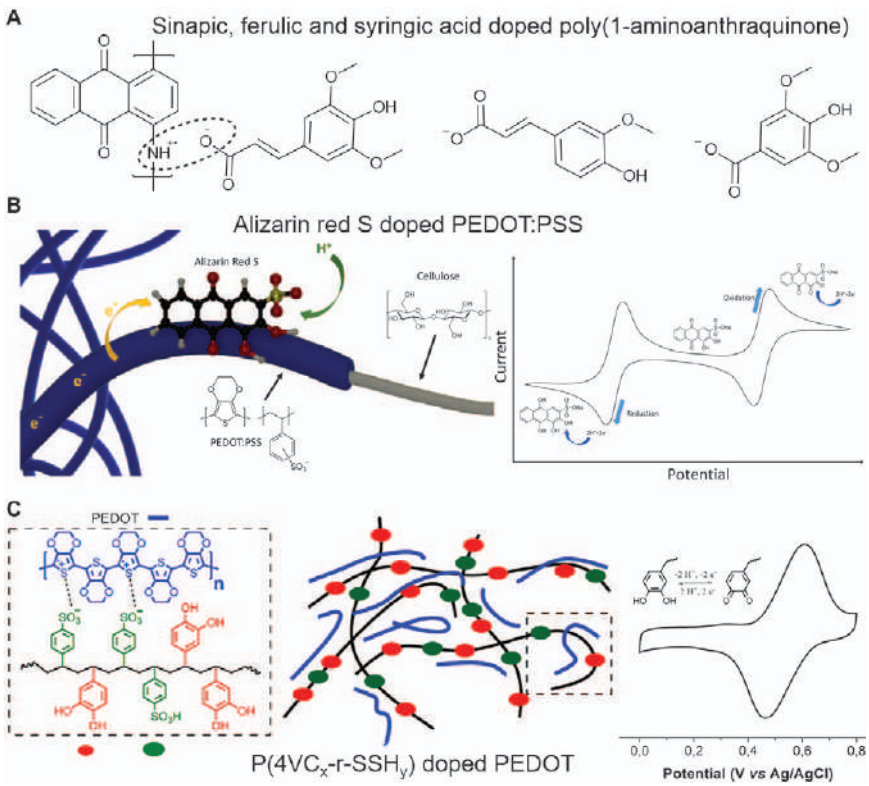


**Figure 7.13** (A) Chemical structure of sinapic, ferulic and syringic acid-doped poly(1-aminoanthraquinone). (B) Schematic depiction of the ''power paper'' fibril network with the molecular structure of its main constituents, along with the CV of Alizarin red S-doped PEDOT: PSS. Reproduced from ref. 25 with permission from John Wiley and Sons, © 2019 Wiley-VCH Verlag GmbH & Co. KGaA, Weinheim. (C) Schematic illustration of poly(4-vinyl catechol-*r*-styrene sulfonic acid)/PEDOT interpenetrating networks, along with the CV of the composite electrode. Reproduced from ref. 61 with permission from the American Chemical Society, Copyright 2019.

compared to the PAAQ (127 $F g^{-1}$). On the contrary, these doped electrodes, respectively, retained a 70%, 90%, and 85% lower capacitance after 1000 cycles, attributed to the leaching of low-molecular-weight dopants from the electrode film during the cycling, while PAAQ endured stable cycling.

Recently, Edberg *et al.* demonstrated a pseudocapacitor made from a ''power paper'' electrode based on PEDOT: PSS co-doped with a plant-based alizarin-S dye and nanocellulose that provides a mechanically strong and nonporous network onto which the electrode components self-organize (Figure 7.13B).[25] The two different quinone groups, residing on the alizarin-S molecule, make it possible to use a bipolar electrode, where the anode component involves electrochemical reactions originating from *para*-quinones, while *ortho*-quinones act as the cathode constituents (see CV in Figure 7.13B). The symmetric device delivered an average voltage output of 1 V with excellent specific capacitance exceeding 400 $F g^{-1}$ and operational stability over more than 1000 cycles.

In addition to the aforementioned examples, poly(4-vinyl catechol), a simple pendant catechol-containing polymer with styrenic backbone was synthesized and tested for pseudocapacitor application after being combined with either carbon black or PEDOT.[29] It was found that poly (4-vinyl catechol) exhibited a moderate electrochemical performance with specific capacity of about 50–54 $mA h g^{-1}$. Moreover, the composite electrode with PEDOT delivered improved rate and cycling compared to that with carbon black. In a further work, Schougaard *et al.* incorporated styrene sulfonic acid comonomer units into the poly(4-vinyl catechol) resulting in a copolymer that can be considered as a simplified analogue of lignosulfonate. Since this copolymer featured both dopant moieties (anionic styrenesulfonic acid) and redox-active building blocks (4-vinyl catechol) in the same copolymer, it served as both electrolyte and dopant for PEDOT electropolymerization.[61] The obtained PEDOT-interpenetrating network with this poly(4-vinyl catechol-*r*-styrenesulfonic acid) dopant (Figure 7.13C) exhibited a higher specific capacity of 52 $mAh g^{-1}$ than PEDOT with the classical poly(styrenesulfonic acid) homopolymer dopant (18 $mAh g^{-1}$).

Pirnat and co-workers developed poly(4-vinyl catechol)-based crosslinked redox-active polymer nanoparticles of different sizes ranging between 40 and 330 nm by (mini)emulsion polymerization with the intention of minimizing solubility and improving mechanical stability related to the conventional linear polymers.[30] These nanoparticles showed reversible redox behavior in aqueous acidic-, neutral- as well as acetonitrile-based electrolytes. Moreover, they found that the nanoparticle size did not have a crucial effect on the electrochemistry as evaluated by CV (Figure 7.14A), but slightly improved cycling stability (Figure 7.14B). They also extended this strategy to include another poly(catechol)-based redox-active polymer nanoparticle derived from 3-vinyl catechol pendants, which presented electrochemical features similar to those of 4-vinyl catechol redox units.

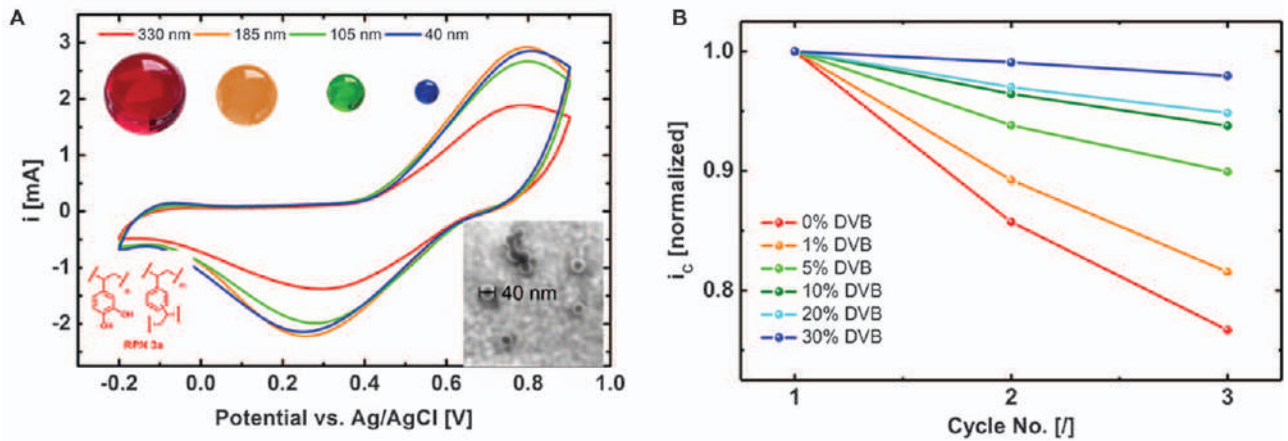


**Figure 7.14** (A) CV and cyclic stability of poly(4-vinyl catechol)-based cross-linked redox-active polymer nanoparticles of different sizes in 0.1 M $HClO_4$ aqueous electrolyte.
Reproduced from ref. 30 with permission from the American Chemical Society, Copyright 2019.

## 7.4.2 Electrodes for Static Batteries

### *7.4.2.1 Carbon Anodes: Carbonization of Catechol Polymers for Alkali Metal-ion Batteries*

Carbon materials are the predominant anodes in commercial metal-ion batteries due to their abundance, low cost, good chemical stability and metal-ion storage ability.[62,63] However, large irreversible capacities associated with solid electrolyte interface (SEI) formation and large volume changes associated with metal-ion insertion/extraction are difficult challenges that need to be addressed. It is worth mentioning that although the use of natural biomass (lignin, *etc.*) to prepare porous carbons is important due to the abundance and renewable character of these compounds, the characteristic redox features exploited in previous examples are totally lost here after carbonization and the electrochemical energy-storage mechanism is identical to other carbon-based anodes.

Zhang *et al.* first developed a hierarchical porous carbon derived from lignin *via* a facile preparation method.[64] A 3D hierarchical macroporous carbon network with abundant mesopores and micropores decorated on carbon walls was obtained by using KOH as both the template and activating agent (Figure 7.15A). This porous carbon had a high specific surface area of 907 $m^2 g^{-1}$, and achieved a much higher capacity of 470 mAh $g^{-1}$ compared to that of pristine non-KOH-treated carbonized lignin anode (180 mAh $g^{-1}$) after 400 cycles at a current density of 200 mA $g^{-1}$ in a lithium-ion half-cell study. Moreover, the unique 3D hierarchical porous structure of this lignin-based carbon provided a high-volume reservoir for lithium and fast lithium ion transportation paths displaying excellent rate capability.

Kraft lignin-based carbon fibers were also synthesized *via* oxidative thermostabilization of pure melt-spun lignin and carbonization at 1000 °C for the optimized electrode.[65] Because of the good mechanical integrity (strength of 628 MPa and a stiffness of 37 GPa) and excellent electrical conductivity ($142 \pm 14$ S $cm^{-1}$) of this carbon electrode, it was applied as a free-standing electrode without the need for current collectors, conductive additives or binders. Consequently, a high specific capacity of 335 mAh $g^{-1}$ (at the electrode level) was obtained in Li-ion half-cell. Finally, a full Li-ion battery was constructed using Kraft lignin-based carbon fibers and lithium iron phosphate as the negative and positive electrodes, respectively. The battery delivered a voltage output of 2.7 V with capacity of 97 mAh $g_{cell}^{-1}$, and retained 98% capacity over 22 cycles at 0.1 C.

Sheng *et al.* prepared nitrogen-doped porous carbon derived from poly(dopamine) using self-assembled colloidal poly(methyl methacrylate) particles as a sacrificial template for the porous carbon structure (Figure 7.15B).[66] The carbonized poly(dopamine) retained its high nitrogen content and also displayed high electrical conductivity as well as mechanical strength. When this electrode was tested as anode in Na-ion half-cell, it delivered a high reversible capacity of 301 mAh $g^{-1}$ and a long cycle lifetime,

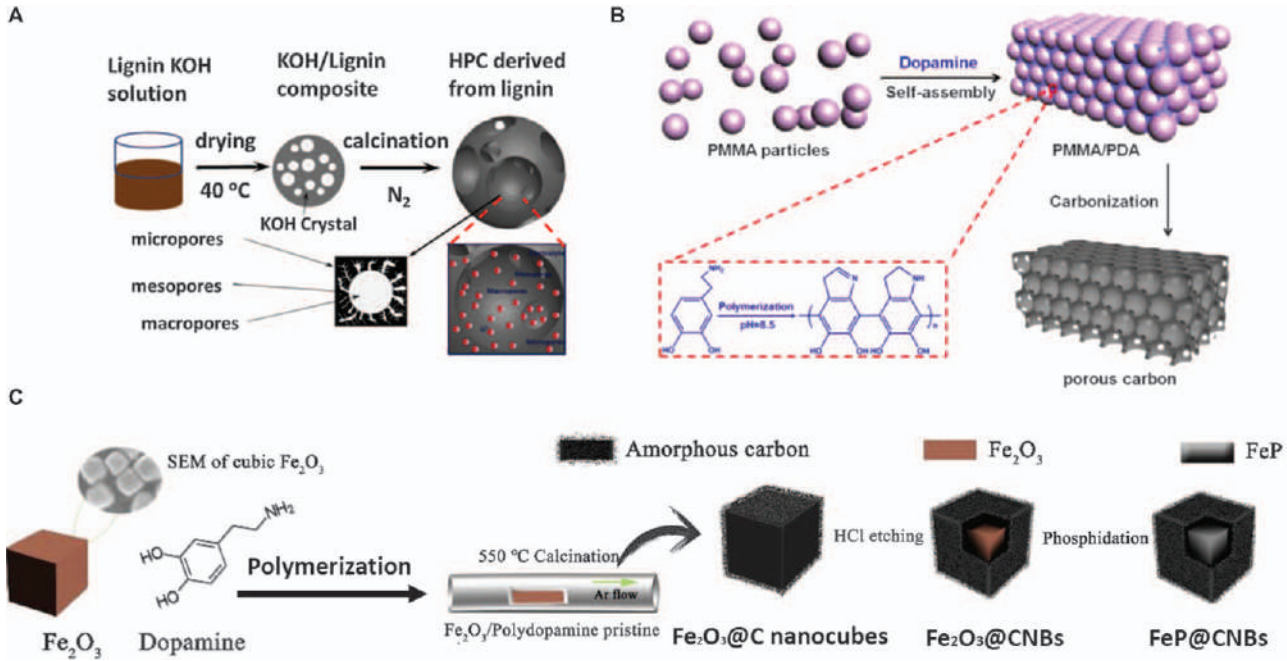


**Figure 7.15** Schematic illustration of the preparation of (A) lignin-based hierarchical porous carbon anode, (B) N-doped porous carbon derived from poly(dopamine), and (C) yolk–shell structured FeP@C nanobox for LIB.
(A) Reproduced from ref. 64 with permission from Elsevier, Copyright 2015. (B) Reproduced from ref. 66 with permission from John Wiley and Sons, © 2019 Wily-VCH Verlag GmbH & Co. KGaA, Weinheim. (C) Reproduced from ref. 67 with permission from John Wiley and Sons, © 2019 Wiley-VCH Verlag GmbH & Co. KGaA, Weinheim.

retaining 80% of the initial capacity after 900 cycles. The full Na-ion battery based on carbonized poly(dopamine) anode and layered $TiS_2$ cathode exhibited a voltage output of 2.5 V with capacity of 86 mAh $g_{cell}^{-1}$, and retained 99% capacity over 50 cycles at 0.06 A $g^{-1}$.

Recently, yolk–shell structured FeP carbon nanoboxes (FeP@CNBs) consisting of FeP nanoparticles surrounded and protected by a carbon shell derived from poly(dopamine) have been also developed as the anode for potassium-ion batteries (Figure 7.15C).[67] Benefiting from its unique structural features, the FeP@CNBs electrode achieved a high reversible capacity of 264 mAh $g^{-1}$, superior rate performance delivering 37 mAh $g^{-1}$ at 2 A $g^{-1}$, and an extremely stable cycling life without an obvious capacity fade over 300 cycles at 0.1 A $g^{-1}$.

### *7.4.2.2 Organic Anodes: Superlithiation (or Sodiation) of Catechol Polymers*

The currently used anode materials for metal-ion batteries are mainly based on carbon electrodes and transition metal oxides, which exhibit many disadvantages, including limited capacity upgrade space, high energy consumption, and the existence of security risks. Recently, the ''superlithiation (in LIB), supersodiation (in SIB) or superpotassiation (in KIB)'' process was proposed to reveal the unexpectedly high lithium (or sodium/potassium) storage capacity of some organic electrode materials.[68] Sun and co-workers were the first to report on the use of poly(dopamine) as a bifunctional anode/binder material for LIBs and SIBs.[17] They fabricated a biodegradable binder-free electrode based on poly(dopamine) that besides the abovementioned *ortho*-quinone redox reaction (step 1 in Figure 7.16A) also undergoes lithiation–delithiation (or sodiation–desodiation) processes through the unsaturated carbon–carbon bonds in the poly(dopamine) derivative (step 2 in Figure 7.16A). The poly(dopamine)/acetylene black delivered exceptional electrochemical performance, including a high capacity (1818 mAh $g^{-1}$ for LIBs and 500 mAh $g^{-1}$ for SIBs; Figure 7.15B, C) and a stable cyclability (93% capacity retention after 580 cycles at a current density of 500 mA $g^{-1}$ for LIBs; 100% capacity retention after 1024 cycles at a current density of 50 mA $g^{-1}$ for SIBs). However, the addition of an external binder, carboxymethyl cellulose was found to deteriorate both the specific capacity and rate performance in LIB (Figure 7.16B).

### *7.4.2.3 Organic Cathodes: Redox Reactions Followed by Coordination/Uncoordination of Metal Cations ($Li^+$, $Na^+$, $Mg^{2+}$, $Zn^{2+}$,* etc.*)*

#### 7.4.2.3.1 Monovalent-ion Batteries

*7.4.2.3.1.1 Lithium-ion Batteries.* In early 2017, Woo Lee *et al.* first reported poly(dopamine)/few-walled carbon nanotubes (FWCNTs) free-standing and flexible $Li^+$ ion cathode material (Figure 7.17A) that exhibited reasonably

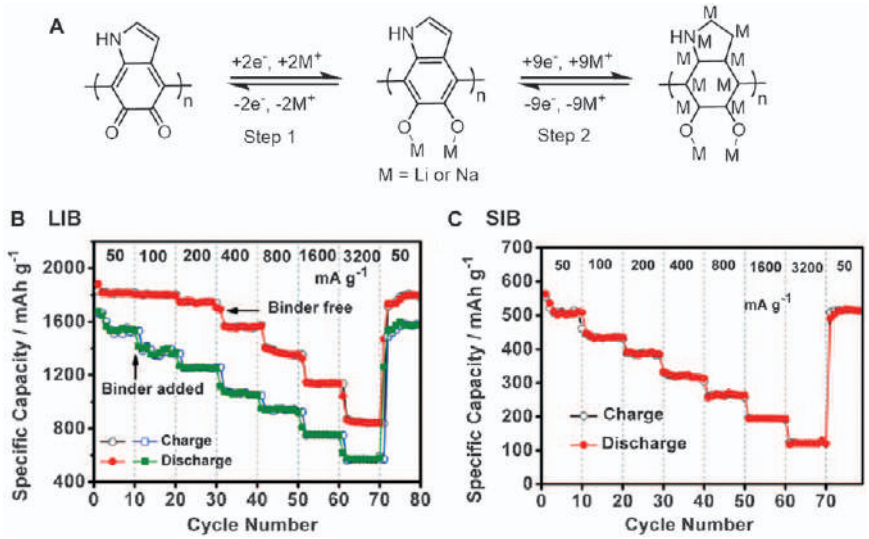


**Figure 7.16** (A) Reversible Li (Na)-ion insertion/extraction mechanism of poly(dopamine). Comparison of rate performance of poly(dopamine) samples in LIB (B) and SIB (C).
Reproduced from ref. 17 with permission from John Wiley and Sons, © 2016 Wiley-VCH Verlag GmbH & Co. KGaA, Weinheim.

high rate performance and high capacity [$\sim$133 mAh $g^{-1}$ normalized by total mass of electrode and 235 mAh $g^{-1}$ normalized by mass of poly(dopamine)].[18] Despite the high capacity of this hybrid electrode, its cycling stability was limited by the kinetics of the redox reactions within the poly(dopamine) film (50% of capacity decay after 100 cycles). Interestingly, a potentiostatic holding process for 5 min at 4.5 or 1.5 V *vs.* Li after each charging/discharging cycle was found to significantly enhance the cycling stability. This suggested that the gradual capacity loss during cycling was due to the kinetic limitation of the redox reactions within the poly(dopamine) film rather than the dissolution of the molecules. Although the system has to be optimized, this work demonstrated that simple bioinspired catechol-based products are very promising candidates for high-performance cathode materials for LIBs.

Inspired by the poly(dopamine) approach from Woo Lee and co-workers, Wang *et al.* developed sandwich-structured mesoporous poly(dopamine)/reduced graphene oxide nanosheets with controllable pore structures.[69] They took advantage of an interfacial self-assembly strategy of controllable block copolymers in solution that led to the generation of 2D nanocomposites with tunable spherical and cylindrical pore structures (Figure 7.17B). The best-performing composite having a large specific surface area (356 $m^2 g^{-1}$) was employed as the cathode in LIB delivering a high specific capacity of 151 mAh $g^{-1}$ at 50 mA $g^{-1}$ (based on the total mass of the electrode), as well as a good rate performance and cycling stability with 89% retention after

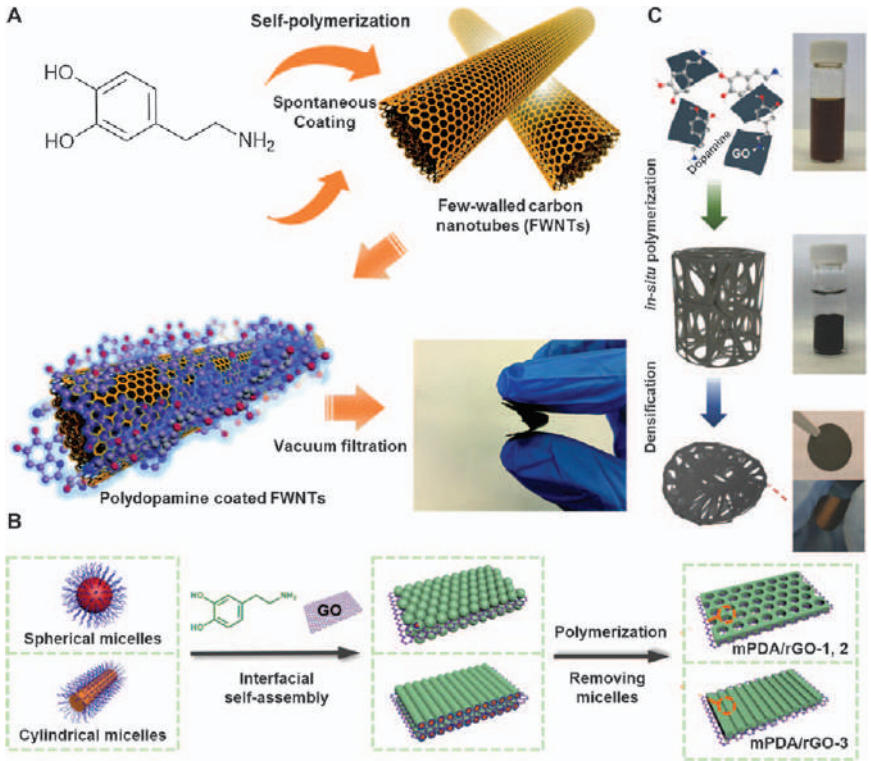


**Figure 7.17** Schematic representation of the preparation of (A) a flexible hybrid film consisting of poly(dopamine)-coated FWCNTs, along with its digital image, (B) poly(dopamine) functionalized graphene film, and (C) poly(dopamine)/reduced graphene oxide nanosheets with tunable pore structures *via* 2D interfacial self-assembly.
(A) Adapted from ref. 18 with permission from the Royal Chemical Society. (B) Adapted from ref. 69 with permission from the American Chemical Society, Copyright 2019. (C) Reproduced from ref. 70 with permission from John Wiley and Sons, © 2018 Wiley-VCH Verlag GmbH & Co. KGaA, Weinheim.

1000 cycles. In another work, graphene oxide was used as both the oxidant for assisting the polymerization of dopamine and the surface area template for the conformal growth of poly(dopamine) to fabricate a poly(dopamine)-coated 3D graphene framework (Figure 7.17C).[70] High-density films were easily attained by compressing the as-prepared aerogels, and directly applied as free-standing and flexible cathodes in LIBs. The authors demonstrated that the electrochemical performance of poly(dopamine)-functionalized graphene film was superior to that of polydopamine-coated graphene flake and pristine polydopamine particles. Moreover, the optimized 3D poly(dopamine)-functionalized graphene exhibited exceptional specific capacity of 230 mAh $g^{-1}$ (based on the total mass of the electrode), volumetric capacity of 150 Ah $L^{-1}$ and a negligible capacity loss over 1000 cycles (under accelerated test). Similar

to previous examples, at each end of the charge and discharge, the voltage was held for 30 min at either 4.5 or 1.5 V *versus* Li (4.2 or 1.3 V *vs.* Na).

Taking advantage of the synthetic possibilities of organic chemistry, Patil *et al.* exploited the macromolecular engineering knowledge to design high-performance redox-active polymers bearing catechol pendants.[28] Such an approach was particularly important from the viewpoint of understanding the structure–property–performance relationship, and therefore directs the chemist to the optimal design of the active materials with controlled structures and superior properties (see Figure 7.18A for the chemical structure of the developed polymers). For instance, the molecular simplification of catechol pendants to design a minimal redox-active unit boosted the specific capacity of poly(4-vinyl catechol)$_{100}$ [P(4VC)$_{100}$] as high as 350 *versus* 217 mAh g$^{-1}$ for the poly(dopamine acrylamide)$_{100}$ [P(DA)$_{100}$] at a low C-rate of 0.2 C (Figure 7.18B).[28] Moreover, the incorporation of ion-conducting lithium styrene sulfonate (LiSS) comonomer units in the structure-optimized copolymer [P(4VC$_{86}$-*stat*-LiSS$_{14}$)], enhanced the rate capabilities compared to its

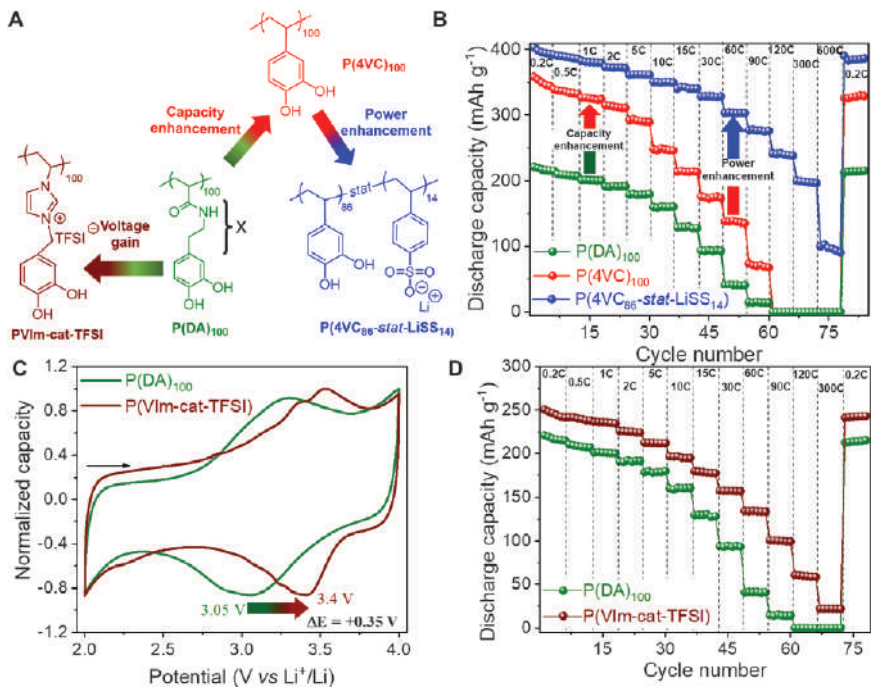


**Figure 7.18** Macromolecular engineering of catechol polymers for LIB cathodes. (A) Chemical structure of different polymers bearing catechol pendants. (B) Rate performance of P(DA)$_{100}$, P(4VC)$_{100}$ and P(4VC$_{86}$-*stat*-LiSS$_{14}$)/MWCNTs in LIB. Reproduced from ref. 28 with permission from John Wiley and Sons, © 2017 Wiley-VCH Verlag GmbH & Co. KGaA, Weinheim. CVs (C) and rate performance (D) of P(DA)$_{100}$ and P(VIm-cat-TFSI)/MWCNTs in LIB. Reproduced from ref. 71 with permission from the American Chemical Society, Copyright 2018.

homopolymer analogue, exhibiting a remarkable specific capacity of 303 *versus* 137 mAh $g^{-1}$ for $P(4VC)_{100}$ at a high C-rate of 60 C (only 1 min of total charge/discharge) (Figure 7.18B). The fast and reversible redox reaction, and the high ion and electron mobilities within the $P(4VC_{86}$-*stat*-$LiSS_{14})$ cathode also enabled the LIBs to be operative at an extreme C-rate of 600 C, which cannot be reached for most of the conventional battery electrode materials. This hybrid system also demonstrated an exceptional ultralong cyclability by retaining 98% of the initial capacity over prolonged 3400 full charge–discharge cycles at 30 C. Furthermore, when the catechol pendants were attached to an electron-withdrawing poly(vinylimidazolium bis(trifluoromethane)sulfonimide) [P(VIm-cat-TFSI)], a huge gain in redox potentials by at least +350 mV was obtained compared to the same redox-active groups confined to a neutral polymer backbone of poly(acrylamide; see CV in Figure 7.18C).[71] The additional ion-conducting nature of the electron-withdrawing group not only enhanced discharge potential of *ortho*-quinones but also improved reversible capacity and capacity retention at higher discharge rates as compared to neutral polymer chain $[P(DA)_{100}]$ (Figure 7.18D).

*7.4.2.3.1.2 Sodium-ion Batteries.* Mecerreyes and co-workers went a step further to test the applicability of lignosulfonate/PEDOT polymers in ''beyond-lithium'' SIBs. In the conventional $NaPF_6$-based liquid electrolyte, lignosulfonate/PEDOT delivered a specific capacity of 50 mAh $g^{-1}$, and the active-material utilization was further boosted to exhibit an improved specific capacity of 159 mAh $g^{-1}$ by combining with C65 carbon additive.[72] Unfortunately, this cathode demonstrated unsatisfactory cycling performance in carbonate-based electrolytes, retaining only 41% initial capacity over 23 cycles at C 20. Later, they implemented a series of pyrrolidinium- and imidazolium-based ionic liquids, containing TFSI and FSI anions and demonstrating that SIB based on PEDOT/lignin cathode with imidazolium-FSI IL electrolyte showed high capacity values reaching 70 mAh $g^{-1}$ with an improved capacity retention of 91% for 100 cycles.[73]

### 7.4.2.3.2 Multivalent-ion Batteries

*7.4.2.3.2.1 Magnesium-ion Batteries.* Jo Kim *et al.* exploited both the redox activity of catechol groups in natural eumelanin and magnesium-ion binding propensity to develop an organic cathode for magnesium-ion aqueous batteries.[74] The half-cell exhibited a specific capacity of 61 mAh $g^{-1}$ at 0.1 A $g^{-1}$ in 0.5 M $Mg(NO_3)_2$, and demonstrated excellent cyclability at 0.1 A $g^{-1}$ over 500 full cycles without deterioration in performance.

*7.4.2.3.2.2 Zinc-ion Batteries.* Recently, poly(catechol)s have been gathering increasing interest for aqueous zinc-ion batteries (AqZIBs) due to their high-water compatibility, excellent kinetics and ability to create a conducive environment for strong, yet reversible, coordination complex formation with $Zn^{2+}$ cations.[75]

Once again, cross-linked poly(dopamine) grafted onto carbon nanotubes was first tested as a flexible, free-standing, binder-free cathode in ZIB (Figure 7.19A) that delivered a moderate specific capacity of 126.2 mAh $g^{-1}$ and long-term cycling stability over 500 cycles, retaining 96% of the stabilized capacity.[76] Very recently, poly(catechol)/reduced graphene oxide 3D hydrogel obtained *via* the successive chemical oxidative polymerization of 1,2-dihydroxybenzene with $FeCl_3$ and hydrothermal reduction process was also validated in ZIB.[77] This system demonstrated a very high specific capacity of 355 mAh $g^{-1}$, one of the highest reported values for zinc-organic batteries, along with good cycling stability, retaining 74% capacity over 3000 cycles at 2 C.

Different from the aforementioned poly(catechol)s that are mostly linear, branched or cross-linked amorphous polymers, conductive metal–organic frameworks (MOFs) are a unique class of crystalline polymers with large specific surface area and porous structures which make ion and electron transport in the framework favorable.[78] In MOFs, the active organic species are immobilized by metal–ligand coordinate covalent bonds, making them a stable framework to alleviate the dissolution issues, associated with organic cathodes. Recently, Woo Nam *et al.* reported a 2D conductive MOF $Cu_3(HHTP)_2$ (HHTP = 2,3,6,7,10,11-hexahydroxytriphenylene), the first example in a MOF-based cathode for AqZIBs (Figure 7.19B).[79] $Cu_3(HHTP)_2$ delivered a high reversible capacity of 228 mAh $g^{-1}$ at 50 mA $g^{-1}$, and still attained 125 mAh $g^{-1}$, when the current density was increased to 4000 mA $g^{-1}$ (~18 C). It is worth mentioning here that $Cu^{2+}/Cu^{+}$ (metal center), catechol/semiquinone (HHTP linker) redox couples and high specific surface area of the MOF collectively contribute to the total capacity of the electrode. Another important merit of this MOF was its unique structure with high electrical conductivity (0.2 S $cm^{-1}$) and large pores (~2 nm) that enabled the active-material loading to be increased to 90% (60% in the previous tests) without sacrificing the specific capacity to a great extent (192 mAh $g^{-1}$, 16% decrease), while maintaining a similar cycle performance.

**7.4.2.3.3 All-polymer Batteries.** The examples of all-polymer batteries involving poly(catechol)s have only sporadically appeared in the literature.[80,81] This is partly due to the formidable challenge that requires careful design of both anode and cathode redox polymer partners to be not only able to sustain their redox activity in the given electrolyte media, but their combination should also deliver a high-voltage output.

Mecerreyes' group reported an all-organic aqueous battery based on perylene polyimide anode and lignosulfonate/PEDOT cathode in the mixed $H^{+}/Na^{+}$ electrolyte (1 M $Na_2SO_4$ and 0.1 M $HClO_4$).[82] This cell worked in a hybrid-ion configuration, where the polyimide anode exhibits an imide/enolate redox process involving $Na^{+}$, while the catechol units in the lignosulfonate/PEDOT cathode undergo classical catechol-to-quinone transformations (Figure 7.20A). The full cell delivered a high voltage

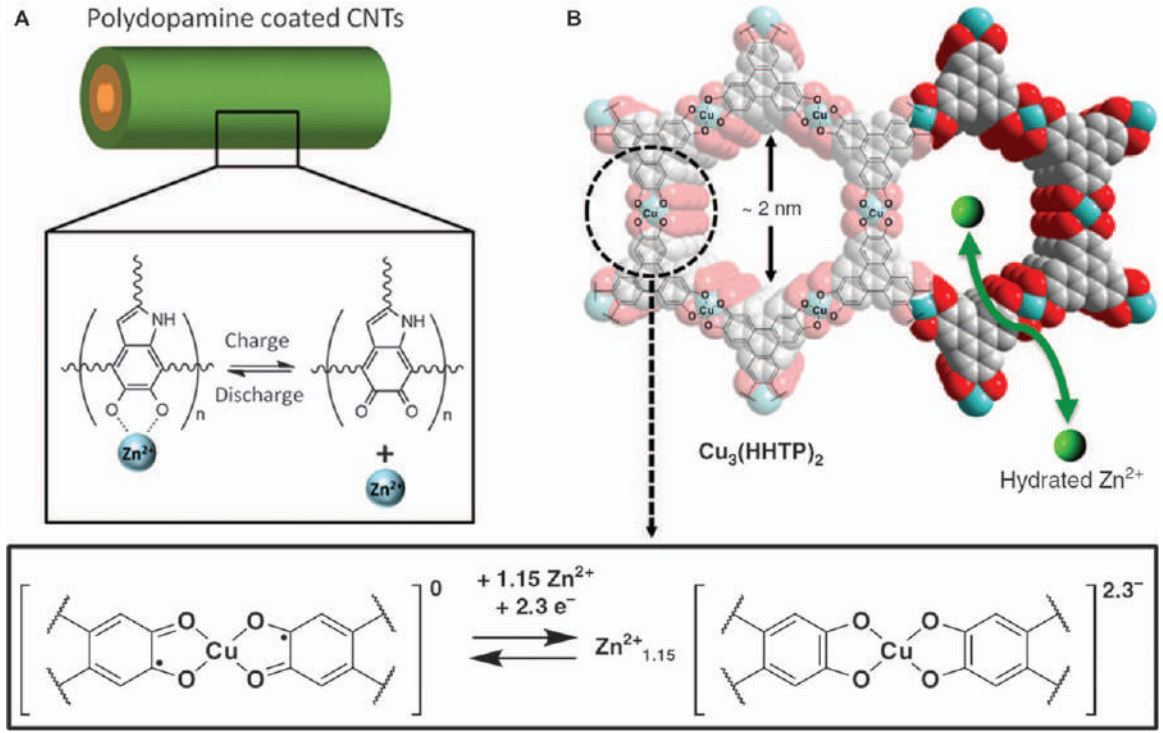


**Figure 7.19** (A) Schematic illustration of poly(dopamine) grafted carbon nanotubes, along with of $Zn^{2+}$ adsorption by catechol and desorption by *ortho*-quinone when poly(dopamine) at discharged or charged states, respectively. Reproduced from ref. 76 with permission from the Royal Chemical Society. (B) Schematic drawing of the rechargeable Zn-2D metal–organic framework cell based on $Cu_3(HHTP)_2$, along with expected redox process. Reproduced from ref. 79 with permission from Springer Nature, Copyright 2019.

output of 0.95 V, reversible capacity of 53 mAh $g^{-1}$ (based on anode weight), and retained 85% capacity over 800 cycles at 100 C. This full cell demonstrated excellent rate capability, which retained ~68% of the capacity at a very high current rate of 200 C compared to that at 10 C (Figure 7.20B).

Taking advantage of the redox properties of *ortho*-quinone derivatives endowing the coordination of both monovalent and multivalent cations, Patil *et al.* evaluated the electrochemical behavior of a catechol copolymer, poly(dopamine acrylamide$_{70}$-*stat*-styrenesulfonic acid$_{30}$) [P($DA_{70}$-*stat*-$AMPS_{30}$)] in aqueous media containing different charge carriers.[83] This polymer exhibited a high redox potential of 0.55 V (*vs.* Ag/AgCl, see Figure 7.21A for CV), high specific capacity (170 mAh $g^{-1}$) and excellent kinetics in 1 M $H_2SO_4$ (Figure 7.21B). Interestingly, when the same polymer was tested in aqueous electrolytes containing different charge carriers, such as $Li^+$, $Zn^{2+}$, $Al^{3+}$, *etc.* separately, it still sustained electroactivity in all these electrolyte media. Moreover, positive shift of redox potentials, typically by at least hundreds of millivolts, in the same order of electroneutralizing cation valences ($M^+ < M^{2+} < M^{3+}$) ascribed to the formation of stronger complexes (between catecholate and charge carriers during the reduction reaction) offers a promising paradigm toward organic electrodes for batteries with tunable cell voltages (Figure 7.21A).

### 7.4.3 Soluble Catechol Polymers for Redox Flow Batteries

The market implementation of a redox flow battery has historically been burdened by the scarcity, toxicity and high costs of redox electrolytes commonly based on vanadium salts.[84] The development of organic redox flow batteries where the vanadium active species are substituted by environmental-friendly and abundant organic-based molecules has recently originated a significant flourishing of this technology.[5,85,86] Mukhopadhyay *et al.* investigated, for the first time, the use of lignin as an abundant biopolymer and extremely low-cost electrolyte in a redox flow battery. They exploited the water solubility of lignosulfonate to demonstrate a proof of concept poly(catechol)-based redox flow battery.[87] They combined 0.1 M lignosulfonate dissolved in 0.1 M perchloric acid as the anolyte ($E_{1/2}$ of 0.50 V *vs.* Ag/AgCl, see Figure 7.22A) with $Br_2$/HBr redox couple ($Br^2 + 2e^- \leftrightarrow 2Br^-$, 0.89 V *vs.* Ag/AgCl) as the catholyte, with an approximate voltage output of 0.43 V and energy capacity of 7 Wh $L^{-1}$ (see Figure 7.4E for the schematic illustration of the flow cell). The flow cell was able to achieve current densities of up to 20 mA $cm^{-2}$ and voltage efficiencies as high as 85% at low current density (Figure 7.22B). Although performance metrics like energy density and cycling stability are not provided in this proof of the concept work, it presents a unique opportunity for a low-cost, metal-free, sustainable-flow battery, and also opens up further possibilities for other poly(catechol)s for such technologies.

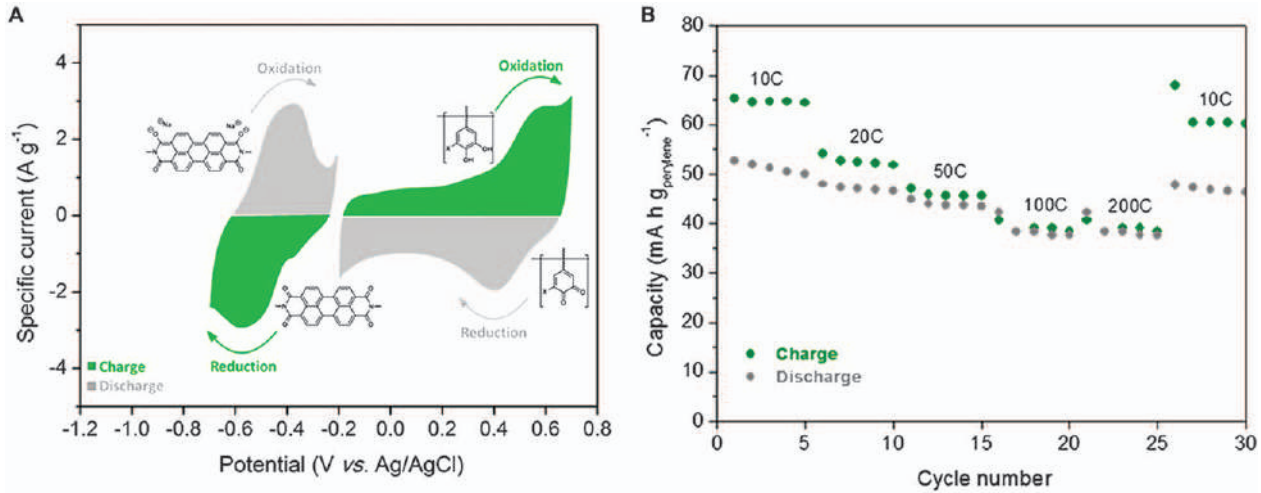


**Figure 7.20** (A) CV and redox reactions of perylene polyimide anode and lignosulfonate/PEDOT cathode in half-cells. (B) Rate capability of perylene polyimide–lignosulfonate/PEDOT full cell.
Reproduced from ref. 82 with permission from the American Chemical Society, Copyright 2018.

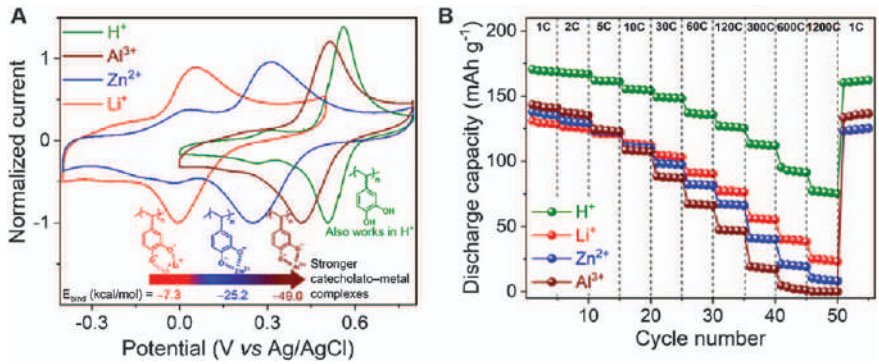


**Figure 7.21** (A) CV and (B) comparative rate capability: discharge capacity *vs* cycle number of poly(dopamine acrylamide$_{70}$-*stat*-styrenesulfonic acid$_{30}$) in aqueous media containing different charge carriers.
Reproduced from ref. 83 with permission from the American Chemical Society, Copyright 2019.

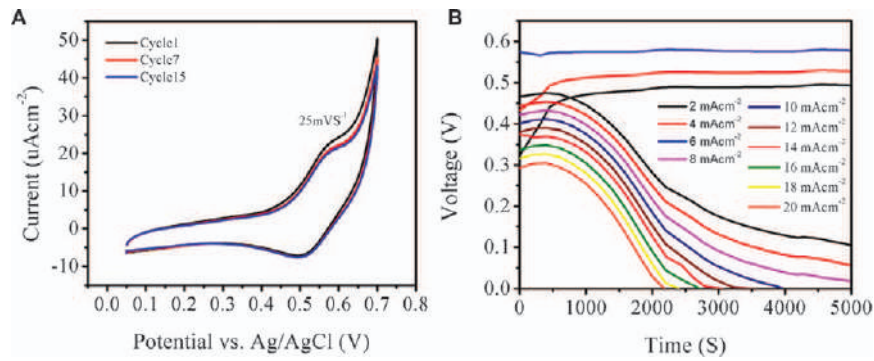


**Figure 7.22** Lignosulfonate and $Br_2$/HBr-based redox flow battery. (A) CV scans of lignosulfonate anolyte in three-electrode setup. (B) Cell voltage *vs.* time at various current densities for the full cell.
Reproduced from ref. 87 with permission from the American Chemical Society, Copyright 2018.

## 7.5 Conclusions and Perspectives

Triggered by the versatility and richness of the poly(catechol) electrochemical and physicochemical properties, involving reversible redox reactions, metal-ion coordination and propensity to interact with aromatic substrates, researchers have been motivated to develop safe, sustainable, multifunctional and bioinspired energy-storage systems. Several energy-storage devices including capacitors, rechargeable static batteries and redox flow batteries have been developed over the past decade. The outstanding electrochemical performance of those devices has directed the interest of the scientific community to this exciting field that is experiencing huge growth.

In this chapter we have presented the relevant physicochemical and electrochemical properties of poly(catechol)s and highlighted their potential as sustainable materials for electrochemical energy storage. We have succinctly described important bioresources of poly(catechol)s (lignin, *etc.*), and also described the feasible synthetic approaches to incorporate catechol groups into (bio)polymers. Among the latter, the radical polymerization of vinyl catechol monomers was presented as a powerful and versatile platform to create well-defined (co)polymers with controlled compositions, functionalities, architectures and improved electrochemical properties.

The last section of this chapter was dedicated to the applications of poly(catechol)s in three important types of energy-storage systems: capacitors, rechargeable static batteries and flow batteries. Particularly, the redox polymer/conductive polymer platform is highly captivating for the fabrication of carbon-free fully pseudocapacitive polymeric electrodes for wearable, flexible, foldable and printable advanced capacitors. Although to a lesser extent, poly(catechol)s were also investigated as active materials in numerous rechargeable static batteries. Interestingly, when used as anodes in alkali metal-ion batteries poly(catechol)s were found to undergo superlithiation (or sodiation) reactions that boosted the specific capacity. Moreover, poly(catechol)s were also implemented as cathodes in monovalent Li-ion, Na-ion, multivalent Mg-ion, Zn-ion and all-polymer batteries and as solubilized active material in redox flow batteries. Metal-free all-polymer aqueous batteries are highlighted as highly promising from the perspective of sustainable electrochemical energy storage development.

From the examples described in this chapter, we see that poly(catechol)s can be used in different electrochemical energy-storage devices, but mainly in capacitors. Despite the fact that they were less explored as organic electrodes for rechargeable batteries, the expectation raised so far in terms of improved energy-storage performance may serve both as an inspiration and stimulus for future research, and put forward the development of this emerging field of potential high impact in our daily life. We hope that this chapter will provide new researchers with a first insight into the field of poly(catechol)s for electrochemical energy storage.

## References

1. M. Li, J. Lu, Z. Chen and K. Amine, *Adv. Mater.*, 2018, **30**, 1800561.
2. D. Larcher and J.-M. Tarascon, *Nat. Chem.*, 2015, **7**, 19–29.
3. S. Muench, A. Wild, C. Friebe, B. Häupler, T. Janoschka and U. S. Schubert, *Chem. Rev.*, 2016, **116**, 9438–9484.
4. J. Kim, J. H. Kim and K. Ariga, *Joule*, 2017, **1**, 739–768.
5. Y. Y. Lai, X. Li and Y. Zhu, *ACS Appl. Polym. Mater.*, 2020, **2**, 113–128.
6. E. J. Son, J. H. Kim, K. Kim and C. B. Park, *J. Mater. Chem. A*, 2016, **4**, 11179–11202.
7. Y. Wu, R. Zeng, J. Nan, D. Shu, Y. Qiu and S.-L. Chou, *Adv. Energy Mater.*, 2017, **7**, 1700278.

8. D. M. Anjos, J. K. McDonough, E. Perre, G. M. Brown, S. H. Overbury, Y. Gogotsi and V. Presser, *Nano Energy*, 2013, **2**, 702–712.
9. T. Nokami, T. Matsuo, Y. Inatomi, N. Hojo, T. Tsukagoshi, H. Yoshizawa, A. Shimizu, H. Kuramoto, K. Komae, H. Tsuyama and J. Yoshida, *J. Am. Chem. Soc.*, 2012, **134**, 19694–19700.
10. Y. Liang, Y. Jing, S. Gheytani, K.-Y. Lee, P. Liu, A. Facchetti and Y. Yao, *Nat. Mater.*, 2017, **16**, 841–848.
11. G. P. Maier and A. Butler, *JBIC, J. Biol. Inorg. Chem.*, 2017, **22**, 739–749.
12. S. Quideau, D. Deffieux, C. Douat-Casassus and L. Pouységu, *Angew. Chem., Int. Ed.*, 2011, **50**, 586–621.
13. N. Patil, C. Jérôme and C. Detrembleur, *Prog. Polym. Sci.*, 2018, **82**, 34–91.
14. P. S. Guin, S. Das and P. C. Mandal, *Int. J. Electrochem.*, 2011, **2011**, 1–22.
15. M. Krogsgaard, V. Nue and H. Birkedal, *Chem. – Eur. J.*, 2016, **22**, 844–857.
16. C. Benoit, D. Demeter, D. Bélanger and C. Cougnon, *Angew. Chem., Int. Ed.*, 2016, **55**, 5318–5321.
17. T. Sun, Z. Li, H. Wang, D. Bao, F. Meng and X. Zhang, *Angew. Chem., Int. Ed.*, 2016, **55**, 10662–10666.
18. T. Liu, K. C. Kim, B. Lee, Z. Chen, S. Noda, S. S. Jang and S. W. Lee, *Energy Environ. Sci.*, 2017, **10**, 205–215.
19. S.-L. Chou, Y. Pan, J.-Z. Wang, H.-K. Liu and S.-X. Dou, *Phys. Chem. Chem. Phys.*, 2014, **16**, 20347–20359.
20. S. Laurichesse and L. Avérous, *Prog. Polym. Sci.*, 2014, **39**, 1266–1290.
21. M. d'Ischia, K. Wakamatsu, A. Napolitano, S. Briganti, J.-C. Garcia-Borron, D. Kovacs, P. Meredith, A. Pezzella, M. Picardo, T. Sarna, J. D. Simon and S. Ito, *Pigm. Cell Melanoma Res.*, 2013, **26**, 616–633.
22. Z. Chang, Q. Zhang, W. Liang, K. Zhou, P. Jian, G. She and L. Zhang, *J. Evidence-Based Complementary Altern. Med.*, 2019, **2019**, 1–26.
23. Y. Liu, K. Ai and L. Lu, *Chem. Rev.*, 2014, **114**, 5057–5115.
24. M. Wagner, T. Rębiś and O. Inganäs, *J. Power Sources*, 2016, **302**, 324–330.
25. J. Edberg, R. Brooke, H. Granberg, I. Engquist and M. Berggren, *Adv. Sustainable Syst.*, 2019, **3**, 1900050.
26. N. Patil, C. Falentin-Daudré, C. Jérôme and C. Detrembleur, *Polym. Chem.*, 2015, **6**, 2919–2933.
27. N. Patil, D. Cordella, A. Aqil, A. Debuigne, S. Admassie, C. Jérôme and C. Detrembleur, *Macromolecules*, 2016, **49**, 7676–7691.
28. N. Patil, A. Aqil, F. Ouhib, S. Admassie, O. Inganäs, C. Jérôme and C. Detrembleur, *Adv. Mater.*, 2017, **29**, 1703373.
29. D. A. Lukyanov, R. V. Apraksin, A. N. Yankin, P. S. Vlasov, O. V. Levin, E. G. Tolstopjatova and V. V. Kondratiev, *Synth. Met.*, 2019, **256**, 116151.
30. K. Pirnat, N. Casado, L. Porcarelli, N. Ballard and D. Mecerreyes, *Macromolecules*, 2019, **52**, 8155–8166.

31. M. Winter and R. J. Brodd, *Chem. Rev.*, 2004, **104**, 4245–4270.
32. Y. Wang, Y. Song and Y. Xia, *Chem. Soc. Rev.*, 2016, **45**, 5925–5950.
33. A. M. Bryan, L. M. Santino, Y. Lu, S. Acharya and J. M. D'Arcy, *Chem. Mater.*, 2016, **28**, 5989–5998.
34. T. Janoschka, N. Martin, U. Martin, C. Friebe, S. Morgenstern, H. Hiller, M. D. Hager and U. S. Schubert, *Nature*, 2015, **527**, 78–81.
35. G. Milczarek and O. Inganas, *Science*, 2012, **335**, 1468–1471.
36. L. Zhang, Z. Liu, G. Cui and L. Chen, *Prog. Polym. Sci.*, 2015, **43**, 136–164.
37. J. L. Espinoza-Acosta, P. I. Torres-Chávez, J. L. Olmedo-Martínez, A. Vega-Rios, S. Flores-Gallardo and E. A. Zaragoza-Contreras, *J. Energy Chem.*, 2018, **27**, 1422–1438.
38. N. Guo, M. Li, X. Sun, F. Wang and R. Yang, *Green Chem.*, 2017, **19**, 2595–2602.
39. L. Liu, N. Solin and O. Inganäs, *RSC Adv.*, 2019, **9**, 39758–39767.
40. S. Chaleawlert-umpon, T. Berthold, X. Wang, M. Antonietti and C. Liedel, *Adv. Mater. Interfaces*, 2017, **4**, 1700698.
41. S. Chaleawlert-umpon and C. Liedel, *J. Mater. Chem. A*, 2017, **5**, 24344–24352.
42. Z. Peng, Y. Zou, S. Xu, W. Zhong and W. Yang, *ACS Appl. Mater. Interfaces*, 2018, **10**, 22190–22200.
43. X. Geng, Y. Zhang, L. Jiao, L. Yang, J. Hamel, N. Giummarella, G. Henriksson, L. Zhang and H. Zhu, *ACS Sustainable Chem. Eng.*, 2017, **5**, 3553–3561.
44. D. H. Nagaraju, T. Rebis, R. Gabrielsson, A. Elfwing, G. Milczarek and O. Inganäs, *Adv. Energy Mater.*, 2014, **4**, 1300443.
45. S. Admassie, A. Elfwing, E. W. H. Jager, Q. Bao and O. Inganäs, *J. Mater. Chem. A*, 2014, **2**, 1974–1979.
46. Z. Peng, C. Wang, Z. Zhang and W. Zhong, *Adv. Mater. Interfaces*, 2019, **6**, 1901393.
47. F. N. Ajjan, N. Casado, T. Rębiś, A. Elfwing, N. Solin, D. Mecerreyes and O. Inganäs, *J. Mater. Chem. A*, 2016, **4**, 1838–1847.
48. F. N. Ajjan, M. Vagin, T. Rębiś, L. E. Aguirre, L. Ouyang and O. Inganäs, *Adv. Sustainable Syst.*, 2017, **1**, 1700054.
49. A. M. Navarro-Suárez, N. Casado, J. Carretero-González, D. Mecerreyes and T. Rojo, *J. Mater. Chem. A*, 2017, **5**, 7137–7143.
50. C. Che, M. Vagin, U. Ail, V. Gueskine, J. Phopase, R. Brooke, R. Gabrielsson, M. P. Jonsson, W. C. Mak, M. Berggren and X. Crispin, *Adv. Sustainable Syst.*, 2019, **3**, 1900039.
51. D. Wu and W. Zhong, *J. Mater. Chem. A*, 2019, **7**, 5819–5830.
52. P. Kumar, E. Di Mauro, S. Zhang, A. Pezzella, F. Soavi, C. Santato and F. Cicoira, *J. Mater. Chem. C*, 2016, **4**, 9516–9525.
53. R. Xu, A. Gouda, M. F. Caso, F. Soavi and C. Santato, *ACS Omega*, 2019, **4**, 12244–12251.
54. J. Y. Oh, Y. Jung, Y. S. Cho, J. Choi, J. H. Youk, N. Fechler, S. J. Yang and C. R. Park, *ChemSusChem*, 2017, **10**, 1644.

55. Y. A. Lee, J. Lee, D. W. Kim, C.-Y. Yoo, S. H. Park, J. J. Yoo, S. Kim, B. Kim, W. K. Cho and H. Yoon, *J. Mater. Chem. A*, 2017, **5**, 25368–25377.
56. C. Xiong, Y. Zou, Z. Peng and W. Zhong, *Nanoscale*, 2019, **11**, 7304–7316.
57. A. Mukhopadhyay, Y. Jiao, R. Katahira, P. N. Ciesielski, M. Himmel and H. Zhu, *Nano Lett.*, 2017, **17**, 7897–7907.
58. S.-K. Kim, J. Cho, J. S. Moore, H. S. Park and P. V. Braun, *Adv. Funct. Mater.*, 2016, **26**, 903–910.
59. C. A. Milroy and A. Manthiram, *ACS Energy Lett.*, 2016, **1**, 672–677.
60. I. K. Ilic, M. Meurer, S. Chaleawlert-umpon, M. Antonietti and C. Liedel, *RSC Adv.*, 2019, **9**, 4591–4598.
61. D. Chhin, L. Padilla-Sampson, J. Malenfant, V. Rigaut, A. Nazemi and S. B. Schougaard, *ACS Appl. Energy Mater.*, 2019, **2**, 7781–7790.
62. M. Winter, J. O. Besenhard, M. E. Spahr and P. Novák, *Adv. Mater.*, 1998, **10**, 725–763.
63. K. Xu, *Chem. Rev.*, 2004, **104**, 4303–4418.
64. W. Zhang, J. Yin, Z. Lin, H. Lin, H. Lu, Y. Wang and W. Huang, *Electrochim. Acta*, 2015, **176**, 1136–1142.
65. A. P. Nowak, J. Hagberg, S. Leijonmarck, H. Schweinebarth, D. Baker, A. Uhlin, P. Tomani and G. Lindbergh, *Holzforschung*, 2018, **72**, 81–90.
66. W. Sheng, P. Zhang, W. Li, T. Zhang, D. Tan, Y. Li, F. Wang, X. Zhuang, X. Feng and R. Jordan, *Energy Technol.*, 2019, **7**, 1800763.
67. F. Yang, H. Gao, J. Hao, S. Zhang, P. Li, Y. Liu, J. Chen and Z. Guo, *Adv. Funct. Mater.*, 2019, **29**, 1808291.
68. X. Han, G. Qing, J. Sun and T. Sun, *Angew. Chem., Int. Ed.*, 2012, **51**, 5147–5151.
69. N. Wang, D. Hou, Q. Li, P. Zhang, H. Wei and Y. Mai, *ACS Appl. Energy Mater.*, 2019, **2**, 5816–5823.
70. T. Liu, B. Lee, B. G. Kim, M. J. Lee, J. Park and S. W. Lee, *Small*, 2018, **14**, 1801236.
71. N. Patil, M. Aqil, A. Aqil, F. Ouhib, R. Marcilla, A. Minoia, R. Lazzaroni, C. Jérôme and C. Detrembleur, *Chem. Mater.*, 2018, **30**, 5831–5835.
72. A. M. Navarro-Suárez, J. Carretero-González, N. Casado, D. Mecerreyes, T. Rojo and E. Castillo-Martínez, *Sustainable Energy Fuels*, 2018, **2**, 836–842.
73. N. Casado, M. Hilder, C. Pozo-Gonzalo, M. Forsyth and D. Mecerreyes, *ChemSusChem*, 2017, **10**, 1783–1791.
74. Y. J. Kim, W. Wu, S. Chun, J. F. Whitacre and C. J. Bettinger, *Adv. Mater.*, 2014, **26**, 6572–6579.
75. J. Cui, Z. Guo, J. Yi, X. Liu, K. Wu, P. Liang, Q. Li, Y. Liu, Y. Wang, Y. Xia and J. Zhang, *ChemSusChem*, 2020, **n/a**, cssc.201903265.
76. X. Yue, H. Liu and P. Liu, *Chem. Commun.*, 2019, **55**, 1647–1650.
77. S. Zhang, W. Zhao, H. Li and Q. Xu, *ChemSusChem*, 2020, **13**, 188–195.
78. W. Xia, A. Mahmood, R. Zou and Q. Xu, *Energy Environ. Sci.*, 2015, **8**, 1837–1866.

79. K. W. Nam, S. S. Park, R. dos Reis, V. P. Dravid, H. Kim, C. A. Mirkin and J. F. Stoddart, *Nat. Commun.*, 2019, **10**, 4948.
80. P. Poizot, F. Dolhem and J. Gaubicher, *Curr. Opin. Electrochem.*, 2018, **9**, 70–80.
81. C. Friebe, A. Lex-Balducci and U. S. Schubert, *ChemSusChem*, 2019, **12**, 4093–4115.
82. G. Hernández, N. Casado, A. M. Zamarayeva, J. K. Duey, M. Armand, A. C. Arias and D. Mecerreyes, *ACS Appl. Energy Mater.*, 2018, **1**, 7199–7205.
83. N. Patil, A. Mavrandonakis, C. Jérôme, C. Detrembleur, J. Palma and R. Marcilla, *ACS Appl. Energy Mater.*, 2019, **2**, 3035–3041.
84. K. Lourenssen, J. Williams, F. Ahmadpour, R. Clemmer and S. Tasnim, *J. Energy Storage*, 2019, **25**, 100844.
85. Y. Ding, C. Zhang, L. Zhang, Y. Zhou and G. Yu, *Chem. Soc. Rev.*, 2018, **47**, 69–103.
86. J. Luo, B. Hu, M. Hu, Y. Zhao and T. L. Liu, *ACS Energy Lett.*, 2019, **4**, 2220–2240.
87. A. Mukhopadhyay, J. Hamel, R. Katahira and H. Zhu, *ACS Sustainable Chem. Eng.*, 2018, **6**, 5394–5400.
88. E. Senokos, R. Marcilla and J. J. Vilatela, in *Carbon Based Nanomaterials for Advanced Thermal and Electrochemical Energy Storage and Conversion*, Elsevier, 2019, pp. 249–278.

CHAPTER 8

# *Redox Polymers for All-organic Batteries*

NICOLAS GOUJON,* XABIER LOPEZ DE PARIZA AND NEREA CASADO

POLYMAT Institution for Polymer Materials, University of the Basque Country, UPV/EHU, Joxe Mari Korta Center, Avda. De Tolosa, 72-3, 20018, Donostia-San Sebastián, Spain
*Email: nicolas.goujon@polymat.eu

## 8.1 Introduction

As illustrated in the preceding chapters, a wide variety of chemistries have already been explored over the years for the synthesis of organic redox polymers, which enable the design of redox materials with various distinct properties (*i.e.*, morphology, porosity, solubility, electronic conductivity, redox potentials, specific theoretical capacity, *etc.*).[1] In general, organic redox polymers can be classified into three classes, depending on the type of electrochemical reactions that they undergo during the discharge process of an electrochemical cell. N-type organic redox polymers are oxidized during discharge, while p-type organic redox polymers are reduced, and b-type organic redox polymers can be both oxidized and reduced, exhibiting both n-type and p-type redox features (see Scheme 8.1).[1] Depending on the type of battery targeted (*i.e.*, alkali metal–organic batteries, alkali ion–organic batteries and all-organic batteries, *etc.*), organic redox polymers can be either used as the anode or cathode, as long as sufficient potential difference is generated between the two electrodes.

The implementation of organic redox polymers as the electrode material of a battery is not a new concept, with the earliest reports dating back to the late

Polymer Chemistry Series No. 34
Redox Polymers for Energy and Nanomedicine
Edited by Nerea Casado and David Mecerreyes

Published by the Royal Society of Chemistry, www.rsc.org

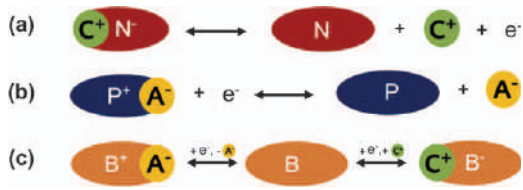


**Scheme 8.1** Redox reaction according to the three classes of organic redox polymers: (a) n-type, (b) p-type and (c) b-type; $C^+$ and $A^-$ are the ions of the electrolyte.

1960s,[2,3] where the fabrication of a Li metal–organic battery was reported using dichloroisocyanuric acid as the cathode material.[3] In the late 1970s, the discovery of conducting polymers[4–9] opened a new battery research avenue, through the development of the first Li–organic polymer battery in the 1980s, which used conducting polymers as the cathode material.[10,11] Two battery products based on either poly(aniline) or poly(pyrrole) were even commercialized by Bridgestone-Seiko and Varta batterie/BASF, respectively.[12] However, these batteries suffered from inherent issues associated with conducting polymers. Indeed, only partial doping/oxidation (0.3–0.5) of the conducting polymer is practically and reversibly achievable (*i.e.*, 0.3–0.5 charge per unit) due to instability of the polymer chain at a high degree of oxidation,[13,14] resulting in batteries with lower energy density than that of conventional batteries at the time of their commercialization.[12] As a result of the aforementioned drawbacks, along with commercialization of the first Li–ion battery by Sony in 1991,[15,16] the commercial exploitation of these Li–organic polymer batteries was discontinued, only 5 years after entering the market.[12] Consequently, tremendous efforts have been made during the last two decades to develop alternative organic redox polymers for application in rechargeable/secondary energy-storage devices. This new class of nonconjugated organic redox polymers generally consists of a nonconducting polymer backbone, bearing redox-active pendant moieties.[17] Such a design concept allows the incorporation of a wide variety of electroactive functionalities, such as carbonyl, catechol, carbazole, phenazine, phenothiazine, triphenylamine and stable organic radicals, expanding the range of redox potentials accessible.[1,18,19] In addition, these nonconjugated organic redox polymers exhibit well-defined redox potentials due to their inherent molecular design, since each redox site is not electrically connected through a conjugated system. This feature is highly favourable for battery applications, as this results in a constant cell voltage profile/plateau during the discharge process. Over the past two decades, nonconjugated organic redox polymers have been intensively investigated for their potential application in alkali metal–organic batteries, alkali ion–organic batteries and all-organic batteries. However, most of the literature reporting on these materials, including review articles, focused on their application in alkali metal–organic batteries, likely due to the ease in characterizing them in a half-cell configuration.[1,18–21] In 2018, Poizot *et al.* attempted to fulfil the lack of a comprehensive review on all-organic batteries, by briefly summarizing all

battery prototypes reported in the literature up until 2018.[22] The aims of this chapter are to expand on this starting point and offer a comprehensive overview of all-organic batteries based on redox polymers, starting with a general introduction on battery terminology and the various cell configurations. Finally, future perspectives on all-organic batteries will be discussed, summarizing the major challenges that are still to be overcome by the current state-of-the-art technology to unlock their commercial implementations.

### 8.1.1 Working Principles and Electrochemical Cell Configurations

Initially, the terminology commonly used in battery research is defined and explained, followed by a brief description of the different components of a battery. An outline of the different electrochemical cell configurations possible is also presented and explained with regard to the type of organic redox polymers used to formulate the electrodes (*i.e.*, n- or p- type).

### 8.1.2 Battery Research Terminology

Several terminologies are commonly employed in battery research, which sometimes leads to confusion. Therefore, the nomenclature used in this chapter will mostly follow the terminology defined in the fifth edition of "Linden's Handbook of Batteries".[23]

Batteries are electrochemical devices, which convert chemical energy into electric energy, through electrochemical oxidation–reduction (redox) reactions of an electroactive material. A battery is by definition a device that is composed of one or more electrochemical cells, which are connected in series, parallel or series-parallel. An electrochemical cell is generally composed of three main components:

- The anode, also called the negative electrode, is oxidized during the discharge process of a battery, providing electrons to the external circuit.
- The cathode, also called the positive electrode, is consequently reduced during the discharge process of a battery, accepting electrons from the external circuit.
- The electrolyte is essentially an ionic conductor material, in liquid or solid state, allowing the migration of charges (*i.e.*, ions) between the anode and the cathode, while being an electronic insulator to prevent an internal short circuit.

To allow comparison of different battery systems, and thus the electroactive materials that compose them, several criteria need to be defined:

- Theoretical capacity ($C_{\text{theo}}$ [mA h]) of an electroactive material corresponds to the total amount of electric charge that can be generated from the redox reactions of the electroactive material. The coulomb

(*i.e.*, 1 C = 1 A s) is the unit of the capacity of an electroactive material, although often expressed in ampere hour (*i.e.*, 1 A h = 3600 * 1 C) in the battery research field. To allow comparison of different electroactive materials, normalization to mass of electroactive material is often implemented to obtain the specific capacity ($C_{spec}$ [mA h $g^{-1}$]), which can be calculated according to eqn (8.1).

$$C_{Spec} = \frac{n \times F}{M_w} = \frac{n \times 96485\left[A\,s\,mol^{-1}\right]}{M_w\left[g\,mol^{-1}\right]} = \frac{n \times 26801}{M_w}\left[mA\,h\,g^{-1}\right] \quad (8.1)$$

where $n$ is the number of electrons involved per redox reaction, $F$ is the Faraday constant and $M_w$ is the molecular weight of the electroactive material. In the case of redox polymers, this refers to the molecular weight of the repeating unit.

- Since the specific capacity is only related to the mass of the electroactive material, the capacity of an electrode is often calculated to compare electrodes and can be quantified in three different ways: per unit of mass of electrode, per unit of volume, or per area, respectively called, gravimetric capacity [mA h $g^{-1}$], volumetric capacity [mA h $cm^{-3}$] and areal capacity [mA h $cm^{-2}$]. As an example, the gravimetric capacity is calculated according to eqn (8.2).

$$C_{gravimetric} = \frac{C_{spec} \times m_{electroactive}[mA\,h]}{m_{electrode}[g]} \quad (8.2)$$

Where $C_{spec}$ is the specific capacity of the electroactive material used to formulate the electrode, $m_{electroactive}$ is the mass of the electroactive materials present in the electrode and $m_{electrode}$ is the mass of all the components of the electrode (*i.e.*, including the electroactive material, carbon additive and binder).

- Theoretical voltage ($V$ [V]) of an electrochemical cell is defined by the potential difference between the standard redox potentials of the anode and cathode as follows:

$$E^0(\text{cell voltage}) = \text{cathode potential} - \text{anode potential} \quad (8.3)$$

- Theoretical energy ($E_{theo}$ [W h]) is also an important parameter of an electrochemical cell and corresponds to the total amount of energy that can be obtained from a defined electrochemical cell, based on their theoretical voltage ($V$) and theoretical capacity ($C_{theo}$), as follows:

$$E_{theo} = C_{theo} \times V \quad (8.4)$$

- Similarly to the specific capacity ($C_{spec}$ [ma h $g^{-1}$]), the specific energy ($E_{spec}$ [W h $g^{-1}$]) is defined by normalization of the theoretical energy by the mass of the electroactive material from the capacity-limiting electrode.

$$E_{spec} = \frac{E_{theo}}{m} \quad (8.5)$$

- Coulombic efficiency ($\eta_c$ [%]) is used to characterize the efficiency in terms of the capacity of an electrochemical cell, through one full charge and discharge cycle and is defined as follows:

$$\eta_{\text{spec}} = \frac{C_{\text{discharge}}}{C_{\text{charge}}} \tag{8.6}$$

- C rate ($C$) is a measure of the loading current applied, normalized by the current required to fully charge a battery in 1 hour and is defined as follows:

$$C = \frac{i_{\text{applied}}}{i_{1h}} \tag{8.7}$$

- Another commonly used measure of the load applied to charge a battery is the current density ($j$ [mA cm$^{-2}$]), which is defined by the current applied, normalized by the cross-sectional area of the limiting electrode.

### 8.1.3 All-organic Polymer Battery: Cell Configuration

All-organic polymer batteries can be classified into three main cell configurations, depending on the doping type of the organic redox polymer used as the anode or cathode (see Figure 8.1). The first two configurations are based on the rocking-chair concept,[24] where a charged species from the electrolyte, either cationic or anionic, is involved in redox reactions of both the anode and cathode. In such a battery configuration, the electrolyte concentration remains constant.[22] The current lithium-ion battery technology is one of the most famous examples of a cationic rocking-chair type battery.[15,16] With regard to all-organic polymer batteries, a cationic rocking-chair cell configuration implies the use of a n-type organic redox polymer as both the anode and cathode materials. In an anionic rocking-chair cell

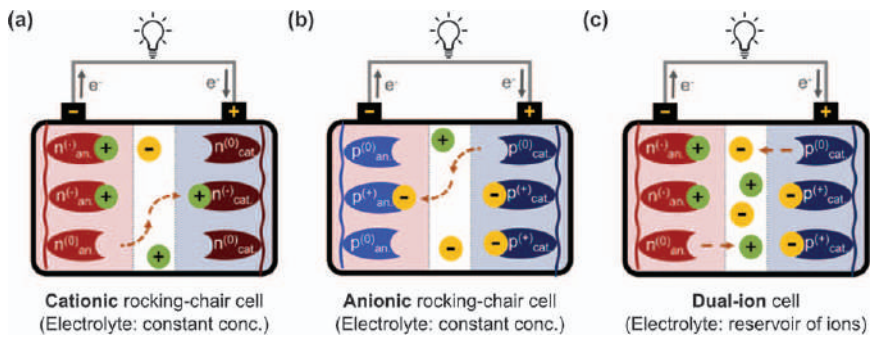


**Figure 8.1** Cell configurations accessible in all-organic polymer batteries, through a combination of n-type and/or p-type organic redox polymers: (a) cationic rocking-chair cell, (b) anionic rocking-chair cell and (c) dual-ion cell.

configuration, both the anode and cathode are composed of a p-type organic redox polymer. The last type of cell configuration accessible in all-organic polymer batteries is based on the dual-ion cell concept, wherein the anode, a cationic charged species is involved in the redox reaction of an n-type organic redox polymer. While in the cathode, a p-type organic redox polymer is used and an anionic charged species is balancing the redox reaction. In a dual-ion battery, the electrolyte acts as a reservoir of ions.[22]

## 8.2 All-organic Polymer Batteries

Over the last two decades, intensive efforts have been made towards the development of organic redox polymers for their potential application in energy storage devices, ranging from large scale-stationary battery systems (see Chapter 7) to battery systems related to the Internet of Things.[1,14,19,21,22] Indeed, the constant increasing demand for more interconnected and mobile systems is urging for new battery systems, with requirements such as flexibility, no toxic/harmful metals, easy processability by roll-to-roll process, made from abundant raw material, fast-charge/discharge and long cycle life, in order to improve user-friendliness.[1] In this regard, organic redox polymers exhibit several advantages compared to the current lithium-ion battery technology (*i.e.*, based on inorganic redox materials), such as easy processability, abundant and environmentally friendly precursors and excellent rate performance. The latter is inherent to the nature of the redox reactions occurring in the organic redox polymer, which is related to a change in the state of charge of the electroactive moiety, enabling fast electron-transfer kinetics. On the contrary, redox reactions in inorganic redox materials generally occur with a change of valence of the transition metal (*i.e.*, cathode material), resulting in slow rate performance.[21] Additionally, the intercalation of Li ions in inorganic intercalation electrodes (*i.e.*, the anode in lithium-ion batteries) is usually accompanied with structural rearrangement of the lattice and layered structures, again resulting in slow kinetics and also heat dissipation, which are unfavourable characteristics for application in the Internet of Things.[25] Finally, inorganic redox materials are usually limited to lithium chemistries as the ion carrier, in contrast to organic redox polymers where the ion carrier can be either cationic (*i.e.*, alkali metal, organic cation or even proton) or anionic, opening the range of battery configurations accessible (see Section 8.1.3 for details), with low-cost and more environmentally friendly electrolytes system.

In the following section, a comprehensive overview of the different prototypes of all-organic polymer batteries reported to date will be discussed. Initially, all-organic polymer batteries based on alkali metal chemistries as ion carriers will be presented, because these have been intensively investigated due to their ease of implementation into Li-ion batteries. Transitioning towards a more environmentally friendly and low-cost battery system (*i.e.*, related to electrolyte), all-organic polymer batteries based on metal-free ion carriers will also be discussed, followed by those based on proton-based ion carriers.

### 8.2.1 All-organic Polymer Batteries based on Li/Na Ion Carriers

Alkali metal salts have been intensively implemented as ion carriers in all-organic batteries, because of the easy translation of organic material electrodes (*i.e.*, as the cathode) into the current lithium-ion battery technology or into the next generation of lithium metal batteries.[1,19,21] Additionally, the reversibility and long-term cycling stability of a novel organic redox polymer can be easily investigated in a half-cell configuration (*i.e.*, organic electrode ‖ alkali metal electrode), prior to assessing them in an all-organic battery, where finding a common electrolyte system for both organic electrodes can be challenging (*i.e.*, different ion carrier, appropriate swelling of organic redox polymer by solvent, *etc.*) and thus the cycling performance can be affected by the cycling stability of both electrodes. The first report on the use of an alkali metal salt as an ion carrier for an organic material electrode dates back to 1981, with the spontaneous n-type doping of poly(acetylene) when dropped in 0.3 M $LiClO_4$ in tetrahydrofuran with a lithium metal strip as counter electrode (*i.e.*, the anode).[26] No further electrochemical characterization was reported.[26] The same year, Chiang reported the first known prototype of an all-solid-state all-organic battery operating at 85 °C, where undoped poly(acetylene) was used as both the anode and cathode, and a solid electrolyte composed of a poly(ethylene-oxide) containing sodium iodide salt was employed.[27] The all-solid-state all-organic battery exhibited an open circuit voltage ranging from 2.8 V to 3.5 V, and a specific energy density of 20 Wh $kg^{-1}$.[27] A few years later, Killian *et al.* reported a quasi-solid-state all-organic battery based on electropolymerized poly(pyrrole) and poly(pyrrole):poly(styrene sulphonate) redox polymers as the cathode and anode, respectively.[28] It is noteworthy that both electrodes needed to be preoxidized and prereduced, respectively, prior to battery assembly. A gel electrolyte based on $LiClO_4$ in poly(acrylonitrile)/ethylene carbonate/propylene carbonate (*i.e.*, over 50 mol.% of solvent components) was used, allowing room temperature battery operation. The all-organic cell displayed a low specific charge capacity of 22 mAh $g^{-1}$ (*i.e.*, relating to the mass of cathode active material), corresponding to 42% of the available specific charge capacity in the cathode, due to the mass loading of the anode electrode and the lower theoretical specific capacity of the poly(pyrrole):poly(styrene sulphonate).[28] Nevertheless, the all-organic cell performed with no capacity loss over 100 cycles.[28] In 2012, Wallace and co-workers described a flexible all-organic battery based on poly(pyrrole):para(toluene sulphonic acid) (pPy-pTS) and poly(pyrrole):indigo carmine (pPy-IC) as the cathode and anode, respectively.[29] Both pPy-pTS and pPy-IC films were prepared by electropolymerization onto polished stainless steel plate, which could be peeled off afterwards, resulting in highly flexible self-standing electrodes. In the discharge process of this dual-ion battery, the poly(pyrrole) in the pPy-IC anode is oxidized from its neutral state, while the poly(pyrrole) in the pPy-pTS cathode is reduced from its oxidized state, and vice and versa during the charging process. The resulting all-organic battery, when using a traditional organic liquid electrolyte (*i.e.*, 1 M $LiPF_6$ in ethylene carbonate/dimethyl

carbonate), revealed an initial specific discharge capacity of 39 mAh $g^{-1}$ at a current density of 0.05 mA $cm^{-2}$, of which 92% remained after 50 cycles. The rate capability was also investigated with current densities ranging from 0.01 mA $cm^{-2}$ to 0.07 mA $cm^{-2}$, exhibiting relatively good performance. In 2013, Zhu *et al.* reported the use of poly(3,4-dihexylthiophene) (PDHT) as an anode material through an n-type doping process.[30] In situ polymerization with 30 wt.% of vapour-grown carbon fibres (VGCFs) was performed to obtain a PDHT/VGCFs composite, which was used for the anode electrode. The Li metal ‖ PDHT/VGCFs half-cell demonstrated a reversible specific discharge capacity of $\sim$250 mAh $g^{-1}$ (*i.e.*, excluding capacity contribution from VGCFs), although irreversible capacity loss was observed in the first 10 cycles, attributed by the authors to electroreduction side reactions of the electrolyte solvent at such negative potential (*i.e.*, +1 V *vs.* $Li/Li^+$).[30] The half-cell also displayed good rate capability with specific discharge capacities of 215 mAh $g^{-1}$ and 120 mAh $g^{-1}$ reached at a current density of 200 mA $g^{-1}$ and 400 mA $g^{-1}$, respectively. An all-organic battery was also constructed by coupling this PDHT/VGCFs anode with an organic cathode based on a poly(triphenylamine) (PTPAn) polymer. This dual-ion battery, which was anode-limited, exhibited a reversible specific discharge capacity of $\sim$250 mAh $g^{-1}$ at a current density of 40 mA $g^{-1}$ and displayed a charging voltage plateau of $\sim$3 V. Unfortunately, no long-term cycling stability data were reported.[30] Using the same p-type PTPAn cathode, Deng *et al.* reported an all-organic sodium-ion battery, by coupling the PTPAn cathode with an n-type poly(antraquinonyl sulphide) anode, enabling an average voltage output of 1.8 V.[31] Although the redox characteristics of both redox polymers were already reported for Li-ion battery,[32,33] their cycling performance was not investigated in a sodium-ion battery, in particular for the poly(antraquinonyl sulphide), which involves the doping/dedoping of sodium ions during the redox reactions. The all-organic sodium-ion battery, anode-limited by design, revealed a specific discharge capacity of 220 mAh $g^{-1}$ at a 1 C rate, indicating full utilization of the anode active materials (*i.e.*, 98%). Additionally, the dual-ion cell displayed a high rate capability, reaching a reversible specific discharge capacity of 118 mAh $g^{-1}$ at a 32 C rate. Excellent long-term cycling stability was also demonstrated with 85% capacity retention after 500 cycles at an 8 C rate. In the pursuit of safer batteries, Zhu *et al.* reported an all-solid-state all-organic sodium-ion battery, which used a plastic crystal electrolyte based on a sodium perchlorate salt dissolved in succinonitrile.[34] The authors employed the aforementioned n-type poly(antraquinonyl sulphide) and a p-type poly(aniline-r-nitroaniline) copolymer (with the latter having been previously reported as cathode material for sodium metal batteries[35]) to construct an all-organic battery which delivered an average output voltage of 1.6 V. The all-solid-state all-organic battery, anode-limited by design, yielded a specific discharge capacity of 200 mAh $g^{-1}$ at a current density of 50 mA $g^{-1}$ when the battery was operated at room temperature, corresponding to 89% of the theoretical capacity of the anode materials. However, a moderate life cycle was observed with 80% capacity retention after 50 cycles.

Following the work by Nishide and co-workers on galvinoxyl-based redox polymers, Schubert and co-workers described the synthesis of poly(acetylene) bearing a (p-ethynylphenyl)hydrogalvinoxyl pendant group for application as anode materials in all-organic batteries.[36] The cycling performance of this anode material was assessed in a half-cell configuration, using a 0.1 M NaCl aqueous solution with 0.01 M tetrabutylammonium hydroxide as the electrolyte. A low specific discharge capacity of 30–35 mAh $g^{-1}$ (*i.e.*, 60% of the theoretical specific capacity) was initially reached. Moreover, a significant capacity fading upon further cycles was also observed with only 50% capacity retention after 40 cycles. The resulting all-organic battery constructed by coupling this anode material with the well-known poly(2,2,6,6-tetramethylpiperidine-*N*-oxyl)methacrylate (PTMA) as the cathode, displayed similar performance.

In 2013, Zhu *et al.* reported an all-organic battery, that used a bipolar redox polymer based on poly(paraphenylene) (PPP).[37] The PPP polymer exhibited both p-type and n-type redox activities, allowing its use as both cathode and anode materials and enabling an average output voltage of $\sim$3 V. In a lithium ‖ PPP half-cell, the specific discharge capacity, associated to the n-type doping of lithium-ion, slightly increased upon cycling, reaching a value of 600 mAh $g^{-1}$ after 60 cycles at a current density of 40 mA $g^{-1}$. High rate capability was also observed for the n-type doping process, delivering a reversible specific discharge capacity of 200 mAh $g^{-1}$ at the impressively high current density of 1280 mA $g^{-1}$. As commonly observed for p-type redox polymers, a lower specific discharge capacity of 80 mAh $g^{-1}$ was observed because of the lower doping degrees of the polymer chains by the bulky anions, due to steric hindrance. Nevertheless, an all-organic battery was constructed with the PPP polymer as both the anode and cathode, in an anode-limited design, delivering a specific discharge capacity of 153 mAh $g^{-1}$. The lower capacity observed, when compared to the lithium metal ‖ PPP half-cell, was attributed by the authors to the incomplete match of the anode and cathode.

In 2017, Schubert and co-workers described two novel synthetic routes for the development of organic redox polymers bearing either a thianthrene or an 11,11,12,12-tetracyano-9,10-anthraquinonedimethane pendant group [*i.e.*, poly(2-vinylthianthrene) and poly(2-methacrylamide-TCAQ), respectively] for application in all-organic batteries[38] (see Figure 8.2). As previously reported,[39] the poly(2-vinylthianthrene) displayed a reversible p-type redox reaction at a potential of 0.78 V (*vs.* $Fc/Fc^+$), associated to the doping/dedoping of anions from the electrolyte. For the poly(2-methacrylamide-TCAQ), a reversible n-type redox reaction was observed at a potential of –0.7 V (*vs.* $Fc/Fc^+$), corresponding to the doping/dedoping of lithium ions onto the polymer chain. Consequently, the all-organic battery resulting from these two redox polymers revealed an average output voltage of 1.35 V, with remarkably flat charge/discharge plateaus. In this case, the all-organic cell was cathode-limited by design and delivered an initial specific discharge capacity of 105 mAh $g^{-1}$, corresponding to 96% of the theoretical capacity of the cathode material. A moderate cycle life was observed with only 67% capacity retention after 250 cycles at a 1 C rate. Rate capability was also reported with

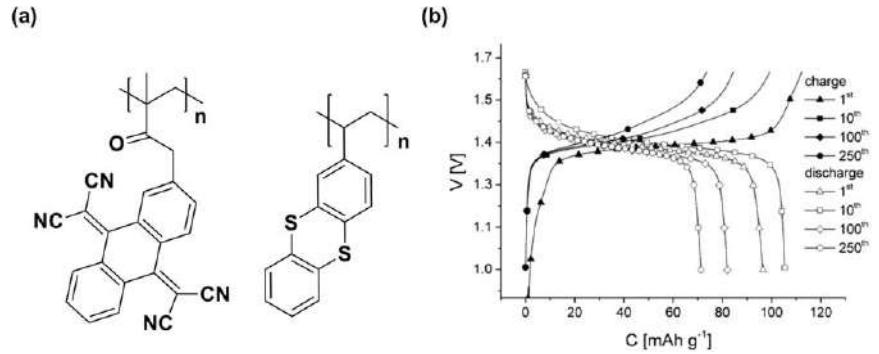


**Figure 8.2** (a) Molecular structures of the poly(2-methacrylamide-TCAQ) (left) and the poly(2-vinylthianthrene) (right) used as anode and cathode, respectively, in the all-organic battery reported by Wild *et al.* (b) Galvanostatic cycling of the resulting cell at a 1 C rate using 1 M $LiClO_4$ in EC/DMC (3/7, v/v) solution. Adapted from ref. 38 with permission from John Wiley and Sons, © 2016 Wiley-VCH Verlag GmbH & Co. KGaA, Weinheim.

no significant capacity loss when increasing C rate from 1 C to 5 C, although only 60% of the initial specific discharge capacity remained at a more elevated C rate of 30 C.

In 2018, Xie *et al.* reported the synthesis of a bifunctional ladderized heterocyclic poly(quinone) (PDB), that could act as both cathode and anode materials[40] (see Figure 8.3). A lithium metal ‖ PDB half-cell was constructed to assess the redox activity and rate capability of the enolization process, revealing an initial specific charge capacity of 255 mAh $g^{-1}$ at a current density of 20 mA $g^{-1}$, corresponding to 79% of its theoretical capacity. The PDB also displayed an astonishing rate capability and cycling stability, reaching a specific charge capacity of 161 mA $g^{-1}$, of which 80% remained after 1000 cycles, at an ultrahigh applied current density of 1.5 A $g^{-1}$. Based on the excellent electrochemical performance of the PDB as cathode, an all-organic (*i.e.*, symmetric) cell was developed using PDB as both the cathode and anode, although a prelithiation process was required for the anode. Slightly lower but still a good rate capability was observed for the all-organic cell, with specific charge capacities of 249 mAh $g^{-1}$ and 55 mAh $g^{-1}$ at a current density of 20 mA $g^{-1}$ and 1 A $g^{-1}$, respectively. The symmetric cell displayed a moderate cycle life, with 68% capacity retention after 250 cycles at 500 mA $g^{-1}$.

Following the design strategy described by Zu *et al.* and Xie *et al.*,[37,40] a dual redox-active polyimide copolymer, having both phenothiazine and naphthlene moieties, was synthesized for application in all-organic batteries by Mecerreyes and co-workers[41] (see Figure 8.4). This dual-redox copolymer displayed three main redox processes, occurring at a potential of 2.3 V, 2.5 V and 3.7 V (*vs.* $Li/Li^+$). The two former redox processes were attributed to the enolization process of the naphthalene units, while the latter corresponded to the oxidation/reduction processes of the phenothiazine moiety. It is noteworthy that no prelithiation process was required to use this dual redox-active copolymer as

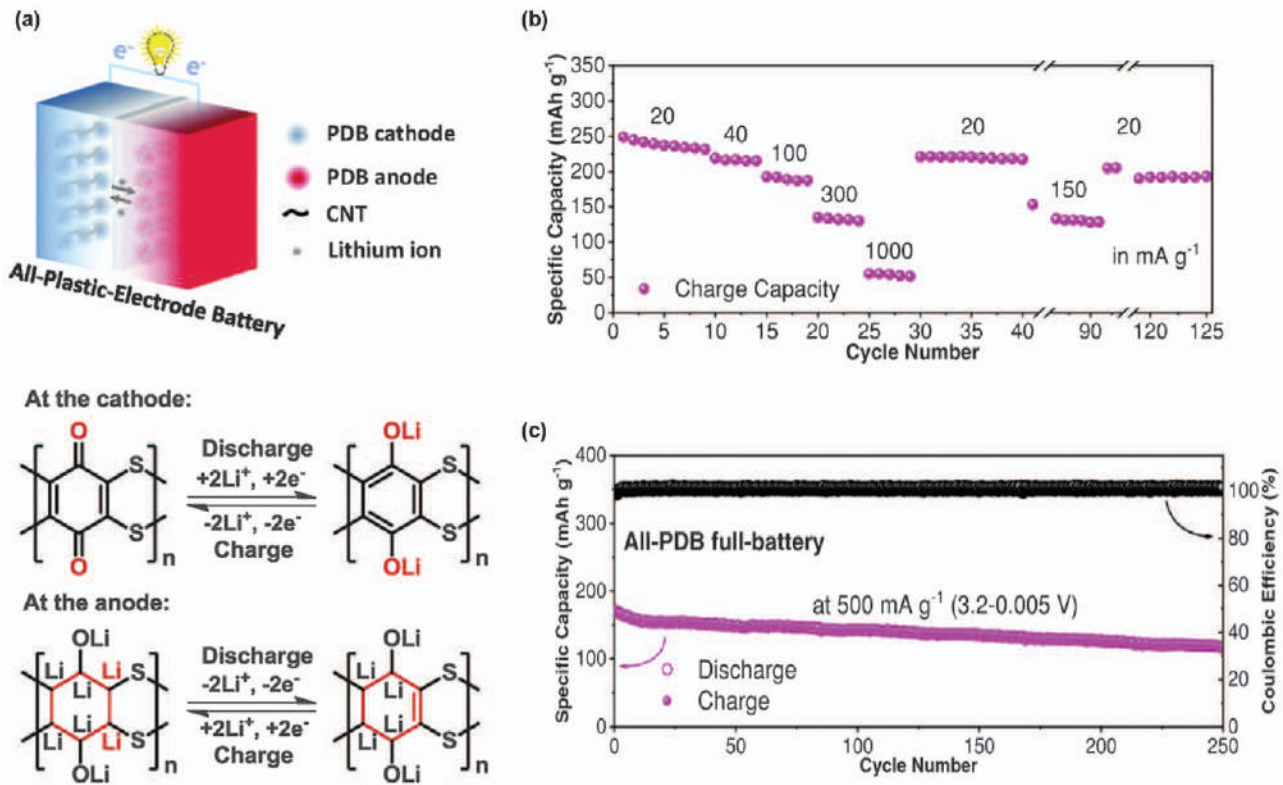


**Figure 8.3** (a) Prototype of the all-PDB-electrode battery as well as the redox reactions associated with the PDB polymer at both the cathode and anode electrodes. (b) Galvanostatic cycling of the resulting cell at different current densities and (c) the long-term cycling for 250 cycles at a current density of 500 mA $g^{-1}$.
Adapted from ref. 40 with permission from John Wiley and Sons, © 2018 Wiley-VCH Verlag GmbH & Co. KGaA, Weinheim.

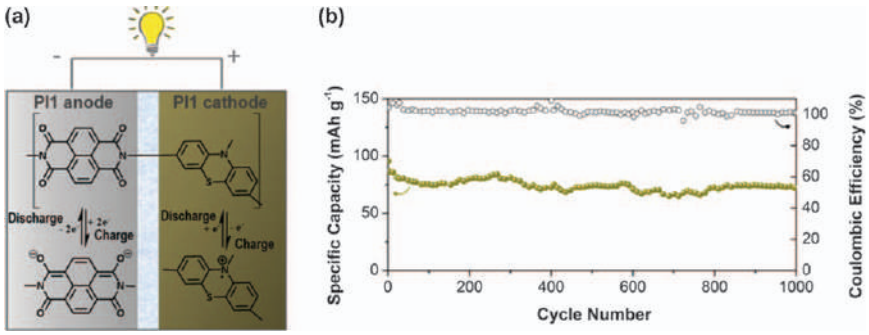


**Figure 8.4** (a) Prototype of the symmetric all-organic battery using the redox-active polyimide copolymer, having phenothiazine and naphthlene moieties, reported by Casado *et al.* (b) Galvanostatic cycling of the resulting cell for 1000 cycles at a high current density of 800 mA $g^{-1}$, demonstrating the long-term stability of the proposed symmetric all-organic battery. Adapted from ref. 41 with permission from John Wiley and Sons, © 2019 Wiley-VCH Verlag GmbH & Co. KGaA, Weinheim.

anode. The symmetric all-organic cell displayed high rate capability, retaining specific discharge capacities of 128 mAh $g^{-1}$ and 124 mAh $g^{-1}$ at current densities of 50 mA $g^{-1}$ and 1000 mA $g^{-1}$, respectively. At the high current density of 800 mA $g^{-1}$, the symmetric cell exhibited long cycling stability, with 94% retention of the initial discharge capacity after 1000 cycles.

In 2018, Mecerreyes and co-workers reported the synthesis of a polyimide copolymer based on perylene and ethylene oxide blocks (perylene polyimide-PEO2000) for cathode materials with application in both aqueous sodium-ion batteries and all-organic batteries[42] (see Figure 8.5). The perylene polyimide-PEO2000 half-cell, using a 1 M sodium sulphate aqueous solution as the electrolyte, displayed a high rate capability, delivering a specific discharge capacity of 94 mAh $g^{-1}$ and 73 mAh $g^{-1}$ (*i.e.*, based on the mass of perylene units) at a 10 C and 600 C rate, respectively. The half-cell also exhibited an outstanding cycle life, with 98% capacity retention after 2000 cycles at a 600 C rate, highlighting the potential of this material as electrode material. The superior electrochemical performance of the perylene polyimide-PEO2000 was attributed to the higher conjugation of the perylene moiety and incorporation of the PEO block, which enhanced the electronic and ionic conductivity of the material, respectively. Encouraged by such promising results, the authors reported the cycling performance of an aqueous all-organic battery, by coupling the perylene polyimide-PEO2000 anode with one of their previously reported poly(3,4-ethylenedioxythiophene)-lignin biopolymer composite cathode (PEDOT-lignin),[43,44] essentially developing a safe, sustainable and low-cost aqueous all-organic battery. This all-organic battery was able to deliver 53 mAh $g^{-1}$ and 39 mAh $g^{-1}$ specific discharge capacities at 10 C and 200 C rates, respectively. Although the cell suffered from low coulombic efficiency at low C rate (*i.e.*, $\leq$ 50 C) due to self-discharge, 85% capacity retention was demonstrated

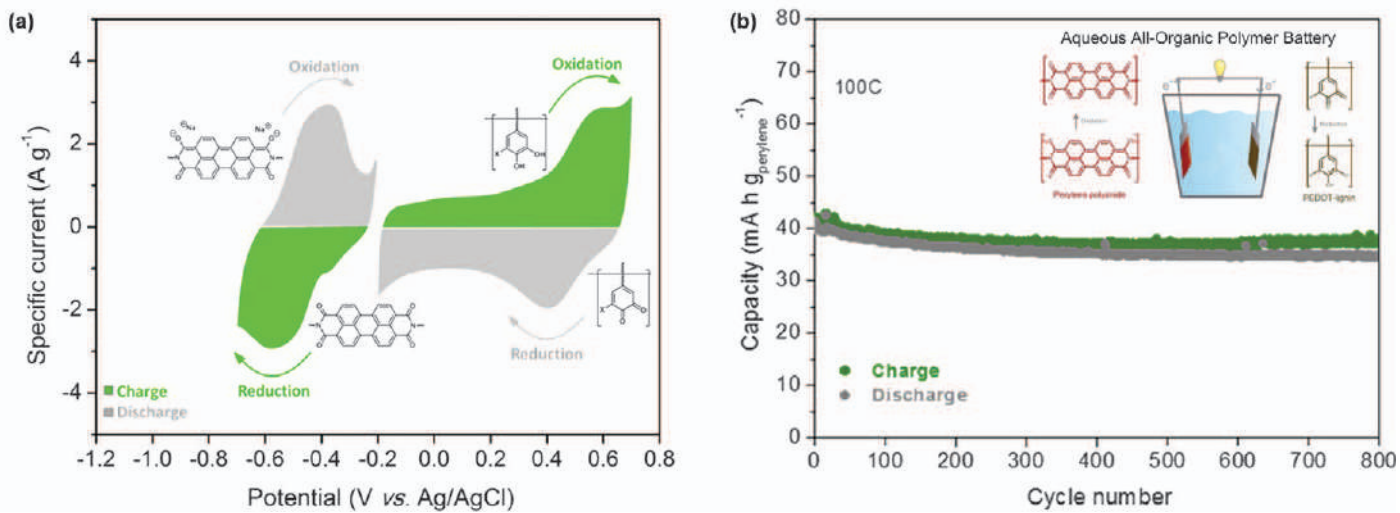


**Figure 8.5** (a) Cyclic voltammetry and redox reactions of perylene polyimide-PEO2000 and PEDOT-lignin polymers in half-cells, (b) long-term galvanostatic cycling of resulting cell for 800 cycles at a 100 C rate.
Adapted from ref. 42 with permission from the American Chemical Society, Copyright 2018.

after 800 cycles at a 100 C rate, highlighting the high rate performance of this all-organic battery.

Although the pursuit of novel organic redox polymers with higher storage capacity, high rate performance and long cycle life are of crucial importance for the next generation of all-organic batteries, the development of high-performance electrolytes is equally important since the aforementioned characteristics could be greatly enhanced by the electrolyte system. In 2017, Dong *et al.* described the use of a novel aqueous electrolyte by the "water-in-salt" concept, where a high concentration of lithium bis(trifluoromethanesulphonyl) imide (LiTFSI) was employed, for application in aqueous all-organic battery[45] (see Figure 8.6). This aqueous electrolyte impeded side reactions related to the water electrochemical stability, extending the electrochemical stability window of the aqueous electrotype, which is generally limited to 1.23 V due to hydrogen/oxygen evolution reactions. As a result, the implementation of a high-voltage organic cathode, which was restricted to battery systems based on organic electrolytes, can now be considered for application in an aqueous all-organic battery. To demonstrate this concept, the author studied the redox activity of a p-type organic cathode material based on poly(triphenylamine) (PTPAn), which suffered from parasitic redox reactions in commonly used aqueous electrolytes, through the competitive absorption of water molecules (*i.e.*, $H_2O/OH^-$) during the oxidation reaction of the nitrogen redox site, consequently promoting oxygen evolution.[32,45] Indeed, the PTPAn cathode displayed no redox activity in common neutral aqueous electrolytes such as 1 M lithium sulphate, 2 M lithium nitrate, 2 M lithium perchlorate and 2 M lithium acetate. To further confirm that the parasitic reaction observed in the aqueous electrolyte involved $H_2O/OH^-$ absorption, the redox activity of the PTPAn

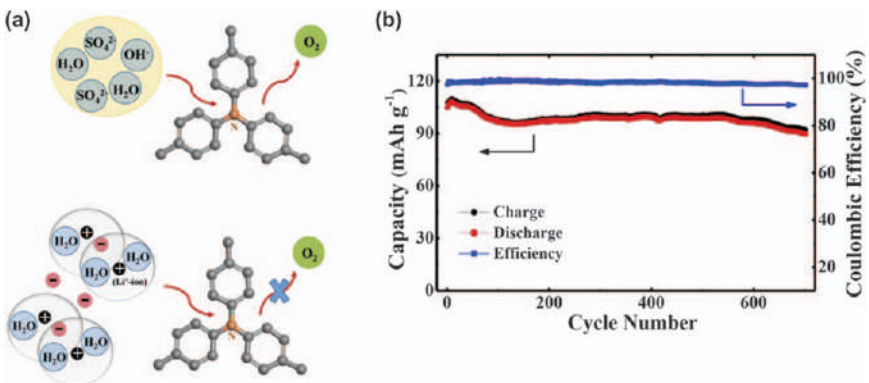


**Figure 8.6** (a) Schematic illustration of the possible oxygen evolution mechanism involved with the poly(triphenylamine) in either 1 M $Li_2SO_4$ (top) or 21 molal LiTFSI aqueous electrolyte (bottom), (b) long-term galvanostatic cycling of the resulting poly(1,4,5,8-naphthalenetetracarboxylic bisimide)/poly(triphenylamine) cell, for 700 cycles at a 1 C rate.
Adapted from ref. 45 with permission from John Wiley and Sons, © 2017 Wiley-VCH Verlag GmbH & Co. KGaA, Weinheim.

cathode was also assessed in an acidic aqueous electrolyte (*i.e.*, 1 M lithium sulphate/1 M sulphuric acid solution), where highly reversible redox activity was indeed observed. However, a reduction of the electrochemical stability window of water is generally observed in acidic electrolytes, due to a shift towards a higher voltage of the hydrogen evolution process, thus limiting the choice of organic anode materials (*e.g.*, excluding redox-based polyimide).[45] To overcome this problem, the authors proposed the use of a neutral ''water-in-salt'' aqueous electrolyte in conjunction with the PTPAn cathode, since no free water is present in this type of electrolyte and thus potentially preventing oxygen evolution side reactions.[46] Indeed, the cyclic voltammogram of the PTPAn cathode in a ''water-in-salt'' electrolyte featured the characteristic two pairs of reversible redox peaks at a potential of 0.2 V and 0.6 V. Furthermore, an all-organic battery consisting of a PTPAn cathode and a poly(1,4,5,8-naphthalenetetracarboxylic bisimide) anode, using the aforementioned ''water-in-salt'' electrolyte was demonstrated. Designed as cathode-limited, the all-organic battery delivered an initial specific discharge capacity of 105 mAh $g^{-1}$ (*i.e.*, 96% of the theoretical specific capacity of the cathode material), at a 1 C rate, of which 85% remained after 700 cycles. The aqueous all-organic cell also displayed good rate capability, by delivering a specific discharge capacity of 48 mAh $g^{-1}$ at an impressive 460 C rate. These results confirmed the potential of the ''water-in-salt'' electrolyte in aqueous all-organic battery applications, potentially unlocking the fabrication of safer, low-cost and environmentally benign battery systems.

One year later, Dong *et al.* reported the development of a novel organic electrolyte based on lithium bis(trifluoromethanesulphonyl)imide dissolved in ethyl acetate, for application in all-organic batteries at ultra-low operating temperatures (*i.e.*, −70 °C).[47] Consequently, an all-organic battery, composed of the previously reported poly(triphenylamine) and poly(1,4,5,8-naphthalenetetracarboxylic bisimide) was assembled using the ethyl acetate-based electrolyte. At a 0.5 C rate, specific discharge capacities of 99 mAh $g^{-1}$ and 69 mAh $g^{-1}$ were obtained at 25 °C and −70 °C, respectively. It is noteworthy that a lithium-ion battery, which was based on lithium intercalation, was not able to operate at such low temperature using the same ethyl acetate-based electrolyte, due to the sluggish desolvation process of lithium ions. Such results highlight the advantages of organic redox polymer materials, in which the redox reaction is related to a change in the state of charge of the electroactive moiety, and thus enabling fast electron-transfer kinetics.[47]

Despite the numerous advantages of organic-based electrodes, in terms of high rate capability and long cycle life, their implementation has been hampered to date by their low areal capacity loading when compared to inorganic-based electrode, due to the high amount of conductive additive required to ensure sufficient electronic conductivity within the electrode (*i.e.*, 30–80 wt.% *vs.* 2–5 wt.% for organic- and inorganic-based electrodes). In 2018, Nishide and co-workers described a novel fabrication method for redox polymer-based electrodes, enabling a high discharge rate up to 1 A $cm^{-2}$ and high active material loading, resulting in an unprecedented areal capacity of 3 mAh $cm^{-2}$, which is 10 to 100 times larger than previous reports[48] (see Figure 8.7).

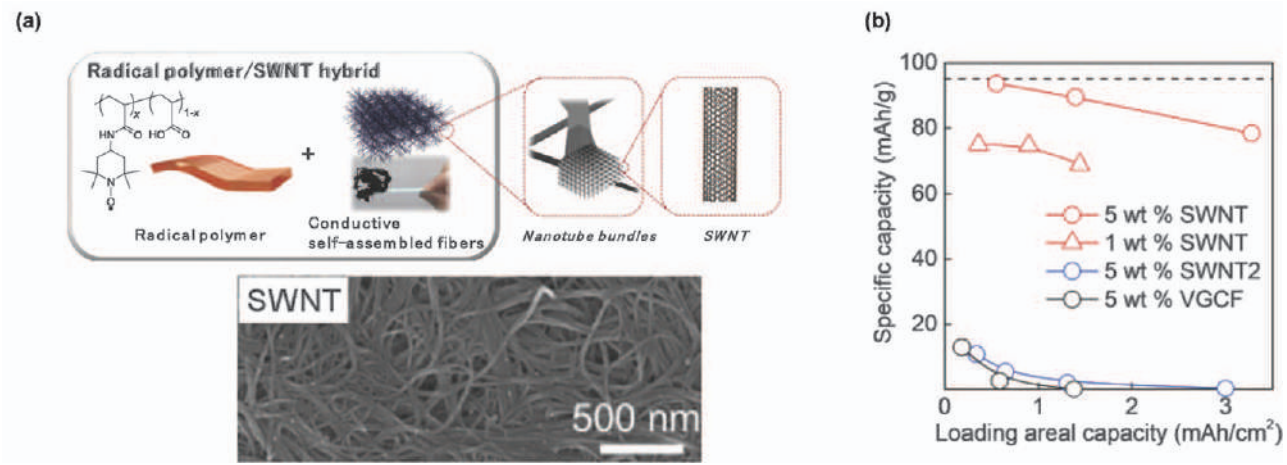


**Figure 8.7** (a) Schematic illustration (top) of the hybrid electrode developed by Nishide and co-workers as well as the corresponding SEM images (bottom), (b) specific discharge capacities delivered by the PTAm/SWNT half-cell as a function of the areal capacity of the PTAm/SWNT electrode.
Adapted from ref. 48 with permission from John Wiley and Sons, © 2018 Wiley-VCH Verlag GmbH & Co. KGaA, Weinheim.

A recently reported new type of single-walled carbon nanotube (SWNT), developed by enhanced-direct-injection-pyrolytic-synthesis, was used as a conductive additive, which self-assembles into a continuous conductive network, enabling high electronic conductivity. A simple hybridization method, *via* physical grinding in an organic solvent, was employed to prepare the organic-based electrode, using either poly(2,2,6,6-tetramethyl-piperidinyloxy-4-yl acrylamide) (PTAm) or poly(anthraquinone-substituted ethyleneimine) (PAQE) for the fabrication of cathode and anode electrodes, respectively. It is noteworthy that only 5 wt.% of SWNTs was required for the formation of a percolating network. The PTAm/SWNTs half-cell, with an areal capacity of 1.4 mAh $cm^{-2}$, displayed an initial specific capacity of 90 mAh $g^{-1}$ at a 10 C rate, which only decreased to 78 mAh $g^{-1}$ when the areal capacity of the electrode was increased to 3.3 mAh $cm^{-2}$. The PTAm/SWNT half-cell also exhibited a high rate capability up to 1 A $cm^{-2}$. A flexible all-organic battery with an areal capacity of 1.1 mAh $cm^{-2}$ was also constructed using the PTAm/SWNT and the PAQE/SWNT electrodes, delivering an average output voltage of 1.1 V. The cell displayed an excellent cycle life considering the high areal capacity of the electrode, with 68% retention of its initial capacity after 1000 cycles at a 10 C rate.

Pursuing their efforts in the development of ultrathin and flexible organic-based electrodes with high rate performance, Nishide and co-workers reported the hybridization of a conductive SWNT mesh material with the aforementioned PTAm and PAQE redox polymers, *via* dip coating.[49] Compared to their previous hybridization method, the dip-coating procedure produced electrodes with a thickness of 100 nm, compared to the previously reported electrode thickness of 100–300 μm.[48,49] Notably, the resulting areal capacity of the electrode was not specified, which would be presumably lower than that formed from the previous hybridization method, due to the higher conductive additive content used in the present method (*i.e.*, 20 wt.% *vs.* 5 wt.%). Nevertheless, thanks to the submicron thickness of the PTAm/SWNT electrode, a specific discharge capacity of 90 mAh $g^{-1}$ was reached even at a high 430 C rate (*i.e.*, 0.4 mA $cm^{-2}$), corresponding to 98% of the theoretical capacity of the PTAm. A micron-thick all-organic battery was constructed, using a 280 nm thick PLA porous separator soaked with a 3 M sodium chloride aqueous solution, corresponding to the thinnest secondary battery reported to date. Despite the submicron thickness of the separator, the cell displayed high coulombic efficiency (*i.e.*, 98%) with no obvious self-discharge and delivered almost its theoretical specific capacity at a 18 C rate.

Although organic polymer–air batteries are not considered as an all-organic battery due to the redox reactions that occur at the cathode side, such battery technology still represents an advantageous alternative to the current lithium-ion battery technology (*i.e.*, based on inorganic redox materials) due to its high energy density, low cost and environmental friendliness. The first prototype of an organic polymer–air battery was presented by Nishide and co-workers in 2011, where a poly(vinylanthraquinone) (PVAQ) anode was employed in conjunction with a basic aqueous electrolyte based on a sodium hydroxide salt[50] (see Figure 8.8). The PVAQ electrode exhibited

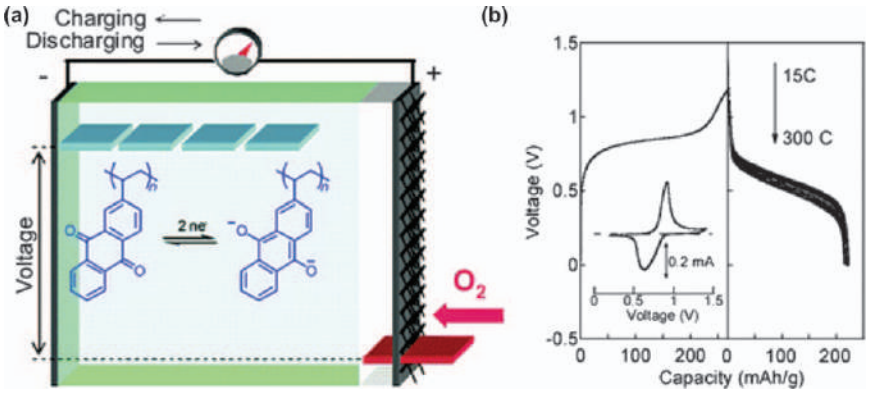


**Figure 8.8** (a) Prototype of the organic polymer–air battery proposed by Nishide and co-workers, using a poly(vinylanthraquinone) as anode, (b) voltage profiles of the resulting cell as a function of C rate, demonstrating high rate performance of the devices.
Adapted from ref. 50 with permission from the American Chemical Society, Copyright 2011.

good redox activity in basic electrolyte (*i.e.*, pH = 13.7), delivering 94% of its specific theoretical discharge capacity, with 100% coulombic efficiency at a current density of 5 $A\,g^{-1}$. On the contrary, only 10% of the theoretical capacity was reached in less basic electrolyte (*i.e.*, pH = 8.3). Such results were in agreement with the p$K_a$ constant of the anthraquinone. A good cycle life stability was also demonstrated for the PVAQ half-cell, with 91% retention of the initial capacity after 300 cycles, due to the robustness of the PVAQ polymer against the basic aqueous electrolyte, with no obvious dissolution of the redox polymer. The organic polymer–air battery, constructed with a conventional $MnO_2$/C air cathode, yielded an average discharge output voltage of 0.5 V and an initial specific discharge capacity of 214 $mAh\,g^{-1}$ under a rapid discharge rate of 34 $A\,g^{-1}$ (*i.e.*, 150 C rate). The polymer–air cell displayed good long-term cycling stability, with only 31% capacity lost after 500 cycles. It is noteworthy that the polymer–air cell was working with no additional oxygen supply, essentially relying on the oxygen solubility of the aqueous electrolyte.

Further optimization of the proposed organic polymer–air battery concept was subsequently reported by Nishide and co-workers, this time using a poly(dianthraquinone-substituted norbornene) (PQNB) as the anode material.[51] In 2019, Li *et al.* described a poly(1,4-anthraquinone)/carbon nanotube composite electrode, for application as the anode in an organic polymer–air battery, yielding a battery system with a high energy density of 165 $Wh\,kg^{-1}$ and good capacity retention of 97% after 100 cycles at a current density of 1 $A\,g^{-1}$.[52]

In parallel, Xuan *et al.* presented the first proof-of-concept of an all-organic polymer–air battery, employing poly(3,4-ethylenedioxythiophene):poly(styrenesulphonate) (PEDOT: PSS) and PEDOT:PSS/poly(ethyleneimine)

**Table 8.1** Overview of all-organic polymer batteries based on Li/Na ion carriers.

| Cell Configuration (ionic carriers) | Anode | Cathode | Electrolyte | Output voltage (V) | Cycling stability: retention, cycle numbers, C rate or current density | Specific capacity ($mAh\,g^{-1}$) | Ref. |
|---|---|---|---|---|---|---|---|
| Dual-ion ($Li^+/ClO^{4-}$) |  |  | 0.3 M $LiClO_4$ | — | —, —, — | — | 26 |
| Dual-ion ($Na^+/I^-$) |  |  | PEO-NaI | 2.8–3.5 | —, —, — | — | 27 |
| Dual-ion ($Li^+/ClO^{4-}$) | 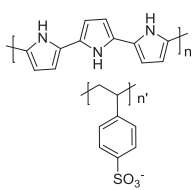 | 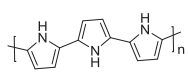 | PAN, $LiClO_4$, EC PC | 0.4 | ~100%, 100 , — | 22 | 28 |
| Dual-ion ($Li^+/PF_6^-$) | 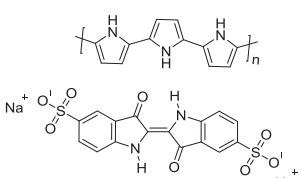 | 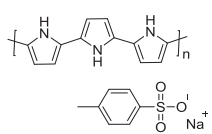 | 1 M $LiPF_6$ in EC : DMC 1 : 1 (v/v) | 1.5 | 92%, 50, 0.05 $mA\,cm^{-2}$ | 36 | 29 |
| Dual-ion ($Li^+/PF_6^-$) | 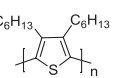 | 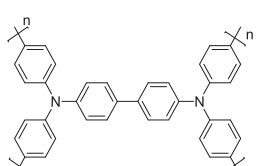 | 1 M $LiPF_6$ in EC : DMC : EMC 1 : 1 : 1 (v/v/v) | 2.35 | —, —, — | 250 (anode-limited) | 30 |

| | | | | | | | |
|---|---|---|---|---|---|---|---|
| Dual-ion ($Na^+/PF_6^-$) | 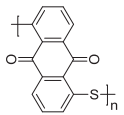 | 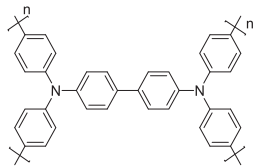 | $NaPF_6$ saturated in DME : DOL 1 : 1 (v/v) | 1.8 | 85%, 500, 8C | 220 | 31 |
| Dual-ion ($Na^+/ClO_4^-$) | 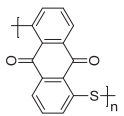 | 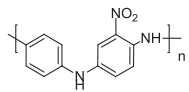 | 5 mol% $NaClO_4$ in succinonitrile | 1.7 | 80%, 50, 50 mA $g^{-1}$ | 200 | 34 |
| Dual-ion ($Na^+/Cl^-$) | 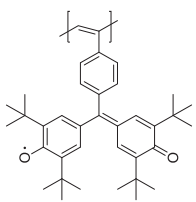 | 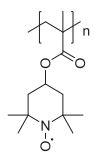 | NaCl 0.1 M and 0.01 M n-$Bu_4NOH$ | ~1.2 | 50%, 40 (anode only) | 27 | 36 |
| Dual-ion ($Li^+/PF_6^-$) | 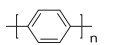 | 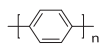 | 1 M $LiPF_6$ in EC : DMC : EMC 1 : 1 : 1 (v/v/v) | 3 | 63%, 60, 40 mA $g^{-1}$ | 153 (anode-limited) | 37 |
| Dual-ion ($Li^+/ClO_4^-$) | 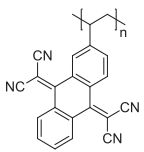 | 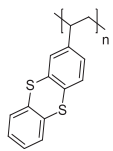 | 1 M LiTFSI in DOL : DME 1 : 1 (v/v) | 1.35 | 67%, 250, 1C | 105 | 38 |
| Li-ion | 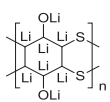 | 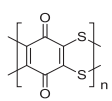 | 1 M LiTFSI in DOL : DME 1 : 1 (v/v) | ~2.0 | 68%, 250, 0.5 A $g^{-1}$ | 174 | 40 |
| Dual-ion ($Li^+/PF6^-$) | 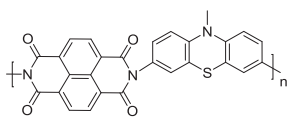 | 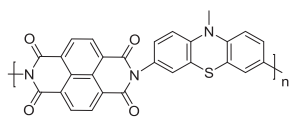 | 1 M $LiPF_6$ EC/DMC | 1.2 | 94, 1000, 800 m A $g^{-1}$ | 77 | 41 |

**Table 8.1** (*Continued*)

| Cell Configuration (ionic carriers) | Anode | Cathode | Electrolyte | Output voltage (V) | Cycling stability: retention, cycle numbers, C rate or current density | Specific capacity ($mAh\,g^{-1}$) | Ref. |
|---|---|---|---|---|---|---|---|
| Na-ion H-ion | 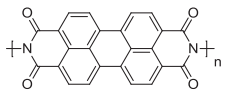 | 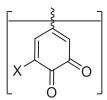 | 1 M $Na_2SO_4$ and 0.1 M HClO4 | 1.0 | 85%, 800, 100C | 53 (10C), 39 (200C) | 42 |
| Dual-ion ($Li^+$/$TFSI^-$) | 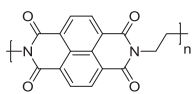 | 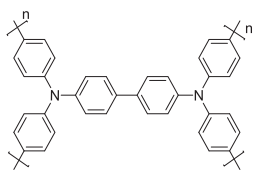 | LiTFSI 21 M (pH 7) | ~0.6 | 85%, 700, 1C | 105 (cathode-limited) | 45 |
| Dual-ion ($Li^+$/$TFSI^-$) | 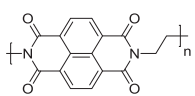 | 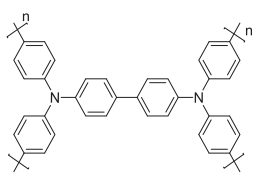 | 2 M LiTFSI in ethyl acetate (55 °C–70 °C) | 1.2 | —, —, — | 69 (anode-limited, −70 °C) | 47 |
| Dual-ion ($Na^+$/$Cl^-$) | 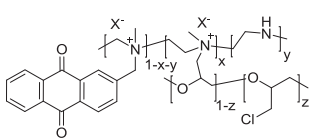 | 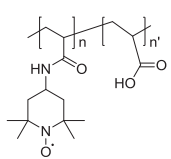 | 3 M NaCl | 1.1 | 68%, 1000, 10C | 80 | 48 |

| | | | | | | | |
|---|---|---|---|---|---|---|---|
| Dual-ion ($Na^+/Cl^-$) | 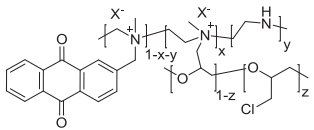 | 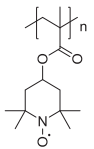 | 3 M NaCl | 1.2 | No loss, 60, 18 C | 95 | 49 |
| Dual-ion ($Na^+/Cl^-$) | 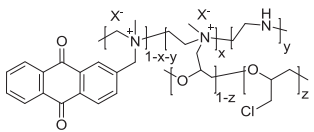 | 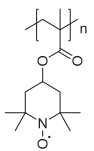 | 3 M NaCl | 1.2 | No loss, 60, 18C | 95 | 49 |
| Dual-ion ($Na^+/Cl^-$) | 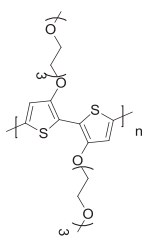 | 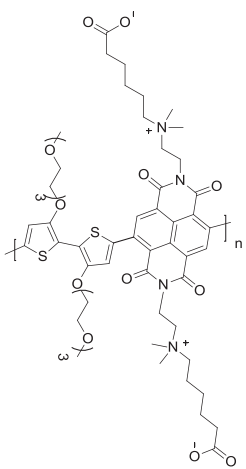 | 0.1 NaCl in $H_2O$ | 1.4 | —, —, — | 21.3 (p-type), 25.9 (n-type) | 58 |

**Table 8.1** (*Continued*)

| Cell Configuration (ionic carriers) | Anode | Cathode | Electrolyte | Output voltage (V) | Cycling stability: retention, cycle numbers, C rate or current density | Specific capacity ($mAh\,g^{-1}$) | Ref. |
|---|---|---|---|---|---|---|---|
| Dual-ion ($Na^+/OH^-$) | 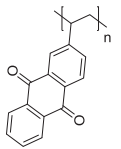 | $MnO_2/CO_2$ | NaOH 30 wt.% | 0.7–0.4 | 69%, 500, 150C | 214 | 50 |
| Dual-ion ($Na^+/OH^-$) | 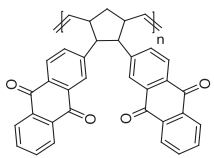 | $O_2$ | 10 M $NaOH_{(aq)}$ | 0.7 | 96%, 300, — | 205 | 51 |
| Dual-ion ($Na^+/OH^-$) | 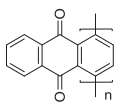 | $O_2$ | 6 M KOH | 0.7 | 95%, 100, 1 $Ag^{-1}$ | 147 | 52 |
| Na-ion | 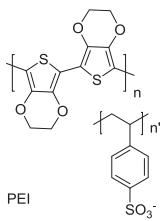  | 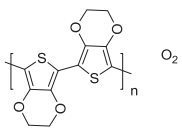 | 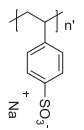 | ~0.3 | —, —, — | — | 53 |
| Na-ion | 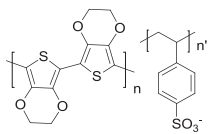 | 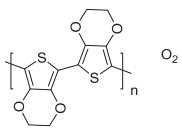 | 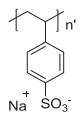 | 0.82–0.85 | —, —, — | — | 57 |

(PEDOT:PSS/PEI) composites, as the cathode and anode materials, respectively.[53] This interesting battery concept relied on the reducing ability of PEI at the anode side to preserve the PEDOT in this neutral state, even in the presence of oxygen. Although no long-term cycling stability data were presented, the all-organic polymer–air battery exhibited a relatively stable discharge plateau at ~0.3 V. Table 8.1 summarizes all-organic polymer battery prototypes based on Li/Na ion carriers reported to date (Table 8.1).

### 8.2.2 All-organic Polymer Batteries based on Metal-free Ion Carriers

In the search for low-cost energy-storage solutions, the transition towards metal-free all-organic batteries has gradually attracted considerable interest through the introduction of the concept of molecular ion batteries. The first example of a metal-free all-organic battery dates back to 1981, when poly(acetylene) films with different oxidation states were used in conjunction with an ammonium-based salt in either tetrahydrofuran (THF) or propylene carbonate (PC) as the electrolyte.[26] Although the long-term cycling stability of these batteries was not investigated in detail, open-circuit cell voltages ranging from 0.5 to 2.5 V were already achieved through the combination of poly(acetylene) films with varying degree of oxidation or reduction.[26] Based on a similar battery concept, a metal-free all-organic polymer battery with poly(thiophene) films as both the anode and cathode was described in 1983.[59] A maximum doping concentration of 24 mol.% was achieved, resulting in a cell with an open-circuit voltage of 3.1 V and a specific energy density of 75 Wh $kg^{-1}$, corresponding to a specific capacity of 24 mAh $g^{-1}$.[59]

More recently, Wang *et al.* presented a flexible textile-based all-organic battery using poly(pyrrole) (pPy) and poly(3′-styryl-4,4″-didecyloxyterthiophene) [poly($OC_{10}$DASTT)] as the cathode and anode, respectively.[54] Poly($OC_{10}$DASTT) films were cast onto Ni/Cu-coated, nonwoven polyester using a simple solvent casting method. For the cathode electrode, poly(pyrrole) was electropolymerized onto a stainless-steel mesh. Although a 1 M $LiPF_6$ solution in ethylene carbonate/dimethyl carbonate was still used as an electrolyte, the lithium was not involved in redox reactions associated with either the pPy cathode or the poly($OC_{10}$DASTT) anode, essentially making an anionic rocking-chair type battery. The flexible textile battery revealed a specific discharge capacity of 39.1 mAh $g^{-1}$, at a current density of 0.02 mA $cm^{-2}$, and an acceptable rate capability, with 53% of the initial specific discharge capacity delivered at a current density of 0.5 mA $cm^{-2}$. The battery displayed a similar cycling stability to that of the previously reported poly(pyrrole) battery systems,[28,60] with no capacity fading observed after 50 cycles at a current density of 0.05 mA $cm^{-2}$.

In 2009, an ultrafast all-polymer paper-based battery was described by Nyström *et al.*, using poly(pyrrole)-reinforced cellulose nanofibres with different oxidation states, as both the anode and cathode, yielded to a symmetric all-organic battery with an open-circuit voltage of 1 V.[61] The chemical oxidation of pyrrole onto the surface of a highly porous cellulose substrate

allowed the fabrication of a pPy-cellulose composite electrode with a high surface area and a nanometre-thick pPy coating, enabling this electrode to operate simultaneously as both a secondary battery and a capacitor. As a result, the symmetric poly(pyrrole) cell demonstrated high rate capability with 70% retention of the initial discharge capacity, even at a current density up to 600 mA $cm^{-2}$.

However, the limiting degree of oxidation achievable in conducting polymers (*i.e.*, 0.3–0.5 charge per unit), due to chemical instability and their characteristic sloping discharge voltage profile, have so far hampered their implementation in battery application.[13,14,62,63]

In 2009, Nishide and co-workers described the first metal-free all-organic battery based on an organic radical polymer, also known as an organic radical battery (ORB),[64] 7 years after Nakahara *et al.* proposed their application in secondary Li-ion–organic batteries as cathode material[65] (see Figure 8.9). In this study, an n-type radical polymer based on poly(galvinoxyl stryrene) was also reported, which delivered a theoretical specific capacity of 51 mAh $g^{-1}$.[64] An organic radical battery was constructed by coupling this n-type radical polymer (*i.e.*, anode) with a poly(norbornene), substituted with two moieties of the well-known p-type nitroxyl radical, 2,2,6,6-tetramethylpiperidinyl-*N*-oxyl (TEMPO), as the cathode. The resulting dual-ion battery exhibited an average output cell voltage of 0.66 V and an interesting power rate capability with an initial specific charge capacity of 32 mAh $g^{-1}$ at a 10 C rate, of which 75% remained after 250 cycles (*i.e.*, based on the weight of redox polymers in both electrodes).[64]

Later, a poleless (symmetric) all-organic battery was reported by the same group, which used a bipolar radical polymer [*i.e.*, poly(nitronylnitroxylstyrene)], as both the anode and cathode.[66] The theoretical specific capacity of the bipolar radical polymer was 103 mAh $g^{-1}$, of which only half of it was accessible due to the symmetric cell configuration. At a 60 C rate, the poleless battery exhibited a good cycle life with an initial specific charge capacity of 44 mAh $g^{-1}$, with only 33% of its initial capacity lost after 250 cycles (*i.e.*, based on the weight of redox polymers in both electrodes). In the same study, the authors also assembled a cationic rocking-chair type battery using this bipolar radical polymer with their previously reported n-type radical polymer based on poly(galvinoxyl styrene), which displayed an average output cell voltage of 0.6 V and retained 91% of its initial specific discharge capacity of 29 mAh $g^{-1}$ after 250 cycles at an impressive 10 C rate (*i.e.*, based on the weight of redox polymers in both electrodes).[66]

In 2010, an all-organic battery based on an aqueous electrolyte was reported, using poly(2,2,6,6-tetramethylpiperidinyloxyl-4-acrylamide) (PTAm) and poly(*N*-4-4′-bipyridinium-*N*-decametylene dibromide) (PV10) as the cathode and anode, respectively.[67] Galvanostatic cycling of a PTAm half-cell revealed excellent long-term cycling stability, with 97% of the initial specific discharge capacity (*i.e.*, 110 mAh $g^{-1}$) retained after 1000 cycles at a 60 C rate. The authors suggested that such a performance was attributed to the good affinity of the PTAm polymer with the aqueous electrolyte (*i.e.*, $BF_4^-$),

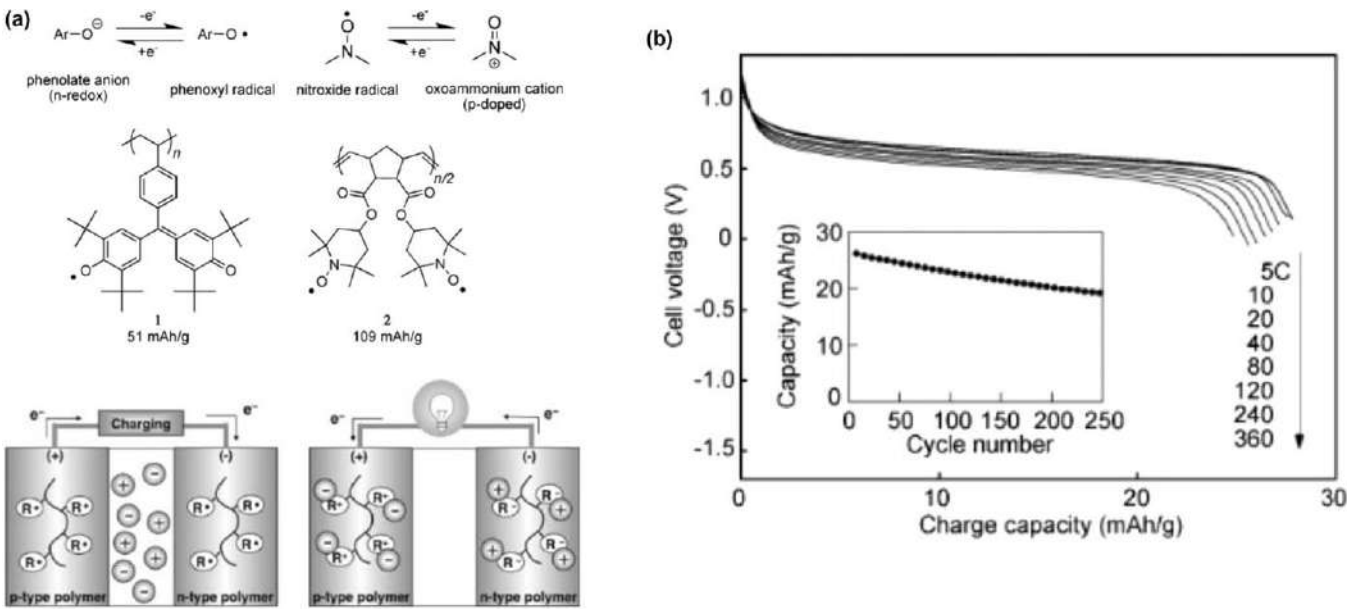


**Figure 8.9** (a) Molecular structure of the poly(galvinoxyl stryrene) (1) and poly(TEMPO-substituted norbornene) (2) and their corresponding redox reactions as well as a schematic illustration of the prototype all-organic battery proposed by Nishide and coworkers. (b) Discharge voltage profiles of the resulting cell as a function of C-rate; inset: long-term galvanostatic cycling of the resulting cell for 250 cycles at a 10 C rate.
Adapted from ref. 64 with permission from John Wiley and Sons, © 2009 Wiley-VCH Verlag GmbH & Co. KGaA, Weinheim.

allowing appropriate swelling of the PTAM polymer while still remaining insoluble. When the PTAM cathode electrode was coupled with the PV10 anode electrode, a specific discharge capacity of 104 mAh $g^{-1}$ was initially obtained. However, a 20% capacity loss was observed after 2000 cycles at a 60 C rate. The authors attributed the difference in cycling performance between the half cell and full cell to the low coulombic efficiency and long-term cycling stability of the PV10 anode.[68]

In 2013, Sen *et al.* developed another viologen-based redox polymer by incorporating viologen moieties either electrostatically or covalently to a poly(pyrrole) polymer backbone (*i.e.*, conducting polymer), for application as anode material[69] (see Figure 8.10). For the electrostatic attachment of viologen, a better incorporation of the viologen during the electropolymerization of the pyrrole monomer was observed for the tetrasulphonated viologen than for the disulphonated analogue (*i.e.* pPy-[VTS] *vs.* pPy-[VDS], respectively). The authors attributed this to the neutral state of the disulphonated viologen upon the formation of a quaternary ammonium during the electropolymerization process.[69] Despite the better attachment of the tetrasulphonated viologen anion onto the poly(pyrrole) polymer backbone, the covalent attachment approach resulted in a more efficient incorporation of the viologen unit (*i.e.*, pPy-$V^{2+}$-Me). Nevertheless, anode electrodes fabricated from both electrostatic and covalent approaches were used to assemble an all-organic battery, where a poly(pyrrole) doped with 2,2′-azino-bis(3-ethylbenzothiazoline-6-sulphonic acid) (pPy[ABTS]) was used as a cathode.[70] The resulting batteries were therefore based on the anionic rocking-chair concept, with $ClO^{4-}$ anions as the ion carriers. The pPy-$V^{2+}$-Me ‖ pPy[ABTS] battery exhibited a better cycling stability with 70% retention of the initial specific discharge capacity after 100 cycles at an applied current density of 0.5 mA $cm^{-2}$, compared to only 38% for the pPy[VTS] ‖ pPy[ABTS] battery.[69] It is noteworthy that the poly(pyrrole) is insulating at the potential where the redox reaction of the viologen occurs, resulting in poor high-rate capability.[69]

In 2013, Nishide and co-workers reported the synthesis of a novel highly cross-linked poly(viologen) hydrogel based on a poly(tripyridiniomesitylene) (PTPM) for application as the anode material for aqueous-based all-organic batteries[71] (see Figure 8.11). The PTPM half-cell displayed high cycling stability with 85% of the initial specific discharge capacity retained after 5000 cycles at a 60 C rate.[71] The superior cycling stability of the PTPM polymer, compared to the previously reported poly(viologen) analogues, was attributed to the highly cross-linked nature of the present system, avoiding elusion or exfoliation of the redox polymer into the electrolyte. Although only one cycle was demonstrated, the PTPM half-cell also showed high rate capability up to a remarkable 1200 C, while still delivering 150 mAh $g^{-1}$ (*i.e.*, 86% of the theoretical capacity). The cycling performance of the PTPM anode was also investigated in an aqueous all-organic battery,[71] by coupling the PTPM anode with the previously reported, poly(2,2,6,6-tetramethylpiperidine-4-yl acrylamide) (PTAm) from the same group. An environmentally benign electrolyte was selected, consisting of an aqueous solution of 0.1 M sodium chloride, in which the chloride ions were used as

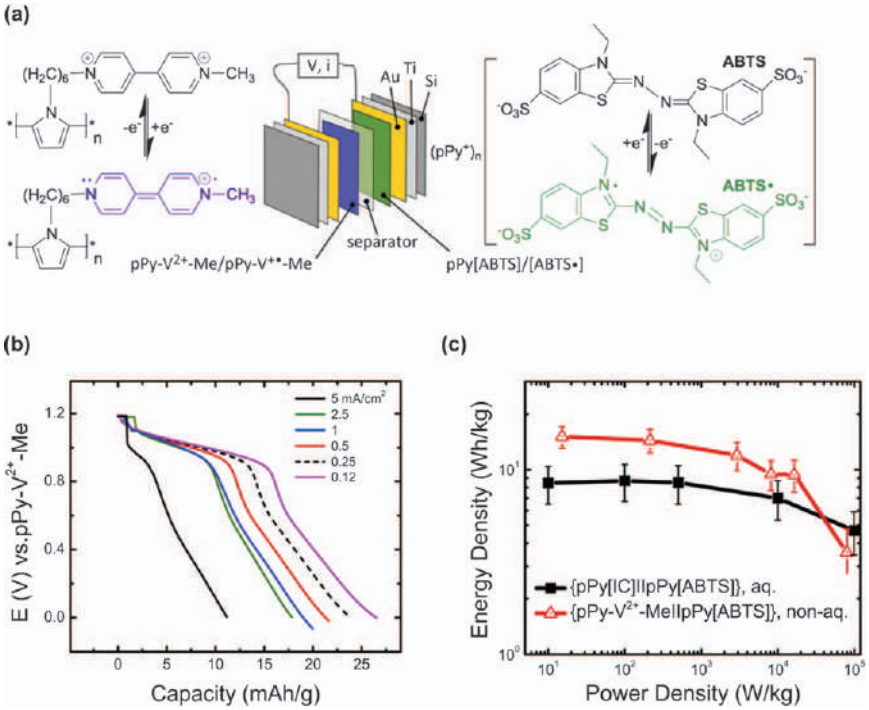


**Figure 8.10** (a) Molecular structures of the poly(pyrrole) based viologen and 2,2′-azino-bis(3-ethylbenzothiazoline-6-sulphonic acid) polymers and their corresponding redox reactions as well as a schematic illustration of the prototype all-organic battery proposed by Sen *et al.* (b) Discharge voltage profiles of the resulting cell at various current densities. (c) Ragone plot illustrating the performance characteristics of the battery system presently developed.
Adapted from ref. 69 with permission from the American Chemical Society, Copyright 2013.

ion carriers for both the anode and cathode. The aqueous all-organic battery also revealed high rate capability and a long cycle life.

Later, Zhang *et al.* proposed an aqueous all-organic battery based on a metal-free aqueous electrolyte,[72] using the previously reported poly(1,4,5,8-naphthalenetetracarboxylic bisimide) (PI-5) and poly(2,2,6,6-tetramethylpiperidin-yloxy-4-yl methacrylate) (PTMA).[65,73] Although the redox activity of PI-5 has been investigated using lithium or sodium chemistries as the ion carriers, it was the first report of an ammonium-based ion carrier. A faster redox kinetic process was found in $(NH_4)_2SO_{4(aq)}$ electrolyte compared with $Li_2SO_{4(aq)}$ or $Na_2SO_{4(aq)}$, resulting in a higher specific discharge capacity at a current density of $1\ A\ g^{-1}$. The authors attributed the enhanced redox performance of the PI-5 polymer in the $(NH_4)_2SO_{4(aq)}$ electrolyte to the smaller size of the hydrated $NH_4^+$ ion, resulting in a higher ionic polarization degree and affinity. Moreover, the higher ionic conductivity of the $(NH_4)_2SO_{4(aq)}$ electrolyte, compared to the

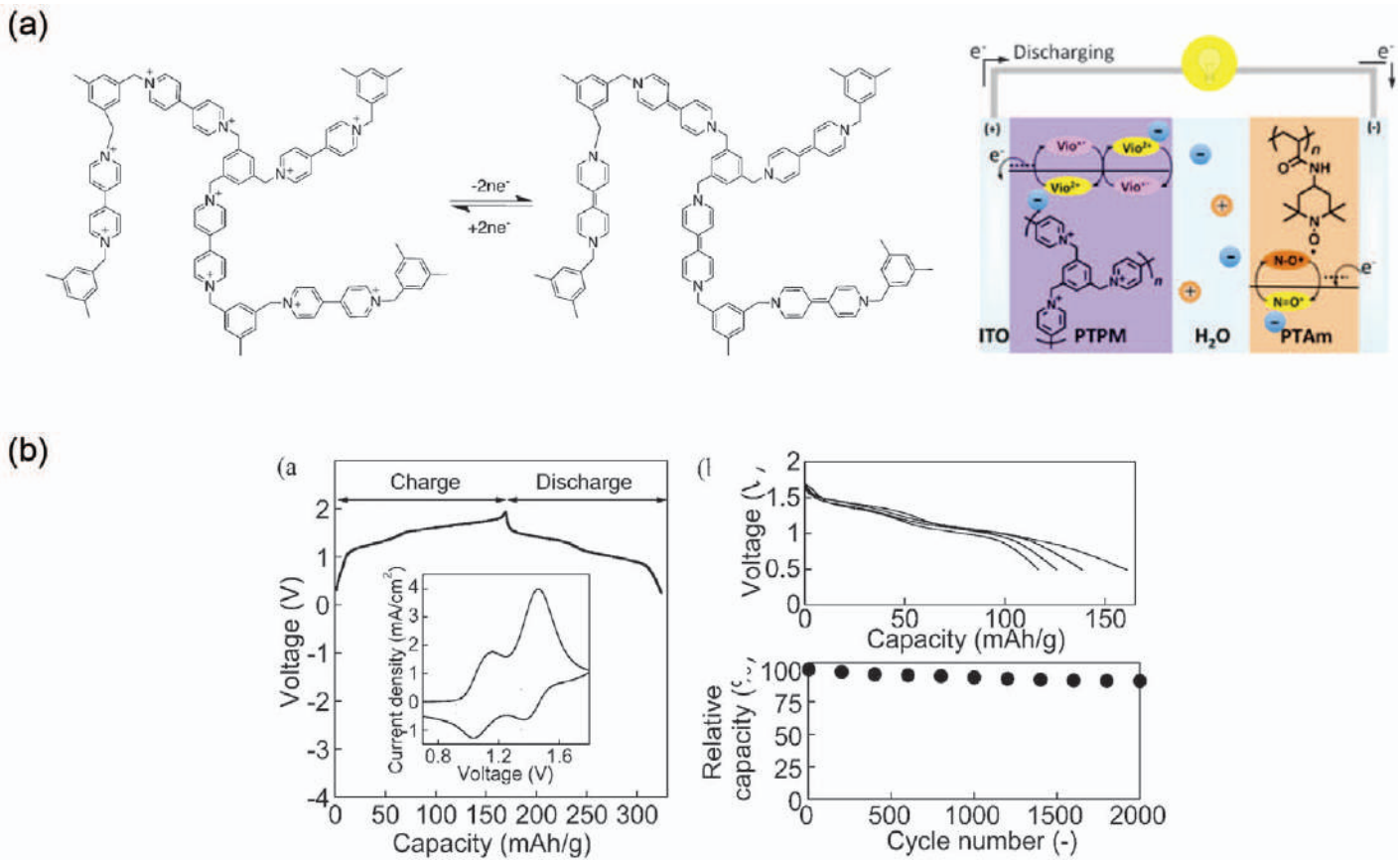


**Figure 8.11** (a) Molecular structure of the poly(tripyridiniomesitylene) (PTPM) as well as a schematic illustration of the prototype all-organic battery proposed by Nishide and co-workers. (b, left) Charging and discharging curves of the PTPM/PTAm cell at a 60 C rate, inset shows a cyclic voltammogram of the PTPM/PTAm cell. (b, top right) Discharging curves of the PTPM/PTAm cell at various C rates (120–1200 C). (b, bottom right) Cycle performance of the PTPM/PTAm cell, with respect to discharging capacity.
Adapted from ref. 71 with permission from the American Chemical Society, Copyright 2013.

$Li_2SO_{4(aq)}$ or $Na_2SO_{4(aq)}$ ones, allowed better power delivery. As a result, a satisfactory rate capability was observed for the PI-5 half-cell, with specific capacities of 157 mAh $g^{-1}$ and 108 mAh $g^{-1}$ delivered at current densities of 0.5 A $g^{-1}$ and 10 A $g^{-1}$, respectively. These results highlight the electrochemical advantage of using molecular ion carriers compared to the alkali metal ion carriers in all-organic batteries. When coupled with the PTMA cathode, the all-organic cell, anode-limited by design, revealed an initial specific discharge capacity of 136 mAh $g^{-1}$ at a current density of 0.5 A $g^{-1}$, of which 72% remained when the current density was increased to 10 A $g^{-1}$, confirming the good rate capability of this device. A maximum energy and power densities of 51 Wh $kg^{-1}$ and 15.8 kW $kg^{-1}$ were demonstrated. The aqueous all-organic battery also exhibited outstanding long-term cycling stability with a capacity retention of 86% after 10 000 cycles at the relatively high current density of 5 A $g^{-1}$.

In 2018, Nishide and co-workers reported a new organic redox polymer based on poly(vinyldibenzothiophenesulphone) for application as the anode electrode in all-organic batteries[74] (see Figure 8.12). This new redox polymer exhibited a two-electron reduction in a single-step reaction at a potential of –1.8 V (*vs.* Ag/AgCl), which opened the design of all-organic batteries with high output voltage. The half-cell of the poly(vinyldibenzothiophenesulphone) displayed a good cycling stability with over 95% capacity retention of its initial specific discharge capacity of 211 mAh $g^{-1}$ after 100 cycles. An all-organic battery was also fabricated using the poly(vinyldibenzothiophenesulphone) and a poly(TEMPO substituted methacrylate) as the anode and cathode, respectively. The full cell exhibited an output of 2.6 V, resulting in a high energy density of 541 mWh $g^{-1}$ with respect to the mass of poly(vinyldibenzothiophenesulphone) in the anode electrode.[74] This example illustrates the potential of designing all-organic batteries with high energy density, through careful selection of the redox potentials of the redox polymers used as the anode and cathode. However,

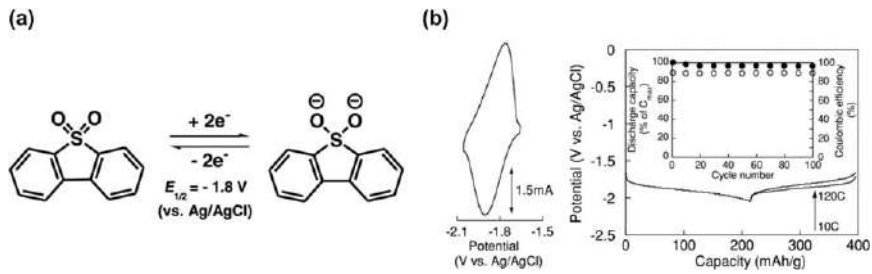


**Figure 8.12** (a) Molecular structure of the poly(vinyldibenzothiophenesulphone) and its corresponding redox reactions. (b, left) Cyclic voltammogram of the poly(vinyldibenzothiophenesulphone) electrode and (b, right) its corresponding charge–discharge curves at various C rates. Inset: Specific discharge capacities and coulombic efficiency as a function of cycle number, demonstrating the cycling stability of the poly(vinyldibenzothiophenesulphone) electrode.
Adapted from ref. 74 with permission from John Wiley and Sons, © 2018 Wiley-VCH Verlag GmbH & Co. KGaA, Weinheim.

new redox polymers with ultralow and high redox potentials (*i.e.*, 0 V and 4.5 V *vs.* $Li/Li^+$) are still required to surpass the high-voltage output of the current Li-ion battery technology (*i.e.*, 4–5 V), based on transition metal oxide cathodes.

One of the main advantages often mentioned for organic redox polymer-based electrodes compared to inorganic-based electrodes is their processability, allowing the use of cheap manufacturing techniques such as roll-to-roll or printing processes.[1] With this in mind, Schubert and co-workers reported a printable ionic liquid-based electrolyte for application in all-organic batteries.[75] The UV-curable gel electrolyte consisted of methacrylate-based monomers [*i.e.*, benzyl methacrylate and poly(ethylene glycol) methyl ether methacrylate], a cross-linker, a functional nanofiller and an ionic liquid. After optimization of the electrolyte system in terms of printability (*i.e.*, composition, oxygen-free printing condition, *etc.*), the printable solid-state electrolyte was tested in an all-organic battery composed of a poly(2,2,6,6-tetramethyl-4-piperidinyl-*N*-oxyl methacrylate) (PTMA) and a poly(2-vinyl-11,11,12,12-tetracyano-9,10-anthraquinonedimethane) [poly(TCAQ)] as the cathode and anode, respectively. It is noteworthy that both the anode and cathode still required prewetting by a liquid electrolyte (*i.e.*, pristine ionic liquid) to allow swelling of the electrode and good penetration of the electrolyte. However, a limited specific discharge capacity was still observed for the all-solid-state all-organic battery, due to the limited affinity of the ionic liquid with the organic redox polymer. Nevertheless, the all-solid-state all-organic battery revealed excellent long-term cycling performance with 77% retention of its initial specific discharge capacity of 24 mAh $g^{-1}$ after 1000 cycles at a 1 C rate.[75] In 2019, Qin *et al.* described the fabrication of a metal-free, solvent-free all-organic battery based on an ionic liquid as the electrolyte, in pursuit of a safer and more environmentally friendly battery.[76] The authors investigated the potential of this electrolyte in an all-organic battery, composed of poly(1,4,5,8-naphthalenetetracarboxylic bisimide) (PI-5) and poly(triphenylamine) (PTPAn), as the anode and cathode, respectively. These organic redox polymers were previously reported for application in a Li–organic battery.[32,73] In addition to the environmental friendliness and safety aspects, the ionic liquid electrolyte allowed a higher rate capability, up to a 200 C rate, when compared to a traditional lithium-based electrolyte (*i.e.*, 1 M LiTFSI in ethylene carbonate/diethyl carbonate). The all-organic battery based on the ionic liquid electrolyte exhibited outstanding long-term cycling stability with 75% capacity retention after 5000 cycles at a 20 C rate. The cycling performance of this battery was also investigated at lower temperature (*i.e.*, −10 °C), and showed enhanced cycling stability compared to that at room temperature, due to a reduction in the number of side reactions occurring, which improved the coulombic efficiency. Later, the authors also reported an enhancement of the working operation towards even lower temperatures (*i.e.*, −80 °C) by developing an optimized ternary electrolyte system, composed of an ionic liquid, acetonitrile and methyl acetate. Table 8.2 summarizes all-organic polymer battery prototypes based on metal-free ion carriers reported to date (Table 8.2).[77]

**Table 8.2** Overview of all-organic polymer batteries based on metal-free ion carriers.

| Cell Configuration (ionic carriers) | Anode | Cathode | Electrolyte | Output voltage (V) | Cycling stability: retention, cycle numbers, rate or current density | Specific capacity ($mAh\,g^{-1}$) | Ref. |
|---|---|---|---|---|---|---|---|
| Dual-ion ($ClO_4^-$/ n-$Bu_4N^+$; $BF_4^-$/n-$BF_4N^+$) |  |  | 0.5 M n-BuN$ClO_4$ in PC; 0.3 M n-$Bu_4NBF_4$ in THF | | —, —, — | — | 26 |
| $PF_6$-ion | 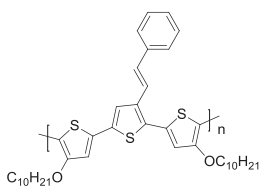 | 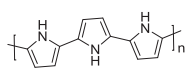 | 1.0 M $LiPF_6$ in 1 : 1 (v/v) EC : DMC | ~0.8 | 100%, 50, 0.05 $mA\,cm^{-2}$ | 39 | 54 |
| Dual-ion ($TBA^+$/ $BF_4^-$) | 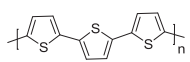 | 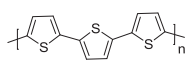 | 0.2 M $TBABF_4$ in ACN | 3.01 | —, —, — | 24 | 59 |
| Cl-ion | 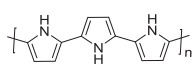 | 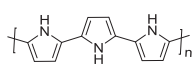 | 2.0 M NaCl | 1 | 94%, 100, 600 $mA\,cm^{-2}$ | 33 | 61 |
| | Reinforced cellulose nanofibers | Reinforced cellulose nanofibers | | | | | |
| Dual-ion (n-$Bu_4N^+$/ $ClO_4^-$) | 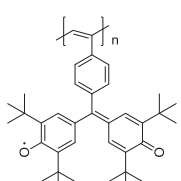 | 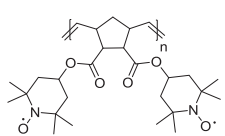 | 0.5 M n-$Bu_4N$ $ClO_4$ + 0.01 M n-$Bu_4NOH$ in ACN | 0.66 | 74%, 250, 10C | 32 | 64 |

**Table 8.2** (*Continued*)

| Cell Configuration (ionic carriers) | Anode | Cathode | Electrolyte | Output voltage (V) | Cycling stability: retention, cycle numbers, rate or current density | Specific capacity ($mAh\,g^{-1}$) | Ref. |
|---|---|---|---|---|---|---|---|
| Dual-ion ($n\text{-}Bu_4N^+$/ $ClO_4^-$) | 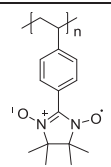 | 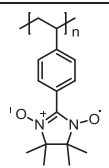 | 0.1 M $n\text{-}Bu_4N$ $ClO_4$ + 0.01 M $n\text{-}Bu_4NOH$ in ACN | 1.33 | 66%, 250, 60C | 44* | 66 |
| $Bu_4N$-ion | 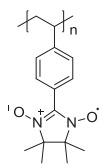 | 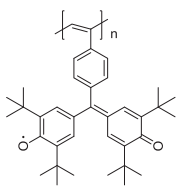 | 0.1 M $n\text{-}Bu_4N$ $ClO_4$ + 0.01 M $n\text{-}Bu_4NOH$ in ACN | 0.6 | 91%, 250, 150C | 29* | 66 |
| $BF_4$-ion | 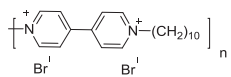 | 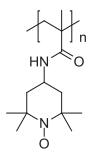 | 0.1 M $NaBF_4$ | 1.2 | 80%, 2000, 60C | 110 (anode-limited) | 67 |
| $ClO_4$-ion | 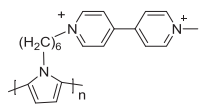 | 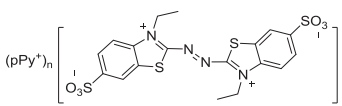 | 0.2 M $LiClO_4$ in $CH_3CN$ | 1 | 70%, 100, 0.5 $mA\,cm^{-2}$ | 16 | 69 |

| | | | | | | |
|---|---|---|---|---|---|---|
| Cl-ion | 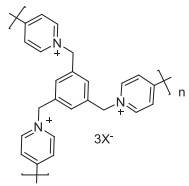 | 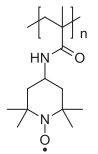 | 0.1 M NaCl | 1.1–1.5 | 80%, 2000, 60C | 110 | 71 |
| Dual-ion ($NH_4^+$/$SO_4^-$) | 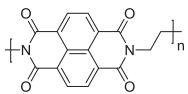 | 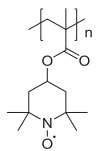 | 1 M $(NH_4)_2SO_4$ | 1.9 | 86%, 10000, 5 $Ag^{-1}$ | 136 | 72 |
| Dual-ion ($Et_4N^+$/($ClO_4^-$) | 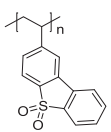 | 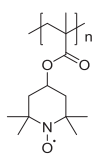 | 1 M $Et_4NClO_4$ in ACN | 2.6 | 95%, 100, 120C | 208 (anode, half-cell) | 74 |
| Dual-ion ($BMIm^+$/ $TFSI^-$) | 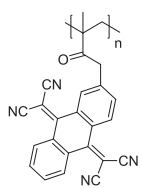 | 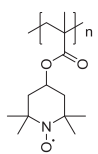 | Vol IL:vol M 2 : 1, CQ-initiated, 10 mol% TEGDMA, 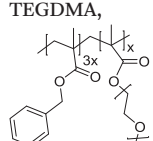 | 1.1 | 77, 1000, 1C | 24 | 75 |

**Table 8.2** (*Continued*)

| Cell Configuration (ionic carriers) | Anode | Cathode | Electrolyte | Output voltage (V) | Cycling stability: retention, cycle numbers, rate or current density | Specific capacity ($mAh\,g^{-1}$) | Ref. |
|---|---|---|---|---|---|---|---|
| Dual-ion ($EMIm^+$/ $TFSI^-$) | 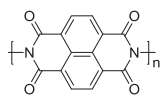 | 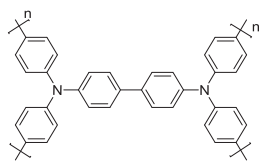 | EMImTFSI | 1.5 | 75%, 5000, 20C | 93 | 76 |
| Dual-ion ($EMIm^+$/ $TFSI^-$) | 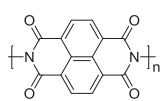 | 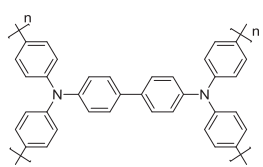 | 1 M EMImTFSI in MA/ACN (1/2, v/v) | 1.3 | 86%, 2000, 5C | 108 | 77 |
| $ClO_4$-ion | 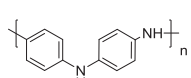 | 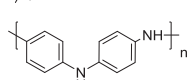 | 0.1 M TEAP in PC | 0.4 | 60%, —, 1C | — | 78 |

*Specific capacity based on the total weight of active polymer in both anode and cathode electrodes

### 8.2.3 All-organic Polymer Batteries based on Proton Ion Carriers

The first prototype of an all-organic proton battery was reported by Surville *et al.* in 1968.[79] A poleless battery was assembled using poly(aniline) pellets with different oxidation states for the electrodes and a sulphuric acid-based electrolyte, delivering a specific capacity of 13 mAh $g^{-1}$.[79] More recently, poly(indole) and poly(aniline) were employed as the anode and cathode material, respectively, in an all-organic proton battery using an $H_2SO_{4(aq)}$ electrolyte (*i.e.*, 40%), which produced a rather flat discharge voltage plateau of ~1.1 V.[80,81] An impressive specific discharge capacity, with respect to a conducting polymer, of 79 mAh $g^{-1}$ was achieved, at a current density of 1 mA $cm^{-2}$, corresponding to 94% of the theoretical capacity of poly(5-nitroindole). The cell could be charged with a current density up to 100 mA $cm^{-2}$, and still retained 82% of the initial capacity, highlighting the high rate capability of the poly(indole)/poly(aniline) battery system. Additionally, the proton battery exhibited an outstanding long-term stability with 80% of its initial discharge capacity after 32 000 cycles at a current density of 1 mA $cm^{-2}$.

In 2016, Sjödin and co-workers presented a new design strategy for the development of redox polymers, where redox-active pendant groups were covalently attached to a conducting polymer backbone; commonly named conducting redox polymers (CRPs) and potentially eliminating the need for conductive additives for organic-based electrode fabrication.[82] An important design criterion for CRPs is the potential matching between the redox reaction of the redox-active moiety and the n-doping region of the conducting polymer, to ensure facile electron transport through the CRP electrode. In this study, hydroquinone and dimethoxy-substituted quinone pendant groups attached onto a poly(pyrrole) polymer backbone were employed as the cathode and anode, respectively, and a proof-of-concept proton battery based on CPRs was constructed using an acidic aqueous electrolyte. The CPR-based battery displayed a low output voltage of 0.15 V, due to the limited potential difference between the two quinone derivatives used in this case. A year later, two new CRPs based on anthraquinone and benzoquinone pendant groups attached to a 3,4-ethylenedioxythiophene polymer backbone (PEDOT-AQ and PEDOT-BQ) were developed by the same group, and employed in an all-organic proton battery using a mixture of pyridine-based proton donors and acceptors as the electrolyte[83] (see Figure 8.13). All-organic batteries were assembled in both anode- and cathode-limited design, in order to assess the electrochemical stability of both PEDOT-AQ and PEDOT-BQ electrodes, yielding a sloping discharge plateau of 0.5 V. In the anode-limited design (*i.e.*, PEDOT-AQ), a specific discharge capacity of 103 mAh $g^{-1}$ (*i.e.*, 78% of its theoretical capacity) was reached at a C/2 rate, of which 87% and 25% remained when increasing the C-rate to 3 C and 160 C, respectively. However, a low coulombic efficiency (*i.e.*, 70%) was observed at low C-rates (*i.e.*, $\leq$15 C) due to an irreversible competing redox process associated with hydrogen evolution.

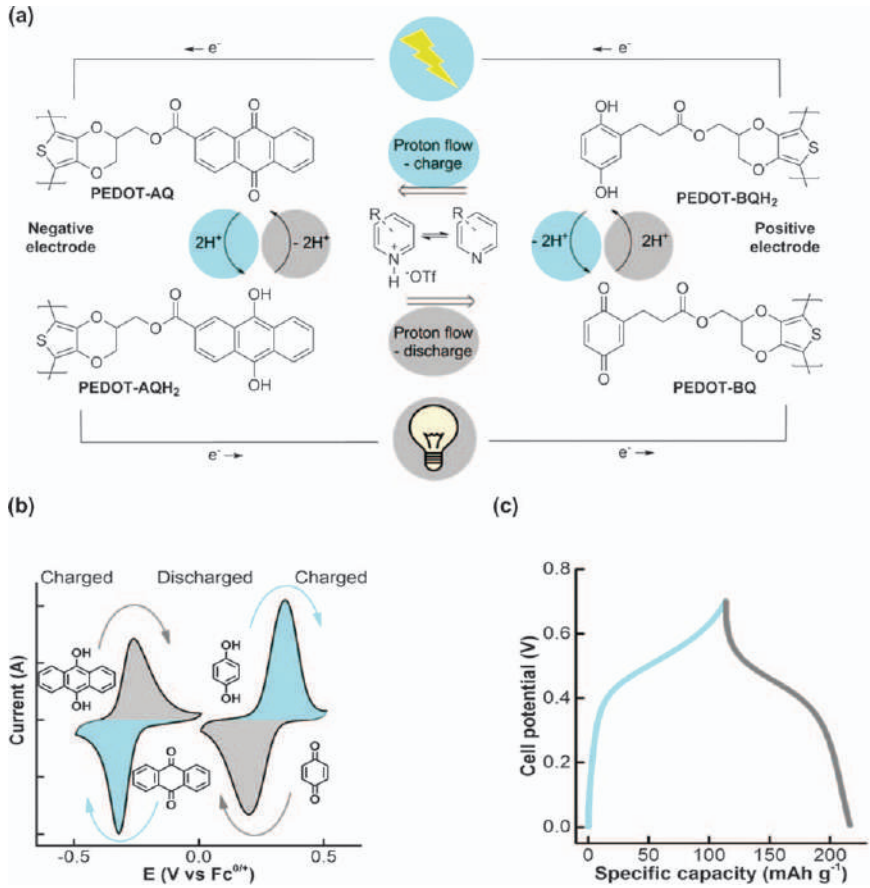


**Figure 8.13** (a) Molecular structure of the two conducting redox polymers based on anthraquinone and benzoquinone pendant groups and their corresponding redox reactions with respect to the operating conditions of the all-organic battery proposed by Sjödin and co-workers, (b) cycling voltammograms of the two conducting redox polymers as well as (c) charge and discharge voltage profiles of the resulting cell.
Adapted from ref. 83 with permission from the American Chemical Society, Copyright 2017.

Moderate long-term cycling stability was achieved, with 98% capacity retention after 100 cycles at a 3 C rate, although rapid capacity fading was observed in the 50 subsequent cycles (*i.e.*, 79% capacity retention). The capacity fading was attributed to the cycling stability of the PEDOT-BQ electrode, as highlighted in the long-term cycling of the cathode-limited design cell. Later, Karlsson *et al.* also reported the development of a novel protic electrolyte based on nonstoichiometric protic ionic liquids for application in all-organic proton batteries based on CRP electrodes.[84]

Recently, Sjödin and co-workers developed a CRP electrode, based on a so-called ''proton-trap technology'', where a copolymer composed of hydroquinone and pyridine monomers was used[85,86] (see Figure 8.14). The pyridine proton/acceptor functionality allowed the quinone redox chemistry to be decoupled from the ion carrier chemistry of the electrolyte, and therefore of the redox counter electrode chemistry. Consequently, such proton-based organic electrodes enabled their use in lithium/sodium metal batteries using traditional organic electrolyte or even ionic liquid-based electrolyte. Such results expand the range of battery applications where proton-based organic electrodes could be used, thus increasing their practical relevance. Table 8.3 summarizes all-organic polymer battery prototypes based on proton ion carriers reported to date (Table 8.3).

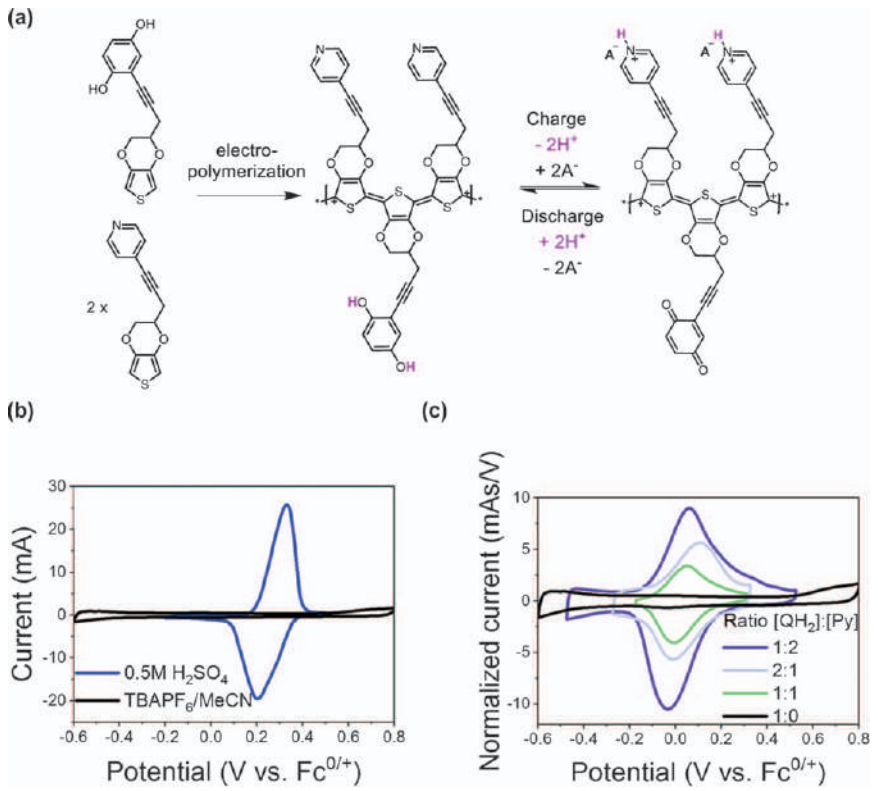


**Figure 8.14** (a) Molecular structure of the conducting redox polymer, based on the proton trap concept proposed by Sjödin and co-workers, cyclic voltammograms of the hydroquinone-based conducting polymer, without (b) or with (c) proton trap function (*i.e.*, pyridine).
Adapted from ref. 86 with permission from the American Chemical Society, Copyright 2019.

**Table 8.3** Overview of all-organic polymer batteries based on proton ion carriers.

| Cell Configuration (ionic carriers) | Anode | Cathode | Electrolyte | Output voltage (V) | Cycling stability: retention, cycle numbers, rate or current density | Specific capacity ($mAh\,g^{-1}$) | Ref. |
|---|---|---|---|---|---|---|---|
| $H^+$ | 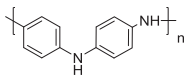 | 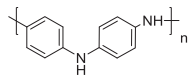 | $H_2SO_4$ | — | —, —, — | 13 | 79 |
| $H^+$ | 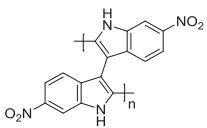 | 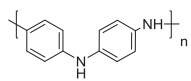 | $H_2SO_4$ 40 % | 1.1 | 80%, 32000, 1 $mA\,cm^{-2}$ | 79 | 80 |
| $H^+$ | 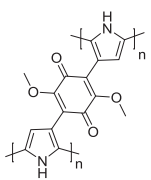 | 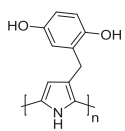 | 1.0 M $NaNO_3$ (pH 2.20) | 0.15 | —, —, — | — | 82 |
| $H^+$ | 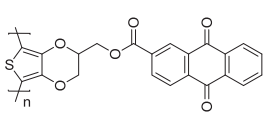 | 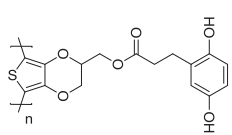 | 2-fluoropyridinium triflate/2-fluoropyridine | 0.5 | 79%, 150, 3C | 103 | 83 |
| $H^+$ | 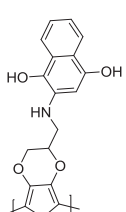 | 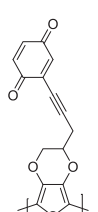 | MeTriHTFSI ($x = 30\%$) | 0.45 | 60%, 100, 140C | 100 | 84 |

## 8.3 Conclusions and Perspectives

During the last few decades, tremendous efforts were made towards the development of organic redox polymers for application in various energy-storage systems, including alkali metal–organic batteries, alkali ion–organic batteries and all-organic batteries.[1,19,22,63] Despite the substantial number of publications on organic redox polymers, limited examples were industrially implemented.[12,87–89] In recent years, all-organic batteries have regained interest within the battery research community, due to the inherent features of organic redox polymers such as processability, flexibility, high rate performance and the perspective to prepare them from renewable resources. The recent emergence of the Internet of Things, smart packaging and clothing as well as mobile devices, has increased the need for low-cost, lightweight and flexible energy-storage systems, making the development of all-organic batteries a highly relevant topic. Additionally, the low cost of aqueous-based all-organic batteries makes them an attractive candidate for stationary energy-storage applications. This chapter provides a comprehensive review of the current state of the art of all-organic batteries, focusing on all battery prototypes reported to date and the nature of the ion carriers involved in their redox reactions. As such, highlighting the gradual research direction transition observed during the development of the all-organic battery technology, going from alkali metal-based ion carrier battery system, similar to the lithium-ion battery, to molecular ion-based and finally proton-based ion carrier battery system. Most successful all-organic battery systems reported to date are based on organic redox polymers containing either quinones, aromatic dimides or stable organic radical moieties. Although such systems exhibited promising electrochemical performance, there is still a need for novel organic redox polymers with higher storage capacity, high rate performance and longer cycle life. The development of organic redox polymers is still at an early stage and many polymer molecular designs are yet to be explored, before exhausting the full range of functional groups and combinations available by organic chemistry.

In parallel, optimization of the fabrication of organic-based electrodes also will be of crucial importance to unlock the industrial implementation of all-organic batteries. Indeed, an organic-based electrode still suffers from low areal capacity, when compared to an inorganic-based electrode (*e.g.*, a Li-ion battery), due to the large amount of conductive additive required to ensure good electronic conductivity within the electrode material. Promising electrode design approaches, where continuous interconnected network of SWNTs or highly porous microfibrillated cellulose (MFC) were employed as substrates, have been already reported, resulting in lower content of conductive additive (5–30 wt.%) and electrodes with practical areal capacity (*i.e.*, 1–3 $mAh\,cm^{-2}$) were made. Alternatively, the covalent attachment of a redox moiety onto a conducting polymer backbone was also reported, making the use of conductive additive redundant.

Finally, the development of high-performance electrolytes, specifically designed for an all-organic battery, is another essential research aspect of this emerging technology, since the cycling performance of an all-organic battery can be greatly affected by the nature of the electrolyte system. Indeed, an inherent challenge in the design of an all-organic battery is finding a sustainable electrolyte for both organic redox polymers, to ensure high rate performance and long battery cycle life. Additionally, the design of application-specific electrolytes such as ultralow battery operation temperature and aqueous electrolyte (*i.e.*, enhancement of the electrochemical stability window), is also highly relevant.

The optimization of the three aforementioned research aspects, along with the development of cheap manufacturing techniques like printing or roll-to-roll processing, will enable all-organic batteries to become a commercial reality.

## References

1. S. Muench, A. Wild, C. Friebe, B. Häupler, T. Janoschka and U. S. Schubert, *Chem. Rev.*, 2016, **116**, 9438–9484.
2. H. Alt, H. Binder, A. Köhling and G. Sandstede, *Electrochim. Acta*, 1972, **17**, 873–887.
3. D. L. Williams, J. J. Byrne and J. S. Driscoll, *J. Electrochem. Soc.*, 1969, **116**, 2.
4. V. V. Walatka, M. M. Labes and J. H. Perlstein, *Phys. Rev. Lett.*, 1973, **31**, 1139–1142.
5. metode penelitian Nursalam, *Phys. Rev. Lett.*, 2016, **1975**(34), 577–579.
6. H. Shirakawa, E. J. Louis, A. G. MacDiarmid, C. K. Chiang and A. J. Heeger, *J. Chem. Soc., Chem. Commun.*, 1977, 578–580.
7. C. K. Chiang, Y. W. Park, A. J. Heeger, H. Shirakawa, E. J. Louis and A. G. MacDiarmid, *J. Chem. Phys.*, 1978, **69**, 5098–5104.
8. M. Audenaert, G. Gusman and R. Deltour, *Phys. Rev. B*, 1981, **24**, 7380–7382.
9. J. L. Bredas and G. B. Street, *Acc. Chem. Res.*, 1985, **18**, 309–315.
10. F. Goto, K. Abe, K. Ikabayashi, T. Yoshida and H. Morimoto, *J. Power Sources*, 1987, **20**, 243–248.
11. T. Matsunaga, H. Daifuku and T. Kawagoe, *Nippon Kagaku Kaishi*, 1990, **1990**, 1–11.
12. J. S. Miller, *Adv. Mater.*, 1993, **5**, 587–589.
13. B. Krische and M. Zagorska, *Synth. Met.*, 1989, **28**, 257–262.
14. J. Heinze, B. A. Frontana-Uribe and S. Ludwigs, *Chem. Rev.*, 2010, **110**, 4724–4771.
15. A. Yoshino, *Angew. Chem., Int. Ed.*, 2012, **51**, 5798–5800.
16. H. Zhang, C. Li, G. G. Eshetu, S. Laruelle, S. Grugeon, K. Zaghib, C. Julien, A. Mauger, D. Guyomard, T. Rojo, N. Gisbert-Trejo, S. Passerini, X. Huang, Z. Zhou, P. Johansson and M. Forsyth, *Angew. Chem., Int. Ed.*, 2020, **59**, 534–538.

17. N. Casado, G. Hernández, H. Sardon and D. Mecerreyes, *Prog. Polym. Sci.*, 2016, **52**, 107–135.
18. P. Novák, K. Müller, K. S. V. Santhanam and O. Haas, *Chem. Rev.*, 1997, **97**, 207–281.
19. B. Häupler, A. Wild and U. S. Schubert, *Adv. Energy Mater.*, 2015, **5**, 1402034.
20. Q. Zhao, C. Guo, Y. Lu, L. Liu, J. Liang and J. Chen, *Ind. Eng. Chem. Res.*, 2016, **55**, 5795–5804.
21. Z. Song and H. Zhou, *Energy Environ. Sci.*, 2013, **6**, 2280–2301.
22. P. Poizot, F. Dolhem and J. Gaubicher, *Curr. Opin. Electrochem.*, 2018, **9**, 70–80.
23. K. W. Beard, *Linden's Handbook of Batteries, Fifth Edition*, 5th edn, McGraw-Hill Education, New York, 2019.
24. B. Scrosat, *J. Electrochem. Soc.*, 1992, **139**, 2776–2781.
25. K. Oyaizu and H. Nishide, *Encycl. Radicals Chem. Biol. Mater*, 2012, 1–8.
26. D. J. MacInnes, M. A. Druy, P. J. Nigrey, D. P. Nairns, A. G. MAcDianrmid and A. J. Heeger, *J. Chem. Soc., Chem. Commun.*, 1981, 317–319.
27. C. K. Chiang, *Polymer.*, 1981, **22**, 1454–1456.
28. J. G. Killian, B. M. Coffey, F. Gao, T. O. Poehler and P. C. Searson, *J. Electrochem. Soc.*, 1996, **143**, 936.
29. I. Sultana, M. M. Rahman, J. Wang, C. Wang, G. G. Wallace and H. K. Liu, *Electrochim. Acta*, 2012, **83**, 209–215.
30. L. M. Zhu, W. Shi, R. R. Zhao, Y. L. Cao, X. P. Ai, A. W. Lei and H. X. Yang, *J. Electroanal. Chem.*, 2013, **688**, 118–122.
31. W. Deng, X. Liang, X. Wu, J. Qian, Y. Cao, X. Ai, J. Feng and H. Yang, *Sci. Rep.*, 2013, **3**, 2671.
32. J. K. Feng, Y. L. Cao, X. P. Ai and H. X. Yang, *J. Power Sources*, 2008, **177**, 199–204.
33. Z. Song, H. Zhan and Y. Zhou, *Chem. Commun.*, 2009, 448–450.
34. X. Zhu, R. Zhao, W. Deng, X. Ai, H. Yang and Y. Cao, *Electrochim. Acta*, 2015, **178**, 55–59.
35. R. Zhao, L. Zhu, Y. Cao, X. Ai and H. X. Yang, *Electrochem. Commun.*, 2012, **21**, 36–38.
36. T. Jähnert, B. Häupler, T. Janoschka, M. D. Hager and U. S. Schubert, *Macromol. Chem. Phys.*, 2013, **214**, 2616–2623.
37. L. M. Zhu, A. W. Lei, Y. L. Cao, X. P. Ai and H. X. Yang, *Chem. Commun.*, 2013, **49**, 567–569.
38. A. Wild, M. Strumpf, B. Häupler, M. D. Hager and U. S. Schubert, *Adv. Energy Mater.*, 2017, **7**, 1601415.
39. M. E. Speer, M. Kolek, J. J. Jassoy, J. Heine, M. Winter, P. M. Bieker and B. Esser, *Chem. Commun.*, 2015, **51**, 15261–15264.
40. J. Xie, Z. Wang, Z. J. Xu and Q. Zhang, *Adv. Energy Mater.*, 2018, **8**, 1703509.
41. N. Casado, D. Mantione, D. Shanmukaraj and D. Mecerreyes, *ChemSusChem*, 2019, cssc.201902856.

42. G. Hernández, N. Casado, A. M. Zamarayeva, J. K. Duey, M. Armand, A. C. Arias and D. Mecerreyes, *ACS Appl. Energy Mater.*, 2018, **1**, 7199–7205.
43. F. N. Ajjan, N. Casado, T. Rębiś, A. Elfwing, N. Solin, D. Mecerreyes and O. Inganäs, *J. Mater. Chem. A*, 2016, **4**, 1838–1847.
44. N. Casado, M. Hilder, C. Pozo-Gonzalo, M. Forsyth and D. Mecerreyes, *ChemSusChem*, 2017, **10**, 1783–1791.
45. X. Dong, H. Yu, Y. Ma, J. L. Bao, D. G. Truhlar, Y. Wang and Y. Xia, *Chem. – Eur. J.*, 2017, **23**, 2560–2565.
46. L. Suo, O. Borodin, T. Gao, M. Olguin, J. Ho, X. Fan, C. Luo, C. Wang and K. Xu, *Science*, 2015, **350**, 938–943.
47. X. Dong, Z. Guo, Z. Guo, Y. Wang and Y. Xia, *Joule*, 2018, **2**, 902–913.
48. K. Hatakeyama-Sato, H. Wakamatsu, R. Katagiri, K. Oyaizu and H. Nishide, *Adv. Mater.*, 2018, **30**, 1800900.
49. K. Hatakeyama-Sato, H. Wakamatsu, K. Yamagishi, T. Fujie, S. Takeoka, K. Oyaizu and H. Nishide, *Small*, 2019, **15**, 1805296.
50. W. Choi, D. Harada, K. Oyaizu and H. Nishide, *J. Am. Chem. Soc.*, 2011, **133**, 19839–19843.
51. T. Kawai, K. Oyaizu and H. Nishide, *Macromolecules*, 2015, **48**, 2429–2434.
52. Y. Li, L. Liu, C. Liu, Y. Lu, R. Shi, F. Li and J. Chen, *Chem*, 2019, **5**, 2159–2170.
53. Y. Xuan, M. Sandberg, M. Berggren and X. Crispin, *Org. Electron.*, 2012, **13**, 632–637.
54. C. Y. Wang, A. M. Ballantyne, S. B. Hall, C. O. Too, D. L. Officer and G. G. Wallace, *J. Power Sources*, 2006, **156**, 610–614.
55. C. Y. Wang, G. Tsekouras, P. Wagner, S. Gambhir, C. O. Too, D. Officer and G. G. Wallace, *Synth. Met.*, 2010, **160**, 76–82.
56. W. Choi, D. Harada, K. Oyaizu and H. Nishide, *J. Am. Chem. Soc.*, 2011, **133**, 19839–19843.
57. M. Reyes-Reyes and R. López-Sandoval, *Org. Electron.*, 2018, **52**, 364–370.
58. D. Moia, A. Giovannitti, A. A. Szumska, I. P. Maria, E. Rezasoltani, M. Sachs, M. Schnurr, P. R. F. Barnes, I. McCulloch and J. Nelson, *Energy Environ. Sci.*, 2019, **12**, 1349–1357.
59. K. Kaneto, K. Yoshino and Y. Inuishi, *Jpn. J. Appl. Phys.*, 1983, **22**, L567–L568.
60. Y. Gofer, H. Sarker, J. G. Killan, T. O. Poehler and P. C. Searson, *Appl. Phys. Lett.*, 1997, **71**, 1582–1584.
61. G. Nyström, A. Razaq, M. Strømme, L. Nyholm and A. Mihranyan, *Am. Chem. Soc.*, 2009, **9**, 3635–3639.
62. A. Mohammadi, O. Inganäs and I. Lundström, *J. Electrochem. Soc.*, 1986, **133**, 947.
63. C. Friebe, A. Lex-Balducci and U. S. Schubert, *ChemSusChem*, 2019, **12**, 4093–4115.
64. T. Suga, H. Ohshiro, S. Sugita, K. Oyaizu and H. Nishide, *Adv. Mater.*, 2009, **21**, 1627–1630.
65. K. Nakahara, S. Iwasa, M. Satoh, Y. Morioka, J. Iriyama, M. Suguro and E. Hasegawa, *Chem. Phys. Lett.*, 2002, **359**, 351–354.

66. T. Suga, S. Sugita, H. Ohshiro, K. Oyaizu and H. Nishide, *Adv. Mater.*, 2011, **23**, 751–754.
67. K. Koshika, N. Chikushi, N. Sano, K. Oyaizu and H. Nishide, *Green Chem.*, 2010, **12**, 1573–1575.
68. N. Chikushi, H. Yamada, K. Oyaizu and H. Nishide, *Sci. China: Chem.*, 2012, **55**, 822–829.
69. S. Sen, J. Saraidaridis, S. Y. Kim and G. T. R. Palmore, *ACS Appl. Mater. Interfaces*, 2013, **5**, 7825–7830.
70. H. K. Song and G. T. R. Palmore, *Adv. Mater.*, 2006, **18**, 1764–1768.
71. N. Sano, W. Tomita, S. Hara, C.-M. Min, J.-S. Lee, K. Oyaizu and H. Nishide, *ACS Appl. Mater. Interfaces*, 2013, **5**, 1355–1361.
72. Y. Zhang, Y. An, B. Yin, J. Jiang, S. Dong, H. Dou and X. Zhang, *J. Mater. Chem. A*, 2019, **7**, 11314–11320.
73. Z. Song, H. Zhan and Y. Zhou, *Angew. Chem., Int. Ed.*, 2010, **49**, 8444–8448.
74. K. Oka, R. Kato, K. Oyaizu and H. Nishide, *Adv. Funct. Mater.*, 2018, **28**, 1805858.
75. S. Muench, R. Burges, A. Lex-Balducci, J. C. Brendel, M. Jäger, C. Friebe, A. Wild and U. S. Schubert, *Energy Storage Mater.*, 2020, **25**, 750–755.
76. J. Qin, Q. Lan, N. Liu, F. Men, X. Wang, Z. Song and H. Zhan, *iScience*, 2019, **15**, 16–27.
77. J. Qin, Q. Lan, N. Liu, Y. Zhao, Z. Song and H. Zhan, *Energy Storage Mater.*, 2020, DOI: 10.1016/j.ensm.2019.12.002.
78. J. Y. Lee, L. H. Ong and G. K. Chuah, *J. Appl. Electrochem.*, 1992, **22**, 738–742.
79. R. De Surville, M. Jozefowicz, L. T. Yu, J. Pepichon and R. Buvet, *Electrochim. Acta*, 1968, **13**, 1451–1458.
80. Z. Cai, M. Geng and Z. Tang, *J. Mater. Sci.*, 2004, **39**, 4001–4003.
81. C. Zhijiang, *J. Polym. Res.*, 2006, **13**, 207–211.
82. R. Emanuelsson, C. Karlsson, H. Huang, C. Kosgei, M. Strømme and M. Sjödin, *Russ. J. Electrochem.*, 2017, **53**, 8–15.
83. R. Emanuelsson, M. Sterby, M. Strømme and M. Sjödin, *J. Am. Chem. Soc.*, 2017, **139**, 4828–4834.
84. C. Karlsson, C. Strietzel, H. Huang, M. Sjödin and P. Jannasch, *ACS Appl. Energy Mater.*, 2018, **1**, 6451–6462.
85. L. Åkerlund, R. Emanuelsson, S. Renault, H. Huang, D. Brandell, M. Strømme and M. Sjödin, *Adv. Energy Mater.*, 2017, **7**, 1700259.
86. L. Åkerlund, R. Emanuelsson, G. Hernández, F. Ruipérez, N. Casado, D. Brandell, M. Strømme, D. Mecerreyes and M. Sjödin, *ACS Appl. Energy Mater.*, 2019, **2**, 4486–4495.
87. K. Nakahara, K. Oyaizu and H. Nishide, *Chem. Lett.*, 2011, **40**, 222–227.
88. S. Iwasa, M. Yasui, T. Nishi and K. Nakano, *NEC Tech. J.*, 2012, **7**, 102–106.
89. S. Iwasa, T. Nishi, H. Sato and S. Nakamura, *J. Electrochem. Soc.*, 2017, **164**, A884–A888.

CHAPTER 9

# *Redox-active Polymers in Biofuel Cells*

GEORGIOS NIKIFORIDIS*[a,b,c] AND SAHIKA INAL*[a]

[a] Organic Bioelectronics Laboratory, Biological and Environmental Science and Engineering, King Abdullah University of Science and Technology (KAUST), Thuwal 23955-6900, Saudi Arabia; [b] Université François Rabelais, Laboratoire PCM2E, Parc de Grandmont, 37200, Tours, France; [c] LE STUDIUM Institute for Advanced Studies, 45000 Orléans, France
*Emails: georgios.nikiforidis@kaust.edu.sa; sahika.inal@kaust.edu.sa

## 9.1 Introduction to Biological Fuel Cells

The increasing cost of energy production, growing population, and environmental hazards that conventional fuels produce have made numerous research groups seek renewable, clean, and green alternatives. Fuels such as waste biomass, solar energy, hydrogen and biofuels are promising, sustainable energy resources that can fulfill the ever-growing energy demands of the world. Several ''energy-harvesting'' technologies have been under development to convert locally available fuels into electricity. Biochemical energy harvesters such as biofuel cells (BFCs) are now justifiably regarded as one of the most promising renewable energy-generation platforms as these devices can convert the energy of biological compounds into electrical energy. The catalysts of BFCs such as catalytic enzymes or living cells, are abundant, and the fuel is plentiful as they are biologically relevant molecules (such as glucose or organic acids). The versatility of BFCs is attested by the different environments in which they can operate, including the human body (blood sugar), flora (tree sap) or fresh-, salt- and wastewater systems

Polymer Chemistry Series No. 34
Redox Polymers for Energy and Nanomedicine
Edited by Nerea Casado and David Mecerreyes

Published by the Royal Society of Chemistry, www.rsc.org

(biodegradable matter).[1] Since catalysts, fuels, and products are biologically derived and biodegradable, the inherent ecological aspect of BFCs compared to conventional fuel cells is huge. BFCs do not require high temperatures for operation, which otherwise leads to the emission of nitrogen oxidase gases, mostly responsible for air pollution.[2] Besides the continuous power output typically independent of temperature gradients, BFCs' main advantages include simple design, use of renewable fuels and nontoxic electrodes and byproducts, reaction selectivity, and a moderately wide range of fuel choices.

There are two general classifications of BFCs in the literature. The first classification identifies a BFC as a device consuming a biofuel and/or bio-oxidant.[3] The second classification is based on the definition of a BFC as a device comprising a biocatalyst such as a redox protein, an organelle or living cells.[4] Since the former BFCs do not rely on biocatalysts, the second class of BFCs is also known as ''biological fuel cells.'' A biological fuel cell converges two-parent technologies, namely fuel cells and biotechnology. Fuel cells are galvanic cells that convert chemical energy into electrical energy.[5] The history of the fuel cell dates back to Grove, who successfully reversed the action of the electrolysis of water in 1839 by recombining hydrogen and oxygen and produced an electrical current. The link between biology and electricity—for BFCs, this link is established by the use of biofuel and a biocatalyst in generating electrical power—was made for the first time in the 1780s by Galvani who discovered that a frog's leg could be made to twitch by the current drawn from an electricity generator (Figure 9.1a). This experiment was a breakthrough in understanding the nervous system and set the stage for Volta's discovery of the electric battery.[6] Following these two discoveries, in 1910, M.C. Potter observed electricity production from an *E. coli* culture, establishing a new type of fuel cell now known as ''microbial fuel cell.'' Cohen *et al.* followed this discovery and, reported a voltage output higher than 35 V by connecting multiple microbial fuel cells in series,[6] along with the demonstration of the first BFC using a cell-free enzyme in 1964 by Yahiro *et al.*[7] In the 1960s, BFCs were built incorporating enzymes and, for the first time, electron mediators, which facilitated mediated electron transfer (MET) between enzymes and electrode surfaces. The next breakthrough came in 1978 when Berezin *et al.* developed a BFC that exhibited direct electron transfer (DET).[8] In 2001, Heller *et al.* built a micron-scale BFC from single carbon fiber as the microelectrode drawing power from bodily fluids, revealing the potential of BFCs as power sources for bioelectronic devices.[9] The development of nanostructured electrodes based on high-performance materials such as graphene has been a milestone for the BFC technology. These electrodes enabled an increased surface area for enzyme loading as well as stable immobilization while promoting the occurrence of DET.[10] BFCs with typical power densities of a few tens of $\mu W\,cm^{-2}$ reached up to *ca.* 2 $mW\,cm^{-2}$ with the incorporation of carbon nanotube (CNT) and graphene-based electrodes.[10] Ever since research has focused on improving the power density and lifetime of devices through various enzyme immobilization techniques, electrode materials and cell designs.[1,11–13] Due to the

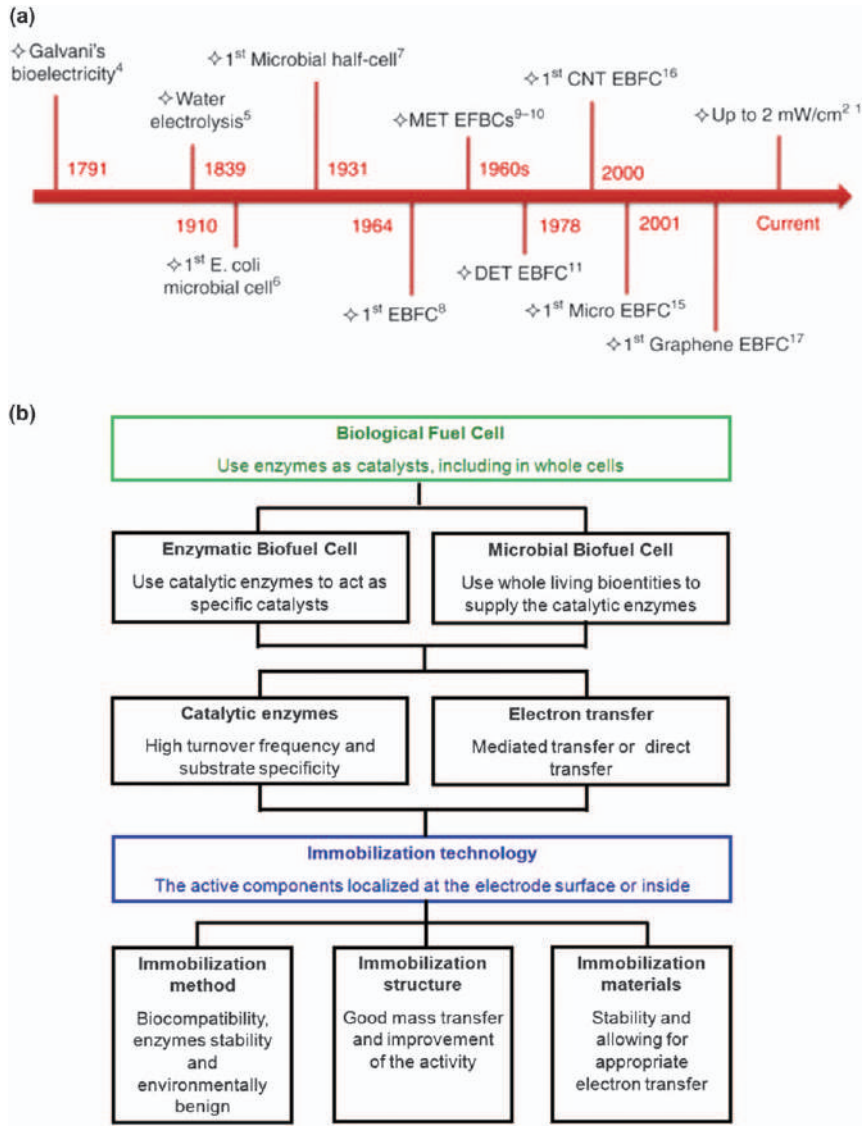


**Figure 9.1** (a) Milestones of biofuel cell technology. Reproduced from ref. 10, https://doi.org/10.1038/s41378-019-0081-2, under the terms of the CC BY 4.0 license, https://creativecommons.org/licenses/by/4.0/. (b) Classification of biofuel cells and biocatalyst immobilization technologies. Reproduced from ref. 2 with permission from the Royal Society of Chemistry.

lower electrical power that BFCs generate compared to conventional fuel cells, the scope of applications is limited for BFCs, at least for now. Their power output fulfills the needs of low-power electronics such as implantable, miniaturized medical devices, *e.g.*, sensors and actuators.[14] For these

applications, the BFC acts as a biobattery that finds the biofuel either contained in one of its compartments or fed through a flow-through system from the biological environment.[15] Despite these flexible design features, the major drawback of BFCs is associated with their lifespan, mostly limited by the environmental instability of immobilized enzymes.[15]

BFC operation is similar to that of conventional fuel cells. During a typical fuel cell operation, oxidation occurs at the anode when the catalyst interacts with its substrate. This reaction releases electrons, which travel to the cathode *via* the external circuit, generating electrical work. The circuit is completed when a compensating charge, often in the form of a cation, moves through the electrolyte to the anode. Typically, fuel cells use small molecules such as hydrogen, ethanol and methanol as fuel (the substrate of the redox reaction) and produce energy, water, and carbon dioxide.[16] BFCs, on the other hand, find their fuel directly in biofluids where it is readily abundant, independently replenished, and cost-effective. We can categorize three biofuel cell configurations, namely microbial, enzymatic, and non-enzymatic biofuel cells, where the former two are also known as biological fuel cells (Figure 9.1b). Microbial fuel cells make use of entire living cells or microorganisms comprising redox intermediates that catalyze the oxidation of a particular fuel.[17] Enzymatic BFCs catalyze chemical reactions by using specific redox enzymes, *i.e.*, catalytic proteins that can be extracted and purified from suitable living organisms. The enzymatic or microbial fuel cells have thus no toxicological, explosive, or flammable risks.[6] Non-enzymatic fuel cells, on the other hand, use platinum alloys or activated carbon as catalysts. Still, the electrochemical reactions they drive are inside a living cell, *i.e.*, *in vivo*, hence relying on biological fuels.[18] In this chapter, our focus will be on the enzymatic BFCs, particularly, those that use glucose and oxygen ($O_2$) as their fuel.

Enzymes (alone or within an organism) are globular proteins that contain reaction sites that catalyze biological reactions in the body. They are preferred over inorganic catalysts as they are biocompatible, renewable, show higher efficiency and activity at mild pH and temperatures, and have superior substrate selectivity.[19] Enzymes work with cofactors such as quinones, flavins and nicotinamides to assist in the catalysis of specific reactions, shuttling of electrons, protons or hydrides.[20] They achieve high catalytic turnovers at mild conditions (*i.e.*, 25–35 °C and pH 5–8). They apply selectively to a variety of fuels that do not require processing steps given that impurities in the fuel do not passivate the catalysts. The high specificity of enzymes toward their substrates allows the anode and cathode to operate in the same compartment, rendering the devices easy to assemble and miniaturize. However, enzymes are labile constituents as they easily degenerate if exposed to environments with conditions differing from their native habitat.

A class of electronic materials that have shown promise to couple with enzymes in BFC electrodes are redox-active polymers. Besides their redox activity (*i.e.*, ability to accept and transfer electrons/holes of an enzymatic reaction), these materials show a unique set of features such as synthetic

tunability, biocompatibility, hydration, modifiable surface energy, porosity and charge transport (valid for those that have conjugated backbones). These properties are ideal for exploiting the construction of high-performance BFC electrodes. In this chapter, we discuss the challenges as well as the opportunities of redox polymer-based enzymatic BFCs. We first provide an overview of the operation principles, components, and characterization of enzymatic BFCs. We then discuss the types of redox-active polymers applied in enzymatic BFCs, the charge transport properties of these polymers, and the function of enzyme-integrated electrodes. Finally, we showcase the performance of a selected set of polymeric BFCs and summarize the state-of-the-art advances in the field with a perspective on the challenges associated with their practical use.

## 9.2 Fundamentals of BFCs: Components, Operation and Characterization

### 9.2.1 BFC Configuration

The typical components of biofuel cells are analogous to those of conventional fuel cells. In the simplest form, two electrodes with appropriate work functions are functionalized with enzymes and placed in an electrolyte that contains the fuel (Figure 9.2a). Classical BFC configurations comprise an ion-conducting membrane or a salt bridge between these two electrodes, which separates the anode from the cathode.[21] Such cells operate in either batch or continuous mode. The incorporation of a membrane is essential to isolate the reaction of the enzyme with the substrate at the surface of its corresponding electrode. The membrane controls the transport of the chemical species (*e.g.*, fuel, $O_2$ and byproducts) involved in the chemical reactions in the solution across the two sides of the BFCs. Membrane material should be carefully selected since the transfer rate of the investigated species affects the performance of the BFC.[1] In a BFC, fuel is supplied to the anode and gets either partially or fully oxidized by the biocatalyst therein, leading to the release of electrons (Figure 9.2a). The electrons travel to the cathode where the oxidants, *e.g.*, $O_2$ or peroxides, are reduced to water.[22,23] The electrode material at the cathode can either perform this reduction reaction by itself or is complexed with an enzyme that catalyzes this reaction. The outcome of these reactions is captured as an electrical current or potential.

BFC electrodes must possess high electrical conductivity alongside the physicochemical properties at the surface favored by the enzyme to ensure interactions that keep them in proximity for long periods. A high surface area is desirable for a high enzyme load, while the electrode has to facilitate efficient mass transport of fuels and oxidants.[3,24] Some of these requirements have been fulfilled by mesoporous structures in the form of nanoparticles (NPs), nanotubes and nanocomposites. Exhibiting such architectures, carbon-based materials [carbon paper, carbon nanotubes (CNTs), graphite, and carbon cloth] are the most widely used electrode materials in BFCs[25] due to their high

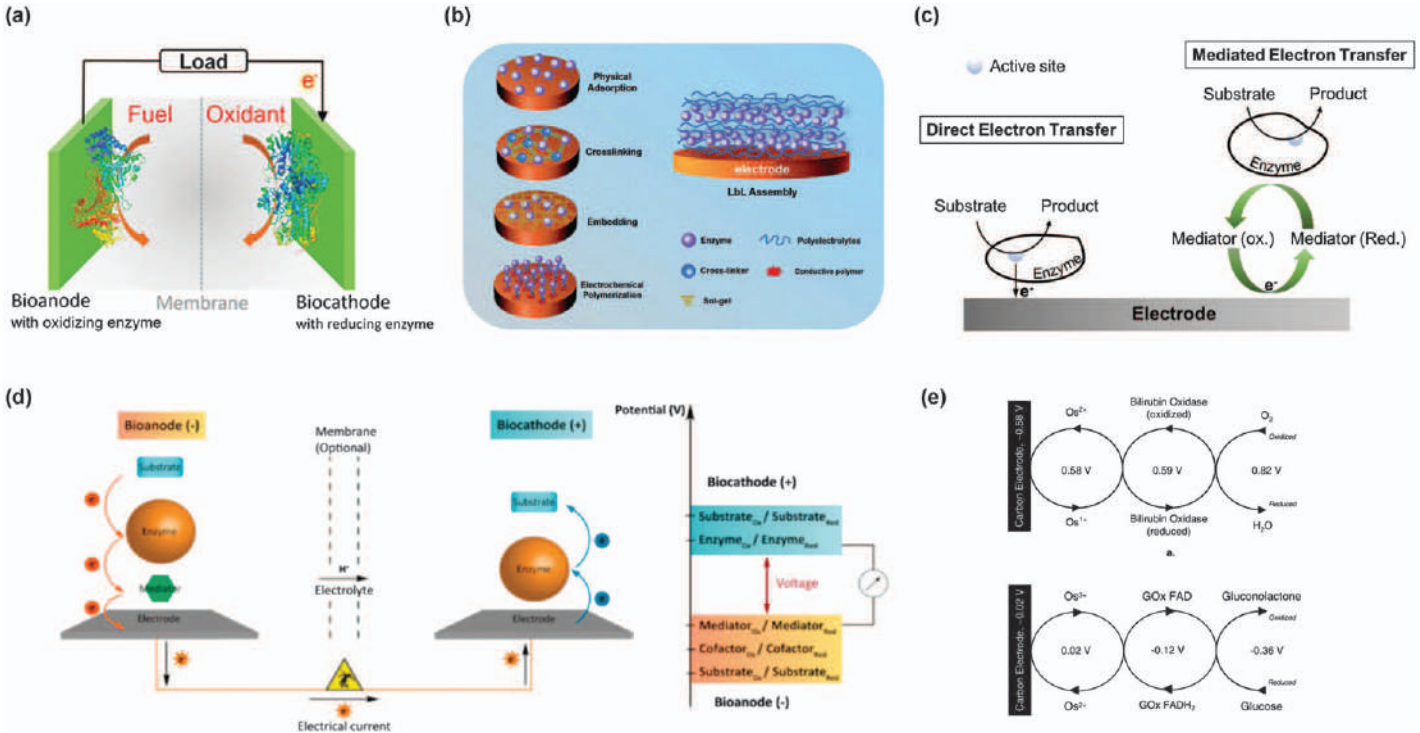


**Figure 9.2** (a) The configuration of an enzymatic BFC consisting of a bioanode and a biocathode. Reproduced from ref. 23 with permission from the American Chemical Society, Copyright 2019. (b) Methods for immobilization of an enzyme on an electrode. Reproduced from ref. 35 with permission from the Royal Society of Chemistry. (c) Direct and mediated electron transfer events on an electrode. (d) An enzymatic BFC utilizing a mediated bioanode and a direct electron transfer-based biocathode. Reproduced from ref. 44 with permission from Elsevier, Copyright 2016. (e) A mediated BFC which contains osmium complexes as redox mediators. All potentials are specified *vs.* SHE (*i.e.*, standard hydrogen electrode). Adapted from ref. 42 with permission from the American Chemical Society, Copyright 2004.

porosity, conductivity, low-cost, biocompatibility, thermal and chemical stability, ease of functionalization and robustness.[3,26] For instance, CNT-based ''Bucky paper'' is commercially available, while another carbon-fiber paper, *i.e.*, ''Toray paper,'' exhibits seamless electronic communication with enzymes because of its high conductivity and porosity.[27,28] These electrodes can be further functionalized with redox-active polymers, as discussed in Section 9.3.

Note that because of the high specificity of enzymes toward their substrates and their activity compatible with mild pH conditions and intermediate ionic strengths, BFCs can sustain operation without a membrane.[29,30] Thus, some BFC configurations have obviated the need for membranes (*i.e.*, one-compartment design) as they can avoid crosstalk (shorting) between the anode and cathode.[21] In 1999, Katz, Willner and co-workers reported the first membrane-free glucose/$O_2$ BFC,[31] and numerous other demonstrations have followed ever since (see Table 9.1 for bioelectrodes and Table 9.2 for membrane-free BFCs made thereof).[11,21,32] The simplicity of assembling all the cell components in one platform is advantageous for miniaturization, shifting the focus toward the development of implantable platforms.

### 9.2.2 Enzyme Immobilization

Efficient energy conversion in a BFC depends on the biocatalytic performance of the anode and the reduction capacity of the cathode (typically for $O_2$ reduction reaction). The bioanode of a BFC defines an electrode functionalized with the catalytic enzyme. The enzyme should be effectively immobilized on the electrically conductive support material selected and, at the same time, preserve its native conformation to ensure long-term stability.[33] For bioanodes comprising electron mediators, the enzyme and mediator should be effectively immobilized at the electrode surface to provide rapid electron transfer rates, decreased enzyme leaching and mitigation of diffusion limitations.[34]

Once attached to their corresponding electrodes, enzymes have efficient channels for electronic communication with the underlying conducting material to achieve high power densities.[33] In the immobilized form, they are more resistant to changes in environmental conditions, such as pH and temperature compared to when they are freely diffusing in electrolytes. During immobilization, one of the major concerns is the denaturation of the enzyme. Enzymes have their catalytic centers typically carried inside their insulating shell. The denaturation of the enzyme involves a transformation of the natural 3D, globular form of the protein into an extended conformation. During this change of conformation, the catalytic centers come closer to the electrode (desired for electrode-catalytic center interactions). However, they get exposed and, in turn, unprotected in this new environment, which can lead to a loss of their activity and subsequently complete dysfunction.

Successfully reported strategies for immobilization/integration of enzymes on solid supports include physical adsorption, covalent binding, cross-

**Table 9.1** A list of redox-active polymers used as bioanodes and cathodes.[a]

| Enzyme | Polymer/anode | Polymer/cathode | $J_{oxidation}$ | Environment | Ref. |
|---|---|---|---|---|---|
| GOx | PVI/[Os(bpy)Cl]/PEGDGE | | 400 mA cm$^{-2}$ | 0.1 M NaCl buffered with 20 mM phosphate, pH = 7.2, 20 °C | 58 |
| Lac | — | [Ru(bipyridine)$_2$(PVI}$)_{10}$Cl Cl | 240 μA cm$^{-2}$ at 0.63 V *vs.* Ag/AgCl | 0.05 M phosphate buffer, pH = 5, 20 °C | 11 |
| Lac | — | Trametes hirsute/Lac/Os-BMCO/GCE | 200 μA cm$^{-2}$ at 0.6 V *vs.* Ag/AgCl | 0.1 M phosphate/citrate buffer, pH = 4.0, (Ar, air and $O_2$), 20 °C | 94 |
| GOx | MgO-carbon/poly(vinyl pyridine) + Os(1,1′-dimethyl-2,2′-biimidazole)$_2$-2-[6-methylpyrid-2-yl]imidazole)$^{2+/3+}$ | — | 50 mA cm$^{-2}$ at 0.3 V *vs.* Ag/AgCl | 0.1 M PBS, 0.5 M glucose, pH = 7, 37 °C | 95 |
| FADGDH | F/Os/MgOC/GC (pore size > 100 nm; (1 mg cm$^{-2}$ hydrogel loading) | — | 100 mA cm$^{-2}$ | 1 M PBS, 0.5 M glucose, pH = 7, 25 °C | 96 |
| FADGDH | FAD-GDH/GC/poly(1-vinylimidazole)-tethered Os(2,2′-bipyridine)$_2$Cl | — | 2.6 mA cm$^{-2}$ at 0.35 V *vs.* Ag/AgCl | 25 °C, 0.1 M PBS, 0.2 M glucose, pH = 7, 25 °C | 97 |
| CDH | *Ct*CDH/CNT/Os-poly(vinylpyridine)-[Os-(*N*,*N*′-methylated-2,2′-biimidalzole)$_3$]$^{2+/3+}$ | — | 0.55 mA cm$^{-2}$ at 0.15 V *vs.* SHE | 50 mM PBS, 50 mM glucose, pH = 7.4 | 98 |
| FADGDH | FADGDH or GOx/PEGDGE/MWCNT/Os | — | 4.2 mA cm$^{-2}$ at 0.12 V *vs.* Ag/AgCl | 0.05 M PBS, pH = 7.4, 0.15 M NaCl, 37 °C | 99 |

[a]Abbreviations are given at the end of the chapter.

**Table 9.2** List of biofuel cells bearing redox-active polymers as electrodes along with their performance.[a]

| Type of BFC | Anode | Cathode | MPD/$E_{cell}$ | Environment | Ref. |
|---|---|---|---|---|---|
| Membraneless glucose/$O_2$ | GOx/PVI-[Os(*N,N′*-dialkylated-2,2′-bisimidazole] $^{2+/3+}$/PEDGE/CF | Lac/PVI-[Os-2,2′,6′,2″-terpyridine-4,4′-dimethyl-2,2′-bipyridine)$_2$Cl] $^{2+/3+}$/PEDGE/CF | 268 μW cm$^{-2}$/0.78 V | 20 mM PBS, 0.14 M NaCl, pH = 7.4 37.5 °C, air | 105 |
| Membraneless β-lactose/air | CDH/Os-polymer/graphite | Lac/Os-polymer cathode/graphite | 1.9 μW cm$^{-2}$/0.6 V | 100 mM phosphate-citrate buffer, pH = 3.5, 34 mM lactose, air | 21 |
| Membraneless glucose/$O_2$ | GOx/PVP-[Os(*N,N′*-alkylanated-2,2′bi-imidazole)$_3$]$^{2+/3}$/CNT fibers | BOD/PAA-PVI-[Os(4,4′-dichloro-2,2′-bipyridine)$_2$Cl]$^{+/2}$/CNT fibers | 740 μW cm$^{-2}$/0.57 V | 20 mM PBS, 0.14 M NaCl, pH = 7.2, 15 mM glucose, 37 °C | 163 |
| Membraneless glucose/$O_2$ | "Wired" GOx//PEGDGE/CF (diameter = 7 μm, 2 cm long) | Lac/PVI/poly(4-vinylpyridine) [Os(*N,N′*-dimethyl-2,2′-biimidazole)$_3$]$^{2+/3+}$)/PEDGE | 350 μW cm$^{-2}$/0.88 V | Stagnant citrate buffer, pH = 5, 15 mM glucose, 37.5 °C | 80 |
| Membraneless glucose/$O_2$ | GOx/[Os(4,4′-dimethoxy-2,2′-bipyridine)2(poly(vinylimidazole))$_{10}$Cl] or [Os(4,4′-dimethyl-2,2′-bipyridine)2(poly(vinylimidazole))$_{10}$Cl]/GA/CNT/graphite | $O_2$-reducing BOx/Au NPs/Au | 275 μW cm$^{-2}$ at 0.3 V MPD$_{human\ blood}$ = 73 μW cm$^{-2}$ | 50 mM PBS, pH = 7.4, 150 mM NaCl, 5 mM glucose, 20 °C | 115 |
| Membraneless glucose/$O_2$ | GOx/[Os(4,4′-dimethoxy-2,2′-bipyridine)$_2$(polyvinylimidazole)$_{10}$Cl]$^+$ and [Os(4,4′-dichloro-2,2′-bipyridine)$_2$(polyvinylimidazole)$_{10}$Cl]$^+$/PEGDGE/graphite | *Th*Lacc or *Mv*BOD/PEGDGE/graphite | 43 μW cm$^{-2}$ at 0.25 V, MPD$_{retention.}$ = 70% after 24 h | PBS, pH = 5.5, 0.1 M glucose, 37 °C | 119 |
| Membraneless (lactate) | LOx/FcMe$_2$-LPEI/EDGE/CNF-Ppy | Lac/An-MWCNT/TBAB-Nafion/CNF-Ppy | 71.2 μW cm$^{-2}$/0.59 V | 0.1 M PBS, pH = 5.7, 40 mM lactate, 37 °C | 120 |
| Membraneless glucose/$O_2$ | GOx/PVP/[Os(*N,N′*-dialkylated-2,2′-bi-imidazole)$_3$]$^{2+/3+}$/PEGDGE/CF | BOx/PAA/PVI/[Os(4,4′-dichloro-2,2′-bipyridine)$_2$Cl]$^{+/2+}$/PEGDGE/CF | 315 μW cm$^{-2}$/0.59 V | 20 mM PBS, 0.14 M NaCl, 15 mM glucose, pH = 7.24, 37 °C | 164 |
| Membraneless glucose/$O_2$ | Poly(MMA-coVFc)/GOx/Au | Poly(MMA-*co*-VFc)/BOD/Au | 323 μW cm$^{-2}$ at 0.4 V | Aerated 100 mM PBS, 10 mM glucose, pH = 7.4, 45 °C | 129 |
| Membraneless glucose/$O_2$ | Poly(TAA-*co*-MT)/Fc/GOx/Au | aPoly(TAA-*co*-MT)/Fc/BOx/Au | 1 μW cm$^{-2}$ at 0.56 V | 100 mM PBS, pH = 7.4, 10 mM glucose | 165 |
| Membraneless glucose/$O_2$ | *Am*PDH/ngDH$_{CtCDHC310Y}$/Os/PEGDGE/graphite | *Mv*BOD/PEGDGE/graphite | 20 μW cm$^{-2}$/0.55 V | 0.1 M PBS, pH = 7.4, 100 mM glucose, 20–35 °C | 166 |
| Membraneless glucose/air | GDH/azine/hydrogel (MG)/EGDGE/MWCNT | Pt (gas permeable)/Vulcan XC-72/Nafion 212 | 106 μW cm$^{-2}$/0.514 V | Phosphate/nitrate buffer, pH = 7.4 | 167 |

| | | | | | |
|---|---|---|---|---|---|
| Membraneless glucose/$O_2$ | GOx/HQS/Ppy (anodic polymerization at 0.9 V *vs.* Ag/AgCl)/carbon tube | Lac/$ABTS^{2-}$/Ppy (anodic polymerization at 0.9 V *vs.* Ag/AgCl)/carbon tube | 27 $\mu W\,cm^{-2}$at 0.25 V | PBS, pH = 5–7, 10 mM glucose, 37 °C, under $N_2$ | 168 |
| Membraneless glucose/air | GOD/Fc/glycerol/graphite disc/BSA/glutaraldehyde | Lac/ABTS/glycerol/graphite/0.1 wt.% Nafion | 23 $\mu W\,cm^{-2}$/0.63 V | 0.1 M PBS, pH = 6, 50 mM glucose, 30 °C | 169 |
| Membraneless fructose/$O_2$ | FDH/CP | Lac/An-MWCNTs/TBAB-modified Nafion/CP | 34.4 $\mu W\,cm^{-2}$/0.707 V | 50 mM citrate, 100 mM fructose, pH = 4.5 | 170 |
| Glucose/$O_2$ | [Os(4,4′-diamino-2,2′bipyridine)$_2$(poly{*N*-vinylimidazole})-(poly{*N*-vinylimidazole})$_9$Cl]Cl/PEGDGE/graphite | [Os(phenanthroline)$_2$(poly{*N*-vinylimidazole})$_2$-(poly{*N*-vinylimidazole})$_8$]$Cl_2$/PEGDGE/graphite | 40 $\mu W\,cm^{-2}$/0.4 V | 0.1 M PBS, pH = 5.5, 10 mM glucose, 0.1 M NaCl, 37 °C | 112 |
| Glucose/$O_2$ | *Af*WrbA/Os redox hydrogel/SWCNT-graphite/PEGDGE | Pt black | 12 $\mu W\,cm^{-2}$/0.165 V | 8 mM NADH in MOPS buffer (0.1 M), pH 7.5, under $O_2$ | 171 |
| Glucose/$O_2$ | Fc/$GO_x$-$FADH_2$/GC (immobilization through irradiation) | BOD-$ABTS^{2-}$/Nafion matrix/FBP | 26 $\mu W\,cm^{-2}$ at 0.2 V/0.55 V | Quiescent saturated PBS, pH = 7.2, 5 mM glucose, $O_2$, 37 °C | 126 |
| Glucose/$O_2$ | GOx/Nafion 117/TMPD/GC | Lac/[Os(2,2′-bipyridine)$_2$(polyvinylimidazole)$_{10}$Cl]$^{+/2+}$ and [Os(4,4′-dichloro-2,2′-bipyridine)$_2$-(polyvinylimidazole)$_{10}$Cl]$^{+/2+}$/PEGDGE/GC | 52 $mW\,cm^{-2}$ at 0.21 V | 0.05 M PBS, 0.1 M glucose, 0.15 M NaCl, pH = 7.4, under $O_2$, 37 °C | 172 |
| Glucose/$O_2$ | PVP/[Os(1,1′-dimethyl-2,2′bisimidazole)$_2$ − 2-(6-methylpyridin-2yl) imidazole]$^{2+/3+}$/PEGDGE/GC | PAA/PVI-[Os(4,4′-dichloro-2,2′-bipyridine)$_2$Cl]$^{+/2+}$ PEGDGE/GC | 129 $\mu W\,cm^{-2}$ at 0.38 V | 8.22 mM glucose in deoxygenated human blood, 37 °C | 173 |
| Glucose/$O_2$ | FAD-*Ct*CDH and PQQ-sGDH/Os/EDT/graphite | MvBOx/graphite | 3 $\mu W\,cm^{-2}$/0.54 V | 12 mM PBS, pH = 7.4, 0.14 M NaCl, 2.7 mM KCl, 5 mM glucose, 30–37 °C | 174 |
| Glucose/$O_2$ | PA/PQQ-GDH/PABSMA/BP | BOD/PQQ-CNT/EDC-NHS solution/BP | 100 $\mu W\,cm^{-2}$/0.71 V $MPD_{saliva}$ = 88 $\mu W\,cm^{-2}$/0.665 V | 100 mM citrate phosphate buffer, 5 mM glucose, pH = 7 | 175 |
| Glucose/$O_2$ | GOx/PANAM/Fc-Ppy/carbon cloth | Gas diffusion membrane (Pt 20% in carbon hot-pressed in Nafion NRE-212 membrane) | 130 $\mu W\,cm^{-2}$/0.416 V | PBS, pH = 5, 0.1 M glucose, 25 °C, air | 140 |
| Glucose/$O_2$ | GC/bi-layer polymer membrane; inner layer: Dp/2-methyl-1,4-naphthoquinone ($K_3$)/KB, outer layer: glucose GDH | Polydimethylsiloxane-coated/Pt | 14.5 $\mu W\,cm^{-2}$/0.62 V | Air-saturated PBS, pH = 7, 0.5 mM NADH, 10 mM glucose, 37 °C | 176 |

**Table 9.2** (*Continued*)

| Type of BFC | Anode | Cathode | MPD/$E_{cell}$ | Environment | Ref. |
|---|---|---|---|---|---|
| Hydrogen/ glucose | *Dv*MF-[NiFe] and (*Dv*H-[NiFeSe]) + P($N_3$MA-BA-GMA)/GOx/$Py_2$Ox or CAT/P(SS-GMA-BA) | Oxidase-HRP/carbon cloth/CMFs/CNT | 530 μW $cm^{-2}$ at 0.85 V/1.15 V | 0.1M phosphate buffer, 3 mM glucose, 20 °C | 177 |
| Glucose/$O_2$ | P(GMA-BA-NIPA)-TB poly(methacrylate)/ GOx/graphite | MvBOx/graphite | 1.2 μW $cm^{-2}$/0.65 V | PBS, pH = 7, 4.8 mM glucose, 20 °C, argon | 178 |
| Glucose/$O_2$ | GC/PaoABC/$[Os(bpy)_2Cl]^+$/PEGDGE/ esterase | CNT/CMF/graphite/BOD/ | 0.63 μW $cm^{-2}$/0.5 V | 0.1 M acetate buffer, pH = 4.5, 20 °C, cathode chamber under $O_2$, Anode chamber under argon | 179 |
| Glucose/$O_2$ | GOx/PVP-[Os(*N*,*N*′-dialkylated-2,2′-bis-imidazole)$_3$]$^{2+/3+}$/PEGDGE/40-Carb (HIPE) | BOD/40-Carb(HIPE) | 205 μW $cm^{-2}$ at 0.4 V | Quiescent, 100 mM PBS, pH = 7.2, 50 mM glucose, 37 °C | 180 |
| Glucose/$O_2$ | GOx/$FcMe_2$-$C_3$-LPEI/GC | Lac/An-MWCNTs/TBAB-modified Nafion | 56.8 μW $cm^{-2}$/0.819 V | Anodic compartment: 50 mM sodium phosphate, 50 mM NaCl, 60 mM glucose, pH = 7.0. Cathodic compartment : 50 mM citrate, pH = 4.5 | 170 |
| Glucose/$O_2$ Microfluidic BFC (double-Y-shaped microchannel) | GOx/Fc-$C_6$-LPEI/EGDGE/PPF | MWCNTs/Lac/TBAB-Nafion/EGDGE/PPF | 64 μW $cm^{-2}$/0.54 V at 70 mL $min^{-1}$ | 100 mM glucose, 100 mM PBS, pH = 7.4, 25 °C Catholyte: 150 mM citrate buffer, pH = 4.5 | 181 |
| NADH/$H_2O_2$ | PQQ/Au/EDC | MP-11/Au/EDC | $W_{max}$ = 8 μW/0.32 V ($W_{max}$: *maximum electrical power*) | 0.1 M Tris–HCl buffer, pH = 8.0 Anodic fuel: 0.001 M NADH and 0.02 M $CaCl_2$. Cathodic oxidizer: 0.001 M $H_2O_2$ | 182 |
| Implantable Tre/$O_2$ | Tre/GOx/Os(dm-bpy)$_2$Cl PEGDGE/carbon rod | BOD/Os(bpy)$_2$Cl/PEGDGE/carbon rod | 100 μW $cm^{-2}$ at 0.2 V | 50 mM Trehalose in PBS, air | 183 |

[a]Abbreviations are given at the end of the chapter.

linking, layer-by-layer encapsulation, and embedding/entrapment (Figure 9.2b).[35] With these strategies, a randomly oriented enzyme layer is formed, either on the surface of the electrode or inside the cavities of an encapsulating matrix or of the electrode itself (given that it is highly porous). Physical adsorption occurs when intermolecular forces between the electrode surface and the enzyme lead to the accumulation of protein(s) therein. Since these interactions are based on weak van der Waals forces, the reasonable approach to ensure long-term enzyme adhesion to the surface is to increase the number of contacts between the surface and the enzyme. This method is simple because no reagents or surface functionalization are required. The enzyme also can be covalently linked to the electrode surface if the latter has reactive groups (such as amides, sulfurs or carboxylic acids). Enzymes are cross-linked inside a network, a process of building covalent bonds typically within and between encapsulating polymer networks and the electrode surface or membrane-like matrices and the enzyme. Bunte *et al.* developed a redox polymer containing cross-linkable benzophenone groups, that entrapped the enzyme inside the network during photo-induced cross-linking.[36] This approach may result in lower enzyme/electrode contacts, yet it provides stability. Enzymes can be physically embedded in sol–gel-like matrices, which are then cast on electrodes. The enzyme layers are cast sequentially between charged polyelectrolyte layers, forming a multilayered assembly of enzymes embedded between polyelectrolyte films. Even at a bilayer configuration, the encapsulation of polymers can prevent the leakage of enzymes. Xiao *et al.* utilized a poly(acrylic acid) coating layer on a GCE coated with an Osmium (Os) redox polymer and lactate oxidase and found an improved catalytic response for high substrate concentrations.[37] Finally, the use of conducting polymers as electrode coatings is closely linked with entrapment techniques. Entrapment entails the polymerization of a monomer (typically, electropolymerization) in the presence of the protein, which results in an entrapped protein inside the conducting polymer network.[34]

The immobilization methods summarized above trade stability for enzyme activity. Chemical bonds formed between the enzyme and a given surface or even physical interactions that are weaker might alter the enzyme structure, hence its function, and affect the electron transfer rates when the orientation of the catalytic center is not preserved. Yet, immobilization results in an improved lifetime as the enzyme cannot readily delink itself from the electrode and remains protected from other species that may be present in the electrolyte. When choosing an enzyme immobilization strategy, the nature of the particular enzyme and the underlying substrate have to be evaluated. The chemical groups and the charge on the enzyme surface, the size of the enzyme as well as its 3D polarity distribution (hydrophobic/hydrophilic regions) have to be considered.[38] Substrate charge, roughness and polarity should be optimized to ensure high enzyme loading and combat leaching. Finally, the properties of the environment where enzyme immobilization takes place must be compatible with the enzyme.

### 9.2.3 Electron Transfer Mechanism in BFCs

For a high power density BFC, an efficient mechanism should rapidly transfer the electrons generated by the catalytic center of the enzyme where the reaction with its substrate takes place. The way that the protein conforms itself on the electrode and the positioning of its catalytic centers determine the electrical coupling with the electrode and in turn the performance of the BFC.

Two main approaches are envisaged in the quest for effective coupling between the enzyme and an electrode: direct and mediated (indirect) electron transfer (Figure 9.2c). Electron transfer (ET) occurs through Marcus-type collisional electron transfer wherein individual redox centers move within short distances and come close enough to facilitate outer-sphere self-exchange reactions.[39] The rate at which electrons move through the enzymatic film limits the overall communication between the enzyme and the electrode.[39] Direct electron transfer (DET), *i.e.*, the tunneling of electrons from the redox-active catalytic center of the enzyme to the electrode surface directly,[40] can be established if the enzyme is in the proximity of the electrode (see Figure 9.2d, biocathode). In this case, the enzyme is positioned in a manner that its active site is oriented toward the electrode, ensuring that its distance to the electrode surface is as short as possible. Dutton and coworkers provided a rule-of-thumb for the DET occurrence within metalloenzyme structures that an electron tunneling distance of less than 14 Å between redox-active sites supports sufficiently fast ET rates and is required so as not to limit the rate of redox catalysis.[41]

Bioelectrodes that rely on mediated electron transfer (MET) contain a low-molecular-weight, redox-active species, known as a mediator (Figure 9.2c). The mediators shuttle electrons between the enzyme-active site and the electrode (see Figure 9.2d, bioanode). They increase the rate of electron transfer between the active site of the enzyme and the electrode, and as such, the stringent electrode design requirements of DET are mitigated. In this case, the enzymatic reaction catalyzes the oxidation or reduction of the redox mediator, and the reduced mediator is simultaneously regenerated on the electrode surface.[42] The mediator (*e.g.*, ferrocene, Prussian blue, methyl viologen) must possess a redox potential close to that of the enzyme cofactor to transfer electrons rapidly upon application of a low voltage (Figure 9.2e). For efficient current collection, ET from the enzyme to the mediator should be at least as fast as the transfer of electrodes from the metabolite to the enzyme. Due to their typically small size, the freely moving redox molecules can readily interact with the cofactor, enhancing the fuel cell performance. Yet, the addition of mediators to the system comes with issues such as mediator leaching over time and increased complexity of the electrode design to immobilize the mediator.

The ET events from the active site of an enzyme to the electrode surface or the immobilized redox-active molecule can be either intermolecular or intramolecular. In the intermolecular case, the enzyme acts as a freely diffusing but high-molecular-weight redox mediator. For the case of

intramolecular ET, the attached redox mediator swings in and out of the active site of its enzyme. The ET rate depends on the interfacial electron transfer rate and the turnover number of the enzyme.[19,43] A BFC electrode can be assembled from electronic materials that perform DET with enzymes or involve mediators (Figure 9.2d). The selection criteria of these materials concern the careful alignment of the energetics of enzymatic reactions and redox-active components. Apart from establishing ET pathways, the design should consider mass transfer processes involved in the BFC reactions, all subject to transfer limitations. These processes can set constraints to the performance of the BFCs and ought to be optimized through careful consideration of the device geometry and materials used.

### 9.2.4 BFC Characterization and Figures of Merit

The performance of a BFC is determined in terms of power output, voltage and current.[19] Typically, linear sweep voltammetry or chronoamperometry is implemented to characterize the BFC performance and to monitor the response of the whole device or the half-cells (anode and cathode, individually). These electrochemical techniques reveal several vital parameters, including onset potentials of the redox reactions, ohmic losses, maximum current extractable from each electrode and theoretical open-circuit voltage. A standardized methodology for testing the BFC performance and reporting figures of merit is indispensable for comparing and benchmarking BFCs in terms of electrode and mediator performance, and configuration. However, the experimental approaches differ in (1) the specific surface area or volume of the electrode, (2) mass transport of the fuel to the surface, (3) coverage, thickness, density and activity of the enzyme or the mediator on the electrode surface and (4) stability of the system. Other differences include variations in operational conditions such as pH, ionic strength, electrolyte composition, concentration and temperature. The reports in the literature involve different techniques to determine current output (such as amperometry, cyclic voltammetry at different scan rates or measurements directly in the BFC configuration) and power density (*i.e.*, fixed load, potentiostatic or galvanostatic control).[45]

The open-circuit voltage (OCV) of the cell is one of the most important BFC figures of merit. It is defined as the voltage output of the BFC when there is no external electric current between the electrodes. OCV depends on the solution composition and follows the Nernst equation:[46]

$$E = E^{\circ} - \frac{RT}{nF}\ln Q \tag{9.1}$$

where $Q$ is the transported charge, $E$ is the cell potential, $R$ stands for the universal gas constant, $T$ is the absolute temperature, $n$ is the number of electrons involved in the reaction, and $F$ is the Faraday constant. The OCV is determined from the difference between the thermodynamic potential of the fuel/oxidized product redox couple (half-reaction of the anode) and of the oxidant/reduced product redox couple (half-reaction of the cathode)

(Figure 9.3a). The difference between the open-circuit potential of the biocathode and the bioanode determines the electrochemical driving force. The difference between the OCV and the apparent standard redox potential of the catalyst ($E^{\circ}$), that is, the overvoltage ($\eta$), defines the deviation of the catalyst from ideal and is thus a measure of its efficiency (Figure 9.3a).[47] From a thermodynamic point of view, the electrochemical efficiency of the cell is expressed by:[15]

$$\text{Efficiency} = \frac{-nF\Delta E}{\Delta H} \tag{9.2}$$

in which $\Delta E$ is the potential difference between anode and cathode, and $\Delta$N represents the enthalpy variation as the anodic reaction occurs ($\Delta H = n \times F \times \Delta E$). This efficiency is lower than in practice, meaning that the measured OCV is not determined solely by the thermodynamics of the reactants and is much lower than the theoretical value of $\Delta E$. This discrepancy arises due to the presence of three types of loss channels: kinetic factors related to the overpotentials for the corresponding reactions at the electrode/electrolyte interface, mass transport due to reactant diffusion limitations and ohmic losses associated with all the resistances in the system.[19] In a typical BFC polarization curve (Figure 9.3b), the measured value of OCV is lower than the theoretical one, the latter determined by the analysis of the individual half-cell responses (Figure 9.3a).

Three mass transfer processes are involved in the BFC reactions, all subject to transfer limitations. A rapid fall in voltage occurs, followed by a smoother and less rapid decline. Although the former is attributed to kinetic parameters caused by a slow rate of reaction at the electrode surface, the limiting second phase is because of resistive (*i.e.*, ohmic) losses. Resistive losses are ascribed to the resistance of electrons through the electrode materials and that of ions through the electrolyte. At the final stages (*i.e.*, higher currents), the voltage falls faster due to the system being mass transport limited. Mass transport limitations arise as the concentration of the reactants on the electrode surface changes with more fuel consumed. Finally, the OCV of glucose/$O_2$ BFCs lies below the thermodynamic limit of 1.18 V.[47,48] BFCs with MET-based electrodes have thermodynamic losses due to the presence of mediators, leading to a smaller cell voltage (recall Figure 9.2d).

The other figure of merit of BFC performance evaluation is its power, depicted in Figure 9.3c and expressed as:[6]

$$P_{\text{cell}} = E_{\text{cell}} \int J_{\text{cell}} \, \mathrm{d}t \tag{9.3}$$

where $E_{\text{cell}}$ stands for the cell voltage, and $J_{\text{cell}}$ is the cell current. The commonly used electrochemical technique to determine $P_{\text{cell}}$ is the polarization at variable load resistances or slow scan rate ($<$0.1 mV $s^{-1}$) cyclic voltammetry. Investigating each electrode separately (half-cell) allows identifying the electrode that limits the electrochemical reaction; hence, the $J_{\text{cell}}$.[19] The current output can be improved by adopting the appropriate immobilization strategy and

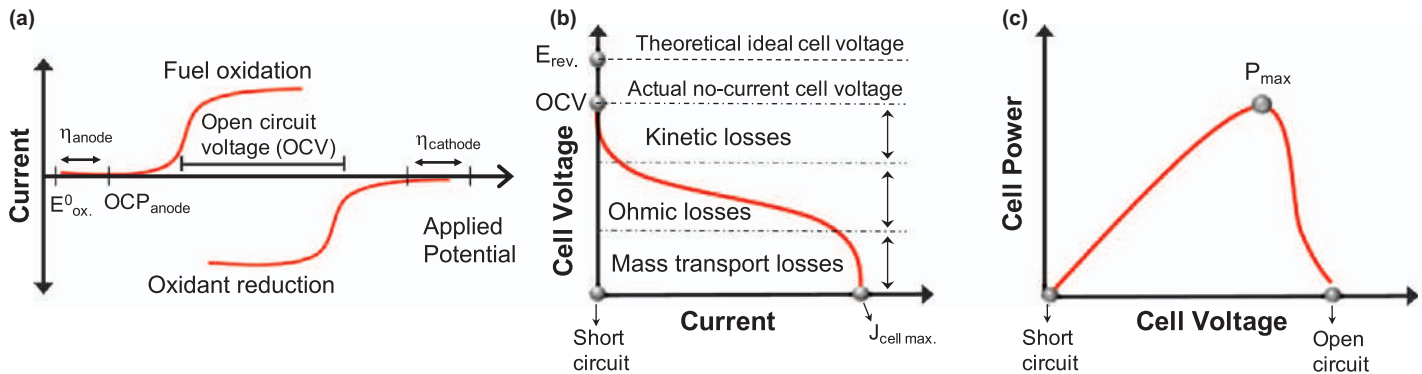


**Figure 9.3** BFC figures of merit. (a) Current *vs.* voltage characteristics of the anode and cathode with the oxidation and reduction events therein the BFC performance (maximum current density of each electrode, their potential losses, the open-circuit voltage). (b) Polarization curve with the respective OCV (current = 0) and short circuit current (V = 0). The theoretical cell voltage is higher than the actual OCV. The three types of losses that lower the OCV are kinetic, ohmic and mass transport losses. (c) A typical BFC power curve with the maximum power output noted. The measured OCV can be extracted from this power density profile or the polarization curve in (b).

promoting the mass transport of reactants and products.[19] Under closed-circuit conditions, the measured $E_{cell}$ is defined as:[19]

$$E_{cell} = E_C - E_A - \sum IR_{ohm} \tag{9.4}$$

in which $E_C$ and $E_A$ are the experimental cathode and anode potentials, respectively. These potentials are related to the equilibrium potential ($E_e$) by the following equation:[49]

$$\eta = E - E_e \tag{9.5}$$

Here, the difference between the resultant potential $E$ and $E_e$ is called polarization. This difference is quantified in terms of an overpotential ($\eta$), *i.e.*, the additional potential (beyond the thermodynamic requirement) required to drive an electrochemical reaction at a certain rate. To maximize the OCV, it is instrumental to bring the starting potential of the electrodes closer to those of the enzymes/mediators so as to lower the overpotential (see Figure 9.3a) (*i.e.*, the difference between the redox potential of the enzyme and that of the electrode).[44]

The maximum electrocatalytic current (or maximum power, $P_{max}$, Figure 9.3c) is the highest power that the fuel cell can achieve. It depends on the density of active catalytic sites and the reaction rate at each active site, which is linked to the turnover number of the enzyme.[19] The power density ($PD$) of the BFC is expressed as:[19]

$$PD = \frac{P_{cell}}{A} \tag{9.6}$$

where $A$ is the geometric area of the electrode. Maximum power density (MPD) of a BFC is the $P_{max}$ normalized by the electrode area.

Overall, the BFC performance is correlated to the ET efficiency between enzyme and electrode surface, which regulates the current, and the potential difference between the bioelectrode pairs that, in turn, dictates the OCV. The biggest hurdles of enzymatic BFCs thus lie in the low power output stemming from impaired electron and mass transfer limitations, and the unmatching cathode and anode potentials. The concentration overpotential is caused by the slow mass transfer rates of reactants and reaction products. Ohmic losses stem from the resistance of the ions that flow in the electrolyte, the impaired proton transfer through the membrane, and the slow flow of electrons through the electrode.[50] The OCV can be improved by maximizing the driving force ($E_C - E_A$) and mitigating the ohmic resistance losses through improved cell design, such as those with narrower interelectrode gaps.[19,24]

It is important to understand the origin of losses in BFCs in order to extract design rules for next-generation devices. Techniques such as infrared microscopy can be implemented to investigate the molecular composition within the localized regions of BFC electrodes.[51] An in-depth assessment of the structure and intermolecular interactions among the components, changes in

enzyme conformation upon the operation, and in its microenvironment will provide insights into loss mechanisms in BFCs that remain unknown.

## 9.3 Redox-active Polymers

Redox-active (or, simply, redox) polymers are macromolecules which contain certain chemical groups that can reversibly change their electrochemical state by losing (oxidation) or gaining (reduction) electrons. They allow to co-immobilize enzymes and redox mediators on the electrode surface. To this end, redox-active polymers are responsible for managing the transfer of both ions and electrons that are generated as their redox-active units interact with substrates. They differ from inorganic electrode materials as they are softer and do not require ions to intercalate into the solid-state structure.[52] Compared to isolated, freely moving redox couples, redox-active polymers covalently immobilize the redox centers, providing stability. Redox properties are governed by the nature of the polymer backbone (conjugated or nonconjugated) and the properties of spatially localized redox groups (if they are present).[53] When combined with biocatalysts, such as enzymes and living cells, redox polymers have not only been implemented in BFCs but also for biosensing, biophotoelectrochemistry and bioelectrocatalysis applications.[54]

The synthesis of redox polymers involves the typical main steps of polymerization, namely, initialization, propagation and termination. An initiator molecule introduced to the reaction mixture triggers the polymerization reaction by reacting with a monomer, attacking its double bond, and forming an unstable-reactive species (*i.e.*, monomer radical). The latter forms another bond with a monomer, sequentially yielding a long chain of monomers, called the macroradical. The reaction is terminated by a chemical reaction that ceases the formation of reactive intermediates. The length of the chains and their polydispersity affect the chemical, electrical and physical properties of the polymer film. The simplicity of the polymer synthesis, as well as its processing into the final form, is essential for its use as a BFC electrode coating since the polymer and the devices made thereof can be easily scaled-up.

Redox polymers transport charge either *via* a mediated electron transfer by way of redox relays or electron-hopping through the polymer (conjugated) backbone (Figure 9.4a).[55,56] They constitute a hydrated electron-conducting system that supports the diffusion of ions, substrates (glucose, $O_2$) and products. The redox relays bound to the polymer backbone can be of organic or inorganic/organometallic origin.[55,57] The electrons that are generated in one enzyme-linked redox unit of the polymer are transferred to another unit through collusions between them. If the redox moiety possesses low reorganization energy, the self-exchange rate is fast,[55] like in the case of Os complexes.[58,59] Here, if the polymer backbone is conducting (*i.e.*, conjugated), the redox-active polymer could act as a conducting wire combining high redox activity of dedicated redox sites with electronic conductivity. A prime example is the electron-transporting polymer, poly{[*N,N′*-bis(2-

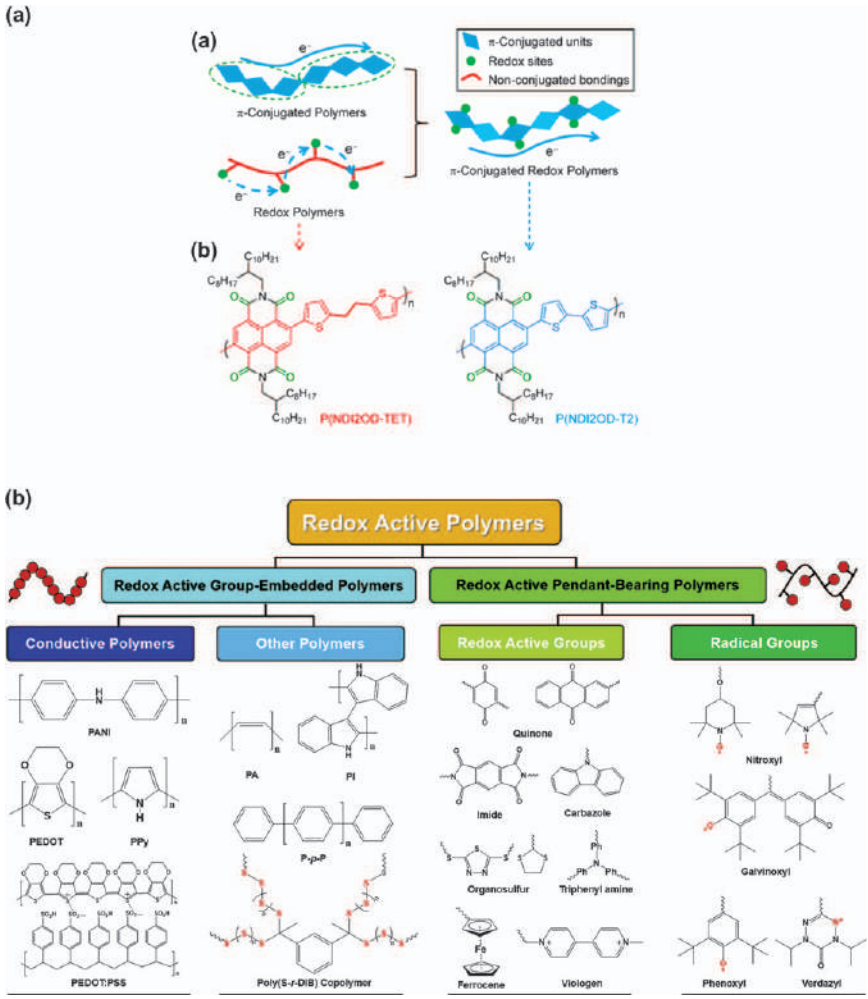


**Figure 9.4** (a) Graphical illustration of charge transport of π-conjugated polymers, redox polymers and π-conjugated redox polymers (top) alongside the molecular structures of the nonconjugated and the π-conjugated n-type redox-polymer (bottom). Reproduced from ref. 63 with permission from the American Chemical Society, Copyright 2015. (b) Classification and chemical structure of representative redox-active polymers and redox-active pendant groups. Reproduced from ref. 61 with permission from Elsevier, Copyright 2017. PANI: Polyaniline; PEDOT: poly(3,4-ethylenedioxythiophene); Ppy: Polypyrrole; PEDOT:PSS: poly(3,4-ethylenedioxythiophene):poly(4-styrenesulfonate); PA: polyacetylene; PI: poly(indole); P-*p*-P: poly(*p*-phenylene); Poly(S-*r*-DIB) copolymer: poly(sulfur-random-(1,3-diisopropenylbenzene).

octyldodecyl)-1,4,5,8-naphthalenedicarboximide-2,6-diyl]-*alt*-5,5′-(2,2′-bithiophene)} [P(NDI2OD-T2)] (Figure 9.4a).[56] Most commonly used conducting polymers in BFCs are however hole-conductors. Polypyrrole (Ppy), polyaniline (PANI) and polythiophene are p-type polymers, which are typically

electropolymerized as films on conductive substrates. While supporting charge transfer, they act as a matrix wherein the enzyme is immobilized.[60]

### 9.3.1 Classification of Redox-active Polymers

Redox-active polymers can be categorized under two groups depending on the location of the redox-active center in the chemical structure: (1) redox-active group-embedded polymers and (2) redox-active pendant-bearing polymers, as depicted in Figure 9.4b.[61] In the first group, the redox units are integrated directly to the backbone, while in the second group, they are grafted to the backbone as pendant side chains. The majority of redox polymers of group 1 have π conjugation in their backbone (an alternation of single and double bonds where $sp^2$ hybridization gives rise to weak π-bonds and reduced bandgaps), which provides them with a semiconducting character. Polarons and bipolarons can propagate an electrical current along the polymer chain as charges hop along the molecule through delocalized π-orbitals, and between molecules which exhibit sufficient π–π overlap.[62] Likewise, sulfur polymers belong to group 1, are highly redox-active but they are not conducting.[61] They have sulfur–sulfur bonds (–S–$S_n$–S–) embedded in a nonconjugated polymer backbone, such as poly(sulfur-random-(1,3-diisopropenylbenzene)[poly(S-*r*-DIB].[61] During the redox process, conjugated, redox-active polymers grant the charge to travel across their chains (Figure 9.4a), leading to electronic communication between redox centers, as well as a shift of the redox potential that would otherwise be expected for the isolated redox centers.[53] Another classification comes from the nature of the redox-active molecule, either organic or inorganic. Overall, these classifications always include exceptions as hybrid forms exist due to the large variety of redox-active polymers that have been developed thanks to the synthetic tunability inherent to polymers.[61]

#### *9.3.1.1 Redox-active Group-embedded Polymers*

Figure 9.4b shows the chemical structures of some of the most common redox-active group-embedded polymers with a conjugated backbone, namely, polyaniline (PANI), poly(3,4-ethylenedioxy thiophene) (PEDOT), poly(3,4-propylenedioxy thiophene) (PProDOT), polythiophene (PT) and polypyrrole (Ppy).[61] Polyacetylene (PA), poly(indole) (PI) and poly(*p*-phenylene) (P-*p*-P) are other redox-active polymers that belong to this group.[64] The similarity of these chemical structures with biological compounds is promising for the activity of the biocatalyst coupled to the polymer film. The electrochemical properties of conjugated polymers depend on their molecular weight, morphology, degree of doping and the nature of dopant ions.[61] These polymers typically undergo redox reactions upon interaction with electrolyte ions transported by an electrical field.

Conjugated polymers can be doped to be p-type and n-type semiconductors. P-type doping suggests the oxidation of the polymer, leading it

to gain a positive charge (in the form of a hole). In contrast, n-type doping occurs when the polymer is reduced and thus possesses a negative charge (*i.e.*, an electron). The n- and p-type character can be controlled by the engineering of HOMO/LUMO levels with electron-rich and electron-poor moieties in the backbone. Heavily and slightly doped p-type doped polymers such as Ppy, PEDOT:PSS, PANI, PEDOT and PT are stable under ambient conditions,[61] unlike most of the n-type conjugated polymers. The difficulty in arriving at a durable n-type material arises from the instability of organic anions, especially carbanions that are oxidized in air and water. To have high stability, the material should have a deep LUMO lower than $-4.0$ eV.[65] A more rigid backbone has been shown to improve charge transport.

Charge carriers are introduced into the conjugated polymer by doping, either chemically or electrochemically. In chemical doping, there is a direct charge transfer from an oxidant to the polymer, such as in the case of PANI getting protonated by acids. Electrochemical doping, on the other hand, requires the application of a voltage on a conjugated polymer film through an electrolyte. The process entails the following elementary steps: electronic charge injection from the metal electrode into the polymer, charge transport across the adjacent localized states, ion injection from the electrolyte into the polymer, ion transport in the free volume between the polymer crystallites or chains, and electrostatic compensation of the two charges in the bulk of the film.[66]

Faradaic charging of a conjugated polymer film implies a current arising from oxidation/reduction reactions happening at the backbone. The CV curves of a conjugated polymer film coated on a conductive substrate display Faradaic and capacitive processes (Figure 9.5a).[66] The CV measures the outcome of a chain of events associated with mixed ionic and electronic conduction that may involve morphology changes, delocalized states and multiple charge compensation (doping) mechanisms.[66] Therefore, CVs are not particularly conclusive in determining the redox activity of conjugated polymer films. A typical figure of merit for polymers that can be delineated from CV or galvanostatic charge–discharge is the capacitance, which is the ability of the polymer film to store charge for a given voltage. For certain polymers, however, the CV curves display discrete features reflecting electron transfer processes localized on single repeat units, stabilized with a cation or anion supplied from the electrolyte.[67] Naphthalene 1,4,5,8-tetracarboxylic-diimide-alkoxybithiophene (NDI-T2)-based n-type polymers, for instance, show distinct features of reduction and oxidation couples in their CV curves and an abrupt change in the film conductivity around the voltages that correspond to the reduction reactions (Figure 9.5b–c).[68] Such Faradaic behavior is possible to observe in CVs if the charge localizes on an individual repeat unit as it does for P(NDI2OD-T2) in Figure 9.5b. The NDI unit undergoes a reversible and rapid doping/dedoping process with Li ions, making this polymer promising to form fast rechargeable Li batteries.[56] Another commonly used redox polymer is PEDOT (the most common form

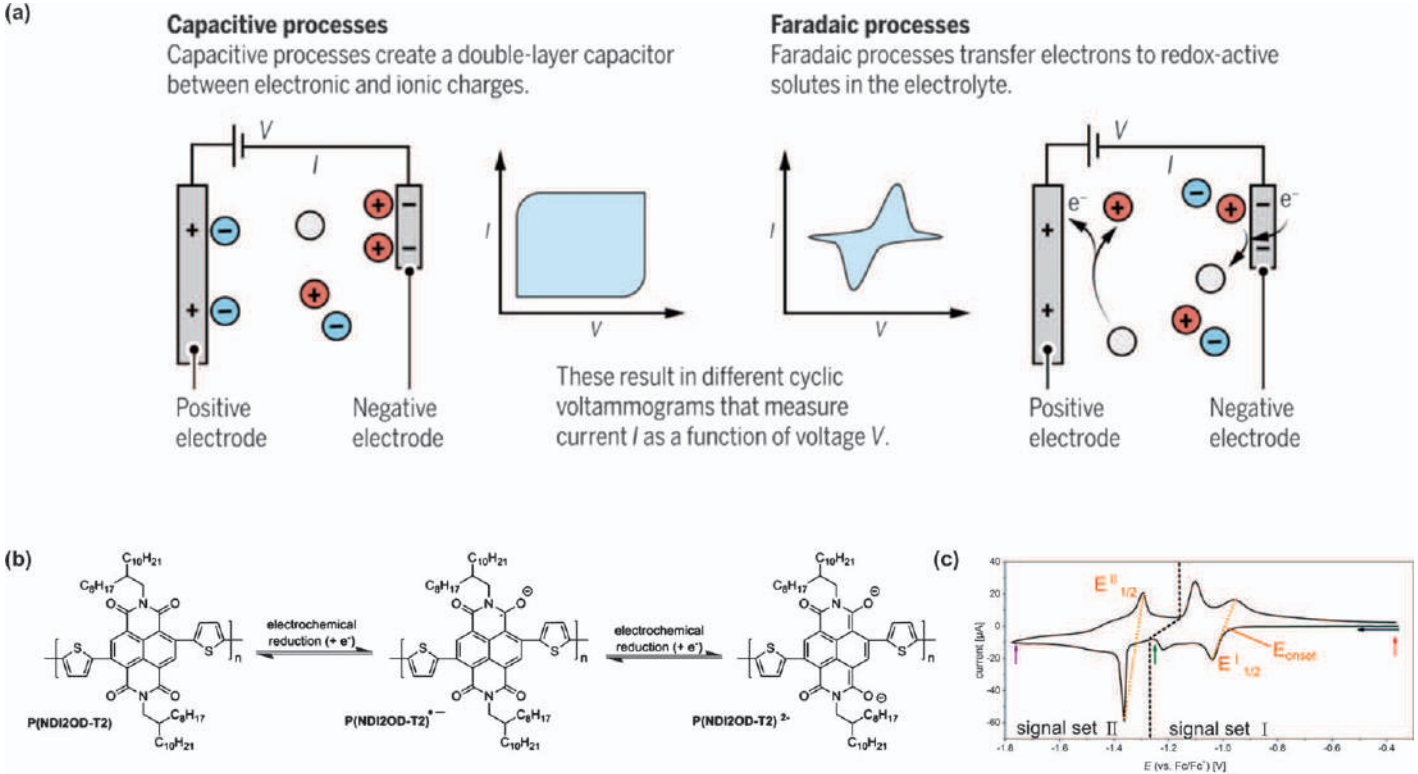


**Figure 9.5** (a) The electrochemical operation of metal electrodes coated with conducting polymers. The conjugated polymer films may show CVs comprising capacitive and Faradaic components. Reproduced from ref. 66 with permission from the American Association for the Advancement of Science, Copyright 2019. (b) Proposed reduction pathways of the n-type semiconducting polymer poly{[*N*,*N*′-bis(2-octyldodecyl)-naphthalene-1,4,5,8-bis (dicarboximide)-2,6-diyl]-*alt*-5,5′-(2,2′-bithiophene), P(NDI2OD-T2), and (c) its cyclic voltammogram recorded in 0.1 M $NBu_4PF_6$/MeCN.
Reproduced from ref. 68 with permission from the American Chemical Society, Copyright 2015.

of this polymer is PEDOT doped with polystyrene sulfonate, PEDOT:PSS) with its dominating capacitive behavior. PEDOT acts as an $O_2$ reduction catalyst in its dedoped form, and gets reoxidized and reduced reversibly upon its interaction with $O_2$ dissolved in aqueous electrolytes.[69,70] As such, this polymer is a strong candidate for a BFC cathode.

### *9.3.1.2 Redox-active Pendant-bearing Polymers*

In this type of redox-active polymers, the redox-active units are attached to the polymer backbone by a tether. The redox units can be either of organic (such as quinones or viologens) or organometallic/inorganic [such as Os, FC, or cobaltocene] origin. An array of redox-active pendant-bearing polymers, mostly on nonconjugated polymer backbones, have been reported. The functional groups include carbonyl compounds, viologen, organosulfur, Fc, quinones and radical compounds such as nitroxyl, phenoxyl and verdazyl groups (Figure 9.4b).[61,71–73] These polymers exhibit a wide electrochemical window depending on the redox unit they possess. The reversible oxidation/reduction potential of common redox couples, deduced from cyclic voltammetry, is displayed in Figure 9.6.[57] The redox potentials depend on experimental parameters, such as electrolyte type and ionic strength, and cell configuration. Although they show high redox activity, the low electrical conductivity of this class of redox polymers due to their insulating backbone necessitates the use of conducting materials in conjunction with these polymers.

These variations in redox potentials make redox polymers advantageous to use in enzymatic BFC electrodes. Ideally, the redox polymer must possess a redox potential close to one of the enzymes and can be adjusted by choice of the redox unit. For instance, the formal potential of the Os-complex bearing redox polymers can be tuned by choosing different combinations of ligands (changing the substituents therein) in the octahedral complex, which modifies the electron density of the central Os center.[74] Moreover, the concentration of the selected redox unit alongside the composition of the polymer backbone, chain length and the spacer that connects the pendant unit to the backbone, can be tailored to fulfill the needs of the biocatalyst and the reaction.

Typical ways to polymerize and introduce redox-active groups to the monomers include polycondensation, oxidative polymerization and free-radical polymerization. Recent works have also employed anionic polymerization, atom-transfer radical polymerization and reversible addition-fragmentation chain transfer polymerization.[61] The most common synthesis route for these polymers is the ''ligand exchange method,'' as well as the covalent binding approach of the (metal) redox complex already bearing the suitable ligand.[75] Poly(N-vinylimidazole) (PVI) or poly(4-vinylpyridine) (PVP) are typical backbones to tether redox units.[45] The success of organometallic compounds as redox components has led to the development of more advanced versions where new synthetic routes have been developed (such as the epoxide opening

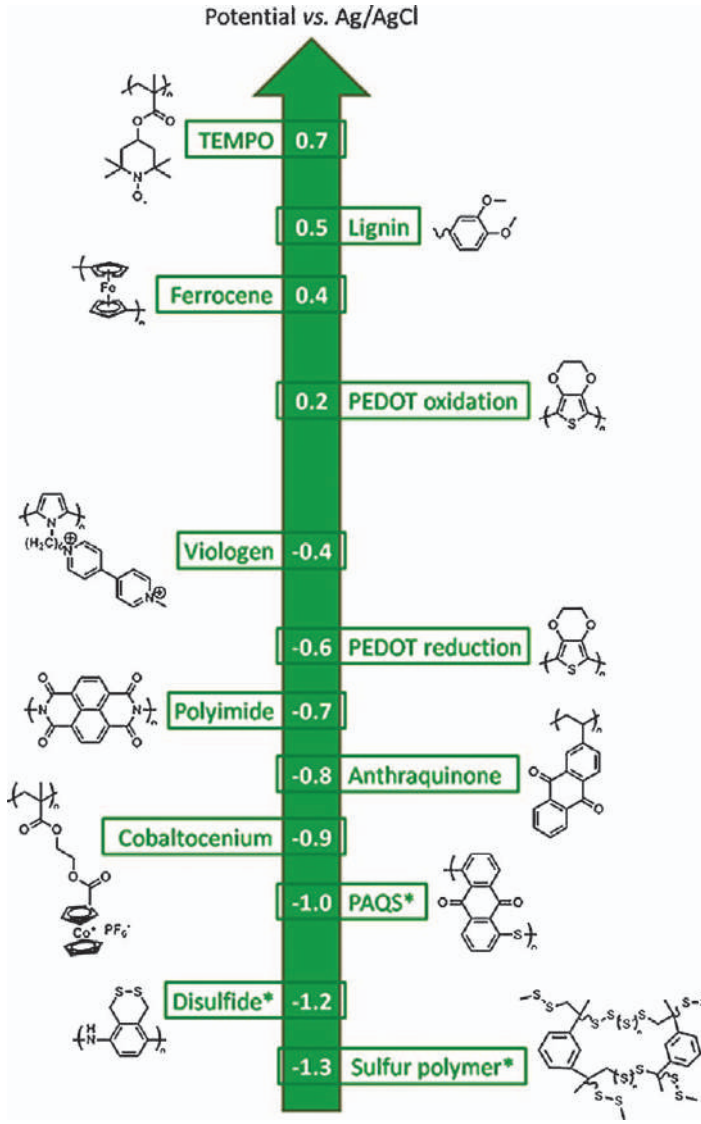


**Figure 9.6** Reversible oxidation/reduction potential of common redox couples found in redox polymers. Potential values are taken from $Li/Li^+$ reference electrode and changed to Ag/AgCl ($Li/Li^+$ is −3.26 V *vs.* Ag/AgCl). Reproduced from ref. 57 with permission from Elsevier, Copyright 2016.

reaction[75]) to enable the immobilization of the enzyme on the redox-polymer surface.[38,57] More recently, Os complexes that bear chelating N-heterocyclic and bipyridine ligands have been synthesized. These units can wire enzymes with nanostructured CNT electrodes through electrografting of the redox polymer or by supramolecular π–π interactions.[76]

### 9.3.2 Kinetics of Redox-active Polymers

The rate of charge transport across redox-active polymer films is critical for the efficient transduction of the enzymatic reaction. This rate can be characterized by an apparent electron diffusion coefficient ($D_{app}$), which is estimated using nonturnover voltammetry of enzyme electrodes in the absence of the enzyme substrate.[45] Typically, the charge transport rate is limited by three processes: the intrinsic barrier to electron self-exchange between polymer-bound redox centers, the transport of ions and the motion of polymer chains (physical displacement).[45] The $D_{app}$ of redox-active polymers is significantly lower ($10^{-8}$–$10^{-9}$ $cm^2$ $s^{-1}$) than the typical $D_{app}$ of small mediators ($10^{-5}$–$10^{-6}$ $cm^2$ $s^{-1}$) as the displacement of redox centers bound to chains is neither rapid nor extensive. The $D_{app}$ stemming from a combination of physical displacement and electron hopping is expressed as:[77]

$$D_{app} = D_{phys} + \frac{k_{ex} C_E \delta^2}{6} \tag{9.7}$$

in which $D_{phys}$ is the diffusion coefficient for the physical displacement of the chains or the redox molecules, $k_{ex}$ is the bimolecular rate constant for electron self-exchange, $C_E$ stands for the concentration of redox species, and $\delta$ is the center-to-center distance between the redox centers (electron-hopping distance). Eqn (9.7) can be recombined to the following:

$$D_{app} = \frac{k_{ex}(\delta^2 + 3\lambda^2) C_E}{6} \tag{9.8}$$

where $\lambda$ is the maximum distance across which the tethered redox unit can move. Eqn (9.8) suggests that $D_{app}$ depends on the concentration of redox couple, and thus $j_{peak}$.[78] We see that polymers, for which the length of spacers between the polymer backbone and the redox unit is long, promise a boost in $D_{app}$. Long tethers can markedly improve the kinetics of the redox polymers, leading to higher power densities when compared to a redox polymer where the mediator has limited freedom of movement.[79] For example, Soukharev *et al.* showed that by wiring the enzyme's reaction centers to the polymer and adding eight-atom long tethers, $D_{app}$ could be markedly increased. For this polymer, $D_{app}$ increased by 100-fold with an overpotential of $-0.07$ V as compared to 0.37 V for platinum.[80]

While charge transport rate limits the current response of redox-active polymers, diffusion-controlled processes affect the efficiency of biocatalysis, particularly for thick polymer layers.[57] To identify the primary limiting process, CV measurements at different scan rates are performed. A linear dependence of the peak current on the scan rate indicates that diffusion of species does not limit the electron transfer rate and that the polymer adheres well to the electrode underneath. Eqn (9.9) and (9.10) describe the

behavior of two types where the redox process is limited by charge transport and diffusion, respectively:[49,81]

$$i_p = \frac{n^2F^2\Gamma}{4RT}\nu \tag{9.9}$$

where $i_p$ is the peak current, $n$ is the number of electrons, $F$ describes the Faraday constant, $\Gamma$ stands for the amount of active material adhered on the electrode surface, $\nu$ represents the scan rate, $R$ is the gas constant, and $T$ is the temperature.

$$i_p = 0.4463nFA\left(\frac{nFD}{RT}\right)^{\frac{1}{2}}C\sqrt{\nu} \tag{9.10}$$

where $A$ is the surface area of the working electrode, $D$ stands for the diffusion coefficient of the electroactive species, and $C$ describes the bulk concentration of the electroactive species. Once the CV curves are recorded, the charge associated with redox reactions can be quantified by dividing the area underneath by the scan rate. The charge normalized by the mass of the polymer on the electrode represents the specific capacity of the polymer film.[82]

## 9.4 Enzymatic Glucose/$O_2$ BFCs and Polymeric Electrodes

Glucose and $O_2$ are an ideal fuel source and oxidant, respectively, because they are readily available in all organic tissues and can be continuously replenished in biological fluids by metabolism. In a typical BFC anode, glucose is catalyzed by the biocatalyst, which is the enzyme, glucose oxidase (GOx) or glucose dehydrogenases (GDH) (Figure 9.7a). The enzyme gets reduced during this reaction. The reaction breaks glucose into gluconolactone and releases electrons, which are then scavenged by $O_2$ or transferred to other electron acceptors at the cathode. As a result, the enzyme cycles back to its natural oxidized form so that it can once more go through its reaction with glucose. Charge flows through the cell as long as glucose and $O_2$ are supplied, generating electricity from the circuit (Figure 9.7a). The half-reactions that place in a glucose/$O_2$ BFC based on redox-active polymers at the bioanode and (bio)cathode are given below:

$$\begin{aligned}
\text{Anode:}\quad & C_6H_{12}O_6 + 2OH^- \rightarrow C_6H_{12}O_7 + H_2O + 2e^- \\
\text{Cathode:}\quad & O_2 + 4H^+ + 4e^- \rightarrow 2H_2O \\
\text{Overall:}\quad & C_6H_{12}O_6 + \tfrac{1}{2}O_2 \rightarrow C_6H_{12}O_7
\end{aligned}$$

Enzymes are nature's catalysts which undergo reduction-oxidation processes thanks to specific subunits, called redox cofactors (Figure 9.7b).[20] GOx is the most common enzyme used at the bioanode owing to its stability on surfaces (up to 20 days), selectivity to glucose, high regeneration ability and commercial availability.[48] The redox cofactor of GOx is flavin adenine dinucleotide (FAD). This catalytic pocket is deeply buried inside the enzyme, hence direct electron transfer is not possible if the enzyme is in its native

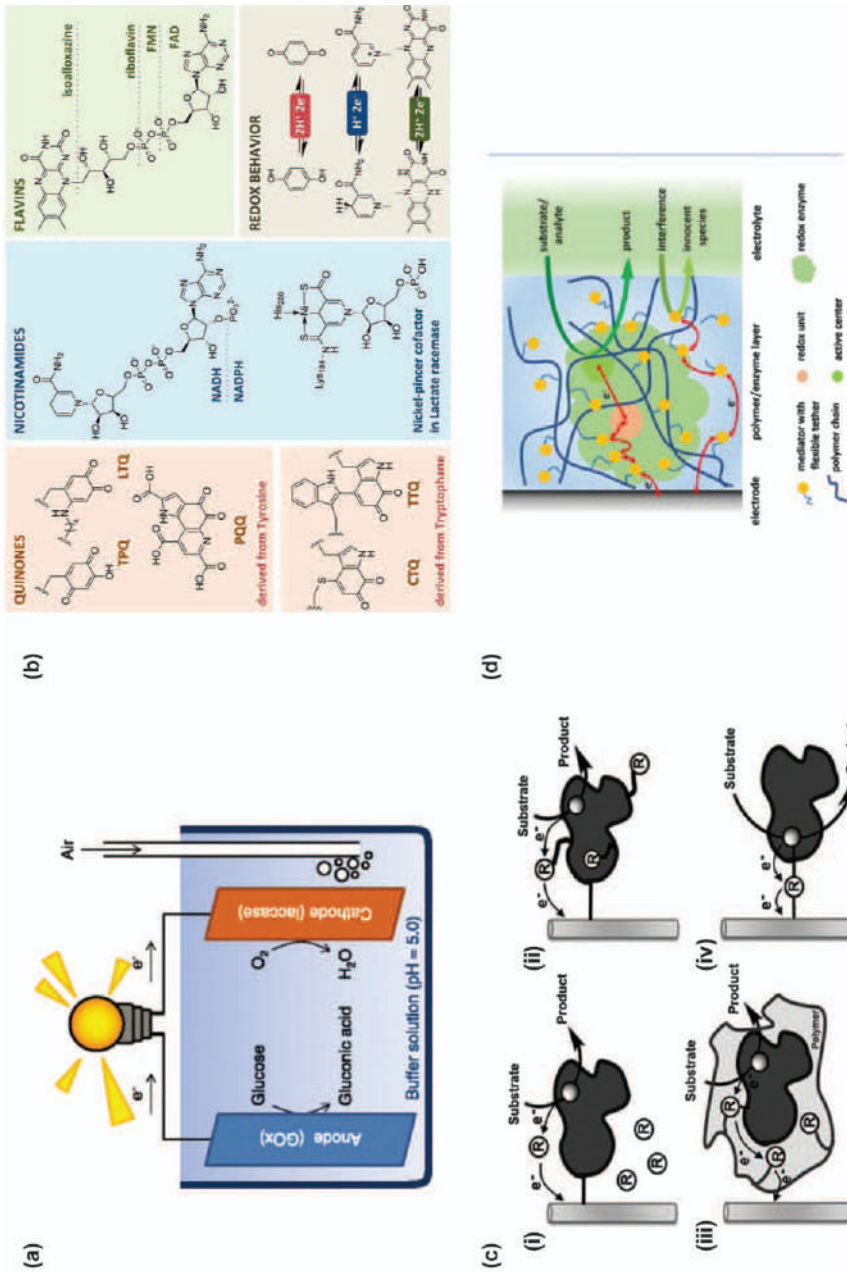
(a)
Air
e⁻
e⁻
Cathode (laccase)
O2
H2O
Glucose
Gluconic acid
Anode (GOx)
Buffer solution (pH = 5.0)
(b)
FLAVINS
Isoalloxazine
riboflavin
FMN
FAD
REDOX BEHAVIOR
2H+ 2e-
H+ 2e-
2H+ 2e-
NICOTINAMIDES
NADH
NADPH
Nickel-pincer cofactor in Lactate racemase
QUINONES
LTQ
TPQ
PQQ
derived from Tyrosine
TTQ
CTQ
derived from Tryptophane
(c)
(i)
Substrate
Product
(ii)
Substrate
Product
(iii)
Substrate
Product
Polymer
(iv)
Substrate
Product
(d)
substrate/ analyte
product
interference
innocent species
electrolyte
electrode
polymer/enzyme layer
redox enzyme
mediator with flexible tether
redox unit
polymer chain
active center

structure. Since $O_2$ competes to take GOx's electrons in its reduced state after the reaction with glucose, the oxidation current decreases alongside the production of hydrogen peroxide ($H_2O_2$). Meanwhile, the concentration of $O_2$ available to the cathode as an oxidant decreases.[48] Therefore, enzymes that do not donate electrons to $O_2$ are an excellent alternative, particularly when the BFC is controlled by the amount of $O_2$ in its compartment. GDHs (glucose dehydrogenases) are oxidoreductases that do not utilize $O_2$ as the electron acceptor and instead transfer electrons to other electron acceptors.[83] GDH can be equipped with redox cofactors found in living systems other than FAD, such as nicotine adenine dinucleotide (NAD), nicotine adenine dinucleotide phosphate (NADP) or pyrroloquinoline quinone (PQQ) (Figure 9.7b).[72,83]

For glucose/$O_2$ BFCs, $O_2$ is the oxidizer at the cathode. Besides, it is the scavenger of electrons in the absence of mediators and ET events in the bioanode (Figure 9.7b). $O_2$ is present in all organs and tissues, which makes it ideal to use as the oxidizer. If the BFC design is a closed system, it should be permeable to $O_2$. For the reduction of $O_2$ at the cathode, enzymes such as laccase (Lac) or bilirubin oxidase (BOx) from the family of enzymes called multicopper oxidases can provide efficient activity with almost no overpotential.[47] Laccases catalyze the four-electron reduction of dioxygen to water coupled with the one-electron oxidation of phenolic substrates.[84] The disadvantage of Lac lies in its optimum pH (between pH 3 and 5), hindering its compatibility with different materials that may not be stable at this pH. BOx, on the other hand, is preferred over Lac when high performance and stability at neutral pH and tolerance toward chloride anions and high temperatures are required.[85]

**Figure 9.7** (a) The two fundamental electron transfers involving reactions taking place at the bioelectrodes of a glucose/$O_2$ BFC. Reproduced from ref. 87 with permission from Elsevier, Copyright 2014. (b) Chemical structures of natural redox cofactors and their redox behavior. Reproduced from ref. 20 with permission from John Wiley and Sons, © 2020 Wiley-VCH Verlag GmbH & Co. KGaA, Weinheim. (c) Schematic illustrations showing different strategies used in the electrical wiring of enzymes and electrodes: (i) the use of solubilized redox (R) units, (ii) covalent attachment of the redox units to the exterior shell of the enzyme, (iii) immobilization of the enzymes in redox-functionalized polymeric matrices, and (iv) the enzyme linked to a redox unit-functionalized electrode surface. Adapted from ref. 88 with permission from John Wiley and Sons, © 2009 Wiley-VCH Verlag GmbH & Co. KGaA, Weinheim. (d) Schematic of a redox polymer-based enzyme electrode. The redox polymer is a hydrogel that provides a solvated environment for the embedded enzyme and serves as an electron relay matrix for the electrical wiring of the enzyme. Electron transport (red arrows) within the hydrogel film is based on self-exchange reactions between adjacent mediator species. Flexible linkers ensure high mobility of the tethered mediator species and favor self-exchange reactions. The oxidized/reduced species can come into close contact, and as such, self-exchange occurs more easily. Reproduced from ref. 54 with permission from Elsevier, Copyright 2017.

For most electrodes, the oxidoreductase enzymes do not comply with direct electron transfer at the anode surface. The sole purpose of redox-active polymers (or low-molecular-weight redox couples) is thus to mediate the electron transfer between the protein and the anode. The redox-active polymers serve as an electron-conducting relay based on self-exchange reactions among their redox species, which are accepting electrons from the reduced enzyme cofactor (Figure 9.7c). The polymer then transports these electrons to the electrode.[86] A counter process happens for the redox-active polymer at the biocathode. The prerequisite is that the redox polymer has a redox potential value close to the one of the enzyme.[57] The inherently soft nature of polymer chains and the tailored hydrophilicity *via* side chains provide a more biologically relevant, solvated environment to the enzyme. Redox polymers are expected to increase the lifetime of enzymes by creating a favorable microenvironment and interface for enzymes to bind. If the polymer films exhibit a porous architecture and water uptake, they allow for the facile diffusion of reaction species to the electrode surface. As such, redox-active polymers fulfill two essential tasks in an enzymatic BFC: (1) immobilization and/or encapsulation of the enzyme and (2) mediating the electrons to the underlying conducting substrate, hence facilitating electrical communication between the electrode underneath and the enzyme cofactor.

For establishing electrical contact with enzymes, aside from linear redox polymers, redox polymer hydrogels have been developed. Redox hydrogels are not different from redox-pendant bearing linear polymers in terms of their redox units or backbone as well as the electron conduction mechanism. The redox centers are chemically bound to the polymer backbone, but the chains are cross-linked (Figure 9.7d). The hydrogels constitute a cross-linked, porous, electron-conducting network in which water-soluble molecules can dissolve and freely diffuse. The rate of the self-exchange of electrons is fastest when the redox units are tethered to the network by flexible spacers that are between 8 and 15 atoms long.[39] As the polymer is cast on an electrode surface, it forms a film that swells substantially in water. The hydration allows for segmental mobility, which in turn increases the frequency of collisions between the redox centers.[89] The denser the cross-linker is, the lower the segmental mobility of redox centers, lowering the rate of self-exchange of electronic charges. Since redox hydrogels can host enzymes, they have a greater possibility to electrically wire the reaction centers of the enzymes to the electrode, irrespective of their spatial orientation.

Moreover, within their 3D network, they can interconnect reaction centers of multiple enzymes, leading to superior current densities compared with enzyme monolayers packed onto electrode surfaces.[39] Heller and co-workers instigated the first attempts of cross-linking the enzyme in a redox–polymer matrix.[90] Immobilization of enzyme by covalently binding it to a cross-linked polymer network provided high enzyme loading and facile transport of fuel/product from/toward the electrodes while enhancing electrode stability.[44] Another example of cross-linking entails the incorporation of photoreactive benzophenone groups into redox polymers.[91] The photochemical cross-

linking upon irradiation with UV light allowed the formation of surface-attached, water-swellable redox hydrogels, and the simple cross-linking chemistry is compatible even with polymers with no specific functionalities. Bunte *et al.* found that such bioanodes photogenerated from mixed solutions of enzyme and redox polymer yield high catalytic current responses upon the addition of glucose, even in the presence of ambient $O_2$.[36]

There are various combinations of redox polymer/enzyme electrodes in the literature used either for biosensing or for BFCs. For instance, Mano *et al.* immobilized BOx inside a cross-linked network of osmium redox copolymer made of polyacrylamide (PAA) and poly(N-vinylimidazole) (PVI).[92] The polymeric biocathode exhibited a redox potential of +0.34 V *vs.* Ag/AgCl and reduced $O_2$ under physiological conditions (pH 7.4, 0.15 M NaCl, 37 °C), reaching 5 mA $cm^{-2}$ when poised at +0.3 V *vs.* Ag/AgCl.[92] When selecting redox polymers in combination with enzymes, other than energetic and polarity compatibility, surface charges ought to be considered. The study of Nieh *et al.* on the interaction of redox polymers (poly(1-vinylimidazole) (PVI[$Fe(CN)_5$]), PVI[$Os(dcbbpy)_2Cl$] (dcbbpy = 4,4′-dicarboxy-2,2′-bipyridine) and PVI[$Os(dmebpy)_2Cl$] (dmebpy = 4,4′-dimethyl-2,2′-bipyridine) with four $H_2O_2$-generating oxidases including glucose oxidase, sarcosine oxidase, choline oxidase (ChOD) and lactate oxidase revealed that electrostatic repulsions and steric hindrance are enhanced with negatively charged polymers, reducing the activity of the oxidases.[93] A few other examples for redox polymers at bioanodes or cathodes are listed in Table 9.1.

In the following sections, we review the fabrication and performance of state-of-the-art glucose/$O_2$ biofuel cells that consist of redox-active polymers. We categorize these devices in two classes, those containing polymeric electrodes with a conjugated backbone and those bearing polymers with a redox-active unit, either pendant or integrated to the backbone. The latter group has a large bandgap due to the absence of π–π conjugation but redox activity inherent to the the special molecular units they have.

### 9.4.1 Redox-active Group-bearing Polymers in Enzymatic Glucose/O2 BFCs

Os-based redox polymers have proved to be up-and-coming candidates integrated both at the cathode and anode of glucose/$O_2$ BFCs.[57,100] Corresponding enzymes were mixed with these redox polymers, typically in addition to a cross-linker such as poly(ethylene glycol) diglycidyl ether (PEGDGE) (Table 9.2). Bioelectrodes were built by simply casting the enzyme–polymer solution onto conducting substrates or making bilayer-type architectures. Heller and co-workers explored the use of Os bearing redox polymers to construct biocatalytic electrodes, setting the state-of-the-art polymeric BFCs.[4,80,101,102] Redox polymers were later incorporated in self-powered and implantable BFC configurations. The first attempt at an implantable BFC with enzymatic catalysts was in 2001, when Katz *et al.* presented a BFC acting as a self-powered implantable biosensor. The device

(a)
(b)
(c)
pyranose dehydrogenase
bilirubin oxidase
glucose
gluconolactone
Anode
Cathode
(d)
Ferrocenyl acrylamide (FcAc)
Surface Initiated ATRP
Cu(I)Cl, Me6TREN
20% dioxane
80% water
GOX-pFcAc
GOX-ATRP initiator (GOX-Cl)
(e)
LPEI
MeOH
12 hrs, R.T.
FAD-GDH
pH 7.4
12 hrs, 4°C
Naphthoquinone-modified linear polyethyleneimine
Naphthoquinone-labeled enzyme
1,2-NQ-4-glycidyl-LPEI (NQ-4-LPEI)
1,4-NQ-2-glycidyl-LPEI (NQ-2-LPEI)
1,2-NQ-4-glycidyl-GDH (NQ-4-GDH)
1,4-NQ-2-glycidyl-GDH (NQ-2-GDH)

gave a 1 μW power output and was based on BOx and GOx immobilized Os-based complexes that made electrical connections to graphite fibers.[103]

A particular advantage of these redox polymers is their versatile chemistry. Coupling of Os complexes, which contain amine functional groups to epoxy-functionalized polymers with different compositions, has provided a new library of redox polymers with various redox potentials and physicochemical properties.[100] There are numerous protocols developed to assemble electrodes based on these polymers for instance, a cross-linking technique taking advantage of the labile $Cl^-$, substituted by the amino acid groups of the enzyme.[104]

Examples of two redox polymers based on the co-ordination of Os complexes to vinylpyridine or vinylimidazole polymers are illustrated in Figure 9.8a and b, respectively.[46] These polymers can efficiently mediate glucose oxidation with co-immobilized GOx. The redox potential of $Os^{2+/3+}$ can be tuned *via* ligand exchange reactions and/or the introduction of functional groups on the bipyridyl ligands.[13] For example, when functionalized with GOx, the Os polymers where the 2,2′-bipyridine ligands of Os (where X represents –H in Figure 9.8a and b) were replaced with 4,4′-diamino-2,2′-bipyridine (where X represents $-NH_2$ in (Figure 9.8a and b) yielded glucose oxidation currents as early as at $\sim -0.1$ V *vs.* Ag/AgCl.[105] Using a cross-linked network of GOx with poly(N-vinyl imidazole[Os(4,4′-dimethyl-2,2′-bipyridine)2Cl]$^{+/2+}$-*co*-acrylimide), Chen *et al.* built a BFC with a power density of 64 μW cm$^{-2}$ at 23 °C, while the performance increased with elevated temperatures.[59]

Besides $GO_X$, GDH was used as an enzyme incorporated with Os-based redox polymers. At the cathode side, Os polypyridine hydrogels have been effective when coupled with BOx, showcasing the use of the redox-polymers with anodic as well as cathodic components. The glucose/$O_2$ biofuel cell made from $Os^{2+/3+}$polymers at both electrodes gave a power output of 58 μW cm$^{-2}$.[106] Another demonstration is that of Cadet *et al.*, who developed a hydrogel-incorporated BFC that functions as a self-powered sensor detecting glucose in

**Figure 9.8** Structures of redox polymers based on the coordination of Os complexes directly to a vinylimidazole polymer (a) or *via* a flexible spacer to a vinylpyridine polymer (b). Reproduced from ref. 45 with permission from the Royal Society of Chemistry. (c) Schematic representation of BFC comprising a bioanode of pyranose dehydrogenase (PDH) and a PVI-bound Os mediator. Reproduced from ref. 115 with permission from the American Chemical Society, Copyright 2016. (d) Schematic representation of the ''grafting from'' ATRP reaction to produce GOx-pFcAc conjugates. Adapted from ref. 116 with permission from Elsevier, Copyright 2016. (e) Naphthoquinone derivatives used as mediators for the fabrication of highly efficient flavin adenine dinucleotide glucose dehydrogenase (FAD-GDH)-based bioanodes. The epoxide group within allows for the covalent attachment to linear poly(ethylenimine)s (LPEI) and to FAD-GDH that bears nucleophilic amino groups in its outer sphere. Reproduced from ref. 118 with permission from the Royal Society of Chemistry.

blood.[107] The anode was prepared by depositing a PEGDGE [poly(ethylene glycol) diglycidyl ether]-based hydrogel on carbon fibers, which comprises the redox polymer PVP-[Os(1,1′-dimethyl-2,2′bisimidazole)$_2$ −2-(6-methylpyridin-2yl)imidazole]$^{2+/3+}$ and GDH. The cathode consisted of the same hydrogel network, this time comprising PAA-PVI-[Os(4,4′-dichloro-2,2′-bipyridine)$_2$Cl]$^{+/2+}$ and BOx. The two polycationic Os redox polymers made electrostatic complexes with the anionic enzymes, improving their stability inside the hydrogel. The polymers had formal potentials matching those of the enzymes, ensuring efficient electron transfer. The BFC exhibited an OCV of 0.65 V, and reached an MPD of 129 μW cm$^{-2}$ at 0.38 V *vs.* Ag/AgCl with *ca.* 8 mM of glucose. Since the device generated a power density scaling with glucose content in human blood, it was employed as a sensor. The authors showed that the loss in power density over time is mainly due to delamination of the polymer from the electrode surface, whereas biofouling (20% loss) and inhibition of the enzymes played minor roles. BFC anodes are realized by using anodic enzymes other than GOx and GDH. Some of these involve cellobiose and fructose dehydrogenase (CDH). CDHs are particularly stable enzymes, and similar to GDH, they suppress $O_2$ conversion in favor of other electron acceptors and are catalytically active in a broad range of pHs.[84] Cellobiose dehydrogenase with an $Os^{2+/3+}$ polypyridine hydrogel yielded a power output of 157 μW cm$^{-2}$ by using a platinum black at the cathode.[108] Another work reported the synthesis of a pH-dependent, two-electron transfer redox polymer based on a methacrylate backbone bearing covalently bound toluidine blue units and its complex with cellobiose dehydrogenase.[109] This polymeric bioanode led to a maximum current density of 60 μA cm$^{-2}$ at −150 mV. When wired together with a BOx biocathode, the BFC gave an OCV of 0.72 V and a power density of 6.1 μW cm$^{-2}$.[109]

Other than BOx, Lac is another widely used enzyme for the cathodes of polymeric BFCs owing to its higher redox potential despite its pH-dependent activity.[110] The redox potential of the Os complex was tuned to match that of the Lac and efficiently reduce $O_2$. For instance, a Lac-entrapped modified Os-based hydrogel, namely, poly [Os(2,2′-bipyridine)$_2$(PVI)$_{10}$Cl]$^+$, led to high current densities when biased even at low potentials (*ca.* 0.2 V *vs.* Ag/AgCl) on GCE.[111] An all-Os redox polymer comprising GOx and Lac as the corresponding electrodes yielded a maximum power density of 16 μW cm$^{-2}$ and an OCV of 0.25 V at pH 7.4.[112] In another case, the $Os^{2+/3+}$ center was tethered to a (2-pyridyl)imidazole based polymer leading to a redox potential (0.72 V *vs.* NHE) close to the potential of the Lac[113] (0.78 V *vs.* NHE at pH 6.5). Shen *et al.* generated a cross-linked network of Os (4,4′-dicarboxylic acid-2,2′-bipyridine) redox units and Lac onto carbon electrodes.[114] The team found a spontaneous cross-linking reaction that involves the exchange of the inner-sphere $Cl^-$ of the Os (4,4′-dicarboxylic acid-2,2′-bipyridine) complex tethered to partially quaternized poly(4-vinylpyridine) (PVP) by a pyridine ligand of a second PVP chain. The reported composite electrode could catalyze $O_2$ electroreduction at 0.58 V (*vs.* Ag/AgCl), indicating effective ET.

Another strategy exploiting the electron mediating of redox-active polymers entails the integration of nanomaterials and metallic NPs that can wire the

enzyme-active site more effectively to the electrode surface. These nanomaterials improved the surface/volume ratio of the electrodes, allowing for the retention of redox polymer and enzyme in the film.[99] For instance, Conghaile *et al.* coupled deglycosylated pyranose dehydrogenase (PDH) as an enzyme catalyst with multiwalled carbon nanotubes (MWCNTs) alongside an Os redox polymer $[Os(4,4'\text{-dimethoxy-}2,2'\text{-bipyridine})_2(\text{poly(vinylimidazole)})_{10}Cl]^+$ (Figure 9.8c).[115] The system was cross-linked using glutaraldehyde. Incorporation of MWCNTs with the redox polymer-mediated bioelectrode surfaces caused an increase in the surface area available for enzyme coupling, and in turn, the catalytic current density.[72] The bioanode was coupled with a biocathode made of BOx, and gold (Au) NPs immobilized on an Au electrode. The resulting BFC gave a maximum power density of 73 and 6 $\mu W\,cm^{-2}$ in 5 mM glucose in human blood and saliva, respectively.[115] In another work, co-immobilized MWCNTs, $[Os(2,2'\text{-bipyridine})_2(PVI)_{10}Cl]^+$ and GOx on GCE resulted in a glucose oxidation current density of 5 $mA\,cm^{-2}$ (100 mM of glucose at 0.35 V *vs.* Ag/AgCl).[118] Current retention of 77% was attained after 24 hours of continuous amperometric testing at 37 °C, pH 7.4 buffered solution containing 100 mM of glucose. Other examples include amine-functionalized graphite electrodes modified with cross-linked films of GOx and $[Os(4,4'\text{-dimethoxy-}2,2'\text{-bipyridine})_2(PVI)_{10}Cl]^+$. The covalently anchored system led to a significant increase in glucose oxidation current density compared to glassy carbon and compared to bare graphite electrodes, the graphite which covalently immobilized the redox polymer had 70% of power retained after 24 h of operation.[119] A novel patch-type BFC device was designed and reported by Escalona-Villalpando *et al.*,[120] who immobilized lactate oxidase and the redox polymer dimethylferrocene with linear polyethyleneimine at the anode. The cathode consisted of a mixture of BOx with anthracene-modified MWCNTs. Despite not being a glucose-based BFC, this wearable BFC produced an OCV of 0.55 V and a short circuit current of 140 $\mu A\,cm^{-2}$, paving the way for new-generation wearable-type BFCs. Haddad *et al.* built a fully polymeric BFC comprising CNT-modified and $HNO_3$-treated carbon cloths that are coated with Os-complex modified redox polymers entrapping Lac or cellobiose dehydrogenase.[121] An MPD of 5.87 $mW\,cm^{-2}$ was achieved, 125 times higher than in the case of the untreated carbon cloth due to the highly porous network with an increased surface area. Tsujimura *et al.* reported a mesoporous carbon electrode coated with a hydrogel based on poly(1-vinylimidazole) complex of $[Os(bpy)_2Cl]$ (PVI-$Os(bpy)_2Cl$). They used a deglycosylated FAD-dependent GDH (d-FAD-GDH) as the biocatalyst.[122] The glucose oxidation current was as high as 100 $mA\,cm^{-2}$ at 25 °C and pH 7 due to efficient enzyme loading in the mesopores, a value 30 times higher than flat carbon electrodes functionalized with the same hydrogel. After a 220-day storage test at 4 °C, almost all of the initial catalytic current remained and 80% of it was conserved after 7 days of continuous operation at 25 °C.

Other than Os-containing redox polymers, Fc-bearing redox polymers have been widely reported[123–126] as they possess properties such as low cost, reversibility of Fc and favorable interactions with GOx despite its relatively high redox potentials.[72,127] A prime example discusses the modification of GOx with

a Fc-comprising redox polymer, namely, poly(*N*-(3-dimethyl(ferrocenyl)methylammonium bromide)propyl acrylamide) (pFcAc) (Figure 9.8d). The polymer was grown on the GOx surface using atom transfer radical polymerization.[116] The BFC comprising GOX-pFcAc bioanodes exhibited over an order of magnitude increase in current output and a fourfold increase in MPD ($\approx$1.7 μW $cm^{-2}$) compared to the BFC with GOx that was physically adsorbed on electrospun polyacrylonitrile fibers integrated with Au NPs and MWCNTs.[128] More recently, GOx and BOx were physically immobilized onto the poly(methyl methacrylate-*co*-vinylferrocene)-modified electrodes.[129] A power density of 323 μW $cm^{-2}$, a value claimed to be higher than other Fc-based fuel cells, was attained with 10 mM of glucose at 0.4 V. Another remarkable example is a redox polymer based on 1,1′-dimethylferrocene-modified linear poly(ethylenimine), which was used to build bioanodes that generated currents of up to 2 mA $cm^{-2}$ at 0.3 V *versus* SCE.[130] The BFC made thereof produced power densities of the order of 146 μW $cm^{-2}$.[130]

Regarding organic redox-active molecules, naphthoquinone (NQ) derivatives are alternative redox mediators to Os- and Fc-based redox polymer hydrogels, promising for increased power densities due to their low redox potentials.[131,132] Minteer *et al.* synthesized low redox potential NQ units that are modified with epoxy units to covalently modify the host polymer (linear polyethyleneimine, LPEI) and GDH directly (Figure 9.8e).[117] The redox potential of the anode could be controlled, ensuring a high OCV (*ca.* 0.85 V). Binding the enzyme directly to the redox sites enabled a high power of *ca.* 2.3 mW $cm^{-1}$ at 0.55 V and 100 mM of glucose as the anode was connected to a BOx-based MWCNT cathode.[117] In another study, GOx and quinone derivatives (p-benzoquinone, naphthoquinone, anthraquinone and 1,5-dihydroxyanthraquinone) were co-embedded in PEI which was then immobilized on CNT substrates.[133] The presence of the two benzene rings of NQ attracted electrons, in turn increasing the catalytic activity for glucose oxidation, corroborated from the high electron transfer rate constant of 1.1 $s^{-1}$. The BFC produced a high power density (57.4 μW $cm^{-2}$) and OCV (0.64 V).[133] Hou *et al.* reported a hydrogel bioanode based on a branched PEI comprising a 1,4-naphthoquinone derivative modified at its electron-withdrawing nitro-group.[134] This modification adjusted the formal potential of the NQ toward more positive values, and the bioanode was completed upon cross-linking the polymer into a hydrogel with the addition of FAD-dependent GDH. When this hydrogel bioanode was combined with a BOx-based biocathode, the single-compartment glucose/$O_2$ BFC produced a power output of 0.28 mW $cm^{-2}$ and an OCV of 0.69 V.

### 9.4.2 Conjugated Polymer-based Enzymatic Glucose/$O_2$ BFCs

Conjugated polymers (mostly in their doped form) have been employed in enzymatic BFCs due to their reduction–oxidation behavior in aqueous media, intrinsic conductivity and softness of their chains. The latter is envisaged to reduce the mechanical mismatch between the rigid, conducting electrode underneath and the soft enzyme. Together with the possibility to

endow the chains with different functional groups, these properties make the materials attractive for BFCs. The variability in processing methods compatible with conjugated polymers has allowed easy integration of enzymes and small redox-active compounds, and enabled different form factors for the electrodes fabricated. Due to their more extensive abundance and water stability, p-type polymers are mostly used in BFCs. Owing to their positive redox potentials, they are frequently integrated at the cathode. For instance, polypyrrole (Ppy) was doped with anionic redox-active compounds such as 2,2′-azino-bis(3-ethylbenzothiazoline-6-sulfonate) (ABTS) during its electropolymerization on conducting substrates.[135] ABTS displays reversible electrochemistry and compatible formal potential (0.62 V *vs.* SHE) compatible with Lac and BOx, ideal for use in biocathodes.[136] Ppy was electropolymerized in the presence of Lac and ABTS to form a polymeric biocathode for $O_2$ reduction, yielding current densities of 3 $mA\,cm^{-2}$ at pH 4.[137]

In the presence of suitable redox mediators, p-type conducting polymers can also be used at the anode. Zebda *et al.* have synthesized two-layered double hydroxides, $Zn_2Cr$–ABTS and $Zn_2Al$–$Fe(CN)_6$, and entrapped the redox mediators alongside the corresponding enzymes inside electropolymerized Ppy films deposited on porous tubular electrodes.[138] Entrapping enzymes in the polymer matrix retained better the enzymes than simple adsorption of the surface and increased their lifetime.[139] Lac combined with $Zn_2Cr$–ABTS cathodic electrode permitted the reduction of $O_2$, whereas the anodic electrode GOx/$Zn_2Al$–$Fe^{III}(CN)_6$ was used for the oxidation of glucose. With a two-compartment configuration comprising these Ppy electrodes, the BFC exhibited an MPD of 45 $\mu W\,cm^{-2}$ at 0.2 V. Crepaldi *et al.* fabricated bioanodes based on polyamidoamine dendrimers that immobilized GOx.[140] The bioanode further contained ferrocenium hexafluorophosphate (FHFP), entrapped in electropolymerized Ppy films. The Ppy material led to an MPD of *ca.* 130 $\mu W\,cm^{-2}$ at pH 5.0 with 100 mM of glucose.[140]

A variety of redox mediators such as porphyrin, Fc, Os and Ru complexes have been entrapped in electropolymerized Ppy, and some act as functional dopants.[141–145] Ppy films comprising FHFP and PQQ promoted ET between GOx and the carbon electrode underneath.[146] Ppy combined with bis-(bipyridine)-(5-amino-phenanthroline) ruthenium bis(hexafluorophosphate) and 4,4-sulfonyldiphenol allowed for ET events at the Lac biocathode.[146] When the electropolymerization was performed in ultrapure water, thicker Ppy films with high conductance could be made.[146] The BFC made of these films showed an MPD of 3.1 $\mu W\,mm^{-2}$ at 0.28 V in PBS (pH 7.4). In human serum, the same cell generated 1.6 $\mu W\,mm^{-2}$ at 0.21 V, despite losing ~11% of its power density each day during a 3-day continuous operation.[146] Cardoso *et al.* prepared Lac-based biocathodes containing different redox mediator species, namely porphyrin, Fc, Os and Ru complexes, all entrapped in an electropolymerized Ppy matrix that is immobilized on carbon-based platforms.[140] Methanol/$O_2$ BFCs reached MPD values of 81 and 71 $\mu W\,cm^{-2}$ for the [Ru(bpy)$_2$Cl$_2$] and [Os(bpy)$_2$Cl$_2$] complexes at pH 4.5, respectively.

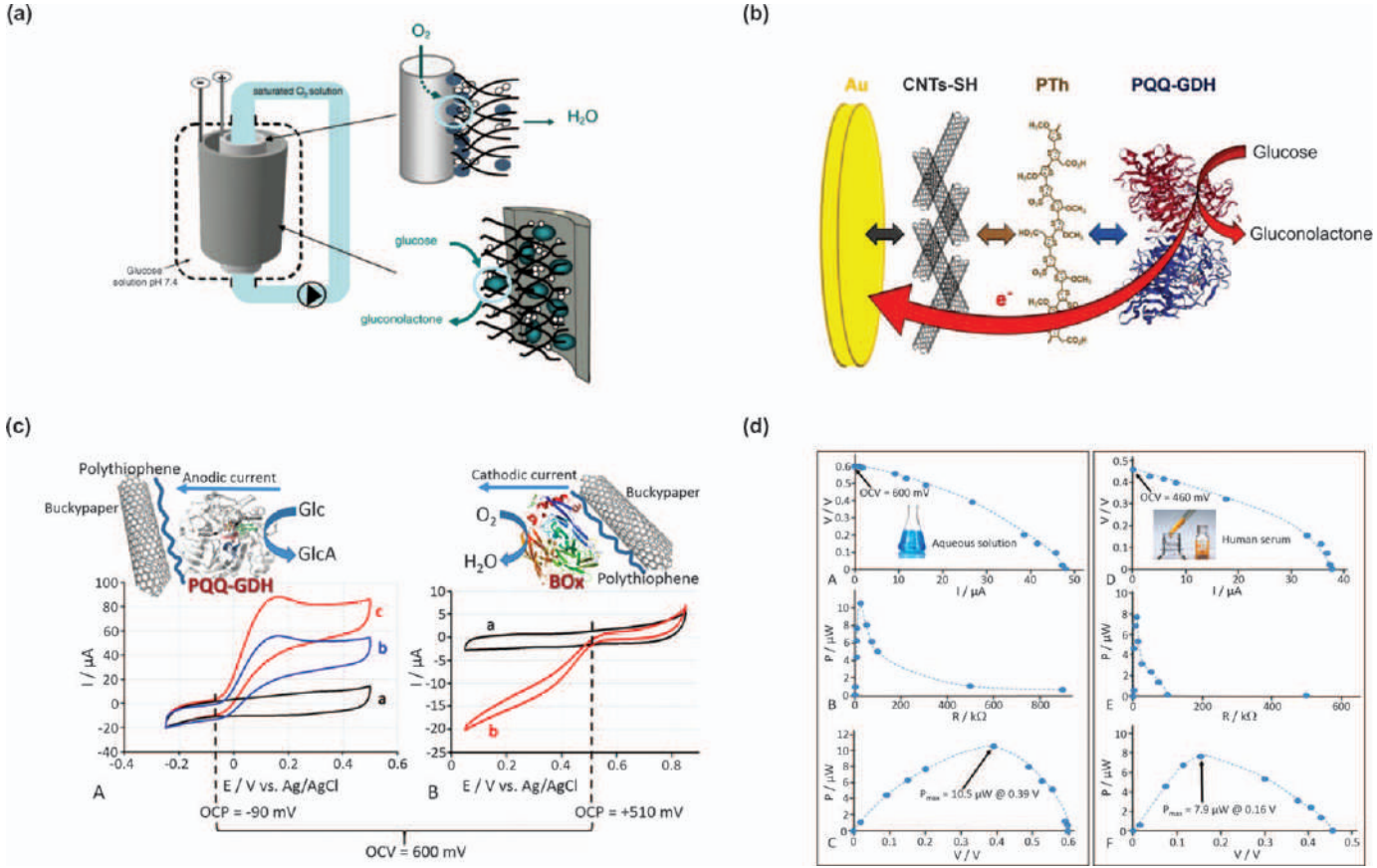
(a)
O2
saturated O2 solution
H2O
glucose
gluconolactone
Glucose solution pH 7.4
(b)
Au
CNTs-SH
PTh
PQQ-GDH
Glucose
Gluconolactone
e-
(c)
Polythiophene
Anodic current
Buckypaper
Glc
GlcA
PQQ-GDH
Cathodic current
Buckypaper
O2
H2O
BOx
Polythiophene
I / µA
E / V vs. Ag/AgCl
A
B
OCP = -90 mV
OCP = +510 mV
OCV = 600 mV
(d)
OCV = 600 mV
Aqueous solution
OCV = 460 mV
Human serum
V / V
I / µA
P / µW
R / kΩ
Pmax = 10.5 µW @ 0.39 V
Pmax = 7.9 µW @ 0.16 V

PPy-based BFC electrodes have been modified with other high-performance carbon nanomaterials. For instance, MWCNT electrodes were functionalized through the electropolymerization of pyrrole monomers that contain pyrene or *N*-hydroxysuccinimide groups.[147] These groups immobilized Lac *via* chemical grafting or noncovalent binding and resulted in high $O_2$ reduction currents (1.85 mA $cm^{-2}$) and enzyme stability (50% after 1 month).[147] Thanks to the ease of chemical modification of the monomer, enzymes can be covalently bound to the conjugated polymer instead of physical entrapment, preventing their leaching and ensuring more stable systems. Merle *et al.* built bioelectrodes where GOx and Lac were covalently grafted onto a poly(-aminopropylpyrrole), which was then electropolymerized onto an electrode surface.[148] The amino groups of the conjugated polymer film reacted with the enzymes, and the flexible alkyl spacer used between the components preserved the enzymatic activity against the denaturation of enzymes. Two redox mediators (HQS and ABTS, at the anode and cathode, respectively) were immobilized in a hydrogel network cast on top of these enzyme-polymer electrodes. The MPD of the resulting BFC was *ca.* 20 μW $cm^{-2}$ with 10 mM glucose in PBS (pH 7.4), and remained constant after intermitted use over 45 days.

Another strategy entailed the use of Ppy as a conducting encapsulation layer. Habrioux *et al.* coated enzymes (BOx and GOx) and mediators (ABTS and HQS) on two carbon tubes, which were encapsulated and separated by an electropolymerized Ppy film (Figure 9.9a).[149] The Ppy film separated the anode and cathode in a tubular, concentric configuration, and dissolved $O_2$ was supplied to the cathode separately from the electrolyte. In this

**Figure 9.9** (a) Schematic configuration of the compartmentalized glucose/$O_2$ BFC where Ppy entraps the components on porous carbon electrodes. Reproduced from ref. 150 with permission from Elsevier, Copyright 2008. (b) Polymer-supported electron transfer of PQQ-dependent glucose dehydrogenase (GDH) at carbon nanotubes (CNTs) modified with electropolymerized polythiophene (PTh) copolymer. Reproduced from ref. 153 with permission from Elsevier, Copyright 2017. (c) CV curves obtained with the PQQ-GDH-modified electrode measured in the absence (curve a) and presence of glucose, 5 and 20 mM (curves b and c, respectively) (A). CV curves obtained with the BOx-modified electrode measured under anaerobic conditions (curve a) and in the presence of $O_2$ (in equilibrium with air, curve b) (B). Background electrolyte was 50 mM phosphate buffer, pH 7.4, containing 100 mM $Na_2SO_4$. Abbreviations used: PQQ-dependent glucose dehydrogenase; BOx: bilirubin oxidase; Glc: glucose; GlcA: gluconic acid (product of Glc biocatalytic oxidation); OCP: open circuit potential (measured *vs.* the reference electrode); OCV is measured between two biocatalytic electrodes. Reproduced from ref. 155 with permission from John Wiley and Sons, © 2020 Wiley-VCH Verlag GmbH & Co. KGaA, Weinheim. (d) Biofuel cell polarization curves and the power release measured with 50 mM phosphate buffer, pH 7.3, containing 100 mM $Na_2SO_4$ and 20 mM glucose (left), or with human serum containing *ca.* 6 mM of glucose (right). Solutions contain $O_2$. The circles in the plots reflect the experimental distribution of the measured parameters. Reproduced from ref. 155 with permission from John Wiley and Sons, © 2020 Wiley-VCH Verlag GmbH & Co. KGaA, Weinheim.

configuration, $O_2$ circulating through the inside of the cathode tube diffused to the external surface of the tube to react with the immobilized BOx.[149] This BFC generated an MPD of *ca.* 42 $\mu W\,cm^{-2}$ at 0.3 V in PBS with 10 mM of glucose.[149] Ppy is also compatible with the layer-by-layer deposition technique to fabricate enzymatic bioanodes.[150] A bioanode was fabricated on a GCE that comprised Ppy, silver NPs, graphene oxide as the electroactive part and horse spleen ferritin protein, and GOx as the catalysts deposited in a layer-by-layer fashion.[151] The electrode yielded a current response of 5.7 $mA\,cm^{-2}$.[151]

Thiophene-based polymers have been also used in bioelectrocatalysis. For instance, the $O_2$-insensitive enzyme, pyrroloquinoline quinone-dependent glucose dehydrogenase (PQQ-GDH), was covalently bound to a PT copolymer electropolymerized on MWCNTs[152] (Figure 9.9b). While the copolymer acted as an immobilization reagent, it allowed for the electrochemical wiring of PQQ-GDH and transferred electrons generated upon glucose oxidation to the electrode, indicated by an anodic current at 0 V *vs.* Ag/AgCl.[153] The OCV of this bioanode in the presence of 5 mM glucose was −0.22 V *vs.* Ag/AgCl, reflecting the efficient communication between PQQ-GDH and MWCNTs.[153]

In another work comprising PT-based polymers, Lac was physically adsorbed on a copolymer containing 3-methylthiophene and thiophene-3-acetic acid, generating a conducting polymer biocathode that gave a large $O_2$ reduction current (*i.e.*, 87 $\mu A\,cm^{-2}$).[155] The same copolymer was used in a BFC comprising the GOx/copolymer at the anode and the BOx/copolymer at the cathode, yielding an MPD of 0.15 $mW\,cm^{-2}$ at 0.35 V.[156] A PQQ-GDH-modified thiophene copolymer film electropolymerized on a Bucky paper composed of compressed MWCNTs was coupled to a (BOx)-MWCNT-based biocathode in a membrane-free configuration (Figure 9.9c).[154] The PQQ-GDH-modified electrode oxidized glucose at potentials more positive than −0.09 mV, and the BOx-modified electrode reduced $O_2$ at potentials more negative than +0.51 mV (Figure 9.9c).[154] A BFC based on these components was built in a small geometry ($2\times3\times2\ mm^3$) and tested in human serum as well as in a living gray garden slug. The BFC power was dependent on glucose and varied between 2–10 μW. In blood, the OCV and power values were lower than those obtained in the buffer (Figure 9.9d). When implanted in the animal which has a typical glucose concentration of *ca.* 0.7 mM in its hemolymph (blood like biofluid of invertebrates), the OCV was *ca.* 0.31 mV and the MPD was 200 $\mu W\,cm^{-3}$, smaller by a factor of *ca.* 2.4 compared to buffer conditions.[154]

Polyaniline (PANI) is another conducting polymer used in BFCs. PANI nanowires have been electrochemically grown on reduced graphene oxide electrode, which was bound to positive-charged (oxidized) PANI nanowire surfaces *via* electrostatic interactions.[157] A bioanode was fabricated as fructose dehydrogenase integrated into the PANI construct. When combined with a Lac-functionalized PT copolymer film, this BFC exhibited an OCV of 0.55 V and a power density of 0.36 $mW\,cm^{-2}$ at a cell voltage of 0.3 V in an $O_2$-saturated acetate buffer solution (0.05 M, pH = 4.5) with 0.2 M of fructose.[158] In addition,

PANI has been reported to electrocatalytically reduce dissolved $O_2$ in acidic conditions, which makes it a promising cathode material.[159]

A similar property is identified for EDOT derivatives, most effective when the polymer is in the reduced (undoped) state. Ohayon *et al.* electropolymerized a copolymer of PEDOT with hydroxyl PEDOT [*i.e.*, p(PEDOT:EDOTOH)] and showed its electrocatalytic activity towards $O_2$ reduction.[160] This polymer film acted as the cathode of a glucose/$O_2$ fuel cell. The anode was an n-type semiconducting polymer (NDI-T2) that was functionalized with an adsorbed layer of GOx (Figure 9.10a and b).[160] The polymer film acted as a redox mediator and a semiconductor and had direct communication with the enzyme, which resulted in an increase in its conductivity upon oxidation of glucose. The BFC generated *ca.* 0.3 V alongside an MPD of 2.8 $\mu W\,cm^{-2}$ for 10 mM of glucose in PBS (Figure 9.10c). The bioelectrode could operate in a complex medium such as human saliva and the polymeric BFC was also used as a circuit component (Figure 9.10d and e). This report is the first demonstration of an enzymatic fuel cell that does not rely on redox mediators while using the conjugated polymers as catalysts.[160]

In addition to the experimental work on redox-polymers in BFCs, computational studies have been reported as early as 2009 as a means to complement further and understand these systems. The outcome of these simulation studies highlights the impact of enzyme loading in the catalyst layer, electrode surface area, and hydrogel film thickness on the performance of the BFC.[79,161,162] Table 9.2 summarizes the performance of the components of selected BFCs that comprise redox-active polymers.

## 9.5 Conclusions and Outlook

Redox-active polymers have received a great deal of attention due to their practicality and effectiveness in an array of energy-storage devices, including BFCs, where they act as electroactive components coating more conducting substrates. The most appealing property of these materials is the wide range of selection of redox-active units and backbones alongside the ease of processing into various forms. It is possible to change the redox potentials, hence the compatibility with the enzymes selected at the electrodes by changing the chemistry of the redox units, their polarity, and how they are bound to the main chain (length of spacers), all affecting the final properties of the polymer. A new polymer tailored to the desired features can be realized via simple chemical modifications, giving a handle to control electron transfer rates and interaction with enzymes as well as reaction species. BFCs, in general, offer competitive advantages over conventional power sources. These include the utilization of renewable and nontoxic components, high reaction selectivity and activity of the biocatalysts, an abundance of biofuels, and physiological operating conditions (human body temperature and near-neutral pH).[184] Next-generation redox-active polymers will certainly need macromolecular engineering to improve their properties. Adapting the

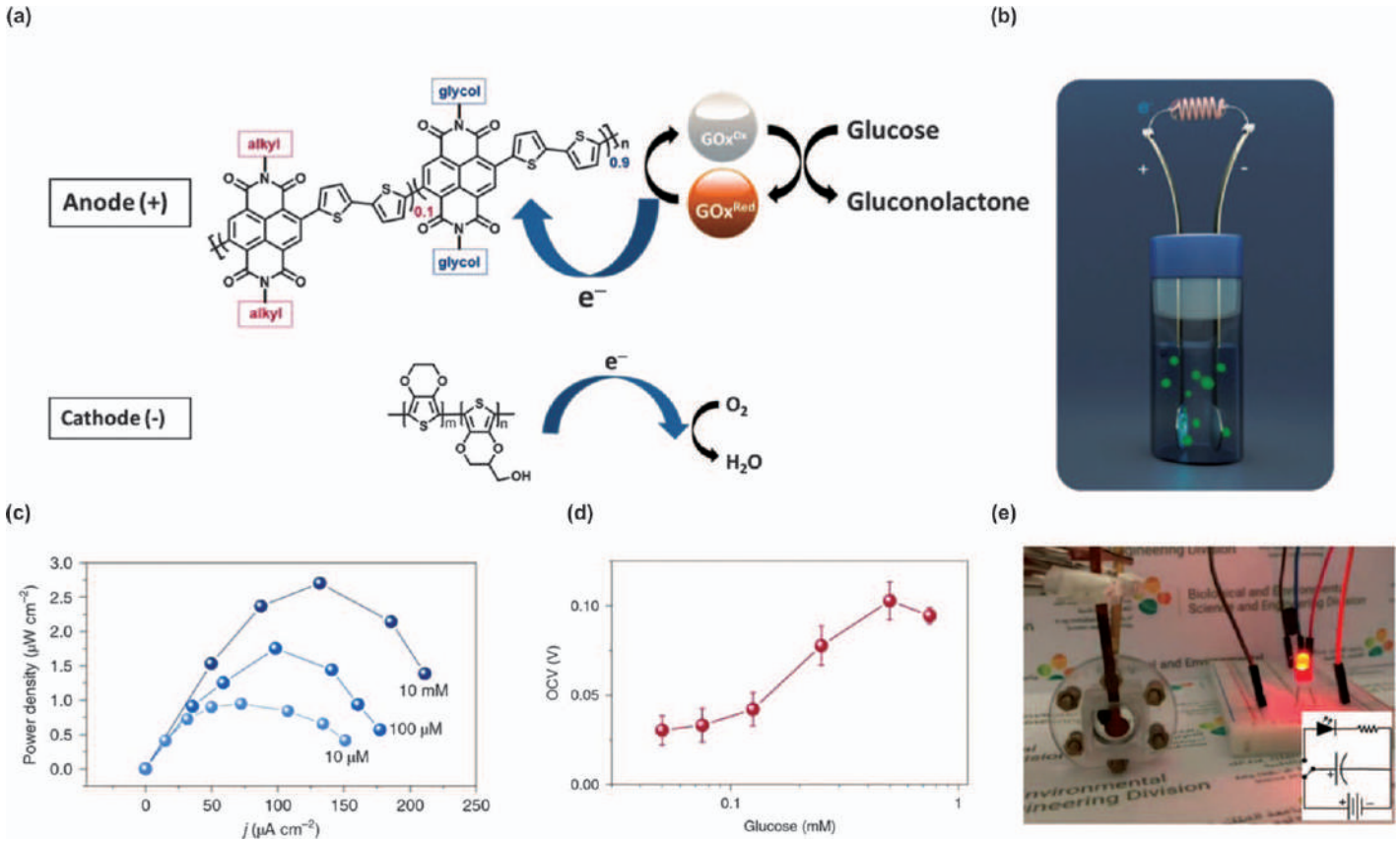


**Figure 9.10** (a) The chemical structure of the n-type copolymer used as the anode. At the anode, electrons from the enzymatic oxidation of glucose by GOx are transferred to the n-type polymer, while p(EDOT-*co*-EDOTOH) electropolymerized at the cathode performs $O_2$ reduction reaction. (b) A schematic of the simple assembly of BFC electrodes. (c, d) The figures of merit of the EFC (power density and open-circuit voltage, OCV) scales with the glucose concentration of the electrolyte. The electrolyte is PBS in (c) and human saliva in (d). (e) Digital photograph of the EFC switching on a light-emitting diode. Inset: configuration of the electrical circuit. Reproduced from ref. 162 with permission from Springer Nature, Copyright 2019.

properties of redox polymers for BFCs will allow immobilization of enzyme more effectively, facilitate electron transfer, design new 3D enzyme–electrode interfaces, and protective matrices, altogether enhancing the power and energy density and, most importantly, the operational stability of the devices. In addition, as the interest in wearable and implantable electronics grows, we will need green power sources coming from the BFCs to power the biosensors and bioactuators. Despite the presence of technical obstacles to overcome, there is a wide range of applications for BFCs. We envision that the next era will see the development of redox-active polymers that are furnished with extra functionalities. These will include biodegradability, flexibility, and self-healing, which will be as crucial as high power outputs for niche applications. For these wearable and implantable device configurations, next-generation redox-active polymers must endorse patterning in small dimensions, where direct electron transfer and effective enzyme immobilization will be needed more than ever.

## Abbreviations

| | |
|---|---|
| An | Anthracene |
| AmPDH | Pyranose dehydrogenase from *Agaricus meleagris* |
| ABTS | 2,2′-azinobis (3-ethylbenzothiazoline-6-sulfonate) diammonium salt |
| BOD | Bilirubin oxidase |
| BMCO | Blue multicopper oxidases |
| BP | Bucky paper |
| BSA | Bovine serum albumin |
| CDH | Cellobiose dehydrogenase |
| CtCDH | *Corynascus thermophiles* cellobiose dehydrogenase |
| CNF | Carbon nanofiber |
| CMFs | Carbon microfibers |
| CAT | Catalase |
| DvMF | *Desulfovibrio vulgaris* Miyazaki F |
| DvH | *Desulfovibrio vulgaris* Hildenborough |
| Dp | Diaphorase |
| $DH_{CtCDH}$ | *Corynascus thermophilus* cellobiose dehydrogenase |
| EDC | 1-ethyl-3-(3-dimethylaminopropyl) carbodiimide |
| EDT | 2,2′-(ethylenedioxy)diethanethiol |
| EGDGE | Ethylene glycol diglycidyl ether |
| FAD-CtCDH | Lavodehydrogenase domain of cellubiose dehydrogenase from *Corynascus thermophiles* |
| FADGDH | Flavin adenine dinucleotide-dependent glucose dehydrogenase |
| fBP | Functionalized Bucky paper |
| FDH | Fructose dehydrogenase |
| GDH | Glucose dehydrogenase |

| | |
|---|---|
| GCE | Glassy carbon electrode |
| GA | Glutaraldehyde |
| HQS | Hydroxyquinolinone-5-sulfonic acid hydrate |
| HRP | Horseradish peroxidase |
| KB | Ketjen black |
| LOx | Lactate oxidase |
| Lac | Laccase |
| MPD | Maximum power density |
| mp | microperoxidase |
| MvBOx | Bilirubin oxidase from *Myrothecium verrucaria* |
| MG | Methylene green |
| MvBOd | *Myrothecium verrucaria* bilirubin oxidase |
| MgOC | MgO-templated carbon |
| MP-11 | Microperoxidase-11 |
| NADH | 1,4-dihydronicotinamide adenine dinucleotide |
| NHS | *N*-hydroxysuccinimide |
| SHE | Standard hydrogen electrode |
| ORR | Oxygen reduction reaction |
| $Os(dmobpy)_2PVI$ | [Os(4,4′- dimethoxy-2,2′-bipyridine)$_2$(polyvinyl imidazole)$_{10}$Cl]Cl |
| PEGDGE | Polyethylene glycol diglycidyl ether |
| PVI | Poly(vinylimidazole) |
| PQQ | Pyrroloquinoline quinone |
| PQQ-sGDH | Apo-enzyme of PQQ-dependent soluble glucose dehydrogenase |
| Ppy | Polypyrrole |
| $P(N_3MA\text{-}BA\text{-}GMA)$ | Poly(3-azido-propyl methacrylate-*co*-butyl acrylate-*co*-glycidyl methacrylate)-viologen |
| $Py_2Ox$ | Pyranose oxidase |
| P(SS-GMA-BA) | Poly(4-styrene sulfonate-*co*-glycidyl methacrylate-*co*-butyl acrylate |
| PQQ-GDH | Pyrroloquinoline quinone-dependent glucose dehydrogenase |
| PANAM | Polyamidoamine |
| PAA | Poluanionic poly(acrylic acid) |
| P(GMA-BA-NIPA | Poly(glycidyl methacrylate-*co*-butyl acrylate-*co*-*N*-isopropylacrylamide) |
| Poly(MMA-*co*-VFc) | Poly(methyl methacrylate-*co*-vinylferrocene) |
| Poly(TAA-*co*-MT) | Poly(3-thiopheneacetic acid-*co*-3-methylthiophene) |
| PaoABC | Aldehyde oxidoreductase isolated from *Escherichia coli* |
| PG | Pyrolytic graphite |
| PBS | Phosphate saline buffer |
| PABMSA | Poly(3-aminobenzoic acid-*co*-2methoxyaniline-5-sulfonic acid) |
| PPF | Pyrolyzed photoresist film |

| | |
|---|---|
| WrbA | Tryptophan (W) repressor-binding proteins from *Escherichia coli* (EcWrbA) and *Archaeoglobus fulgidus* (AfWrbA) |
| Tre | Trehalase |
| ThLacc | *Trametes hirsuta* laccase |
| TB | Toluidine Blue |
| Tr | Disaccharide trehalose |
| TMPD | *N,N,N′,N′*-tetramethyl-*p*-phenylenediamine |
| TBAB | Tetrabutylammonium bromide. |

## References


1. Z. Ghassemi and G. Slaughter, *Membranes*, 2017, **7**, 3.
2. X.-Y. Yang, G. Tian, N. Jiang and B. L. Su, *Energy Environ. Sci.*, 2012, **5**, 5540–5563.
3. S. Shleev, L. Gorton and A. Bergel, *Bioelectrochemistry*, 2015, **106**, 1–248.
4. M. Falk, C. W. Narváez Villarrubia, S. Babanova, P. Atanassov and S. Shleev, *ChemPhysChem*, 2013, **14**, 2045–2058.
5. F. Mashayekhi Mazar, M. Alijanianzadeh, Z. Jamshidy Nia and A. Molaei Rad, *Energy Sources, Part A*, 2017, **39**, 419–425.
6. R. A. Bullen, T. C. Arnot, J. B. Lakeman and F. C. Walsh, *Biosens. Bioelectron.*, 2006, **21**, 2015–2045.
7. A. T. Yahiro, S. M. Lee and D. O. Kimble, *Biochim. Biophys. Acta, Spec. Sect. Biophys. Subj.*, 1964, **88**, 375–383.
8. Y. Song and C. Wang, *Microsyst. Nanoeng.*, 2019, **5**, 46.
9. A. Heller, *Phys. Chem. Chem. Phys.*, 2004, **6**, 209–216.
10. Y. Song and C. Wang, *Microsyst. Nanoeng.*, 2019, **5**, 46.
11. F. Barrière, Y. Ferry, D. Rochefort and D. Leech, *Electrochem. Commun.*, 2004, **6**, 237–241.
12. A. De Poulpiquet, A. Ciaccafava and E. Lojou, *Electrochim. Acta*, 2014, **126**, 104–114.
13. D. Leech, P. Kavanagh and W. Schuhmann, *Electrochim. Acta*, 2012, **84**, 223–234.
14. S. Cosnier, A. J. Gross, F. Giroud and M. Holzinger, *Curr. Opin. Electrochem.*, 2018, **12**, 148–155.
15. L. Carrette, K. A. Friedrich and U. Stimming, *ChemPhysChem*, 2000, **1**, 162–193.
16. G. D. Najafpour, Biofuel Production, *Biochemical Engineering and Biotechnology*, 2nd edn, Elsevier, Amsterdam, 2015, pp. 527–555.
17. V. Oncescu and D. Erickson, *Sci. Rep.*, 2013, **3**, 1226.
18. P. Atanassov, M. Y. El-Naggar, S. Cosnier and U. Schröder, *ChemElectroChem*, 2014, **1**, 1702–1704.
19. R. A. S. Luz, A. R. Pereira, J. C. P. de Souza, F. C. P. F. Sales and F. N. Crespilho, *ChemElectroChem*, 2014, **1**, 1751–1777.

20. M. Desage-El Murr, *ChemCatChem*, 2020, **12**, 53–62.
21. L. Stoica, N. Dimcheva, Y. Ackermann, K. Karnicka, D. A. Guschin, P. J. Kulesza, J. Rogalski, D. Haltrich, R. Ludwig and L. Gorton, *Fuel Cells*, 2009, **9**, 53–62.
22. S. Shleev, V. Andoralov, D. Pankratov, M. Falk, O. Aleksejeva and Z. Blum, *Electroanalysis*, 2016, **28**, 2270–2287.
23. X. Xiao, H. Xia, R. Wu, L. Bai, L. Yan, E. Magner, S. Cosnier, E. Lojou, Z. Zhu and A. Liu, *Chem. Rev.*, 2019, **119**, 9509–9558.
24. P. Atanassov, C. Apblett, S. Banta, S. Brozik, S. C. Barton, M. Cooney, B. Y. Liaw, S. Mukerjee and S. D. Minteer, *Interface Electrochem. Soc.*, 2007, **16**, 28–31.
25. S. Cosnier, M. Holzinger and A. Le Goff, *Front. Bioeng. Biotechnol.*, 2014, **2**, 45.
26. Y. Yan, W. Zheng, L. Su and L. Mao, *Adv. Mater.*, 2006, **18**, 2639–2643.
27. R. L. D. Whitby, T. Fukuda, T. Maekawa, S. L. James and S. V. Mikhalovsky, *Carbon*, 2008, **46**, 949–956.
28. D. Ivnitski, K. Artyushkova, R. A. Rincon, P. Atanassov, H. R. Luckarift and G. R. Johnson, *Small*, 2008, **4**, 357–364.
29. C. Liu, S. Alwarappan, Z. Chen, X. Kong and C. Z. Li, *Biosens. Bioelectron.*, 2010, **25**, 1829–1833.
30. M. Christwardana, K. J. Kim and Y. Kwon, *Sci. Rep.*, 2016, **6**, 30128.
31. E. Katz, I. Willner and A. B. Kotlyar, *J. Electroanal. Chem.*, 1999, **479**, 64–68.
32. N. Mano, F. Mao, W. Shin, T. Chen and A. Heller, *Chem. Commun.*, 2003, 518–519.
33. B. Persson, L. Gorton, G. Johansson and A. Torstensson, *Enzyme Microb. Technol.*, 1985, **7**, 549–552.
34. S. D. Minteer, *Enzyme stabilization and immobilization*, New York, NY, Springer New York, 2017.
35. J. Zhang, X. Huang, L. Zhang, Y. Si, S. Guo, H. Su and J. Liu, *Sustain. Energy Fuels*, 2020, **4**, 68–79.
36. C. Bunte, O. Prucker, T. König and J. Rühe, *Langmuir*, 2010, **26**, 6019–6027.
37. X. Xiao, P. Ó. Conghaile, D. Leech and E. Magner, *ChemElectroChem*, 2019, **6**, 1344–1349.
38. M. J. Cooney, V. Svoboda, C. Lau, G. Martin and S. D. Minteer, *Energy Environ. Sci.*, 2008, **1**, 320–337.
39. A. Heller, *Curr. Opin. Chem. Biol.*, 2006, **10**, 664–672.
40. R. A. Marcus, *J. Phys. Chem.*, 1963, **67**, 853–857.
41. C. C. Page, C. C. Moser, X. Chen and P. L. Dutton, *Nature*, 1999, **402**, 47.
42. S. Calabrese Barton, J. Gallaway and P. Atanassov, *Chem. Rev.*, 2004, **104**, 4867–4886.
43. A. Okamoto, K. Hashimoto, K. H. Nealson and R. Nakamura, *Proc. Natl. Acad. Sci. U. S. A.*, 2013, **110**, 7856–7861.
44. M. Rasmussen, S. Abdellaoui and S. D. Minteer, *Biosens. Bioelectron.*, 2016, **76**, 91–102.

45. P. Kavanagh and D. Leech, *Phys. Chem. Chem. Phys.*, 2013, **15**, 4859–4869.
46. S. D. Minteer, B. Y. Liaw and M. J. Cooney, *Curr. Opin. Biotechnol.*, 2007, **18**, 228–234.
47. N. Mano and A. de Poulpiquet, *Chem. Rev.*, 2018, **118**, 2392–2468.
48. D. Leech, P. Kavanagh and W. Schuhmann, *Electrochim. Acta*, 2012, **84**, 223–234.
49. L. R. Faulkner and A. J. Bard, *Electrochemical Methods: Fundamentals and Applications*, John Wiley and Sons, 2002.
50. S. Babanova, Y. Hubenova, M. Mitov and P. Mandjukov, *Fuel Cells*, 2011, **11**, 824–837.
51. Y. Liang, R. Cai, D. P. Hickey, J. P. Kitt, J. M. Harris, S. D. Minteer and C. Korzeniewski, *ChemElectroChem*, 2019, **6**, 818–826.
52. B. A. Helms and D. S. Seferos, *Macromolecules*, 2019, **52**, 1349–1353.
53. R. Gracia and D. Mecerreyes, *Polym. Chem.*, 2013, **4**, 2206–2214.
54. A. Ruff, *Curr. Opin. Electrochem.*, 2017, **5**, 66–73.
55. P. Pinyou, V. Blay, L. M. Muresan and T. Noguer, *Mater. Horizons*, 2019, **6**, 1336–1358.
56. Y. Liang, Z. Chen, Y. Jing, Y. Rong, A. Facchetti and Y. Yao, *J. Am. Chem. Soc.*, 2015, **137**, 4956–4959.
57. N. Casado, G. Hernández, H. Sardon and D. Mecerreyes, *Prog. Polym. Sci.*, 2016, **52**, 107–135.
58. T. J. Ohara, R. Rajagopalan and A. Heller, *Anal. Chem.*, 1993, **65**, 3512–3517.
59. T. Chen, S. C. Barton, G. Binyamin, Z. Gao, Y. Zhang, H. H. Kim and A. Heller, *J. Am. Chem. Soc.*, 2001, **123**, 8630–8631.
60. P. N. Barlett and J. M. Cooper, *J. Electroanal. Chem.*, 1993, **362**, 1–12.
61. J. Kim, J. H. Kim and K. Ariga, *Joule*, 2017, **1**, 739–768.
62. W. Schuhmann, *Biosens. Bioelectron.*, 1995, **10**, 181–193.
63. Z. Li, M. S. Pan, L. Su, P. C. Tsai, A. F. Badel, J. M. Valle, S. L. Eiler, K. Xiang, F. R. Brushett and Y. M. Chiang, *Joule*, 2017, **1**, 306–327.
64. S. Muench, A. Wild, C. Friebe, B. Häupler, T. Janoschka and U. S. Schubert, *Chem. Rev.*, 2016, **116**, 9438–9484.
65. H. Sun, J. Gerasimov, M. Berggren and S. Fabiano, *J. Mater. Chem. C*, 2018, **6**, 11778–11784.
66. M. Berggren and G. G. Malliaras, *Science*, 2019, **364**, 233–234.
67. B. D. Paulsen, K. Tybrandt, E. Stavrinidou and J. Rivnay, *Nat. Mater.*, 2020, **19**, 13–26.
68. D. Trefz, A. Ruff, R. Tkachov, M. Wieland, M. Goll, A. Kiriy and S. Ludwigs, *J. Phys. Chem. C*, 2015, **119**, 22760–22771.
69. B. Winther-Jensen, O. Winther-Jensen, M. Forsyth and D. R. MacFarlane, *Science*, 2008, **321**, 671–674.
70. E. Mitraka, M. Gryszel, M. Vagin, M. J. Jafari, A. Singh, M. Warczak, M. Mitrakas, M. Berggren, T. Ederth, I. Zozoulenko, X. Crispin and E. D. Głowacki, *Adv. Sustainaable Syst.*, 2019, **3**, 1800110.
71. F. Mao, N. Mano and A. Heller, *J. Am. Chem. Soc.*, 2003, **125**, 4951–4957.

72. M. T. Meredith and S. D. Minteer, *Annu. Rev. Anal. Chem.*, 2012, **5**, 157–179.
73. I. Kong, *Polymers with Nano-Encapsulated Functional Polymers*, William Andrew Publishing, Boston, ch. 7, 2016, pp. 125–154.
74. D. A. Guschin, J. Castillo, N. Dimcheva and W. Schuhmann, *Anal. Bioanal. Chem.*, 2010, **398**, 1661–1673.
75. S. Pöller, Y. Beyl, J. Vivekananthan, D. A. Guschin and W. Schuhmann, *Bioelectrochemistry*, 2012, **87**, 178–184.
76. D. J. Garrett, P. Jenkins, M. I. J. Polson, D. Leech, K. H. R. Baronian and A. J. Downard, *Electrochim. Acta*, 2011, **56**, 2213–2220.
77. D. N. Blauch and J. M. Saveant, *J. Am. Chem. Soc.*, 1992, **114**, 3323–3332.
78. A. Prévoteau, O. Courjean and N. Mano, *Electrochem. Commun.*, 2010, **12**, 213–215.
79. T. Tamaki, T. Ito and T. Yamaguchi, *Fuel Cells*, 2009, **9**, 37–43.
80. V. Soukharev, N. Mano and A. Heller, *J. Am. Chem. Soc.*, 2004, **126**, 8368–8369.
81. J. Broadhead and H. C. Kuo, *Handb. Batter*, 2001, 1–2.
82. R. Ramya, R. Sivasubramanian and M. V. Sangaranarayanan, *Electrochim. Acta*, 2013, **101**, 109–129.
83. S. Ferri, K. Kojima and K. Sode, *J. Diabetes Sci. Technol.*, 2011, **5**, 1068–1076.
84. T. Nöll and G. Nöll, *Chem. Soc. Rev.*, 2011, **40**, 3564–3576.
85. N. Mano, *Appl. Microbiol. Biotechnol.*, 2012, **96**, 301–307.
86. A. Ruff, *Curr. Opin. Electrochem.*, 2017, **5**, 66–73.
87. S. Cosnier, A. Le Goff and M. Holzinger, *Electrochem. Commun.*, 2014, **38**, 19–23.
88. R. Tel-Vered and I. Willner, *ChemElectroChem*, 2014, **1**, 1778–1797.
89. J. F. Rusling and R. J. Forster, *J. Colloid Interface Sci.*, 2003, **262**, 1–15.
90. B. A. Gregg and A. Heller, *Anal. Chem.*, 1990, **62**, 258–263.
91. C. Bunte and J. Rühe, *Macromol. Rapid Commun.*, 2009, **30**, 1817–1822.
92. N. Mano, H.-H. Kim, Y. Zhang and A. Heller, *J. Am. Chem. Soc.*, 2002, **124**, 6480–6486.
93. C.-H. Nieh, S. Tsujimura, O. Shirai and K. Kano, *J. Electroanal. Chem.*, 2013, **689**, 26–30.
94. Y. Beyl, D. A. Guschin, S. Shleev and W. Schuhmann, *Electrochem. Commun.*, 2011, **13**, 474–476.
95. A. Suzuki, N. Mano and S. Tsujimura, *Electrochim. Acta*, 2017, **232**, 581–585.
96. S. Tsujimura and S. Takeuchi, *Electrochim. Acta*, 2020, 136110.
97. K. Murata, W. Akatsuka, T. Sadakane, A. Matsunaga and S. Tsujimura, *Electrochim. Acta*, 2014, **136**, 537–541.
98. M. N. Zafar, I. Aslam, R. Ludwig, G. Xu and L. Gorton, *Electrochim. Acta*, 2019, **295**, 316–324.
99. I. Osadebe and D. Leech, *ChemElectroChem*, 2014, **1**, 1988–1993.
100. P. Ó. Conghaile, S. Pöller, D. MacAodha, W. Schuhmann and D. Leech, *Biosens. Bioelectron.*, 2013, **43**, 30–37.

101. N. Mano, F. Mao and A. Heller, *J. Am. Chem. Soc.*, 2002, **124**, 12962–12963.
102. P. Rowinski, C. Kang, H. Shin and A. Heller, *Anal. Chem.*, 2007, **79**, 1173–1180.
103. E. Katz, A. F. Bückmann and I. Willner, *J. Am. Chem. Soc.*, 2001, **123**, 10752–10753.
104. Z. Gao, G. Binyamin, H. Kim, S. C. Barton, Y. Zhang and A. Heller, *Angew. Chem., Int. Ed.*, 2002, **41**, 810–813.
105. H. H. Kim, N. Mano, Y. Zhang and A. Heller, *J. Electrochem. Soc.*, 2003, **150**, A209–A213.
106. S. Tsujimura, K. Kano and T. Ikeda, *Electrochemistry*, 2002, **70**, 940–942.
107. M. Cadet, S. Gounel, C. Stines-Chaumeil, X. Brilland, J. Rouhana, F. Louerat and N. Mano, *Biosens. Bioelectron.*, 2016, **83**, 60–67.
108. F. Tasca, L. Gorton, W. Harreither, D. Haltrich, R. Ludwig and G. Nöll, *J. Phys. Chem. C*, 2008, **112**, 13668–13673.
109. M. Shao, S. Pöller, C. Sygmund, R. Ludwig and W. Schuhmann, *Electrochem. Commun.*, 2013, **29**, 59–62.
110. A. Le Goff, M. Holzinger and S. Cosnier, *Cell. Mol. Life Sci.*, 2015, **72**, 941–952.
111. P. Kavanagh, P. Jenkins and D. Leech, *Electrochem. Commun.*, 2008, **10**, 970–972.
112. F. Barrière, P. Kavanagh and D. Leech, *Electrochim. Acta*, 2006, **51**, 5187–5192.
113. Y. Ackermann, D. A. Guschin, K. Eckhard, S. Shleev and W. Schuhmann, *Electrochem. Commun.*, 2010, **12**, 640–643.
114. W. Shen, H. Deng, A. K. L. Teo and Z. Gao, *J. Power Sources*, 2013, **226**, 27–32.
115. P. Ó. Conghaile, M. Falk, D. MacAodha, M. E. Yakovleva, C. Gonaus, C. K. Peterbauer, L. Gorton, S. Shleev and D. Leech, *Anal. Chem.*, 2016, **88**, 2156–2163.
116. A. S. Campbell, H. Murata, S. Carmali, K. Matyjaszewski, M. F. Islam and A. J. Russell, *Biosens. Bioelectron.*, 2016, **86**, 446–453.
117. R. D. Milton, D. P. Hickey, S. Abdellaoui, K. Lim, F. Wu, B. Tan and S. D. Minteer, *Chem. Sci.*, 2015, **6**, 4867–4875.
118. D. MacAodha, M. L. Ferrer, P. Ó. Conghaile, P. Kavanagh and D. Leech, *Phys. Chem. Chem. Phys.*, 2012, **14**, 14667–14672.
119. S. Rengaraj, P. Kavanagh and D. Leech, *Biosens. Bioelectron.*, 2011, **30**, 294–299.
120. R. A. Escalona-Villalpando, L. G. Arriaga, S. D. Minteer and J. Ledesma-García, in *Journal of Physics: Conference Series*, IOP Publishing, **vol. 1052**, 2018, p. 12066.
121. R. Haddad, W. Xia, D. A. Guschin, S. Pöller, M. Shao, J. Vivekananthan, M. Muhler and W. Schuhmann, *Electroanalysis*, 2013, **25**, 59–67.
122. S. Tsujimura, K. Murata and W. Akatsuka, *J. Am. Chem. Soc.*, 2014, **136**, 14432–14437.
123. H. Deng, W. Shen and Z. Gao, *Sens. Actuators, B*, 2012, **168**, 238–242.

124. P. A. Fiorito, C. M. A. Brett and S. I. Córdoba, de Torresi, *Talanta*, 2006, **69**, 403–408.
125. R. Pietschnig, *Chem. Soc. Rev.*, 2016, **45**, 5216–5231.
126. C. Bunte, L. Hussein and G. A. Urban, *J. Power Sources*, 2014, **247**, 579–586.
127. J. Shim, G. Y. Kim and S.-H. Moon, *J. Electroanal. Chem.*, 2011, **653**, 14–20.
128. A. S. Campbell, H. Murata, S. Carmali, K. Matyjaszewski, M. F. Islam and A. J. Russell, *Biosens. Bioelectron.*, 2016, **86**, 446–453.
129. S. Korkut, M. S. Kiliç and B. Hazer, *Asia-Pac. J. Chem. Eng.*, 2019, **14**, e2374.
130. M. T. Meredith, D.-Y. Kao, D. Hickey, D. W. Schmidtke and D. T. Glatzhofer, *J. Electrochem. Soc.*, 2011, **158**, B166–B174.
131. D. Fapyane, Y. Lee, C. Y. Lim, J. Ahn, S. Kim and I. S. Chang, *ChemElectroChem*, 2014, **1**, 1844–1848.
132. J. He, Y. Guan and Y. Zhang, *J. Appl. Polym. Sci.*, 2013, **129**, 3070–3076.
133. K. Hyun, S. Kang and Y. Kwon, *Korean J. Chem. Eng.*, 2019, **36**, 500–504.
134. C. Hou, Q. Lang and A. Liu, *Electrochim. Acta*, 2016, **211**, 663–670.
135. H.-K. Song and G. T. R. Palmore, *Adv. Mater.*, 2006, **18**, 1764–1768.
136. W. E. Farneth, B. A. Diner, T. D. Gierke and M. B. D'Amore, *J. Electroanal. Chem.*, 2005, **581**, 190–196.
137. J. Fei, H. K. Song and G. T. R. Palmore, *Chem. Mater.*, 2007, **19**, 1565–1570.
138. A. Zebda, S. Tingry, C. Innocent, S. Cosnier, C. Forano and C. Mousty, *Electrochim. Acta*, 2011, **56**, 10378–10384.
139. G. Merle, A. Habrioux, K. Servat, M. Rolland, C. Innocent, K. B. Kokoh and S. Tingry, *Electrochim. Acta*, 2009, **54**, 2998–3003.
140. L. B. Crepaldi, S. A. Neto, F. P. Cardoso, P. Ciancaglini and A. R. De Andrade, *Electrochim. Acta*, 2014, **136**, 52–58.
141. F. P. Cardoso, S. A. Neto, L. B. Crepaldi, S. Nikolaou, V. P. Barros and A. R. De Andrade, *J. Electrochem. Soc.*, 2014, **161**, F445–F450.
142. K. Min, J. H. Ryu and Y. J. Yoo, *Biotechnol. Bioprocess Eng.*, 2010, **15**, 371–375.
143. J. Kim, S. I. Kim and K. H. Yoo, *Biosens. Bioelectron.*, 2009, **25**, 350–355.
144. M. Ammam and J. Fransaer, *Biotechnol. Bioeng.*, 2012, **109**, 1601–1609.
145. M. Şenel, *Synth. Met.*, 2011, **161**, 1861–1868.
146. M. Ammam and J. Fransaer, *Biosens. Bioelectron.*, 2010, **25**, 1474–1480.
147. N. Lalaoui, K. Elouarzaki, A. Le Goff, M. Holzinger and S. Cosnier, *Chem. Commun.*, 2013, **49**, 9281–9283.
148. G. Merle, A. Habrioux, K. Servat, M. Rolland, C. Innocent, K. B. Kokoh and S. Tingry, *Electrochim. Acta*, 2009, **54**, 2998–3003.
149. A. Habrioux, G. Merle, K. Servat, K. B. Kokoh, C. Innocent, M. Cretin and S. Tingry, *J. Electroanal. Chem.*, 2008, **622**, 97–102.
150. Z. Li, T. Konno, M. Takai and K. Ishihara, *Biosens. Bioelectron.*, 2012, **34**, 191–196.
151. R. Perveen, Inamuddin, A. Nasar, Beenish and A. M. Asiri, *Int. J. Biol. Macromol.*, 2018, **106**, 755–762.

152. G. Fusco, G. Göbel, R. Zanoni, E. Kornejew, G. Favero, F. Mazzei and F. Lisdat, *Electrochim. Acta*, 2017, **248**, 64–74.
153. G. Fusco, G. Göbel, R. Zanoni, M. P. Bracciale, G. Favero, F. Mazzei and F. Lisdat, *Biosens. Bioelectron.*, 2018, **112**, 8–17.
154. P. Bollella, I. Lee, D. Blaauw and E. Katz, *ChemPhysChem*, 2020, **21**, 120–128.
155. T. Kuwahara, K. Nakata, M. Kondo and M. Shimomura, *Synth. Met.*, 2016, **214**, 30–34.
156. T. Kuwahara, T. Homma, M. Kondo and M. Shimomura, *Synth. Met.*, 2009, **159**, 1859–1864.
157. L. Xia, J. Xia and Z. Wang, *RSC Adv.*, 2015, **5**, 93209–93214.
158. T. Kuwahara, M. Kameda, K. Isozaki, K. Toriyama, M. Kondo and M. Shimomura, *React. Funct. Polym.*, 2017, **116**, 87–91.
159. V. G. Khomenko, V. Z. Barsukov and A. S. Katashinskii, *Electrochim. Acta*, 2005, **50**, 1675–1683.
160. D. Ohayon, G. Nikiforidis, A. Savva, A. Giugni, S. Wustoni, T. Palanisamy, X. Chen, I. P. Maria, E. Di Fabrizio, P. M. F. J. Costa, I. McCulloch and S. Inal, *Nat. Mater.*, 2020, **19**, 456–463.
161. L. Rajendran, M. Kirthiga and E. Laborda, *Curr. Opin. Electrochem.*, 2017, **1**, 121–132.
162. R. Pathak and S. Basu, *Electrochim. Acta*, 2013, **113**, 42–53.
163. F. Gao, L. Viry, M. Maugey, P. Poulin and N. Mano, *Nat. Commun.*, 2010, **1**, 2.
164. F. Gao, O. Courjean and N. Mano, *Biosens. Bioelectron.*, 2009, **25**, 356–361.
165. S. Korkut and M. S. Kilic, *Environ. Prog. Sustain. Energy*, 2016, **35**, 859–866.
166. M. Shao, M. N. Zafar, M. Falk, R. Ludwig, C. Sygmund, C. K. Peterbauer, D. A. Guschin, D. MacAodha, P. Ó. Conghaile, D. Leech, M. D. Toscano, S. Shleev, W. Schuhmann and L. Gorton, *ChemPhysChem*, 2013, **14**, 2260–2269.
167. M. T. Meredith, F. Giroud and S. D. Minteer, *Electrochim. Acta*, 2012, **72**, 207–214.
168. L. Brunel, J. Denele, K. Servat, K. B. Kokoh, C. Jolivalt, C. Innocent, M. Cretin, M. Rolland and S. Tingry, *Electrochem. Commun.*, 2007, **9**, 331–336.
169. S. Cosnier, D. Shan and S.-N. Ding, *Electrochem. Commun.*, 2010, **12**, 266–269.
170. M. T. Meredith, M. Minson, D. Hickey, K. Artyushkova, D. T. Glatzhofer and S. D. Minteer, *ACS Catal.*, 2011, **1**, 1683–1690.
171. M. N. Zafar, F. Tasca, L. Gorton, E. V. Patridge, J. G. Ferry and G. Nöll, *Anal. Chem.*, 2009, **81**, 4082–4088.
172. P. Kavanagh, S. Boland, P. Jenkins and D. Leech, *Fuel Cells*, 2009, **9**, 79–84.
173. M. Cadet, X. Brilland, S. Gounel, F. Louerat and N. Mano, *ChemPhysChem*, 2013, **14**, 2097–2100.
174. P. Pinyou, A. Ruff, S. Pöller, S. Ma, R. Ludwig and W. Schuhmann, *Chem. – Eur. J.*, 2016, **22**, 5319–5326.

175. G. Göbel, M. L. Beltran, J. Mundhenk, T. Heinlein, J. Schneider and F. Lisdat, *Electrochim. Acta*, 2016, **218**, 278–284.
176. F. Sato, M. Togo, M. K. Islam, T. Matsue, J. Kosuge, N. Fukasaku, S. Kurosawa and M. Nishizawa, *Electrochem. Commun.*, 2005, **7**, 643–647.
177. A. Ruff, J. Szczesny, N. Marković, F. Conzuelo, S. Zacarias, I. A. C. Pereira, W. Lubitz and W. Schuhmann, *Nat. Commun.*, 2018, **9**, 3675.
178. F. Lopez, S. Zerria, A. Ruff and W. Schuhmann, *Electroanalysis*, 2018, **30**, 1311–1318.
179. A. Contin, S. Frasca, J. Vivekananthan, S. Leimkühler, U. Wollenberger, N. Plumeré and W. Schuhmann, *Electroanalysis*, 2015, **27**, 938–944.
180. V. Flexer, N. Brun, M. Destribats, R. Backov and N. Mano, *Phys. Chem. Chem. Phys.*, 2013, **15**, 6437–6445.
181. M. J. González-Guerrero, J. P. Esquivel, D. Sánchez-Molas, P. Godignon, F. X. Muñoz, F. J. del Campo, F. Giroud, S. D. Minteer and N. Sabaté, *Lab Chip*, 2013, **13**, 2972–2979.
182. I. Willner, G. Arad and E. Katz, *Bioelectrochem. Bioenerg.*, 1998, **44**, 209–214.
183. M. Rasmussen, R. E. Ritzmann, I. Lee, A. J. Pollack and D. Scherson, *J. Am. Chem. Soc.*, 2012, **134**, 1458–1460.
184. G. T. R. Palmore and G. M. Whitesides, *Microbial and Enzymatic Biofuel Cells*, ACS Publications, 1994, pp. 271–290.

CHAPTER 10

# *Conductive Polymers Building 3D Scaffolds for Tissue Engineering*

NURIA ALEGRET,*[a,b] ANTONIO DOMINGUEZ-ALFARO[a,c] AND DAVID MECERREYES*[a,d]

[a] POLYMAT University of the Basque Country UPV/EHU, Avenida de Tolosa 72, 20018 Donostia-San Sebastián, Spain; [b] Cardiovascular Institute, School of Medicine, Division of Cardiology, University of Colorado Denver Anschutz Medical Campus, 12700 E.19th Avenue, Bldg. P15, Aurora, CO, 80045, USA; [c] Carbon Nanobiotechnology Group, CIC biomaGUNE, Paseo de Miramón 182, 2014 Donostia-San Sebastián, Spain; [d] Ikerbasque, Basque Foundation for Science, 48013 Bilbao, Spain
*Emails: nuria.alegret@ehu.es; david.mecerreyes@ehu.es

## 10.1 Importance of using Conductive Scaffolds in Tissue Engineering

The human body works with electric signals in many functions, such as neural communication, embryonic development, tissue healing and cardiac contraction.[1] The nervous system is the largest infrastructure with electric properties, followed by the heart and other muscles.[2,3] Neurons transmit information between each other through electric synapses; heart cells produce rhythmical electrical impulses, known as beats, that travel through the entire organ and generate its contraction. On the other side, when damage takes place in a tissue, it is often accompanied by scar formation. This scar is

Polymer Chemistry Series No. 34
Redox Polymers for Energy and Nanomedicine
Edited by Nerea Casado and David Mecerreyes

Published by the Royal Society of Chemistry, www.rsc.org

insulating and cannot conduct the electricity, thus hindering the communication of the electrochemical signals between the surrounding healthy cells. Its regeneration requires the connection of a variety of physiological inputs with biochemical, mechanical and electrical changes to avoid such a barrier. For example, the activation of selected inputs can drive stem cells to migrate into the injury site and guide them to differentiate, promoting regeneration. In addition, several studies have also demonstrated that other tissues with no electric properties, such as bone marrow, use conductivity to regenerate themselves.[4] Therefore, it is essential that the materials used as supports for tissue engineering of electrically sensitive tissues must also be conductive to enhance the biological response to external stimuli.

Conducting polymers (CPs) are conjugated polymers containing an oxidized backbone, which is the main key feature that makes them electrically conductive. Conducting polymers are a particular type of redox polymer due to their ability to be oxidized and reduced in a reversible manner. In addition, to counterbalance the overall charge, negatively charged species, called dopants, are also introduced in the CP composition. The combination among the conjugated backbone, the oxidized state and the dopant allows free and rapid electronic movement along the polymeric structure. CPs are usually highly biocompatible, thus, together with their ability to provide conductivity, they have become an optimal choice for the design of devices and scaffolds with electric properties.[5] Polypyrrole (PPy), polyaniline (PANI) and poly(3,4-ethyl-enedioxythiophene) (PEDOT) have been by far the most employed CPs in tissue engineering, and are the only ones used in the development of conductive 3D architectures, as illustrated in Figure 10.1.[6]

Conductive material can not only provide a structure and mechanical properties of natural-like tissues but also transmit electrical signals between

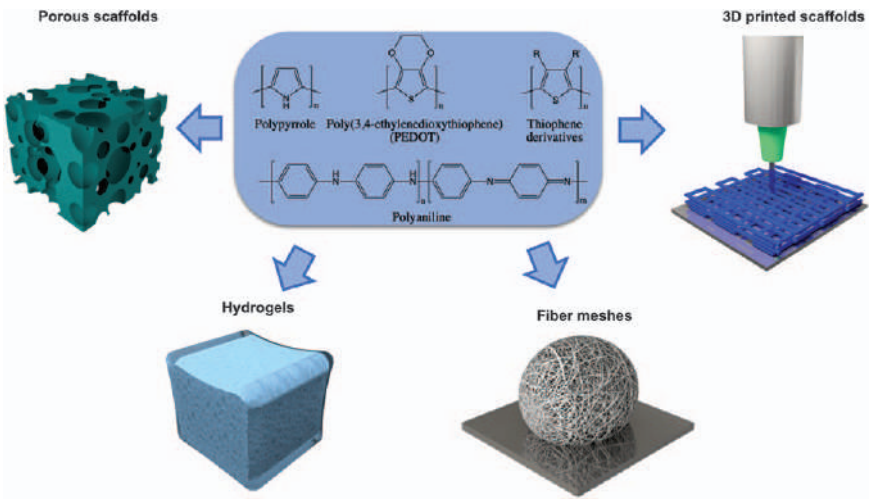


**Figure 10.1** Conductive 3D architectures manufactured from conjugated polymers.

cells. Such materials possess the ability to conduct electrical signals, binding the gap between cells, promoting their adherence, migration, proliferation, and, when required, differentiation.[7] Furthermore, they have a sensitive response against small changes or stimuli in the external environment, such as pH, temperature, light, electricity and magnetism.

### 10.1.1 Redox State Effect on Cell Cultures

Focusing on redox changes, Svennersten and co-workers showed how PEDOT:tosylate films modulated the epithelial formation using electrochemical stimulation. In 2009, it was demonstrated that changes in the redox state can be used to produce direct changes on the cell adhesion and proliferation. MDCK cells were cultured onto the different zones of the substrate, and the results confirmed the formation of tight junctions, actin stress fibers and large macromolecular focal adhesion complexes. Reduced PEDOT:tosylate films presented functional fibronectin on the surface that promoted cellular adhesion, while the oxidized state did not, due to the interference with the ECM-protein.[8]

Other cell lines such as mouse fibroblast (3T3-L1) were evaluated in redox conductive polymers. PEDOT:tosylate was also used to explore the formation of fibronectin in redox substrates culturing mouse fibroblasts on both the oxidized and reduced states. $\alpha 5\beta 1$ integrins, one of the most important receptors responsible for cell adhesion to fibronectin, were blocked to inhibit the binding through $\beta 1$ function-blocking antibody; it was identified in higher concentration in reduced states of the film.

In the final example, commercial PEDOT:PSS was also used: adhesion and protein conformation were modulated by the redox state of a conductive polymer.[9] In this case, redox performance was not only carried out onto two-dimensional material: Malliaras and co-workers replicated these results using a three-dimensional structure formed of PEDOT:PSS cross-linked with a silane. These authors showed that their three-dimensional structure was able to support fibroblast growth and find changes in the fibronectin adherence depending on the redox state.[10]

### 10.1.2 Importance of 3D Cell Cultures

To favor their acceptance in tissue engineering, the implants are required to mimic the biological environment's porosity, permeability and mechanical stability to avoid possible rejection from the host tissue. Current *in vitro* studies are based on bidimensional cell cultures to analyze the material's biocompatibility, being far from the complexity and heterogeneity of real systems. One alternative is animal models, although they are expensive and time-consuming, and the ethical issues make them unfeasible for most projects, keeping them for final studies. Thus, tridimensional scaffolds appear to be an effective strategy for tissue

regeneration not only because the result can be obtained faster, but also because they allow cultures similar to *in vivo* tissues, having large surface areas for cell or biomaterial attachment, proliferation, sensing, *etc.*[11] Several studies have demonstrated that cells have behaviors and responses when cultured in a 3D organization that is more similar to the *in vivo*, providing a more realistic predictive outcome.[12]

A suitable scaffold must obey the following characteristics: (i) porous structure in the three dimensions, with pore sizes large enough to allow cellular penetration and growth, as well as nutrient and metabolic waste flow; (ii) mechanical properties similar to the tissue of interest; and (iii) an appropriate surface composition and morphology to allow cellular adhesion and interaction.[13] The last is the main issue to ensure successful adaptability inside the biological environment. A large variety of biocompatible polymers, dopants, compositions and biomaterials have been developed as CP 3D scaffolds to regulate and improve material–cell interactions. Most are composed of a nonconductive polymer matrix coated with CPs to provide conductivity.[11]

## 10.2 Fabrication Methods of 3D Scaffolds Based on Conducting Polymers

### 10.2.1 Porous Scaffolds

The major obstacle in using CPs is the difficulty to manipulate and process them. Also, they have poor mechanical properties, *i.e.*, they are stiff, brittle and insoluble, leading the final device to suffer from delamination and poor durability. The combination of CPs with other malleable nonconductive matrices with better properties for tissue engineering has become an effective solution.[6,14] Due to their low processability, preparing 3D CP-based materials is tricky; however, the number of different strategies to manufacture these devices, summarized in Figure 10.2, has increased significantly in recent years. Such processing methods are based on the use of a

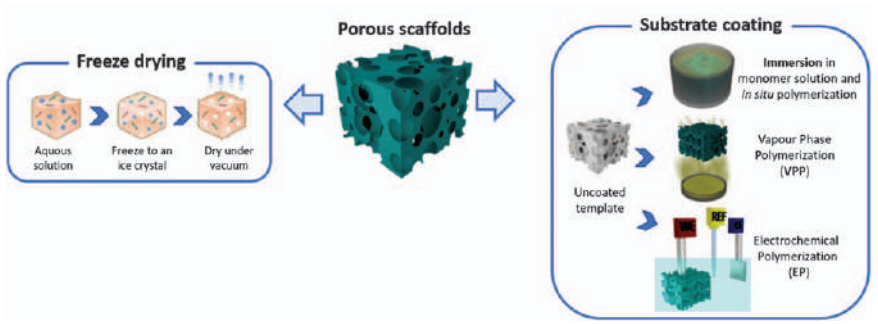


**Figure 10.2** Processing methods to manufacture porous scaffolds.

nonconducting template to define the 3D geometrical shape as well as the internal configuration, and a post-coating with CP to provide conductivity.

The nonconducting template can be formed from a previously manufactured polymer matrix or through freeze-drying or lyophilization. The latter uses frozen solvent as a template to build the tridimensional structure: the solution of interest is poured into the desired mold and frozen, and then, through ice sublimation, a cast 3D network is formed, retaining the solute particles in their original position and conformation.[15–17] Freeze-drying is a versatile and facile method to produce 3D macroporous structures with any shape and dimensions.[18] It has been demonstrated that the conditions and porosity of the final substrate can be modulated with the freezing and/or sublimation rate and temperatures.[18]

Polymerization of the monomer in solution in the presence of an oxidant and the nonconductive matrix is the most conventional method.[19] Sajesh and co-workers published the first attempt at manufacturing a 3D porous conductive scaffold in 2013. They functionalized polypyrrole (PPy) with alginate (Alg), a natural biopolymer that allows cell penetration and encapsulation, *via* chemical oxidation with $FeCl_3$ of a pyrrole solution containing Alg. Afterwards, the blend was incorporated into a chitosan solution, which was then lyophilized and cross-linked with glutaraldehyde.[20]

*In situ* polymerization is the most common method to coat a nonconductive 3D matrix with CPs.[21,22] Such a coating can be performed *via* immersion, vapor phase polymerization (VPP) or electropolymerization. Synthesis through VPP, in contrast to conventional chemical polymerizations, occurs through a monomer in its vapor state, which allows control of the deposition of highly conductive films. In this process, the 3D matrix is soaked into an oxidant solution; then placed in a closed chamber with the monomer solution. It has to be noted that both components inside the chamber must not be in direct contact. Finally, the coated substrate is rinsed in an alcohol solvent and water to remove any unreacted species. The monomer vapor can be formed through heat, high vacuum under an inert atmosphere or both.[23,24] In some cases, the vapor has been stored or produced in a separated connected chamber, and guided through pressure differences to the reacting chamber.[25] The monomer vapor polymerizes chemically when it reacts with the oxidant inside the 3D substrate. Iandolo *et al.* added pyridine or the triblock copolymer PEG-PPG-PEG into the oxidant solution to reduce the oxidant reactivity, thus slowing down the PEDOT polymerization process.[24]

In some cases, the template has been removed at the end of the polymerization and produced the 3D replica structure. As an example, polystyrene (PS) and poly(lactic-*co*-glycolic acid) (PLGA) microspheres have been used for this role, since they can be selectively eliminated by the addition of DCM.[11,26]

Apart from the chemical polymerization, also electrochemical deposition has been employed for coating 3D substrates. Song *et al.* used nickel foam as a template to manufacture foam-like scaffolds composed of reduced-

graphene oxide (rGO) and PPy.[27] They combined an electrostatic layer-by-layer (LBL) assembly methodology to first absorb the rGO nanosheets within the template *via* electrodeposition, and then polymerized PPy on top. Finally, the Ni was etched, yielding a porous flexible scaffold. In another example, a bulk sponge made of carbon nanotubes (CNTs) has been directly used as a working electrode to electrodeposit PANI using a three-electrode cell.[28]

Severt and co-workers combined both chemical and electrochemical polymerization to sequentially deposit CP onto sponge-like silk substrates.[14] They first deposited a layer of PPy chemically, and then used the resulting substrates as working electrodes for a posterior electropolymerization of either PPy, PEDOT or PEDOT-OH. The authors concluded that the second conductive layer reduced the overall resistivity and increased its stability during long-term storage.

The last processing strategy to produce porous scaffolds does not include a polymerization step, thus it is the simplest method reported. In this approach, the CPs used are commercially available, such as the commonly used PEDOT:PSS Clevios PH-1000, from Heraeus. Ding and co-workers coated a melamine sponge by immersion into a PEDOT:PSS solution.[29] Although such a strategy is the fastest and easiest to generate conductive 3D scaffolds ever published, delamination does occur more often than in the other processes abovementioned due to the weak interaction between the CP and the substrate. For this reason, instead of only dipping and letting dry, the commercial CP solutions are usually mixed with other nonconjugated polymers, placed in molds and freeze-dried.[18] Most these works used cross-linkable matrices, such as gelatin, chitosan or collagen, to improve the mechanical properties and stability of the final porous scaffolds.[16,30–32]

### 10.2.2 Hydrogels Composed of Conjugated Polymers

The highly hydrated nature, flexibility and softness of hydrogels make them outstanding biomimetic materials for soft-tissue applications.[33–35] Conductive hydrogels also provide electrical properties and can be used as bioelectrodes while interfacing with soft tissues.[36,37] Similar to the conductive porous scaffolds in the previous section, the conductivity can be incorporated by addition of CPs through polymerization before, after or even at the same time as the gel is cross-linked (Figure 10.3).[38]

Classic methodologies to produce hydrogels are easy and feasible. In most cases, these strategies used natural biopolymers, such as chitosan or gelatin, as the backbone hydrogel.[39–41] Yang *et al.* polymerized PPy chemically inside an already cross-linked alginate (Alg) hydrogel, a natural polysaccharide.[38] In their work, the authors introduced the monomer within the gel by immersion of the hydrogel in an aqueous pyrrole solution. Afterwards, the polymerization was produced by the addition of $FeCl_3$ oxidant, and obtained highly homogeneous PPy/Alg hydrogels. Using a similar strategy, Xia and co-workers filled poly(acrylic acid) (PAA) with aniline monomers and then polymerized them within the gel by immersion into an APS solution.[42] In

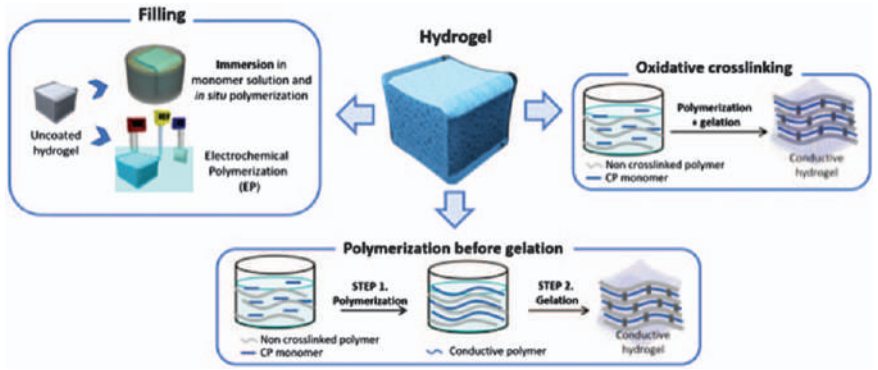


**Figure 10.3** Processing methods for manufacturing conductive hydrogels.

other examples, the order of incorporating the reagents within the hydrogel was inverted. Xu and co-workers immersed cross-linked carboxymethyl chitosan (CMCS) hydrogels into an oxidant solution of ammonium persulfate (APS), and then into EDOT/hexane solution. In this case, the authors used a vibrator to facilitate the polymerization process.[43] This effect, *i.e.*, facilitating the synthesis of the CP, has also been achieved with the incorporation of PSS inside PEG-diacrylate hydrogel matrix before the polymerization of PEDOT.[44] The hydrogel produced showed higher conductivity, which was further enhanced by $H_2SO_4$ treatment.

Electrochemical polymerization within a gel has also been performed. Mario Cheong and co-workers prepared a sericin and PVA hydrogel coated on a glass substrate with a prelayer of PEDOT/pTS.[45] This combination enhances the adherence of hydrogels to substrates and provides conductivity, making it feasible as an electrode. Then, the electropolymerization of PEDOT was achieved at low charge density, achieving a slow uniform deposition throughout the substrate. Such homogeneity is, according to the authors, essential to avoid increased voltage across the electrode, which would damage the hydrogel.

In a second strategy, CPs are polymerized at the same time that the hydrogel is cross-linked. In this case, two solutions must be prepared: one containing the biopolymer and the CP monomer, and the other the oxidant and cross-linker. Both the polymerization and gelation start as soon as the solutions are mixed.[46] Shin and co-workers reported the use of sodium periodate ($NaIO_4$) as a double agent, acting both as oxidant and cross-linker, and performed the oxidative cross-linking of PEDOT/catechol-functionalized hyaluronic acid (HA-CA).[47] Instead, Hur *et al.* took advantage of the temperature-dependent gelation of agarose to polymerize PPy inside melted agarose (40 °C) containing the oxidative agent while decreasing the temperature to RT.[48]

In the last methodology, a solution of CP, which can be synthesized in the laboratory or commercially, is the starting point. First the hydrogel precursor is added and, afterwards, the addition cross-linker forms the final gel.[49]

Using this strategy, Mawad *et al.* prepared N-(3-aminopropyl) methacrylamide hydrochloride (APMA)-derived PEDOT cross-linked with acrylic acid (AA) in the presence of poly(ethylene glycol) diacrylate (PEG-DA).[50]

Hydrogels composed of a single component, instead of the CP/nonconductive matrix mixture, have also been achieved. Dai *et al.* developed hydrogels composed uniquely of PEDOT/PSS through a kind of ionic cross-linking using an excess of $Fe^{3+}$ ions.[51] Also, gels from monomer derivatives have been synthesized *via* cross-linking of the side chains,[52] but also without such a cross-linking effect: Du and co-workers used spherical micelles composed of an amphiphilic EDOT monomer and, after oxidation, converted them into a PEDOT-based hydrogel with sheet-like building blocks.[53]

### 10.2.3 Electrospun Fiber Meshes

Fibers are the third type of 3D scaffolds used in tissue engineering.[54] Their shape and distribution mimic the extracellular matrix (ECM) more effectively than hydrogels and, in general, porous scaffolds, becoming the materials with higher potential to achieve improved cellular growth and functional expression.[55] Natural or synthesized fibers are nonconductive, and the introduction of electrical properties, unlike in the other types of scaffolds, has only been achieved through coating of the CP. In the few examples existing in the literature, the most common coating process used was chemical polymerization by immersing the 3D fibrous mesh in the corresponding monomer and oxidant solutions.[56] This has sometimes been a difficult task since the CP monomer usually prefers to polymerize within the liquid phase rather than on the fiber surface.[56] We anticipate that any of the methods used to deposit CP onto 3D substrates described so far in this chapter could also be applied in fibrous meshes. For example, Chen *et al.* reported an *in situ* interfacial polymerization of EDOT on bacterial cellulose membranes previously immersed in aqueous PSS.[57] Similarly, Yow *et al.* developed an interfacial polyelectrolyte complexation (IPC) technique, where the chemical polymerization occurred at the interphase of the aqueous solutions containing oppositely charged electrolytes.[58]

Fibers are usually synthesized in membranes using electrospinning, either randomly dispersed or patterned meshes, which are not tridimensional. Briefly, a high-voltage electrostatic field is applied to a polymer solution or melt until a charged liquid jet is formed and, as it flies toward a collector, the solvent is dried, resulting in homogeneous fibers with diameters of a few hundred nanometers. Thus, the challenge is to produce 3D structures with this approach, and there exist scarce examples in the literature that succeeded in the manufacture of 3D structures using new and original strategies. Jin *et al.* developed a special collector, consisting of a hemispheric plastic dish embedded with stainless-steel probes and covered with aluminum foil, and fabricated a 3D ''fluffy'' PPy-coated conductive fibrous PLLA scaffold.[59] In another example, Pelton and co-workers prepared a

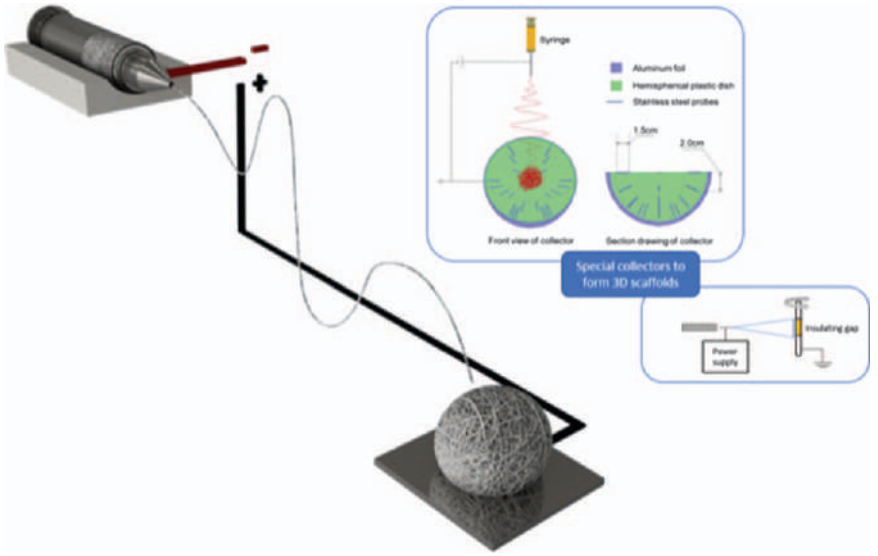


**Figure 10.4** Schematic representation of the fabrication of 3D electrospun fibrous scaffolds.
Reproduced from ref. 62 with permission from the Royal Society of Chemistry.

tridimensional fibrous scaffold by extrusion of a poly-96L/4D-lactide (PLA) filament and then manually carded the fibers into sheets and punched them until they obtained a nonwoven scaffold of 2 mm thickness.[60] Xu *et al.* reported the use of electrospinning to accumulate 3D polyacrylonitrile (PAN) nanofibers into a collector filled with ethanol, which was shaken every few minutes to ensure the homogeneity of the fibers along the 3D structure.[61] In all these reports, PPy was *in situ* chemically polymerized after the formation of the 3D fibrous structure by immersion into the monomer solution, first, and the oxidant solution, afterwards.[59,62]

Interestingly, there exist two examples in the literature where the electrospinning solution already contains a mixture of the biopolymer and the CP. Subramanian and co-workers were able to electrospin a solution of PLGA containing PHT and collect 3D axially aligned nanofibers. The authors designed a collector as a grounded rotating mandrel, shown in Figure 10.4, with a small insulating gap dividing the rod into two independent-like electrodes, thus allowing the deposition of longitudinally oriented fibers.[63] PANi was also blended with PLGA and PCL solutions and then a 3D scaffold was formed in two steps: the inner core was prepared through a wet electrospinning system, where the fiber was deposited vertically in a water bath and collected by guidance rings; the outer cylindrical sheath was prepared with a two-nozzle electrospinning system, where two oppositely charged nozzles were placed horizontally facing each other and a neutral rod in the middle keeping the previously prepared scaffold's core.[64]

### 10.2.4 3D Printing for Conjugated Polymers

3D printing has emerged as a promising industrial manufacturing strategy since it became commercially available in the early 2010s. The development of two key concepts, replication machine and OpenCode sharing information, started the quick development of this additive manufacturing technology. 3D printing has the advantage, against other conventional manufacturing techniques, that it allows the design and fabrication of more complex customized shapes. Accordingly, areas requiring specific structures, such as electrode printing, tissue engineering or aeronautics, have become the cradle where these techniques are being developed. Due to the infancy of the field, the terminology used has not yet been standardized worldwide, and different words are used to name the same technique. In this chapter, we are using the same criteria of naming the techniques as most of the scientific community working in the field. It has to be noted that other terminology could also be found in the literature.

For tissue engineering, 3D printing represents a powerful tool due to the possibility to customize complex architectures and produce structures at the micrometric scale. Typically, this additive manufacturing process is used to create different types of tridimensional structures. Moreover, 3D printing offers the possibility to use functional inks that are not available commercially. Their attractive properties can be tailored to specific requirements incorporating functional groups, specific polymers or other biological components. The key to 3D printing for biomedical applications resides basically in the possibility to use conducting polymers to design any structure we have in mind with high conductivity, improvement in the mechanical properties, biocompatibility and mimicking the extracellular matrix.

As already mentioned, conducting polymers with redox-active properties have attracted the interest of researchers for tissue engineering due to electrochemical impulses that are the primary means of intercellular communication between electroactive cells. Conductive materials are deposited through a nozzle on a substrate of interest (*e.g.*, tissue culture well plate). A key challenge is to ensure the shape stability of the printed structures, caused by, for example, the recovery of the prior sheared hydrogel or by cross-linking of the printed structure directly after printing (*e.g.*, ionic, covalent by UV light). However, 3D printing of conductive structures has a very low number of publications. This might be because one of the principal problems of conductive polymers is their low processability.

Each type of 3D printing methodology, showed in Figure 10.5, has several advantages and limitations for producing robust tissue constructs. Each technique gives the possibility to produce materials with different physicochemical properties, thus playing a crucial role in the final application. In this section, we discuss them, focusing on those methodologies that use conductive polymers: light-based printing, ink-jet printing, bioplotting and electrohydrodynamic printing.[65]

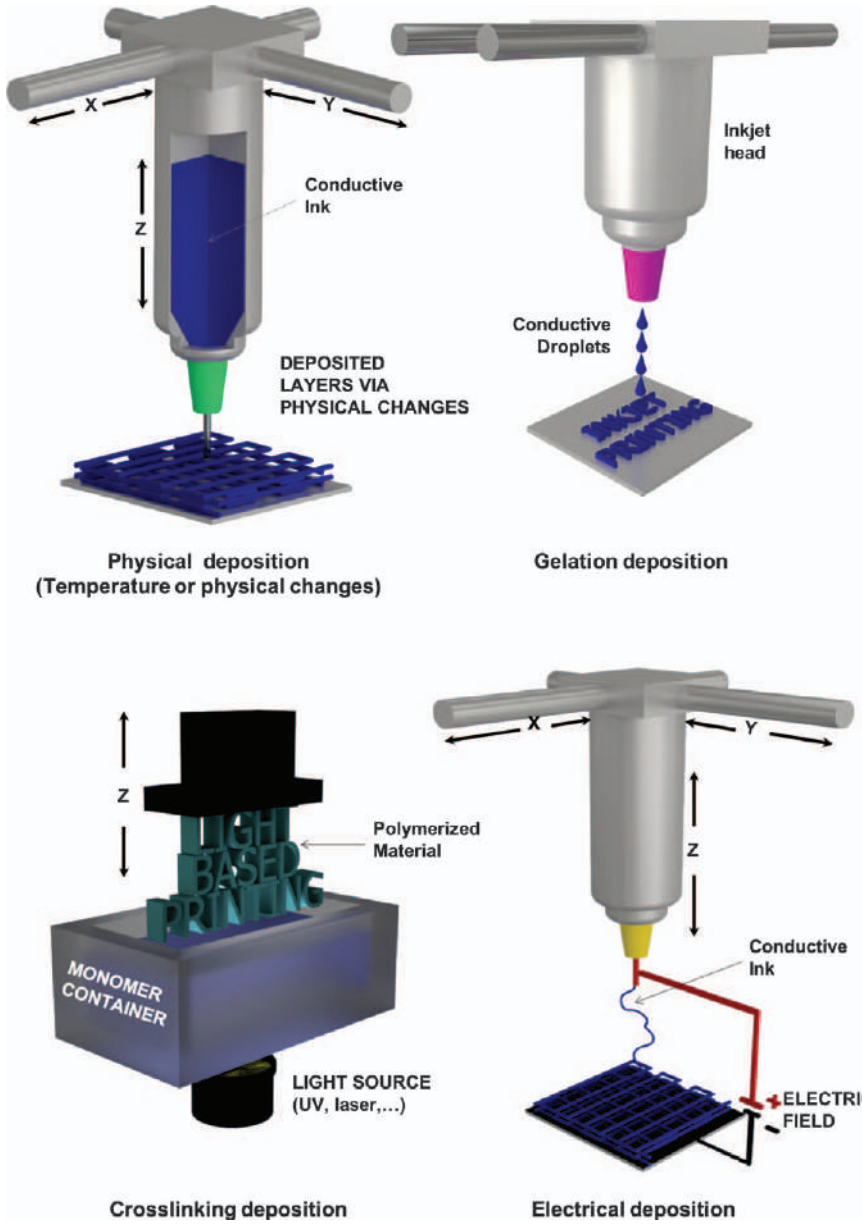


**Figure 10.5** 3D printing systems for the development of conductive scaffolds.

### *10.2.4.1 Inkjet Printing*

Inkjet printing is based on the capability to deposit a water-based liquid or polymer on a planar substrate like glass or paper. In general terms, it is the more similar to a regular printer. Specifically, inkjet printing is an inexpensive

3D printing platform broadly used in biomaterials development due its low requirements when patterning a material. It is capable of dispensing and handling biological and polymer solutions in a highly controlled manner. Moreover, it allows noncontact and simultaneous deposition of different cell types in a precise orientation at the micrometer scale.[65]

Zhenan Bao and co-workers developed the first methodology to include conductive polymers in printing techniques using two inks: a solution containing the oxidative initiator was printed, followed by printing a second solution that contained the phytic acid and aniline monomer. Phytic acid induced a gelation process and at the same time worked as a doping agent of PANI. This approach allows the obtention of a nonsoluble hydrogel with a designed shape.[66] Inkjet printing is also a suitable technique to deposit a conductive layer over a specific surface. Weng *et al.* used a single ink composed of polypyrrole (PPy) and collagen to perform micropatterns on polyarylate film.[67] In 2014, an interesting strategy was reported, where a PANi layer was printed on top of already electrospun fibers of PCL/osteo/Gel/SG5.[68] Inkjet printing represents a versatile tool to make any kind of substrate conductive. PEDOT:PSS and different ionic conductors were deposited layer by layer on a polyimide textile aimed at monitoring and recording body movements.[69]

### *10.2.4.2 Extrusion-based 3D Printing*

3D bioplotting is the most extended printer technique commercially available. It can process a wide variety of different materials, including polymer melts, thermoset resins, polymer solutions, high-filler pastes, cement and bioactive proteins. The main differences with other printers reside in the viscosity of the printing material: here, the material is inserted in an extruder and it then flows down by the action of a piston or compression system.

PPy-decorated chitosan was used to generate self-healing hydrogels. In fact, Darabi *et al.* took advantage of this property to print a patterned device: the hydrogel was destroyed while passing through the needle, printed with a certain design and self-recovered after a short period of time. The hydrogel was prepared with physically and chemically cross-linked networks through a two-step synthesis. In the first step, PPy was grafted to chitosan and then acrylic acid (AA) monomers were chemically polymerized on top of the PPy-grafted chitosan, in the presence of iron ions, to form poly(acrylic acid) (PAA).[70]

Another different approach to printing conducting polymers is based on using polyester viscous inks.[71] For example, taking advantage of the properties of polymers such as PLLA, which can be both melted and solubilized, forming viscous mixtures. Spheres and nanowires of PPy were mixed in different ratios with PLLA, generating a viscous ink, and deposited layer by layer to manufacture scaffolds and membranes.

As explained above, conductive polymers require counterions to stabilize their negative charge. However, there can be remaining charge that can be used to induce gelation, as proved by Spencer *et al.* in their work.[72] These authors were able to cross-link together GelMA and PEDOT:PSS ionic and covalently.

First, GelMA/PEDOT:PSS blend was ionically cross-linked while injected into a support bath containing aqueous calcium chloride at 4 °C. The resulting hydrogel was then covalently cross-linked through photopolymerization of the methacryloyl groups on GelMA. In addition, this approach allowed cell encapsulation during the printing and cross-linking processes.

### *10.2.4.3 Light-based Printing*

Light-based printing techniques are based in the irradiation of UV–Vis or laser beam on a resin-based monomer that induces a curing process in designed regions by fabricating photo-cross-linkable structures in a layer-by-layer method. Usually, the resins used are composed of acrylates, urethane acrylates or vinyl ether groups. Among the existing techniques, those used with conjugated polymers are stereolithography (SLA) and digital light processing (DLP). SLA is typically a bottom-up approach that uses a laser beam as source; the polymerization occurs on a liquid surface, with the stage moving downwards after each layer is solidified. On the contrary, DLP uses a UV light source projected on a transparent surface at the bottom of a vat, which holds the photosensitive resin; the light goes through an optical transparent window and the polymerization process works with the stage moving upwards upon layer formation.

There are two different strategies in the literature to combine the resin with the conjugated polymer: post-polymerization and *in situ* polymerization. In the former, an already manufactured 3D structure, normally from acrylic resin, is soaked in an oxidant solution and transferred to a monomer solution. The oxidative polymerization occurs as an interfacial polymerization, covering the three-dimensional network with the electroconductive material. On the other side, *in situ* printing requires a previous synthesis of the electroconductive material before being photo-cross-linked in the presence of the resin.

In 2016, Wu and co-workers developed a hydrogel composed of methacrylic gelatin by SLA. Once the membrane was manufactured, the gel was first immersed in an oxidant solution of ammonium persulfate (in HCl 1M) and then in an hexane solution of aniline, avoiding oxidant leakage and limiting the oxidative reaction. This approach resulted in a hybrid hydrogel with electronic conductivity.[73] Subsequently, Fantino *et al.* carried out a similar procedure to obtain a PPy coating of a manufactured PEG-diacrylate scaffold *via* DLP, using $FeCl_3$ as the oxidant.[74] In addition, nanostructures like LAPONITE® have also been included in the formula. LAPONITE® consists of silicate nanoplatelets of 25 nm that are negatively charged in their inner faces. Such structural charge density was used as dopant to attract the PEDOT polymer.[75]

*In situ* light-based printings allow to encapsulate cells during the cross-linking process. Sawyer and co-workers manufactured PANi through oxidative polymerization and mixed them with gel methacrylate (GelMA), which was then cured *via* SLA with UV light in the presence of human osteosarcoma cells. The final hybrid material showed a high conductivity (up to 20 kΩ) and a modulable young modulus.[76] Also, commercially available

crystallized PEDOT:PSS was also blended with a matrix of poly(ethylene glycol) diacrylate and *in situ* printed through SLA.[77]

#### *10.2.4.4 Electrohydrodynamic Printing*

Electrohydrodynamic (EHD) printing is based on the deposition of a material, dissolved in a polarizable liquid, which suffers ion mobility by the action of an electric field. The high-voltage field is typically placed between a nozzle and a conductive substrate. EHD printing possesses high resolution, thus high precision of fabricating micro/nanoscale structures, and overcomes the limitations of the nozzle found with extrusion and inkjet printing. It can be used under a pulse or jet mode, creating dots or a continuous fibrous layer. The quality of the print is affected by the ink properties, such as viscosity, surface tension, electrical conductivity or dipole moment, and many process-related factors including applied voltage, pressure and flow rate.[78] Mainly by controlling the electric field near the nozzle flow, among other parameters, EHD can control the patterning and therefore the size, porosity and alignment, overcoming limitations of electrospinning and other electric-based techniques.[79]

A recent study reported the EHD printing of PPy mixed with PCL in different ratios. The addition of conductive polymer produced an increment in the scaffold's roughness structure and in the final conductivity of the material. Moreover, the degradation of the polymer was also increased with the amount of PPy in the final PPy/PCL system.[80] Also, the EHD printed was used to manufacture PCL/PEDOT:PSS-PEO nanofibers layer by layer with different orientations. At the beginning, PCL melted was deposited using a micropumping system and then PEDOT:PSS-PEO conductive fibers with a spacing of 50 μm were printed on the top with a similar orientation.

## 10.3 Characterization of 3D Materials

### 10.3.1 Common Characterization of 3D Scaffolds

Scaffolds envisioned for tissue regeneration are designed to enhance the cell–scaffold interaction and favor cellular attachment. Thus, the composition and the functional groups in the backbone of the polymeric matrix are a key factor taken into account for a successful interaction. Fourier transform infrared spectroscopy (FTIR) is the best technique to determine the composition of the scaffolds,[15,20,42] although XPS gives an accurate percentage of the elements present within the devices manufactured.[13,21] Thermogravimetric analyses (TGA) give information on the thermal stability of the entire scaffold, and also allow the quantification of the percentage of each species within the matrix. CPs are very stable thermally;[81–83] thus, large amounts of CP increase the thermal decomposition temperature of the mixed substrates when compared to the pristine natural polymer.[20] This effect can be explained due to the high electrostatic interaction occurring

between the two polymers. However, when the matrix is composed of less than 10% CP, it shows no effect on thermal stability.[30,32,56]

A key requirement for the regenerative substrates is the appropriate pore size to allow cellular infiltrations, and homogeneous interconnected porosity to enhance the medium and nutrient flow to the seeded cells. Macroporous scaffolds have the better pore size for this application, ranging from a few tens to several hundreds of micrometers;[15,21,30] however, fibers and hydrogels have a much smaller porosity, below a few tens of micrometers, that can hinder the cellular penetration inside the 3D structure.[11,62] In addition, the orientation of the pores defines the kind of tissues the scaffold mimics and, therefore, the potential application of the device. Patterned structures should be optimal for directional tissues, such as muscle cells, while randomly distributed pores mimic tissues with undefined directionality, such as brain tissues.[84–86] Scanning electron microscopy (SEM) is a very powerful technique to analyze the internal and/or external morphology of the scaffolds, although only 2D cross-sections of the entire assembly can be analyzed.[20] To obtain the tridimensional image of the internal structure, microcomputed tomography (μCT) can be a suitable alternative. This nondestructive technique gives a detailed 3D model reconstruction of the entire skeleton.[30] More detailed analyses on the surface area can be obtained from porosimetry techniques, such as ethanol displacement,[20] Brunauer–Emmett–Teller (BET)[32] or mercury porosimetry.[18]

Tridimensional porous scaffolds have porosities between 60%–90%,[21,30,31] and the incorporation of the CP does not always change such values in the same direction. In some cases, the addition of CP *decreased* the overall porosity of the scaffolds; on others, such addition *increased* the porosity and surface area.[32] Yazdimamaghani *et al.* demonstrated that the pore size of gelatin and bioactive glass increased when blended with PEDOT:PSS, but they decreased when the PEDOT:PSS concentration was raised.[30,31] Regarding fibrous materials, it is reasonable to expect thicker fibers after CP coating, resulting in smaller pore size. However, most studies did not show a significant difference, likely because the coating layer is usually in the nanometric range.[56] Furthermore, Chen *et al.* observed thinner fibers with an excess of the PSS within the conductive matrix.[57] In hydrogel materials, the pore size is usually below 20 μm, smaller than in porous scaffolds, and seems to be more dependent on the hydrogel backbone, addends and cross-linking level.[87]

CP coating produces characteristic nano- and microscale topography roughening the surface of the matrix (Figure 10.6).[16] This effect might modulate the cell adhesion, improving the cellular attachment, proliferation and, in some cases, differentiation.[24]

Implanting scaffolds *in vivo* might induce swelling in some materials; thus, its previous analyses are extremely important for tissue engineering. On one hand, water uptake facilitates the migration and infiltration of the cells, the diffusion of the nutrients and waste removal.[32] But on the other hand, an uncontrolled increase of the substrate can affect the surrounding living tissue and lead to severe inflammation.[88,89] Porous or fibrous

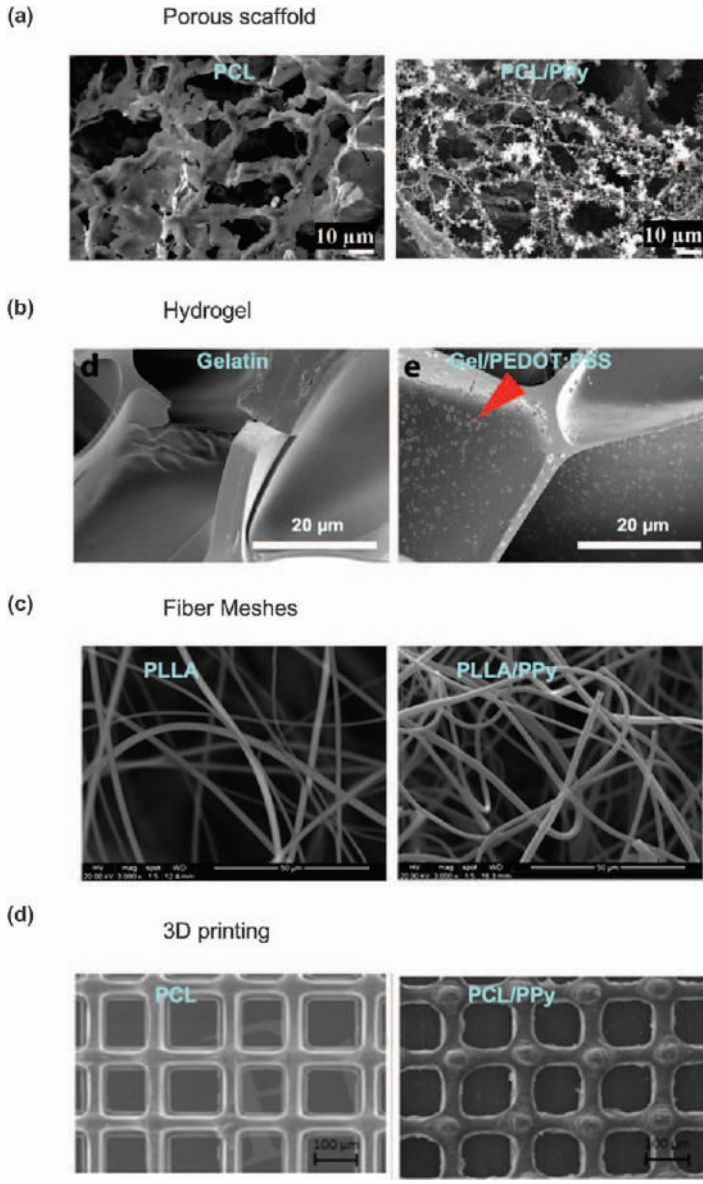


**Figure 10.6** SEM images of (a) PCL and PCL/PPy porous scaffolds, (b) gelatin and gelatin/PEDOT:PSS hydrogel, (c) novel fluffy-PLLA scaffold , fluffy-PPy scaffold fabricated by improved electrospinning, and (d) PCL and 2% PCL/PPy electrohydrodynamic scaffold.
Adapted from ref. 21 with permission from Elsevier, Copyright 2016, from ref. 111 with permission from the American Chemical Society, Copyright 2018, from ref. 62 with permission from the Royal Society of Chemistry, and from ref. 80 with permission from Frontiers, Copyright 2019.

materials do not generally suffer a significant change in volume and the swelling ability is directly related to the porosity:[30] it was determined that a decrease in the porosity yields a decrease in the water uptake.[20] Swelling in hydrogels is more important, and is significantly affected by the composition, amount of hydrophilic groups present and pH of the media.[42,87] In literature there are several discrepancies about the effect that the introduction of a CP has within the hydrogel matrix. Some reports observed a reduction in the swelling after incorporating CPs, and concluded that the main factor governing this phenomenon was the hydrophobicity of the conjugated matrix.[15,32,47,90] The solution given to reverse such hydrophobicity was to alter the matrix composition to improve the swelling ability.[91] The presence of more hydrophilic carboxylate groups in PAA-based hydrogels is strongly dependent on the pH of the media: increasing the pH increases the absorption of water due to the ionization of the free carboxylic groups.[42] In that line, Mawad *et al.* obtained a higher ratio of swelling by mixing functionalized PEDOT-COOH with polyacrylic acid.[50]

The mechanical properties are mainly defined with the Young's modulus, usually determined using a compression mechanical testing apparatus or, in the case of hydrogels, rheology. The Young's modulus is obtained by measurement of the elastic deformation response of the material against the applied force. The stiffer the material, the lower the elastic deformation.[38,47,49] Although the Young's modulus can be altered by dopants, monomer concentrations, hydrophobic polymer content or cross-linking density,[32,87,91] herein we only focus those alterations coming from the conjugated backbone. Usually, the compressive modulus in dry conditions is increased by the addition of CP into the matrix even at low CP concentrations.[17,21,27,30,58] This effect has been attributed to the highly conjugated, and thus rigid and stiff, nature of the CP.[47,56,90] Furthermore, in the case of fibrous substrates, Niu and co-workers presumed that such an increase may also come from the deposition within the interstices, which act as cross-links and reduce the sliding of neighboring microfibers in contact with each other.[56] Abedi and co-workers hypothesized that a reduction in the fiber diameter would reduce the structural imperfections during fiber formation, thus increasing the tensile strength and stiffness of the resulting substrate, as confirmed with samples containing PEDOT:PSS.[92] Alternatively, Yang *et al.* hypothesized that clustered PPy within alginate hydrogels may be connected, thus strengthening the internal network with hydrogel portions.[38]

To determine the correct Young's modulus, experiments must be performed in wet conditions, since the biological tissues are in aqueous media. Hydrogels formed *via* 3D printing were observed to reduced their Young's modulus by around 30% when PEDOT:PSS was included within a gelatin methacryloyl matrix.[93] Furthermore, the swelling can greatly affect the scaffold strength. Del Agua *et al.* observed a reduction of the value by half after swelling compared to dry conditions.[17] Wang *et al.* rationalized that this effect was due to the weakened matrix resistance to external compression caused by the presence of water molecules within the structure.[90]

The redox state of the conjugated polymer can also affect the mechanical strength of the material, which can be rationalized due to secondary bond formation within the structure,[50] or even by electrostatic interaction between the CP and the nonconductive matrix.[38]

### 10.3.2 Electrochemical Characterization

CP, as a conductive species, have the ability to transport electrons through their conjugated bonds. Such electrical conductivity can be useful in repairing electrophysiological functions, such as neural or cardiac communication; substrates with electrical properties were shown to have a positive effect on cellular differentiation.[94,95] Moreover, conductivity is indispensable to use scaffolds as electrodes and, thus, record electrical activity in the biological material and stimulate the cells or tissue during regeneration. The intensity current of the biological processes happening in the human body was found to be in the order of nanoamperes:[96] the highest conductivity value reported for cardiac tissue is in the order of $1.0{\cdot}10^{-2}$ S m$^{-1}$, while native neural tissue was reported around $2.0{\cdot}10^{-3}$ S m$^{-1}$,[97,98] meaning that the conductivity provided by the CP-based scaffolds is close to those and, thus, they are suitable for tissue regeneration applications.

The electrical properties are directly related to the amount of CP present within a substrate. It is worth noting that the comparison of the conductivity values between different 3D substrates manufactured has been challenging, since each work undertook experiments using different conditions. There are several methods to measure the conductivity. (i) Direct measures common for 2D films that give an absolute value in S cm$^{-1}$, such as digital multimeter or four-point probe analyzer (4PP),[15,17,21,31,43,56,90,99] placing the 3D scaffold in direct contact with the electrode or between two metal plate electrodes.[14,38,100] (ii) By cyclic voltammetry (CV) and evaluation of the current passing through the scaffold at a fixed voltage range.[23,57,87] (iii) Indirect measurement from the resistivity obtained with electrochemical impedance spectroscopy (EIS), which results in the inverse of the conductivity.[45,50] EIS shows the signal as a function of frequency at a constant potential, resulting in a very sensitive methodology and useful for cell monitoring after seeding to evaluate attachment and development.[17,91] (iv) Some reports have constructed an electrical circuit that includes the scaffold, a LED bulb and a power supply connected in series.[11,26,29,48] The pass of electricity is then confirmed if the bulb lights up once the circuit is closed. (v) Finally, scanning electrochemical microscopy (SECM) also can be useful in analyses of the distribution of the surface current of a substrate.[20]

The principal aim in the addition of CP into nonconductive matrices, either porous scaffolds, fibers or hydrogels, is to increase the conductivity of the resulting material.[15,38,56] For example, Shahini *et al.* observed a 70% increase in conductivity in a scaffold containing only 0.3% of PEDOT.[30,31] The method of fabrication is the key factor to achieving the final properties desired. It has been shown that electropolymerization produces the most

conductive CPs; from the chemical methods, vapor phase polymerization is the method that yields the highest conductivity.[11,24] Severt and co-workers demonstrated that such electrical properties can be even more enhanced if, after a first chemical polymerization, a second coating layer is deposited *via* electrodeposition.[14]

The kind and amount of dopant introduced within the matrix can also have an impact on the electrical properties of the system.[49,57,87] An excessive concentration of dopant can lead to structural damage, as observed by Chen and co-workers, since it may disturb the polymerization deposition, thus leading to, in their case, thinner coated layers.[57]

To evaluate the electrical properties, it is important to work in biological conditions and hydrated samples. Semiconducting substrates, such as chitosan/gelatin hydrogels containing CP, showed an increased conduction ability when hydrated.[90] However, Niu and co-workers detected a reduction in the conductivity of PEDOT/PLLA after more than 100 h of cell incubation, what was related to the biodegradation of the scaffold.[56]

### 10.3.3 Biodegradability

A regular scaffold in tissue engineering is either reabsorbed by the biological system, becoming part of the tissue, or biodegraded at the same rate that new tissue is generated.[90] In general, all implants must remain in the implanted site long enough to provide the desired support and/or connective effect, but no longer than necessary as they may become a hindrance to repair the damaged tissue.[101] Biodegradation refers to degradation occurring through disintegration, hydrolytic mechanisms or enzymatic activity, and is tested *in vitro* under physiological conditions.[102] Apart from the appropriate degradation rate, the degradation products of the scaffold should not be cytotoxic, so cell viability studies of the biodegradation solution are typically performed.[90] In addition, the scaffolds can be designed with side chains or dopants known to have no foreign body response, such as polyethylene glycol (PEG), poly(glycerol-sebacate) (PGS), and poly(tetrafluoroethylene) (PTFE).[102]

PEDOT and PPy are considered highly biocompatible materials, since they showed no signs of cytotoxicity with different types of cells. However, their use as long-term implants can, somehow, be considered an issue due to their high stability over time. In fact, the degradability of CP-containing substrates is higher than the homologous nonconductive systems,[47] attributed to the increased hydrophobicity from CP nanoparticles present along the scaffold's surface:[15,30] hydrophobicity reduces the contact area between the water containing the degradation enzyme and the substrate and, thus, its effect.[90]

Degradation of conductive substrates usually happens because of delamination of the CP coatings. Severt and co-workers performed a second coated layer through electrodeposition on a CP-coated silk scaffold to reduce such delamination, while improving the stability and increasing the overall conductivity.[14] On the other hand, the lower biodegradation of

functionalized CP, such as PEDOT-COOH, can be rationalized due to the increase in stability from the higher cross-linking level.[15]

## 10.4 Application in Tissue Engineering

Even though conjugated 3D devices have been used in a wide range of biomedical applications, most of the scaffolds have been designed for tissue regeneration (Table 10.1).[103] It is worth noting that among the different CPs, PANi has shown certain toxicity and very low biodegradability, what limits its implementation in the biomedical field.[104] Tissue engineering is focused on the repair or replacement of damaged or diseased tissues with synthetic and/or natural implants. The tridimensional conductive scaffolds reviewed in this chapter present great potential for such purposes, not only because they mimic the biological environment, but also due to their controllable processing morphology and composition,[87] as well as the facility of tuning them with chemical groups, bioactive agents such as drugs, growth factors and dopants to enhance cellular adhesion and proliferation, as shown in Figure 10.7.[91,105] For instance, the incorporation of hydroxyapatite (HAp), known as a bone mineral, shows strong adhesion and excellent proliferation with mouse MC3T3-E1 pre-osteoblasts.[27] Also, scaffold designed for tissue engineering must also maintain the health of cells inside its structure for long periods of time, thus *in vitro* cultures of at least 5 days are those discussed in this chapter.

The regeneration of tissues employing 3D CP-incorporating scaffolds is in its early stages, thus its success as supports to generate a full artificial organ or tissue has not been yet achieved.

There are few examples in the literature with real applications. PPy/Alg hydrogels were subcutaneously implanted *in vivo* for 8 weeks, inducing moderate immune reactions.[38] Recently, the *in vitro* and *in vivo* reconstruction of a spinal cord injury culturing nerve cells inside a PCL/PANI-PLGA fibrous scaffold has been reported.[64]

SEM and fluorescent microscopy are very powerful techniques used to image the morphology and dispersion of cells incubated within 3D structure scaffolds, thus testing their ''healthy' growth.''[61] The cell proliferation has also been evaluated through analyses of characteristic cell functions with specific protein markers: the concentration of vascular endothelial growth factor (VEGF) in 3T3-L1s fibroblasts was characterized to quantify its pro-angiogenic potential;[18] neurotransmitters are useful to evaluate the proliferation of neurons.[16,19,50] Inal and co-workers used the inherent electrical sensitivity of cells to monitor cell growth within CP-based porous scaffolds with *in situ* impedance measurements.[91] Moreover, phenotyping and gene expression characterization have become useful tools to follow up cellular behavior studies.[15,90]

There are three main types of cells reported that have been incubated inside tridimensional conductive structures, all of which are electrically sensitive: bone, neuronal and cardiac cells. The articles related to bone tissue engineering used pre-osteoblasts, *i.e.*, mesenchymal stem cells that

**Table 10.1** Summary of the of the CP-based structures and properties for tissue engineering highlighted in this chapter.

| Structure | Composition | Fabrication method | Max. pore size | Conductivity/ resistance | Swelling ratio | YM (kPa) | Biodegradability | Biomedical Application | Ref. |
|---|---|---|---|---|---|---|---|---|---|
| Porous | PPy-Alg/chitosan | Immersion | 100 μm | 1000 nA | 9% | — | 30% after 4 weeks | Tissue engineering | 20 |
| | Cs/Gel/PEDOT | Immersion | 250 μm | $10^{-1}$ S cm$^{-1}$ | 400% | 30 | 37% after 8 weeks | Tissue engineering | 91 |
| | rGO/PPy/CPP | Immersion | 200 μm | — | — | 186 MPa | — | Stem cells differentiation | 13 |
| | PTMC/PPy | Immersion | 250 μm | 1 kΩ sq$^{-1}$ | — | — | — | Stem cells differentiation | 22 |
| | PPy/PCL | Immersion | 328 μm | $10^{-1}$ S cm$^{-1}$ | — | 12 MPa | 2% after 10 weeks | Tissue engineering | 21 |
| | PEDOT/PS and PPy/PS | VPP | 150 μm | — | — | — | — | Tissue engineering | 11 |
| | PEDOT/PCL | VPP | 600 μm | — | — | $10^3$ | — | Stem cells differentiation | 24 |
| | PEDOT-HA/Cs/Gel | Freeze-drying | 300 μm | $10^{-3}$ S cm$^{-1}$ | 700% | 55 | 43% after 8 weeks | Tissue engineering | 15, 16 |
| | Gel/PEDOT/PSS | Freeze-drying | 300 μm | 210 μS m$^{-1}$ | — | — | — | Tissue engineering | 31 |
| | PEDOT/PSS/GOPS | Freeze-drying | 40 μm | $10^1$ kΩ | — | 4.5 | — | Tissue engineering | 18 |
| | Gel/BaG/PEDOT/PSS | Freeze-drying | 250 μm | 170 μS m$^{-1}$ | 240% | 35 MPa | 35% after 90 days | Stem cells differentiation | 30 |
| | HAp/Gel/Si/PPy | Freeze-drying | 350 μm | — | 250% | 110 MPa | — | Tissue engineering, drug delivery | 32 |
| | rGO/PPy/HAp | EP | 400 μm | — | — | 186 MPa | — | Tissue engineering | 27 |
| Hydrogel | HA/CNT/PPy | Ox. crosslinking | — | 12.6 kΩ sq$^{-1}$ | ~30% | 3.2 | 100% after 2 days | Stem cells differentiation | 47 |
| | Alg/PPy | Filling | 1 μm | 31.1×10$^{-4}$ S cm$^{-1}$ | | ~2000 | — | Stem cells differentiation | 38 |
| | CMCS/PEDOT | Filling | 100 μm | 4.7×10$^{-3}$ S cm$^{-1}$ | 1700% | 12.5 | 35% after 10 weeks | Tissue engineering | 43 |
| | GelMa/PEDOT/PSS | Filling | 50 μm | 261 kΩ sq$^{-1}$ | 600% | 7.6 | 25 % after 2 weeks | Tissue engineering | 88 |
| | HEMA/PAA/PEDOT | Polym. before gelation | 30 μm | — | ~2500% | ~100 | — | Tissue engineering | 87 |
| | PAA/PEG-DA/APMA-PEDOT | Polym. before gelation | — | — | ~5000% | ~45 | — | Tissue engineering | 50 |
| | PTAA | Side-chain crosslinking | 50 μm | ~10$^{-5}$ S cm$^{-1}$ | 300–800% | — | — | Tissue engineering | 52 |

**Table 10.1** (*Continued*)

| Structure | Composition | Fabrication method | Max. pore size | Conductivity/ resistance | Swelling ratio | YM (kPa) | Biodegradability | Biomedical Application | Ref. |
|---|---|---|---|---|---|---|---|---|---|
| Fibers | PLA/PEDOT | Immersion | — | 0.4 $k\Omega\,sq^{-1}$ | — | 15.7 | — | Tissue engineering | 57 |
| | PAN/PPy | Immersion | 30 μm | — | — | — | — | Tissue engineering | 62 |
| | PLA/PPy | Immersion | 200 μm | 1700 $\Omega\,sq^{-1}$ | — | — | — | Stem cells differentiation | 61 |
| | PLLA/PPy | Immersion | 100 μm | — | — | — | — | Tissue engineering | 54, 60 |
| 3D Printing | PCL/PPy | EHD | 125 μm | 1.2 $mS\,cm^{-1}$ | — | 40 MPa | 50% after 14 days | Tissue engineering | 80 |
| | PANI/GelMA | SLA/Inmersion | — | 2.9 kΩ | 90% | 15 | — | Tissue engineering/ Biosensing | 73 |
| | PEDOT:PSS/GelMA | Extrusion based | — | $2.5{\cdot}10^{-5}$ Ω | 1100% | 16.3 kPa | — | Tissue Enginering/ Implants | 94 |
| | PANI/Phytic acid | Ink jet | — | 0.23S $cm^{-1}$ | — | — | — | Tissue engineering/ Electrode | 66 |
| | PEDOT:PSS/GelMA | SLA | 287 μm | 0.91 $\Omega\,sq^{-1}$ | — | 30 Mpa | — | Tissue engineering | 77 |

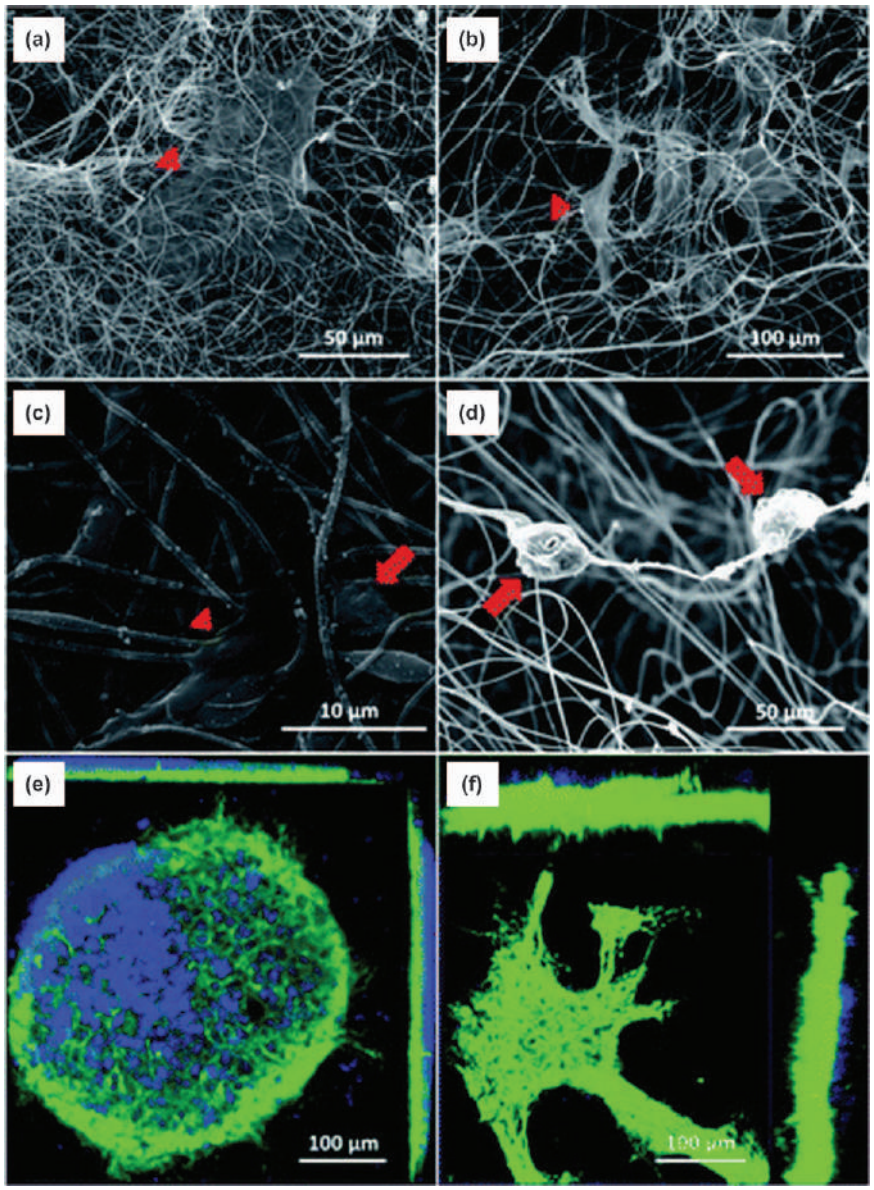


**Figure 10.7** SEM of cortical cells cultured in 2D-CNFs (a and c), 3D-CNFs (band d) and confocal microscopic ortho-images of cell culture in 2DCNFs (e) and 3D-CNFs (f). The red arrows and triangles indicate two different cell morphologies, respectively. Green: MAP2; blue: DAPI.
Reproduced from ref. 61 with permission from the Royal Society of Chemistry.

differentiate into bone cells. The most employed neural model is rat pheochromocytoma-derived (PC12) cells.[15,35,43,90] Neonatal rat ventricular cardiomyocytes and mouse myoblast C2C12 cells have also been analyzed as models for heart regeneration, resulting in a good beating behavior and excellent contractility.[50,62,87,106] Other kinds of nonconductive cells that have been employed as models for cell viability and proliferative ability of 3D architectures include epithelial cells[17] and fibroblasts.[91]

### 10.4.1 Biomineralization for Bone Tissue Engineering

In order to determine the suitability of a potential scaffold for biological regeneration, the key is to evaluate its biological integration with the surrounding tissue. In bone engineering, a reliable way to mimic the bone regeneration and evaluate the osteointegration is through *in vitro* mineralization of the substrate. In this process, the material is immersed in saturated simulated body fluid (SBF), a supersaturated calcium phosphate solution with composition similar to human plasma, for several periods at 37 °C. The formation of bioactive minerals, such as hydroxyapatite (HA), which is similar to the minerals present in the bone, and their rate of deposition on the surface is then evaluated with SEM, EDX and Alizarin Red staining (see Figure 10.8).[20] The faster the HA formation rate, the more feasible and stronger the osteointegration of the scaffold within the host tissue. Although the mineral covers the entire surface, it is essential to determine the existence of pores afterwards to ensure proper cellular penetration and nutrient and media flow.[13,31,32]

### 10.4.2 Stem Cells Differentiation

One of the strategies used in tissue engineering to develop artificial tissues in the laboratory could be direct differentiation of pluripotent or mesenchymal stem cells inside a 3D structure. In order to guide the differentiation into the desired type of cells, usually growth factors and specific proteins are introduced in the culture media. However, the mechanical properties of the materials also play an important role in such differentiation.[91]

Human mesenchymal stem cells (hMSCs), mainly extracted from the bone marrow, are the most frequently used cells to differentiate into bone, cartilage and fat, as well as neuronal and endodermal lineages.[24,30,31,38,60,107] MC3T3-E1 mesenchymal cells derived from mouse skull have also been used for osteoblast differentiation and shown to form calcified bone tissue *in vitro*.[11,13] Neural stem cells (NSCs) are self-renewing, multipotent cells used to generate neurons, astrocytes and oligodendrocytes.[16,47] Heart tissue differentiation has been achieved through C2C12 cells, a mouse myoblast cell line commonly used as an *in vitro* model to study muscle differentiation.[50]

Also, human embryonic stem cell-derived neural crest stem cells (hESC-NCSCs) showed improved and accelerated proliferation and differentiation when cultured in 3D-printed scaffolds of PPy/PCL when compared to pure

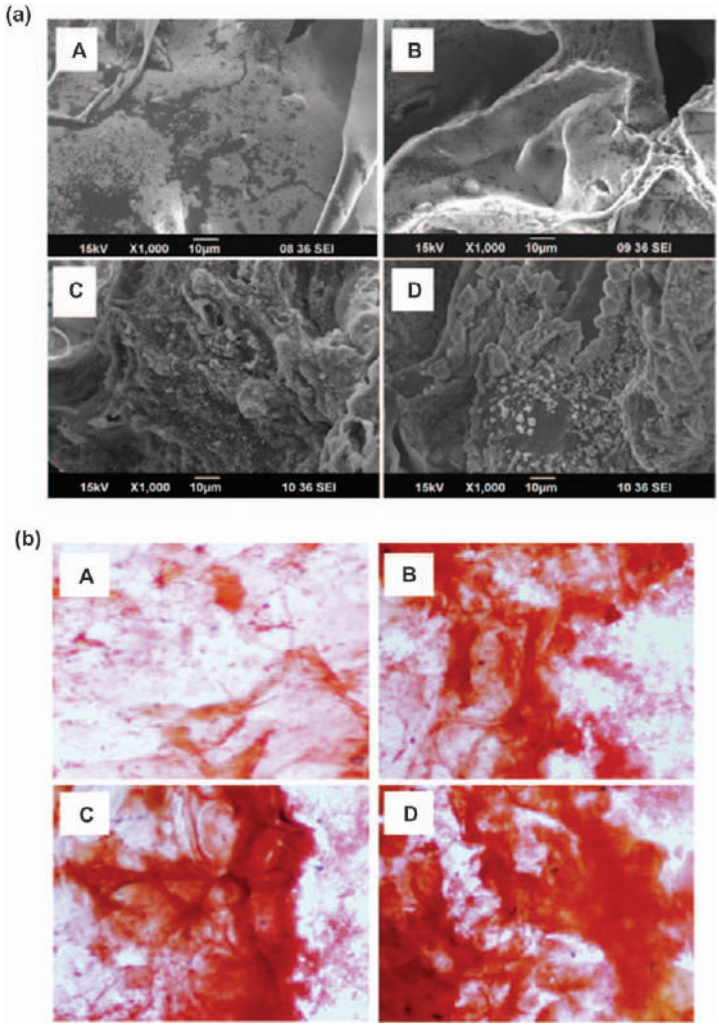


**Figure 10.8** (a) SEM images and (b) Alizarin Red staining showing mineralization of chitosan on (A) 7th and (C) 14th day, and chitosan/PPy–Alg on (B) 7th and (D) 14th day.
Adapted from ref. 20 with permission from Elsevier, Copyright 2013.

PCL scaffolds. Among all the compositions tested, the scaffold with 0.5% of PPy gave the best results.[80]

### 10.4.3 Electric Stimulation

Conjugated scaffolds are usually designed for electrical stimulation of electrical-sensitive cells and tissues, thus providing a new kind of interaction with biological systems.[56] Several studies have demonstrated that local

electrical stimulation (ES) favored and accelerated the regeneration and healing processes of electroactive tissues, enhancing cell–cell and cell–substrate interactions.[108] Although ES has not always had a significant effect in cell cultures, there are no reports of possible damage to the cells.[11] Clinically, pulsed electromagnetic fields have been previously applied to treat bone fractures and enhance spinal fusions.[109] The combination of CP scaffolds and ES can be a safer tool in clinics for that purpose: since the current applied goes through the scaffold structure, the electrolysis of the biological medium and, thus, the production of cytotoxic agents, are minimized.[21]

After a detailed revision of the literature, we observe that most of the scaffolds used for ES stimulation are composed of PPy. Zhang and co-workers demonstrated that the application of 200 μA (4 h per day, 21 days) on human adipose-derived mesenchymal stem cells (ADM-SCs) cultured in PPy/polycaprolactone (PCL) porous scaffolds promoted cell migration into deep regions of the scaffold and enhanced their osteogenic differentiation.[21] Furthermore, ES of neurons and glial cells at the beginning of the cultures reduces the formation of clusters in the PPy-coated structure, while improving their proliferation and accelerating their maturation.[61] Björninen *et al.* developed a device able to stimulate simultaneously 24 scaffolds for long times to differentiate adipose stem cells (ASCs) into smooth muscle cells (SMCs). The PPy coating was shown to improve the SMC expression and proliferation.[22]

Furthermore, the shape of the structure is not significant in the stimulation results. Neurons derived from immortalized dorsal root ganglion (DRG) were obtained inside hydrogel scaffolds with different shapes by their electric stimulation over 2 days.[77] Neurogenesis produced by ES was also confirmed after the culture of PC12 cells inside PPy/collagen scaffolds, showing improved cell adherence and growth.[67]

## 10.5 Conclusions and Future Perspectives

Conducting 3D scaffolds are indicated as the next-generation platforms to move toward real *in vivo* regeneration, providing a cost-effective, reliable and effective tool to enhance tissue formation in the laboratory before subsequent clinical trials. However, manufacturing in the third dimension is not always an easy task, since CPs are insoluble, and their layer-by-layer stacking makes them difficult to manipulate. Few groups have overcome such limitations and succeeded in the manufacture of 3D substrates. Here, we present a comprehensive overview of the state-of-the-art processing methodologies and the characterization techniques necessary to analyze correctly the properties in the tridimensional disposition. Nevertheless, this field is in its infancy and we anticipate that it will be exponentially expanded in the coming years, with a special highlight in emerging 3D printing techniques: we believe the future lies in the preparation of conductive printable inks that can be used to construct the 3D scaffold *in situ*.[49,110]

The main area where conductive 3D scaffolds have the most potential is tissue engineering of electroactive tissue, such as neurons, bones and heart

cells. Apart from tissue engineering, it is clear that all the other biomedical areas require 3D scaffolds that mimic as close as possible the *in vivo* tissue for a successful application. For the highest effectiveness, the substrates should obey the following criteria: homogeneous porosity with pore sizes large enough to host the cells, providing large surface area for cell attachment and proliferation; have similar mechanical properties to the tissue, including elastic modulus and wettability; and have a suitable surface composition to enhance the cell–substrate interaction. Nevertheless, biodegradation remains an issue that has still to be resolved.

Moreover, localized electric stimulation can play an important role in any of the cellular or tissue incubation steps. Initial studies demonstrated its potential, but further and extended investigations are in demand. Furthermore, the same implanted scaffold can be imagined as a single platform that can complete the different objectives at the same time. For instance, scaffolds loaded with drugs or growth factors and receptors could be used as monitoring devices for the regeneration of cells during their growth inside the scaffold. The next demand is to move forward *in vivo* assays, getting one step closer to the clinical application.

## Abbreviations

| | |
|---|---|
| CP | conducting polymer |
| PEDOT | poly(3,4-ethyl-enedioxythiophene) |
| PPy | polypyrrole |
| PANi | polyaniline |

## References

1. R. H. W. Funk, T. Monsees and N. Özkucur, *Prog. Histochem. Cytochem.*, 2009, **43**, 177–264.
2. M. Scanziani and M. Häusser, *Nature*, 2009, **461**, 930.
3. R. H. Clayton, O. Bernus, E. M. Cherry, H. Dierckx, F. H. Fenton, L. Mirabella, A. V. Panfilov, F. B. Sachse, G. Seemann and H. Zhang, *Prog. Biophys. Mol. Biol.*, 2011, **104**, 22–48.
4. F. Vasquez-Sancho, A. Abdollahi, D. Damjanovic and G. Catalan, *Adv. Mater.*, 2018, **30**, 1705316.
5. T. Nezakati, A. Seifalian, A. Tan and A. M. Seifalian, *Chem. Rev.*, 2018, **14**, 6766–6843.
6. R. Balint, N. J. Cassidy and S. H. Cartmell, *Acta Biomater.*, 2014, **10**, 2341–2353.
7. L. Jiang, Y. J. Wang, Z. Q. Liu, C. Y. Ma, H. Yan, N. Xu, F. L. Gang, X. M. Wang, L. Y. Zhao and X. D. Sun, *Tissue Eng., Part B*, 2019, **25**, 398–411.
8. K. Svennersten, M. H. Bolin, E. W. H. Jager, M. Berggren and A. Richter-Dahlfors, *Biomaterials*, 2009, **30**, 6257–6264.

9. M. Marzocchi, I. Gualandi, M. Calienni, I. Zironi, E. Scavetta, G. Castellani and B. Fraboni, *ACS Appl. Mater. Interfaces*, 2015, **7**, 17993–18003.
10. A. M.-D. Wan, S. Inal, T. Williams, K. Wang, P. Leleux, L. Estevez, E. P. Giannelis, C. Fischbach, G. G. Malliaras and D. Gourdon, *J. Mater. Chem. B*, 2015, **3**, 5040–5048.
11. J. S. Choi, J. S. Park, B. Kim, B. T. Lee and J. H. Yim, *Polymer*, 2017, **124**, 95–100.
12. M. Ravi, V. Paramesh, S. R. Kaviya, E. Anuradha and F. P. Solomon, *J. Cell. Physiol.*, 2015, **230**, 16–26.
13. W. Jie, F. Song, X. Li, W. Li, R. Wang, Y. Jiang, L. Zhao, Z. Fan, J. Wang and B. Liu, *RSC Adv.*, 2017, **7**, 34415–34424.
14. S. Y. Severt, N. A. Ostrovsky-Snider, J. M. Leger and A. R. Murphy, *ACS Appl. Mater. Interfaces*, 2015, **7**, 25281–25288.
15. S. Wang, S. Guan, Z. Zhu, W. Li, T. Liu and X. Ma, *Mater. Sci. Eng., C*, 2017, **71**, 308–316.
16. S. Wang, S. Guan, J. Xu, W. Li, D. Ge, C. Sun, T. Liu and X. Ma, *Biomater. Sci.*, 2017, **5**, 2024–2034.
17. I. del Agua, S. Marina, C. Pitsalidis, D. Mantione, M. Ferro, D. Iandolo, A. Sanchez-Sanchez, G. G. Malliaras, R. M. Owens and D. Mecerreyes, *ACS Omega*, 2018, **3**, 7424–7431.
18. A. M. Wan, S. Inal, T. Williams, K. Wang, P. Leleux, L. Estevez, E. P. Giannelis, C. Fischbach, G. G. Malliaras and D. Gourdon, *J. Mater. Chem. B*, 2015, **3**, 5040–5048.
19. T. Vishnoi and A. Kumar, *BioMed Res. Int.*, 2013, **2013**, 294679.
20. K. M. Sajesh, R. Jayakumar, S. V. Nair and K. P. Chennazhi, *Int. J. Biol. Macromol.*, 2013, **62**, 465–471.
21. J. Zhang, M. Li, E.-T. Kang and K. G. Neoh, *Acta Biomater.*, 2016, **32**, 46–56.
22. M. Björninen, K. Gilmore, J. Pelto, R. Seppänen-Kaijansinkko, M. Kellomäki, S. Miettinen, G. Wallace, D. Grijpma and S. Haimi, *Ann. Biomed. Eng.*, 2017, **45**, 1015–1026.
23. T. Giffney, M. Xie, M. Sartelet and K. C. Aw, *AIMS Mater. Sci.*, 2015, **2**, 414–424.
24. D. Iandolo, A. Ravichandran, X. Liu, F. Wen, J. K. Chan, M. Berggren, S. H. Teoh and D. T. Simon, *Adv. Healthcare Mater.*, 2016, **5**, 1505–1512.
25. W. E. Tenhaeff and K. K. Gleason, *Adv. Funct. Mater.*, 2008, **18**, 979–992.
26. S. W. Kim, S. W. Lee, J. Kim, J.-H. Yim and K. Y. Cho, *Polymer*, 2016, **102**, 127–135.
27. F. Song, W. Jie, T. Zhang, W. Li, Y. Jiang, L. Wan, W. Liu, X. Li and B. Liu, *RSC Adv.*, 2016, **6**, 92804–92812.
28. W. Zhao, Y. Li, S. Wu, D. Wang, X. Zhao, F. Xu, M. Zou, H. Zhang, X. He and A. Cao, *ACS Appl. Mater. Interfaces*, 2016, **8**, 34027–34033.
29. Y. Ding, J. Yang, C. R. Tolle and Z. Zhu, *ACS Appl. Mater. Interfaces*, 2018, **10**, 16077–16086.

30. A. Shahini, M. Yazdimamaghani, K. J. Walker, M. A. Eastman, H. Hatami-Marbini, B. J. Smith, J. L. Ricci, S. V. Madihally, D. Vashaee and L. Tayebi, *Int. J. Nanomed.*, 2014, **9**, 167–181.
31. M. Yazdimamaghani, M. Razavi, M. Mozafari, D. Vashaee, H. Kotturi and L. Tayebi, *J. Mater. Sci.: Mater. Med.*, 2015, **26**, 274.
32. N. Zanjanizadeh Ezazi, M. A. Shahbazi, Y. V. Shatalin, E. Nadal, E. Mäkilä, J. Salonen, M. Kemell, A. Correia, J. Hirvonen and H. A. Santos, *Int. J. Pharm.*, 2018, **536**, 241–250.
33. L. Qingyong, N. Zhengxiang, R. Jiaoyan and L. Wenzhen, *Curr. Med. Chem.*, 2018, **25**, 963–981.
34. F. Zhao, D. Yao, R. Guo, L. Deng, A. Dong and J. Zhang, *Nanomaterials*, 2015, **5**, 2054.
35. M. B. Runge, M. Dadsetan, J. Baltrusaitis, T. Ruesink, L. Lu, A. J. Windebank and M. J. Yaszemski, *Biomacromolecules*, 2010, **11**, 2845–2853.
36. A. Guiseppi-Elie, *Biomaterials*, 2010, **31**, 2701–2716.
37. F. Ketabat, S. Khorshidi and A. Karkhaneh, *Polym. Int.*, 2018, **67**, 975–982.
38. S. Yang, L. K. Jang, S. Kim, J. Yang, K. Yang, S. W. Cho and J. Y. Lee, *Macromol. Biosci.*, 2016, **16**, 1653–1661.
39. B. Guo, A. Finne-Wistrand and A.-C. Albertsson, *Biomacromolecules*, 2011, **12**, 2601–2609.
40. X. Zhao, P. Li, B. L. Guo and P. X. Ma, *Acta Biomater.*, 2015, **26**, 236–248.
41. J. Yang, G. Choe, S. Yang, H. Jo and J. Y. Lee, *Biomater. Res.*, 2016, **20**, 31.
42. Y. Y. Xia and H. L. Zhu, *Soft Matter*, 2011, **7**, 9388–9393.
43. C. Xu, S. Guan, S. Wang, W. Gong, T. Liu, X. Ma and C. Sun, *Mater. Sci. Eng., C*, 2018, **84**, 32–43.
44. Y. S. Kim, K. Cho, H. J. Lee, S. Chang, H. Lee, J. H. Kim and W.-G. Koh, *React. Funct. Polym.*, 2016, **109**, 15–22.
45. G. L. Mario Cheong, K. S. Lim, A. Jakubowicz, P. J. Martens, L. A. Poole-Warren and R. A. Green, *Acta Biomater.*, 2014, **10**, 1216–1226.
46. R. Ravichandran, J. G. Martinez, E. W. H. Jager, J. Phopase and A. P. F. Turner, *ACS Appl. Mater. Interfaces*, 2018, **10**, 16244–16249.
47. J. Shin, E. J. Choi, J. H. Cho, A. N. Cho, Y. Jin, K. Yang, C. Song and S. W. Cho, *Biomacromolecules*, 2017, **18**, 3060–3072.
48. J. Hur, K. Im, S. W. Kim, J. Kim, D.-Y. Chung, T.-H. Kim, K. H. Jo, J. H. Hahn, Z. Bao, S. Hwang and N. Park, *ACS Nano*, 2014, **8**, 10066–10076.
49. Q. Wu, J. Wei, B. Xu, X. Liu, H. Wang, W. Wang, Q. Wang and W. Liu, *Sci. Rep.*, 2017, **7**, 41566.
50. D. Mawad, A. Artzy-Schnirman, J. Tonkin, J. Ramos, S. Inal, M. M. Mahat, N. Darwish, L. Zwi-Dantsis, G. G. Malliaras, J. J. Gooding, A. Lauto and M. M. Stevens, *Chem. Mater.*, 2016, **28**, 6080–6088.

51. T. Dai, X. Jiang, S. Hua, X. Wang and Y. Lu, *Chem. Commun.*, 2008, 4279–4281.
52. D. Mawad, E. Stewart, D. L. Officer, T. Romeo, P. Wagner, K. Wagner and G. G. Wallace, *Adv. Funct. Mater.*, 2012, **22**, 2692–2699.
53. R. Du, Y. Xu, Y. Luo, X. Zhang and J. Zhang, *Chem. Commun.*, 2011, **47**, 6287–6289.
54. J. M. Holzwarth and P. X. Ma, *J. Mater. Chem.*, 2011, **21**, 10243–10251.
55. A. S. Tayi, E. T. Pashuck, C. J. Newcomb, M. T. McClendon and S. I. Stupp, *Biomacromolecules*, 2014, **15**, 1323–1327.
56. X. Niu, M. Rouabhia, N. Chiffot, M. W. King and Z. Zhang, *J. Biomed. Mater. Res., Part A*, 2015, **103**, 2635–2644.
57. C. Chen, Y. Yu, K. Li, M. Zhao, L. Liu, J. Yang, J. Liu and D. Sun, *Cellulose*, 2015, **22**, 3929–3939.
58. S. Z. Yow, T. H. Lim, E. K. F. Yim, C. T. Lim and K. W. Leong, *Polymers*, 2011, **3**, 527–544.
59. L. Jin, Z. Q. Feng, M. L. Zhu, T. Wang, M. K. Leach and Q. Jiang, *J. Biomed. Nanotechnol.*, 2012, **8**, 779–785.
60. J. Pelto, M. Bjorninen, A. Palli, E. Talvitie, J. Hyttinen, B. Mannerstrom, R. Suuronen Seppanen, M. Kellomaki, S. Miettinen and S. Haimi, *Tissue Eng., Part A*, 2013, **19**, 882–892.
61. Q. Xu, L. Jin, C. Li, S. Kuddannayai and Y. Zhang, *RSC Adv.*, 2018, **8**, 11027–11035.
62. L. Jin, T. Wang, Z. Q. Feng, M. Zhu, M. K. Leach, Y. I. Naim and Q. Jiang, *J. Mater. Chem.*, 2012, **22**, 18321–18326.
63. S. Anuradha, K. Uma Maheswari and S. Swaminathan, *Biomed. Mater.*, 2011, **6**, 025004.
64. F. Zamani, M. Amani-Tehran, A. Zaminy and M. A. Shokrgozar, *Fibers Polym.*, 2017, **18**, 1874–1881.
65. S.-J. Lee, T. Esworthy, S. Stake, S. Miao, Y. Y. Zuo, B. T. Harris and L. G. Zhang, *Adv. Biosyst.*, 2018, **2**, 1700213.
66. L. Pan, G. Yu, D. Zhai, H. R. Lee, W. Zhao, N. Liu, H. Wang, B. C. K. Tee, Y. Shi, Y. Cui and Z. Bao, *Proc. Natl. Acad. Sci. U. S. A.*, 2012, **109**, 9287.
67. B. Weng, X. Liu, R. Shepherd and G. G. Wallace, *Synth. Met.*, 2012, **162**, 1375–1380.
68. I. Rajzer, M. Rom, E. Menaszek and P. Pasierb, *Mater. Lett.*, 2015, **138**, 60–63.
69. E. Bihar, T. Roberts, E. Ismailova, M. Saadaoui, M. Isik, A. Sanchez-Sanchez, D. Mecerreyes, T. Hervé, J. B. De Graaf and G. G. Malliaras, *Adv. Mater. Technol.*, 2017, **2**, 1600251.
70. M. A. Darabi, A. Khosrozadeh, R. Mbeleck, Y. Liu, Q. Chang, J. Jiang, J. Cai, Q. Wang, G. Luo and M. Xing, *Adv. Mater.*, 2017, **29**, 1700533.
71. C. Y. Ma, L. Jiang, Y. J. Wang, F. L. Gang, N. Xu, T. Li, Z. Q. Liu, Y. J. Chi, X. M. Wang, L. Y. Zhao, Q. L. Feng and X. D. Sun, *Materials*, 2019, **12**, 2491.

72. A. R. Spencer, E. Shirzaei Sani, J. R. Soucy, C. C. Corbet, A. Primbetova, R. A. Koppes and N. Annabi, *ACS Appl. Mater. Interfaces*, 2019, **11**, 30518–30533.
73. Y. B. Wu, Y. X. Chen, J. H. Yan, D. Quinn, P. Dong, S. W. Sawyer and P. Soman, *Acta Biomater.*, 2016, **33**, 122–130.
74. E. Fantino, I. Roppolo, D. Zhang, J. Xiao, A. Chiappone, M. Castellino, Q. Guo, C. F. Pirri and J. Yang, *Macromol. Mater. Eng.*, 2018, **303**, 1700356.
75. C. Tondera, T. F. Akbar, A. K. Thomas, W. L. Lin, C. Werner, V. Busskamp, Y. X. Zhang and I. R. Minev, *Small*, 2019, **15**, 8.
76. S. W. Sawyer, P. Dong, S. Venn, A. Ramos, D. Quinn, J. A. Horton and P. Soman, *Biomed. Phys. Eng. Express*, 2017, **4**, 015005.
77. D. N. Heo, S. J. Lee, R. Timsina, X. Y. Qiu, N. J. Castro and L. G. Zhang, *Mater. Sci. Eng. C Mater. Biol. Appl.*, 2019, **99**, 582–590.
78. Y. W. Han and J. Y. Dong, *J. Micro. Nanomanuf.*, 2018, **6**, 20.
79. S. Vijayavenkataraman, S. Zhang, S. Thaharah, G. Sriram, W. F. Lu and J. Y. H. Fuh, *Polymers*, 2018, **10**, 753.
80. S. Vijayavenkataraman, S. Kannan, T. Cao, J. Y. H. Fuh, G. Sriram and W. F. Lu, *Front. Bioeng. Biotechnol.*, 2019, **7**, 14.
81. J. C. Thiéblemont, A. Brun, J. Marty, M. F. Planche and P. Calo, *Polymer*, 1995, **36**, 1605–1610.
82. R. Kiebooms, A. Aleshin, K. Hutchison and F. Wudl, *J. Phys. Chem. B*, 1997, **101**, 11037–11039.
83. K. Pielichowski, *Solid State Ionics*, 1997, **104**, 123–132.
84. Z. Huan, H. K. Chu, H. Liu, J. Yang and D. Sun, *Biomed. Microdevices*, 2017, **19**, 102.
85. C. Hwang, D. H. Jung Min, K. Tae-Yun, J. Jin Woo, H. Dong-Heon and C. Dong-Woo, *J. Micromech. Microeng.*, 2012, **22**, 125002.
86. S. J. Florczyk, K. Wang, S. Jana, D. L. Wood, S. K. Sytsma, J. G. Sham, F. M. Kievit and M. Zhang, *Biomaterials*, 2013, **34**, 10143–10150.
87. L. Jiang, C. Gentile, A. Lauto, C. Cui, Y. Song, T. Romeo, S. M. Silva, O. Tang, P. Sharma, G. Figtree, J. J. Gooding and D. Mawad, *ACS Appl. Mater. Interfaces*, 2017, **9**, 44124–44133.
88. A. H. Dewi, I. D. Ana and J. Jansen, *J. Biomed. Mater. Res., Part A*, 2016, **104**, 768–774.
89. H. Kwon, L. Sun, D. M. Cairns, R. S. Rainbow, R. C. Preda, D. L. Kaplan and L. Zeng, *Acta Biomater.*, 2013, **9**, 6563–6575.
90. S. Wang, C. Sun, S. Guan, W. Li, J. Xu, D. Ge, M. Zhuang, T. Liu and X. Ma, *J. Mater. Chem. B*, 2017, **5**, 4774–4788.
91. S. Inal, A. Hama, M. Ferro, C. Pitsalidis, J. Oziat, D. Iandolo, A.-M. Pappa, M. Hadida, M. Huerta, D. Marchat, P. Mailley and R. M. Owens, *Adv. Biosyst*, 2017, **1**, 1700052.
92. A. Abedi, M. Hasanzadeh and L. Tayebi, *Mater. Chem. Phys.*, 2019, **237**, 121882.
93. A. R. Spencer, E. S. Sani, J. R. Soucy, C. C. Corbet, A. Primbetova, R. A. Koppes and N. Annabi, *ACS Appl. Mater. Interfaces*, 2019, **11**, 30518–30533.

94. W. Guo, X. Zhang, X. Yu, S. Wang, J. Qiu, W. Tang, L. Li, H. Liu and Z. L. Wang, *ACS Nano*, 2016, **10**, 5086–5095.
95. O. Akhavan, *J. Mater. Chem. B*, 2016, **4**, 3169–3190.
96. M. Carter and J. Shieh, in *Guide to Research Techniques in Neuroscience*, 2nd edn, ed. M. Carter and J. Shieh, Academic Press, San Diego, 2015, pp. 89–115.
97. Miklavčič, D., Pavšelj, N. and Hart, F.X. (2006). Electric Properties of Tissues. In *Wiley Encyclopedia of Biomedical Engineering*, M. Akay (Ed.). , DOI: 10.1002/9780471740360.ebs0403.
98. J. D. Bronzino, *The Biomedical Engineering Handbook*, 2nd edn, CRC Press, 1999.
99. S. Sayyar, M. Bjorninen, S. Haimi, S. Miettinen, K. Gilmore, D. Grijpma and G. Wallace, *ACS Appl. Mater. Interfaces*, 2016, **8**, 31916–31925.
100. A. Subramanian, U. M. Krishnan and S. Sethuraman, *J. Mater. Sci.: Mater. Med.*, 2012, **23**, 1797–1809.
101. Kenry and B. Liu, *Biomacromolecules*, 2018, **19**, 1783–1803.
102. L. A. Reis, L. L. Chiu, N. Feric, L. Fu and M. Radisic, *J. Tissue Eng. Regen. Med.*, 2016, **10**, 11–28.
103. R. Dong, X. Zhao, B. Guo and P. X. Ma, *Biomacromolecules*, 2017, **18**, 2808–2819.
104. B. W. Walker, R. P. Lara, E. Mogadam, C. H. Yu, W. Kimball and N. Annabi, *Prog. Polym. Sci.*, 2019, **92**, 135–157.
105. J.-W. Lee, F. Serna, J. Nickels and C. E. Schmidt, *Biomacromolecules*, 2006, **7**, 1692–1695.
106. Q. Lei, J. K. He and D. C. Li, *Nanoscale*, 2019, **11**, 15195–15205.
107. S.-Z. Yow, T. H. Lim, E. K. F. Yim, C. T. Lim and K. W. Leong, *Polymers*, 2011, **3**, 527–544.
108. R. Balint, N. J. Cassidy and S. H. Cartmell, *Tissue Eng., Part B*, 2012, **19**, 48–57.
109. C. Daish, R. Blanchard, K. Fox, P. Pivonka and E. Pirogova, *Ann. Biomed. Eng.*, 2018, **46**, 525–542.
110. S. L. Dong, L. Han, C. X. Du, X. Y. Wang, L. H. Li and Y. Wei, *Macromol. Rapid Commun.*, 2017, **38**, 1600551.
111. A. R. Spencer, A. Primbetova, A. N. Koppes, R. A. Koppes, H. Fenniri and N. Annabi, *ACS Biomater. Sci. Eng.*, 2018, **4**(5), 1558–1567.

CHAPTER 11

# *Redox Polymers for Drug Delivery*

L. ROMERO-AZOGIL, E. BENITO, N. IGLESIAS, E. GALBIS, M.-V. DE-PAZ AND M.-G. GARCÍA-MARTÍN*

Departamento de Química Orgánica y Farmacéutica, Facultad de Farmacia, Universidad de Sevilla, C /Prof. García González, s/n, 41012-Seville, Spain
*Email: graciagm@us.es

## 11.1 Introduction

Polymers containing redox cleavage linkages are termed redox polymers and they are the stimuli-responsive polymers most extensively studied as drug-delivery systems (DDS) to date. In their response to different redox potentials according to the physiological microenvironments, *i.e.*, cytosol and extracellular fluids, they can undergo chemical and physical transformations, ultimately triggering the release of the therapeutic agent they carry. The promising applications of redox polymers in cancer therapy, as nanovehicles for targeted intracellular drug and gene delivery, are confirmed by the high number of reviews that have appeared in recent years.[1–15]

The pair glutathione/glutathione disulfide (GSH/GSSG) is the bio-redox agent most profuse in animal cells, it is known that the levels of GSH in cytosol and nuclei range from 1 to 10 mM, which are 100 to 1000 times higher than those found in the blood circulation and extracellular fluids (2–20 μM).[16] This difference in the concentration of GSH is able to destabilize the nanotransporters sensitive to reducers once they have been internalized in the cells. Besides, *in vivo* studies have demonstrated that the GSH levels in tumor tissues is four times higher than those found in healthy

Polymer Chemistry Series No. 34
Redox Polymers for Energy and Nanomedicine
Edited by Nerea Casado and David Mecerreyes

Published by the Royal Society of Chemistry, www.rsc.org

tissues.[17] Quinn and Davies[7] have recently reviewed the applications of GSH-responsive polymers in drug delivery through physical or conjugate encapsulation of drugs including genetic material. They also refer signaling molecules, fluorescence, magnetic resonance imaging and protein therapy.

On the other hand, reactive oxygen species (ROS), which are products derived from aerobic metabolism, are critical for the production of various hormones, the regulation of cell signaling, among others. However, high concentrations of ROS such as peroxynitrite ($ONOO^-$), hydrogen peroxide ($H_2O_2$), singlet oxygen ($^1O_2$), superoxide ($O_2^-$), and hydroxyl radicals ($HO^\bullet$) have been detected in some damaged tissues. Furthermore, excess ROS is closely associated with DNA mutations and the development of several cancer types.[18] The mucosal ROS concentrations in inflammatory tissues and colon cancer are 10–100-fold higher than those of normal tissues, so ROS-response polymer nanoparticles can control targeted drug/gene release.[2,4,8,12,19] Although GSH-based reduction-responsive systems have been studied for many years, great interest has been generated by ROS systems more recently.[2] In addition to the number of recent reviews, we highlight herein some relevant research work published to date. In an illustrative manner, the most significant functional groups responsible for the redox character of the polymers are presented in Scheme 11.1.

## 11.2 Reduction-responsive Drug-delivery Systems

Reduction-responsive DDS have been used both to supply simple molecules and macromolecules such as proteins and genetic material. In this regard, disulfide- and diselenide-based polymers have been the most widely explored materials up to date.

### 11.2.1 Disulfide-based Systems

The difference in redox potential in different physiological compartments (extracellular and cytoplasm) is crucial for the success of DDS containing disulfide (S–S) reductive links. However, it is just not a matter of specificity, the speed of reduction for a determined S–S link in the cytoplasm is faster compared with the extracellular media.[20] Once the stabilized disulfide-based materials are internalized in the cells they suffer exchange with the thiol group of the intracellular GSH, what causes destabilization of the systems with the consequent release of the cargo. The S–S bonds have been incorporated either in the main backbone, in cross-linked segments or into side chains by grafting.

The biodegradability rate varies depending on the S–S link location. Hence, fast biodegradability is achieved when the S–S bond is contained in the polymer backbone, while the tridimensional structure is lost when such a bond is responsible for cross-linking. Incorporation of disulfide linkages has been mainly achieved by thiol–disulfide exchange reaction, Michael addition, and thiol–thioester exchange, as Quinn and Davis have masterfully reviewed.[7] The developments of living/controlled polymerization as atom transfer radical

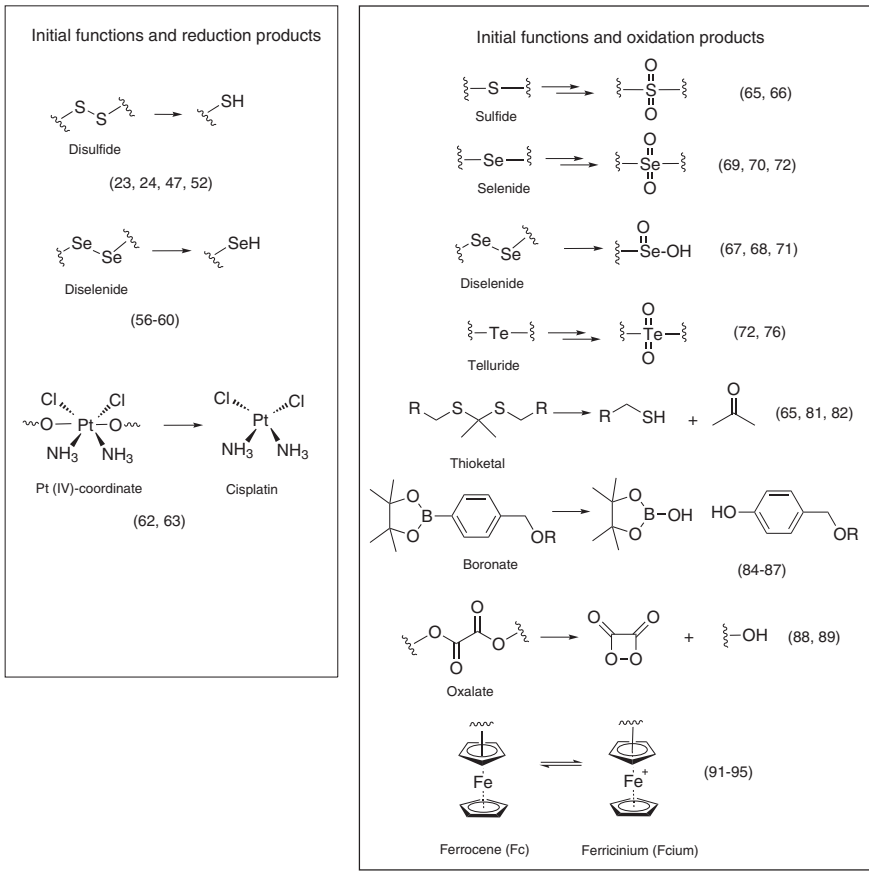


**Scheme 11.1** Most common reactive functional groups found in redox polymers; recent references are included.

polymerization (ATRP), reversible addition-fragmentation chain transfer polymerization (RAFT) and ring-opening polymerization (ROP) have greatly contributed to achieve polymers with well-defined S–S end groups.[12,21]

The thiol–disulfide exchange reaction has been extensively exploited for constructing redox-responsive prodrugs, and gene and drug carriers.[12] Nevertheless, the same exchange due to the action of the GSH on polymeric materials (films, hydrogels) and particles (micelles, nanogels, vesicles, mesoporous silica nanoparticles) containing S–S links results in their degradation, emitting low-molecular-weight fragments which are more polar in general terms whether these links are in the main chain or in other cross-linking positions.[7] Such an exchange is also triggered to initiate controllable changes in the material properties (*i.e.*, hydrogel modulus)[22] by forming and subsequently dissolving hydrogels. The hydrogels were formed *in situ* by covalent cross-linking of polymer chains through reversible S–S bonds. The hydrogels were based on 8-arm-PEG-SH cross-linked in the presence of either $H_2O_2$ or 8-arm-PEG-S-TP

(S-TP = sulfur-thiopyridine) in phosphate buffer solution (pH 8.0). GSH was identified as the dissolution agent since the hydrogel was dissolved by the thiol/disulfide interchange. The hydrogels were loaded with doxycycline and evaluated in the treatment of mustard-gas-injured skin in an *in vivo* mouse model and epidermal re-epithelialization was observed.

Pyridyl disulfide chemistry has become an important strategy in the preparation of GSH-responsive materials. Ge *et al.* have recently investigated a sequential tumor pH-promoted cellular internalization and intracellular stimuli-responsive drug release.[23] The ring-opening reaction of drug-conjugated thiolactones released thiol groups *via* aminolysis by *N*-(3-aminopropyl)-imidazole, which further reacted with poly(ethylene glycol)-*block*-poly(pyridyldisulfide ethylmethacrylate) (PEG-PDSEMA) to produce imidazole and disulfide bonds-incorporated block copolymer prodrugs (BCPs) (Figure 11.1). Taking paclitaxel (PTX), PTX BCPs exhibited high drug-loading content (>50%) and low critical micellization concentration ($5 \times 10^{-3}$ g $L^{-1}$), which could self-assemble into micellar nanoparticles in aqueous solution with a small size (~40 nm). The nanoparticles showed high accumulation and uniform distribution in hypopermeable tumors *via* systemic administration. The imidazole moieties endowed nanoparticles with pH-sensitive charge transition from nearly neutral to positive, which promoted cellular internalization.

Additionally, disulfide bonds could be cleaved by intracellular GSH of cancer cells, which accelerated the release of PTX. Lastly, highly aggressive murine breast cancer 4T1 tumor and hypopermeable human pancreatic adenocarcinoma BxPC3 tumor were completely ablated after treatment by PTX BCP nanoparticles.

More recently, Perrier *et al.*[24] have developed an efficient strategy toward cyclic-peptide polymer conjugates capable of self-assembling into supramolecular polymeric nanotubes driven by the strong multiple hydrogen bonding interactions between the cyclic peptides. Reactions between a cysteine-containing cyclic peptide (CP-SH) and pyridyl disulfide-containing polymers were initially studied, leading to the quantitative formation of cyclic peptide – polymer conjugates (Figure 11.2). The disulfide linker formed by the pyridyl disulfide reaction was then selectively reduced to thiol in the presence of a reductant, enabling the transition of the conjugates from non-assembling unimers to self-assembled supramolecular polymeric nanotubes. In addition, the introduction of a responsive linker between the cyclic peptide and the polymer would endow these materials with stimuli-responsive properties, offering great potential regarding their application as DDS and as antimicrobial drugs.

Polyurethanes (PU) containing disulfide links in the main chain were successfully self-assembled into micelles for intracellular drug delivery.[25,26] In a rational design of polymers that could be used as carrier systems for drug delivery under the reductive conditions of the colon, we prepared disulfide-based PU,[27–32] some of them derived from monosaccharides. For instance, functionalization of reduction-sensitive L-arabinitol-based PU[28] was achieved by thiol-ene click reactions. Degradation of these materials

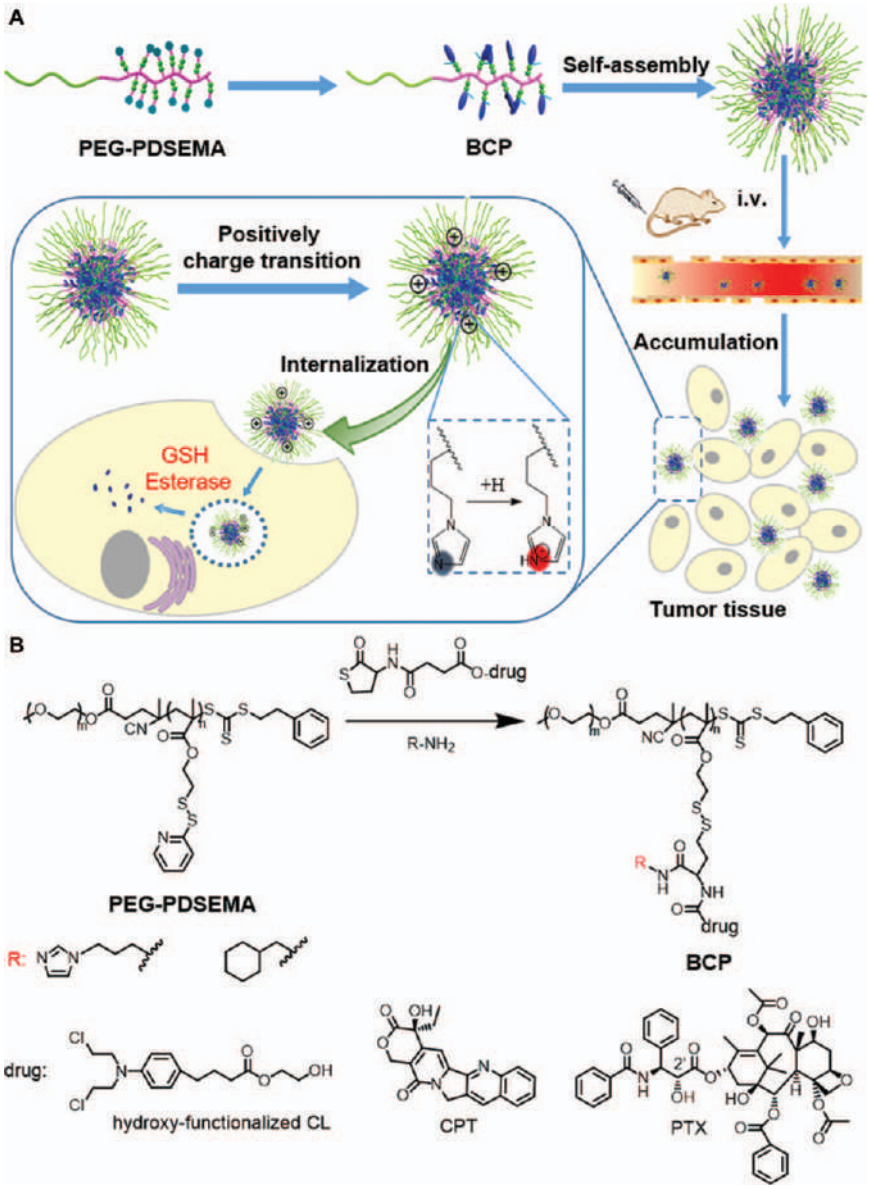


**Figure 11.1** (A) Schematic illustration of the construction of BCPs, self-assembly into micellar nanoparticles, and subsequent transporting processes including efficient accumulation and positively charge transition in the tumor extracellular microenvironment followed by increased tumor penetration, cellular internalization and effective drug release inside cells. (B) Synthetic routes of varying BCPs *via* thiolactone chemistry reaction among thiolactone-functionalized drug molecules, functional moiety-containing amines, and PEG-PDSEMA.
Reproduced from ref. 23 with permission from Elsevier, Copyright 2018.

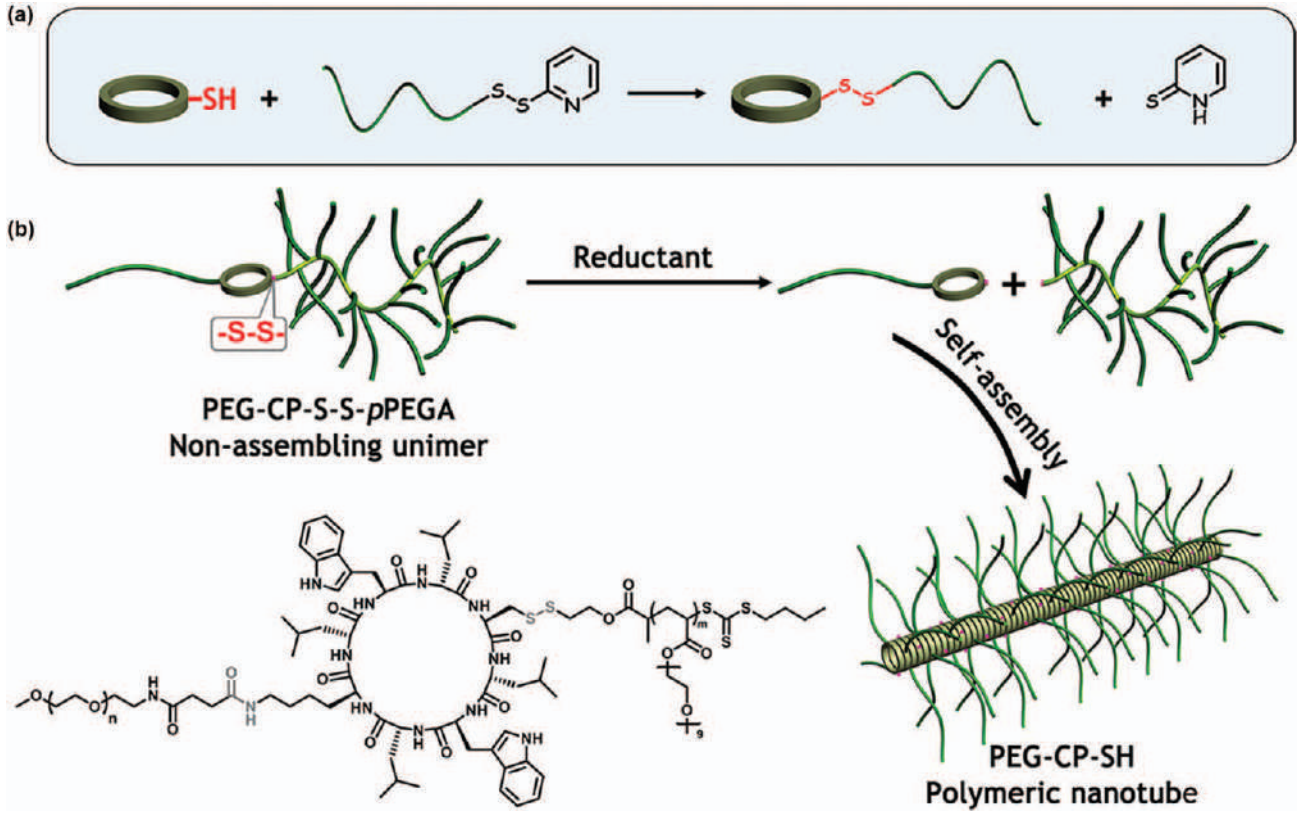


**Figure 11.2** (a) Reaction between a thiol-containing cyclic peptide and a pyridyl disulfide-containing polymer to fabricate cyclic peptide – polymer conjugate; (b) chemical structure and redox-responsiveness of the asymmetric conjugate PEG-CP-S-S-pPEGA.
Reproduced from ref. 24 with permission from the American Chemical Society, Copyright 2019.

was achieved by GSH under physiological conditions due to the presence of S–S groups along the polymer backbone. Atomic force microscopy (AFM) on solid-supported multilayered dry polymer films—prepared by spin-coating from dimethylsulfoxide solutions—was used to study the morphology of the polymers and the degradation process. Matrix systems containing the polymers selected according to their rheological properties were also investigated as modulated methotrexate-release systems. Later, we prepared a set of D-mannitol-based PU containing S–S links and demonstrated that it is possible to modulate the GSH response by finely tune the hydrophilicity of the polymers.[30] We also demonstrated the use of this type of PU for sustained and site-specific drug release in the gastrointestinal tract in the presence of GSH.[32]

Disulfide-containing cross-linkers such as dithiodipropionic acid, bis(2,2′-hydroxyethyl)disulfide, cystamine and their derivatives have been often used to create tridimensional reduction-responsive polymers.[12] We also studied the scope and limitations of aqueous dispersions prepared from a novel cross-linked chitosan-*N*-acetyl-D,L-homocysteine conjugate polymer (Figure 11.3), as a controlled DDS for topical use.[33] The neutral anhydrous theophylline and the cationic diltiazem hydrochloride were selected for controlled-release formulations, paying special attention to the influence of the new-polymer concentration (1 and 3% w/v) in drug release. Additionally, the use of texture profile analysis as a convenient method for the mechanical characterization of topical preparations was also discussed.

It has been described[34] how in a very efficient way cross-linked micelles retained drug in circulation before reaching the target, where they were later disassembled to deliver the drug. Since cross-linking may slow down the response rate, a surface-cross-linked micelle with extremely rapid release of the encapsulated pyrene was obtained.[35] The fast release profile was associated with electrostatic repulsion among the headgroups. Once the covalent cross-linking shell was broken by the stimuli, the micelle exploded rapidly.

Polymers with a disulfide group within the chains have been prepared by ATRP, resulting in polymers that can be cleaved into two thiol-terminated chains upon exposure to a variety of reducing agents.[21] Likewise, ring-opening polymerization affords this type of structure, *i.e.*, a synthesized functional monomer having a S–S bond was polymerized into hyperbranched polyphosphate by self-condensing ROP.[36] The hydrophobic and hydrophilic domains contained the disulfide bond and phosphate groups, respectively. The polymers could self-assemble into multi-core–shell micelles with potential applications in drug release. Kataoka *et al.*[37] synthesized a series of block copolymers (PEG–SS–P(Asp), PEG–SS–P[Asp(DET)] and PEG–P[Asp(DET)]) by ROP, and the electrostatic attractions between the polycation and polyanion blocks led them to self-assemble into polyion complex micelles. These micelles re-assemble into hollow nanocapsules under reduction by dithiothreitol (DTT).

Polymers with disulfide bonds hanging on the side chain can be easily obtained by the polymerization of disulfide-containing monomers. By this strategy

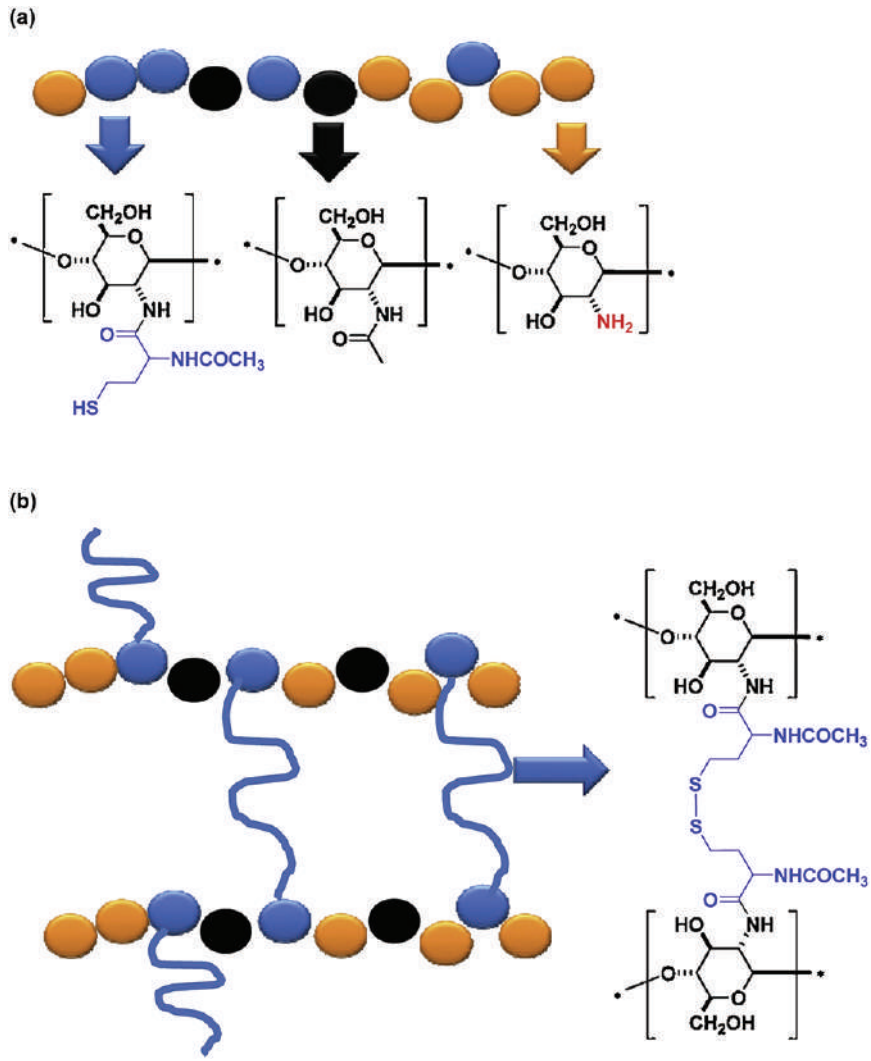


**Figure 11.3** Chemical structures of (a) chitosan-*N*-acetyl-D,L-homocysteine conjugate and (b) cross-linked chitosan-*N*-acetyl-D,L-homocysteine conjugate. Reproduced from ref. 33 with permission from Elsevier, Copyright 2016.

it was possible to achieve a tunable balance between the hydrophobic and hydrophilic blocks, and once the balance was broken by cleaving the disulfide bond, the assemblies would collapse to release the drugs.[38] Moreover, according to the amount of DTT added, a micelle-to-nanogel transition could take place that provided a more complex release profile. This transition afforded a facile technique to solve the drug leakage problem of uncross-linked polymeric carriers in clinical applications. Self-cross-linked nanogels were synthesized by RAFT polymerization of oligoethyleneglycol methacrylate and pyridyl disulfide

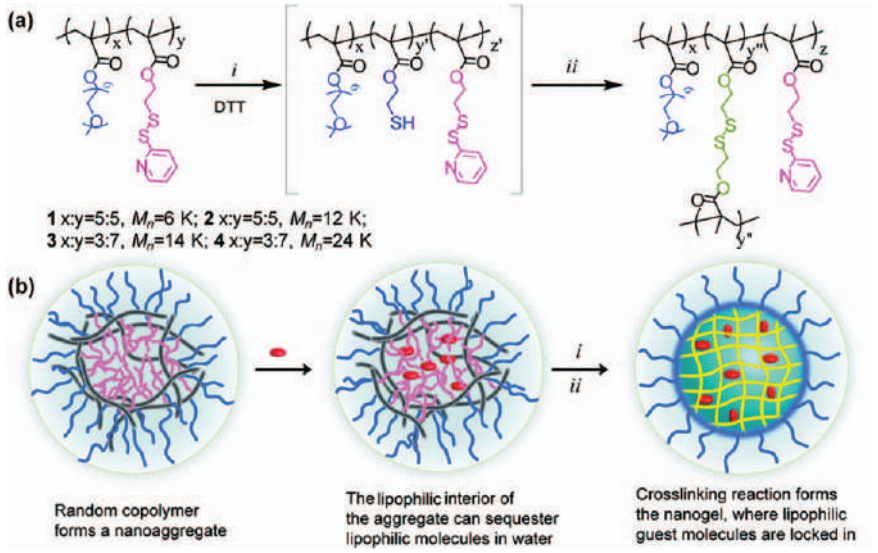


**Figure 11.4** (a) Structure of the polymer precursors and nanogels: (i) cleavage of a specific amount of PDS group by DTT, and (ii) nanogel formation by inter/intrachain cross-linking. (b) Schematic representation of the preparation of the biodegradable nanogels.
Reproduced from ref. 39 with permission from the American Chemical Society, Copyright 2010.

ethyl methacrylate.[39] Nanogels with controlled size and guest release rate were formed after adding a certain amount of DTT into the precursor solution (Figure 11.4). Fluorescence resonance energy transfer (FRET) was used to study the stability of the nanogels and their encapsulation ability, and no green fluorescence emission indicated that the FRET occurred among the dye molecules in the network. However, after adding 20 mM DTT, the breakage of the nanogels enabled the dyes to migrate to the hydrophobic domain of the dioleoyl phosphatidylcholine bilayer vesicles, which caused a decrement of the FRET ratio.

Engler *et al.* synthesized polycarbonate-based brush polymers with detachable, disulfide-linked side chains.[40] In another approach, a thiol-containing drug was incorporated in the side chain *via* exchange reaction,[41] and it was found that a herceptin-functionalized camptothecin nanoparticle (HCN) was supersensitive to the trigger of elevated redox potential, releasing all payloads in less than 30 minutes. Even cellulose-based nanogels with GSH reactive cross-links were prepared by grafting polymeric pendants *via* ATRP.[42] Ghosh *et al.* reported the synthesis of ABA triblock copolymers incorporating a central poly(disulfide) domain bracketed by segments of poly(triethyleneglycol monomethyl ether)methacrylate.[43] The poly(disulfide) domain was synthesized by step polymerization of 2,2′-dithiodipyridine with either 2,2′-(ethane-1,2-diylbis(oxy))-diethanethiol or 1,6-hexanedithiol. The resulting pyridyl disulfide capped prepolymer was then reacted with mercaptoethanol to give hydroxyl terminated poly(disulfide). The terminal hydroxyls were then reacted with

2-bromoisobutyrylbromide affording a macromolecular initiator for ATRP. These initiators were used to polymerize 2-(2-(2-methoxyethoxy) ethoxy)ethyl methacrylate, giving the ABA triblock copolymer. The resulting polymers assembled into micelles, encapsulated a dye (Nile Red) and showed degradation by GSH with corresponding dye release.

In 2014, other particles based on poly(2-ethyl-2-oxazoline) brushes with pendant thiol groups were described.[44] The brushes were synthesized by ATRP of oligo(2-ethyl-2-oxazoline)methacrylate and glycidyl methacrylate (GMA). Incorporation of pyridyl disulfide groups was attained by ring opening of the oxirane-GMA. The polymer brushes were assembled into thin films on either planar or colloidal substrates. After cross-linking, exposure to 5 mM GSH caused disintegration of the particles in a few hours. In this case, poly(2-ethyl-2-oxazoline) embodies an alternative antifouling polymer to the most common employed PEG.

Gene transfection is a nonviral tool for therapy on gene-based diseases by delivering nucleic acids into the target cells and change gene functions or protein expressions. Nonetheless, toxicity and low transfection efficiency are the main drawbacks to overcome. Disulfide redox-polymers have been widely explored as gene-delivery systems to increase the transfection efficiency of nucleic acids. Hence, Cai and Li *et al.*[45] developed redox-responsive nonviral gene-delivery nanocarriers based on neutral cationic brush copolymers. The copolymer effectively condensed pDNA into polyplex nanoparticles and released the plasmid under reductive conditions. Moreover, the enhanced efficiency of gene transfection by magnetofection has been investigated,[46] which uses magnetic fields to concentrate magnetic nanoparticles (MNPs) containing nucleic acid into the target cells. MNPs are usually modified with cationic compounds such as polyethylenimine (PEI). Here a redox-responsive disulfide bond was used to link PEI to MNPs (Scheme 11.2), generating detachable PEIs for DNA protection, endosomal escape and nuclear entry. The magnetic gene carrier exhibited not only efficient DNA transfection but also a gene-silencing effect as tested in both HeLa and HepG2 cells. The modified redox-responsive MNPs released plasmid DNA by the action of GSH.

Ren and Feng *et al.*[47] reported a bioreducible poly(ethyleneglycol)-*b*-poly(disulfide-L-lysine) cationic polymer (PEG–SSL) *via* a Michael addition reaction of poly(ethyleneglycol)tetraacrylate PEG$(Ac)_4$ and the terminal amine group of poly(disulfide-L-lysine) (Scheme 11.3). PEG–SSL efficiently condensed the plasmid pZNF580, forming nano-sized polyplexes. When exposed to a reducing environment of 5 mM DTT, it rapidly released genes at higher weight ratios of the PEG–SSL polymer in the PEG–SSL/pDNA complexes. *In vitro* transfection and cytotoxicity were investigated in EA.hy926 cells showing that PEG–SSL successfully delivered pZNF580 into the cells with less cytotoxicity compared to PEI25kDa. The flow cytometry and confocal scanning laser microscopy results indicated that PEG–SSL polyplexes exhibited good cellular uptake and nuclear colocalization rates.

Thiol-thioester exchange is another strategy used on polymers having pendant thioester groups for the preparation of GSH-responsive polymers.

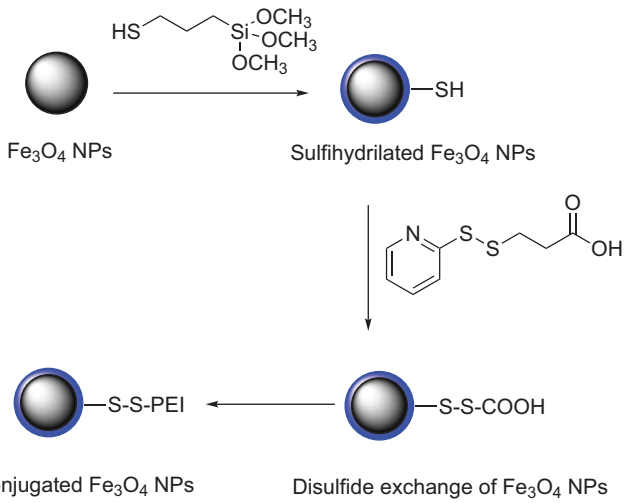


**Scheme 11.2** Schematic illustration of the synthesis of $Fe_3O_4$@-$SiO_2$-SS-PEI nanoparticles.
Adapted from ref. 46 with permission from the Royal Society of Chemistry.

Liu *et al.*[48] prepared copolymers of *N*,*N*-dimethylacrylamide and pyridyl disulfide ethylacrylamide *via* RAFT polymerization. By sequentially reacting the pyridyl disulfide functional polymers with tris(2-carboxyethyl)phosphine and thymine thioester, they obtained a thymine-conjugated biodynamer (see Scheme 11.4). Such a conjugate containing reversible thioester linkages could interact with the adenine-modified molecule mediated by hydrogen bonding, and demonstrate L-glutathione (GSH)-responsiveness. It could also interact with melamine and adenosine-5′-triphosphate (ATP) and form spherical aggregates in water.

A novel type of GSH-responsive DDS is nanoporous or mesoporous silica because the pores can incorporate high drug loading and can act as "gates." In 2008, Feng *et al.*[49] first reported the preparation of mesoporous silica with disulfide functionalized polymeric gates and since then this area has been deeply explored by many authors. Thus, Giménez *et al.*[50] coated MCM-41 mesoporous silica with PEG chains tied *via* a disulfide linkage. In this case, the dye safranin-O was first loaded into the particles and the surface was provided with thiol groups using (3-mercaptopropyl)trimethoxysilane. Reaction with 2,2′-dipyridyl disulfide provided pyridyl disulfide functionalized mesoporous silica particles. A GSH-responsive PEG coating was then afforded by reacting the pyridyl disulfide with *O*-(2-mer-captoethyl)-*O*′-methyl-hexa(ethylene glycol) (Figure 11.5). Release of safranin-O (or preloaded DOX) was able to be triggered by exposure to a physiological concentration of GSH (10 mM).

Based on this approach, different methods have been used to prepare thiol-terminated PEG polymer[51] showing similar release profiles in the

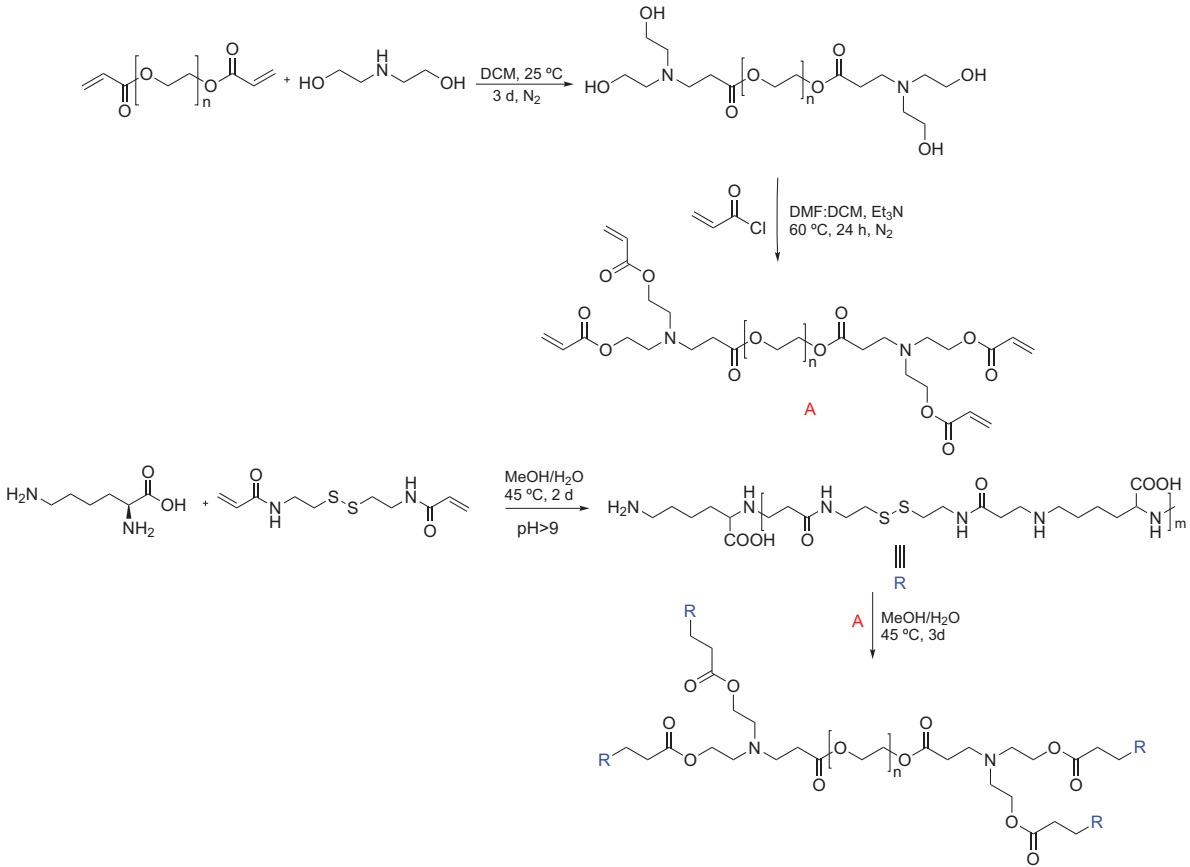


**Scheme 11.3** Synthesis of poly(ethyleneglycol)-*b*-poly(disulfide-L-lysine) (PEG-SSL). R: poly(disulfide-L-lysine). Adapted from ref. 47 with permission from the Royal Society of Chemistry.

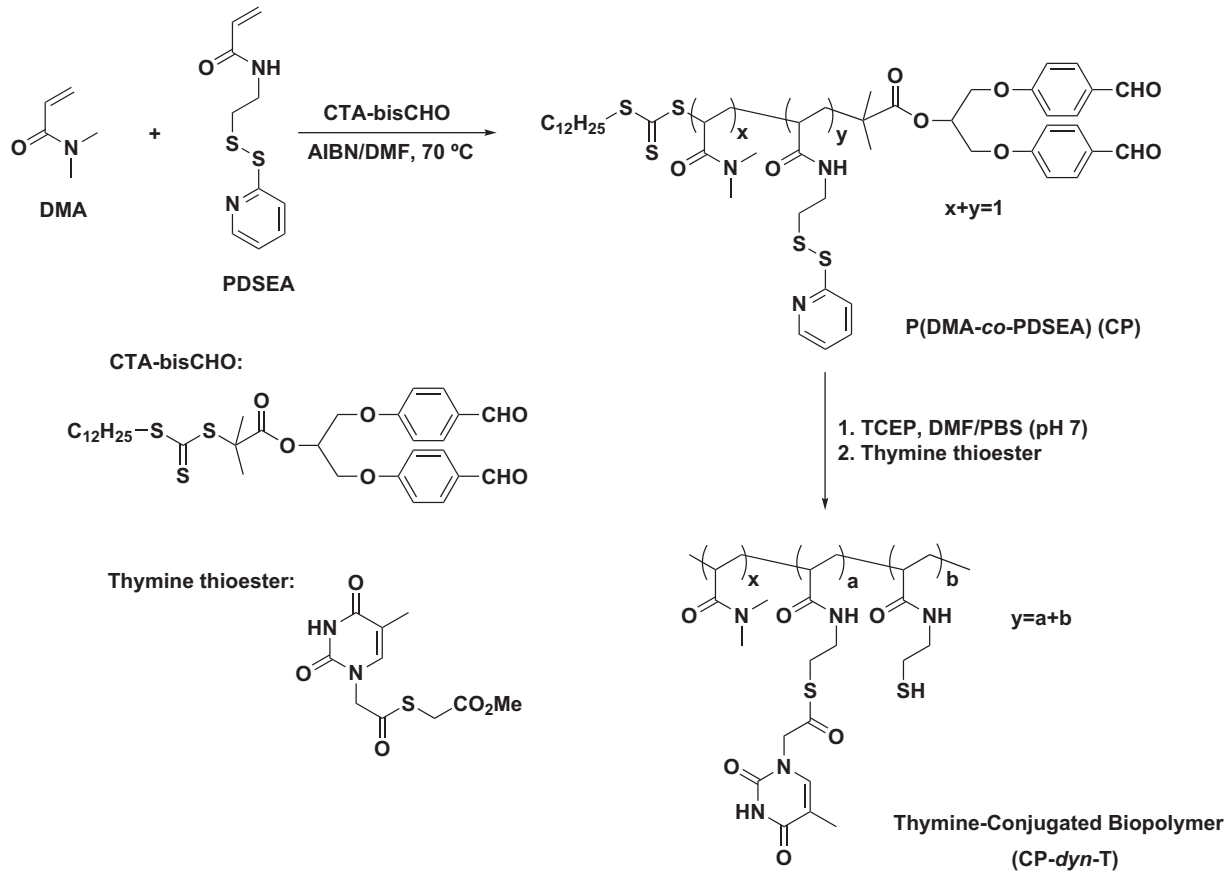


**Scheme 11.4** Synthesis of PDS-functionalized copolymer P(DMA-*co*-PDSEA) by RAFT polymerization and thymine-conjugated biodynamer *via* a thiol–thioester exchange reaction.
Adapted from ref. 48 with permission from the Royal Society of Chemistry.

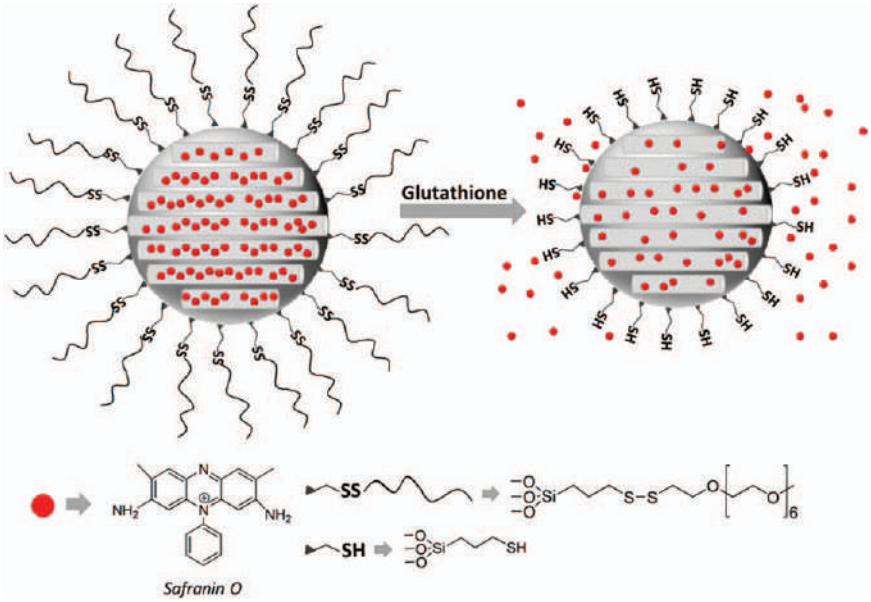


**Figure 11.5** Schematic representation of gated material S1 capped with PEG chains through disulfide linkages.
Reproduced from ref. 50 with permission from the American Chemical Society, Copyright 2015.

presence of GSH. Another class of stimuli-responsive systems that has generated great expectation lately is metal–organic frameworks (MOFs).[52] They have high drug-loading capacity, easy functionalization, good biodegradability and good biocompatibility. MOFs can respond to a single stimulus and multiple endogenous stimuli, *i.e.*, pH, redox and ATP, in addition to exogenous stimuli. Liu *et al.*[53] synthesized GSH-responsive nanoscale coordination polymers (NCPs) composed of manganese ions ($Mn^{2+}$) and dithiodiglycolic acid as the disulfide-containing organic linker for drug delivery. These Mn–SS NCPs were loaded with DOX *via* hydrophobic interactions to produce Mn-SS/DOX NPs, which were then coated with a layer of polydopamine (PDA) and further modified with PEG to yield spherical Mn-SS/DOX@PDA–PEG NPs (see Figure 11.6). Owing to S–S linkage within dithiodiglycolic acid cleavage in the presence of GSH, the efficient dissociation of these NCPs and DOX release were achieved. In addition, the protonation of the amino group on DOX provoked faster release at lower pH values. Furthermore, the $Mn^{2+}$ ions in these NCPs provided a strong T1 contrast during magnetic resonance imaging. These Mn-SS/DOX@PDA–PEG NPs also exhibited improved *in vivo* therapeutic efficacy compared to free DOX. These inherently biodegradable NCPs have the potential for clinical translation.

Similarly, Wang, Qi *et al.*[54] reported the novel GSH-sensitive MOF M-DTBA (M = Fe, Al, or Zr, as metal connecting points) and 4,4′-dithiobisbenzoic

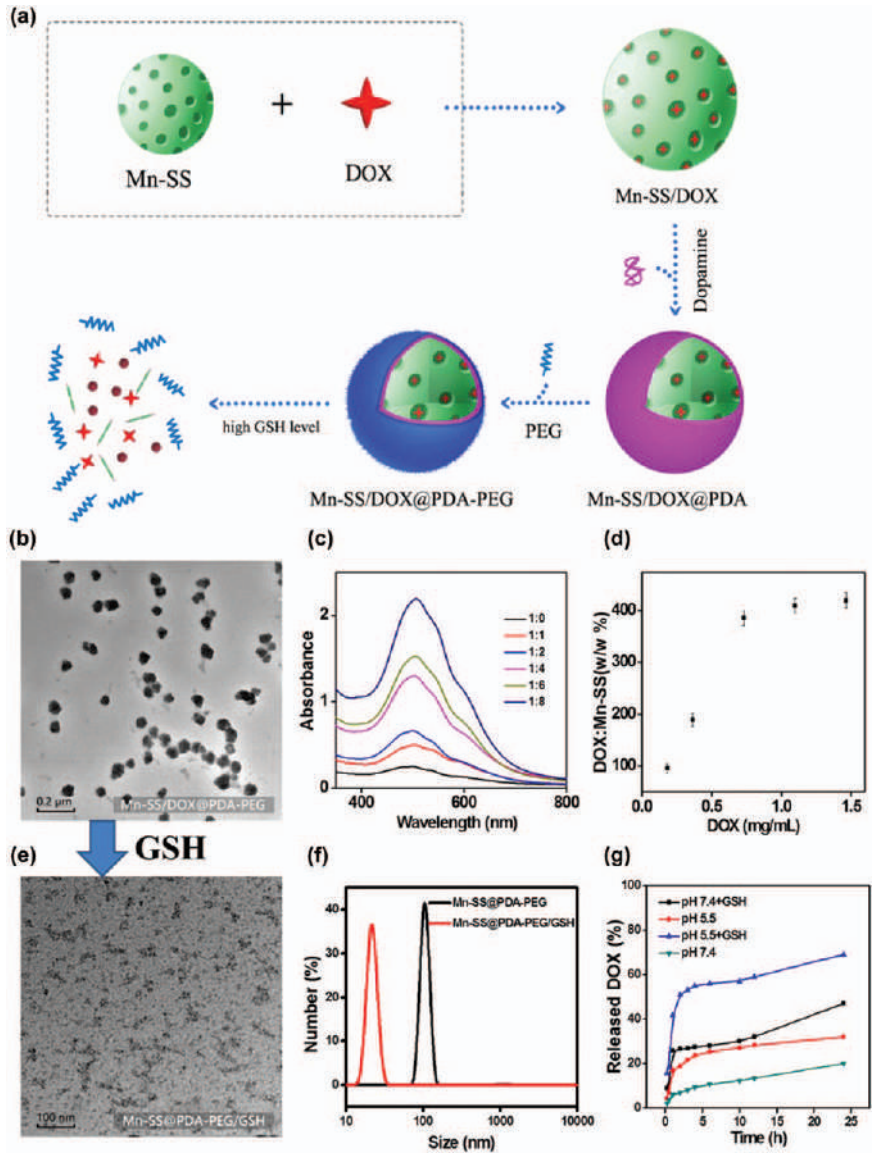


**Figure 11.6** Drug loading and release. (a) Scheme showing the preparation of DOX-loaded NCPs, as well as GSH-triggered nanoparticle decomposition and drug release. (b) TEM image of Mn-SS/DOX@PDA-PEG nanoparticles. (c) Ultraviolet – visible (UV – vis) – NIR spectra of DOX-loaded Mn-SS with different concentrations of added DOX, varying from 0 to 1.5 mg $mL^{-1}$. (d) Quantification of DOX loadings at different feeding DOX concentrations. (e) TEM image of Mn-SS@PDA-PEG 0.25 h post incubation with 10 mM GSH. (f) Hydrodynamic diameters of Mn- SS/DOX@PDA-PEG before and after incubation with GSH. (g) Cumulative release profiles of DOX from Mn-SS/DOX@PDA-PEG in PBS with different pHs without or with 10 mM GSH. Reproduced from ref. 53 with permission from the American Chemical Society, Copyright 2017.

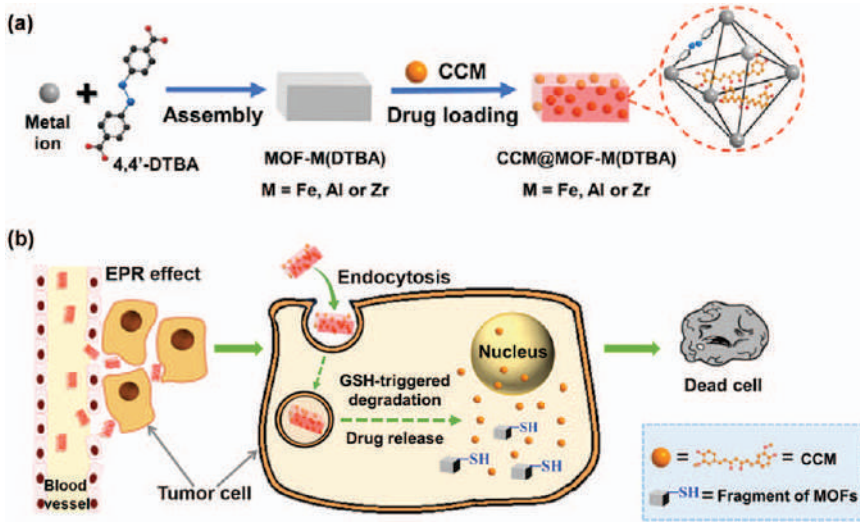


**Figure 11.7** Schematic illustration of (a) the preparation of CCM@MOF-M(DTBA), and (b) the redox-responsive degradation of CCM@MOF-M(DTBA) in tumor cells for cancer therapy.
Reproduced from ref. 54 with permission from the American Chemical Society, Copyright 2018.

acid (4,4′-DTBA) as the GSH-sensitive organic bridging ligand. MOF-Zr(DTBA) displayed the appropriate size and properties as a drug carrier. By incorporating curcumin (CCM) into MOF-Zr(DTBA), CCM@MOF-Zr(DTBA) nanoparticles displayed a faster release behavior *in vitro* and enhanced the cell death compared with free CCM (Figure 11.7). The release of CCM reached 87.4% after 22 h in phosphate buffer solution (pH 7.4). The *in vivo* anticancer experiments indicated that the NPs exhibited much higher anti-tumor efficacy than free CCM. This strategy for constructing responsive MOF-based nanocarriers might open new possibilities for the application of MOFs in drug delivery, molecular imaging and theragnostics.

### 11.2.2 Diselenide-containing Systems

Diselenide linkage is an improving strategy to access redox-responsive systems based on the lower bond dissociation energy of Se–Se and C–Se bonds compared to S–S and C–S bonds. Diselenide bonds can respond to both oxidants and reductants, thus diselenide bonds can be oxidized to seleninic acid and reduced to selenol in the presence of a reducing environment. They display high potential as more efficient and specific DDS but introduction of the diselenide linkage in the polymeric chains is not as easy as that of the disulfide linkage.[6,12,14,55] Besides, many inconveniences related to insolubility, toxicity and efficient synthetic methods are being revised currently. For instance, Yi, Zhang *et al.*[56] have very recently investigated mesoscale simulations of DOX distribution of the star polymer [PCL-*b*-

P(HEMASe-Se˜)-*b*-PPEGMA]$_6$ diselenide cross-linked micelles with different diselenide cross-linking levels (CLs). The self-assembly process results obtained by dissipative particle dynamics (DPD) simulations revealed the formation of three-layer spherical micelles with the loaded DOX mainly distributed at the interfacial regions of the inner PCL core and middle HEMA layer. Furthermore, the nearest media–bead bond breaking principle was applied to study the effect of breaking the Se–Se bond on the drug-release properties. A low CL gave rise to intense drug release, increasing the toxic side effects on the system. With the increase in the CL, the micelles showed the transformation from local cross-linking to compact cross-linking, leading to slower drug release. Therefore, this work could provide some guidance on the mesoscale for the design and controlled building of reversible cross-linked micelles for smart DDS. Another approach recently proposed is the synthesis of a redox-responsive amphiphilic polymer, Bi(mPEG-PLGA)-$Se_2$ from mPEG-PLGA and 3,3′-diselanediyldipropanoic acid using DCC/DMAP as coupling agents.[57] Due to its amphiphilic nature, the polymer self-assembled into stable micelles in aqueous solution with a hydrodynamic size of $123.9 \pm 0.85$ nm, which exhibited DOX-loading content of 6.61 wt.% and encapsulation efficiency (EE) of 54.9%. The DOX-loaded micelles released 73.94% and 69.54% of their cargo within 72 h upon treatment with 6 mM GSH and 0.1% $H_2O_2$, respectively, under physiological conditions. The MTT (3-[4,5-dimethylthiazol-2-yl]-2,5-diphenyltetrazolium bromide) assay results demonstrated that Bi(mPEG-PLGA)-$Se_2$ did not present toxicity and the DOX-loaded micelles showed pronounced antitumor activities against HeLa cells, 44.46% of cells were viable at a maximum dose of 7.5 mg $mL^{-1}$. Cellular uptake experiments confirmed the internalization of DOX-loaded micelles and drug release by redox stimuli in cytosol and nuclei of cancer cells.

In this same line, a similar study has been made with triblock copolymer Bi(mPEG-SeSe)-PCL.[58] This amphiphilic triblock copolymer could self-assemble into uniform nanoparticles in aqueous medium and disassemble upon redox stimuli. The copolymer nanoparticles showed a DOX loading content of 5.1 wt.% and a loading efficiency of 49%. *In vitro* drug-release studies showed that about 62.4% and 56% of DOX was released from the nanoparticles during 72 h at 37 °C in phosphate buffer solution containing 6 mM GSH and 0.1% $H_2O_2$, respectively, whereas only about 30% of DOX was released in PBS under the same conditions. The cell viability (MTT assays) results showed that the synthesized material was biocompatible with above 90% cell viability, and that the DOX-loaded Bi(mPEG-SeSe)-PCL nanoparticles had a high antitumor activity against HeLa cells and low antitumor activity against HaCaT cells, during a 24-h incubation period. Three-dimensional (3D) spheroids of HeLa cells were established for the evaluation of localization of the DOX-loaded nanoparticles into spheroid cells and the successfully inhibition of 3D tumor spheroid growth. The results indicated that the synthesized material Bi(mPEG–SeSe)-PCL was biocompatible and it could be a potential candidate for an anticancer drug-delivery system.

An interesting study that investigates the redox sensitivity differences between diselenide- and disulfide-containing micelles has been recently published.[59] Tri-block copolymer micelles (mPEG-PCL-SeSe-PCL-mPEG) and (mPEG-PCL-SS-PCL-mPEG) were synthesized, and the changes of micelles in size and structure were investigated in the presence of GSH or $H_2O_2$. It was found that the size and PDI of $(mPEG\text{-}PCL\text{-}Se)_2$ micelles presented more significant variations under redox condition compared with $(mPEG\text{-}PCL\text{-}S)_2$ micelles. The DOX released faster and to a greater extent from diselenide micelles than disulfide micelles. The $IC_{50}$ of $(mPEG\text{-}PCL\text{-}Se)_2$/DOX micelles was lower than that of $(mPEG\text{-}PCL\text{-}S)_2$/DOX micelles against 4T1 and HeLa cells. The amount of intracellular drug release from diselenide micelles was higher than from disulfide micelles in HeLa cells with GSH 4.6 mM. Therefore, it was demonstrated that those diselenide micelles were more sensitive stimuli-responsive drug carriers. Folic acid has also been incorporated into an amphiphilic triblock copolymer, PCL-(SeSe-mPEG/PEG-FA)$_2$, and micelles at concentrations higher than the critical micelle concentration in an aqueous medium were obtained.[60] DLS and TEM analyses showed that the micelles were spherical, with an average diameter of 120 nm. The hydrophobic anticancer drug paclitaxel was loaded into micelles, and its triggered release behavior under different redox conditions was verified. Folate-targeting micelles showed an enhanced uptake in 4T1 breast cancer cells and *in vitro* cytotoxicity by flow cytometry and MTS [3-(4,5-dimethylthiazol-2-yl)-5-(3-carboxymethoxyphenyl)-2-(4-sulfophenyl)-2H-tetrazolium] assay, respectively. Delayed tumor growth was confirmed in subcutaneously implanted 4T1 breast cancer in mice after intraperitoneal injection. The proposed redox-responsive copolymer offers a new type of biomaterial for drug delivery into cancer cells *in vivo*.

Wu *et al.*[61] developed an injectable dual redox-responsive Se–Se-containing PEG hydrogel with potential applications in stimuli-responsive drug release. The mechanical properties, cross-linking, oxidation and reduction-responsive degradation behaviors of the hydrogels were studied. Rhodamine B was encapsulated as a model drug in the hydrogel, and the degradation experiments were in accordance with a dual redox-responsive release profile.

Apart from sulfur- and selenium-based DDS, other reduction-responsive systems have also been successfully used. For instance, cisplatin is a broad-spectrum anticancer drug that must be conjugated with polymers to reduce the severe side effects to healthy cells.[62] Among them one of the most interesting is platinum(IV)-coordinate containing reduction responsive polymers.[63] Methodologically, cisplatin is first oxidized to a diol, then polycondensation reactions are conducted. This conjugate should be reduced selectively in tumor cells releasing cisplatin.

Trimethyl-locked benzoquinone (TMBQ) is another interesting option that has been used as a redox-responsive building block in DDS. Reduction of TMBQ produced a much more hydrophilic polymer due to the free amine groups generated. This change in solubility induced by the redox stimuli allows drug release.[64]

## 11.3 Oxidation-responsive Drug-delivery Systems

### 11.3.1 Sulfur- and Selenium-containing Systems

The most relevant progress in the biological applications of ROS (reactive oxygen species)-responsive polymers as drug carriers, and ROS probes medications for certain ROS-related diseases, have been recently reviewed.[1,2,4,6,10] Conversely to sulfur, selenium-based polymers present higher responsiveness toward ROS. For instance, polysulfides can be oxidized by ROS to polysulfoxides, thus achieving hydrophobic–hydrophilic transition. However, the major limitation of the sulfur-containing materials is the relative high stability of the sulfur, and the response to ROS may not be as sensitive. Nonetheless, recent examples on sulfur-containing ROS-responsive polymers are found. Thus, Gao, He *et al.*[65] synthesized three amphiphilic copolymers of mPEG-poly(ester-thioether), mPEG-poly(thioketal-ester) and mPEG-poly(thioketal-ester-thioether), and the ROS-sensitivity was demonstrated by NMR, DLS and SEM. Their corresponding nanoparticles showed enhanced cellular uptake and anticancer efficacy comparing to the control mPEG-*b*-PCL nanoparticles (Figure 11.8). However, DOX-loaded nanoparticles of the former exhibited the best ROS sensitivity and the fastest drug release rate.

Thayumanavan *et al.*[66] synthesized amphiphilic homopolymers with high densities of functional groups, by means of thiol-yne nucleophilic click reactions. An electron-deficient alkyne group bearing methacrylate monomer was polymerized by reversible addition-fragmentation chain-transfer (RAFT). Subsequently, the electron-deficient alkyne group on the polymer side chain was readily reacted with a thiol reagent using triethylamine as catalyst under mild conditions. The resultant homopolymer-bearing thiol vinyl ether functional groups could perform a second thiol addition with a stronger base, such as triazabicyclodecene, thus multifunctional homopolymers were accessed. Furthermore, these functionalized polymers bearing dithioacetal groups are sensitive to ROS, which compromises the host–guest properties of the assembly in response to this stimulus.

In 2017, Xu *et al.*[67] reported the fabrication of dual-responsive core–shell-structured metal–organic framework (MOF) nanocomposites as multi-responsive drug carriers. They synthesized a diselenide-containing triblock polyurethane (PEG-PUSeSe-PEG) which could self-assemble into micelles in aqueous solution. Then, the drug-loaded micelles were used as templates to promote the growth of MOFs. The chemical structure endowed the nanocomposites with redox/pH dual responsiveness. In acidic solution (pH 5.0), the shell of the nanocomposites slowly disintegrated, but the disintegration of the core of the nanocomposites could be expedited by both 1 mM GSH and 1 mM $H_2O_2$. In tumors, the drug could be released due to the higher acidity and abundance of GSH and ROS. Compared with sulfur-containing drug carriers, this drug-delivery system was much more sensitive to oxidation.

In the same year they reported[68] the preparation and light-induced cytotoxicity of diselenide and porphyrin-containing hyperbranched polymer. The

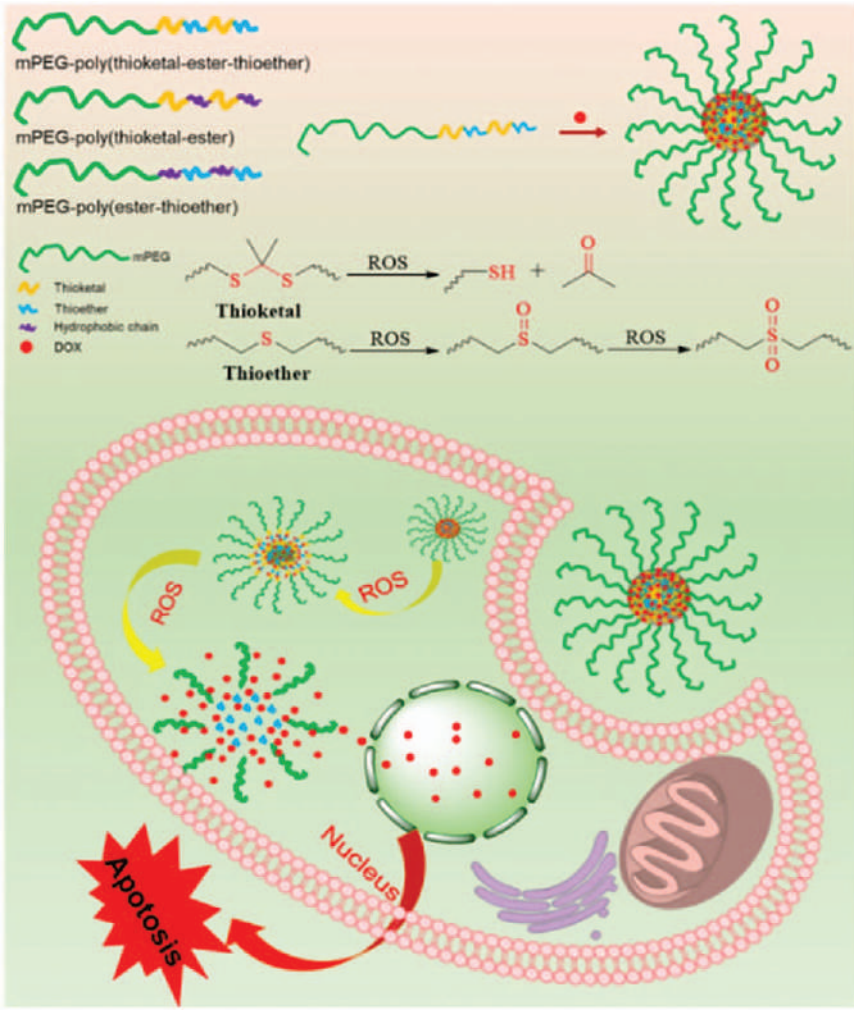


**Figure 11.8** Illustration of ROS-responsive nanoparticles to induce cell apoptosis. Reproduced from ref. 65 with permission from Elsevier, Copyright 2019.

polymer backbone contained porphyrin which could generate singlet oxygen upon visible light irradiation. The singlet oxygen species could cleave the Se–Se bonds *in situ*, provoking polymer disintegration. The oxidation product was confirmed to be seleninic acid. At concentrations ranging from 10 to 200 $\mu g\,mL^{-1}$, the nanoparticles were nontoxic to MDA-MB 231 human breast cancer cells, but cell viability was significantly reduced upon visible light irradiation. However, two important aspects should be overcome, such as the control of the hyperbranched polymer structure and the penetration of visible light into tissues of living organisms.

Du and Li demonstrated[69] another important difference between sulfur- (PS) and selenium-containing polymers (PSe) as phenylseleno esters might

undergo β-elimination upon oxidation. They reported the synthesis and ROS responsiveness of three kinds of biodegradable poly(ε-caprolactone) (PCL) with pendant sulfide or selenide groups. The sulfide groups of PS were completely oxidized to sulfoxide, becoming hydrophilic and water soluble. On the contrary, the oxidized PSe was unable to retain the selenoxide structure and again became amphiphilic copolymers once the elimination occurred. In this line, Xu *et al.*[70] have recently studied the ROS responsiveness and biodegradability of polymers containing selenide moieties in the main chain. However, only few ROS-responsive polymers currently are based on this reaction, hopefully they will be explored in the future.

In order to overcome the difficulties involved in the treatment of neurodegenerative diseases by transplanting exogenous neural stem cells (NSCs) into degenerated human brain, Zhang *et al.*[71] have utilized a strategy based on an amphiphilic ROS-responsive polyprodrug. They synthesized poly(carboxibetaine)-based, PCB-Se-Se-simvastatin (PCB-Se-Se-Sim) to utilize exogeneous NSCs as the source of brain-derived neurotrophic factor (BDNF) through traceable synergistic therapy (Figure 11.9). They tried to combine gen let-7b antisense oligonucleotide and simvastatin together, and managed to utilize superparamagnetic iron oxide nanocubes (SPIONs) to achieve the tracing of NSCs.

Due to the high concentration of ROS in NSCs, ROS-labile Se–Se bonds were selected as the linker. The polymer could efficiently absorb let-7b at N/P ratio of 5, and 80% of the simvastatin could be released within 24 h in phosphate buffer solution in the presence of 0.01% $H_2O_2$. The amount of brain-derived BDNF was

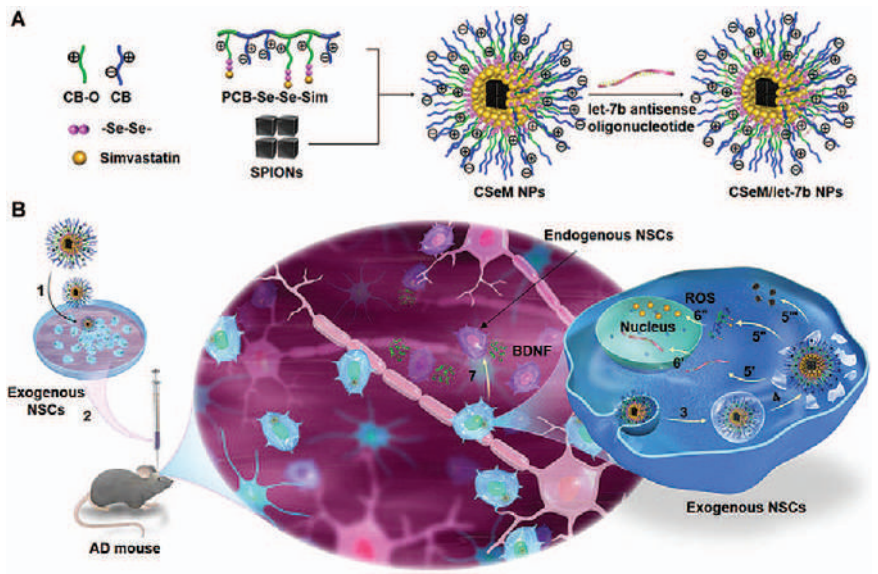


**Figure 11.9** Illustration of the strategy for construction and functionalization of the traceable CSeM/let-7b NPsa.
Reproduced from ref. 71 with permission from the American Chemical Society, Copyright 2018.

significantly decreased during the differentiation of NSCs. They successfully rescued the memory deficits of memory-deficient 2xTg-AD mice using the amphiphilic polyprodrug, and the track of SPIONs could be monitored by magnetic resonance imaging. The authors believe they have found a new path for the treatment of Alzheimer disease and other neurodegenerative disorders.

ROS-responsive aliphatic polycarbonates[72] synthesized by the controlled anionic ring-opening polymerization (ROP) of three six-membered cyclic carbonate monomers with Et selenide, Ph selenide or Et telluride groups, catalyzed by DBU (1,8-diazabicyclo[5.4.0]undec-7-ene) have been reported. With PEG macroinitiator, three series of amphiphilic block copolymers were prepared. They formed spherical nanoparticles of ~100 nm, which were stable in neutral phosphate buffer but dissociated rapidly under triggering of $H_2O_2$. However, it was observed that the telluride-containing nanoparticles degraded at the fastest rate, while the Ph selenide-based ones degraded most slowly. These ROS-responsive nanoparticles could load photosensitizer chlorin e6 (Ce6) and anticancer drug DOX. Under red light irradiation, Ce6 sensitized production of singlet oxygen, that triggered the degradation of nanoparticles, resulting in an accelerated payload release. *In vitro* cytotoxicity assays demonstrated that the NPs co-loaded with DOX and Ce6 exhibited a synergistic cell-killing effect against MCF-7 cells, representing a novel responsive nanoplatform for photodynamic therapy and/or chemotherapy. Another example of radiotherapy-controllable chemotherapy from ROS-responsive polymeric nanoparticle tumors has been reported by Chiu *et al.*[73] for effective local dual modality treatment of malignant.

### 11.3.2 Tellurium-based Systems

Tellurium-containing polymers constitute an emerging type of ROS-responsive DDS, to which Xu *et al.*[2] have paid special attention over recent years. They reported the first water-soluble tellurium-containing hyperbranched polymer sensitive to 0.1 mM $H_2O_2$.[74] By co-assembling tellurium-containing molecules and phospholipids, the biocompatibility of tellurium was improved, and the oxidation responsiveness of tellurium was retained.[75] A side-chain tellurium-containing polymer was shown to coordinate with cisplatin and could combine radiotherapy together with chemotherapy.[76] In 2015, the same group reported an ultrasensitive oxidation-responsive tellurium-containing polyurethane.[77] Upon the addition of 0.1mM $H_2O_2$, the micelles swelled significantly after 8 h. These micelles were more sensitive to $H_2O_2$ compared with their selenium- or sulfur-containing counterparts. They also showed that the polymer responded to ionizing radiation (generating ROS in aqueous solution) oxidizing the telluride and releasing the payload in the micelle. The polymer was responsive to 2 Gy gamma-ray radiation, a normal dosage utilized in clinical radiation therapy, and the oxidation process was completed within 1 h. This polymer represents a DDS that combines chemotherapy and radiotherapy. They also explored a synergistic therapy nanoplatform[78] that combines chemotherapy, photodynamic therapy and photothermal therapy. The

coordination between tellurium and platinum enhanced the loading capacity, prolonged the circulation time and prevented premature drug release. By incorporating indocyanine green (ICG) into this system, tellurium could be oxidized by the singlet oxygen generated under near-infrared light irradiation, thus releasing cisplatin from the polymer. The nanoparticles made from PEG-PUTe-PEG were stable in 10% fetal bovine serum in the dark, but most of the cisplatin could be released after being irradiated with an 808-nm laser for 10 min. The vehicles could be effectively internalized by MDA-MB-231 cells and showed no obvious cytotoxicity in the dark. In addition, circulation time, tumor-targeting ability and antitumor effects were tested *in vivo*.

Xu's group has also reported[79] the hierarchical oxidation behavior of a selenium- and tellurium-containing amphiphilic block copolymer which could be stepwise oxidized by both chemical oxidants and electrochemical oxidants. The hydrophobic blocks were selenium- and tellurium-containing polyurethane, and the hydrophilic blocks were PEG monomethyl ethers. This amphiphilic copolymer could spontaneously self-assemble into micelles in aqueous solution. By tuning the concentration of oxidants and oxidation periods, self-assembly behaviors could be tuned by stepwise chemical oxidation (Figure 11.10).

In the presence of a low concentration of $H_2O_2$ or a short oxidation period, only tellurium was oxidized. However, both tellurium and selenium were oxidized by increasing the concentration of $H_2O_2$ or the oxidation time. During the entire oxidation process, the polymer micelles only showed a cross-linking phenomenon without any swelling, regardless of the concentration of the oxidant or the oxidation period. Similarly, in electrochemical oxidation, the voltages and the oxidation periods affected the level of oxidation. In addition, the length of the PEG blocks would also affect the degree of electrochemical oxidation. Although these were only preliminary results, this research is expected to be continued in the future.

### 11.3.3 Systems with Thioketal Units

The interest in the thioketal link in relation to ROS materials is revealed as follows. Biodegradable poly(1,4-phenyleneacetone dimethylene thioketal) (PPADT) nanoparticles were successfully developed by Nam *et al.*[80] as an intracellular delivery carrier for anticancer therapeutic applications. PPADT was synthesized through condensation polymerization of 2,2-dimethoxypropane and 1,4-benzenedimethanethiol. PPADT afforded polymeric nanoparticles, which encapsulated Nile red and paclitaxel. The presence of ROS facilitated polymer degradation *via* breakage of the thioketal bonds, resulting in disruption of the nanoparticle structure and release of the encapsulated molecules. The paclitaxel-loaded PPADT nanoparticles demonstrated therapeutic effects on PC-3 prostate cancer cells, while no significant cytotoxic effects of placebo PPADT nanoparticles were observed. The same group[81] has recently reported a method that efficiently increased the *in vivo* anticancer drug efficacy levels through the photodynamic degradation of tumor-targeted nanocarriers. Folate-decorated poly(ethylene glycol)-polythioketal micelles were synthesized to encapsulate

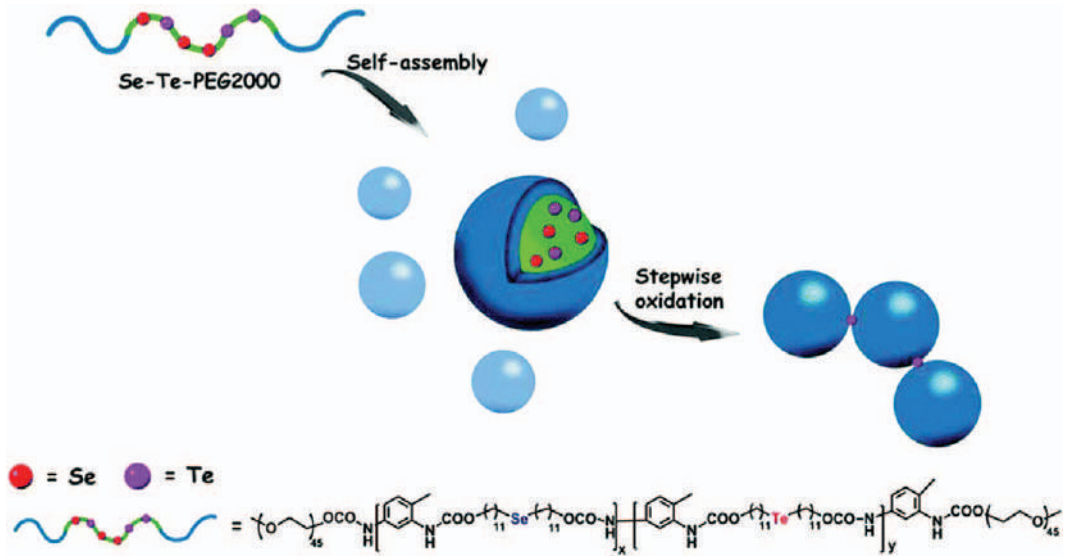


**Figure 11.10** Self-assembly and stepwise oxidation of the selenium- and tellurium-containing block copolymer. Reproduced from ref. 79 with permission from the Royal Society of Chemistry.

paclitaxel and porphyrins. ROS were generated by photo-excitation within the micelles to split the polythioketal backbone efficiently which enabled drug release only at the illuminated tumor site. Intravenous injection of a murine xenograft model with a low dose of paclitaxel within the micelles, 1 mg drug per kg (mouse), with a drug content that is less than that of Taxol by an order of magnitude, induced dramatic tumor regression without any severe systemic inflammation response or organ toxicity under low-power irradiation (55 mW $cm^{-2}$) at 650 nm. These researchers have also demonstrated[82] that on-demand drug release from tumor-targeted nanocarriers can reduce the effective dosage of anticancer drugs by rapidly increasing local drug concentration in tumor tissues. A near-infrared (NIR) photodynamic method triggered drug release from tumor-targeted polymer nanoparticles *via* ROS-mediated polymer degradation. Paclitaxel and silicon 2,3-naphthalocyanine bis(trihexylsilyloxide) were co-encapsulated as an anticancer drug and photosensitizer, respectively, within biotin-decorated PEG-polythioketal micelles. Upon NIR irradiation under the maximum permissible exposure level, the photoexcited naphthalocyanine generated ROS cleaved of the thioketal groups in the micelles to release the encapsulated paclitaxel. The photodynamically induced release of paclitaxel dramatically reduced the half maximal inhibitory concentration of paclitaxel by 39.9-fold and eliminated lung adenocarcinoma at a concentration one order of magnitude smaller than its maximum tolerated dose.

### 11.3.4 Systems with Aryl Boronic Ester Functional Groups

Many reports and patents regarding the incorporation of boronic ester groups in DDS have emerged recently. In the view of the fact that ROS-responsive polymeric or supramolecular hydrogels often present low sensitivity, slow response, instability and low mechanical strength, Li *et al.*[83] prepared a novel type of oxidation-responsive degradable hydrogel by means of the redox-initiated radical polymerization of a 4-arm-PEG acrylic macromonomer that owns a $H_2O_2$-cleavable phenylboronic acid linker in each of its arms. The macroscopic hydrogels presented good cytocompatibility, moderate mechanical strength, and a fast response toward $H_2O_2$ at low concentration, due to the covalently cross-linked hydrophilic PEG network and high sensitivity of the linker. The hydrogels could encapsulate molecules such as insulin and glucose oxidase (GOx) with high efficacy, affording a new glucose-responsive insulin-delivery platform on the basis of enzymic transformation of a biochemical signal (glucose) into an oxidative stimulus ($H_2O_2$). The *in vitro* results demonstrated that the same GOx-loaded hydrogel exhibited unequal degradation modes by different activating molecules, *i.e.*, bulk degradation by $H_2O_2$, and surface erosion by glucose. Moreover, compared to the macroscopic hydrogel, the nanogel with a diameter of ~160 nm prepared by inverse emulsion polymerization showed a much higher degradation rate even by activation through $H_2O_2$ at 20 mM concentration.

Ischemic stroke is the leading cause of long-term disability and death worldwide and lacks satisfactory drug-delivery systems. In the light of the up-regulation of ROS in the ischemic neuron, Xin *et al.*[84] have developed a

bioengineered ROS-responsive nanocarrier for stroke-specific delivery of a neuroprotective agent, NR2B9C, against ischemic brain damage. The nanocarrier is composed of a dextran polymer core modified with ROS-responsive boronic ester and a red blood cell (RBC) membrane shell with stroke homing peptide (SHp) inserted. These SHp-RBC-NP nanoparticles could control the release of NR2B9C triggered by high intracellular ROS in ischemic neurons after targeting ischemic brain tissues (see Figure 11.11). The therapeutic potential of such NPs for the treatment of ischemic stroke was systematically evaluated *in vitro* and in rat models with middle cerebral artery occlusion (MCAO).

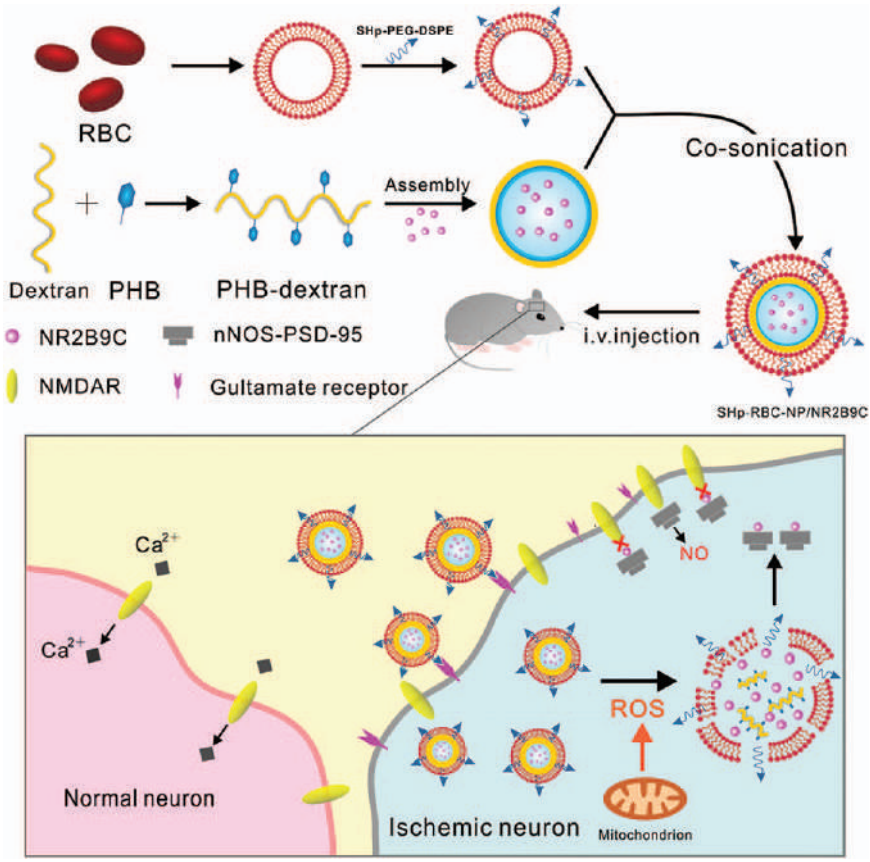


**Figure 11.11** Schematic design of the SHp-RBC-NP/NR2B9C. After intravenous injection, the SHp-RBC-NP/NR2B9C could prolong the circulation life with the RBC-mimicking properties and then target the ischemic brain site *via* stroke homing peptide-mediated transcytosis. When internalized into ischemic neurons, the NR2B9C is released from the PHB-dextran polymer nanoparticles attributable to the high levels of intracellular ROS and then selectively disrupted the NMDARs with PSD-95 to prevent the overproduction of nitric oxide (toxic signaling agent).
Reproduced from ref. 81 with permission from the American Chemical Society, Copyright 2018.

*In vitro* results showed that the SHp-RBC-NPs had great protective effects on glutamate-induced cytotoxicity in PC-12 cells. In addition, *in vivo* studies demonstrated that these NPs could drastically prolong the systemic circulation of NR2B9C, enhance the active targeting of the ischemic area in the MCAO rats and reduce ischemic brain damage.

By combining therapies that use dual drug-delivery systems (DDDS), the use of high doses and the increase of drug resistance are avoided. A DDDS based on nanogel-incorporated injectable hydrogel (NHG) was designed for sequential local delivery of combretastatin-A4 phosphate (CA4P) and DOX for anti-angiogenesis and anticancer combination therapy.[85] The injectable hydrogel was prepared for loading and quick release of the hydrophilic drug CA4P, while the nanohydrogel, incorporated into the injectable hydrogel through a pH-responsive boronate ester bond, was responsible for the sustained and long-term delivery of DOX. The DDDS released CA4P and DOX sequentially and exhibited high inhibitory activities on the proliferation of cancer cells *in vitro*. Likewise, a single injection displayed superior therapeutic efficacy *in vivo*. Immunohistochemistry analyses suggested a synergistic therapeutic effect through tumor vascular collapse caused by CA4P and tumor cell apoptosis induced by DOX.

Concerning immunotherapy to vaccinate or treat a broad range of illnesses, including cancer, infectious diseases and autoimmune disorders, Broaders *et al.*[86] recently stated that the rate of antigen release from nano/microparticles (MPs) can impact both the type and quality of the immune response they elicit. The lysosomes of antigen-presenting cells are highly oxidizing and so, an oxidation-sensitive system could enable a significant improvement in effective MP immunotherapy. With this objective in mind, this research group has just developed a bunch of aryl boronate-modified dextran polymers. Highly stable boronic esters were obtained using pinanediol (PD). MPs could be prepared by emulsion, nanoprecipitation and electrospray techniques. $H_2O_2$-triggered degradation of MPs was quantified calorimetrically, and the mechanism was confirmed by $^1$H NMR. Preliminary *in vitro* studies showed their low cytotoxicity and ability to deliver an immunostimulatory agent.

Wei *et al.*[87] recently synthesized a di-block copolymer containing boronic esters and *N*-isopropyl acrylamide *via* RAFT polymerization, which presented synergies between the esterase and ROS stimuli (Figure 11.12). Aryl boronic esters could be oxidized by ROS and the ester bonds could be hydrolyzed by esterases. This copolymer can successfully self-assemble into polymer micelles in water with a narrow distribution, and it loaded DOX up to 6.99 wt.%, showing an entrapment efficiency of 76.9%. Compared to the common DDS, this copolymer exhibits high entrapment efficiency and drug-loading capacity, and the synergetic characteristics of two stimuli.

### 11.3.5 Systems Containing Oxalate Units

Polyoxalates also play an important role as ROS-responsive DDS. Wu and Guan[88] recently developed a prodrug by linking podophyllotoxin (POD) to poly(ethylene glycol) monomethacrylate (POD-PEG) with a $H_2O_2$-responsive oxalate ester

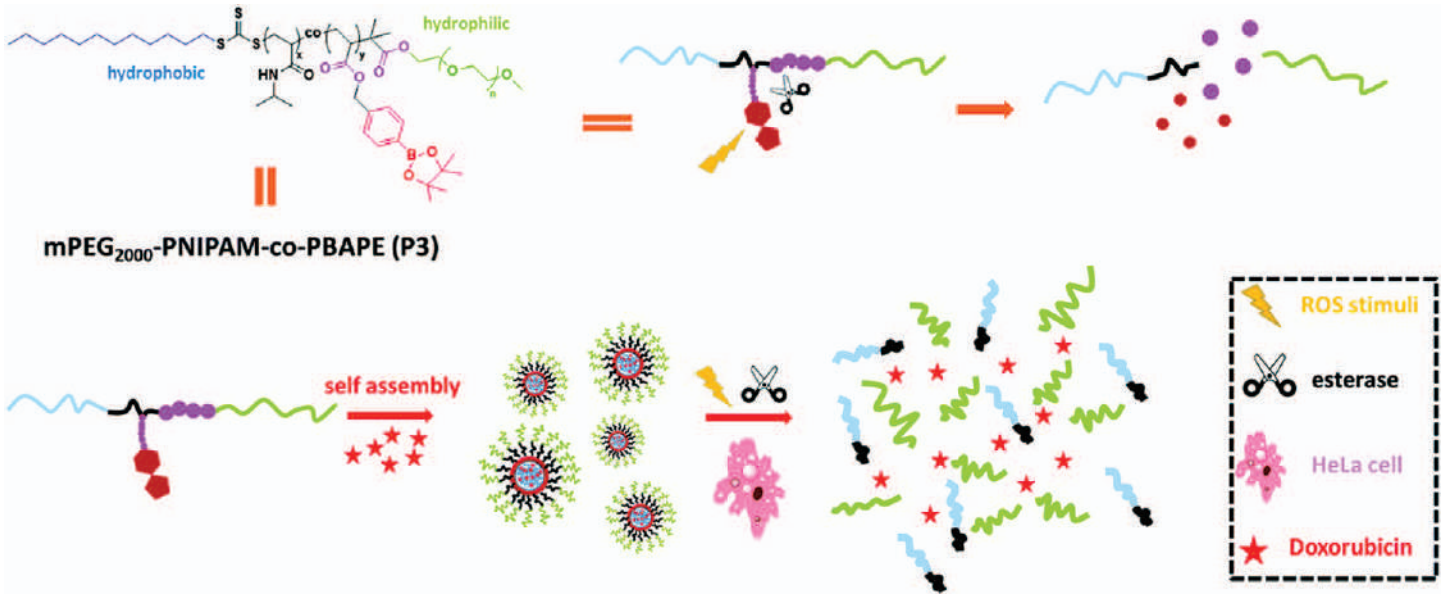


**Figure 11.12** Self-assembly properties and stimuli-responsive release properties of a copolymer with a dual-stimulus response. Reproduced from ref. 87 with permission from the Royal Society of Chemistry.

bond, able to increase the concentration of the anticancer podophyllotoxin in the tumor microenvironment to enhance the therapeutic effect (see Figure 11.13). POD-PEG self-assembled into stable nanoparticles, and *in vitro*

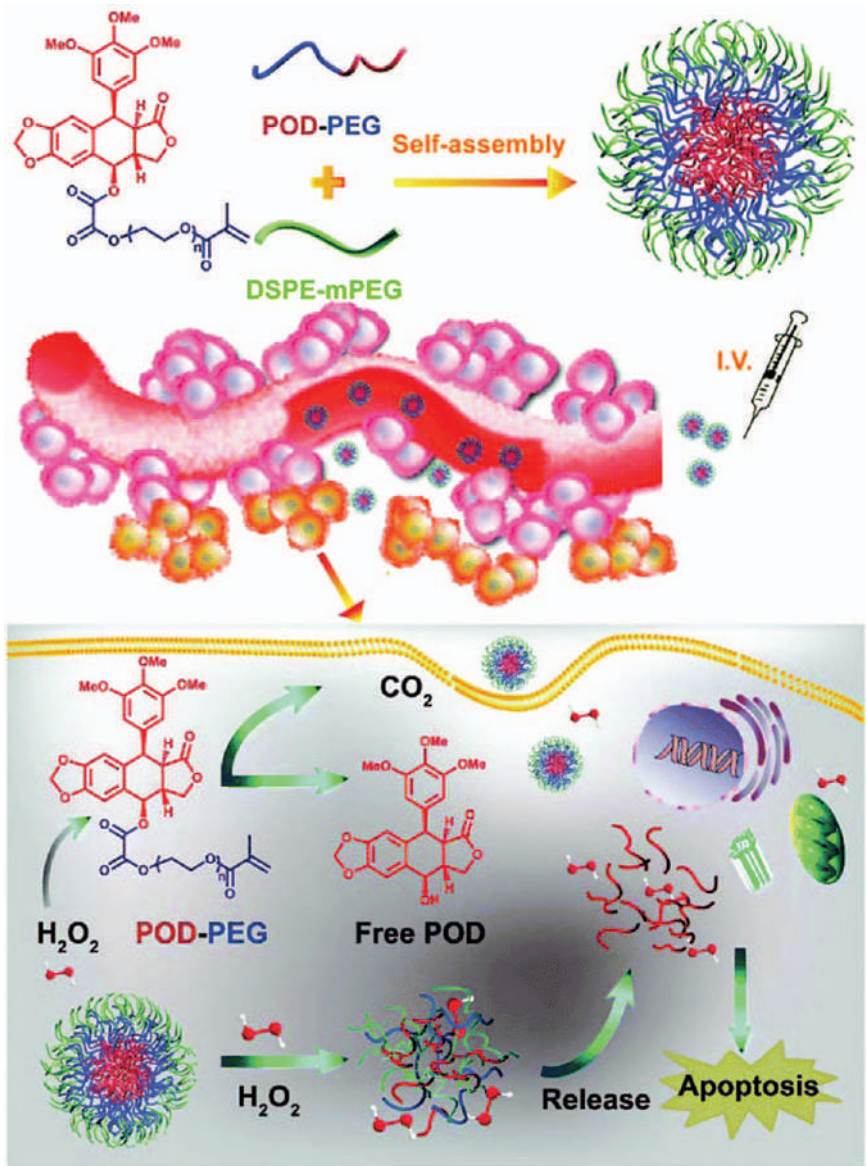


**Figure 11.13** Schematic illustration of the $H_2O_2$-responsive linkage-bridged prodrug POD-PEG nanoparticles for anticancer drug delivery. In the tumor cells, NPs can respond to $H_2O_2$ and release podophyllotoxin.
Reproduced from ref. 88 with permission from the Royal Society of Chemistry.

experiments demonstrated that they could be activated by $H_2O_2$ releasing podophyllotoxin, a highly toxic drug against colon carcinoma CT26 cells. The prolonged POD-PEG nanoparticle circulation in the blood, and effective accumulation at the site of the tumor due to the PEGylated prodrug strategy, improved the antitumor efficacy. So, intravenous injection of the nanoparticles into CT26 tumor-bearing Balb/c mice showed a significantly enhanced therapeutic efficacy against tumors, with no significant systemic toxicity.

A transferrin (Tf) variant (oxalate Tf) was used to improve the targeted delivery of DOX-encapsulated nanoparticles in PLGA porous scaffolds to PC3 prostate cancer cells.[89] This innovative DDS consisted of DOX-loaded poly(lactide-*co*-glycolide) (PLGA) nanoparticles (DP) conjugated with PEG and transferrin (Tf) to form Tf-PEG-DPs (TPDPs), which were incorporated into three-dimensional PLGA porous scaffolds. Such scaffolds provided a continuous release of DOX. The MTS assays of native and oxalate TPDPs showed a 3.0-fold decrease in $IC_{50}$ values between the native version and the oxalate TPDPs. Thus, with this oxalate modification, a lower concentration of drug was required to achieve the same therapeutic effect.

In vitro cisplatin release was also explored from functionalized chitosan with poly-carboxylic acid nanocomposites.[90] The encapsulation of cisplatin on chitosan cross-linked with oxalic acid-EG, succinic acid-EG, citric acid-EG and tartaric acid-EG carriers were carried out by the ionic gelation technique. The nanocomposites showed excellent drug-release kinetics and good biocompatibility *in vitro*. The unloaded nanocomposites had a low inherent cytotoxicity, whereas the loaded nanocomposites were as active as free cisplatin in the MCF-7 cancer cell line.

## 11.4 Ferrocene-containing Redox-responsive Drug-delivery Systems

Ferrocene-containing polymers possess a dual responsive character because they are sensitive to both oxidizing and reducing agents. Ferrocene (Fc) can be incorporated in the backbone, side chain and terminal group of the polymers. The Fc molecule consists of two cyclopentadienyl rings bound on opposite sides of a central iron atom, forming a Fe(II) 18-electron neutral sandwich complex. This complex can be oxidized using a relatively low voltage of around +0.4 V to a Fe(III) 17-electron cationic form, ferricinium (Fcium), then can be returned to its original neutral form using an appropriate reductant. The reversible Fc/Fcium redox conversion takes place without substantial structural changes. Conversely, changes in properties such as electrophilic/nucleophilic reactivity, hydrophobic/hydrophilic balance, neutral/cationic character, complexation/dissociation, among others, are observed. This is the reason why this system has found a wide range of applications, for instance, in nano- and biomedicine, due to properties such as its biocompatibility and stability, easy structural modification, large surface area, good electrical conductivity and excellent redox properties. Gu, Astruc *et al.* published in 2018 a review[3] on the redox-stimuli-responsive

drug-delivery systems with supramolecular ferrocenyl-containing polymers for controlled release. The chemically and electrochemically reversible Fc/Fcium redox pair is a dynamic redox switching of DDS that also responds to external redox stimuli. The Fc-containing polymers involve main-chain, side-chain and dendritic topologies in which the polymers assemble in various supramolecular fashions. Fc-based DDS are found as micelles, vesicles, nanoparticles, nanotubes, multilayer films and bulk hydrogels, able to respond to electrochemical stimuli, redox reagents, pH and temperature.

For example, Gu *et al.*[91] reported the preparation of a block co-polynorbornene PNFc-*b*-PNAd with side-chains containing Fc and adamantane (Ad) units. The well-defined block copolymer was synthesized by the ring-opening metathesis polymerization using a third-generation Grubbs catalyst. A polycationic amphiphilic block copolymer PNFcium-*b*-PNAd was then obtained by the stoichiometric oxidation of Fc into Fcium cations. Its redox-controlled reversible self-assembly behavior in water was demonstrated by SEM and DLS with glutathione as reductant and $FeCl_3$ as oxidant. Benzocaine was used as a model drug and the loading ability of the cationic micelles formed by the copolymer, and the reduction of Fcium led to rapid release of the loaded drug. Additionally, a new supramolecular copolymer PNFc-*b*-PNAd@β-CD was prepared by mixing PNFc-*b*-PNAd and β-cyclodextrin (β-CD) with equimolar quantity to Ad units, in which host–guest interactions were mainly observed between β-CD and pendant Ad (Figure 11.14). This new amphiphilic copolymer exhibited redox-controlled self-assembly behavior in water. The oxidation-triggered release of benzocaine from the supramolecular micelles was observed in a slow and long-lasting way.

Liao *et al.*[92] recently revised the application of mesoporous silica nanoparticles with a gated switch as DDS. Switchable gatekeepers based on β-CD hosts with different guest moieties such as benzimidazole, azobenzene and ferrocene groups respond to different stimuli modes (pH, light and redox, respectively) that change the host – guest interactions and trigger the drug release.

Guo *et al.*[93] prepared noncovalent amphiphilic polymers through host–guest interactions between β-CD-grafted dextran (Dex-CD) and Fc-terminated poly(ε-caprolactone) (PCL-Fc). Because of the presence of Fc groups, the inclusion complex between Fc and β-CD could be reversibly controlled by an external stimulating voltage, leading to reversible formation and disassembly of the micelles. The formation of the inclusion complex between Fc and β-CD was confirmed by cyclic voltammetry and 2D NOESY NMR experiments. Meloxicam was selected as a model drug and it was found that its release rate and its final cumulative release could be effectively controlled by the external voltage (Figure 11.15).

Regarding cancer therapy, the synthesis of Fc-containing amphiphilic diblock and random copolymers PN(Fc-*b*-TEG) and PN(Fc-*r*-TEG) [PN = polynorbornene; TEG = triethylene glycol], respectively, *via* ring-opening metathesis polymerization showing tunable redox responses and excellent capability to entrap therapeutic anticancer drugs, such as DOX, has been recently reported.[94] Both copolymers could self-assemble into globular

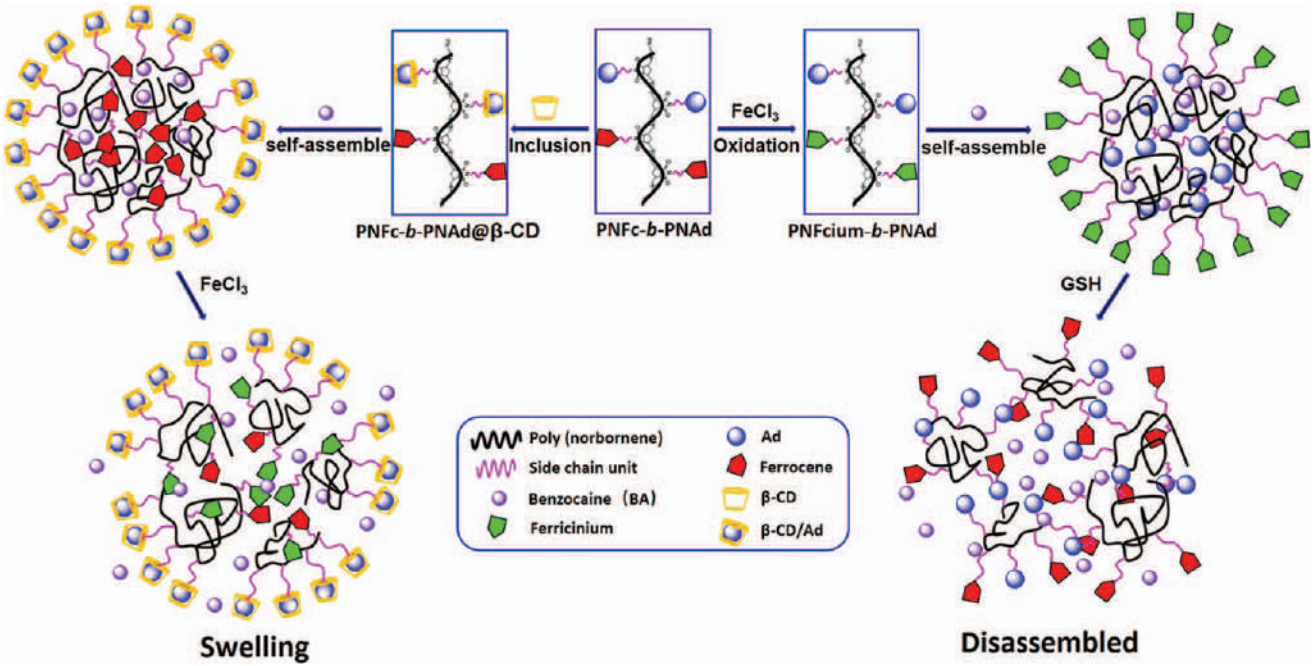


**Figure 11.14** Schematic illustration for the formation of cationic PNFcium-*b*-PNAd and supramolecular PNFc-*b*-PNAd@β-CD, and their self-assembly, cargo-loading and redox-triggered release behaviors.
Reproduced from ref. 91 with permission from Elsevier, Copyright 2018.

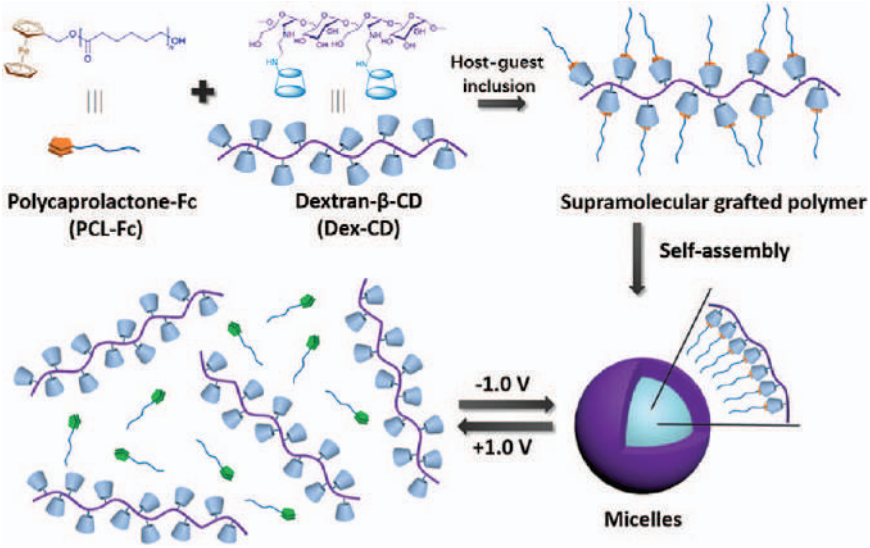


**Figure 11.15** Schematic illustration of the preparation of redox-controlled voltage-responsive micelles through the self-assembly of noncovalently grafted polymers.
Reproduced from ref. 93 with permission from the American Chemical Society, Copyright 2019.

nanoscale core–shell micelles in aqueous solution and showed tunable redox responses. Meanwhile, the DOX-loaded micelles exhibited oxidation-controlled drug release, and the release rate could be mediated by the concentration of oxidants.

In order to achieve the proper synergetic treatment for the tumor, some self-assembly amphiphilic Fcium-based polymers have been designed to form cationic micelles capable of interacting with hyaluronic acid through electrostatic interactions.[95] Thus, the resulting neutralized micelles were used to deliver DOX under a high GSH concentration in the tumor area (see Figure 11.16). These outcomes suggested that these promising micelles are useful delivery systems that improve the effects of synergistic antineoplastic therapy.

Multistimuli-responsive Fc-based DDS are also capable of responding to other external stimuli, simultaneously or at different times, generating an intense interest in the scientific community. For instance, well-defined Fc-containing homopolymers were synthesized by RAFT polymerization[96] of an acrylate monomer bearing an Fc unit and an *N*,*N*-diethylamino ethyl (DEAE) group; the monomer was the 2-(3-(*N*-(2-(diethylamino)ethyl)-acrylamido)-propanoyloxy)ethyl ferrocenecarboxylate (Fc-DEAE-AM). Due to the redox- and pH/$CO_2$-responsive character provided by the Fc and DEAE groups, the polymer exhibited distinct phase transition in aqueous solution. It could also form typical spherical particles in acidic aqueous solution, and the redox agent could lead to changes in the size and morphology of the

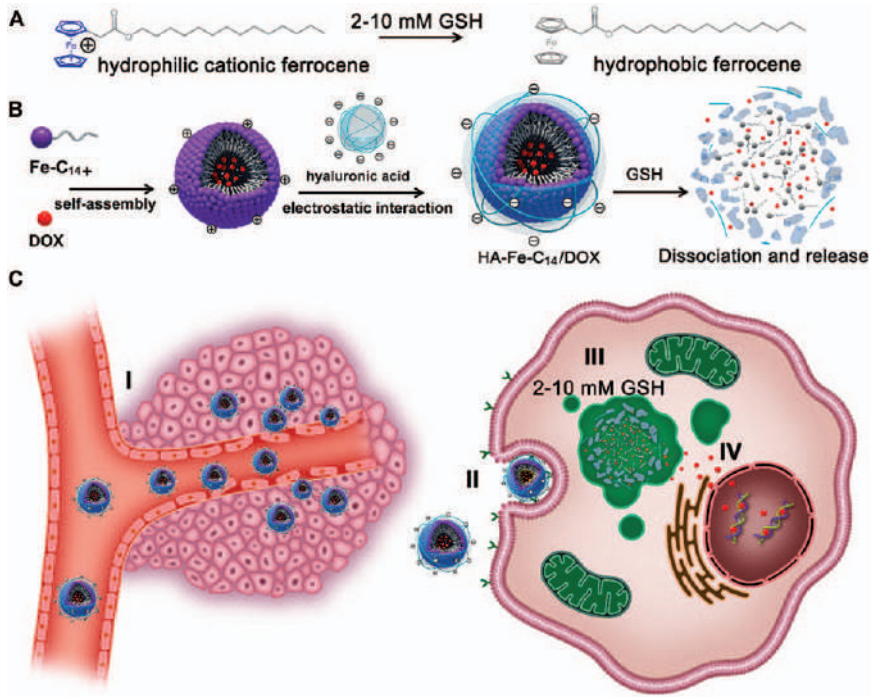


**Figure 11.16** Illustration of the drug-release process of GSH-responsive HA-Fe-$C_{14}$/DOX micelles. (A) Mechanism of GSH-triggered dissociation based on the charge change of Fe-$C_{14}$ under the GSH microenvironment. (B) Schematic diagram illustrating the assembly of HA-Fe-$C_{14}$/DOX micelles and the mechanism of GSH-triggered release of DOX from HA-Fe-$C_{14}$/DOX. (C) GSH-responsive delivery of DOX by HA-Fe-$C_{14}$ prodrug micelles for combination treatment of tumor. (I) Accumulation of HA-Fe-$C_{14}$/DOX at the tumor through passive and active targeting. (II) Receptor-mediated endocytosis. (III) GSH-triggered DOX release into the cytosol. (IV) DOX entering the nucleus to kill tumor cells.
Reproduced from ref. 95 with permission from the American Chemical Society, Copyright 2019.

aggregates. Therefore, this is an interesting building block for the fabrication of triple-stimuli-responsive functional materials.

Despite what has been described above, for future applications of these materials as drug-delivery systems, there are still some aspects that should be improved, such as low water solubility, stability, chemical performance, production cost or specificity.

## 11.5 Conclusions and Outlook

The advances in current chemotherapy are largely due to the effectiveness shown by anticancer drug-transport systems to deliver them in tumor tissues, which additionally helps to silence resistance to multiple drugs. Redox polymers can generate carrier systems for anticancer drugs capable of

releasing their cargo as a function of the redox conditions in extracellular and intracellular microenvironments of diseased cells. Nowadays, it is worth noting the interest aroused by systems able to respond to both endogenous—redox, pH, enzymes—and exogenous—light, temperature, ultrasound, magnetism—stimuli. However, in many cases, it remains a proof of concept. Hopefully, the breakthrough experienced by synthetic and nanotechnological methodologies will allow access to more biocompatible and biodegradable drug-delivery systems for the specific release of therapeutic molecules in the desired tissue. Therefore, toxicity and immunogenicity problems would be attenuated. Transferring results to *in vivo*, and finally to the clinic is the long-awaited goal. We must also take into account the voices that advocate for simpler, less sophisticated polymer structures that can be synthesized by routine strategies. However, accomplishing all these requirements is not an easy task, mainly because these carriers must incorporate structural features capable of mimicking natural biomolecules and responding specifically to physiological stimuli. It can be envisioned that, in the near future, the scientific community will be able to simultaneously tune the physicochemical properties and response rates of yet-undiscovered sustainable polymers. The latter will inspire the design of a new class of stimulus-responsive supramolecular materials capable of empowering the emerging field of redox-sensitive DDS.

## References

1. J. Zhang, X. Jiang, X. Wen, Q. Xu, H. Zeng, Y. Zhao, M. Liu, Z. Wang, X. Hu and Y. Wang, *J. Phys. Mater.*, 2019, **2**, 032004.
2. Z. Fan and H. Xu, *Polym. Rev.*, 2019, 1.
3. H. Gu, S. Mu, G. Qiu, X. Liu, L. Zhang, Y. Yuan and D. Astruc, *Coord. Chem. Rev.*, 2018, **364**, 51.
4. N. V. Rao, Y. Ko, J. Lee and J. H. Park, *Front. Bioeng. Biotechnol.*, 2018, **6**, 110.
5. X. Guo, Y. Cheng, X. Zhao, Y. Luo, J. Chen and W.-E. Yuan, *J. Nanobiotechnol.*, 2018, **16**, 1.
6. X. Zhang, L. Han, M. Liu, K. Wang, L. Tao, Q. Wan and Y. Wei, *Mater. Chem. Front.*, 2017, **1**, 807.
7. J. F. Quinn, M. R. Whittaker and T. P. Davis, *Polym. Chem.*, 2017, **8**, 97.
8. T. Fukino, H. Yamagishi and T. Aida, *Adv. Mater.*, 2017, **29**, 1603888.
9. N. Casado, G. Hernández, H. Sardon and D. Mecerreyes, *Prog. Polym. Sci.*, 2016, **52**, 107.
10. Q. Xu, C. He, C. Xiao and X. Chen, *Macromol. Biosci.*, 2016, **16**, 635.
11. H. Wen and Y. Li, *Med. Chem.*, 2014, **4**, 748.
12. M. Huo, J. Yuan, L. Tao and Y. Wei, *Polym. Chem.*, 2014, **5**, 1519.
13. M. H. Lee, Z. Yang, C. W. Lim, Y. H. Lee, S. Dongbang, C. Kang and J. S. Kim, *Chem. Rev.*, 2013, **113**, 5071.
14. H. Xu, W. Cao and X. Zhang, *Acc. Chem. Res.*, 2013, **46**, 1647.
15. S. Mura, J. Nicolas and P. Couvreur, *Nat. Mater.*, 2013, **12**, 991.

16. R. Cheng, F. Feng, F. Meng, C. Deng, J. Feijen and Z. Zhong, *J. Controlled Release*, 2011, **152**, 2.
17. P. Kuppusamy, H. Li, G. Ilangovan, A. J. Cardounel, J. L. Zweier, K. Yamada, M. C. Krishna and J. B. Mitchell, *Cancer Res.*, 2002, **62**, 307.
18. D. Trachootham, J. Alexandre and P. Huang, *Nat. Rev. Drug Discovery*, 2009, **8**, 579.
19. C. C. Song, F. S. Du and Z. C. Li, *J. Mater. Chem. B*, 2014, **2**, 3413.
20. C. Wu, S. Wang, L. Brulisauer, J. C. Leroux and M. A. Gauthier, *Biomacromolecules*, 2013, **14**, 2383.
21. D. J. Siegwart, J. K. Oh and K. Matyjaszewski, *Prog. Polym. Sci.*, 2012, **37**, 18.
22. M. D. Konieczynska and M. W. Grinstaff, *Acc. Chem. Res.*, 2017, **50**, 151.
23. W. Ke, W. Yin, Z. Zha, J. F. Mukerabigwi, W. Chen, Y. Wang, C. He and Z. Ge, *Biomaterials*, 2018, **154**, 261.
24. Q. Song, J. Yang, S. Hall, C. L. Stephen, P. Gurnani and S. Perrier, *ACS Macro Lett.*, 2019, **8**, 1347.
25. N. Song, M. Ding, Z. Pan, J. Li, L. Zhou, H. Tan and Q. Fu, *Biomacromolecules*, 2013, **14**, 4407.
26. S. Yu, J. Ding, C. He, Y. Cao, W. Xu and X. Chen, *Adv. Healthcare Mater.*, 2014, **3**, 752.
27. M.-V. De-Paz, F. Zamora, B. Begines, C. Ferris and J. A. Galbis, *Biomacromolecules*, 2010, **11**, 269.
28. C. Ferris, M.-V. De-Paz, A. Aguilar-de-Leyva, I. Caraballo and J. A. Galbis, *Polym. Chem.*, 2014, **5**, 2370.
29. B. Begines, M.-V. de-Paz, A. Alcudia and J. A. Galbis, *J. Polym. Sci., Part A: Polym. Chem.*, 2016, **54**, 3888.
30. L. Romero-Azogil, E. Benito, M. G. García-Martín and J. A. Galbis, *Eur. Polym. J.*, 2017, **94**, 259.
31. L. Romero-Azogil, E. Benito, A. Martínez, de Ilarduya and M. G. García-Martín, *Polym. Degrad. Stab.*, 2018, **153**, 262.
32. M. D. Campiñez, E. Benito, L. Romero-Azogil, A. Aguilar-de-Leyva, M. G. García-Martín, J. A. Galbis and I. Caraballo, *Eur. J. Pharm. Sci.*, 2017, **100**, 285.
33. M. J. Lucero, C. Ferris, C. A. Sánchez-Gutiérrez, M. R. Jiménez-Castellanos and M.-V. de-Paz, *Carbohydr. Polym.*, 2016, **151**, 692.
34. Y. Li, K. Xiao, J. Luo, W. Xiao, J. S. Lee, A. M. Gonik, J. Kato, T. Dong and K. S. Lam, *Biomaterials*, 2011, **32**, 6633.
35. S. Zhang and Y. Zhao, *J. Am. Chem. Soc.*, 2010, **132**, 10642.
36. J. Liu, W. Huang, Y. Pang, P. Huang, X. Zhu, Y. Zhou and D. Yan, *Angew. Chem.*, 2011, **123**, 9328.
37. W.-F. Dong, A. Kishimura, Y. Anraku, S. Chuanoi and K. Kataoka, *J. Am. Chem. Soc.*, 2009, **131**, 3804.
38. Q. Zhang, S. Aleksanian, S. M. Noh and J. K. Oh, *Polym. Chem.*, 2013, **4**, 351.
39. J.-H. Ryu, R. T. Chacko, S. Jiwpanich, S. Bickerton, R. P. Babu and S. Thayumanavan, *J. Am. Chem. Soc.*, 2010, **132**, 17227.

40. A. C. Engler, J. M. W. Chan, K. Fukushima, D. J. Coady, Y. Y. Yang and J. L. Hedrick, *ACS Macro Lett.*, 2013, **2**, 332.
41. K. C. R. Bahadur, B. Thapa and P. Xu, *Mol. Pharmaceutics*, 2012, **9**, 2719.
42. K. Rahimian, Y. Wen and J. K. Oh, *Polymer*, 2015, **72**, 387.
43. D. Basak, R. Bej and S. Ghosh, *Polym. Chem.*, 2015, **6**, 6465.
44. K. Kempe, S. L. Ng, S. T. Gunawan, K. F. Noi and F. Caruso, *Adv. Funct. Mater.*, 2014, **24**, 6187.
45. X. Cai, C. Dong, H. Dong, G. Wang, G. M. Pauletti, X. Pan, H. Wen, I. Mehl, Y. Li and D. Shi, *Biomacromolecules*, 2012, **13**, 1024.
46. L. Zhang, Y. Li, J. C. Yu and K. M. Chan, *RSC Adv.*, 2016, **6**, 72155.
47. I. Ullah, J. Zhao, S. Rukh, K. Muhammad, J. Guo, X. Ren, S. Xia, W. Zhang and Y. Feng, *J. Mater. Chem. B*, 2019, **7**, 1893.
48. L. Liu, L. Wu, J. Tan, L. Wang, Q. Liu, P. Liu and L. Liu, *Polym. Chem.*, 2015, **6**, 3934.
49. R. Liu, X. Zhao, T. Wu and P. Feng, *J. Am. Chem. Soc.*, 2008, **130**, 14418.
50. C. Giménez, C. de la Torre, M. Gorbe, E. Aznar, F. Sancenón, J. R. Murguía, R. Martínez-Máñez, M. D. Marcos and P. Amorós, *Langmuir*, 2015, **31**, 3753.
51. Z. Xie, H. Gong, M. Liu, H. Zhu and H. Sun, *J. Biomater. Sci., Polym. Ed.*, 2016, **27**, 55.
52. W. Cai, J. Wang, C. Chu, W. Chen, C. Wu and G. Liu, *Adv. Sci.*, 2019, **6**, 1801526.
53. Y. Zhao, Y. Yang, X. Han, C. Liang, J. J. Liu, X. J. Song, Z. Ge and Z. Liu, *ACS Appl. Mater. Interfaces*, 2017, **9**, 23555.
54. B. Lei, M. Wang, Z. Jiang, W. Qi, R. Su and Z. He, *ACS Appl. Mater. Interfaces*, 2018, **10**, 16698.
55. J. Zeng, J. Zhu, X. Pan, Z. Zhang, N. Zhou, Z. Chen, W. Zhang and X. Zhu, *Polym. Chem.*, 2013, **4**, 3453.
56. W. Lin, Z. Xue, L. Wen, Y. Li, Z. Liang, J. Xu, C. Yang, Y. Gu, J. Zhang, X. Zu, H. Luo, G. Yi and L. Zhang, *Colloids Surf., B*, 2019, **182**, 110313.
57. Y. S. Birhan, B. Z. Hailemeskel, T. W. Mekonnen, E. Y. Hanurry, H. F. Darge, A. T. Andrgie, H.-Y. Chou, J.-Y. Lai, G.-H. Hsiue and H.-C. Tsai, *Int. J. Pharm.*, 2019, **567**, 118486.
58. B. Z. Hailemeskel, W.-H. Hsu, K. D. Addisu, A. T. Andrgie, H.-Y. Chou, J.-Y. Lai and H.-C. Tsai, *Mater. Sci. Eng., C*, 2019, **103**, 109803.
59. L. Zhang, Y. Liu, K. Zhang, Y. Chen and X. Luo, *Colloid Polym. Sci.*, 2019, **297**, 225.
60. F. Behroozi, M.-J. Abdkhodaie, H. S. Abandansari, L. Satarian, M. Molazem, K. T. Al-Jamal and H. Baharvand, *Acta Biomater.*, 2018, **76**, 239.
61. C. Gong, M. Shan, B. Li and G. Wu, *J. Biomed. Mater. Res., Part A*, 2017, **105**, 2451.
62. M. Callari, J. R. Aldrich-Wright, P. L. de Souza and M. H. Stenzel, *Prog. Polym. Sci.*, 2014, **39**, 1614.
63. H. Xiao, R. Qi, S. Liu, X. Hu, T. Duan, Y. Zheng, Y. Huang and X. Jing, *Biomaterials*, 2011, **32**, 7732.

64. L. P. Lv, Y. Zhao, N. Vilbrandt, M. Gallei, A. Vimalanandan, M. Rohwerder, K. Landfester and D. Crespy, *J. Am. Chem. Soc.*, 2013, **135**, 14198.
65. L. Xu, M. Zhao, W. Gao, Y. Yang, J. Zhang, Y. Pu and B. He, *Colloids Surf., B*, 2019, **181**, 252.
66. H. He, B. Liu, M. Wang, R. W. Vachet and S. Thayumanavan, *Polym. Chem.*, 2019, **10**, 187.
67. W. Zhou, L. Wang, F. Li, W. Zhang, W. Huang, F. Huo and H. Xu, *Adv. Funct. Mater.*, 2017, **27**, 1605465.
68. C. Sun, S. Ji, F. Li and H. Xu, *ACS Appl. Mater. Interfaces*, 2017, **9**, 12924.
69. L. Yu, M. Zhang, F.-S. Du and Z.-C. Li, *Polym. Chem.*, 2018, **9**, 3762.
70. L. Wang, K. Zhu, W. Cao, C. Sun, C. Lu and H. Xu, *Polym. Chem.*, 2019, **10**, 2039.
71. Y. Li, Y. Li, W. Ji, Z. Lu, L. Liu, Y. Shi, G. Ma and X. Zhang, *J. Am. Chem. Soc.*, 2018, **140**, 4164.
72. L. Yu, Y. Yang, F.-S. Du and Z.-C. Li, *Biomacromolecules*, 2018, **19**, 2182.
73. T. I. Liu, Y.-C. Yang, W.-H. Chiang, C.-K. Hung, Y.-C. Tsai, C.-S. Chiang, C.-L. Lo and H.-C. Chiu, *Biomacromolecules*, 2018, **19**, 3825.
74. R. Fang, H. Xu, W. Cao, L. Yang and X. Zhang, *Polym. Chem.*, 2015, **6**, 2817.
75. L. Wang, F. Fan, W. Cao and H. Xu, *ACS Appl. Mater. Interfaces*, 2015, **7**, 16054.
76. F. Fan, S. Gao, S. Ji, Y. Fu, P. Zhang and H. Xu, *Mater. Chem. Front.*, 2018, **2**, 2109.
77. W. Cao, Y. Gu, T. Li and H. Xu, *Chem. Commun.*, 2015, **51**, 7069.
78. F. Li, T. Li, W. Cao, L. Wang and H. Xu, *Biomaterials*, 2017, **133**, 208.
79. L. Wang, W. Wang, W. Cao and H. Xu, *Polym. Chem.*, 2017, **8**, 4520.
80. J. S. Kim, S. D. Jo, G. L. Seah, I. Kim and Y. S. Nam, *J. Ind. Eng. Chem.*, 2015, **21**, 1137.
81. G. L. Seah, J. H. Yu, M. Y. Yang, W. J. Kim, J.-H. Kim, K. Park, J.-W. Cho, J. S. Kim and Y. S. Nam, *J. Controlled Release*, 2018, **286**, 240.
82. G. L. Seah, L. Geok, J. H. Yu, B. I. Koo, D. J. Lee and Y. S. Nam, *J. Mater. Chem. B*, 2018, **6**, 7737.
83. M. Zhang, C.-C. Song, F.-S. Du and Z.-C. Li, *ACS Appl. Mater. Interfaces*, 2017, **9**, 25905.
84. W. Lv, J. Xu, X. Wang, X. Li, Q. Xu and H. Xin, *ACS Nano*, 2018, **12**, 5417.
85. W. J. Yang, P. Zhou, L. Liang, Y. Cao, J. Qiao, X. Li, Z. Teng and L. Wang, *ACS Appl. Mater. Interfaces*, 2018, **10**, 18560.
86. A. J. Manaster, C. Batty, P. Tiet, A. Ooi, E. M. Bachelder, K. M. Ainslie and K. E. Broaders, *ACS Appl. Bio Mater.*, 2019, **2**, 3755.
87. N. Wang, X.-C. Chen, R.-L. Ding, X.-L. Yang, J. Li, X.-Q. Yu, K. Li and X. Wei, *RSC Adv.*, 2019, **9**, 2371.
88. K. Ou, Y. Kang, L. Chen, X. Zhang, X. Chen, Y. Zheng, J. Wu and S. Guan, *Biomater. Sci.*, 2019, **7**, 2491.
89. A. M. Lopes, K. Y. Chen and D. T. Kamei, *Mater. Sci. Eng., C*, 2017, **73**, 373.

90. M. Rajan, M. Murugan, D. Ponnamma, K. K. Sadasivuni and M. A. Munusamy, *Biomed. Pharmacother.*, 2016, **83**, 201.
91. L. Zhang, G. Qiu, F. Liu, X. Liu, S. Mu, Y. Long, Q. Zhao, Y. Liu and H. Gu, *React. Funct. Polym.*, 2018, **132**, 60.
92. S. Yi, J. Zheng, P. Lv, D. Zhang, X. Zheng, Y. Zhang and R. Liao, *Bioconjugate Chem.*, 2018, **29**, 2884.
93. Z. Yuan, J. Wang, Y. Wang, Y. Zhong, X. Zhang, L. Li, J. Wang, S. F. Lincoln and X. Guo, *Macromolecules*, 2019, **52**, 1400.
94. G. Qiu, X. Liu, B. Wang, H. Gu and W. Wang, *Polym. Chem.*, 2019, **10**, 2527.
95. H.-L. Mao, F. Qian, S. Li, J.-W. Shen, C.-K. Ye, L. Hua, L.-Z. Zhang, D.-M. Wu, J. Lu, R.-T. Yu and H.-M. Liu, *Mol. Pharmaceutics*, 2019, **16**, 987.
96. X. Jiang, R. Li, C. Feng, G. Lua and X. Huang, *Polym. Chem.*, 2017, **8**, 2773.

CHAPTER 12

# *Conducting Polymers as Redox Electroactive Materials for Soft Microelectromechanical Systems*

K. ROHTLAID,[a] T. M. G. NGUYEN,[a] C. SOYER,[b] E. CATTAN,[b] F. VIDAL[a] AND C. PLESSE*[a]

[a] LPPI (EA2528), Institut des Matériaux, Université de Cergy-Pontoise, 5 mail Gay Lussac, Neuville sur Oise, F-95031 Cergy Cedex, France; [b] Univ. Polytechnique des Hauts de France, CNRS, Univ. Lille, Yncrea, Centrale Lille, UMR 8520 - IEMN, DOAE, F-59313 Valenciennes, France
*Email: cedric.plesse@u-cergy.fr

## 12.1 Introduction

Artificial muscle is a general term for a group of materials or devices that are intended to mimic the functionality of natural muscles. Electroactive polymers (EAPs) have been intensively investigated for this purpose, since they are soft, lightweight, easily processed and manufactured. The main functionality of these materials is that through external electric stimulus they are able to generate reversible contraction and expansion, which leads to changing their shape or size similarly to natural muscles. Based on their activation mechanism, EAPs are classified into two main categories: electronic EAPs and ionic EAPs.

The electronic EAPs are driven by an electric field[1,2] and this group includes dielectric elastomers, ferroelectric polymers, also called piezoelectric polymers, and electrostrictive polymers.[3–6] In an example of dielectric elastomer actuators, the actuation mechanism is caused by the electrostatic

Polymer Chemistry Series No. 34
Redox Polymers for Energy and Nanomedicine
Edited by Nerea Casado and David Mecerreyes

Published by the Royal Society of Chemistry, www.rsc.org

forces between two electrodes, which apply Maxwell pressure to a soft dielectric elastomer and result in plane expansion of the device. Electronic EAPs are known to produce relatively large actuation forces, respond rapidly (order of a millisecond) and to operate in open air for a long time. A perceived drawback with these types of actuators is their need for high voltage (up to 150 MV $m^{-1}$), although some recent research has succeeded in reducing it significantly,[7] which may be disadvantageous for many applications. Indeed, high voltage could be close to the electrical breakdown level and even dangerous if not handled carefully.

The ionic EAPs are driven by the electrical potential which induces mobility or diffusion of ions between their two electrodes. This group of materials includes electronically conducting polymers (ECPs), ionic polymer–metal composites (IPMC), carbon nanotubes (CNTs), carbide-derived carbon (CDC) and ionic polymer gels (IPGs).[2,8–18] Compared to the electronic EAPs, the main advantage of the ionic EAPs is their low operating voltages (1–5 V). Additionally, they are also capable of generating an electrical signal in response to mechanical stimulation, *i.e.*, they behave as sensors, providing dual behaviour, *i.e.*, actuation/sensing, as the so-called proprioception of biological muscles.

Among ionic EAPs, most of the investigated materials are based on a capacitive behaviour where ions are attracted by oppositely charged electrodes. However, the working principle of ECP-based EAPs is significantly different due to the redox nature of the polymer. Indeed, ECP actuators are driven by the ion diffusion inside/outside the polymer during a redox process in the presence of an electrolyte, resulting in volume variation of the materials. ECPs are flexible and lightweight materials, able to operate at low potentials and offer the possibility of processability and miniaturization, making them attractive for the development of soft microelectromechanical systems (MEMS).

MEMS is a generic term to describe multifunctional and intelligent integrated microscale systems combining different elements (electrical, mechanical, optical, magnetic, thermal, chemical, fluidic). They are usually fabricated with semiconductor processing techniques. Miniaturization and MEMS fabrication allow reducing the size and manufacturing costs and could possibly improve the performances of the microdevices. MEMS are usually classified into two main categories: actuators and sensors. Actuators are devices able to produce mechanical work from energy (electrical, chemical, mechanical, thermal, magnetic, *etc.*) and sensors are devices able to convert a specific variable (pressure, strain, flow, heat, chemicals, biological elements, *etc.*) into a measurable signal. Microfabrication technology has advanced over the years and allowed the development of different MEMS, used in a wide range of applications (aeronautics, satellites, automotive, computers, video game consoles, displays, printers, phones, medical devices, *etc.*) covered by most scientific and technical fields (physics, chemistry, materials science, biology, medicine, electronics, mechanics, computer science, robotics, *etc.*). Nevertheless, the general and powerful trend of moving from stiff to soft electronics requires the synthesis, understanding and integration of new smart polymeric materials.

This chapter focuses on ECPs as redox polymers for the development of soft actuators and more specifically on their potential for being used as soft MEMS in soft electronics (flexible substrates, soft robotics, biomedicine, microbiology, *etc.*).

After a brief description of the basics on ECPs (discovery history, structures and conductivity mechanism), the chapter focuses on their synthesis and on their use as active layers for ionic actuators. The different strategies for the development of ECP-based microactuators, the possibility to integrate them into complex microsystems, and the issues and challenges that these exciting materials are still facing are then presented and discussed.

## 12.2 Electronically Conducting Polymers

Conducting polymers were discovered in 1977 after a mistake by a PhD student in Shirakawa's group, who applied a thousand times higher amount of Ziegler-Natta catalyst into acetylene. The accelerated reaction rate resulted in the formation of a silvery film on the walls of the reaction vessel.[19] This obtained metallic-looking material was then additionally investigated by MacDiarmid and Shirakawa. It was discovered that the material is conductive because of the conjugated double bonds and the obtained iodine-doped polyacetylene resulted in an electronic conductivity of $10^3$ S cm$^{-1}$. Shortly after this discovery, a series of conducting polymers, like polypyrrole (PPy), polyaniline (PAn) and polythiophene (PTh) were reported and promoted the research of conducting polymers. In 2000, Heeger, MacDiarmid and Shirakawa shared the Nobel prize "for the discovery and development of conducting polymers" (polyacetylene).[20]

The electronically conducting polymers (ECPs) or π-conjugated polymers have a bonding pattern consisting of alternating single (σ-bonds) and double (π-bonds) carbon bonds along the backbone of the polymer chain. Such conjugation leads to a structure with continuous overlapping π-molecular orbitals along the polymer backbone. In their neutral form, ECPs are insulators or poorly conducting semiconductors since they do not have intrinsic charge carriers.

The conductivity is obtained by partial addition (n-doping) or removal (p-doping) of electrons to or from the neutral and insulating polymer chains, which provides charge carriers able to move along the orbital system. Depending on their doping level, the conductivity values of ECPs can range between insulators and conductors.[21] Doping is generally a reversible oxidation-reduction reaction by chemical or electrochemical means and results in positive or negative charges on the polymer chain. Most commonly, p-doping is used because it is more stable compared to n-doping and will be the focus of the subsequent discussion. During p-doping, π-electrons are removed from the polymer chains. As a consequence, surrounding anions, acting as dopants, are incorporated within the polymer chains to maintain the charge neutrality of the

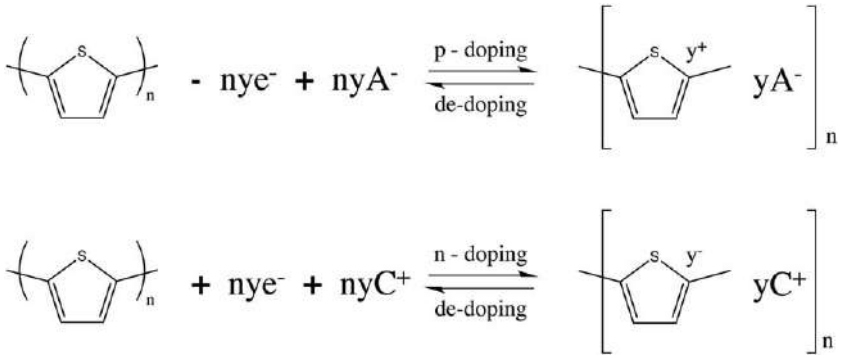


**Figure 12.1** Reversible p- and n-doping mechanisms of polythiophene.

system. The de-doping reaction corresponds to a return to the neutral state of ECPs (see Figure 12.1).

Several types of charge carriers may appear during p-doping and for ECPs they are typically referred to as polarons, bipolarons or charged solitons.[22,23] According to the band theory, the electrical properties of these materials are determined by their electronic structure and the electrons move within discrete energy states, called bands. The highest occupied molecular orbital (HOMO) corresponds to the valence band (VB), usually described for inorganic semiconductors and the lowest unoccupied molecular orbital (LUMO) to the conduction band (CB). The energy difference between them is called the band gap (see Figure 12.2). The bands should be partially filled, in order to obtain the electrical conductivity of the materials. Semiconductors have completely full VB and completely empty CB and need to be doped to change their band structures and to become conductors. In the example of p-doped ECPs, the polarons are created when one electron is removed from the top of the VB. The removal of the second electron on a chain results in the formation of a bipolaron through dimerization of two polarons. The number of polarons and bipolarons increases with the doping level. High doping levels lead to new energy bands through which electrons can flow and metal-type conductivity can be achieved.[24]

Therefore, the appearance of the charge carriers along the macromolecular chains results in drastic changes in the electrical properties of the polymers. Depending on the state of the polymer (neutral or doped) and the type of doping, the electronic properties of ECPs can be very different. Some conjugated polymers with their chemical structures, doping nature and conductivities are presented in Table 12.1.

The reversible redox process, *i.e.*, the ability to switch between the two states (neutral and oxidized/reduced) is then a property of conducting polymers. In addition to changing the conductivity, several other properties are dependent on the redox level, which allows their use in different applications such as supercapacitors, electrochromic devices and actuators. This work and the next sections will be focused on actuator-related applications.

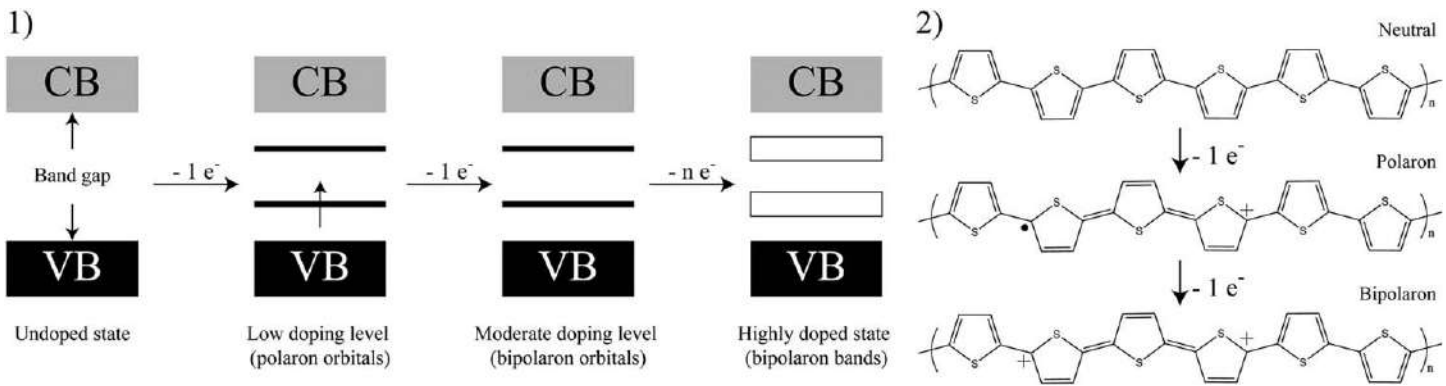


**Figure 12.2** Schematic representation of a: (1) band structure as a function of doping level; (2) p-doping of polythiophene.

**Table 12.1** Doping nature (n or p), conductivities and structures for some electronically conducting polymers.

| Polymer | Doping nature | Conductivity ($S\,cm^{-1}$) | Structure |
|---|---|---|---|
| Polyacetylene (PA) | n, p | $10^{5}$ [25] | 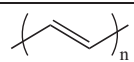 |
| Polyaniline (PANI) | n, p | $10^{2}$ [26] | 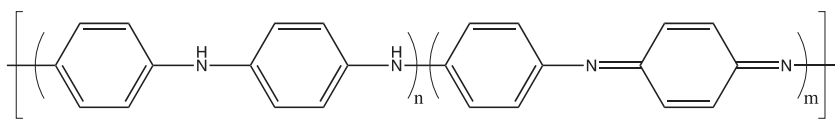 |
| Polypyrrole (PPy) | p | $10^{3}$ [27] | 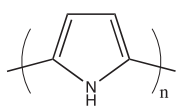 |
| Polythiophene (PT) | p | $10^{3}$ [28] | 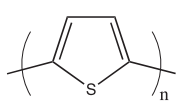 |
| Poly(3,4-ethylene-dioxythiophene) (PEDOT) | n, p | $10^{3}$ [29] | 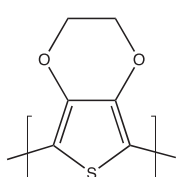 |

## 12.3 Electronically Conducting Polymer Actuators

Electronically conducting polymer actuators are electromechanically active devices that are able to change their shape or size in response to the electrical stimulus. They have attracted lots of interest due to their low operating voltages, relatively large forces and biocompatibility.[11] The following subsections will describe first the working principle of ECPs and different synthesis methods used in the actuators field. Moreover, an overview of the ECP actuators will be given based on their operation environment (in solution and in open air).

### 12.3.1 Oxidation, Reduction and the Volume Variation of Conducting Polymers

The working principle of ECP actuators is based on the electrochemically driven insertion or expulsion of ions, occurring during their reversible redox process. During the oxidation-reduction process, positive charges are created (p-doping) or removed (de-doping) from the polymer backbone. As a consequence of this charge modification, ions from a surrounding electrolyte are being inserted in or expelled from the polymer chains in order to maintain the charge neutrality. Consequently, this ion exchange mechanism induces the expansion or contraction of the polymer, leading to a volume variation of the ECPs.[30–32]

The switching between oxidized and reduced state can be achieved either by (1) expulsion of anions or (2) insertion of cations:

(1) During oxidation of the conducting polymer, the (electro)chemically generated positive charges will be compensated by the insertion of anions (and accompanying solvent molecules) within the material, leading to a volume expansion. During reduction (de-doping), positive charges are removed and anions are expelled, leading to a volume contraction.[33,34]
(2) If the polymer is doped during the synthesis with large and immobile anions, or if the mobility of anions is low compared to that of cations, the opposite mechanism takes place. During oxidation, cations will be expelled from the material in order to maintain the electroneutrality, resulting in volume contraction. During reduction, cations are inserted among the polymer chains and a volume expansion can be observed.[35,36]

Figure 12.3 illustrates these two reversible mechanisms during redox reaction with poly(3,4-ethylenedioxythiophene) (PEDOT) chosen as an example.

In some cases, when both ions have comparable size and/or mobility, the two redox mechanisms can take place concomitantly or consecutively. This results in opposite volume variations and can lead to a decrease in final

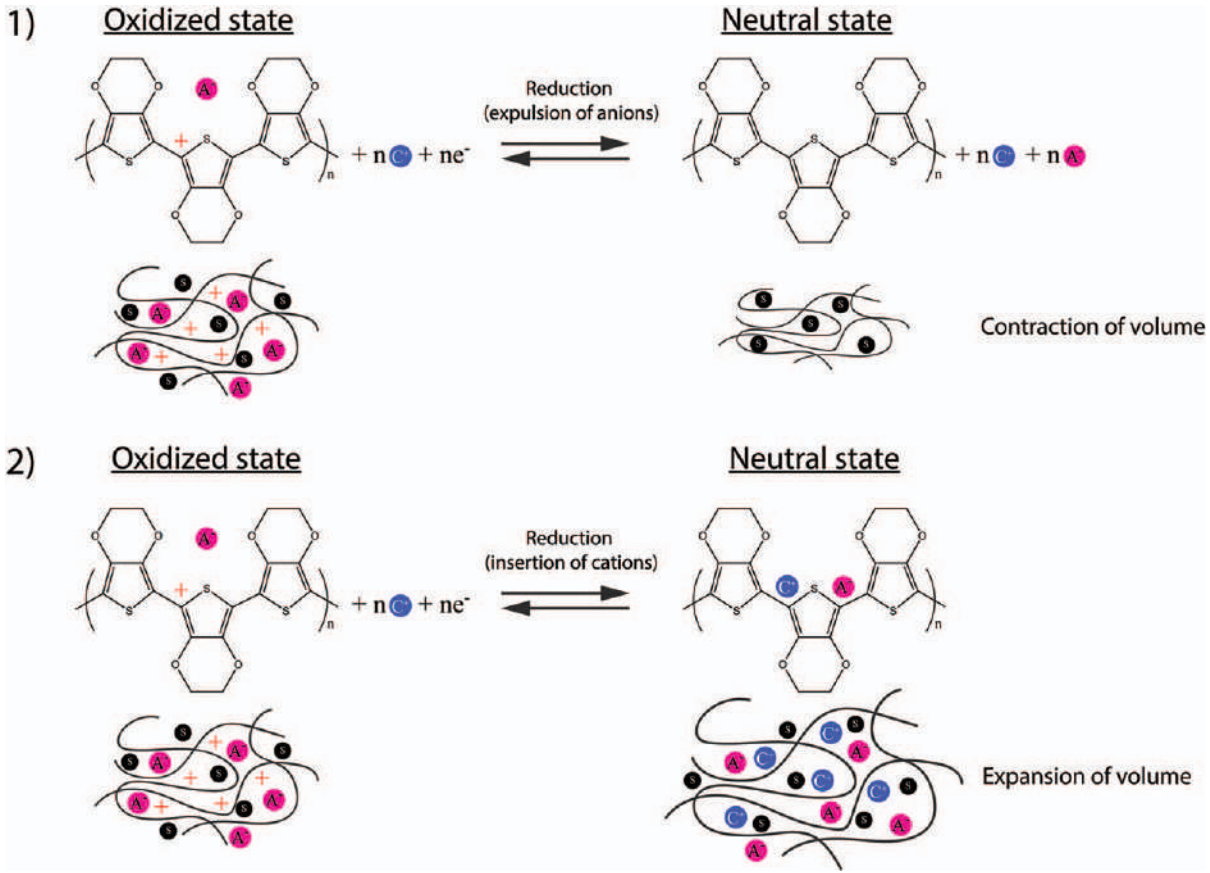


**Figure 12.3** Volume variation mechanism of conducting polymers on an example of PEDOT.

expansion/contraction.[37] In addition to the size and mobility of ions, also the nature of the solvent and conformational changes in the polymer can affect the redox process and consequently also the volume changes.[38–40] In general, the ion exchange mechanism is the main factor concerning the redox process and volume variation of ECPs. This unique volume-changing characteristic of ECPs can be used for actuator applications.

The volume variation of electronically conducting polymers, *i.e.*, the strain $\varepsilon$, depends on the volumetric charge density $\rho$ ($C\,m^{-3}$) of the ECP and on an empirical electromechanical coupling coefficient, so-called strain-to-charge ratio $\alpha$ ($m^3\,C^{-1}$), by the relationship: $\varepsilon = \alpha\rho$.[41] Therefore, high volume variation requires high electrochemical charge density, *i.e.*, a high number of expelled/inserted ions, and high elementary volume variation for each exchanged charge. The sign of $\alpha$ depends on the involved mechanism. A positive value of $\alpha$ corresponds to an anion mechanism, since during oxidation ($\rho > 0$), the insertion of the negatively charged ions in the ECP promotes an expansion and therefore a positive volume variation ($\varepsilon > 0$). On the opposite side, a negative value of $\alpha$ corresponds to a cation mechanism since during oxidation ($\rho > 0$), the expulsion of the positively charged ions from the ECP promotes a contraction, resulting in a negative volume variation ($\varepsilon < 0$).

### 12.3.2 Synthesis of Conducting Polymers for Actuator Purposes

There are several possibilities to synthesize conducting polymers, but the most commonly used and described methods in the literature for ECP actuators are the chemical and electrochemical oxidative polymerizations. Both of these methods lead to p-doped conducting polymers, *i.e.*, in their oxidized state after synthesis. The choice of the method (chemical or electrochemical) has an effect on the resulting polymer's morphology, crystallinity, doping level, conductivity and molecular weight. The most commonly used and described ECPs for actuator applications are PANI, PPy and PEDOT.

The electrochemical synthesis of ECPs is usually carried out employing the galvanostatic or potentiostatic method or by cyclic voltammetry. This synthesis method allows the control of a wide range of parameters, such as the nature of counter-ions, usually chosen according to the solubility in the selected solvent, the polymerization temperature and the potential or current.[42] It is an effective process which allows reproducibility and more precise control on electropolymerization kinetics, morphology and the thickness of the resulting ECP layers. However, the process is limited to the synthesis of electronic conducting substrates and large deposition areas can suffer from the lack of film uniformity. Usually thin metal layers are used in order to deposit the ECP layers. Recently, Temmer *et al.* proposed a different method for ECP actuators by replacing the metal layer with chemically oxidized PEDOT, where afterwards PPy was electrochemically deposited.[37,43]

The chemical oxidative polymerization method is realized in the presence of a monomer (pyrrole, EDOT, *etc.*) and an oxidant. The most commonly

used oxidants for chemical oxidation are iron(III) chloride ($FeCl_3$) and iron(III) tosylate [$Fe(OTs)_3$]. Using $FeCl_3$ as the oxidant for the chemical oxidation, directly mixed with the monomer, results in highly conductive, but brittle and insoluble powder, which is usually not applicable for self-standing film or actuator fabrication.[42] Host materials are most commonly used for ECP actuators in order to obtain the ECP as a film. In this case, the host material is swollen with the monomer, which is then immersed into the oxidant solution and allows the formation of ECP film directly at the interface of the host material.[44] Generally, the chemical oxidation is a cheap and facile method and the polymerization can be obtained on nonconductive substrates, which is not possible with electrochemical polymerization.

Vapour phase polymerization (VPP) is another route of chemical oxidation, which is usually carried out by introducing the monomer vapour to the oxidant-covered substrate. This polymerization method was first described by Mohammadi *et al.* in 1986 and allows the formation of thin and uniform ECP layers.[45]

ECPs are also commercially available, for example in the form of poly(3,4-ethylenedioxythiophene):poly(styrene sulphonate) (PEDOT:PSS) dispersion. This ink-type conducting polymer dispersion was first commercialized under the trade name of Baytron® and is currently manufactured by Heraeus under the trade name of Clevios™.[46] It is the most successful commercialized conducting polymer ink in terms of practical applications (conductive coatings, antistatic coatings, electroluminescent devices, capacitors, *etc.*). A deep blue PEDOT:PSS microdispersion can be obtained through aqueous oxidative polymerization of the hydrophobic EDOT monomer in the presence of polystyrene sulphonic acid (PSS) (see Figure 12.4a). The resulting aqueous mixture is a colloidal dispersion of PEDOT:PSS particles with hydrophobic and positively charged (doped) PEDOT core surrounded by hydrophilic and negatively charged PSS shell (see Figure 12.4b).[47] The PSS has two functions in the PEDOT:PSS complex: (i) it serves as the charge-balancing counter-ion for the doped PEDOT, and (ii) it disperses and stabilizes the PEDOT particles in water and other solvents.[42,48] The ink-type nature of PEDOT:PSS dispersion has the advantage of easy processing through various methods, such as drop casting, spray coating, spin coating and ink-printing techniques.[49–58] The resulting material possesses many unique properties, such as flexibility, intrinsic conductivity, biocompatibility and high chemical stability.[42] The electrical conductivity of PEDOT:PSS is influenced by different synthetic conditions, processing additives or post-treatment techniques.[59–66]

### 12.3.3 Conducting Polymer Actuators Operating in Liquid Electrolyte

The use of conducting polymers as actuators was first demonstrated by Baughman in the 1990s (see Figure 12.5b).[8,11,68] This actuator was constructed to operate in electrolytic solution in a bending mode. Ever since, great advances and improvements in this field have been made and

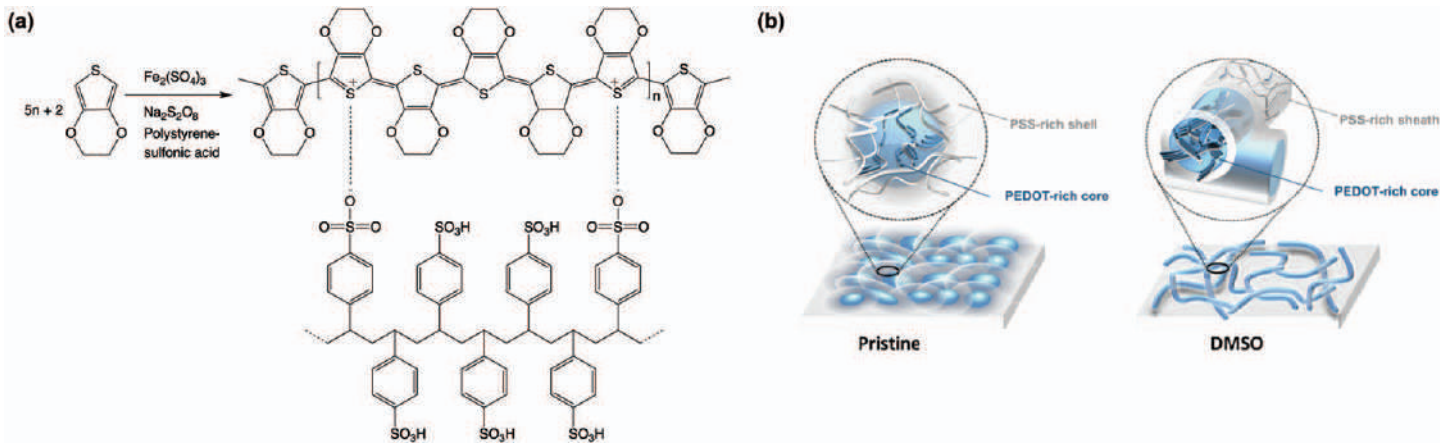


**Figure 12.4** (a) Oxidative polymerization of EDOT monomer in the presence of PSS and a primary structure of PEDOT:PSS; (b) scheme representing the morphology and effects of additives of PEDOT:PSS.
Reproduced from ref. 67 with permission from the American Chemical Society, Copyright 2019.

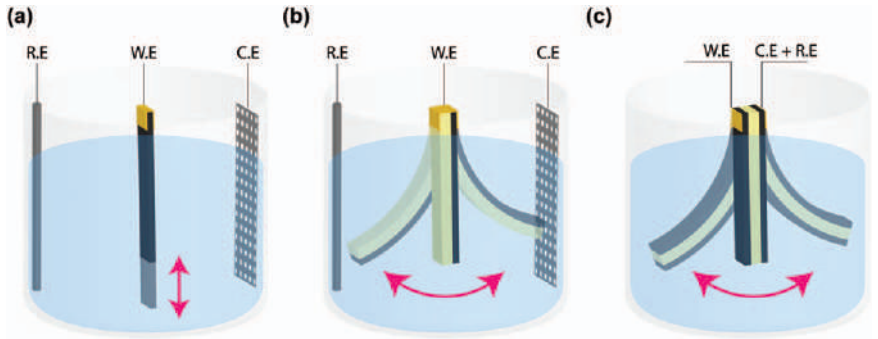


**Figure 12.5** Schematic view of different actuators operating in liquid electrolyte in a three-electrode configuration: (a) freestanding linear actuator, (b) bilayer bending actuator and (c) trilayer bending actuator.

reported. Conducting polymer actuators can be divided into different categories based on: active ECP material, operating environment (in solution, open air), number of layers (freestanding, bilayers, trilayers), motion type (linear or bending) and dimensions (nano-, micro-, macroscale). The overview of ECP actuators in these sections is based on their operating environment and will be discussed subsequently.

Conducting polymer actuators operating in liquid electrolyte can be constructed as freestanding films, bilayer actuators or trilayer actuators. The freestanding films (see Figure 12.5a) were initially used in their most basic form to understand the fundamental performances of conducting polymers. The volume change of the ECP is isotropic, but if the configuration of the polymer is anisotropic as a film, a linear deformation can be obtained.[69,70]

Bilayer actuators are usually two-layer structures consisting of a passive layer (constant volume) and an ECP layer (see Figure 12.5b). The fabrication of a bilayer actuator is usually obtained by the electrochemical synthesis of a conducting polymer layer directly on a flexible substrate with a thin layer of sputtered metal.[12,71–73] The substrate, *i.e.*, the passive materials, can be a plastic or a piece of paper.[11,74–77] Another possibility to realize bilayer actuators is to fabricate both layers (passive and conductive) separately and later manually attaching them.[78,79]

The actuation of these freestanding and bilayer devices has to be performed in a three-electrode configuration when immersed in liquid electrolyte. The ECP layer acts as a working electrode (WE). Metal grids or wires (platinum, gold, silver, stainless steel) are usually used as a counter electrode (CE) and classical reference electrode (RE) is added to control the potential of the system. The electrochemical oxidation/reduction of the WE when applying potential difference or current results in reversible volume variation of the ECP layer and consequently leads to a linear (freestanding film) or bending (bilayer actuator) movement.[35,70,80–83]

Two-electrode configuration can be used if the device is elaborated with a trilayer configuration. In this case, a second ECP electrode is deposited on

the other side of the passive film (see Figure 12.5c). One ECP layer is then connected to the WE and the second ECP layer to the CE + RE. Electrical stimulation of the trilayer, still immersed in electrolyte, promotes opposite electrochemical reactions in the electrodes, one being oxidized (anode) while the second one (cathode) is concomitantly reduced. As a consequence, one layer expands while the other contracts, leading to the bending movement of the actuator.[84,85] A trilayer configuration has the advantage of producing higher output forces compared to the bilayer actuator due to the presence of the two electrodes instead of one. However, the operation in liquid electrolyte may reduce their potential areas of applications.[79,86]

### 12.3.4 Conducting Polymer Actuators Operating in Open Air

Air operation of ECP actuators allows broadening of their application field. Since these ionic actuators require an ion source in order to operate, the strategy was to replace the previously described passive film for trilayer configuration with an ionically conducting film, behaving as an ion reservoir. In other words, the necessary ions are incorporated directly in the self-standing trilayer device (see Figure 12.6).

The redox process takes place in the same way as for the trilayers in the liquid electrolyte, except that the ion exchange occurs between the electrodes with the electrolyte are directly included in the separator membrane. When applying a potential, the ions will be inserted into one ECP layer and expulsed from the other ECP layer resulting in an open-air bending movement of the actuator. The ion reservoir membranes and the open-air trilayer actuators will be described in the following sections.

#### *12.3.4.1 Ionic Membranes for Conducting Polymer Actuators*

Different ECPs (PPy, PEDOT, *etc.*) and different ion reservoir membranes (gel electrolyte, porous membrane filled with electrolyte, solid polymer electrolyte) have been used for actuator fabrication.[80,87–91] The ion reservoir membrane has an important role in the actuator configuration by providing the system with ionic conductivity and mechanical properties. Nowadays,

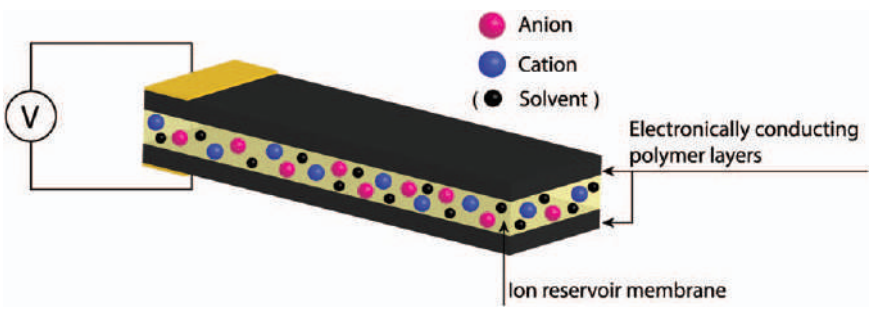


**Figure 12.6** Schematic view of a trilayer actuator for operating in the open air.

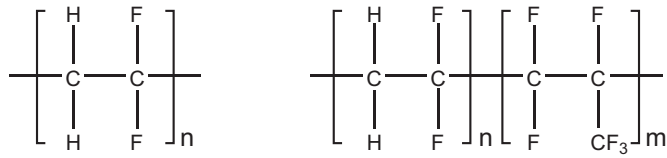


**Scheme 12.1** Chemical structures of poly(vinylidene fluoride) (PVdF) and poly(vinylidene fluoride)-*co*-hexafluoropropylene (PVdF-HFP).

most commonly used ion reservoir membranes for actuators are based on microporous poly(vinylidene fluoride) (PVdF)-containing electrolyte, based on single networks or on an interpenetrating polymer network (IPN) architecture swollen with electrolyte.

Poly(vinylidene fluoride) (PVdF) and its copolymers (Scheme 12.1) are widely used as porous membranes mainly for filtration purposes.[92,93] For actuation applications, they are mostly used because of their commercial availability, allowing fast and simple actuator fabrication and because of their porous nature allowing strong anchoring of the ECP layer to avoid delamination issues. PVdF is a semicrystalline polymer with the repeat unit of $-(CH_2CF_2)_n-$, presenting high mechanical strength and stability, good chemical resistance and it is often used as a commercial thermoplastic membrane (Millipore®).[94] This polymer presents good compatibility with liquid electrolytes, which simply fill the porous structure without solvating the membrane. The porous copolymer poly(vinylidene fluoride)-*co*-hexafluoropropylene (PVdF-HFP) is often used for electrochemical applications due to good electrochemical stability.[95,96] PVdF-HFP has both, crystalline VdF and amorphous HFP units. The crystalline phase provides the structural properties to support a freestanding film and the amorphous phase is capable of trapping a large amount of electrolyte which contributes to increasing the swelling rate of the polymer and then provides the ionic conductivity.

The use of single networks for ion reservoir membranes has been demonstrated by different research groups. The first ion reservoir membrane for open-air actuators was developed by Sansiñena *et al.* and was based on poly(epichlorohydrin-*co*-ethylene oxide) [P(ECH-*co*-EO)] and lithium perchlorate ($LiClO_4$).[87] The resulting gel-like membrane presented good ionic conductivity but relatively poor mechanical properties. Vidal *et al.* demonstrated the fabrication of a dangled chain PEO network since it favours ionic mobility.[44] The single PEO network was obtained by free-radical copolymerization of poly(ethylene glycol) dimethacrylate (PEGDM) and poly(ethylene glycol) methyl ether methacrylate (PEGM), later swollen in 0.1 M $LiClO_4$ aqueous solution. However, the resulting material presented poor mechanical properties due to the brittle nature of this PEO network and was not satisfying as an ionic reservoir membrane for actuator fabrication. Cho *et al.* proposed the use of a high-molecular-weight nitrile butadiene rubber (NBR) network swollen in ionic liquid as an ionic membrane for actuator fabrication.[97,98] The presence of NBR could fulfil the mechanical requirements,

but the membrane's ionic conductivity was not sufficient for use as an ionic reservoir. The use of polyurethane (PU) containing $Mg(ClO_4)_2$ as an ion reservoir membrane was demonstrated by Choi *et al.*,[99] however with poor ionic conductivity. The ionic conductivity of the similar PU system was further improved by the group of Okuzaki using ionic liquid (IL) as an electrolyte to develop IL/PU gels suitable for the actuator fabrication.[100,101]

Another type of ionic membrane for actuators is based on interpenetrating polymer network (IPN) architecture containing an electrolyte. IPNs are defined as the combination of two or more cross-linked polymers, synthesized in the presence of each other.[102,103] It is the only way to combine cross-linked polymer networks and provide usually good dimensional and morphological stability. Depending on their synthesis pathway, the relative weight ratio of components and their relative cross-linking kinetics, different morphologies can be obtained. In order to combine the intrinsic properties of each polymer partner, co-continuous morphology across the material is usually desired. Semi-IPNs can also be obtained if one of the polymer partners is not cross-linked. In this case, it remains as linear macromolecules interpenetrated and entangled in the cross-linked structure of the second network.

There are many ways to synthesize IPNs. In the *sequential pathway*, the precursors of the second network (monomer 2, cross-linker, initiator) are introduced, usually by swelling, and subsequently polymerized in an already-formed single network of the first partner. In the *in situ* pathway, all the precursors, *i.e.*, monomers, cross-linkers, initiators and/or catalysts, are mixed together, eventually with a solvent, and polymerized. Polymerization of both networks can be performed simultaneously or sequentially. When networks are polymerized simultaneously, it corresponds to the *in situ simultaneous pathway.* It must be mentioned here that noninterfering polymerization mechanisms are used, like free-radical polymerization for one network and step polymerization for the other. If networks are polymerized sequentially, it corresponds to the *in situ sequential pathway*. In this case, the polymerization mechanism can be similar but monomers have to present significantly different reactivity (see Figure 12.7).

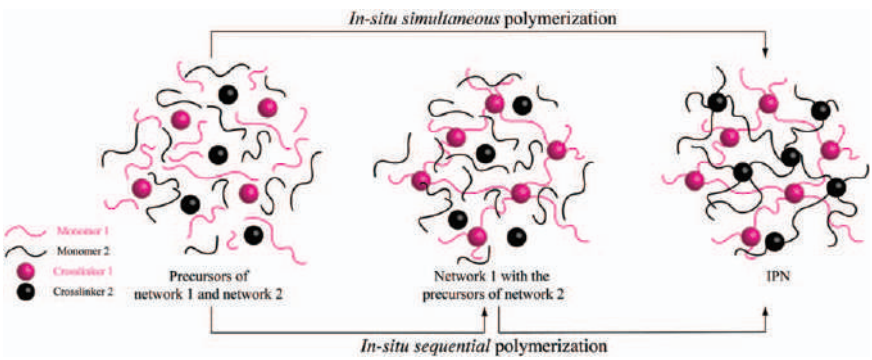


**Figure 12.7** Schematic view of the two polymerization routes to fabricate IPNs from the precursors of network 1 and network 2.

The first IPN-based membrane for ionic reservoir in actuator application was elaborated as poly(ethylene oxide) (PEO)/polycarbonate (PC) IPN, obtained by *in situ sequential* polymerization. From a reactive mixture containing all the network precursors, the PEO network was obtained by free-radical copolymerization of poly(ethylene glycol) dimethacrylate (PEGDM), poly(ethylene glycol) methyl ether methacrylate (PEGM) and PC network by free radical polymerization at higher temperature of the less reactive monomer di(ethylene glycol) bis(allyl carbonate) (DEGBAC).[91] Unfortunately, this membrane was not suitable for long-life operation of the actuator due to the brittle nature of PEO and PC and finally the poor mechanical properties of the resulting IPNs after swelling with electrolyte. Optimized materials were proposed later by replacing the glassy PC network with those based on elastomers, such as polybutadiene (PB),[104,105] polytetrahydrofurane (PTHF)[106] and NBR.[107] When phase co-continuity is obtained, the PEO phase can act as an efficient ionic conducting medium while the elastomer phase acts as mechanical reinforcement due to its rubber properties. Upon swelling in an electrolyte, the resulting membrane can be used as an ionic reservoir for actuators. Ionic conductivities up to $10^{-3}$ S cm$^{-1}$ and strain at break above 150% have been demonstrated using 1-ethyl-3-methylimidazolium bis(trifluoromethylsulphonyl)imide (EMImTFSI) as electrolyte.[108] These results demonstrated the advantage of IPN architecture in the synthesis of highly ionically conductive and robust ion reservoir membranes by combining the intrinsic properties of each partner. The chemical structures of these used polymers are illustrated in Scheme 12.2.

### *12.3.4.2 Trilayer Conducting Polymer-based Bending Actuators*

The first trilayer actuator operating in open air was described by the MacDiarmid group in 1994.[109] This electrochemical actuator consisted of two PANI films which were affixed on both sides of double-sided cellophane tape and wetted in hydrochloric acid aqueous solution. The deformation of the actuator at maximum bending was estimated to be approximately 1%, with an applied voltage of 4.0 V. A few years later, the wetted cellophane tape was replaced by a gel-like membrane.[87] The polymeric electrolyte solution was dropped on two electropolymerized PPy electrodes, which were affixed together after solvent evaporation. The actuator resulted in 90° angular bending and demonstrated efficient fabrication of all polymer actuator.

The development of actuators had to overcome different problems related to the mechanical properties or lifetime of the actuators. The gel electrolytes that were used as ion reservoir membranes for actuators were mostly insufficient due to poor mechanical properties. Another common problem was the use of electrolytic solutions (salt/organic solvent or salt/water) which were limiting the lifetime of the actuators due to the solvent evaporation. This issue can be solved if an ionic liquid is used as an electrolyte. Ionic liquids are salts in liquid state at ambient temperature.[110] They present large electrochemical windows, high ionic conductivity, do not require the use of any additional solvent, are nonvolatile but also nonflammable.[111] They were

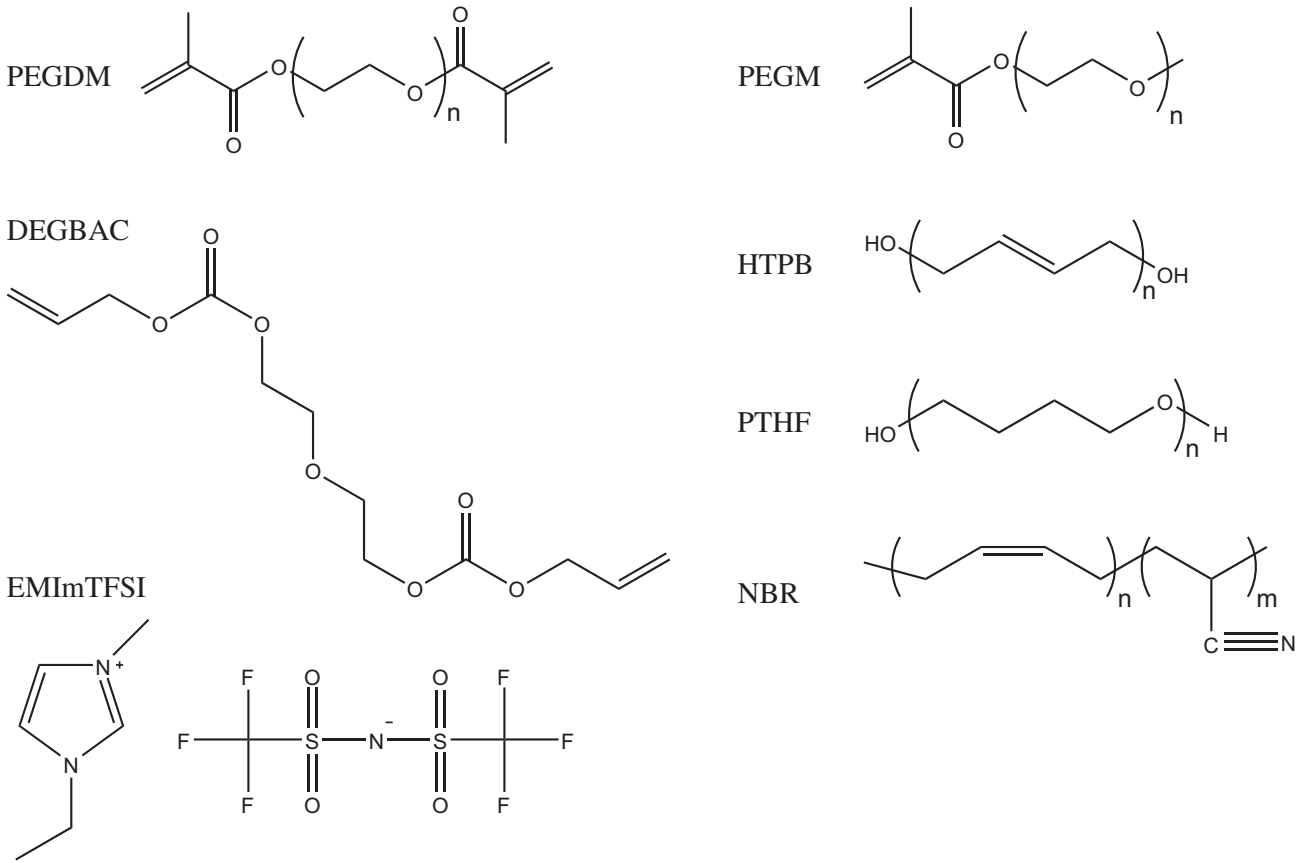


**Scheme 12.2** Chemical structures of PEGDM, PEGM, DEGBAC, HTPB, PTHF, NBR and EMImTFSI ionic liquid.

described for the first time in 2002 by Lu *et al.* as electrolytes for π-conjugated polymer electrochemical devices with an enhanced lifetime (up to 1 million cycles).[89] In 2003, ionic liquids were used in actuator application for linear systems operating in solution[112] and for open-air bending trilayers.[90] Since then, many systems have been described and demonstrated high lifetime of the resulting actuators.[113]

The second issue was related to the delamination occurring at the interfaces of the layers due to the repeated electromechanical deformation of ECP electrodes. This problem has been solved thanks to several approaches at the same period as the introduction of ionic liquids. First, as mentioned earlier, the use of microporous PVdF membranes helped to improve the anchoring of the ECP layers on the central membrane.[90] For instance, Zhou *et al.* electropolymerized Py onto previously platinized commercial PVdF membrane.[90] Combined with the use of ionic liquids, the resulting PPy/PVdF/PPy trilayer actuators demonstrated 90° bending to either side and exceeded more than 3600 cycles without any obvious delamination between the electroactive PPy and the platinized PVdF layers. The use of commercially available PVdF membranes with defined thickness and dimensions may limit the possibility of tuning the geometry and performances of the resulting actuators. To overcome these issues, Gaihre *et al.* demonstrated the possibility to control the porosity and final thickness of homemade PVdF membrane for actuator applications.[114]

The delamination problem of the layers was also solved according to another approach by the synthesis of conducting IPNs (C-IPNs).[44,104,113,115] Instead of depositing the ECP layer on top of already fabricated membrane, ECP layers are interpenetrated within the membrane with their concentration decreasing from the surface to the central part of the film. Providing that no electrical connection occurs between the two electrodes, one-piece pseudo-trilayers are obtained, resolving de facto any delamination problem. This 3D interface, compared to the 2D interface of classical trilayer systems, may also improve the charge exchanges between the ECP electroactive layers and the ion reservoir membrane. Interpenetration of the electrodes was realized by chemical oxidative polymerization of EDOT with 1.5 M $FeCl_3$ aqueous solution in two steps. First, the EDOT monomers are introduced in the membrane by swelling and the resulting swollen membrane is immersed in oxidant solution. Due to opposite diffusion processes, *i.e.*, desorption of the EDOT from the membrane and absorption of the oxidant in the membrane, polymerization occurs within the surface of the membrane, resulting in the expected pseudo-trilayer configuration (see Figure 12.8).

The first C-IPN actuators, operating in open air, were introduced by the LPPI group in 2002, but a short life time was reported due to the appearance of cracks during bending deformation.[91] In this case, the ion reservoir membrane was already an IPN combining PEO network and polycarbonate (PC) network, as mentioned earlier, the interpenetrated ECP electrodes were made of PEDOT and the electrolyte was $LiClO_4/H_2O$. The brittleness of these first C-IPN actuators was solved by the synthesis of robust ionic membranes, and more

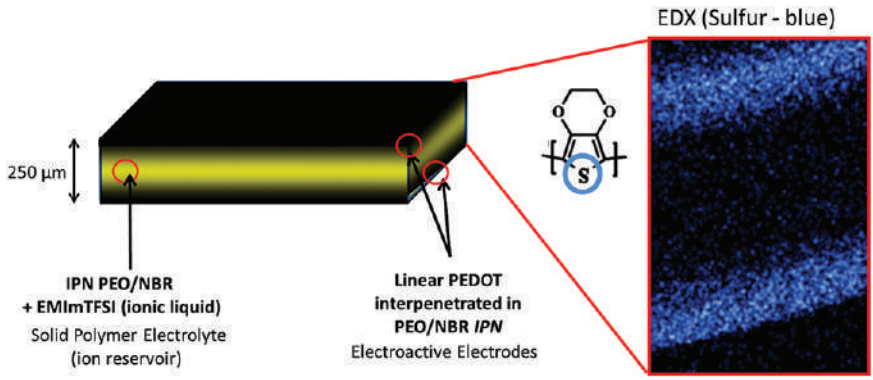


**Figure 12.8** Conducting interpenetrating polymer network (C-IPN): schematic view of the configuration and EDX mapping of sulphur (blue) corresponding to PEDOT. In this example, the ion reservoir membrane displays an IPN macromolecular architecture with a total thickness of *ca.* 250 µm.

specifically by replacing the vitreous PC network by short-chain elastomer networks, such as PB[113,116] and PTHF[106] or by a second PEO network.[117] The synthesis of C-IPNs has also been described from a single network of high-molecular-weight rubber, such as NBR[97,98] and by PEO/NBR IPNs.[108] With the use of ionic liquids, strains up to 2.4% under $\pm 2.0$ V, forces in the range of tens of mN (depending on device dimensions) and long life time (up to $7 \times 10^6$ cycles at a frequency of 10 Hz) have been obtained. It is also interesting to mention that the C-IPN architecture provides a control on the mechanical and electromechanical properties of the electrodes. Indeed, ECP chains are surrounded by other macromolecular chains in C-IPNs. As a consequence, a modification of ECP local concentration in the electrodes[118] or the introduction of another polymer partner[119] appears as a powerful tool for tuning the Young's modulus and the volumetric charge density of the electrodes, in order to control the final performances of the devices.

## 12.4 Electronically Conducting Polymer Microactuators

Electronically conducting polymer-based microactuators are promising candidates to enable a broad range of applications for new generation of soft microsystems where large strains are required. The concept and possible designs of microelectromechanical actuators based on ECPs were first described by Baughman in 1991.[120] He conceptually analyzed material properties and device designs based on experimental verifications on a macroscale to propose different approaches for fabricating ECP microactuators. Then, the combination of different microfabrication technologies (photolithography, etching techniques, metal deposition methods and laser ablation) allowed the design and fabrication of conducting polymer-based microsystems with a variety of configurations for different purposes.

The next subsections will give an overview of ECP microactuators based on their operation environment (in electrolytic solution and in open air).

### 12.4.1 Microactuators Operating in an Electrolytic Solution

The first microactuators were developed in bilayer configuration and operated in electrolytic solution. Smela *et al.* reported a work on bilayer strips of gold (Au) and dodecylbenzenesulphonate (DBS)-doped polypyrrole (PPy) in 1993.[71] They used standard photolithography of positive photoresist S1828 to fabricate millimetre-scale polymer fingers. After the dissolution of a sacrificial layer, the polymer fingers were connected to the Si wafer at one end but were free for the movement at the other. These fingers were stimulated in 0.1 M NaDBS aqueous solution and resulted in curling and uncurling with a response time of approximately 5 seconds. The same authors presented the possibility of a more complex configuration by combining the same DBS-doped PPy and Au bilayers with stiff parts.[82] The realization of these devices was done by combining standard photolithography, wet chemical etching and reactive ion etching (RIE). This work also demonstrated the differential adhesion method to release the bilayers by pulling themselves from the substrate when the electrical stimulation was applied. These microactuators with rigid elements had a configuration of an unfolded box. During electrical stimulation in NaDBS solution, the bilayer hinges achieved 180° bending, allowing the planar configuration microsystem to fold into an octahedron configuration (see Figure 12.9). Smela continued the research and demonstrated the fabrication of microsystems with a different release method.[121] The microactuator was fabricated using many different microfabrication technologies with the combination of standard photolithography, RIE, wet chemical etching, chemical vapour deposition (CVD) and metal evaporation. The novelty of this fabrication method was the release of the microsystems by finally etching through the Si wafer. These microsystems were electrically stimulated in NaDBS solution and the PPy/Au bilayer hinges were capable of lifting and positioning rigid Si and benzocyclobutene (BCB) plates.

**Figure 12.9** Octahedron of PPy/Au bilayer hinge microactuators with rigid elements by M. Krogh *et al.*, Micromuscle AB, inspired by Smela *et al.*[82] Reproduced from ref. 122 with permission from Elsevier, Copyright 2007.

Jager *et al.* demonstrated the fabrication of different microstructures for different purposes. They fabricated on-chip microsystems based on moveable PPy/Au bilayers with all the necessary electrodes (working, counter and reference) directly on a chip.[123] They found that the speed of the microactuators was the same compared to the usual device where macroscale electrodes were used. The next work proposed more complex design of a micro robot arm, consisting of an elbow, a wrist and a hand with fingers.[72] The joint parts were made of PPy/Au bilayers that were connected to stiff elements of benzocyclobutene (BCB). Different joints were stimulated separately, allowing the microarm to move, to grab and lift a 100 μm glass bead and to move it over a distance of 200–50 μm. The design and operation ability in different environments (salt solutions, blood plasma, urine and cell culture medium) make them attractive for biomedical applications. Over the years they reported studies on different designs of microstructures as microfluidic system, cell clinic and microactuators for different biomedical applications.[12,124–126]

A relatively simpler procedure of a PEDOT:PSS-based bilayer microactuator was proposed by Taccola *et al.*[127] The PEDOT:PSS/SU-8 bilayers with a final thickness of less than 600 nm (PEDOT:PSS 220 nm and SU-8 340 nm) were constructed by standard photolithography of SU-8 and wet chemical etching of PEDOT:PSS. The contacts were also included in the system but with manual wiring, after the fabrication of the microstructures. The system consisted of many fingers, which were stimulated at the same time in NaDBS aqueous solution and resulted in displacement from 220 to 2090 μm.

These bilayers have been integrated into complex microsystems for various applications over the past few decades. The operation in liquid electrolyte, especially in salt solutions, blood plasma, urine and cell culture medium, is mostly advantageous for biological and biomedical applications. In order to broaden the application field, the microactuator needs to be able to operate in open air. As mentioned earlier, for operation in the open air, the actuator needs to have a trilayer configuration with two electroactive electrodes sandwiching an ion storage membrane.

### 12.4.2 Microactuators Operating in the Open Air

The first air-operating microactuator was demonstrated by Alici *et al.* in 2009.[128] The microactuator was fabricated as a conventional macroscale actuator using a commercial PVdF membrane with a thickness of 110 μm and electropolymerizing PPy electrodes on both sides of the Au-coated PVdF membrane. The downscaling of the device was performed using a laser ablation technique, resulting in microactuators with dimensions 799×217×155 μm (length×width×thickness). Gaihre *et al.* presented the synthesis of PVdF thin films in order to decrease the final thickness of these PPy microactuators to 54 μm.[129] After synthesizing thinner PVdF films, they found that the actuator (850×250×54 μm) with PVdF membrane containing 0.05 M LiTFSI resulted in the highest tip displacement of 0.253 mm.[114] They also demonstrated that miniaturization of the actuators resulted in higher

strain energy per unit of mass or volume.[130] These trilayer microactuators were simple and obtained by a laser ablation technique or by manually cutting, later operated in the same manner as macroscale actuators, manually connecting the PPy microactuators to the macroscopic power supply.

Using similar PPy-Au-PVdF-based trilayer actuators, Jager *et al.* proposed a method to fabricate individually controllable actuators on a commercial flexible printed circuit board (FPCB).[131] The fabrication of the millimetre-scale actuators involved patterning of the Au on both faces of the PVdF membrane by flipping the substrate using wet chemical etching. Subsequently, the PPy electrodes were electropolymerized on the Au patterns simultaneously, resulting in trilayer actuators. The interface was fabricated separately and manually connected later with the resulting actuators. The actuators, 9 mm long and 2 mm wide, with FBCB interfacing, resulted in 18 mm tip displacement when stimulated under 1.5 V.

Another actuator composition and microfabrication method were proposed by Khaldi *et al.*[132,133] The microactuator was fabricated as a C-IPN composed of PEO/PTHF IPN as the ion reservoir membrane and PEDOT as interpenetrated electrodes. The low thickness of the resulting trilayer actuator (12 μm) allowed the use of RIE for patterning the actuators. The trilayer structure was manually placed on a PVA sacrificial layer in order to maintain it fixed and planar during the etching process, using photoresist as a mask. After the etching, microbeams were swollen in ionic liquid EMImTFSI before characterization. The microbeams with dimensions of $900\times300\times17$ μm resulted in a large displacement amplitude of 950 μm, corresponding to the strain of 1.1%. The same authors optimized the thickness of these actuators and glued SU-8 parts on the microbeams to mimic the wings of a crane fly.[134] This work demonstrated improvement of the actuation frequency of 50 Hz, compared to the previous 0.05 Hz.

A further decrease of the thickness was demonstrated by Maziz *et al.* by the fabrication of C-IPN-based trilayer microactuators with an interpenetrating polymer network of PEO and nitrile butadiene rubber (NBR).[135,136] The PEDOT electrodes were here also obtained through chemical oxidative polymerization on both sides of the PEO/NBR layer. The involvement of a spin-coating step into the fabrication process allowed tuning of the thickness of the membrane layer from 600 nm to 30 μm. The actuators were patterned using standard photolithography and RIE, resulting in microactuators with final thicknesses of 6, 12 and 19 μm. These microactuators demonstrated strain differences up to 0.9% and output forces in the range of μN. More importantly, reducing the final thickness of the microactuators allowed demonstrating actuation at a high resonant frequency of 930 Hz.

Recently, another interesting work was demonstrated by Khaldi *et al.* about patterning techniques for conducting polymers.[137] They presented two patterning methods: micro-contact printing (μCP) and syringe-based printing. The PDMS stamp was used for μCP, where an oxidant solution layer was deposited through the stamp on PVdF membrane and followed by the vapour phase polymerization (VPP) of EDOT, resulting in well-defined micropatterned electrodes. The PDMS stamp and μCP allow patterning of the device architecture in

a single step with individually controllable actuators, wires and contact pads. Unfortunately, they did not succeed in using this technique on PEO-NBR membrane due to the insufficient affinity between the oxidant solution and the PEO-NBR membrane. Consequently, they used the second patterning method. Syringe-based printing requires different affinity and the PEO-NBR membrane was found to be suitable for this process. They fabricated the trilayer actuator based on a layer-stacking method. First, an oxidant solution was deposited in the desired shape using syringe-based printing followed by the EDOT VPP. The PEO-NBR network precursors were deposited through spin-coating, followed by a short curing and the second electrode was obtained in the same way as the first one. The final systems were cut out from the membrane using laser ablation and fabricated milli/micro hand actuator resulting in a 2.2% strain difference, stimulated at $\pm$2.0 V with a thickness of 70 μm. This work proposed printing methods that have not been used so far for microactuator fabrication. Nonetheless, electrical connections were not integrated to the system requiring the use of macroscopic connections to electrically stimulate the resulting microactuators.

Except the work of Jager, all reported attempts on air-operated microactuators have been reported without the integration of electrical connections. As said earlier, in order to fabricate an efficient microsystem, electrical contacts have to be integrated in the system, and ideally directly during its fabrication, to connect the actuator with an electrical supply. For this purpose, Khaldi *et al.* proposed a bottom-up process to fabricate a system with individual control of the system.[138,139] The process combined standard photolithography, wet chemical etching, evaporation and sputtering. The reported work proposed a fabrication of millimetre-scale actuators, resulting in a relatively low strain of 0.01% at $\pm$1.0 V. Even though the fabrication process was successful and two electrical connections were incorporated, the final samples were manually cut out of the substrate, which makes it harder to manipulate, if the sample dimensions are decreased.

On the other hand, Maziz *et al.* reported a microactuator fabrication method on a flexible substrate, called the top-down approach.[140] This process is the first to integrate one electrical connection into an open-air actuating microdevice without any kind of manual handling, using different microsystem technologies. The realization of the trilayer actuator was performed using a layer-stacking method, *i.e.*, by sequentially stacking layers on top of the previous layers. Using spin-coating to deposit the layers allows precise control over the thickness of each layer and allows the fabrication without any manual handling during the synthesis. The PEDOT electrodes were obtained through EDOT vapour phase polymerization (VPP) and the membrane layer through radical polymerization of spin-coated PEO-NBR solution precursors. The PEDOT/PEO-NBR/PEDOT trilayer microactuators were fabricated on a SU-8 substrate with bottom electrical contact by combining standard photolithography, evaporation and RIE (see Figure 12.10). The second contact was obtained by placing a micromechanical gold tip on top of the trilayer. The microactuator (650$\times$100$\times$10 μm) was electrically

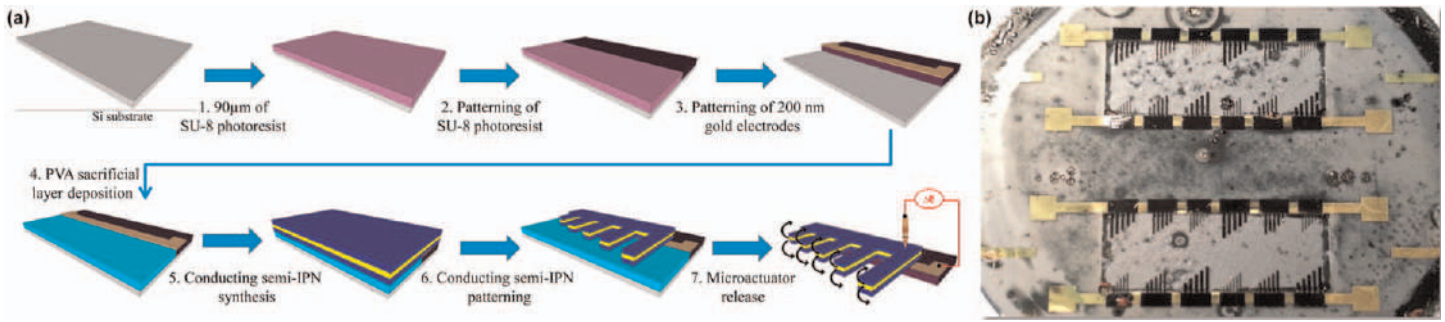


**Figure 12.10** (a) Overview of the fabrication steps and (b) photograph of the microactuators fabricated with the layer-stacking method and with integrated bottom electrical contact.
Reproduced from ref. 140 with permission from the American Chemical Society, Copyright 2016.

stimulated in air (±4.0 V) and resulted in a strain difference of 0.13% and an output force of 0.75 μN. This work presented a great improvement compared to previous works with full integration of bottom electrical contact and subsequent operation on a soft substrate and resulted in a functioning microactuator after all the microfabrication processing steps. The disadvantage of this method remains in the absence of the second electrical contact from the top of the PEDOT electrode, requiring manual connection of this electrode for the characterization and relatively low performances.

More recently, Zhong *et al.*[141] demonstrated the fabrication of a photopatternable ionic reservoir membrane composed of bisphenol A ethoxylate dimethacrylate (BEMA) and poly(ethylene glycol) methyl ether methacrylate (PEGMA) networks with the necessary ions for the redox process directly incorporated before the photopolymerization. The microsystem was realized by locally electropolymerizing PPy electrodes in photoresist holes on a gold-coated wafer. Subsequently, the membrane was micropatterned locally on top of the PPy layer using photolithography, resulting in bilayer microactuators. The final release was performed by wet chemical etching to form the device layout. After the etching, the working electrodes were movable but still attached to the wafer. The final microdevice was fabricated with parallel electrode configuration. In this case, the working and counter electrodes were placed parallel under the actuator, between which the ions were shuttled during the electrical stimulation (see Figure 12.11). This novel method and the development of the photopatternable ionogel would be advantageous for microstructure fabrication. Although the novel fabrication method was reported, the performances of the actuators were almost nonexistent, probably due to the low ionic conductivity of the BEMA gel after all the processing steps.

Finally, Plesse *et al.* described the synthesis of trilayer microactuators and microsensors fully compatible with microsystem processes and with integrated electrical connections. Commercially available poly(3,4-ethylenedioxythiophene):poly(styrene sulphonate) (PEDOT:PSS) dispersion was chosen as an electrode material for the fabrication of microactuators. The poor electrical, mechanical and electrochemical properties of pristine PEDOT:PSS electrodes were improved significantly by formulation of the commercial dispersion with polar reactive additive based on methacrylic poly(ethylene glycol) and its subsequent polymerization within the PEDOT:PSS material leading to a PEDOT:PSS:PEO electrode. The synthesis of PEDOT:PSS:PEO trilayers was performed according to the layer stacking method (see Figure 12.12a). Patterning was performed first by laser ablation to obtain PEDOT:PSS-based microactuators. While electrically connected manually, these PEDOT:PSS/PEO microactuators presented high performances with a maximum strain of 0.82% and maximum output force of 472 μN under ±2.2 V (see Figure 12.12b).[142] More importantly, the mechanical sensing behaviour was demonstrated for the first time at the microscale and presented enhancement of the sensitivity compared to the macroscale ECP-based actuators (maximum output voltage 0.42 mV at 0.5% strain). The full microsystem process was then performed to integrate such electroactive

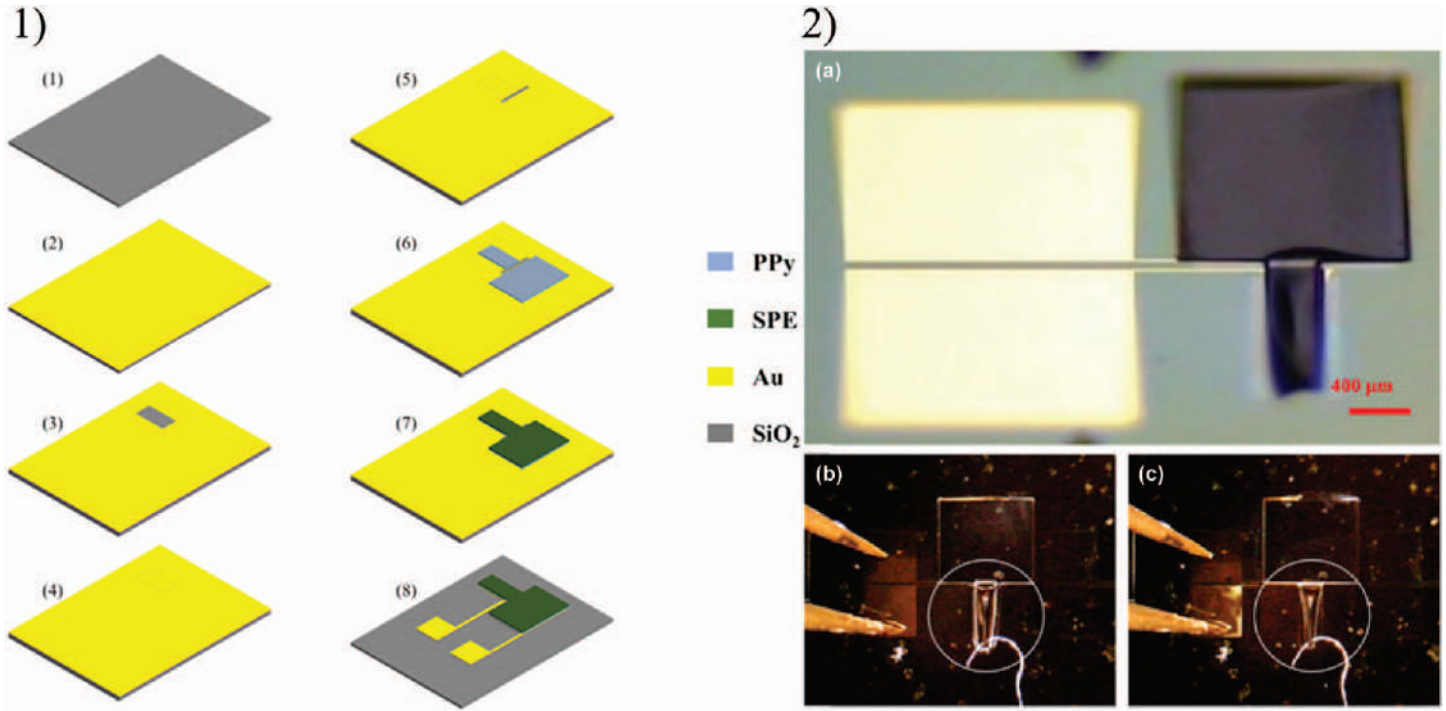


**Figure 12.11** Solid-state polypyrrole microactuator: (1) overview of the fabrication steps and (2) photographs of the microactuator, (a) as fabricated, (b) and (c) actuation results showing folding motion.
Reproduced from ref. 141, https://doi.org/10.1088/1361-665X/aabe42, under the terms of the CC BY 3.0 licence, https://creativecommons.org/licenses/by/3.0/.

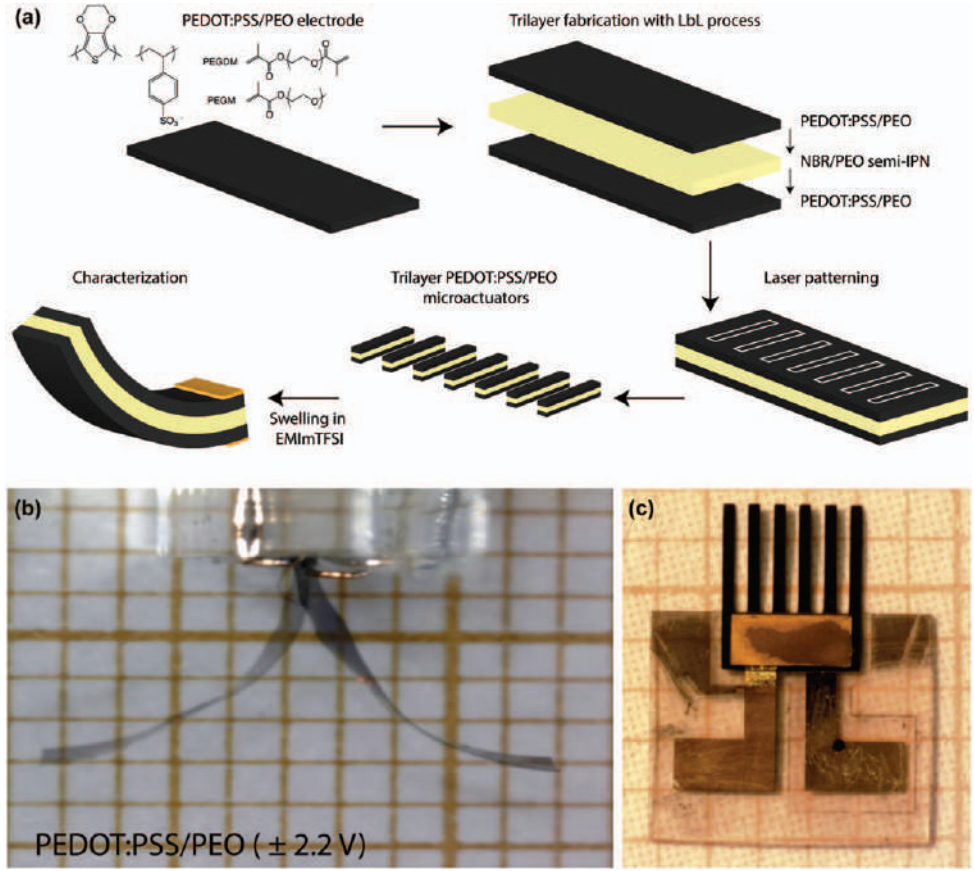


**Figure 12.12** (a) PEDOT:PSS/PEO microactuator fabrication with the layer-stacking method; (b) PEDOT:PSS/PEO microactuator under electrical stimulation of ±2.2 V; (c) fully integrated PEDOT:PSS/PEO microsystem with two electrical contacts directly on a flexible substrate.
Part (a) reproduced from ref. 142 with permission from John Wiley and Sons, © 2019 Wiley-VCH Verlag GmbH & Co. KGaA, Weinheim.

microdevices into microsystems with two electrical contacts directly on a flexible substrate (see Figure 12.12c).[143] The microfabrication process was realized by combining different microfabrication technologies (photolithography, etching, metal evaporation) and the microsystems were developed by reversing the steps, *i.e.*, fabricating the microactuators first and finally encapsulating them into SU-8 to obtain the flexible support. The resulting process allows the fabrication of microsystems with different configurations and designs, for example, the realization of the actuator-sensor microsystem with two separate pairs of electrical contacts. The resulting microsystems demonstrated a maximum strain of 0.66% and maximum output force of 105 μN under ±3.0 V. Additionally, the mechanical sensing behaviour was demonstrated for the first time for microsystems with integrated electrical contacts, resulting in a maximum output voltage of 0.35 mV at 0.34% strain. In other words, this electromechanical ECP microdevice is to date the closest demonstration of air-operating soft MEMS based on ECPs and theoretically ready for further integration into complex systems.

## 12.5 Conclusions and Perspectives

This chapter depicted the state of the art in the field of conducting polymers as redox materials for the development of soft microelectromechanical systems. This multidisciplinary field gathers polymer and material chemistry, electrochemistry, physics, microfabrication and engineering. While impressive and eye-catching demonstrators have been proposed 20 years ago on ''in-electrolyte'' operation, still suitable for biology-related applications, it took the efforts of numerous groups to push this technology forward and demonstrate it in the open air. Integrated and soft microactuators/microsensors have been finally demonstrated and are now opening promising perspectives for applications in soft electronics and microelectronics. Among others, the development of open-air microgrippers with haptic feedback can now be explored where interfaced microactuators and microsensors acting as finger, wrist and elbow may allow grabbing and ''feeling'' micro-objects. Micropatterned sheets with bumping area can be also envisioned for texturing the surfaces of smart screens (phone, TV, cars) or for the development of soft, light, rollable and refreshable braille displays. Integration of micromuscle to actuate flapping wings or legs also makes the development of a scale-1 microdrone mimicking fly or crawling insects one step closer.

However, several challenges and issues remain. The ''wet'' nature of these materials, requiring the presence of an ionic conducting phase, may cause evaporation and leaking issues. Ionic liquid electrolyte could overcome the evaporation issue, nevertheless the electrolyte leaking can be a major drawback if these devices are to be used for medicinal purposes. A solution could come from the development of ''dry'' ionic devices by the use of polymeric ionic liquids. These materials are a sub-class of polyelectrolyte bearing ionic liquid-type functions along their polymer backbones. They can then bring together the best of both worlds, *i.e.*, ionic conductivity of ionic liquids and mechanical properties of polymers. Unfortunately, to date, their ionic conductivity remains low compared to the corresponding ionic liquids,

and any further improvement is usually at the expense of the mechanical properties, critical for electromechanical applications. Another question, common with all of the new soft organic electronics, is related to the end-of-life. While bio-based and biodegradable membranes and bio-compatible ionic liquids are widely studied nowadays, the possibility to synthesize efficient and (bio-)degradable conducting polymers remains a hurdle. Blending with bio-degradable compounds is of course an identified and studied path, but the development of truly (bio-)degradable conjugated and electrically conducting polymer chains will require the efforts of chemists in the next decade to allow these materials to develop their full potential while respecting the necessary constraints of an environmentally responsible (friendly) world.

## References

1. Y. Bar-Cohen, in *SPIE EAPAD*, San Diego, California, March, 2005.
2. Y. Bar-Cohen, *Electroactive Polymer (EAP) Actuators as Artificial Muscles: Reality, Potential, and Challenges, SPIE – The International Society for Optical Engineering*, 2nd edn, Washington, 2004.
3. R. Pelrine, R. Kornbluh, Q. Pei and J. Joseph, *Science*, 2000, **287**, 836–839.
4. H. S. Nalwa, *Ferroelectic Polymers – Chemistry, Physics and Applications*, Marcel Dekker, Inc., New York, 1995.
5. V. D. Kugel, B. Xu, Q. M. Zhang and L. E. Cross, *Sens. Actuators, A*, 1998, **69**, 234–242.
6. J. Y. Li and N. Rao, *J. Mech. Phys. Solids*, 2004, **52**, 591–615.
7. X. Ji, A. El Haitami, F. Sorba, S. Rosset, G. T. M. Nguyen, C. Plesse, F. Vidal, H. R. Shea and S. Cantin, *Sens. Actuators, B*, 2018, **261**, 135–143.
8. R. H. Baughman, *Makromol. Chem., Mocromol. Symp.*, 1991, **51**, 193–215.
9. Y. Osada and J. Gong, *Prog. Polym. Sci.*, 1993, **18**, 187–226.
10. P. Calvert, J. O'Kelly and C. Souvignier, *Mater. Sci. Eng., C*, 1998, **6**, 167–174.
11. R. H. Baughman, *Synth. Met.*, 1996, **78**, 339–353.
12. E. W. H. Jager, E. Smela and O. Inganäs, *Science*, 2000, **290**, 1540–1545.
13. M. Shahinpoor, Y. Bar-Cohen, O. J. Simpson and J. Smith, *Smart Mater. Struct.*, 1998, **7**, R15.
14. R. H. Baughman, C. Cui, A. A. Zakhidov, Z. Iqbal, J. N. Barisci, G. M. Spinks, G. G. Wallace, A. Mazzoldi, D. De Rossi, A. G. Rinzler, O. Jaschinski, S. Roth and M. Kertesz, *Science*, 1999, **284**, 1340–1344.
15. T. Sugino, K. Kiyohara, I. Takeuchi, K. Mukai and K. Asaka, *Sens. Actuators, B*, 2009, **141**, 179–186.
16. I. Takeuchi, K. Asaka, K. Kiyohara, T. Sugino, N. Terasawa, K. Mukai, T. Fukushima and T. Aida, *Electrochim. Acta*, 2009, **54**, 1762–1768.
17. R. Dash, J. Chmiola, G. Yushin, Y. Gogotsi, G. Laudisio, J. Singer, J. Fischer and S. Kucheyev, *Carbon N. Y.*, 2006, **44**, 2489–2497.
18. J. Torop, M. Arulepp, J. Leis, A. Punning, U. Johanson, V. Palmre and A. Aabloo, *Materials*, 2010, **3**, 9–25.
19. H. Shirakawa, E. J. Louis, S. C. Gau, A. G. MacDiarmid, C. K. Chiang, C. R. Fincher, Y. W. Park and A. J. Heeger, *Phys. Rev. Lett.*, 1977, **39**, 1098–1101.

20. A. J. Heeger, A. G. MacDiarmid and H. Shirakawa, *Nobel Prize Chemistry, 2000 Conductive Polymers*, Royal Swedish Academy of Sciences, Stockholm, Sweden, 2000.
21. A. G. MacDiarmid, *Synth. Met.*, 2002, **125**, 11–22.
22. J. L. Brédas, J. C. Scott, K. Yakushi and G. B. Street, *Phys. Rev. B*, 1984, **30**, 1023–1025.
23. J. L. Brédas and G. B. Street, *Acc. Chem. Res.*, 1985, **18**, 309–315.
24. T. C. Chung, J. H. Kaufman, A. J. Heeger and F. Wudl, *Phys. Rev. B*, 1984, **30**, 702–710.
25. H. Naarmann and N. Theophilou, *Synth. Met.*, 1987, **22**, 1–8.
26. P. N. Adams, P. Devasagayam, S. J. Pomfret, L. Abell and A. P. Monkman, *J. Phys.: Condens. Matter*, 1998, **10**, 8293–8303.
27. Y. Nogami, J. P. Pouget and T. Ishiguro, *Synth. Met.*, 1994, **62**, 257–263.
28. R. D. McCullough, S. P. Williams, R. D. Lowe, M. Jayaraman and S. Tristram-Nagle, *J. Am. Chem. Soc.*, 1993, **115**, 4910–4911.
29. B. Winther-Jensen, D. W. Breiby and K. West, *Synth. Met.*, 2005, **152**, 1–4.
30. M. R. Gandhi, P. Murray, G. M. Spinks and G. G. Wallace, *Synth. Met.*, 1995, **73**, 247–256.
31. Q. Pei and O. Inganäs, *Solid State Ionics*, 1993, **60**, 161–166.
32. T. F. Otero, H. Grande and J. Rodriguez, *J. Phys. Org. Chem.*, 1996, **9**, 381–386.
33. Y. Qiu and J. R. Reynolds, *Polym. Eng. Sci.*, 1991, **31**, 417–421.
34. C. Lopez, M. F. M. Viegas, G. Bidan and E. Vieil, *Synth. Met.*, 1994, **63**, 73–78.
35. Q. Pei and O. Inganäs, *J. Phys. Chem.*, 1992, **96**, 10507–10514.
36. T. Matencio, M. A. De Paoli, R. C. D. Peres, R. M. Torresi and S. I. Cordoba de Torresi, *Synth. Met.*, 1995, **72**, 59–64.
37. R. Temmer, A. Maziz, C. Plesse, A. Aabloo, F. Vidal and T. Tamm, *Smart Mater. Struct.*, 2013, **22**, 1–16.
38. Y. Sonoda, W. Takashima and K. Kaneto, *Synth. Met.*, 2001, **119**, 267–268.
39. B. Qi, W. Lu and B. R. Mattes, *J. Phys. Chem. B*, 2004, **108**, 6222–6227.
40. H. Okuzaki, T. Kondo and T. Kunugi, *Polymer*, 1999, **40**, 995–1000.
41. J. D. W. Madden, PhD thesis Massachusetts Inst. Technol., 2000.
42. A. Elschner, S. Kirchmeyer, W. Lövenich, U. Merker and K. Reuter, *PEDOT – Principles and Applications of an Intrinsically Conductive Polymer*, Taylor & Francis Group, Boca Raton, 2011.
43. R. Temmer, I. Must, F. Kaasik, A. Aabloo and T. Tamm, *Sens. Actuators, B*, 2012, **166–167**, 411–418.
44. F. Vidal, J. F. Popp, C. Chevrot and D. Teyssié, *Smart Struct. Mater. 2002 Electroact. Polym. Actuators Devices*, 2002, **4695**, 95–103.
45. A. Mohammadi, M. A. Hasan, B. Liedberg, I. Lundström and W. R. Salaneck, *Synth. Met.*, 1986, **14**, 189–197.
46. L. Groenendaal, F. Jonas, D. Freitag, H. Pielartzik and J. R. Reynolds, *Adv. Funct. Mater.*, 2000, **12**, 481–494.
47. Y. Wang, C. Zhu, R. Pfattner, H. Yan, L. Jin, S. Chen, F. Molina-Lopez, F. Lissel, J. Liu, N. I. Rabiah, Z. Chen, J. W. Chung, C. Linder, M. F. Toney, B. Murmann and Z. Bao, *Sci. Adv.*, 2017, **3**, 1–10.

48. T. A. Skotheim and J. R. Reynolds, *Conjugated Polymers, Theory, Synthesis, Properties, and Characterization*, 3rd edn, Taylor & Francis Group, Boca Raton, 2007.
49. F. Louwet, L. Groenendaal, J. Dhaen, J. Manca, J. Van Luppen, E. Verdonck and L. Leenders, *Synth. Met.*, 2003, **135–136**, 115–117.
50. N. Kim, S. Kee, S. H. Lee, B. H. Lee, Y. H. Kahng, Y. R. Jo, B. J. Kim and K. Lee, *Adv. Mater.*, 2014, **26**, 2268–2272.
51. Y. Xia, K. Sun and J. Ouyang, *Adv. Mater.*, 2012, **24**, 2436–2440.
52. M. Cai, Z. Ye, T. Xiao, R. Liu, Y. Chen, R. W. Mayer, R. Biswas, K. M. Ho, R. Shinar and J. Shinar, *Adv. Mater.*, 2012, **24**, 4337–4342.
53. Z. Zhao, G. F. Richardson, Q. Meng, S. Zhu, H. C. Kuan and J. Ma, *Nanotechnology*, 2016, **27**, 42001.
54. H. Yan, T. Jo and H. Okuzaki, *Polym. J.*, 2009, **41**, 1028–1029.
55. H. Okuzaki, H. Suzuki and T. Ito, *Synth. Met.*, 2009, **159**, 2233–2236.
56. A. Simaite, B. Tondu, P. Souères and C. Bergaud, *ACS Appl. Mater. Interfaces*, 2015, **7**, 19966–19977.
57. A. Simaite, F. Mesnilgrente, B. Tondu, P. Souères and C. Bergaud, *Sens. Actuators, B*, 2016, **229**, 425–433.
58. I. Põldsalu, K. Rohtlaid, T. Minh, G. Nguyen, C. Plesse, F. Vidal, M. S. Khorram, A. Peikolainen, T. Tamm and R. Kiefer, *Sens. Actuators, B*, 2018, **258**, 1072–1079.
59. J. Huang, P. F. Miller, J. C. De Mello, A. J. De Mello and D. D. C. Bradley, *Synth. Met.*, 2003, **139**, 569–572.
60. A. Moujoud, S. H. Oh, H. S. Shin and H. J. Kim, *Phys. Status Solidi Appl. Mater. Sci.*, 2010, **207**, 1704–1707.
61. J. Y. Kim, J. H. Jung, D. E. Lee and J. Joo, *Synth. Met.*, 2002, **126**, 311–316.
62. C. Badre, L. Marquant, A. M. Alsayed and L. A. Hough, *Adv. Funct. Mater.*, 2012, **22**, 2723–2727.
63. B. Fan, X. Mei and J. Ouyang, *Macromolecules*, 2008, **41**, 5971–5973.
64. Y. Xia and J. Ouyang, *Org. Electron. physics, Mater. Appl.*, 2010, **11**, 1129–1135.
65. Y. Xia, H. Zhang and J. Ouyang, *J. Mater. Chem.*, 2010, **20**, 9740.
66. Y. Xia and J. Ouyang, *ACS Appl. Mater. Interfaces*, 2010, **2**, 474–483.
67. E. Dauzon, A. E. Mansour, M. R. Niazi, R. Munir, D. M. Smilgies, X. Sallenave, C. Plesse, F. Goubard and A. Amassian, *ACS Appl. Mater. Interfaces*, 2019, **11**, 17570–17582.
68. R. H. Baughman, L. W. Shacklette, R. L. Elsenbaumer, E. Plichta and C. Becht, *Conducting Polymer Electromechanical Actuators*, Kluwer Academic Publishers, Dordrecht, 1990.
69. P. Chiarelli, D. De Rossi, A. Della Santa and A. Mazzoldi, *Polym. Gels Networks*, 1994, **2**, 289–297.
70. M. Kaneko, M. Fukui, W. Takashima and K. Kaneto, *Synth. Met.*, 1997, **84**, 795–796.
71. E. Smela, O. Inganäs, Q. Pei and I. Lundström, *Adv. Mater.*, 1993, **5**, 630–632.

72. E. W. H. Jager, O. Inganäs and I. Lundström, *Science*, 2000, **288**, 2335–2338.
73. T. F. Otero and J. Rodríguez, *Intrinsically Conducting Polymers: An Emerging Technology*, 1992.
74. S. J. Higgins, K. V. Lovell, R. M. Gamini Rajapakse and N. M. Walsby, *J. Mater. Chem.*, 2003, **13**, 2485.
75. S. D. Deshpande, J. Kim and S. R. Yun, *Synth. Met.*, 2005, **149**, 53–58.
76. S. D. Deshpande, J. Kim and S. R. Yun, *Smart Mater. Struct.*, 2005, **14**, 876–880.
77. G. Alici, A. Punning and H. R. Shea, *Sens. Actuators, B*, 2011, **151**, 72–84.
78. T. F. Otero, E. Angulo, J. Rodríguez and C. Santamaría, *J. Electroanal. Chem.*, 1992, **341**, 369–375.
79. Q. Pei and O. Inganas, *Adv. Mater.*, 1992, **4**, 227–278.
80. T. F. Otero, J. M. Sansinena and J. M. Sansiñena, *Bioelectrochem. Bioenerg.*, 1995, **38**, 411–414.
81. M. Kaneko and K. Kaneto, *React. Funct. Polym.*, 1998, **37**, 155–161.
82. E. Smela, O. Inganäs and I. Lundström, *Science*, 1995, **268**, 1735–1738.
83. E. Smela, *J. Micromech. Microeng.*, 1999, **9**, 1–18.
84. M. Fuchiwaki and T. F. Otero, *J. Mater. Chem. B*, 2014, **2**, 1954–1965.
85. T. F. Otero and J. G. Martinez, *Sens. Actuators, B*, 2014, **199**, 27–30.
86. Q. Pei, O. Inganäs, G. Gustafsson and M. Granström, *Synth. Met.*, 1993, **55**, 1221–1226.
87. J. M. Sansinena, V. Olazabal, T. F. Otero, C. N. Polo da Fonseca and M. A. De Paoli, *Chem. Commun.*, 1997, **22**, 2217–2218.
88. T. W. Lewis, L. A. P. Kane-Maguire, A. S. Hutchison, G. M. Spinks and G. G. Wallace, *Synth. Met.*, 1999, **102**, 1317–1318.
89. W. Lu, A. G. Fadeev, B. Qi, E. Smela, B. R. Mattes, J. Ding, G. M. Spinks, J. Mazurkiewicz, D. Zhou, G. G. Wallace, D. R. MacFarlane, S. A. Forsyth and M. Forsyth, *Science*, 2002, **297**, 983–987.
90. D. Zhou, G. M. Spinks, G. G. Wallace, C. Tiyapiboonchaiya, D. R. MacFarlane, M. Forsyth and J. Sun, *Electrochim. Acta*, 2003, **48**, 2355–2359.
91. F. Vidal, J. F. Popp, C. Plesse, C. Chevrot and D. Teyssié, *J. Appl. Polym. Sci.*, 2003, **90**, 3569–3577.
92. M. Khayet and T. Matsuura, *Ind. Eng. Chem. Res.*, 2001, **40**, 5710–5718.
93. X. Wang, C. Xiao, H. Liu, Q. Huang and H. Fu, *J. Appl. Polym. Sci.*, 2018, **135**, 46711.
94. M. Qtaishat, T. Matsuura, B. Kruczek and M. Khayet, *Desalination*, 2008, **219**, 272–292.
95. G. Li, Z. Li, P. Zhang, H. Zhang and Y. Wu, *Pure Appl. Chem.*, 2008, **80**, 2553–2563.
96. X. Tang, R. Muchakayala, S. Song, Z. Zhang and A. R. Polu, *J. Ind. Eng. Chem.*, 2016, **37**, 67–74.
97. M. S. Cho, H. J. Seo, J. D. Nam, H. R. Choi, J. C. Koo, K. G. Song and Y. Lee, *Sens. Actuators, B*, 2006, **119**, 621–624.
98. M. S. Cho, H. J. Seo, J. D. Nam, H. R. Choi, J. C. Koo and Y. Lee, *Smart Mater. Struct.*, 2007, **16**, S237.

99. H. J. Choi, Y. M. Song, I. Chung, K. S. Ryu and N. J. Jo, *Smart Mater. Struct.*, 2009, **18**, 1–6.
100. Y. Li, R. Tanigawa and H. Okuzaki, *Smart Mater. Struct.*, 2014, **23**, 1–8.
101. H. Okuzaki, S. Takagi, F. Hishiki and R. Tanigawa, *Sens. Actuators, B*, 2014, **194**, 59–63.
102. L. H. Sperling, *Adv. Chem.*, 1994, **239**, 3–38.
103. A. D. Jenkins, P. Kratochvíl, R. F. T. Stepto and U. W. Suter, *Pure Appl. Chem.*, 1996, **68**, 2287–2311.
104. C. Plesse, F. Vidal, C. Gauthier, J. M. Pelletier, C. Chevrot and D. Teyssié, *Polymer*, 2007, **48**, 696–703.
105. C. Gauthier, C. Plesse, F. Vidal, J. M. Pelletier, C. Chevrot and D. Teyssié, *Polymer*, 2007, **48**, 7476–7483.
106. C. Plesse, A. Khaldi, Q. Wang, E. Cattan, D. Teyssié, C. Chevrot and F. Vidal, *Smart Mater. Struct.*, 2011, **20**, 1–8.
107. N. Festin, C. Plesse, P. Pirim, C. Chevrot and F. Vidal, *Sens. Actuators, B*, 2014, **193**, 82–88.
108. N. Festin, A. Maziz, C. Plesse, D. Teyssié, C. Chevrot and F. Vidal, *Smart Mater. Struct.*, 2013, **22**, 104005.
109. K. Kaneto, M. Kaneko, Y. Min and A. G. MacDiarmid, *Synth. Met.*, 1995, **71**, 2211–2212.
110. P. Bonhôte, A.-P. Dias, N. Papageorgiou, K. Kalyanasundaram and M. Grätzel, *Inorg. Chem.*, 1996, **35**, 1168–1178.
111. M. Galiński, A. Lewandowski and I. Stepniak, *Electrochim. Acta*, 2006, **51**, 5567–5580.
112. J. Ding, D. Zhou, G. Spinks, G. Wallace, S. Forsyth, M. Forsyth and D. MacFarlane, *Chem. Mater.*, 2003, **15**, 2392–2398.
113. F. Vidal, C. Plesse, D. Teyssié and C. Chevrot, *Synth. Met.*, 2004, **142**, 287–291.
114. B. Gaihre, G. Alici, G. M. Spinks and J. M. Cairney, *Sens. Actuators, B*, 2011, **155**, 810–816.
115. F. Vidal, C. Plesse, H. Randriamahazaka, D. Teyssie and C. Chevrot, *Mol. Cryst. Liq. Cryst.*, 2006, **448**, 95–102.
116. H. Randriamahazaka, C. Plesse, F. Vidal, C. Gauthier, C. Chevrot and D. Teyssie, *Smart Structures and Materials 2004: Electroactive Polymer Actuators and Devices*, 2004, **vol. 5385**, 294–301.
117. C. Plesse, F. Vidal, D. Teyssie and C. Chevrot, *Adv. Sci. Technol.*, 2008, **61**, 53–58.
118. A. Fannir, R. Temmer, G. T. M. Nguyen, L. Cadiergues, E. Laurent, J. D. W. Madden, F. Vidal and C. Plesse, *Adv. Mater. Technol.*, 2018, **1800519**, 1–8.
119. V. Woehling, G. T. M. Nguyen, C. Plesse, S. Cantin, J. D. W. Madden and F. Vidal, *Sens. Actuators, B*, 2018, **256**, 294–303.
120. R. H. Baughman, L. W. Shacklette, R. L. Elsenbaumer, E. J. Plichta and C. Becht, *Micro Electromechanical Actuators Based on Conducting Polymers*, Springer, Dordrecht, 1991.
121. E. Smela, M. Kallenbach and J. Holdenried, *J. Microelectromech. Syst.*, 1999, **8**, 373–383.

122. S. A. Wilson, R. P. J. Jourdain, Q. Zhang, R. A. Dorey, C. R. Bowen, M. Willander, Q. U. Wahab, M. Willander, S. M. Al-hilli, O. Nur, E. Quandt, C. Johansson, E. Pagounis, M. Kohl, J. Matovic, B. Samel, W. van der Wijngaart, E. W. H. Jager, D. Carlsson, Z. Djinovic, M. Wegener, C. Moldovan, E. Abad, M. Wendlandt, C. Rusu and K. Persson, *Mater. Sci. Eng. R Reports*, 2007, **56**, 1–129.
123. E. W. H. Jager, E. Smela and O. Inganäs, *Sens. Actuators, B*, 1999, **56**, 73–78.
124. P. F. Pettersson, E. W. H. Jager and O. Inganas, *1st Annu. Int. IEEE-EMBS Spec. Top. Conf. Microtechnologies Med. Biol. Proc.* (Cat. No.00EX451), 2000, **56**, 1999–2000.
125. E. W. H. Jager, C. Immerstrand, K. H. Peterson, K. E. Magnusson, I. Lundström and O. Inganäs, *Biomed. Microdevices*, 2002, **4**, 177–187.
126. C. Immerstrand, E. W. H. Jager, K.-E. Magnusson, T. Sundqvist, I. Lundström, O. Inganas and K. H. Peterson, *Med. Biol. Eng. Comput.*, 2003, **41**, 357–364.
127. S. Taccola, F. Greco, B. Mazzolai, V. Mattoli and E. W. H. Jager, *J. Micromech. Microeng.*, 2013, **23**, 117004.
128. G. Alici and M. J. Higgins, *Smart Mater. Struct.*, 2009, **18**, 065013.
129. B. Gaihre, G. Alici, G. M. Spinks and J. M. Cairney, *Sens. Actuators, A*, 2010, **165**, 321–328.
130. B. Gaihre, G. Alici, G. M. Spinks and J. M. Cairney, *J. Microelectromech. Syst.*, 2012, **21**, 574–585.
131. E. W. H. Jager, N. Masurkar, N. F. Nworah, B. Gaihre, G. Alici and G. M. Spinks, *Sens. Actuators, B*, 2013, **183**, 283–289.
132. A. Khaldi, C. Plesse, C. Soyer, E. Cattan, F. Vidal, C. Legrand and D. Teyssié, *Appl. Phys. Lett.*, 2011, **98**, 164101.
133. A. Khaldi, C. Plesse, C. Soyer, C. Chevrot, D. Teyssié, F. Vidal and E. Cattan, *Proc. SPIE - Smart Mater. Struct.*, 2012, **8340**, 83400J–1-83400J–9.
134. A. Khaldi, C. Plesse, C. Soyer, E. Cattan, F. Vidal, C. Chevrot and D. Teyssié, *Proc. ASME 2011 Int. Mech. Eng. Congr. Expo.*, 2011, **1**, 1–3.
135. A. Maziz, C. Plesse, C. Soyer, C. Chevrot, D. Teyssié, E. Cattan and F. Vidal, *Adv. Funct. Mater.*, 2014, **24**, 4851–4859.
136. A. Maziz, C. Plesse, C. Soyer, E. Cattan and F. Vidal, *Proc. SPIE*, 2015, **9430**, 1–8.
137. A. Khaldi, D. Falk, K. Bengtsson, A. Maziz, D. Filippini, N. D. Robinson and E. W. H. Jager, *ACS Appl. Mater. Interfaces*, 2018, **10**, 14978–14985.
138. A. Khaldi, A. Maziz, G. Alici, G. M. Spinks and E. W. H. Jager, *SPIE Smart Struct. Mater. Nondestruct. Eval. Heal. Monit.*, 2015, **9430**, 94301R.
139. A. Khaldi, A. Maziz, G. Alici, G. M. Spinks and E. W. H. Jager, *Sens. Actuators, B*, 2016, **230**, 818–824.
140. A. Maziz, C. Plesse, C. Soyer, E. Cattan and F. Vidal, *ACS Appl. Mater. Interfaces*, 2016, **8**, 1559–1564.
141. Y. Zhong, S. Lundemo and E. W. H. Jager, *Smat Mater. Struct.*, 2018, **27**, 1–7.
142. K. Rohtlaid, G. T. M. Nguyen, C. Soyer, E. Cattan, F. Vidal and C. Plesse, *Adv. Electron. Mater.*, 2019, **5**, 1–11.
143. K. Rohtlaid, *PhD thesis Univ. Paris-Seine*, 2019.

CHAPTER 13

# *Polymers/PEDOT Derivatives for Bioelectronics*

MARY J. DONAHUE,*[a,b] CHRISTOPHER M. PROCTOR[c] AND XENOFON STRAKOSAS[a]

[a] Laboratory of Organic Electronics, Linköping University, 60174 Norrköping, Sweden; [b] Department of Physical Chemistry and Materials Science, Interdisciplinary Excellence Centre, University of Szeged, Rerrich Square 1, Szeged H-6720, Hungary; [c] University of Cambridge, Dept. of Eng., Electrical Eng. Division, 9 JJ Thomson Avenue, Cambridge CB3 0FA, UK
*Email: maryjdonahue@gmail.com

## 13.1 Introduction

The evolution of polymer materials over the past few decades has brought significant advancement to next-generation organic electronic devices. These devices range from consumer electronics such as flexible displays for cell phones, tablets, and large area displays, to optoelectronic applications like solar cells and light-emitting diodes, to bioelectronic devices with the potential to improve the quality of medical care. In this chapter, we look specifically into the field of bioelectronics and the ongoing development that has been made possible through the use of redox polymers. The field of organic bioelectronics demands a different set of requirements when compared to traditional solid-state electronic devices. Although some overlap of these ''special requirements'' exists with other domains, in particular with flexible optoelectronics or photovoltaic systems, direct contact with biological tissue presents specific complications. When dealing with

Polymer Chemistry Series No. 34
Redox Polymers for Energy and Nanomedicine
Edited by Nerea Casado and David Mecerreyes

Published by the Royal Society of Chemistry, www.rsc.org

bioelectronic interfaces, various combinations of the following attributes are essential:

- **Biocompatibility**—To avoid damage or death of biological cells/tissue, nontoxic materials must be employed.
- **Flexibility**—To reduce invasiveness and mitigate biological effects such as the foreign body response.
- **Conformability**—To reduce invasiveness and improve close physical proximity of electronic/biological interfaces.
- **Stretchability**—Particularly important for artificial muscle, soft robotics and wearable or skin-mounted devices. Stretchability is needed to follow the natural movement of biological systems
- **Long-term stability**—Depending on the desired application, stability in the range of hours up to decades may be required. Long-term medical implants such as pacemakers, cochlear implants and deep-brain stimulators demand many years of functionality.

Redox/conducting polymers demonstrate great potential for bioelectronic applications as they are inherently more flexible and conformable than traditional metals and materials used from the silicon-based electronics industry. In addition, polymers may be tuned or modified through a variety of methods to attain the desired material properties for a given application. This material tuning begins with the conditions of the polymerization process used to create the polymers. In the previous chapter, polymerization processes are discussed in detail, however here a short description of the methods most often utilized for bioelectronic applications is given as well. These processes include electrochemical polymerization, chemical oxidative polymerization and vapor phase polymerization or chemical vapor deposition.

In general, and detailed in other chapters here, various classifications exist for redox polymers.[1] Oxidation or reduction of redox polymers may take place in a redox-active side group, but also on the conjugated backbone of conductive polymers. With the use of this definition, *intrinsically conductive polymers* (CPs) may be categorized under the main classification of redox polymers. It should be noted that *extrinsically* conducting polymers are a separate category, in which conductive materials are incorporated into a nonconductive polymer matrix. In this chapter we discuss only redox polymers, and for the most part CPs, as bioelectronic applications to date have predominantly employed conjugated CP systems. Section 13.2 will investigate biological recording and stimulation devices, Section 13.3 will focus on biosensors, and Section 13.4 explores drug-delivery systems.

Before looking into the polymerization methods, the concept of doping is introduced as this is important for conjugated conducting polymer systems. This doping differs from the atomic doping of traditional inorganic semiconductor materials.[2,3] Doping of CP films occurs when a counterion, or ''dopant,'' is introduced into the polymer during the oxidation or reduction process, thus balancing the electronic charge of the positive or negative charge

carries induced on the conjugated backbone. The discovery of CPs in 1977 depended on this concept, where halogen vapor doping of polyacetylene films after polymerization dramatically increased the conductivity.[4] For the processes discussed here, doping typically takes place during the polymerization process, however ''secondary dopants'' or additives may also be employed during or post-polymerization, affecting the final film properties. The dopant is an anion in the case of oxidative processes for p-type polymers, or a cation for reductive polymerization of n-type materials. Oxidative polymerization is far more common due to instability issues of n-type polymers, a result of radical anions which form during the process. These are readily oxidized when exposed to air or other oxidizing atmospheres and are therefore highly unstable under standard conditions.[5] The most often employed CPs in the field of bioelectronics are polypyrole (PPy), polyaniline (PAni) and polythiophene, or EDOT-based derivatives (see Figure 13.1a). Stability issues, in particular those due to overoxidation in biologically relevant environments, have pushed the focus to polythiophenes, which provide a higher level of stability regarding irreversible overoxidation. Among this family of polymers, PEDOT-based materials and in particular the commercially available poly(3,4-ethylenedioxythiophene) doped with poly(styrenesulfonate) (PEDOT:PSS) have received an enormous amount of attention. In all conducting polymer classes, the utilized counterion(s), process parameters, pre- and/or post-treatments, and polymerization method all have significant impact on the resulting film.[6] Some examples will be provided in the following descriptions of polymerization processes.

### 13.1.1 Electrochemical Polymerization

Electrochemical polymerization is carried out through the anodic oxidation or cathodic reduction of a monomer at a conductive substrate. In general, electrochemical oxidation of aromatic heterocyclic compounds is the preferred and most common route for this polymerization method. This is a result of the previously mentioned instability of n-type polymers. The electrochemical process is often carried out in a three-electrode set-up and requires a conductive substrate to apply the desired electrical signal in order to induce charge transfer and polymerization (see Figure 13.2b, top). This polymerization occurs at the working electrode, with a reference electrode and counter electrode also present in the electrolyte to set the potential and provide a pathway for current flow, respectively. Typical electrochemical processes used for this polymerization include potentiostatic, galvanostatic, or pulsed deposition, or cyclic voltammetry (CV). Signal parameter variations in each of these deposition techniques may also be made, such as the scan speed or deposition charge density. The various methods or parameters, as well as the counterion and other molecules present in the reaction solution, affect the mechanical, electrical and electrochemical properties of the resulting polymer. An example of this may be visually observed in Figure 13.1b (bottom), where the surface morphology significantly varies as a result of

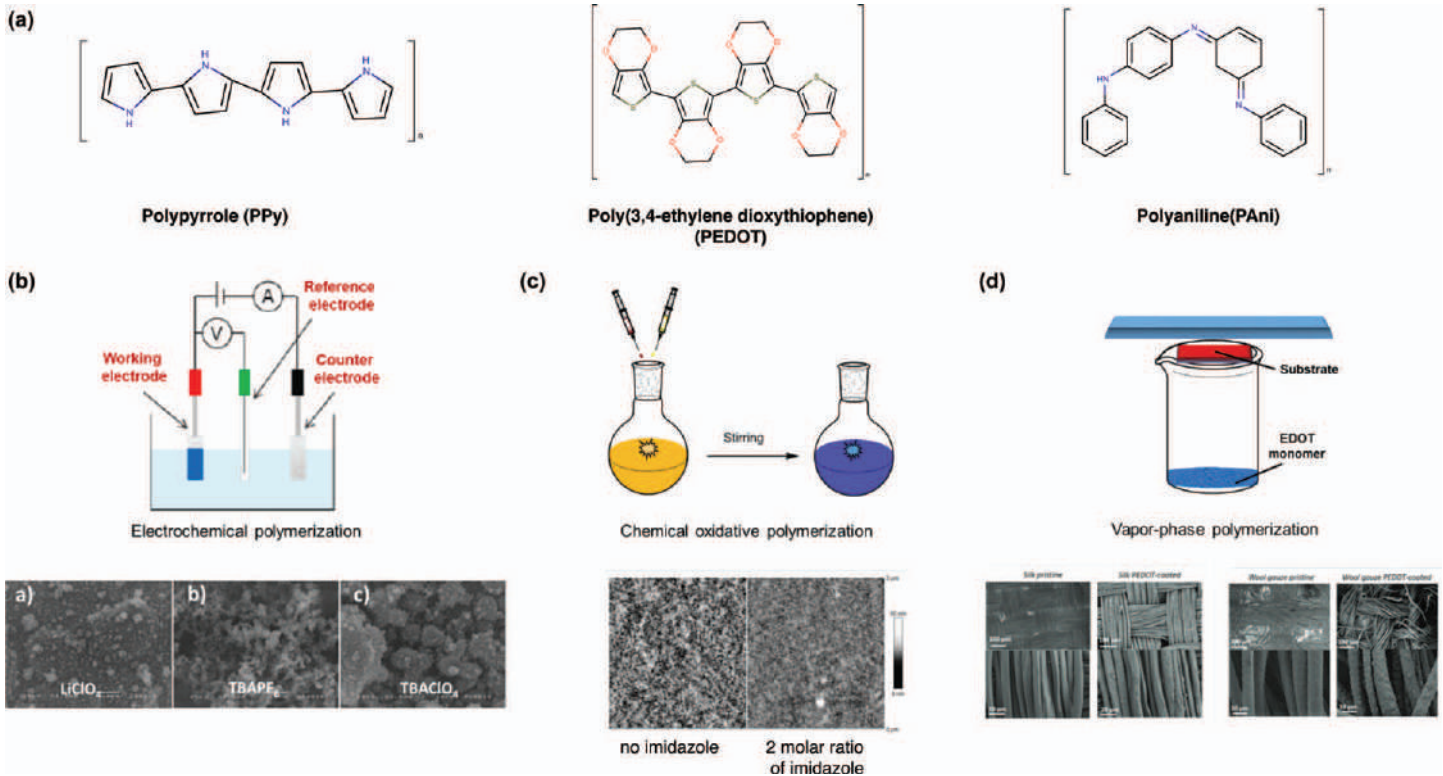


**Figure 13.1** (a) Commonly used conducting polymers in bioelectronic applications. Polymerization methods to obtain conducting polymer films: (b) Electrochemical polymerization with examples of surface morphology differences as a result of cation or counteranion variation. (c) Chemical polymerization with film variation examples resulting from the use of an alkaline reaction rate inhibitor. (d) Vapor-phase polymerization with examples of deposition on complex substrates such as silk and wool. Adapted from ref. 6 with permission from Elsevier, Copyright 2020. Adapted from ref. 7 with permission from Springer, Copyright 2009. Adapted from ref. 8 with permission from John Wiley and Sons, © 2004 Wiley-VCH Verlag GmbH & Co. KGaA, Weinheim. Adapted from ref. 9 with permission from John Wiley and Sons, © 2017 Wiley-VCH Verlag GmbH & Co. KGaA, Weinheim.

differing ions. Overall electrochemical polymerization facilitates a wide range of counterion possibilities and is a useful technique when use of a conductive substrate is possible and large numbers of electrodes or devices (*i.e.*, mass production) are not needed.

### 13.1.2 Chemical Oxidative Polymerization

Chemical oxidative polymerization (Figure 13.1c) makes use of a chemical oxidizing agent to induce polymerization. This is different from electrochemical polymerization, where oxidation or reduction of the monomer is caused by the application of a current or potential. Although the chemical oxidative process also allows for the use of a wide variety of counterions, those practically employed are fewer in number when compared to electrochemical polymerization. This is because the role of the oxidizing agent is typically played by the salt providing the charge-balancing counterion for the polymer complex. The most often employed and studied oxidizing agents to date are iron(III) chloride ($FeCl_3$) and iron(III) tosylate, and ammonium persulfates. A great benefit of chemical polymerization is the solution preparation and consequent possibility of film deposition on a variety of substrates through standard fabrication methods such as spin-coating, printing, dip-coating or drop-casting. This method additionally facilitates large-scale processing when relevant. Finally, tailoring and optimizing the resulting films for the intended application are straightforward with a large parameter space available for variation. These parameters include solution concentrations, counterions, processing conditions, as well as additives that may be easily added to the solution mixture. Figure 13.1c (bottom) shows examples of surface morphology variation resulting from the addition of an alkaline reaction rate-inhibitor (imidazole) during polymerization of EDOT using iron(III) toulenesulfonate [$Fe(OTs)_3$–Tos].

### 13.1.3 Vapor-phase Polymerization/Chemical Vapor Deposition

Vapor-phase polymerization (VPP) and chemical vapor deposition (CVD) (Figure 13.1d) are subgroups of chemical oxidative polymerization as the polymerization process is also induced chemically, using an oxidizing agent. In this case, the process is carried out in what is often called a ''dry'' or solvent-less deposition. This is a special advantage for insulating and/or complex surfaces, such as the wool and silk fibers shown in Figure 13.1d (bottom). The chemical oxidizing agent in the case of VPP is applied to the substrate surface (requiring chemical compatibility and wettability) and the vapor-phase deposition of the monomer is typically carried out using rather simple equipment, without strict vacuum requirements. For the CVD process, the oxidizing agent is brought into the chamber as a vapor during the deposition process and requires higher vacuum levels. Under ideal

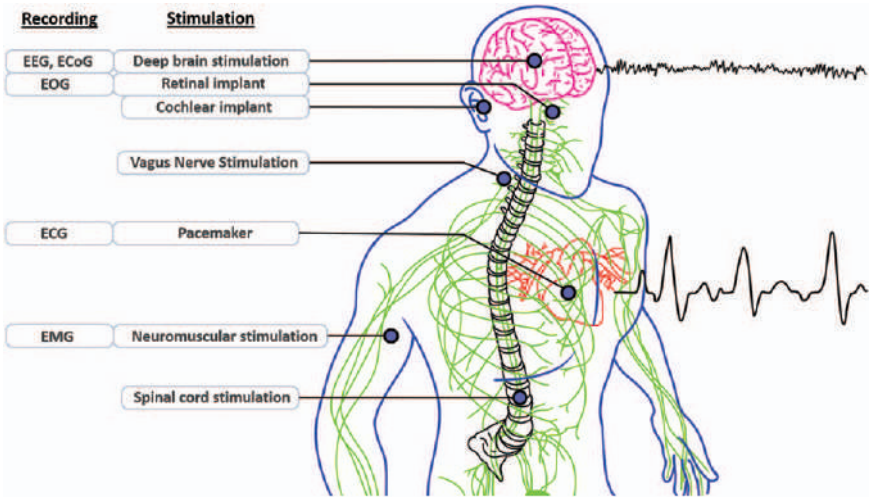


**Figure 13.2** Clinical recording (listed on the left) and stimulation (right) technologies. Example interfacing regions of the human body are shown, along with cardiac and brain wave signals.

conditions a careful layer-by-layer deposition of the polymer occurs, providing a high level of crystallinity. This has resulted in the highest conductivity attained for CPs.

Overall, each polymerization method possesses advantages and disadvantages, some extremely application dependent. For example, nonconductive wearable devices necessitate the use of chemical oxidative techniques to allow drop casting, dip-coating or vapor phase/chemical vapor techniques. In other cases, electrodeposition is extremely useful for small-dimension conductive areas, where other fabrication procedures may be difficult or impossible. In general, a high degree of adjustability is available when it is desired to fine-tune the mechanical and electrical properties. The following sections will introduce bioelectronic technologies making use of polymer systems and their tunability.

## 13.2 Polymers for Biological Recording and Stimulation

The physiological state of a biological system may be monitored through a variety of methods, including measurement of the electrical activity of an organ, tissue or single cells. Depending on the signal shape, frequency and magnitude, conclusions may be made as to the state of the biological system. The biomedical field dedicated to monitoring and understanding electrical phenomena of biological systems is called *electrophysiology*. Examples of electrophysiological signal measurement include monitoring the cardiac cycle (electrocardiography, ECG), electrical signals from skeletal muscle (electromyography, EMG), eye movement (electrooculography, EOG), or

neurological rhythms (electroencephalography, EEG; electrocorticogram, ECoG). In order to carry out electrophysiological measurements, a variety of devices and materials are employed. Some example signals and recording or stimulation methods are given in Figure 13.2. The devices employed in these techniques, as well as most of those historically used for electrophysiology recordings, utilize electrodes or arrays of electrodes to capture the biological signals. These recording electrodes should ideally provide an *intimate electronic/biological interface*, measure the desired signal with the *highest possible signal-to-noise ratio (SNR)*, and with sufficient *sampling rates*. Considering that biological signals range from approximately 0.5 Hz up to 1 kHz, sampling rates of greater than 10 kS $s^{-1}$ may be necessary. This primarily sets the requirements of the complementary back-side electronics used for signal acquisition and data storage needs, however the recording device must also be capable of resolving such frequencies (mainly a concern for transistors).

Regarding the SNR, and noise in general, an assortment of factors must be considered. The electronic noise and interference of the environment (50–60 Hz of electrical mains, electronic noise of nearby machines, *etc.*) may be reduced through the use of Faraday cages, proper grounding and filtering. These techniques, in addition to engineering considerations such as materials and device designs, aid in improving the SNR of the acquired signal. The bioelectronic interface is also of extreme importance for this matter. This has to do with the proximity of the recording device to the electrophysiological signal, transduction of the ionic fluctuations to electronic signals and the issue of invasiveness. Traditionally used hard/stiff materials, or those with poor biocompatibility, will cause tissue damage, inflammation, scarring and/or rejection of the device. Tissue inflammation or scarring creates a physical, insulating distance between the signal source and recording device, thus reducing signal amplitude and SNR (addressed in the following and in Figure 13.3). The case of negative biological reactions and potential implanted biomedical device rejection is known as the *foreign body response*. This must be avoided or limited as much as possible to improve/maintain sensitive recordings. Reducing invasiveness and improving the physical proximity to the signal source as well as the transduction of this signal, are largely engineering questions. The field of research dedicated to improving the materials, devices and measurement/stimulation techniques for this biological interaction is growing at a rapid rate. Within this field, redox/conducting polymers have shown a great deal of promise, in particular regarding:

- *Electronic/biological interfaces*
- *Recording signal quality*
- *Stimulation efficiency*

The last member of this list, stimulation efficiency, concerns active interaction with cells or organs, whereas most of the discussion so far has alluded to biological recording applications. While the recording devices ideally obtain high-quality signals with minimal influence on the biological

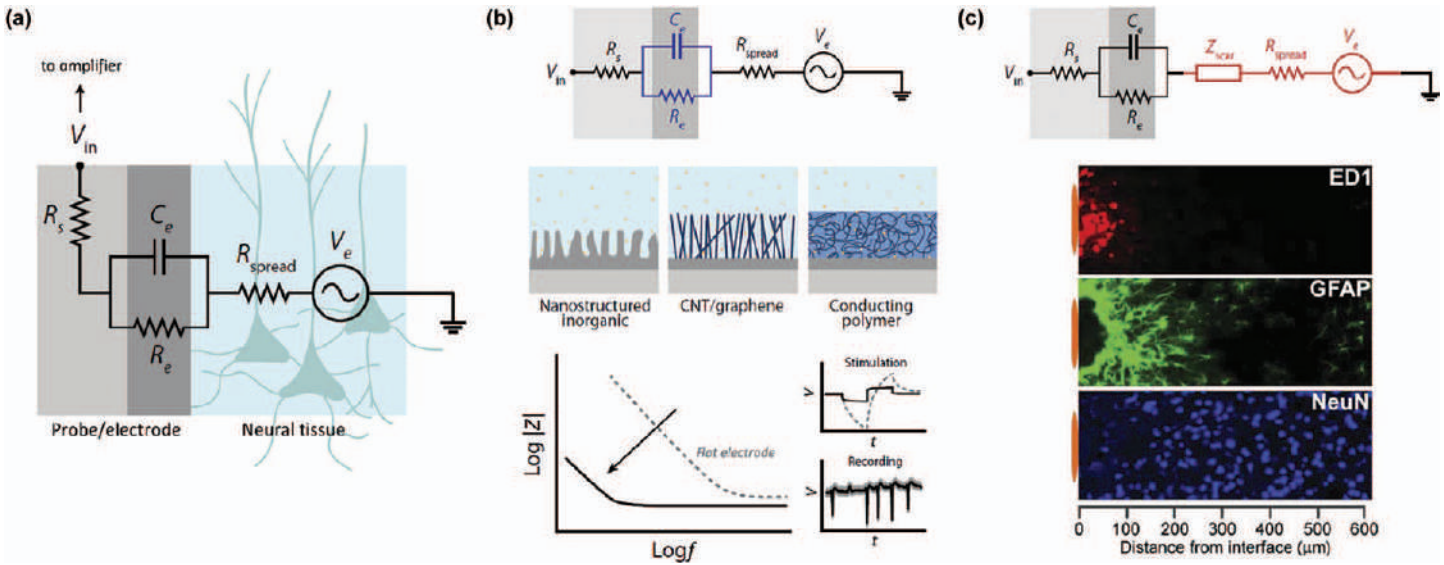


**Figure 13.3** Electrochemical interface between biology and electronics. (a) Equivalent circuit model elements describing the overall electrochemical circuit. (b) Possibilities to improve electrode performance through surface modifications, the affected part of the electrochemical circuit model is highlighted in blue. The associated reduction in the EIS curve, lower voltage transients and improved SNR are illustrated (bold curves represent example measurements with modified electrodes *versus* unmodified represented by gray dashed curves). (c) Neural tissue staining to portray the effects of an implanted probe, with inflammatory cells (ED1), astrocyte development (GFAP) and physically distanced neurons (NeuN). The influenced part of the electrochemical circuit model is highlighted in red.
Adapted from ref. 14, http://dx.doi.org/10.1126/sciadv.1601649, under the terms of the CC BY 4.0 license, https://creativecommons.org/licenses/by/4.0/.

system, the goal of stimulation devices is to efficiently elicit a specific response in the cell(s) or organ of interest. Well-known examples include the cardiac pacemaker, deep-brain stimulation (DBS) electrodes, cochlear implants, vagus nerve stimulation and retinal implants. This area of applications also benefits greatly from materials, devices and measurement techniques that allow for close bioelectronic interfaces and efficient transduction between electrical and ionic signals.

The concepts introduced here will be further explained in this section, with literature sources provided as well for further information and detail. Overall, the use of polymers to advance biological interfacing for recording and stimulation will be covered, as well as their role in the improvements that have or continue to be made.

### 13.2.1 Biological Interfaces

The significance of the bioelectronic interface has already been emphasized and is important from several points of view. Included in this list are the following:

- Mechanical material characteristics
  - Hard or stiff materials cause discomfort or irritation when considering skin-mounted or wearable electronics, whereas ''soft'' flexible or elastic materials enable unobtrusive interfaces.
  - In the case of implantable devices, normal human movement and the soft nature of biological tissue are not compatible with rigid structures. Tissue is displaced by such materials and may be physically compacted,[10] inflamed, and may develop scar tissue through protective mechanisms.
- Invasiveness/physical proximity to the area of interest
  - Electrophysiological signal fluctuations are attenuated as they pass through biological tissue and fluids. Proximity to the signal source therefore improves the ability to detect these fluctuations.
  - To stimulate cells or tissue, close physical contact of the stimulation electrode greatly enhances spatial accuracy and reduces the voltage levels needed (further discussed in the following). These factors are related to the above-mentioned signal attenuation as well as current spread in the tissue.
  - The previous points on mechanical compliancy go hand-in-hand with this topic as well. Softer, less invasive materials/devices prevent biological reactions (*i.e.*, inflammation, scar tissue) that create physical space between the cells and electronic device.
- Electrochemical transduction
  - Bidirectional (ionic-to-electronic and *vice versa*) signal transduction is extremely important for bioelectronic device performance. Biological conduction and current fluxes are primarily ionic, while electronic conduction takes place as a result of negative and positive

charge carriers (electrons and holes). Efficient transduction between these two conduction mechanisms is of great importance.

The first two concepts may be relatively well-understood already by the short descriptions given. Redox/conducting polymers have a great deal to offer regarding these topics as a result of their inherent soft nature and flexibility, conformability or stretchability. Material softness may be quantified by the Young's modulus, one of the elastic moduli used to characterize materials. Whereas the Young's moduli of biological tissue ranges from ~1 kPa (*i.e.*, fat, bone marrow, brain tissue) up to ~1 MPa (cartilage) or 15–20 MPa (cancellous bone), the moduli of silicon or noble metals are on the order of ~100 GPa or greater. This large mismatch between the materials and biological tissue contributes to the issues of adverse biological reactions to biomedical devices (*i.e.*, inflammation, scarring) and the resulting reduced bidirectional signal transduction efficiency. Great advancement has been made regarding this issue by using polymer-based materials to reduce this elastic modulus, in some cases approaching the tens of kPa range, similar to that of soft tissue types. The tunability of these systems through chemical and engineering approaches, and the resulting advancements in application-based bioelectronic studies will be further discussed in the following section.

The final concept in the previous list, the electrochemical signal transduction, is a more complex topic that will be briefly introduced here. Electrical resistance is a commonly known concept, involving the resistance of a circuit to current flow.[11,12] Electrical *impedance* expands on this idea to include nonideal circuit elements and support the understanding and modeling of real-world systems. The concept of *electrochemical impedance* further expands these possibilities through the inclusion of chemical influences. Measurement of the electrochemical impedance of a system provides a way to understand interactions between electronic and ionic environments. This measurement is often carried out by electrochemical impedance spectroscopy (EIS), an important tool for the analysis and comparison of materials and devices for bioelectronic applications.

#### *13.2.1.1 Electrochemical Impedance*

A good introduction to this concept may be found in *Gambry Basics of Electrochemical Spectroscopy*[11] or the classic electrochemistry textbook by Allen Bard *et al. Electrochemical methods: fundamentals and applications.*[12] The electrochemical impedance of an electrode interface gives an indication of how effectively the ionic to electronic transduction process is carried out. A low electrochemical impedance is desired for biological recording and stimulation applications.[13] As is demonstrated in Figure 13.3a, rather simple equivalent circuit elements may be employed to model the overall electrochemical circuit of the bioelectronic interface. When dealing with real systems, which may have material imperfections or limitations as a result of

(for example) diffusion within the electrolyte, other more complicated circuit elements may be needed to find a correct model. In the illustrated example case, however, a simple resistor ($R_{spread}$) represents the solution resistance of the extracellular space, while a parallel resistor and capacitor ($R_e$, $C_e$) represent the electrode interface. The remaining $R_s$ circuit element here results from additional resistances, such as conductive lines which then lead to the ''back-side'' electronics, *i.e.*, amplifiers (transimpedance, feedback, *etc.*) of the recording system.

The $R_{spread}/(R_e \| C_e)$ circuit is important for characterization and analysis of electrodes or devices. Determining these values allows one to compare electrode materials or structuring methods and judge the expected performance. The desired low electrochemical impedance translates to a high capacitance when considering the proportionality between the two:

$$Z_C = 1/j\omega C$$

As a result of the size dependence:

$$C = \varepsilon_0 \varepsilon_r A/d$$

larger electrode areas result in lower electrochemical impedance. While in some applications large electrodes may be acceptable, in other cases high spatial resolution and reduced invasiveness are crucial. This is the case for most implantable recording and stimulation devices, where electrode miniaturization and the smallest possible overall device size are desired. Small electrode performance, however, may suffer due to high electrochemical impedances and the ensuing poor signal quality of recording and low stimulation efficiency (resulting in an increase of necessary voltages). To improve the performance of small electrodes, a variety of methods have been developed in order to increase the capacitance (and reduce the impedance). These include surface roughening or structuring (to increase the effective surface area of the electrode) and the use of electrode coatings.[13,15,16] Examples of electrode surface modifications are given in Figure 13.3b, including material nanostructuring, the use of high surface-area materials such as graphene or carbon nanotubes (CNTs), and conducting polymer coatings.[14] The circuit elements affected by such modifications are highlighted in blue. Typical EIS characterization curves are given in the lower left with an indicated lowering of impedance across the frequency range for useful modifications. This improvement in electrochemical impedance translates to superior ionic-electronic transduction efficiency. This in turn provides higher signal-to-noise ratios (SNRs), as well as improved stimulation efficiency of the electrode. This is portrayed in Figure 13.3b (lower right), where improved SNR allows for higher quality recordings (bold curve) and enables acquisition of low-amplitude signals, which may otherwise be lost in the background noise.

In the case of stimulation, a certain amount of charge must be ''injected'' into the biological environment when aiming to induce a response in biological tissue. The amount of injected charge is equal to the applied current magnitude multiplied by the duration of time (*i.e.*, 1 coulomb = 1 ampere×1 second).

The voltage level needed to attain charge injection into the ionic environment is an extremely important factor. When the level of voltage needed to drive the required current (and inject the necessary charge into neighboring tissue) becomes too large, tissue damage is imminent. A variety of redox reactions may occur, creating damaging chemical species. In order to quantify the voltages needed for such stimulation pulses, electrochemical measurements may be carried out. The desired stimulation current pulse is applied to the electrode under characterization in a physiologically relevant electrolyte environment. The voltage required to attain the set current level is measured and is referred to as the voltage transient (see Figure 13.3b, lower right side). The geometrical size of the stimulation electrode again plays an important role, with larger electrodes requiring lower voltages, however suffering from loss of spatial resolution and increase of overall device size. Utilization of electrode modification methods, such as polymeric interfaces, again provides a possibility for significant improvement. The low-impedance system provides a large charge injection capacity, which allows the desired stimulation pulse to be delivered using lower voltages and offers the opportunity to reduce electrode size.

As a result of highly increased capacitance compared to standard metal electrodes, polymeric coatings have demonstrated great potential for electrode modification. This is a result of mixed ionic–electronic conduction characteristics, in which case the polymer may be called a ''mixed conductor.'' This means that both electronic charge and ionic charge may be transported within the material. When ions are injected into this type of polymer, they may interact with the entire volume of the film.[17–19] Depending on the ionic charge (positive/negative) and the charge carriers within the polymer (n-type/p-type), doping or de-doping processes will take place, modifying the electrochemical state of the system. This process modulates the conductivity of the polymer, providing efficient transduction between ions and electrons—ideal for bioelectronic applications.

Figure 13.3c portrays the biological influence on the overall electrochemical circuit. The circuit elements corresponding to this effect are highlighted in red. Fluorescence staining of brain tissue following implantation of a neural probe displays the density of various cell types as a function of distance from the electrode interface. Red (ED1) staining indicates the location of inflammatory cells, green (GFAP) shows astrocytes and neurons are displayed in purple (NeuN). The insulating distance between the electrode surface (represented on the left) and the neuron cell bodies is evident. This distance between the cells of interest and the recording site results in the aforementioned problematic signal attenuation.

#### *13.2.1.2 Bidirectional Interaction—Recording and Stimulation Devices*

Classically, metal electrodes have been employed for bioelectronic recording and stimulation interactions. Luigi Galvani is credited with the first instance of such an interaction, with his discovery of bioelectricity through the first-known

experiment in the field of bioelectronics. The stimulation of a frog leg, due to the differing metals of the steel dissection scalpel and brass hook used to hold the leg in place in this initial experiment, was the basis of Galvani's discovery; at the time he called this "animal electricity."[20] The publication of this event is highlighted in the bioelectronics development timeline of Figure 13.4, along with several other historically significant events.

In early bioelectronic studies, rather crude and simple set-ups were often employed. For example, the neural interfacing microelectrodes of Hodgkin and Huxley, used to develop a model describing action potential propagation, were simple encapsulated silver wires, and those of Hubel and Wiesel, used to map the visual cortex of a feline model, were tungsten microwires encapsulated with epoxy to leave the tip free, obtaining the spatial resolution needed for single-neuron recordings. In other cases, the set-up was complicated and cumbersome. The string galvanometer is a good example, created by Williem Einthoven to attain more reliable results for ECG than the previously used Lippmann electrometer by Augustus Desiré Waller.[24] The quartz filament utilized in this system was prepared using a bow and arrow to pull long, thin filaments, subsequently silver coated and placed between two electromagnets. This was placed in a large overall set-up (see the 1901 entry of Figure 13.4), with additional big cylinders of electrolyte used to provide the "bioelectronic interface" to the human body. The research involved in this development as well as many other early biomedical-related works is fascinating and the reader is encouraged to read the publications.[20,25–29]

Although a great deal has been discovered about the cardiac, visual, muscular and nervous systems with the devices and materials of past centuries, the development of more sophisticated technologies provides the opportunity for a deeper understanding. The desire to attain this deeper understanding and to improve diagnostic tools and injury or disease treatments has driven biomedical research toward solutions of reduced invasiveness and improved performance. Biomedical technologies currently being developed strive to achieve this reduced invasiveness, through increased flexibility/elasticity, and reduced overall thickness or size for implantable devices. For skin-mounted or wearable electronics, thin, conformable and nonperceptible characteristics are sought. Additionally, increased electrode density and spatial accuracy (*i.e.*, reduced size) are frequently desired. High electrode densities are often essential for implantable devices, where size and pliability are also of great concern.

Nonredox/conductive polymers with intrinsic flexibility or stretchability have demonstrated promise as substrate materials. In research studies, as well as some clinical biomedical technologies, polymer substrate materials such as polysiloxanes (*i.e.*, silicones, like PDMS), Parylene C, SU-8 and polyimide have been employed. Most clinical work uses millimeter-scale thicknesses, where the polymer flexibility provides some advantage, but this is limited due to the overall size. The early 21st century has begun to revolutionize biomedical device research. Micron- or even nano-scale devices are

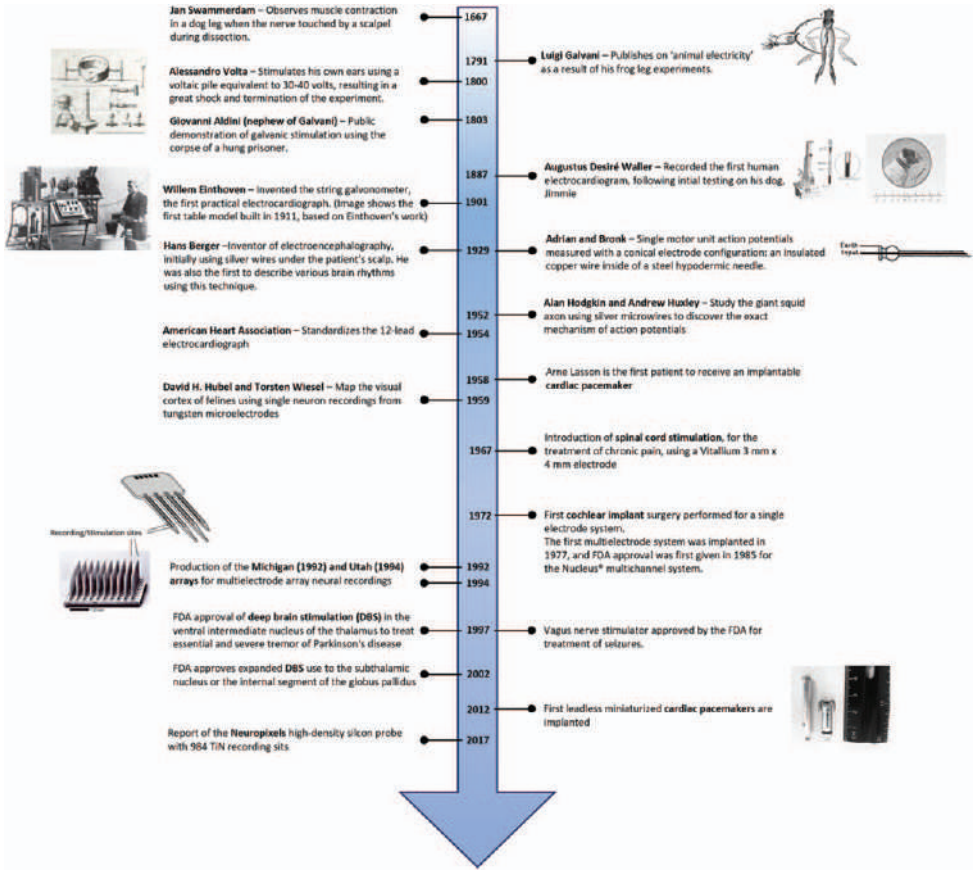


**Figure 13.4** Bioelectronics development timeline. Key achievements throughout history relating to bioelectronic interactions. Conical electrode image adapted from ref. 21 with permission from John Wiley and Sons, © 1929 The Physiological Society. Utah array image adapted from ref. 22 with permission from Springer Nature, Copyright 2006. Leadless pacemaker image adapted from ref. 23 with permission from Elsevier Copyright 2017.

emerging with reduced invasiveness, in addition to improved performance and the inclusion of other functionalities (see Sections 13.3 on biosensors and 13.4 on drug delivery).

Redox/conducting polymers have made a great contribution to the new generation of bioelectronic research. The intrinsic material properties of these polymer provide a natural path toward flexible/stretchable conductive lines, active sites and overall devices. In addition, as a result of the previously discussed benefits in electrochemical impedance through the use of mixed electronic/ionic CPs, electrode miniaturization is facilitated as well with these materials. Initial studies taking advantage of CPs employed these as an electrode coating on standard silicon- or metal-based probes, improving recording and stimulation performance.[16,30–32] These polymers, however, have also produced a new generation of devices that may be fully flexible, stretchable and/or conformal to human tissue, thereby achieving a more ideal bioelectronic interface. In general, often used conducting polymers for biomedical applications are those presented in Figure 13.1. Specific research and clinical examples making use of these polymers for recording and stimulation applications are given in the following section.

Before moving to the application examples, an alternative technological possibility is presented. Whereas electrodes allow passive signal recording (*i.e.*, no energy supplied to the overall circuit), active transistor elements present the opportunity to benefit from signal amplification, in some cases directly at the recording site. Two main organic transistor types have been developed and adapted to take advantage of this local amplification for biological applications: electrolyte-gated organic field effect transistors (EGOFETs) and organic electrochemical transistors (OECTs). Both offer the advantage of interacting directly with the electrolyte, a key benefit when working in liquid biological environments. In the case of EGOFETS, ionic charge accumulates at the gate/electrolyte (except in some floating or buried gate instances) and the semiconducting channel/electrolyte interface, similar to the case of standard FETs with electronic charge accumulation, however here ionic capacitively coupled charges play a large role. OECTs, on the other hand, again take advantage of the mixed-conducting characteristics of certain semiconducting polymer materials and can reversibly exchange ions with the electrolyte. Through this process the electrochemical state of the polymer channel is modulated. In both EGOTFETs and OECTs, the obtained signal is amplified by a factor depending on the transistor characteristics. Introductory material and further details on the operation of these transistors may be found in the following: EGOFETs,[33–36] and OECTs.[37–39] The potential benefit of utilizing these transistors at biological interfaces has been demonstrated in numerous applications, some of which are highlighted in the following research examples. In addition, a great deal of work has also been done to utilize functionalization techniques and employ OECTs and EGOFETs for biosensor applications (Section 13.3).

## 13.2.2 Current Uses/Applications

In the previous section we considered traditionally used bioelectronic materials and devices, and established areas where redox polymers may offer possibilities toward improvement. Potential advantages include enhanced device performance, reduced (unwanted) biological response such as scar tissue, and intimate tissue contact allowing interaction with select populations of cells through recording or stimulation. Together these benefits provide the opportunity for brain mapping, spatially accurate therapeutic stimulation (spinal cord stimulation, cardiac pacemakers, deep-brain stimulation, *etc.*), or restoration of vision or hearing.[40] Here we look into research examples aimed at such applications.

### *13.2.2.1 Surface-mounted Recording Applications—ECG/EEG/EMG*

Often research demonstrations of new bioelectronic recording devices utilize electrocardiogram (ECG or EKG) and electroencephalogram (EEG) applications. This stems from the minimally invasive skin-mounted testing capability and, in the case of ECG, high-amplitude signals. The ECG is an essential diagnostic tool that captures a tracing of cardiac electrical impulses through the use of electrodes, or ''leads.'' EEG records electrical activity of the brain, employing devices placed on the scalp. In both cases the interface between the skin and the electrode plays a critical role. To date, the electrodes have been metal-based, typically Ag/AgCl, and a conductive electrolyte gel is employed to improve the bioelectronic interface. In cases where long-term recording is necessary, an adhesive pad is used to maintain cutaneous contact. As motion artifacts, signal quality, evaporation of the ion-conductive gel, and overall comfort of the electrodes pose potential drawbacks of current systems, alternative materials and measurement techniques have been sought. A wide variety of materials have been investigated to improve the problematic issues of traditionally used electrodes, including an assortment of metal particle-infused nonconductive polymers (*i.e.*, extrinsically conductive polymers), however these will not be discussed here. Redox/conductive polymers are promising candidates due to potential improvements in all the stated problematic areas.

For ECG and EEG recording electrodes, PEDOT-based, and especially PEDOT:PSS-based, technologies have played the largest role in biomedical research utilizing CPs. Figure 13.5a shows an example of simple gold electrodes compared to the same electrodes coated with PEDOT:PSS and used for EEG recordings.[41] The signal acquisition process is carried out by placing the exposed circular gold surface in contact with the skin; in this case of EEG the electrodes are placed on the scalp. Alternatively, the electrode is coated with a PEDOT:PSS layer and applied to the skin. The black insulating layer indicated in Figure 13.5a (left, and observable in the center image) defines the electrode area and ensures that the electrodes are equivalent in size for comparison. The recorded EEG signals are shown on the right-hand side for

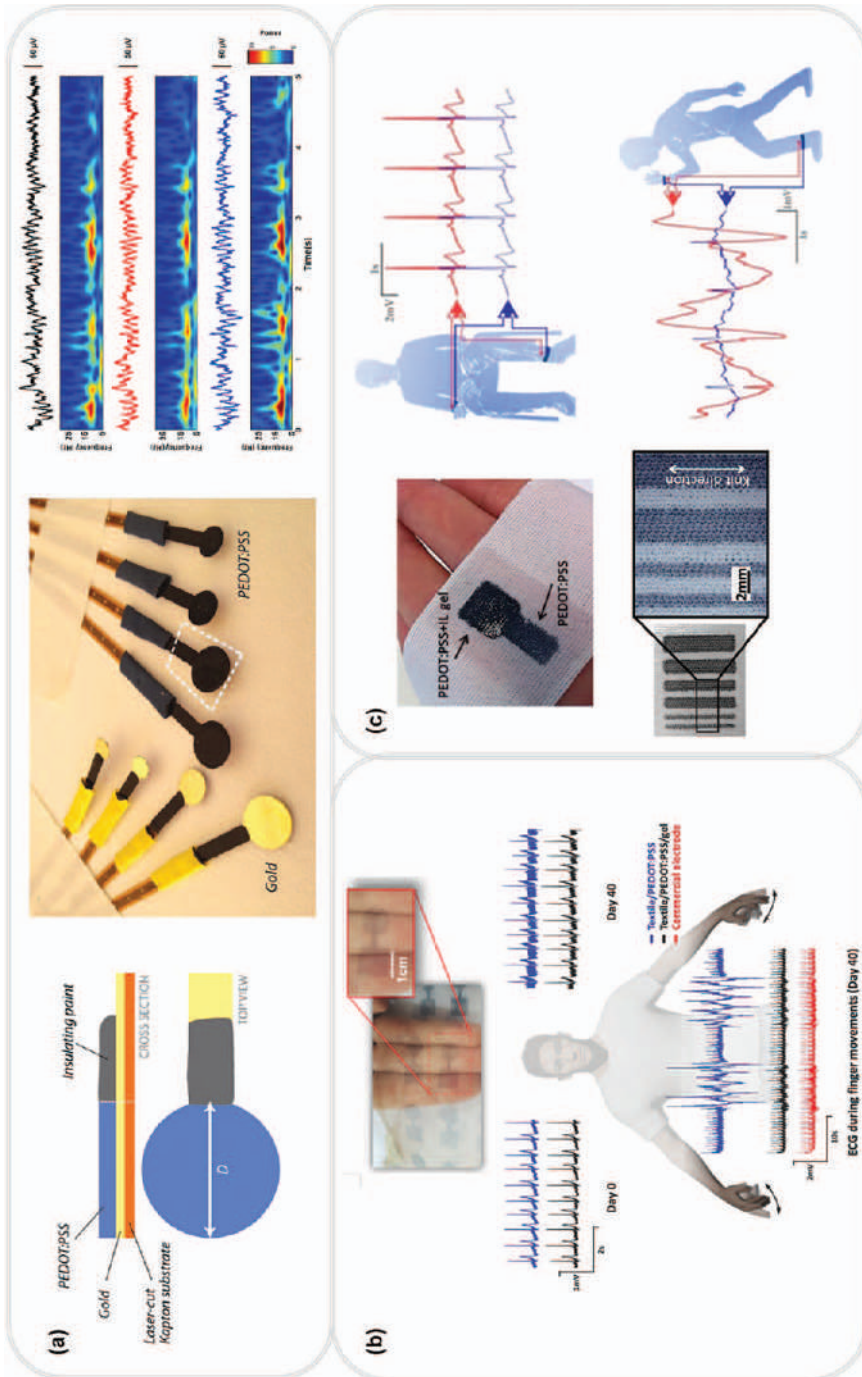
(a)
PEDOT:PSS
Insulating paint
Gold
Laser-cut Kapton substrate
CROSS SECTION
TOP VIEW
D
Gold
PEDOT:PSS
(b)
1cm
Day 0
Day 40
2mV
2s
Textile/PEDOT:PSS
Textile/PEDOT:PSS/gel
Commercial electrodes
ECG during finger movements (Day 40)
(c)
PEDOT:PSS+IL gel
PEDOT:PSS
2mm
knit direction

a standard Ag/AgCl electrode with ion-conductive gel (top, black), dry gold electrode (center, red), and a dry PEDOT:PSS-coated electrode. With calculated SNR values of 24.4 dB and 24.9 dB for the PEDOT:PSS and gel-assisted electrode, respectively, and 21.3 dB for the Au electrode, the polymer coating demonstrates potential. As a result of the time-consuming preparation and aforementioned evaporation issues, the possibility to achieve analogous SNR performance using PEDOT:PSS in its dry state is a significant benefit. In addition, the polymer-based electrodes are considerably more flexible than typical EEG technologies, and have also been fabricated on extremely thin, flexible substrates for maximum conformability.[41,42]

Wearable technologies represent an attractive research field for providing intimate cutaneous bioelectronic interfaces and minimizing discomfort. These technologies are very interesting for both medicine and sports applications. The example in Figure 13.5b shows PEDOT:PSS electrodes printed directly onto a textile substrate, commercial pantyhose made of 100% polyamide. In this work, an ionic liquid gel (based on biocompatible cholinium lactate) was employed to improve the bioelectronic interface and was also deposited by ink-jet printing.[43] Demonstrative ECG recordings were carried out, placing the textile electrodes on the forearm and utilizing hand opening/closing to create motion artifacts. It may be seen that the gel-assisted textile/PEDOT:PSS performs analogously to the commercial electrode and experiences only slight degradation over 40 days. An alternative, simple approach to directly pattern PEDOT:PSS coatings to specific areas of knit cloth may be observed in Figure 13.5c (left). Using a technique inspired by the Japanese kimono, the conductive polymer electrodes are patterned onto the cloth and shown to perform (blue trace) similarly to medical Ag/AgCl electrodes (red trace) when the patient is stationary (Figure 13.5c, right, upper).[42] However, during movement, the textile electrodes significantly outperform the medical electrodes, where the biological signal may be completely lost in the motion artifacts (Figure 13.5c, right, lower).

As discussed at the end of Section 13.2.1, transistors such as EGOFETs and OECTs exhibit great potential for signal amplification directly at the biological

**Figure 13.5** Conducting polymer electrodes for skin-mounted bioelectronic applications. (a) Gold- and PEDOT:PSS-coated EEG electrodes. The use of PEDOT:PSS shows analogous performance to clinically used Ag/AgCl electrodes, with increased flexibility and without the need for application of an ion-conductive gel. Adapted from ref. 41 with permission from John Wiley and Sons, © 2013 Wiley-VCH Verlag GmbH & Co. KGaA, Weinheim. (b) Textile inkjet-printed PEDOT:PSS electrodes with printed ionic liquid gel for ECG measurement. Gel-assisted textile electrodes performed equally well as clinical electrodes, while providing a higher degree of comfort. Adapted from ref. 43 with permission from John Wiley and Sons, © 2017 Wiley-VCH Verlag GmbH & Co. KGaA, Weinheim. (c) Wearable PEDOT:PSS electrode technology for ECG recording with reduced motion artifacts. Adapted from ref. 42, https://doi.org/10.1038/srep15003, under the terms of the CC BY 4.0 license, https://creativecommons.org/licenses/by/4.0/.

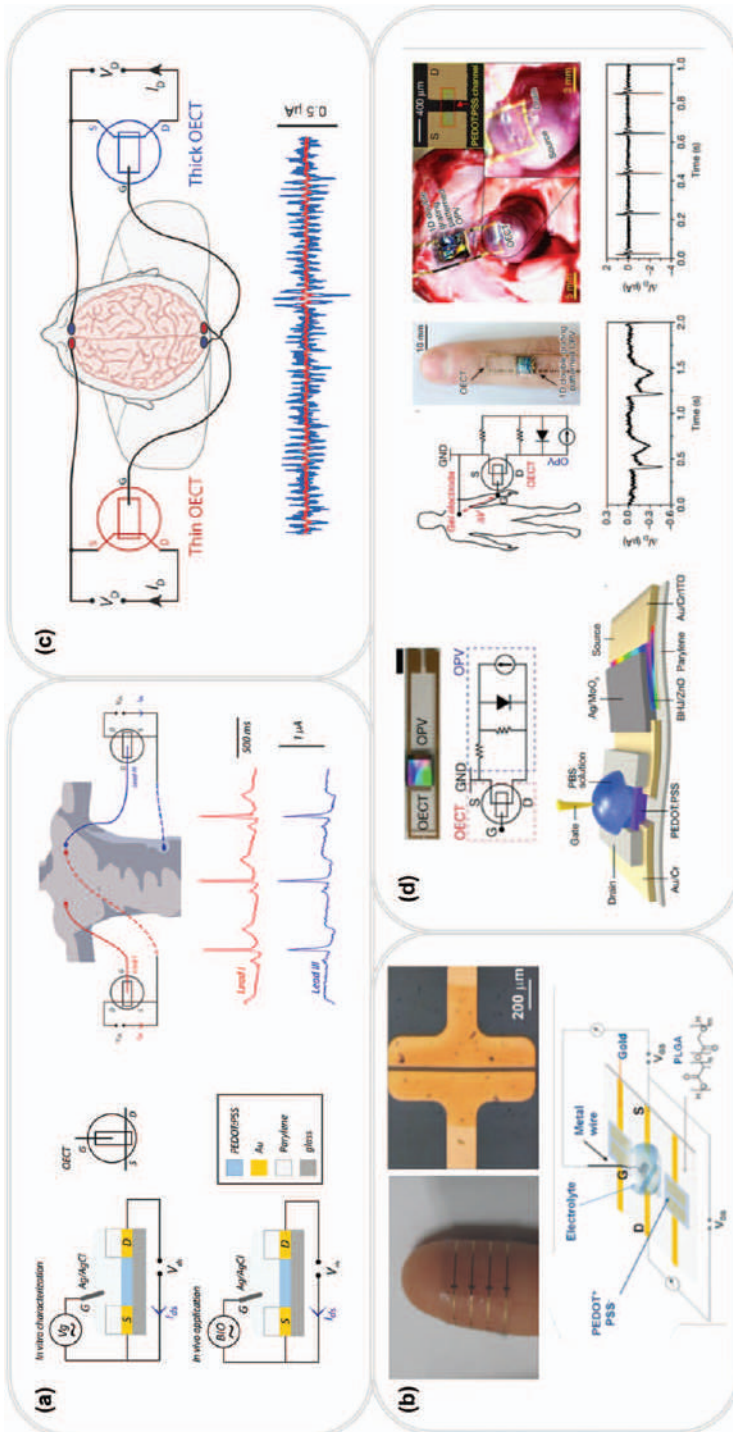
(a)
In vitro characterization
In vivo application
OECT
PEDOT:PSS
Au
Parylene
glass
500 ms
1 µA
Lead I
Lead III
(b)
200 µm
Electrolyte
Metal wire
Gold
PEDOT:PSS
(c)
Thin OECT
Thick OECT
0.5 µA
(d)
OECT
OPV
GND
Gate
Drain
Source
PBS solution
PEDOT:PSS
Au/Cr
Ag/MoO3
BHJ/ZnO
Parylene
Au/Cr/ITO
Time (s)

recording site. Research studies aimed at exploiting this bioelectronic application of transistors have primarily focused on OECTs with PEDOT:PSS as the active channel material. Some examples are given in Figure 13.6, again utilizing ECG and EEG records to demonstrate the promise of the developed devices. An illustrated cross-sectional view and connection scheme of the OECT is given in Figure 13.6a. With the polymer channel in direct contact with the ionic environment, $V_{ds}$ is applied between the source and drain contacts, $V_{gs}$ between the gate (also in contact with the electrolyte or tissue) and source. The channel current, $I_{ds}$, is read out. Example ECG recordings are presented in Figure 13.6a (right side). Good signal quality may be observed in this ''two-limb'' recording set-up with one OECT measuring the potential difference between the right and left arms, and the second between the left arm and left leg. This may additionally be expanded in a straight-forward manner to the standard clinical 12-lead measurement Cardiac signal recording was also successfully achieved by the OECTs in Figure 13.6b, however in this case a dissolvable poly(L-lactide-*co*-glycolide) (PLGA) substrate layer was utilized. This resorbable bioscaffold provides a method for extremely thin overall devices, once again aiding in the conformable bioelectronic interface.

The study in Figure 13.6c demonstrates the importance of the transistor geometry and how this may be tuned depending on the application.[37] Here an OECT with a thicker PEDOT:PSS channel (blue schematic and signal) is compared with that of a thinner channel (red) of the same transistor width and length (*i.e.*, W/L ratio). As a result of the mixed conduction channel properties of OECTs, and the ensuing volumetric performance dependence, the thicker channel provides higher amplification with a lower cutoff frequency, while the thinner channel possesses a higher cutoff frequency but lower amplification. Both OECTs in this study can resolve the EEG signal frequency (~10 Hz), which may be observed through the similar signal pattern of the blue and red curves, however the blue curve is highly amplified in comparison. A final example of OECT application is presented in Figure 13.6d through a self-powered combined OECT-OPV approach.[46] This ultra-flexible device is composed of a

**Figure 13.6** Electrophysiological recordings using transistor technologies. (a) ECG recordings using OECTs. Adapted from ref. 44 with permission from John Wiley and Sons, © 2014 Wiley-VCH Verlag GmbH & Co. KGaA, Weinheim. (b) OECT fabricated on a resorbable bioscaffold for ECG recording. Adapted from ref. 45 with permission from John Wiley and Sons, © 2014 Wiley-VCH Verlag GmbH & Co. KGaA, Weinheim. (c) EEG measurement with different signal amplitudes as a result of OECT geometry tuning. Adapted from ref. 37 with permission from AAAS, © the authors, some rights reserved; exclusive licensee American Association for the Advancement of Science. Distributed under a CC BY-NC License 4.0 http://creativecommons.org/licenses/by-nc/4.0/ Copyright 2015. (d) Combination of OECT and OPV cell for self-powered ECG measurement. Adapted from ref. 46 with permission from Springer Nature, Copyright 2018.

bulk heterojunction using poly[4,8-bis(5-(2-ethylhexyl)thiophen-2-yl)benzo[1,2-*b*;4,5-*b*′]dithiophene-2,6-diyl-*alt*-(4-octyl-3-fluorothieno[3,4-*b*]thiophene)-2-carboxylate-2-6-diyl] (PBDTTT-OFT) polymer with [6,6]-phenyl-C71-butyric acid methyl ester ($PC_{71}BM$) making up the photoactive layer. The electron-transporting layer is made up of zinc oxide nanoparticles (ZnO NPs). This OPV cell was wired to a PEDOT:PSS OECT and could be driven using infrared illumination. Demonstrations of the OECT powered in this wireless manner were given on a human finger and the heart of a rodent.

Two final applications that will be mentioned shortly are electromyography (EMG) and cardiac patches. EMG studies employing conducting polymers are fewer in number than, for example, ECG, and the approaches are typically similar. Roll-to-roll processing was employed in one instance to create conductive polymer nanosheets.[47] PEDOT:PSS with butylene glycol (BG, dermatologically approved) as a secondary dopant was deposited on a poly(D, L-lactic acid) (PDLLA) layer which could be subsequently peeled from the main polypropylene substrate. This freestanding, conductive PEDOT:PSS/PDLLA bilayer nanosheet was then used for EMG measurements from the arm of healthy human subjects. Other examples include electrodes fabricated through ink-jet printing of PEDOT:PSS on textiles or tattoo paper[48] and flexible PPy electrodes coated on nonwoven fabric sheets with the potential of patient-specific customization to improve the myoelectric control of prosthetic hands.[49] The cardiac patch application is an interesting bioelectronic use of CPs and application-specific material tuning, which does not rely on electronic read-out or stimulation. Patients who have undergone myocardial infarction subsequently suffer as a result of the nonconductive nature of the developed cardiac scar tissue. The use of flexible or stretchable conductive materials, that also bind well to challenging tissue surfaces over time, have demonstrated beneficial aspects simply by providing a conductive pathway to restore biological impulse propagation. Successful work regarding this form of treatment includes PPy/chitosan[50] and poly-3-amino-4-methoxybenzoic acid (PAMB)/gelatin[51] hydrogels, PPy/chitosan gelfoam patches and PAni/phytic acid/chitosan films.[52]

#### *13.2.2.2 Central and Peripheral Nervous System—Recording and Stimulation*

When looking into more invasive, implantable bioelectronic interfaces, the material properties of flexible and stretchable electronic devices once again offer great potential. Implanted devices requiring surgical operation demand a higher level of stability, biocompatibility and long-term functionality when compared to skin-mounted devices. An excellent overview of the challenges and achievements regarding materials for implantable device technologies may be found from Wellman *et al.*[53] For these technologies, CPs remain prominent among the emerging attractive candidates.

The earliest use of a CP coating in an effort to advance neural interfacing electrodes was carried out by Foos *et al.* in 1986.[54] Polypyrrole/anthraquinone

(PPy/AQ) was compared with PPy using voltage transients and cyclic voltammetry (CV) cycling. PPy/AQ proved to be more electrochemically and mechanically stable, and required less voltage when applying biphasic current pulses, while PPy suffered from delamination issues (refer to the voltage transient discussion in the *electrochemical impedance* subsection and look ahead to Figure 13.8 for examples). Over the decades following this report, an immense number of variations on PPy, PAni and polythiophene (polymer chemical structure in Figure 13.1) films have been studied. Alternative polymers have been employed as well, particularly in recent years, and ongoing research to synthesize new materials continues, however the stated polymer families have played the main roles to date. Preliminary experiments to determine the electrochemical and mechanical benefits are often employed alongside biocompatibility and tissue response studies on conducting polymers in general. These studies are extremely useful in determining the material appropriateness before moving on to complicated bio-interfacing probes and long-term measurements. Good examples of such preliminary work include George *et al.*, comparing cultured primary cell growth on PPy samples doped with (PSS) or sodium dodecylbenzenesulfonate (NaDBS) prior to implantation of PPy, Teflon and ''stab wounds'' (*i.e.*, no implant, control case of damage from the insertion method itself) in the rodent cortex,[55] and an *in vitro* study by Runge *et al.* on various polycaprolactone fumarate and polypyrrole (PCLF/PPy) composites for nerve regeneration (see Figure 13.7a, b).[56] The latter study visually shows the effect of various dopants on dorsal root ganglia (DRG) attachment and neurite extension, as well as differences in PC12 cultures as a result of variation of the polymeric material composition. These reports of course represent only two examples of thousands available on biocompatibility and cellular response studies involving CPs.

The neurite outgrowth study is particularly relevant to nerve regeneration applications, extremely important in respect to spinal cord and peripheral nerve injury, a promising field for the application of redox polymers. In 1997, Schmidt *et al.* were one of the first to report on the use of a CP scaffold or guidance channel to promote neuronal outgrowth and encourage nerve regeneration.[57,58] PPy was used in this report, demonstrating biocompatibility as well as significantly longer neurite outgrowth when electrical stimulation was applied. Over the following decades, further work has demonstrated the potential of such platforms. Durgam *et al.* developed electrically conductive, biodegradable block co-polymers aimed at nerve regeneration.[58] These co-polymer scaffolds consisted of PPy with either poly(ε-caprolactone) (PCL) or poly(ethyl cyanoacrylate) (PECA). The co-polymers performed well *in vitro*, showing no toxic effects, and PPy–PCL demonstrated the highest number of neurite-bearing cells and longest neurite outgrowth when electrical stimulation was used. Implantation into a sciatic nerve injury rodent model was also carried out, with no inflammatory response, however no electrical stimulus was provided in this case. Similarly, Xu *et al.* utilized PPy/poly(D,L-lactic acid) (PPy/PDLLA) to promote nerve regeneration in a 2014 study.[59] Again, the material composition is varied and the number of neurite-bearing cells and

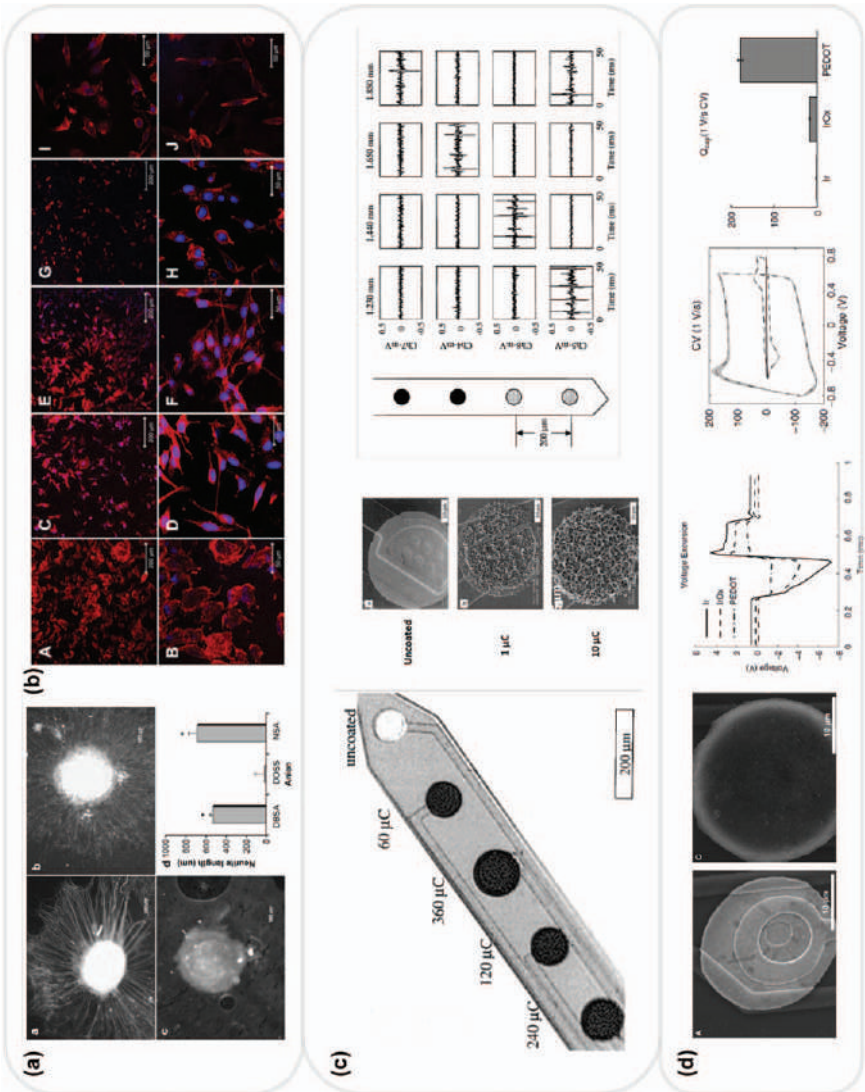
(a)
(b)
(c)
(d)
DBSA
DOSS
NSA
Axon
Uncoated
1 µC
10 µC
60 µC
120 µC
240 µC
360 µC
200 µm
PEDOT
IrOx
Ir
CV (1 V/s)
Voltage (V)

neurite outgrowth length are assessed. Optimized PPy/PDLLA compositions were applied to a severed sciatic nerve with a more in-depth *in vivo* study, however also in this case no electrical stimulation was applied. PPy/PDLLA is compared to the gold standard for nerve repair, an autologous graft, in addition to only PDLLA which is often used in peripheral nerve tissue engineering. PPy/PDLLA significantly outperformed PDLLA alone and performed similarly to the autologous graft, an important result which could eliminate challenges such as donor site morbidity, limited donor sources and size mismatch.

In the early 2000s, Cui *et al.* were pioneers in the field of conductive polymer coatings for neural implants. In 2001, two reports on PPy-based coatings were reported using micromachined Michigan neural depth probes.[30,61] This work employed typically used counterions, such as $ClO_4^-$ or PSS, as well as building on previous studies incorporating biomolecules in CP films as the dopant. Figure 13.7c shows PPy:PSS electrode coatings deposited at various deposition charges (left) and zoomed-in views of PPy:silk-like polymer having fibronectin fragment (SLPF) films, demonstrating the ''fuzzy'' morphology (center images). The magnitude and SNR of recordings using PPy:SLPF coatings are similar to the bare gold electrodes (Figure 13.7c, right). This acute *in vivo* experiment was carried out in the cerebellum of a guinea pig, with the neural probe advanced in 10 um steps to ensure that each electrode site passed by the same neuron(s). As previously discussed, the physical proximity to the biological signal source has a large influence on the recording quality, thus this stepping of the probe is important for a fair comparison between uncoated and coated electrode sites. Although this early study simply demonstrates recording capability, without improved signal quality, a beneficial aspect of the CP use was demonstrated through preferential cell binding of specific cell types to biomolecule-based coatings when compared to bare gold electrodes. In general, the use of biomolecules is an interesting approach, investigated by multiple research

**Figure 13.7** Polymeric material compatibility study on the use of PCLF/PPy for nerve regeneration applications. Differences in (a) neurite outgrowth of DRG due to counterion variation and (b) PC12 culture growth as a result of PCLF/PPy ratio variation. Adapted from ref. 56 with permission from Elsevier, Copyright 2010. (c) Electropolymerization of PPy:PSS (left) or PPy:SLPF (center) on neural probe electrode sites using different deposition charge parameters. An acute experiment in the guinea pig cerebellum demonstrated similar recording capability of uncoated gold (right image, channels 5, 8) and coated PPy:SLPF (channels 4, 7) electrode sites. The probe was advanced in 10 μm steps to ensure that the electrodes each passed by the same neuron(s). Adapted from ref. 30 with permission from John Wiley and Sons, © 2001 John Wiley & Sons, Inc. (d) Comparison of IrOx (leftmost image) and PEDOT:PSS (second from left) for electrostimulation application. Comparison of the voltage transients for 45 μA current pulses of 200 μs phase duration (center), CV curves (second from right) and calculated charge storage capacities (rightmost) of the electrode coatings. Adapted from ref. 60 with permission from Frontiers, Copyright 2009.

groups in an attempt to increase biocompatibility and encourage acceptance of electronic devices in the tissue.[62–65] A great deal of biomolecule counterion candidates have been studied, including DNA, proteins, heparin, poly(hyaluronic acid), nerve growth factors and even red blood cells.

Further, the studies carried out by Cui *et al.* looked into the electrochemical stability of such electrode coatings, as well as the effects of dopant or polymer variation (mainly PPy and PEDOT).[16,31] Over the subsequent decades a great deal of work has gone into improving stability, adhesion and signal transduction of polymeric coatings on neural probes. A good demonstration of improving recording efficiency was given by Ludwig *et al.* in 2011, utilizing electrochemically deposited PEDOT:$ClO_4$ on gold electrode sites of neural probes to improve the SNR of recorded activity. Visual morphology variation of deposited PEDOT:$ClO_4$ films as a result of deposition parameters was shown and significant recorded signal differences were observable. Spiking activity, or action potentials, is evident in the recordings from polymer-coated sites, while these are partially lost in the background noise of the bare metal sites.

On the subject of biological stimulation, the aforementioned voltage transients and cyclic voltammograms are often employed to evaluate electrode performance. Examples of this characterization may be viewed in Figure 13.7d in a study from Wilks *et al.*[60] Here PEDOT:PSS coatings are compared to iridium (Ir) and iridium oxide (IrOx) electrodes. This comparison stems from the fact that clinical implants such as deep-brain stimulators (DBS) or cochlear implants typically utilize Ir, platinum (Pt) or alloys of these. In addition, when working towards small-area neural stimulation electrodes that maintain a good level of charge injection capacity, IrOx films have demonstrated promise as a result of the high electrochemical surface area. When delivering a specific current pulse, in the example of Figure 13.7d this is a biphasic pulse with 200 μs phase durations and 45 μA amplitude, the voltage needed is dependent on the electrode size and material. Figure 13.7 (center) shows that the voltage needed for a PEDOT:PSS-coated electrode is significantly lower than that of IrOx and Ir electrodes of the same size. The ability to stimulate excitable tissue with lower voltage prevents reaching the tissue-damaging threshold.[66] Material assessment may also be understood when observing the CVs of the various electrodes. A larger area under the measured curve corresponds to a larger charge injection capacity (see Figure 13.7e, right two images). This is complemented by the lack of redox peaks which would indicate potentially damaging faradaic reactions that may take place. Once more it is possible to see the potential of PEDOT:PSS for stimulation applications from the great increase in charge injection capacity when compared to Ir and IrOx.

Once the beneficial use of CP coatings was established for bioelectronic recording and stimulation applications, significant focus was put into tackling the problematic issues of these films. This goes back to some of the important factors emphasized throughout this chapter, such as long-term mechanical and electrochemical stability, as well as improved mechanical characteristics to reduce adverse biological

reactions. Regarding the long-term stability, a great deal of work has gone into improving the adhesion of such electrode coatings, as many of the original studies did not provide a covalent bond between the polymer and the electrode surface that is often comprised of noble metals. This has been greatly improved through the use of techniques including functionalized monomers, such as aminopropyltriethoxysilane EDOT (APTES-EDOT), which is useful for adhesion to substrates containing surface hydroxyl groups,[67] or grafting of molecules providing covalent bonding possibility, such as the electrochemical grafting of a "home-made" diazonium salt to improve polymer adhesion to platinum and PtIr surfaces.[68]

As a result of mechanical or electrochemical degradation (among other long-term *in vivo* measurement difficulties), many *in vivo* studies to date using CP recording sites have only lasted up to two weeks. One of the longest reported chronic recordings was achieved by Kozai *et al.* over a period of 154 days.[69] PEDOT polymerized with carboxylic acid-functionalized carbon nanotubes (CNTs) was used to realize this achievement, and a comparison was made with PEDOT:PSS. Although PEDOT:PSS electrodes maintained lower electrochemical impedance values over a significant portion of the study duration, the recordings using PEDOT:CNT films provided higher overall signal quality. Additionally, the recording capability of PEDOT:CNT-coated electrodes extended approximately 2 months past the point where PEDOT:PSS recordings were lost. This represents a good demonstration of the possibility to enhance device performance through straightforward methods such as dopant variation.

Following the validation studies of CP application to rigid bioelectronic devices, flexible implants have been sought after to combine the advantageous recording or stimulation capabilities with improved mechanical properties. A vast number of fabrication-based research examples may be found exploring methods to pattern and utilize conducting polymers and conductive interconnects on flexible, stretchable and conformable substrates. An example from Hassarati *et al.* investigates the use of conductive hydrogels (CHs) as coatings for perimodiolar cochlear implants.[70] The Pt electrode sites of a clinical cochlear implant were first coated with a thin layer of PEDOT doped with para-toluenesulfonate (PEDOT/pTs) using electrochemical polymerization. The array was then dipped in a hydrogel comprised of poly(vinyl alcohol) (PVA) and heparin methacrylate (Hep-MA), with a photoinitiator to cross-link the hydrogel. Lastly, the growth of the PEDOT coating is continued *through* the hydrogel, again using electrochemical polymerization, however in this case the negatively charged immobilized sulfate ions of heparin in the CH act as the counterions. An increase of the charge injection capacity using this CH approach was shown through cyclic voltammograms. In addition, improved stability of impedance values of the hydrogel coatings over time was shown compared to Pt electrodes with a cycling period of up to 2 billion current pulses.

Two final examples are presented here to demonstrate possibilities resulting from the use of redox polymers for bioelectronic devices. The first is the Neurogrid (Figure 13.8a), a cortical surface recording array from

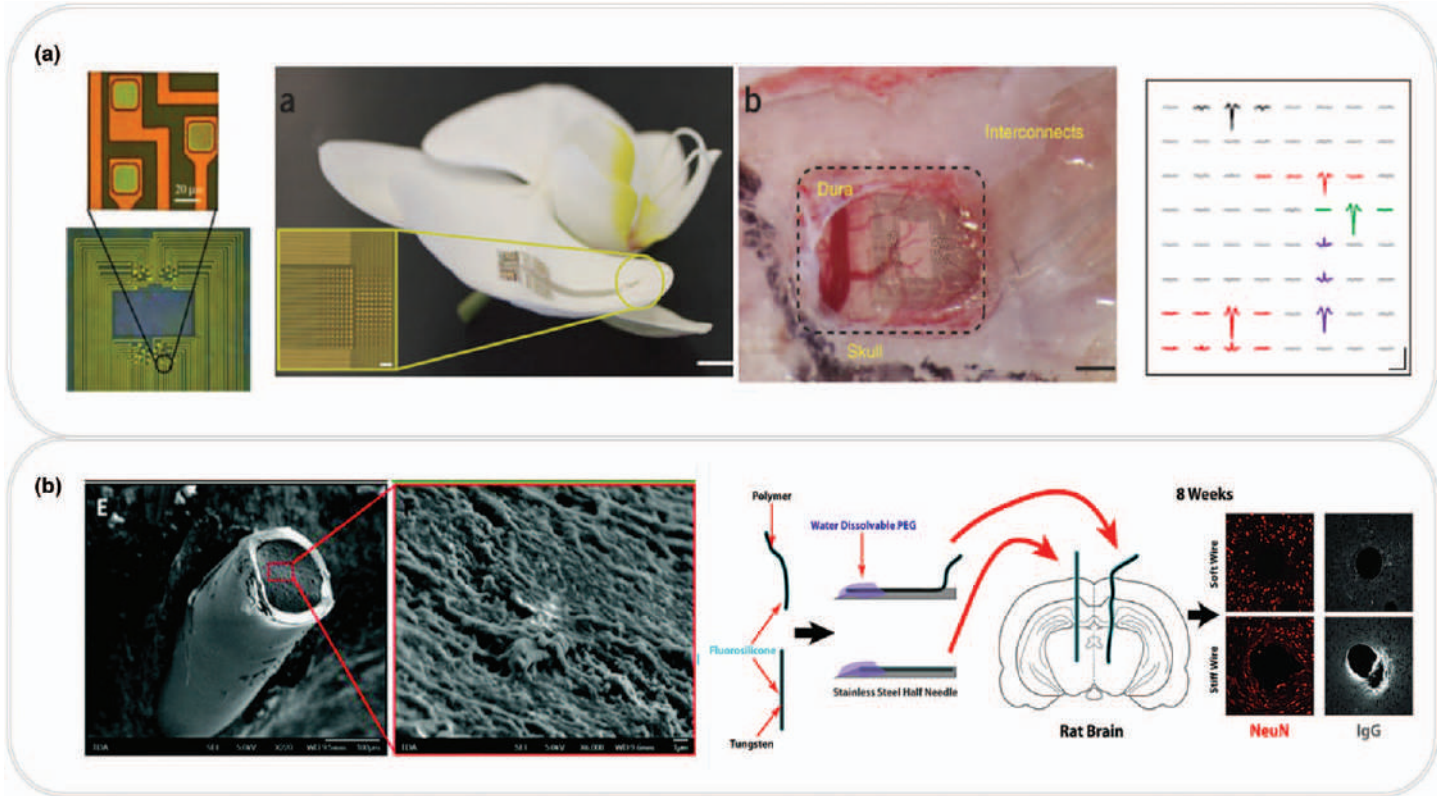


**Figure 13.8** Flexible neural implant development. (a) Cortical surface electrode array using conformable parylene C substrates and PEDOT:PSS electrode coatings. The superior recording capability is shown through the possibility to record action potentials from the surface of the brain (rightmost image). Adapted from ref. 71 with permission from Nature Springer, Copyright 2015. (b) Soft penetrating microwires with a Young's modulus of ~970 kPa are achieved using a PDMS and a lauryl terminated PEDOT–PEG copolymer blend as the conductive core, with a fluorosilicone layer used as the outer insulation. Good biological response compared to tungsten microwires is shown *via* tissue staining. Adapted from ref. 72 with permission from the Royal Society of Chemistry. Adapted from ref. 73 with permission from Elsevier, Copyright 2017.

Khodagholy *et al.*[71] The use of this thin (~4 um), conformable parylene C substrate and patterned micron-scale PEDOT:PSS electrodes was also developed by Khodagholy *et al.*,[74] expanded to 256 electrodes in this case. Action potential recordings from the surface of the brain were achieved (Figure 13.8b, right) through the use of these low-impedance electrodes; an impressive accomplishment for a nonpenetrating probe. In addition, the use of this Neurogrid has been extended to studies on the human brain,[75] an important demonstration of the progression toward clinical application of these materials.

Lastly, we take a look at studies from Kolarcik *et al.* and Du *et al.* on the development of penetrating microwires comprised of soft, elastomeric materials[72] and utilized for chronic recordings.[73] This is a good example of combining positive aspects of various materials and approaches to achieve, in this case, low elastic modulus, reduced invasiveness and good recording capability. An example microwire and the morphology of the conductive inner core are shown in Figure 13.8c (left). This core is made up of PDMS and a lauryl terminated PEDOT–PEG copolymer, while fluorosilicone is used for the outer insulating layer. The Young's modulus of the resulting microwires is ~970 kPa, five orders of magnitude lower than the compared common neural tungsten microwires. This represents one of the lowest elastic modulus values among conducting polymer-based neural electrodes. To achieve this, the ratio of elastomer to conducting polymer was varied in order to optimize the flexibility of the elastomer and maintain good impedance. Hundreds of bending/unbending cycles were applied with conductivity levels remaining constant, and neural activity from the rodent visual cortex was recorded as a result of drifting bar stimulation. Evidence of improved biological tissue response, compared to tungsten microwires, was given through tissue-staining techniques. Neural cell body density appears undisturbed when using the soft microwires and glial activation is highly reduced, indicating a reduced inflammatory response (Figure 13.8e, right).

## 13.3 Polymers for Biosensors

### 13.3.1 Introduction

Disease diagnosis at an early stage is a cost-effective method that can reduce healthcare expense. This approach is often considered more important than the medical treatment itself. Monitoring the physiological concentration of relevant metabolites can greatly aid in this early-stage diagnosis. This is one factor that has driven the development of biosensors, contributing significantly to the well-being of our society. For example, diabetic patients routinely monitor their glucose levels at home by using miniaturized glucose sensors.[76] However, sensing and diagnosis of a wide variety of other important diseases is still in the early phases. Consequently, researchers and companies around the world focus a great deal of effort and resources toward the advancement of biosensors.[77]

A biosensor is comprised of an electronic device, often coupled with biological components in order to sense biological or chemical species, or a biochemical reaction, and to transduce this reaction to an observable signal (Figure 13.9). The output signal of the biological reaction can be electrical, optical or thermal in nature.

A good biosensor must exhibit sensitive, selective, rapid and reproducible detection. Moreover, low cost and miniaturization are critical parameters for large-scale production. When implantable and continuous monitoring are of importance, the biosensor must be stable and biocompatible. Electrochemical biosensors offer a combination of the stated properties, in contrast to optical and calorimetric biosensors. Low-cost, disposable sensors are achievable through the use of printing techniques. Contrary to optical sensors, electrochemical sensors provide label-free detection. When considering the transduction mechanism, two main categories exist for electrochemical biosensors:

1. Faradaic charge transfer between the biological components and transducer
2. Capacitive coupling between ions/molecules in the biological environment and the surface of a transducer

The first process occurs when the reaction between the recognition element and the analyte produces an electrochemically active by-product. This product will in turn undergo faradaic charge transfer with the transducer. As an example, the reaction an enzyme catalyzes with the corresponding analyte results in redox molecules (reactive oxygen species). These molecules can further transfer or receive a charge on the surface of an electrode acting as the transducer. The enzymes are typically located in close proximity to the electronic transducer to maximize the sensing efficiency. The second broad category of sensors relies on the ionic coupling between ions and biomolecules in the vicinity of the transducer. These reactions are electrochemically inert, with no charge transfer occurring. The accumulation of charge at the interface of the transducer, however, can generate a transient signal that is proportional to the concentration of the analyte of interest. By using this operating principle, biosensors can detect affinity-binding reactions between, for example, antibody and antigen.

When redox-active polymers, including CPs, are used as active electrodes in place of metals they offer a plethora of advantages. The possibility to use uncomplicated fabrication methods, such as solution processable techniques including inkjet and screen printing, can result in low-cost mass production of sensors. As a result of the high effective surface area of CPs, large amounts of biorecognition elements can be immobilized spatially close to the electrode surface. This proximity is an important factor that can increase the sensitivity and detection speed. Moreover, polymers with mixed ionic/electronic conduction and the resulting, previously discussed high volumetric capacitance (Section 13.2.1), provide an opportunity to scale down the

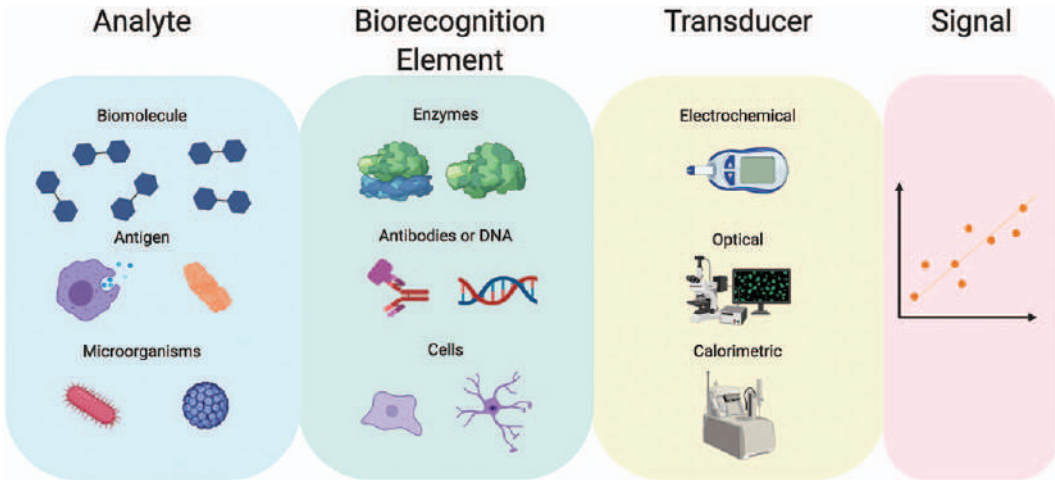


**Figure 13.9** Illustration of a biosensor (left three panels), which is made up of three distinctive parts—the analyte, recognition element and transducer. Analytes include biomolecules, antigens and microorganisms. The analyte interacts with the biorecognition elements, examples of these are given in the second panel. The recognition elements are usually coupled with an electronic device, and upon interaction with the target analyte, a change in the surrounding of the transducer is caused. Finally, the electronic transducer produces a signal that is proportional to the reaction rate (concentration, affinity) between the analyte and biorecognition element.

electrode size without adversely affecting the performance. These aspects constitute redox polymers as excellent candidates for ion to electron transducers.

Finally, as introduced in Section 13.1, semiconducting polymers can be used as active channel and/or gate materials in organic transistors. White *et al.* first developed a PPy-based organic transistor, in which the conducting polymer coated both channel and gate electrodes, and direct contact with the electrolyte could be made. A positive voltage at the gate electrode induced oxidation of pyrrole and the source drain current was measured at various degrees of oxidation.[78] Nishizawa *et al.* showed that the conductivity of the channel could be modulated not only by the gate potential but also by the concentration of protons (pH) in the electrolyte.[79] Similarly, Paul *et al.* demonstrated transistor modulation with pH variation and redox mediators by using PAni as the active channel material.[80]

Recently, OECTs based on PEDOT:PSS, and EGOFETs based on P3HT or small-molecule organic nanocrystal films have been used as enzymatic sensors, as well as small-molecule sensors, based on affinity reactions. First-, second- and third-generation transistor-based glucose sensors have been realized by immobilizing redox enzymes, usually at the gate of OECTs. Additionally, the ability to monitor the binding of proteins and small molecules using antibodies or aptamers has been demonstrated through the use of EGOFETs.

### 13.3.2 Enzymatic Biosensors

Enzymatic sensors were primarily developed to monitor the glucose levels in diabetic patients. The first biosensor of this kind was reported by Clarks and Lyons in 1962. Historically, three generations of glucose sensors have been developed and are categorized according to the process by which the electron transfer (ET) takes place, as the charge moves from the enzymatic active site to the electrode surface (see Figure 13.10).

The 1st generation of electrochemical sensors was based on the Clark electrode, designed for sensing oxygen using a catalytic platinum (Pt) surface. In this case, the concentration of oxygen is measured through its conversion to water at the Pt electrode in a one- or two-step process. In the former, four electrons are transferred to $O_2$ and $4H^+$ forming $2H_2O$.[81] In the latter, two electrons are first transferred from the Pt surface to $O_2$ and $2H^+$ creating $H_2O_2$ as an intermediate product and subsequently $H_2O_2$ receives two electrons, forming $2H_2O$. Taking advantage of the second step in this reduction process, $H_2O_2$ to $H_2O$, a glucose sensor may be created if the electrode is coated with glucose oxidase (GOx) enzyme. In this case the GOx enzyme, in the presence of glucose and oxygen, will produce $H_2O_2$ as a by-product, which in turn will be converted into water at a negatively biased electrode surface or is converted to $O_2$ at a positive electrode as shown in Figure 13.10a. The resulting current corresponds to the enzymatic activity as well as the glucose concentration. The speed of the sensors, when setting

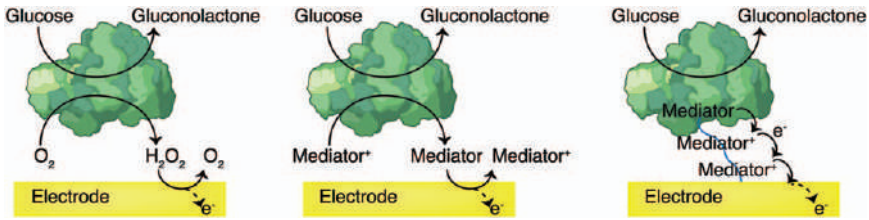


**Figure 13.10** Operating mechanism of electron transfer between the enzymatic active site and the electrode transducer for 1st-, 2nd- and 3rd-generation enzymatic sensors. (a) First-generation sensors use the conversion of oxygen to hydrogen peroxide as the mediator. (b) The 2nd-generation approach uses small redox molecules with low redox potentials as mediators. (c) Third-generation sensors use cross-linked small-molecule mediators that reach the active site deep in the enzyme structure, and through a hopping mechanism charge is transferred between cross-linked mediators and the electrode.

aside enzyme kinetics and analyte concentration, also depends on the diffusion of $H_2O_2$. As a result of neutrality, diffusion away from the electrode occurs and the sensitivity and response time of the sensor may be limited as a result. An additional shortcoming of first-generation glucose sensors is the depletion of $O_2$ in solution due to the reduction into $H_2O_2$ by GOx. This reduces the mediator concentration, thus diminishing the performance of the sensors.

In order to overcome such limitations, redox molecules (ferrocene, quinones, iodine) have been employed as mediators (2nd-generation glucose sensors, Figure 13.10b). Redox mediators have small redox potentials, meaning that they can efficiently transport electrons at potentials where other species present in complex solutions do not become oxidized or reduced. This prevents interference from reactions with such undesirable species. The redox mediator concentration can be optimized in order to limit their depletion. A major disadvantage of this approach, however, is their toxicity if leached into a biological environment. A wide variety of electrodes can be used to accept the electrons from the redox molecules.

Third-generation glucose sensors (Figure 13.10c) were pioneered by Adam Heller[82,83] in an attempt to achieve direct electron transfer from the active site of the enzyme to the electrode surface. This takes place through redox oligomer/polymer ''relays'' that are covalently functionalized on side groups of amino acids existing on the surface of enzymes. Ferrocene and osmium complexes have been bound to GOx, reaching inside the flavin adenine dinucleotide (FAD) active site. Heller speculated that, after the conversion of glucose, the electron from FAD would transfer to the redox relay, if this relay is very close to the redox active site (Figure 13.11a). Afterward, the electron would reach the surface of the enzyme through a hopping mechanism and could be transferred to the electrode if the enzyme is located spatially close to the electrode surface. The output current from these modified enzymes was proportional to the glucose concentration (Figure 13.11b). To avoid

limitation of electron transfer near the surrounding of the electrode, and to extend the surface available for this process, osmium complex redox polymers were employed and cross-linked with GOx enzymes, creating a three-dimensional network of enzymes and redox polymers. A part of the osmium

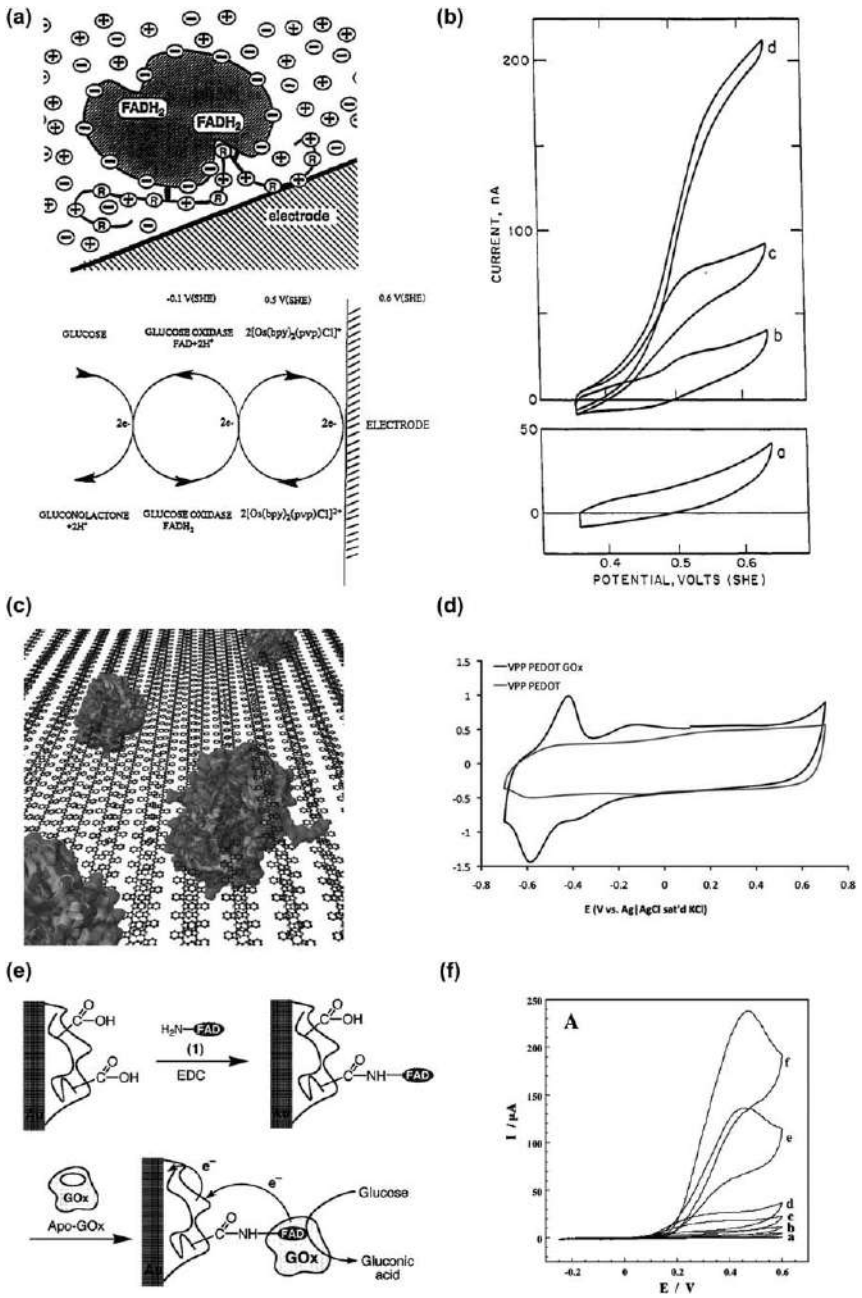

complex penetrates the enzyme close to the FAD active site and receives the electron, which in turn is transferred to the surface of the electrode from the redox wire under the influence of an applied voltage. Cross-linking the enzyme with redox polymers improves the stability of the sensors, preventing both the enzyme and mediator from leaching out in solution over time as they are covalently bound to the electrode. This concept is useful for implantable biosensors, where leaching of toxic mediators in the biological environment can be a bottleneck in development. In addition, the low redox potential of these mediators allows for more selective measurements in complex solutions by reducing interference with common acids that can be oxidized at the electrode surface. Finally, the fact that electron hopping is a quantum effect would theoretically allow for more efficient charge transfer compared to diffusion.

Following Heller, many research groups have investigated direct wiring of enzymes to conducting polymers in order to improve the electron transfer efficiency. Electropolymerization in the presence of various enzymes has been attempted with claimed success in instances of enzymes with redox active sites that are fairly exposed as well as those with sites deeply buried inside the structure of the enzymes. However, for enzymes such as GOx, which contain deeply buried FAD sites, claims of direct wiring are under discussion.[86] An attempt to wire GOx to vapor-phase polymerized PEDOT:tosylate (PEDOT:Tos) has been made, as shown in Figure 13.11c, by washing the deposited film with a GOx-containing solution during the process step to remove residual iron(II) oxidant. It is evident from the CV measurement (Figure 13.11d) that the enzyme is entrapped in the PEDOT:Tos polymer structure, however glucose detection was not possible. The

**Figure 13.11** (a) First reported enzyme wiring through redox relays which penetrate the GOx enzyme close to the FAD active site. During glucose catalysis, an electron transfers from the FAD located inside the enzyme to the electrode surface by a hopping mechanism along the redox relays. (b) Cyclic voltammetry (current *vs.* voltage) for different concentrations of glucose. The current increases with the addition of 0.8 mM and 5mM glucose. Adapted from ref. 83 with permission from the American Chemical Society, Copyright 1990. (c) Illustration of GOx wiring to PEDOT:Tos during a washing step of removing the iron(II) oxidant from the film. The film collapses entrapping the enzyme. (d) Cyclic voltammetry showing the redox peaks that correspond to the transfer of electron from FAD to PEDOT:Tos and *vice versa*. The absence of peaks in the absence of GOx shows that the enzyme is wired to the conducting polymer electrode. Adapted from ref. 84 with permission from John Wiley and Sons, © 2010 Wiley-VCH Verlag GmbH & Co. KGaA, Weinheim. (e) Schematic showing the immobilization of FAD on a PAni/poly(acrylic acid) film and the subsequent reconstruction of GOx by addition of a GOx apoenzyme. (f) Cyclic voltammetry of an Au electrode coated with PAni/poly(acrylic acid) and functionalized using the technique in (e) in the presence of various glucose concentrations: (a) 0, (b) 5, (c) 10, (d) 20, (e) 35, and (f) 50 mM. Adapted from ref. 85 with permission from the American Chemical Society, Copyright 2002.

hypothesized issue was denaturing of the enzyme during the process.[84] Another approach that has been investigated involves reconstitution of apo-enzymes, which are essentially enzyme structures without the active site. CPs may be functionalized with this active site (*i.e.*, FAD, FMN, NAD), thus the modified site can be attached close to the electrode surface (Figure 13.11e). Subsequently, the apo-enzyme is reconnected to this site, creating an active enzyme that is closely wired to the electrode.[85] So far, this method has typically been carried out using PAni mixed with polyacrylic or polysulfonic acid and has shown positive results for glucose sensitivity (Figure 13.11f).

#### *13.3.2.1 Immobilization of Enzymes on Conducting Polymers*

The importance of biorecognition element immobilization as close as possible to the electrode surface has been stressed. The immobilization process can be accomplished through a variety of methods. The simplest approach involves the adsorption of a biorecognition element onto the surface of the transducer. Adsorption occurs due to electrostatic attraction, hydrophilic/hydrophobic interactions or weak van der Waals forces. This process is possible as most biorecognition elements exhibit a net charge on their surface, resulting from the charged side groups of amino acids or lipids. Although adsorption is a very simple immobilization method, it suffers from stability issues. In electrolytes with high ionic concentrations, ions can desorb the biorecognition elements.

In order to improve the sensor stability, covalent attachment of biomolecules to the electrode surface is necessary. Covalent immobilization may be achieved using functional groups induced on the electrode surface, which can covalently bind to targeted functional side groups of amino acids in biomolecules (SH, COOH, $NH_2$). The strong covalent bond results in long-term stability and reproducibility of the enzyme concentration. As this process of biomolecule surface-attachment is dependent on the available electrode surface area, limitations may arise when considering the case of microelectrodes made of traditional metals or inorganic materials with small geometric surface areas.

Conducting polymers provide an opportunity to attain small electrode sizes while maintaining a highly effective surface area. The polymers may be patterned through controlled deposition techniques, and allow for the attachment of a larger number of biorecognition elements when compared to flat metal surfaces (Figure 13.12a, b). Furthermore, conducting polymers can be combined either by simple blending, or through copolymerization, with other nonconducting polymers that contain functional groups. This allows for covalent immobilization of biomolecules close to the conducting polymer electrode without altering the chemical structure. Additionally, when utilizing electropolymerization, conducting polymers can entrap biomolecules resulting in a 3-D network of biorecognition elements in the bulk of the polymer scaffold (Figure 13.12c). During an oxidative electropolymerization process, monomers are oxidized at the surface of a positively charged

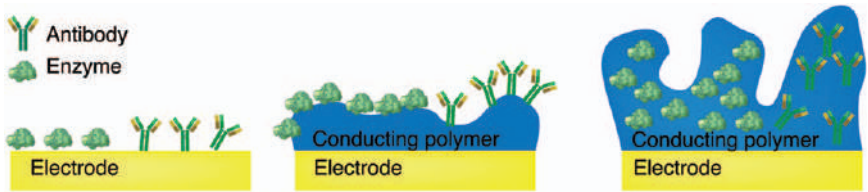


**Figure 13.12** Illustration showing the advantages of conducting polymers for both surface immobilization and immobilization of enzymes in the bulk of the polymer.

conductive substrate and further polymerize into oligomers that precipitate onto the surface of the electrode. If a biomolecule is present in solution, such as an enzyme, due to the net negative charge, it will be attracted toward the electrode surface. As this attraction takes place while the polymer is simultaneously growing, a blend of conducting polymer and biorecognition elements is created.

### *13.3.2.2 Enzymatic Sensor Research Examples*

As already discussed, the immobilization of enzymes through physical adsorption is a simple yet powerful approach. A large number of enzymes, DNA and antibodies exhibit a net negative charge in physiological conditions of pH 7 due to their low isoelectric point.[87] This charge can facilitate electrostatic interaction with positively charged surfaces, whereas in other cases chemical binding or a cross-linking method must be used. An example of a cross-linking method was demonstrated by Zhai *et al.* through the development of PAni CP hydrogels (Figure 13.13a). In this study the PAni was doped with phytic acid, creating a hydrogel, and was subsequently coated on a Pt surface and modified with Pt nanoparticles grown by reduction chemistry throughout the gel. GOx was then applied in solution to the electrode, allowed to diffuse through the structure, and finally glutaraldehyde was added for cross-linking purposes. This resulted in a 3D hydrogel structure with immobilized GOx and Pt nanoparticles. A very low glucose detection limit (700 nM) and fast response time of approximately ~2 seconds were achieved (Figure 13.13b). The Pt nanoparticles are important for the attained performance as they increase the catalytic area and reduce the diffusion time of produced $H_2O_2$. The combination of a high surface area and porous structure enables a large amount of immobilized enzyme and Pt nanoparticles, greatly improving the performance of this 1st-generation glucose sensor.[88]

A more stable functionalization technique can be achieved though the blending of CPs and non-CPs in appropriate ratios. This method can induce functional chemical groups for covalent attachment of biomolecules on the surface of a CP transducer. A good example is found in a study using polyvinyl alcohol (PVA) added to PEDOT:PSS in a mass ratio of 1 : 4. The result is a blend in which the conductivity of PEDOT:PSS is not significantly affected, however, many OH groups are introduced. These hydroxyl groups enable

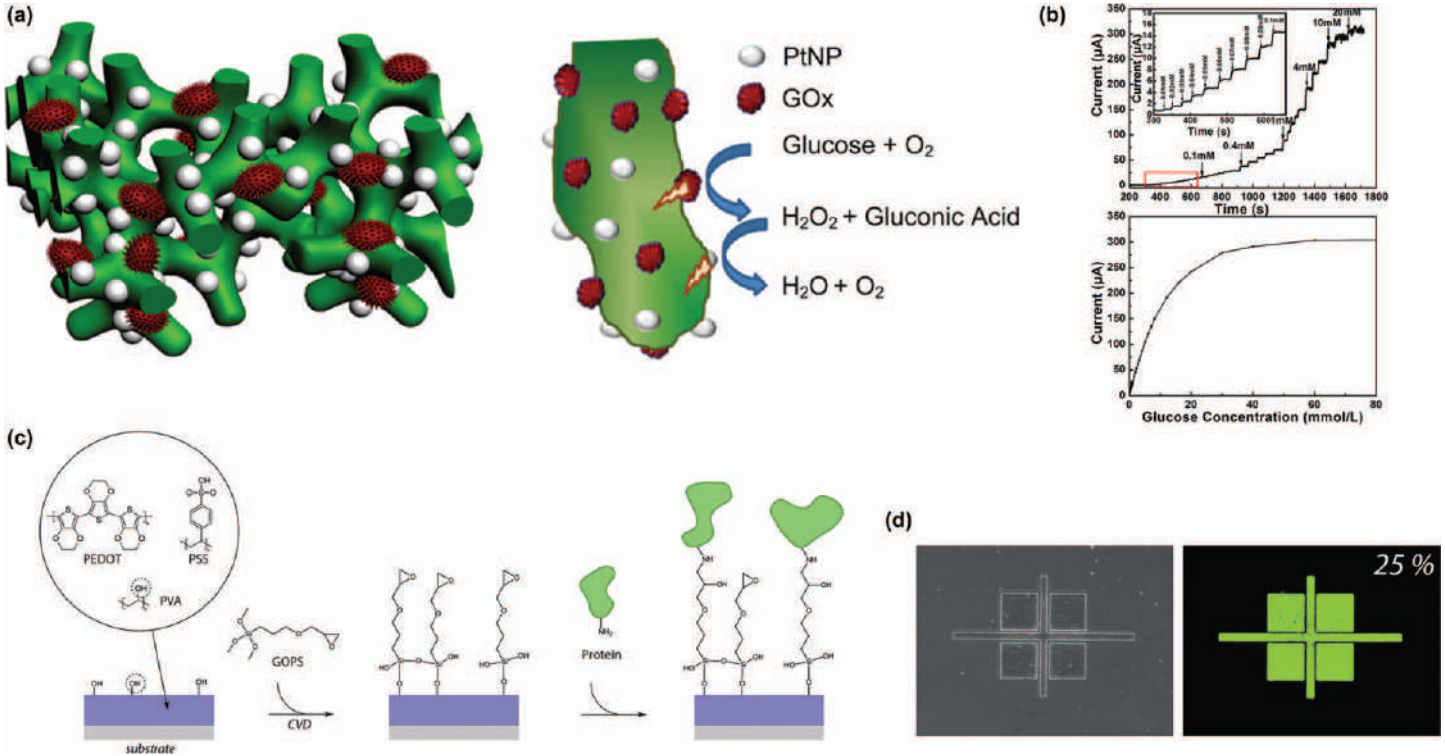


**Figure 13.13** (a) Schematic of PAni-based hydrogel modified with platinum nanoparticles and GOx enzyme. (b) Current response and calibration curve of the sensor in (a) showing high sensitivity and fast response times for glucose detection. Adapted from ref. 88 with permission from the American Chemical Society, Copyright 2013. (c) Schematic showing the functionalization process of PEDOT:PSS modified with PVA. PVA provides hydroxyl groups on the surface of PEDOT:PSS and an epoxy silane is used for binding proteins to this surface. (d) Bright field and fluorescence images of immobilized poly-lysine using the procedure from (c), used to optimize the ratio of PVA to PEDOT:PSS. Adapted from ref. 89 with permission from the Royal Society of Chemistry.

enzyme immobilization by various chemistries (Figure 13.13c, d).[89] Similarly, aniline has been electropolymerized on electrodes coated with poly(-vinyl sulfonate) or poly(acrylic acid). PAni is redox active in acidic conditions, limiting integration of enzymes that exist in physiological pH 7. This obstacle can be overcome through the use of composites, for example, PAni and poly(vinyl sulfonate) or poly(acrylic acid), which enable redox activity at physiological pH. Raitman *et al.* made use of this approach, electropolymerizing PAni in the presence of poly(acrylic acid), which not only improved the redox properties of the CP, but also provided useful poly(acrylic acid) functional groups. Modified amino-FAD sites were covalently bound to the available functional groups of the CP composite, and subsequently a solution containing an apoezyme (apo-GOx) was applied to the electrode surface. Through this process a third-generation glucose sensor successfully realized (refer to Figure 13.11e, f with measurements from this work).[85]

A method for enzyme immobilization in CPs, without the need for chemical functional groups, is entrapment during the electropolymerization process. As the enzyme is entrapped close to the electrode surface during film growth, the immobilization and polymerization may be carried out in one step avoiding chemical modification processes. Additionally, the CP formation and immobilization of enzymes are spatially controlled, with deposition on top of a specific electrode. This allows for the use of different enzymes, sequentially entrapped on separate electrodes, enabling the development of multianalyte sensors. Furthermore, multilayers of different enzymes can be sequentially immobilized on top of each other on the same electrode. PPy has been used as a prominent polymer for enzyme immobilization. Polymerization can be carried out at relatively low oxidation potentials and the thickness of the film can be well-controlled by the injected charge. As a result of the low isoelectric point and net negative surface charge, enzymes can be attracted to the surface of the electrodes upon application of positive charge. The amount of immobilized enzyme can be controlled by controlling the thickness of the polymerized film as well as the concentration of the enzyme that exists in solution. Similarly, PAni and poly(indole) have been utilized for enzyme entrapment. The importance of deposition parameters was shown in this case, however, with denaturing of the enzyme structure occurring at high voltages.[86]

### *13.3.2.3 Organic Transistors*

OECTs have been utilized as an alternative technology for enzymatic sensors. These transistors employ CPs as a channel material and, in many cases, as the gate material as well. The goal of OECT use in sensor applications is to take advantage of beneficial characteristics when compared to electrodes, such as the high amplification properties, quantified by the transconductance.[90] As briefly described previously, the conductivity of the channel in OECTs may be modulated by a gate voltage or ionic imbalances and electrochemical reactions that occur in the electrolyte. The transistor transconductance

(*i.e.*, amplification) is defined as the modulation of the channel current for specific gate voltage modulations. These changes in gate voltage can be a result of mechanisms such as charge transfer resulting from enzyme functionalization and analyte detection. Tang *et al.* demonstrated an example of this transistor-based sensor using immobilized GOx entrapped in a chitosan matrix on top of a gate electrode modified with Pt nanoparticles. The achieved glucose detection limit was in the nanomolar range.[91] 2nd-generation OECT-based enzymatic sensors have also been realized by integrating ferrocene redox mediators.[92] Recently, the development of n-type polymers that operate in aqueous electrolytes has allowed for the creation of 3rd-generation n-type OECT sensors (Figure 13.14a).[93,94] In these studies, n-type OECT-based lactate and glucose sensors employ a copolymer named P-90 (Figure 13.14b). The enzyme of interest was immobilized through adsorption on top of both the gate and channel. The P-90 n-type polymer accepts electrons from the catalysis of lactate or glucose by the corresponding enzymes lactate oxidase (LOx) or GOx. This electron transfer results in doping of the OECT polymer channel and thus an increase of the drain current ($I_D$). The drain current increase is proportional to the analyte concentration, in the case of Figure 13.14c glucose sensitivity is demonstrated. To validate the hypothesis of direct electron transfer, cyclic voltammograms of P-90 working electrodes in the presence of GOx were employed, showing oxidation peaks upon addition of glucose in air-equilibrated and deoxygenated solutions. In ref. 93 it was shown that various concentrations of $H_2O_2$ introduced into the electrolyte produced a lower current modulation compared to that resulting from addition of the analyte. As no mediator was present, direct electron transfer from the enzyme active site to the channel electrode is presumed.

### 13.3.3 Immunosensors and DNA Sensors

Immunosensors are based on the integration of antibodies, DNA, aptamers or even whole cells as biorecognition elements with electronic transducers. The realization of immunosensors is important for the detection of various diseases, such as viral and bacterial infections, sensing of genes that are responsible for inherited diseases, or sensing of biomarkers for the detection of cancer. Traditionally, immunosensing was performed through immunoassays that indirectly measured antigens. This was mainly carried out through an enzymatic reaction using enzymes attached to antibodies, or through antibodies tagged with fluorescent dyes. In contrast to optical sensors or immunoassays, electrochemical sensors provide label-free detection. This means that the analyte of interest does not necessitate tagging with a fluorescent dye or attachment of enzymes to antibodies, thus reducing steps and complexity. Electrochemical sensors function based on biochemical interactions or reactions that cause a change in voltage, current or impedance, and result in an electronic signal which is proportional to the analyte concentration. For example, the binding between antibody and antigen in the vicinity of an electrode causes fluctuation of charge due to the

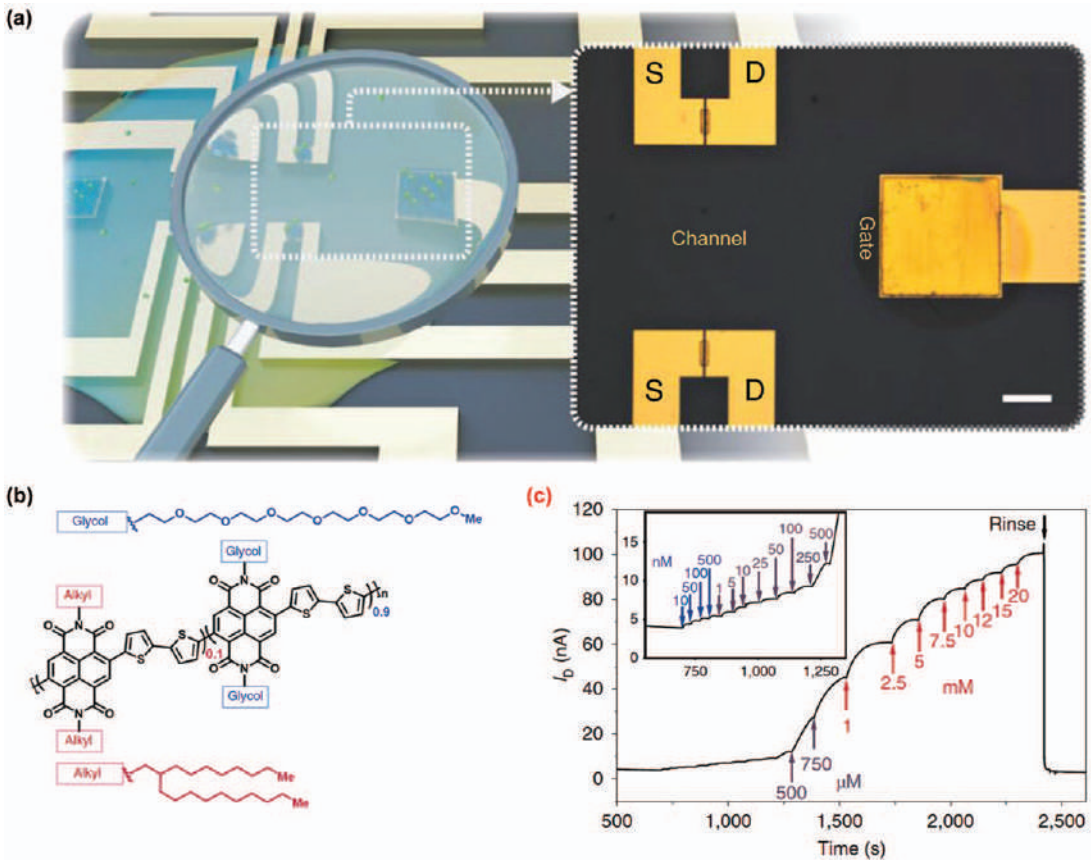


**Figure 13.14** N-type OECT-based glucose sensor. (a) Illustration of the OECT with n-type gate and channel. (b) Chemical structure of the n-type polymer. (c) Calibration curves of glucose addition at various concentrations, the inset displays low concentrations of glucose not visible on the larger scale.
Adapted from ref. 94 with permission from Springer Nature, Copyright 2019.

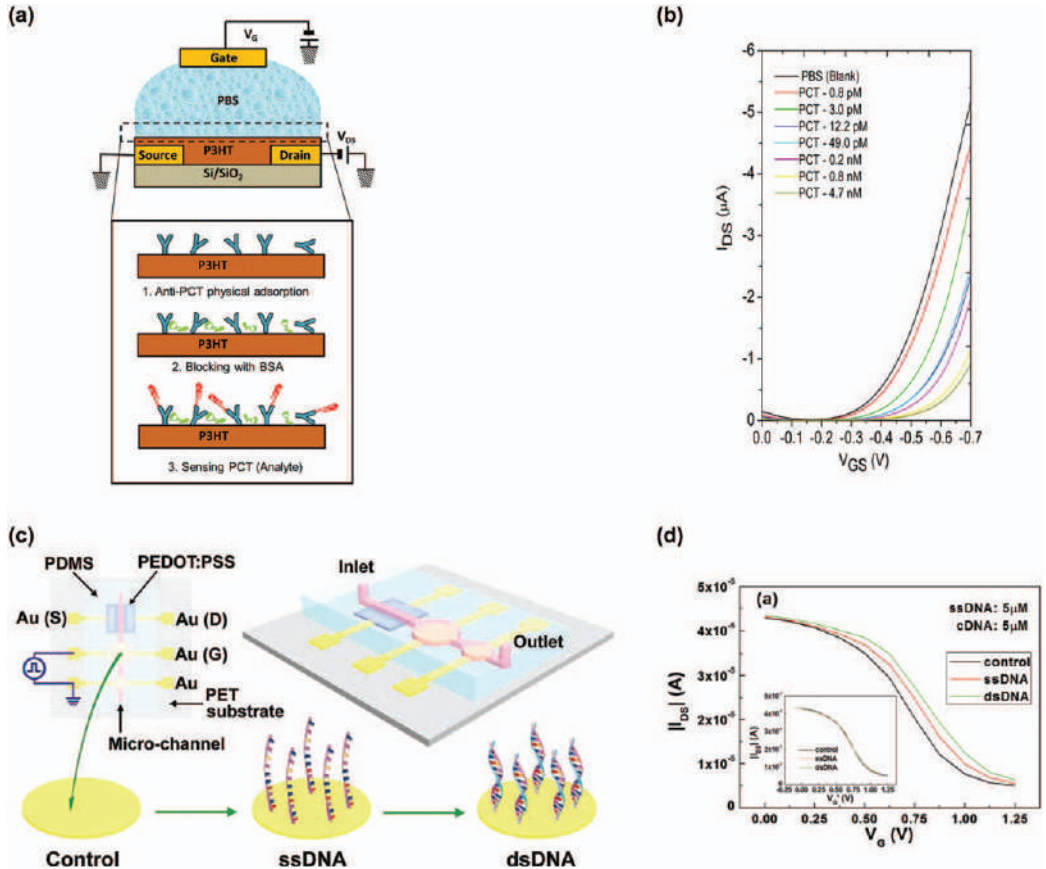
(a)
Gate
PBS
Source
P3HT
Drain
Si/SiO2
1. Anti-PCT physical adsorption
2. Blocking with BSA
3. Sensing PCT (Analyte)
(b)
PBS (Blank)
PCT - 0.8 pM
PCT - 3.0 pM
PCT - 12.2 pM
PCT - 49.0 pM
PCT - 0.2 nM
PCT - 0.8 nM
PCT - 4.7 nM
IDS (μA)
VGS (V)
(c)
PDMS
PEDOT:PSS
Au (S)
Au (D)
Au (G)
Au
PET substrate
Micro-channel
Inlet
Outlet
Control
ssDNA
dsDNA
(d)
(a)
ssDNA: 5μM
cDNA: 5μM
control
ssDNA
dsDNA
|IDS| (A)
VG (V)

net charge that exists on the surface of the proteins. This event brings about changes in the capacitance of the electrode. Production of recombinant antibodies provides the opportunity for highly diverse antibody-based sensors for the detection of different diseases.[95] As was the case for enzymatic sensors, the realization of highly sensitive and efficient immunosensors, DNA sensors and small-molecule sensors depends on the integration of the biorecognition element as close as possible to the transducer.

CPs have been used extensively for electrochemical immunosensors and DNA sensors because they offer advantages similar to those previously mentioned, including high surface area, which does not limit the amount of immobilized recognition element. The biorecognition elements can also be immobilized through adsorption, covalent attachment or entrapment during electrodeposition. Immunosensor operation is based on modification of the CP oxidation state due to affinity reactions, which are then translated to changes in current or voltage output.[96–100] EGOFETS have been reported to be highly sensitive when sensing small concentrations of antigens. An advantage of this type of transistor results from the fact that the biorecognition element can be immobilized on the gate as well as the channel (Figure 13.15a, in this case the antibody is immobilized at the channel).[101] The gate material can be a metal, such as gold, or a conducting polymer. When operating an EGOFET, a negative gate bias attracts positive ions from the bulk electrolyte to the gate interface, and negative ions accumulate at the solution channel interface. This results in an accumulation of positive charges (vacancy of electrons) at the conducting polymer channel side of the interface. If a voltage is applied between the source and drain, the charges at the interface can move freely.[102] A gate threshold voltage exists, at which the transistor switches from ''OFF'' (no channel current) to ''ON'' (where current is observed). When the transistor gate is functionalized with antibodies, this threshold voltage shifts to more negative values, as a result of the fixed charge on the antibodies. This results in a higher voltage (effective gate voltage) needed to turn the transistor to the ON state (Figure 13.15b). In the same way, when the antigen, in this example case procalcitonin (PCT), binds to the antibody, the localized charge either attracts positive ions or repels them, again shifting the effective gate voltage and thus the threshold voltage.

**Figure 13.15** (a) Schematic of an EGOFET-based immunosensor for the detection of procalcitonin antigen. Here the immobilization of antibodies occurs at the P3HT CP channel. (b) The effective gate voltage changes when biomolecules bind to the channel, shifting the threshold voltage and characteristic curves. Reproduced from ref. 101 with permission from Elsevier, Copyright 2018. (c) An OECT integrated with microfluidics for the detection of complementary DNA. Single-stranded DNA is immobilized on the Au gate electrode. (d) Shifts in the effective gate voltage, seen through the transfer characteristics of an OECT, result from the detection of complementary DNA by immobilized single-stranded DNA. Reproduced from ref. 103 with permission from John Wiley and Sons, © 2011 Wiley-VCH Verlag GmbH & Co. KGaA, Weinheim.

An example of this shift may be observed in Figure 13.15b, proportional to the concentration of the antigen. In an analogous way, OECTs have been used to monitor DNA hybridization.[103] Single-stranded DNA was immobilized on an Au gate, while PEDOT:PSS was used as an active channel material (Figure 13.15c). Like EGOFETs, addition of the analyte shifts the effective gate voltage, which is proportional to the DNA concentration. Unlike EGOFETs, OECTs typically operate in depletion mode, meaning that the channel is initially in a highly conductive state. This means that if a positive voltage is applied to the gate, positive ions are injected into the channel and compensate the $PSS^-$ anions. In order for charge conservation to be maintained in the channel, a positive hole is extracted from PEDOT, reducing the conductivity. Therefore, when complementary single-stranded DNA binds to the immobilized DNA, the effective gate voltage shifts to higher values (Figure 13.15d). This shift is proportional to the concentration of DNA.

### 13.3.4 Conclusions and Future Outlook

Conducting polymers and redox polymers offer a wide variety of advantages for the development of electrochemical biosensors. Here we have investigated some of the polymers, processes, operating principles and new devices that are currently used for electrochemical biosensors. As a result of the redox activity and mixed electronic/ionic conductivity, CPs operating in solution can be used as effective transducers. Simple fabrication techniques, such as printing, solution processing, vapor deposition and electrodeposition, allow for the development of low-cost sensors. A variety of immobilization techniques such as adsorption, covalent immobilization and entrapment through electropolymerization, allow for intimate coupling between the biorecognition element and the CP transducers. Doped CPs allow for the realization of transistor-based highly sensitive biosensors. As a future perspective, the goal of continuous monitoring devices that can be integrated with the human body is of importance. From a device perspective two main parameters—stability and biocompatibility—need to be improved. Newly synthesized polymers with long-term stability and biocompatibility will be valuable for developing electrode and organic transistor devices.

## 13.4 Polymers in Bioelectric Drug Delivery

Local drug delivery has been an active area of research and development in the field of polymer bioelectronics. The combination of traditional electronics and polymers presents unique opportunities to have precise control over drug release. This work is motivated by the desire to improve efficacy and reduce side effects for a variety of health problems, ranging from chronic pain to cancer and epilepsy. For instance, local release of drugs, only at the site where they are needed, can avoid side effects that come from off-target drug interactions during systemic drug delivery. Local release thus provides the possibility for delivery of higher concentrations of drugs and/or a wider range of

highly effective drugs than can be delivered systemically. Additionally, and importantly, releasing drugs only when they are needed can increase effectiveness and mitigate long-term habituation. This control over administration allows for drug therapies to maintain a high level of efficacy for longer periods.

A variety of polymer-based bioelectronic devices have been reported for controlled local drug delivery. These systems can be broadly classified into two categories: drug-loaded polymer electrodes (DLPEs) and drug reservoir-containing electrophoretic drug-delivery devices (DREDDDs). These topics, as well as the critical active polymer materials and mechanisms, are described below. It should be noted that there have been also reports of systems with electronically controlled pumps and valves—including intrathecal pumps which currently have clinical use.[104] However, these systems typically do not leverage active polymer materials and therefore will not be discussed in detail here.

### 13.4.1 Drug-loaded Polymer Electrodes

Drug-loaded polymer electrodes offer the benefit of controlled, local drug release. In short, the concept involves an implantable electrode coated with a drug-loaded polymer, which then actively controls the release of drugs from the polymer by applying a potential to the electrode (relative to a secondary electrode). Several material systems and release mechanisms have been investigated, ranging from redox reactions, electrophoresis and electrically controlled volume changes. Commonly used conducting polymers for this application include PPy, PEDOT and PAni.

The primary DLPE design paradigms are highlighted in Figure 13.16.[105] Perhaps the most straightforward approach is loading a conducting polymer film with the charged drug(s) of interest.[106–109] This loading is often carried out during polymerization, with the drug serving as a dopant, counter-ion, or simply an entrapped species. Once the DLPE is implanted in the target tissue, an applied electric potential can drive drugs out of the film on demand, as has been shown for PEDOT-[107,108,110] and PPy-based[106] films. Commonly used drugs include methylene blue, oleanolic acid and dexamethasone. A variety of applied potential schemes have been demonstrated, including cyclic voltammetry and biphasic current pulses. The quantity of drug that can be loaded scales with the film thickness as well as the size and charge of the drug. However, the loading capacity can be limiting in standard drug-loaded polymer films as many therapeutic targets require relatively high concentrations to be effective.

The drug-loading capacity of conducting polymer films can be significantly increased by nano- and micro-scale structuring of the films to effectively increase their surface area[111–113] (Figure 13.16b). Such structuring also affects the release kinetics as drugs may be more readily released from a film with higher porosity. While this may allow for a higher rate of active drug release, it can also increase the rate of passive drug release, which may or may not be desirable. Film structuring has been achieved by forming drug-loaded conducting polymer film around microbeads as well as electrospun fibers. Once the film is formed, the microbeads or fibers are selectively dissolved or

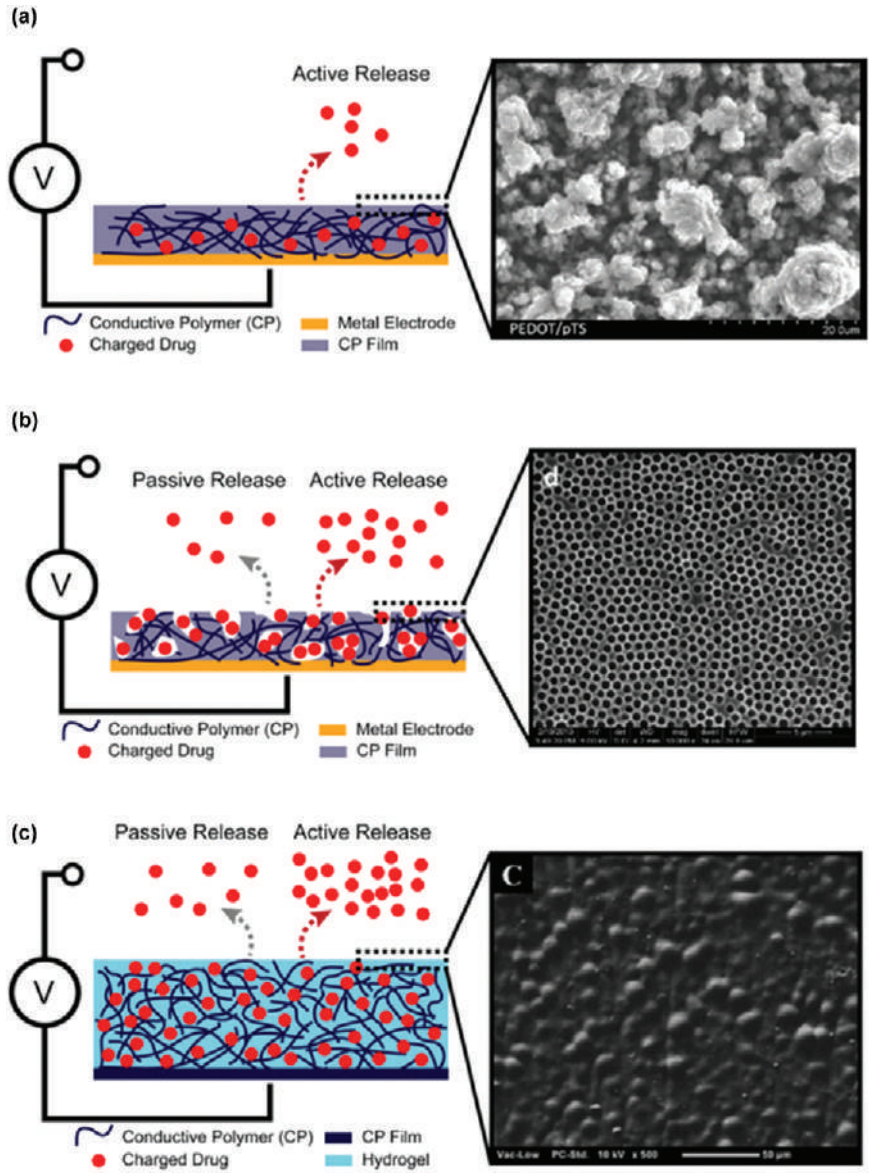


**Figure 13.16** Common drug-loaded polymer electrode designs, including (a) charged drugs imbedded in CP films, (b) nano- or micro-structured DLPEs and (c) a CP hydrogel matrix with charged drugs.
Adapted from ref. 105 with permission from AIP Publishing, Copyright 2020.

degraded, leaving behind voids in the polymer. A bilayer method of alternating structured and unstructured layers has also been reported in an effort to reduce the fast rate of drug elution in microstructured films.[114]

A third approach to DLPEs is to mix a drug, CP and a hydrogel matrix[115,116] (Figure 13.16c). The conducting polymer can be mixed directly into the hydrogel before it is cross-linked or it may be polymerized within the hydrogel. The drug release can be controlled by electrostatic repulsion due to an applied potential as in other DLPEs. Alternatively, drug release can be controlled by electric field-induced volumetric changes in hydrogel DLPEs. Hydrogel DLPEs offer the advantage of a high drug-loading capacity, as drugs can be readily loaded into the hydrogel matrix. The high water content of the hydrogel also facilitates relatively fast diffusion of drugs, which in turn leads to a high rate of both passive and active drug delivery.

### 13.4.2 Drug Reservoir-containing Electrophoretic Drug-delivery Devices

Drug reservoir-containing electrophoretic drug-delivery devices have attracted much interest in recent years. As the name suggests, DREDDDs have a reservoir containing charged drugs in solution and the release of these drugs is controlled by an applied electric field. The applied field electrophoretically drives drugs across a polymeric membrane from the reservoir to the target tissue. The rate of drug delivery can be controlled by tuning the strength of the applied electric field as well as the concentration of drug in the reservoir. The incorporation of a drug reservoir allows for one to reload or exchange the drug solution *in situ*. Thus, DREDDDs are ideally suited for cases where long-term delivery of drugs and/or the ability to change the drug(s) during treatment is desirable.

DREDDDs encompass devices such as organic electronic ion pumps[117–123] (OEIPs) and microfluidic ion pumps[124–127] (uFIPs), as well as iontophoresis devices[128–130] (Figure 13.17). The exact design and formulation of these devices varies; however, they share some fundamental features. DREDDDs have a drug reservoir that is in direct contact with a polymer membrane. This membrane acts as a bridge material between the reservoir and the target tissue. DREDDDs are typically two-terminal devices with a source electrode in contact with the drug reservoir and a target electrode on the other side of the polymeric membrane. The target electrode must be in contact with the target tissue and/or electrolyte/bodily fluid that is in contact with the tissue of interest. This target electrode may be integrated into the device, creating an independent implantable or wearable device, or the target electrode may be physically independent. DREDDDs are typically driven by an external power source that can set either a current or potential to drive an ionic flux between the source and target electrodes.

The structural differences between the different types of DREDDDs can be seen in Figure 13.17, in which examples of OEIPs, uFIPs and iontophoresis devices are highlighted. OEIPs typically have a lateral structure with drug transport from the drug reservoir to the target tissue on mm to cm length scales. This structure has shown potential to be a highly effective approach for applications including pain management,[123] studying chemical effects in

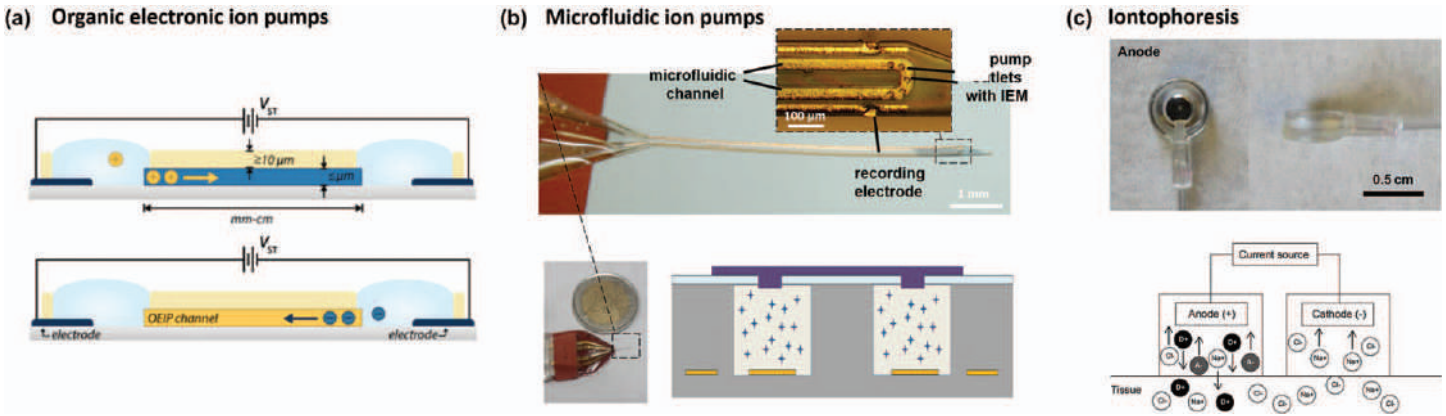


**Figure 13.17** Drug reservoir electrophoretic drug-delivery devices. (a) Cross-sectional schematic of the organic electronic ion pump, a device that has been implanted in the spinal column of rats.[123,131] Adapted from ref. 131 with permission from John Wiley and Sons, © 2018 The Authors. Published by Wiley-VCH Verlag GmbH & Co. KGaA, Weinheim. (b) The microfluidic ion pump design, with a photograph of a device for deep-brain therapy in rodent models. Adapted from ref. 125 with permission from AAAS, © The Authors, some rights reserved; exclusive licensee American Association for the Advancement of Science. Distributed under a CC BY-NC License 4.0 http://creativecommons.org/licenses/by-nc/4.0/ Copyright 2018. (c) Picture and schematic of an implantable iontophoresis device. Adapted from ref. 130 with permission from Elsevier, Copyright 2015.

brain tissue slices,[118,132] and interfacing with cochlear nerves.[119] The OEIP concept has also been incorporated into capillary fiber-like structures to deliver chemicals to plant tissues.[120,133] The uFIP structure differs from OEIPs in that it has a microfluidic channel that serves the dual purpose of acting as the drug reservoir and transporting drugs along the length of the device.[124] These devices have a vertical transport direction as shown in the cross-sectional structure of Figure 13.17b. Using integrated microfluidics can accelerate the chemical transport as the drugs can be transported through convection up to the delivery outlet. At this point the drugs need only be electrophoretically driven through some microns of a polymer membrane to reach the target tissue. The uFIP design has been incorporated into electrocorticography devices allowing for drug delivery to be coupled with real-time sensing of neuronal activity on the surface of the brain.[126] uFIPs have also been engineered to create depth probes for deep-brain therapy, showing evidence of the potential for seizure control.[125,127] While OEIPs and uFIPs are relatively new developments, the concept of iontophoresis and iontophoretic devices is more than a century old.[134] Iontophoresis devices have primarily focused on drug delivery through the skin; however, there are also numerous reports of intraocular delivery as well as iontophoresis devices targeting nondermatological cancers.[129,130]

The primary difference between iontophoresis and OEIPs concerns the polymeric membrane through which drugs are electrophoretically transported. A standard approach for iontophoresis devices is the use of a cellulose-based membrane. Cellulose membranes are well known for their biocompatibility and have been used extensively in microdialysis applications. They offer the benefit of tunable porosity, allowing for size selection of chemical species. Cellulose membranes could, in theory, transport a range of chemicals from the single atomic level (*i.e.*, $Na^+$) to proteins and strips of genetic materials, which can be over 100 kDa. Iontophoresis with cellulose membranes may also allow for electro-osmotic effects, further enhancing the flux of drug delivery.

In contrast, the OEIP employs a polymeric ion exchange membrane (IEM) to selectively transport chemicals according to the ionic charge. The IEM may be either a polyanion or polycation. Polyanions have fixed anionic groups with cationic counterions, thereby allowing for selective transport of cations when an external electric field is applied. Conversely, polycations selectively transport anions. It should be noted that ion-selective transport is only possible if the drug source concentration is significantly less than the fixed-ion concentration in the IEM.[135] Examples of IEM materials that have been used in OEIPs to date are shown in Figure 13.18. The advantage of drug transport with an IEM lies in the selectivity of these membranes, which prevents the back-flow of ions from the target tissue *into* the source drug reservoir. The benefit of this property is the minimization of disturbance to the surrounding tissue (as native salts are not extracted). Ion-selective transport also allows for more drug to be delivered per unit of electrode capacitance, as the back-flow of ions can otherwise account for a significant portion of the ionic current between source and target electrodes. The

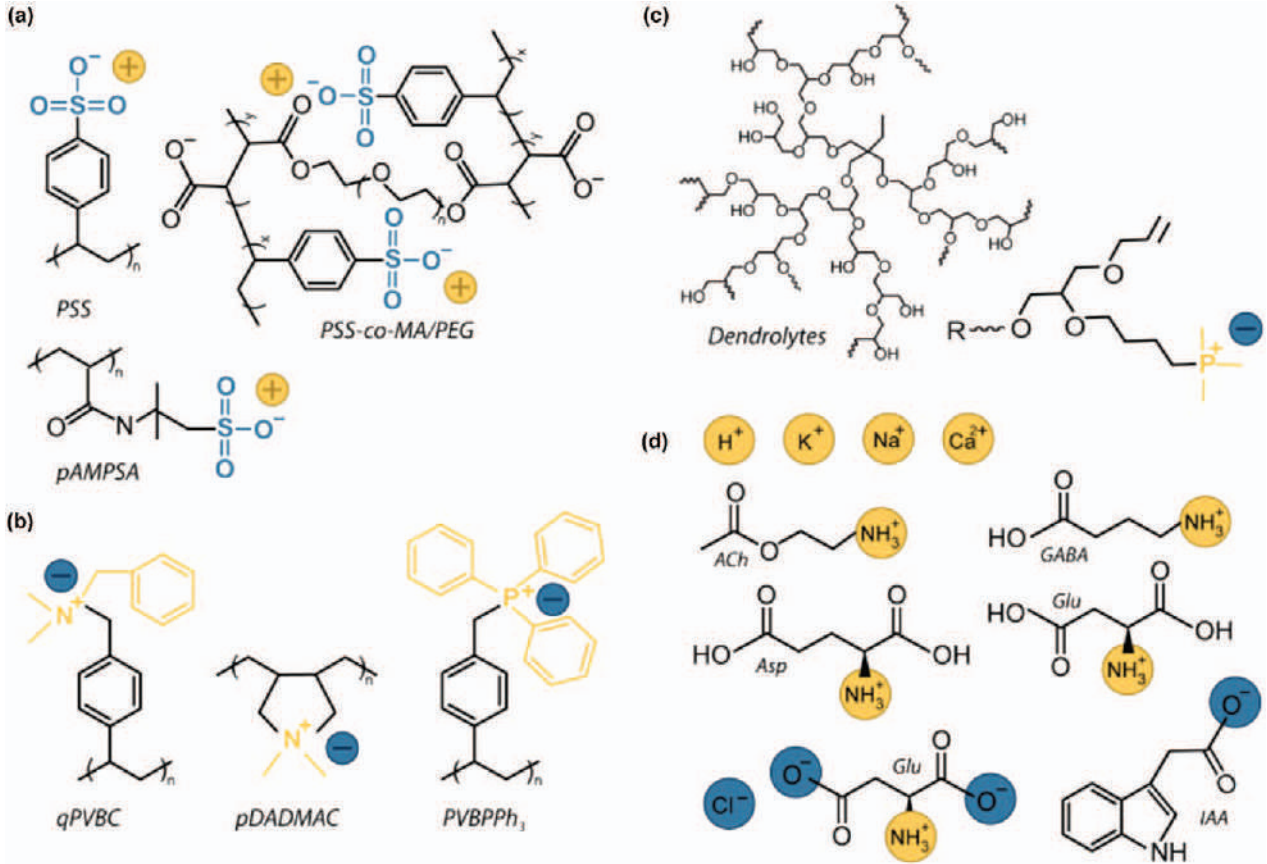


**Figure 13.18** Chemical structure of commonly used polyanions (a) and polycations (b) as well as dendrimer-based polycations (c) and (d) commonly used ionic drugs that have been used in DREDDDs.
Adapted from ref. 131 with permission from John Wiley and Sons, © 2018 The Authors. Published by Wiley-VCH Verlag GmbH & Co. KGaA, Weinheim.

downside of using an IEM for drug transport is the inherent size limitation of drugs that can be transported. IEMs typically only allow for transport of small ions, less than 300 Da, such as $Na^+$, $Ca^{2+}$, acetylcholine and gamma aminobutyric acid (Figure 13.18d). The recent development of IEMs capable of selectively transporting aromatic compounds has expanded the library of deliverable chemicals to include substances such as auxin and dopamine. It remains to be seen if it is possible to design polymer membranes that can allow for ion-selective transport of larger compounds.

A final material consideration for DREDDDs concerns the electrodes themselves. For implantable applications in animal models or for clinical use, only polarizable electrodes may be used. This results from toxicity concerns, which exclude the use of any known faradaic electrodes such as Ag/AgCl. Consequently, DREDDDs can be considered capacitive devices with maximum drug-delivery rate coupled to the electrode capacitance. CP coatings such as PEDOT:PSS have been employed in DREDDDs, particularly OEIPs and uFIPs, to significantly increase the electrode capacitance and therefore increase the capacity to deliver drugs. Similar materials have also been employed to engineer ionic circuitry in order to overcome the limit of electrode capacity.[136]

## References

1. N. Casado, G. Hernández, H. Sardon and D. Mecerreyes, Current trends in redox polymers for energy and medicine, *Prog. Polym. Sci.*, 2016, **52**, 107–135.
2. J. L. Bredas and G. B. Street, Polarons, Bipolarons, and Solitons in Conducting Polymers, *Acc. Chem. Res.*, 1985, **18**, 309–315.
3. B. Wei, J. Liu, L. Ouyang, C. C. Kuo and D. C. Martin, Significant Enhancement of PEDOT Thin Film Adhesion to Inorganic Solid Substrates with EDOT-Acid, *ACS Appl. Mater. Interfaces*, 2015, **7**, 15388–15394.
4. H. Shirakawa, T. Ito, S. I.-D. M. Chemie 1978, undefined. Electrical properties of polyacetylene with various cis-trans compositions. Wiley Online Libr.
5. D. M. De Leeuw, M. M. J. Simenon, A. R. Brown and R. E. F. Einerhand, Stability of n-type doped conducting polymers and consequences for polymeric microelectronic devices, *Synth. Met.*, 1997, **87**, 53–59.
6. M. J. Donahue, *et al.*, Tailoring PEDOT properties for applications in bioelectronics, *Mater. Sci. Eng. R: Rep.*, 2020, **140**, 100546.
7. A. I. Melato, M. H. Mendonça and L. M. Abrantes, Effect of the electropolymerisation conditions on the electrochemical, morphological and structural properties of PEDOTh films, *J. Solid State Electrochem.*, 2009, **13**, 417–426.
8. Y. H. Ha, *et al.*, Towards a transparent, highly conductive poly (3,4-ethylenedioxythiophene), *Adv. Funct. Mater.*, 2004, **14**, 615–622.
9. L. Zhang, M. Fairbanks and T. L. Andrew, Rugged Textile Electrodes for Wearable Devices Obtained by Vapor Coating Off-the-Shelf, Plain-Woven Fabrics, *Adv. Funct. Mater.*, 2017, **27**, 1–9.

10. A. Gilletti and J. Muthuswamy, Brain micromotion around implants in the rodent somatosensory cortex, *J. Neural Eng.*, 2006, **3**, 189–195.
11. A. B.-F. Applications 2001, undefined. Electrochemical Methods. ci.nii.ac.jp.
12. Basics of EIS: Electrochemical Research-Impedance. https://www.gamry.com/application-notes/EIS/basics-of-electrochemical-impedance-spectroscopy/.
13. S. F. Cogan, Neural Stimulation and Recording Electrodes, *Annu. Rev. Biomed. Eng.*, 2008, **10**, 275–309.
14. J. Rivnay, H. Wang, L. Fenno, K. Deisseroth and G. G. Malliaras, Next-generation probes, particles, and proteins for neural interfacing, *Sci. Adv.*, 2017, **3**, e1601649.
15. S. J. Wilks, S. Richardson-burns and J. L. Hendricks Neural Interface Material for Electrostimulation material for electrostimulation, 2017, **2**, 1–8.
16. X. T. Cui and D. D. Zhou, Poly (3,4-ethylenedioxythiophene) for chronic neural stimulation, *IEEE Trans. Neural Syst. Rehabil. Eng.*, 2007, **15**, 502–508.
17. J. Rivnay, *et al.*, Structural control of mixed ionic and electronic transport in conducting polymers, *Nat. Commun.*, 2016, **7**, 1–9.
18. C. M. Proctor, J. Rivnay and G. G. Malliaras, Understanding volumetric capacitance in conducting polymers, *J. Polym. Sci., Part B: Polym. Phys.*, 2016, **54**, 1433–1436.
19. A. V. Volkov, *et al.*, Understanding the Capacitance of PEDOT:PSS, *Adv. Funct. Mater.*, 2017, **27**, 1700329.
20. L. G.-B. T. I. delle Scienze undefined. D viribus electricitatis in motu musculari: Commentarius. adsabs.harvard.edu, **4**, 1791; 58, p. 1791.
21. E. D. Adrian and D. W. Bronk, The discharge of impulses in motor nerve fibres, *J. Physiol.*, 1929, **67**, 9–151.
22. L. R. Hochberg, *et al.*, Neuronal ensemble control of prosthetic devices by a human with tetraplegia, *Nature*, 2006, **442**, 164–171.
23. M. F. El-Chami, F. M. Merchant and A. R. Leon, Leadless Pacemakers, *Am. J. Cardiol.*, 2017, **vol. 119**, 145–148.
24. G. E. Burch and N. P. DePasquale, *A History of Electrocardiography*, Novato, Norman Publishing, 1990.
25. A. L. Hodgkin and A. F. Huxley, The components of membrane conductance in the giant axon of Loligo, *J. Physiol.*, 1952, **116**, 473–496.
26. A. L. Hodgkin and A. F. Huxley, A quantitative description of membrane current and its application to conduction and excitation in nerve, *J. Physiol.*, 1952, **117**, 500–544.
27. A. L. Hodgkin, A. F. Huxley and B. Katz, Measurement of current-voltage relations in the membrane of the giant axon of Loligo, *J. Physiol.*, 1952, **116**, 424–448.
28. D. H. Hubel and T. N. Wiesel, Receptive fields of single neurones in the cat's striate cortex, *J. Physiol.*, 1959, **148**, 574–591.

29. W. Einthoven, Ein neues Galvanometer, *Ann. Phys.*, 1903, **317**, 1059–1071.
30. X. Cui, *et al.*, Surface modification of neural recording electrodes with conducting polymer/biomolecule blends, *J. Biomed. Mater. Res.*, 2001, **56**, 261–272.
31. X. Cui and D. C. Martin, Electrochemical deposition and characterization of poly (3, 4-ethylenedioxythiophene) on neural microelectrode arrays, *Sens. Actuators, B*, 2003, **89**, 92–102.
32. K. A. Ludwig, *et al.*, Poly(3,4-ethylenedioxythiophene) (PEDOT) polymer coatings facilitate smaller neural recording electrodes, *J. Neural Eng.*, 2011, **8**, 014001.
33. L. Kergoat, B. Piro, M. Berggren, G. Horowitz and M. C. Pham, Advances in organic transistor-based biosensors: From organic electrochemical transistors to electrolyte-gated organic field-effect transistors, *Anal. Bioanal. Chem.*, 2012, **vol. 402**, 1813–1826.
34. E. Macchia, *et al.*, About the amplification factors in organic bioelectronic sensors, *Mater. Horizons*, 2020, DOI: 10.1039/c9mh01544b.
35. G. Palazzo, *et al.*, Detection beyond Debye's length with an electrolyte-gated organic field-effect transistor, *Adv. Mater.*, 2015, **27**, 911–916.
36. T. Cramer, A. Kyndiah, M. Murgia, F. Leonardi, S. Casalini and F. Biscarini, 2012, undefined. Double layer capacitance measured by organic field effect transistor operated in water. aip.scitation.org.
37. J. Rivnay, *et al.*, High-performance transistors for bioelectronics through tuning of channel thickness, *Sci. Adv.*, 2015, **1**, 1–5.
38. D. A. Bernards and G. G. Malliaras, Steady-State and Transient Behavior of Organic Electrochemical Transistors, *Adv. Funct. Mater.*, 2007, **17**, 3538–3544.
39. J. Friedlein, R. McLeod and J. R.-O Electronics, 2018, undefined. Device physics of organic electrochemical transistors. Elsevier.
40. G. G. Wallace, S. E. Moulton and G. M. Clark, Electrode-Cellular Interface, *Science*, 2009, **324**, 185–187.
41. P. Leleux, *et al.*, Conducting Polymer Electrodes for Electroencephalography, *Adv. Healthc. Mater*, 2014, **3**, 490–493.
42. S. Takamatsu, *et al.*, Direct patterning of organic conductors on knitted textiles for long-term electrocardiography, *Sci. Rep.*, 2015, **5**, 1–7.
43. E. Bihar, *et al.*, Fully Printed Electrodes on Stretchable Textiles for Long-Term Electrophysiology, *Adv. Mater. Technol.*, 2017, **2**, 1600251.
44. P. Leleux, *et al.*, Organic electrochemical transistors for clinical applications, *Adv. Healthc. Mater.*, 2015, **4**, 142–147.
45. A. Campana, T. Cramer, D. T. Simon, M. Berggren and F. Biscarini, Electrocardiographic recording with conformable organic electrochemical transistor fabricated on resorbable bioscaffold, *Adv. Mater.*, 2014, **26**, 3874–3878.
46. S. Park, *et al.*, Self-powered ultra-flexible electronics via nano-grating-patterned organic photovoltaics, *Nature*, 2018, **vol. 561**, 516–521.

47. A. Zucca, *et al.*, Roll to roll processing of ultraconformable conducting polymer nanosheets, *J. Mater. Chem. C*, 2015, **3**, 6539–6548.
48. E. Bihar, *et al.*, Fully printed all-polymer tattoo/textile electronics for electromyography, *Flex. Print. Electron.*, 2018, **3**, 034004.
49. Y. Jiang, M. Togane, B. Lu and H. Yokoi, sEMG Sensor Using Polypyrrole-Coated Nonwoven Fabric Sheet for Practical Control of Prosthetic Hand, *Front. Neurosci.*, 2017, **11**, 33.
50. A. Mihic, *et al.*, A Conductive Polymer Hydrogel Supports Cell Electrical Signaling and Improves Cardiac Function After Implantation into Myocardial Infarct, *Circulation*, 2015, **132**, 772–784.
51. C. Zhang, *et al.*, A self-doping conductive polymer hydrogel that can restore electrical impulse propagation at myocardial infarct to prevent cardiac arrhythmia and preserve ventricular function, *Biomaterials*, 2020, **231**, 119672.
52. D. Mawad, *et al.*, A Conducting polymer with enhanced electronic stability applied in cardiac models, *Sci. Adv.*, 2016, **2**, e1601007.
53. S. M. Wellman, *et al.*, A Materials Roadmap to Functional Neural Interface Design, *Adv. Funct. Mater.*, 2018, **28**, 1–38.
54. J. S. Foos, Rate Enhancement in Modified Polypyrrole Electrodes, *J. Electrochem. Soc.*, 1986, **133**, 1983.
55. P. M. George, *et al.*, Fabrication and biocompatibility of polypyrrole implants suitable for neural prosthetics, *Biomaterials*, 2005, **26**, 3511–3519.
56. M. Brett Runge, *et al.*, The development of electrically conductive polycaprolactone fumarate-polypyrrole composite materials for nerve regeneration, *Biomaterials*, 2010, **31**, 5916–5926.
57. C. E. Schmidt, V. R. Shastri, J. P. Vacanti and R. Langer, Stimulation of neurite outgrowth using an electrically conducting polymer, *Proc. Natl. Acad. Sci. U. S. A.*, 1997, **94**, 8948–8953.
58. H. Durgam, *et al.*, Novel degradable co-polymers of polypyrrole support cell proliferation and enhance neurite out-growth with electrical stimulation, *J. Biomater. Sci., Polym. Ed.*, 2010, **21**, 1265–1282.
59. H. Xu, *et al.*, Conductive PPY/PDLLA conduit for peripheral nerve regeneration, *Biomaterials*, 2014, **35**, 225–235.
60. S. Wilks, Poly(3,4-ethylene dioxythiophene) (PEDOT) as a micro-neural interface material for electrostimulation, *Front. Neuroeng.*, 2009, **2**, 7.
61. X. Cui, J. F. Hetke, J. A. Wiler, D. J. Anderson and D. C. Martin, Electrochemical deposition and characterization of conducting polymer polypyrrole/PSS on multichannel neural probes, *Sens. Actuat., Phys.*, 2001, **93**, 8–18.
62. R. Green, N. Lovell and L. P.-W. Biomaterials, undefined, Cell attachment functionality of bioactive conducting polymers for neural interfaces, Elsevier, 2009.
63. R. Green, N. Lovell and L. P.-W.-A. biomaterialia, undefined, Impact of co-incorporating laminin peptide dopants and neurotrophic growth factors on conducting polymer properties, Elsevier, 2010.

64. M. Asplund, *et al.*, Toxicity evaluation of PEDOT/biomolecular composites intended for neural communication electrodes, *Biomed. Mater.*, 2009, **4**, 045009.
65. M. Asplund, H. von Holst and O. Inganäs, Composite biomolecule/PEDOT materials for neural electrodes, *Biointerphases*, 2008, **3**, 83–93.
66. S. F. Cogan, K. A. Ludwig, C. G. Welle and P. Takmakov, Tissue damage thresholds during therapeutic electrical stimulation, *J. Neural Eng*, 2016, **13**, 021001.
67. S. Carli, L. Casarin, G. Bergamini, S. Caramori and C. A. Bignozzi, Conductive PEDOT covalently bound to transparent FTO electrodes, *J. Phys. Chem. C*, 2014, **118**, 16782–16790.
68. D. Chhin, *et al.*, Diazonium-based anchoring of PEDOT on Pt/Ir electrodes via diazonium chemistry, *J. Electrochem. Soc.*, 2018, **165**, G3066–G3070.
69. T. D. Y. Kozai, *et al.*, Chronic In Vivo evaluation of PEDOT/CNT for stable neural recordings, *IEEE Trans. Biomed. Eng.*, 2016, **63**, 111–119.
70. R. T. Hassarati, *et al.*, Improving cochlear implant properties through conductive hydrogel coatings, *IEEE Trans. Neural Syst. Rehabil. Eng*, 2014, **22**, 411–418.
71. D. Khodagholy, *et al.*, NeuroGrid: Recording action potentials from the surface of the brain, *Nat. Neurosci.*, 2015, **18**, 310–315.
72. C. L. Kolarcik, *et al.*, Elastomeric and soft conducting microwires for implantable neural interfaces, *Soft Matter*, 2015, **11**, 4847–4861.
73. Z. J. Du, *et al.*, Ultrasoft microwire neural electrodes improve chronic tissue integration, *Acta Biomater.*, 2017, **53**, 46–58.
74. D. Khodagholy, *et al.*, Highly conformable conducting polymer electrodes for in vivo recordings, *Adv. Mater.*, 2011, **23**, 268–272.
75. D. Khodagholy, *et al.*, Organic electronics for high-resolution electrocorticography of the human brain, *Sci. Adv.*, 2016, **2**, e1601027.
76. M. J. Tierney, J. A. Tamada, R. O. Potts, L. Jovanovic and S. Garg, Clinical evaluation of the GlucoWatch® biographer: A continual, non-invasive glucose monitor for patients with diabetes, *Biosens. Bioelectron.*, 2001, **16**, 621–629.
77. M. Senior, Novartis signs up for Google smart lens, *Nat. Biotechnol.*, 2014, **vol. 32**, 856.
78. H. S. White, G. P. Kittlesen and M. S. Wrighton, Chemical Derivatization of an Array of Three Gold Microelectrodes with Polypyrrole: Fabrication of a Molecule-Based Transistor, *J. Am. Chem. Soc.*, 1984, **106**, 5375–5377.
79. M. Nishizawa, T. Matsue and I. Uchida, Fabrication of a pH-sensitive microarray electrode and applicability to biosensors, *Sens. Actuators, B*, 1993, **13**, 53–56.
80. E. W. Paul, A. J. Ricco and M. S. Wrighton, Resistance of polyaniline films as a function of electrochemical potential and the fabrication of polyaniline-based microelectronic devices, *J. Phys. Chem.*, 1985, **89**, 1441–1447.
81. L. C. Clark and E. W. Clark, Differential anodic enzyme polarography for the measurement of glucose, *Adv. Exp. Med. Biol.*, 1973, **37 A**, 127–133.

82. A. Heller, Electrical connection of enzyme redox centers to electrodes, *J. Phys. Chem.*, 1992, **vol. 96**, 3579–3587.
83. J. Michl and A. Heller, ARTIC LES Electrical Wiring of Redox Enzymes Relaying of Electrons in Enzymes, *Acc. Chem. Res.*, 1990, **vol. 23**, 128–134.
84. B. C. Thompson, O. Winther-Jensen, J. Vongsvivut, B. Winther-Jensen and D. R. MacFarlane, Conducting Polymer Enzyme Alloys: Electromaterials Exhibiting Direct Electron Transfer, *Macromol. Rapid Commun.*, 2010, **31**, 1293–1297.
85. O. A. Raitman, E. Katz, A. F. Bückmann and I. Willner, Integration of polyaniline/poly(acrylic acid) films and redox enzymes on electrode supports: An in situ electrochemical/surface plasmon resonance study of the bioelectrocatalyzed oxidation of glucose or lactate in the integrated bioelectrocatalytic system, *J. Am. Chem. Soc.*, 2002, **124**, 6487–6496.
86. P. N. Bartlett and P. R. Birkin, The application of conducting polymers in biosensors, *Synth. Met.*, 1993, **61**, 15–21.
87. E. D. Wills and A. Wormall, Isoelectric points of enzymes as determined by inhibition with suramin, *Nature*, 1950, **165**, 813–814.
88. D. Zhai, *et al.*, Highly sensitive glucose sensor based on pt nanoparticle/polyaniline hydrogel heterostructures, *ACS Nano*, 2013, **7**, 3540–3546.
89. X. Strakosas, *et al.*, A facile biofunctionalisation route for solution processable conducting polymer devices, *J. Mater. Chem. B*, 2014, **2**, 2537–2545.
90. D. Khodagholy, *et al.*, High transconductance organic electrochemical transistors, *Nat. Commun.*, 2013, **4**, 2133.
91. H. Tang, F. Yan, P. Lin, J. Xu and H. L. W. Chan, Highly sensitive glucose biosensors based on organic electrochemical transistors using platinum gate electrodes modified with enzyme and nanomaterials, *Adv. Funct. Mater.*, 2011, **21**, 2264–2272.
92. G. Scheiblin, *et al.*, Screen-printed organic electrochemical transistors for metabolite sensing, *MRS Commun.*, 2015, **5**, 507–511.
93. A.-M. Pappa, *et al.*, Direct metabolite detection with an n-type accumulation mode organic electrochemical transistor, *Sci. Adv.*, 2018, **4**, eaat0911.
94. D. Ohayon, *et al.*, Biofuel powered glucose detection in bodily fluids with an n-type conjugated polymer, *Nat. Mater.*, 2020, **19**, 456–463.
95. B. Hock, Antibodies for immunosensors. A review, *Anal. Chim. Acta*, 1997, **347**, 177–186.
96. G. G. Wallace, M. Smyth and H. Zhao, Conducting electroactive polymer-based biosensors, *TrAC – Trends Anal. Chem.*, 1999, **18**, 245–251.
97. A. Sargent and O. A. Sadik, Monitoring antibody-antigen reactions at conducting polymer-based immunosensors using impedance spectroscopy, *Electrochim. Acta*, 1999, **44**, 4667–4675.
98. O. A. Sadik, Bioaffinity Sensors Based on Conducting Polymers: A Short Review, *Electroanalysis*, 1999, **11**, 839–844.

99. A. Sadik, *et al.*, Pulsed Amperometric Detection of Thaumatin Using Antibody-containing Poly(pyrro1e) Electrodes, *Analyst*, 1994, **vol. 11**, 1997–2000.
100. G. G. Wallace and L. A. P. Kane-Maguire, Manipulating and Monitoring Biomolecular Interactions with Conducting Electroactive Polymers, *Adv. Mater.*, 2002, **14**, 953–960.
101. P. Seshadri, *et al.*, Low-picomolar, label-free procalcitonin analytical detection with an electrolyte-gated organic field-effect transistor based electronic immunosensor, *Biosens. Bioelectron.*, 2018, **104**, 113–119.
102. L. Torsi, M. Magliulo, K. Manoli and G. Palazzo, Organic field-effect transistor sensors: A tutorial review, *Chem. Soc. Rev.*, 2013, **42**, 8612–8628.
103. P. Lin, X. Luo, I. M. Hsing and F. Yan, Organic electrochemical transistors integrated in flexible microfluidic systems and used for label-free DNA sensing, *Adv. Mater.*, 2011, **23**, 4035–4040.
104. Y. N. Wang and L. M. Fu, Micropumps and biomedical applications – A review, *Microelectron. Eng.*, 2018, **195**, 121–138.
105. C. A. R. Chapman, E. A. Cuttaz, J. A. Goding and R. A. Green, Actively controlled local drug delivery using conductive polymer-based devices, *Appl. Phys. Lett.*, 2020, **116**, 010501.
106. R. Wadhwa, C. F. Lagenaur and X. T. Cui, Electrochemically controlled release of dexamethasone from conducting polymer polypyrrole coated electrode, *J. Control. Release*, 2006, **110**, 531–541.
107. C. Boehler, F. Oberueber and M. Asplund, Tuning drug delivery from conducting polymer films for accurately controlled release of charged molecules, *J. Control. Release*, 2019, **304**, 173–180.
108. C. Boehler, *et al.*, Actively controlled release of Dexamethasone from neural microelectrodes in a chronic in vivo study, *Biomaterials*, 2017, **129**, 176–187.
109. K. Krukiewicz, *et al.*, Advancing the delivery of anticancer drugs: Conjugated polymer/triterpenoid composite, *Acta Biomater.*, 2015, **19**, 158–165.
110. J. A. Goding, A. D. Gilmour, P. J. Martens, L. A. Poole-Warren and R. A. Green, Small bioactive molecules as dual functional co-dopants for conducting polymers, *J. Mater. Chem. B*, 2015, **3**, 5058–5069.
111. D. Uppalapati, B. J. Boyd, S. Garg, J. Travas-Sejdic and D. Svirskis, Conducting polymers with defined micro- or nanostructures for drug delivery, *Biomaterials*, 2016, **vol. 111**, 149–162.
112. D. Esrafilzadeh, J. M. Razal, S. E. Moulton, E. M. Stewart and G. G. Wallace, Multifunctional conducting fibres with electrically controlled release of ciprofloxacin, *J. Control. Release*, 2013, **169**, 313–320.
113. M. R. Abidian, D.-H. Kim and D. C. Martin, Conducting-Polymer Nanotubes for Controlled Drug Release, *Adv. Mater.*, 2006, **18**, 405–409.
114. B. Massoumi and A. Entezami, Controlled release of sulfosalicylic acid during electrochemical switching of conducting polymer bilayers, *Eur. Polym. J.*, 2001, **37**, 1015–1020.

115. C. Kleber, K. Lienkamp, J. Rühe and M. Asplund, Electrochemically Controlled Drug Release from a Conducting Polymer Hydrogel (PDMAAp/PEDOT) for Local Therapy and Bioelectronics, *Adv. Healthc. Mater*, 2019, **8**, 1801488.
116. R. A. Green, S. Baek, L. A. Poole-Warren and P. J. Martens, Conducting polymer-hydrogels for medical electrode applications, *Sci. Technol. Adv. Mater.*, 2010, **11**, 014107.
117. J. Isaksson, *et al.*, Electronic control of Ca2 + signalling in neuronal cells using an organic electronic ion pump, *Nat. Mater.*, 2007, **6**, 673–679.
118. A. Williamson, *et al.*, Controlling Epileptiform Activity with Organic Electronic Ion Pumps, *Adv. Mater.*, 2015, **27**, 3138–3144.
119. D. T. Simon, *et al.*, Organic electronics for precise delivery of neurotransmitters to modulate mammalian sensory function, *Nat. Mater.*, 2009, **8**, 742–746.
120. I. Bernacka-Wojcik, *et al.*, Implantable Organic Electronic Ion Pump Enables ABA Hormone Delivery for Control of Stomata in an Intact Tobacco Plant, *Small*, 2019, **15**, 1902189.
121. M. Seitanidou, R. Blomgran, G. Pushpamithran, M. Berggren and D. T. Simon, Modulating Inflammation in Monocytes Using Capillary Fiber Organic Electronic Ion Pumps, *Adv. Healthc. Mater*, 2019, **8**, 1900813.
122. T. Arbring Sjöström, *et al.*, Cross-Linked Polyelectrolyte for Improved Selectivity and Processability of Iontronic Systems, *ACS Appl. Mater. Interfaces*, 2017, **9**, 30247–30252.
123. A. Jonsson, *et al.*, Therapy using implanted organic bioelectronics, *Sci. Adv.*, 2015, **1**, e1500039.
124. I. Uguz, *et al.*, A Microfluidic Ion Pump for In Vivo Drug Delivery, *Adv. Mater.*, 2017, **29**, 1–6.
125. C. M. Proctor, *et al.*, Electrophoretic drug delivery for seizure control, *Sci. Adv.*, 2018, **4**, eaau1291.
126. C. M. Proctor, *et al.*, An Electrocorticography Device with an Integrated Microfluidic Ion Pump for Simultaneous Neural Recording and Electrophoretic Drug Delivery In Vivo, *Adv. Biosyst*, 2019, **3**, 1800270.
127. A. Slezia, C. M. Proctor, A. Kaszas, G. G. Malliaras and A. Williamson, Electrophoretic delivery of γ-aminobutyric acid (GABA) into epileptic focus prevents seizures in mice, *J. Vis. Exp*, 2019, e59268.
128. G. B. Kasting, Theoretical models for iontophoretic delivery, *Adv. Drug Deliv. Rev*, 1992, **9**, 177–199.
129. J. Byrne, J. Yeh and J. D.-J. Release, undefined. Use of iontophoresis for the treatment of cancer, Elsevier, 2018.
130. J. D. Byrne, *et al.*, Local iontophoretic administration of cytotoxic therapies to solid tumors, *Sci. Transl. Med.*, 2015, **7**, 273ra14.
131. T. Arbring Sjöström, *et al.*, A Decade of Iontronic Delivery Devices, *Adv. Mater. Technol*, 2018, **3**, 1700360.

132. A. Jonsson, *et al.*, Bioelectronic neural pixel: Chemical stimulation and electrical sensing at the same site, *Proc. Natl. Acad. Sci. U. S. A.*, 2016, **113**, 9440–9445.
133. D. J. Poxson, *et al.*, Regulating plant physiology with organic electronics, *Proc. Natl. Acad. Sci. U. S. A.*, 2017, **114**, 4597–4602.
134. J. B. Sloan and K. Soltani, Iontophoresis in dermatology: A review, *J. Am. Acad. Dermatol.*, 1986, **15**, 671–684.
135. Y. Tanaka and I. M.-S. Series, undefined. Fundamentals and Applications, 2007.
136. E. O. Gabrielsson, P. Janson, K. Tybrandt, D. T. Simon and M. Berggren, A Four-Diode Full-Wave Ionic Current Rectifier Based on Bipolar Membranes: Overcoming the Limit of Electrode Capacity, *Adv. Mater.*, 2014, **26**, 5143–5147.

# *Subject Index*